Studies on Functionalised Macrocyclic Ligands

Lorenzo Tei

Thesis submitted to the University of Nottingham
for the degree of Doctor of Philosophy, June, 2001

To Elisabetta

Acknowledgements

First and foremost, I would like to thank my supervisor, Professor Martin Schröder, for the opportunity he has given me to work at the University of Nottingham and for his enduring guidance and advice throughout the course of my PhD. Furthermore, I would like to express my thanks to Dr. Alexander Blake (Sandy) either for his invaluable assistance with the X-ray crystal structures presented in this thesis and for his help and comments to every chapter of this work. Last but not least, I am also very grateful for all the support Sandy has given me correcting all the mistakes I could not avoid in a language that is not my own mother tongue.

Many people have contributed and assisted the work of this thesis in a way or another. I would like to acknowledge Dr. Andrea Bencini and Dr. Barbara Valtancoli from the University of Florence for the potentiometry measurements they carried out with the two [15]aneN_3O_2 derivatives which have been very useful in completing the work with those ligands. I am also grateful to Dr. Claire Wilson who helped me with some very complicated X-ray crystal structures and to Dr. Julia Weinstein and Dr. Mike George for the luminescence measurements reported in Chapter 5.

The time I spent in the laboratory would not have been so pleasant without many of past and present members of the Schröder group. Among all lab-mates I have collected during the years in Nottingham I would like to offer my special thanks to Dan Doble and Richard Kay for the very stimulating and valuable discussions about lanthanide chemistry. During these three years the homesickness has been alleviated by the presence of many Italians among which Vito Lippolis, Michele Galatola and Francesca Morale who made me feel more at home. In particular, Francesca kept my Italian language in good shape by talking to me almost every day even against Martin's dispositions. A special mention for keeping the time spent in the laboratory very enjoyable goes to Simon Chung, Doug Spencer, Alex Mackrell, and Mark Glenny.

I am also grateful to the technical, analytical and administrative staff of the School of Chemistry in particular to Meryl Richardson, Bob Fleming and Shaz Aslam. Finally, I would like to thank the Universities of Nottingham and Florence for their financial support.

Chapter 1: INTRODUCTION TO MACROCYCLIC CHEMISTRY

Chapter 2: LANTHANIDES AND MEDICINAL CHEMISTRY

Chapter 3: LANTHANIDE COMPLEXES OF IMINO-CARBOXYLATE DERIVATIVES OF [9]aneN_3

Chapter 5: LANTHANIDE COMPLEXES OF ASYMMETRIC DERIVATIVES OF [9]aneN_3

Chapter 8: MACROCYCLIC LIGANDS FOR THE SYNTHESIS OF POLYMERIC Ag^I COMPLEXES

Abstract

The work presented in this thesis hinges on three main topics: a) the co-ordination chemistry of symmetric and asymmetric derivatives of [9]aneN$_3$ towards lanthanide ions; b) the transition metal co-ordination chemistry of nitrile and amino derivatives of [9]aneN$_3$ and [15]aneN$_3$O$_2$; c) the use of macrocyclic ligands for the synthesis of polymeric Ag^{I} complexes.

Chapter 3 describes the Ln^{III} complexes of the ligand obtained by Schiff-base condensation of 1,4,7-*tris*(2-aminoethyl)-1,4,7-triazacyclononane (L) with three molar equivalents of sodium pyruvate using the Ln^{III} ion as templating agent. The mononuclear complexes [Ln(L^{a})] (Ln^{III} = Y^{III}, Sm^{III}, Gd^{III}, Dy^{III}, Eu^{III}, Yb^{III}, La^{III}) have been prepared and characterised, and in most cases the crystal structure has also been determined. NMR spectroscopic studies on the diamagnetic [Y(L^{a})] and [La(L^{a})] complexes and on paramagnetic [Yb(L^{a})] and [Sm(L^{a})] complexes have been carried out. Variable temperature ^{1}H NMR behaviour of the [Y(L^{a})] and [Yb(L^{a})] complexes has also been investigated. Hydrolysis experiments on the [La(L^{a})] complex in D_2O at neutral and acidic pH have been performed in order to determine the stability of such a complex in *in vivo* conditions. Moreover, lanthanide properties such as relaxivity of the Gd^{III} complex and Dysprosium Induced Shift (DIS) have been determined in order to obtain information either about the efficiency as contrast agent of the Gd^{III} complex and the number of water molecules bound to the metal centre.

After the study on the nine co-ordinate complexes [Ln(L^{a})] discussed in Chapter 3, Chapter 4 reports the Ln^{III} complexes obtained by changing the ketone employed for the Schiff-base condensation with the triamine L. Two different acetylphosphonate monoesters have been used in order to form novel nine co-ordinate Ln^{III} complexes: the synthesis of [Ln(L^{b})] (Ln^{III} = Y^{III}, Gd^{III}, Yb^{III}, La^{III}) and [Ln(L^{c})] (Ln^{III} = Y^{III}, Gd^{III}, Eu^{III}) complexes has been achieved by Schiff-base condensation of the triamine (L) with methyl sodium acetyl phosphonate and methoxybenzyl sodium acetyl phosphonate, respectively, using the Ln^{III} ion as templating agent. These Ln^{III} complexes have been studied again by X-ray crystallography and NMR spectroscopy. Since the nine co-ordinate lanthanide complexes such as [Ln(L^{b})] and [Ln(L^{c})] contain three chiral phosphorus centres, four possible diastereomers, each of them with two enantiomers, could

be distinguished and NMR spectroscopic studies have been carried out in order to determine the four different diastereomers present in solution. As in Chapter 3, hydrolysis experiments on the Y^{III} complexes with L^b and L^c and relaxivity of the Gd^{III} complexes have been determined.

The ligands discussed in Chapter 5 have been synthesised in order to provide a set of seven or eight donor atoms for the co-ordination of lanthanide ions, leaving one or two co-ordination sites available for the binding of water molecules. Therefore, 4,7-*bis*(2-aminoethyl)-1,4,7-triazacyclononane (L^2), 1-(carboxymethyl)-4,7-*bis*(2-aminoethyl)-1,4,7-triazacyclononane (HL^3) and 1-(2-hydroxyethyl)-4,7-*bis*(2-aminoethyl)-1,4,7-triazacyclononane (HL^4) have been synthesised and then reacted with two equivalents of sodium pyruvate, methyl sodium acetyl phosphonate or methoxybenzyl sodium acetyl phosphonate using the Ln^{III} ion as templating agent. A large number of lanthanide complexes with formulations $[Ln(L^{2a})(CH_3CO_2)]$, $[Ln(L^{2b})(CH_3CO_2)]$, $[Ln(L^{2c})(CH_3CO_2)]$, $[Ln(L^{3a})]$, $[Ln(L^{3b})]$, $[Ln(L^{4a})]$ and $[Ln(L^{4b})]$ have been synthesised and characterised. The single crystal X-ray diffraction analysis of $[Gd(L^{2a})(CH_3CO_2)]\cdot CH_3OH$, the ^1H and ^{13}C NMR spectra and the hydrolysis experiments on the Y^{III} complexes with L^{2a}, L^{2b}, L^{2c}, L^{3a}, L^{3b}, L^{4a} and L^{4b} are reported. Relaxivity of the Gd^{III} complexes and Dysprosium Induced Shift on $[Dy(L^{2a})(CH_3CO_2)]$, $[Dy(L^{3a})]$ and $[Dy(L^{4a})]$ have been determined.

Chapter 6 describes the co-ordination chemistry of symmetric and asymmetric derivatives of $[9]aneN_3$ towards transition metal ions. The two ligands *tris*(cyanomethyl)- and *tris*(2-cyanoethyl)-1,4,7-triazacyclononane (L^1 and L^5, respectively) form peculiar complexes with Cu^{II}: using $Cu(BF_4)_2\cdot 4H_2O$ in MeOH at 65°C, the methanolysis of two nitriles with formation of imino-ether groups have produced square-based pyramidal Cu^{II} complexes. However, from the reaction of L^5 with $CuCl_2\cdot 2H_2O$ in CH_3CN at room temperature, the distorted square-based pyramidal Cu^{II} complex $[Cu(L^5)Cl_2]$ with the nitrile pendant arms left uncoordinated has been formed. Cu^{II} and Zn^{II} complexes with 1-(2-aminoethyl)-1,4,7-triazacyclononane (L^7), Mn^{II}, Ni^{II}, Cu^{II} and Zn^{II} complexes with L^2, Mn^{II}, Cu^{II} and Zn^{II} complexes with 1,4,7-*tris*(3-aminopropyl)-1,4,7-triazacyclononane (L^6) and Mn^{II} and Zn^{II} complexes with HL^3 and HL^4 have been prepared and characterised, and in most cases the crystal structure has

also been determined. Furthermore, the EPR spectra of the Cu^{II} complexes and the ^{13}C NMR spectroscopic data for the Zn^{II} complexes are reported.

Synthesis, solution studies and structural characterisation of complexes with [15]aneN_3O_2 derivatives are the topics of Chapter 7. The two ligands 1,4,7-*tris*(cyanomethyl)-1,4,7-triaza-10,13-dioxacyclopentadecane (L^8) and 1,4,7-*tris*(2-aminoethyl)-1,4,7-triaza-10,13-dioxacyclopentadecane (L^9) have been synthesised and their co-ordination chemistry towards transition and post-transition metal ions (Cu^{II}, Zn^{II}, Cd^{II} and Pb^{II}) has been studied. Most of the complexes have been structurally characterised and they all show interesting structures: the pendant nitrile arms of L^8 are not involved in co-ordination of the metal except for the Pb^{II} crystal structure and with L^9 only larger metal ions such as Cd^{II} and Pb^{II} are bound to all the donor atoms of the ligand. The protonation equilibria of the two ligands and the formation of the Cu^{II}, Zn^{II}, Cd^{II} and Pb^{II} complexes with L^8 and L^9 have been studied by means of potentiometric measurements. The protonation constants of the ligands and the stability constants of the complexes are reported and compared to other ligands with similar macrocyclic framework and donor atoms. In order to further investigate the structural features of the complexes in solution, ^1H NMR spectra of diamagnetic complexes have also been recorded at various temperatures.

In Chapter 8, the nitrile pendant arm derivatives L^1, L^5, L^8 and L^{10} have been used as building blocks for the synthesis of extended inorganic architectures by reaction with Ag^I. The complexes $\{[Ag(L^1)]PF_6\}_\infty$, $\{[Ag(L^1)]BF_4\}_\infty$, $\{[Ag(L^8)]BF_4\}_\infty$ and $[Ag(L^{10})]PF_2O_2$ have been prepared and structurally characterised. Analogously to other complexes of the same type prepared in the Schröder group, these compounds show nuclearity and dimensionality strictly dependent upon the number and length of the nitrile functionalised pendant arms present in the ligand: these act as linkers between different metal centres. Ag^I complexes of [9]aneN_3 and [15]aneN_3O_2 derivatives bearing three 7-methylquinoline pendant arms have also been prepared and characterised. The crystal structure of the Ag^I complex with 1,4,7-*tris*(7-methylquinolyl)-1,4,7-triaza-10,13-dioxacyclopentadecane (L^{12}) shows the formation of a dimer $\{[Ag_{2.5}(L^{12})(PF_2O_2)_{2.5}\cdot CH_3CN]_2\}$ with one Ag^I co-ordinated linearly by two heterocyclic N-donors and bridging the two units.

Ligands and lanthanide (Ln^{III}) complexes reported in the thesis

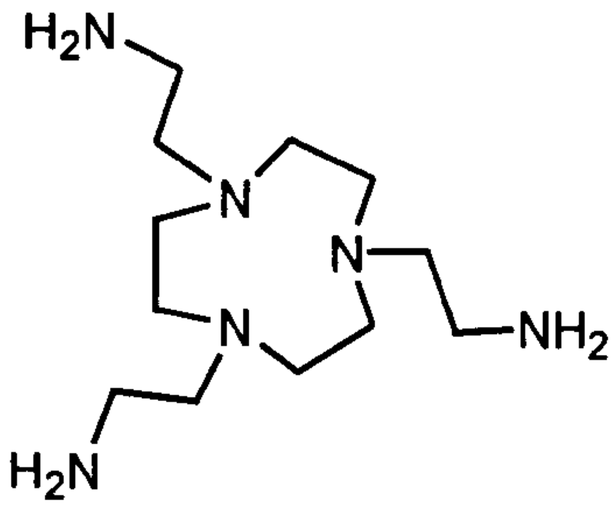

L

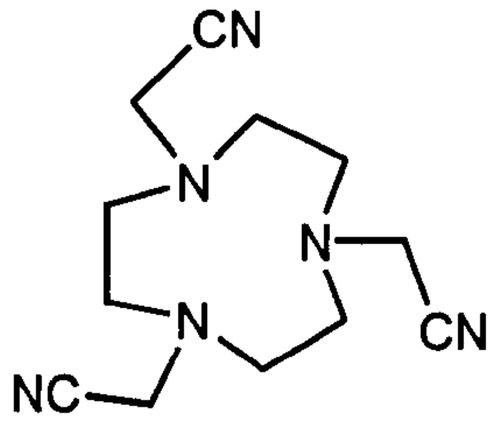

L^1

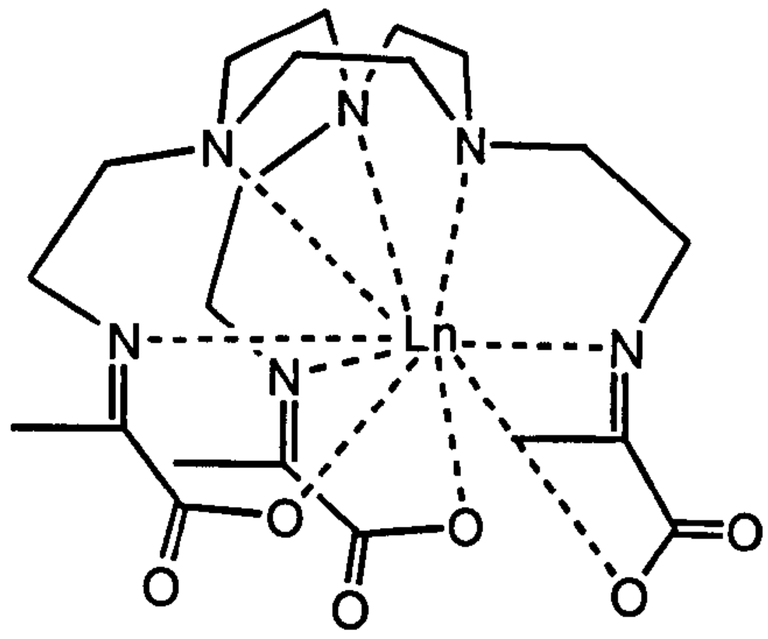

$[Ln(L^a)]$

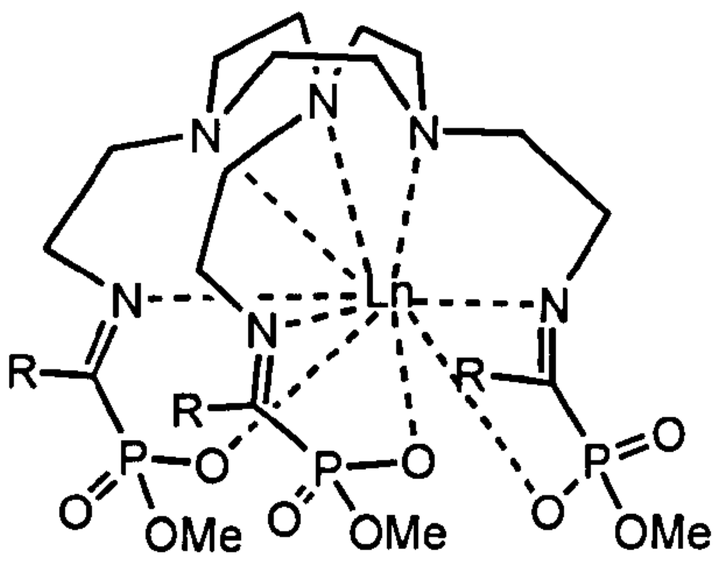

R = Me: $[Ln(L^b)]$
R = Methoxybenzyl: $[Ln(L^c)]$

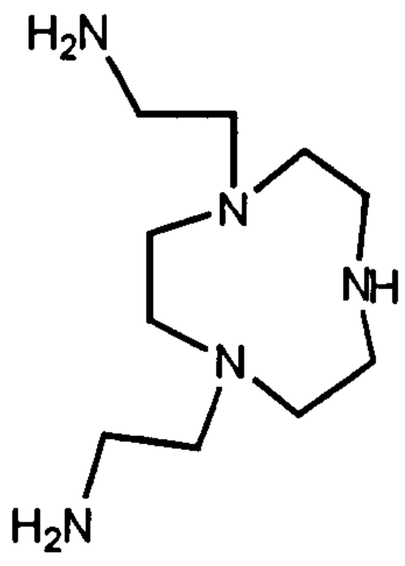

L^2

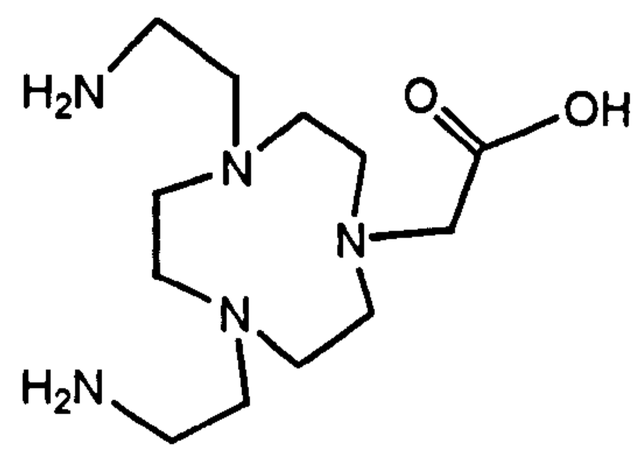

HL^3

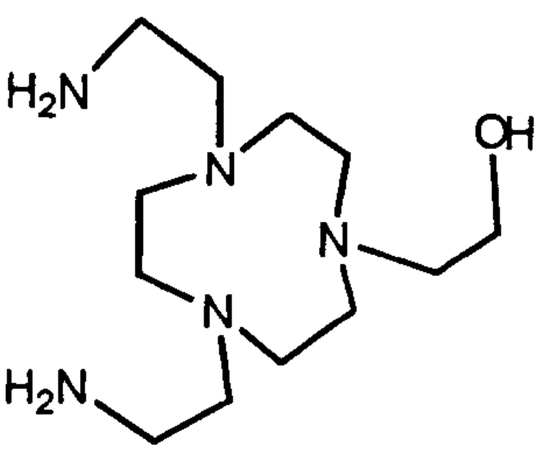

HL^4

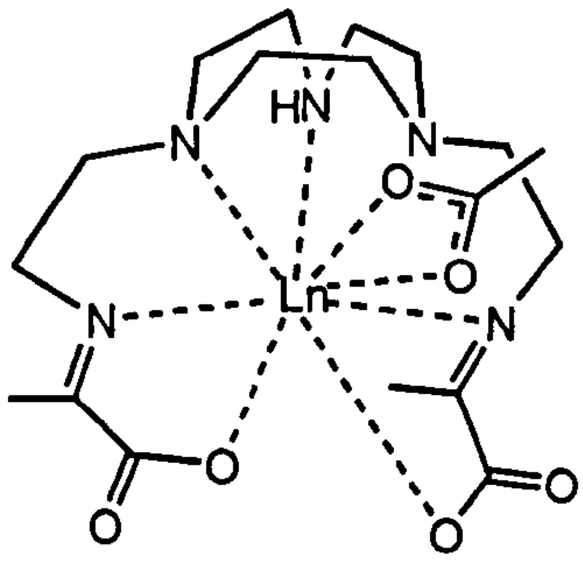

$[Ln(L^{2a})(CH_3CO_2)]$

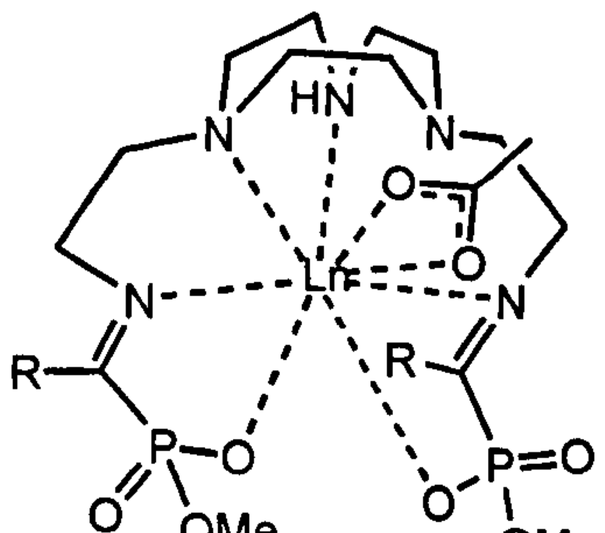

$[Ln(L^{2b})(CH_3CO_2)]$
with R = Me;
$[Ln(L^{2c})(CH_3CO_2)]$
with R =Methoxybenzyl

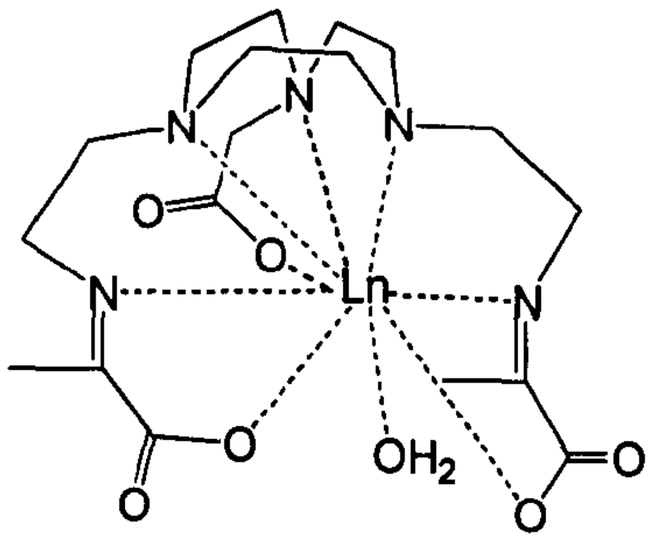

$[Ln(L^{3a})]\cdot H_2O$

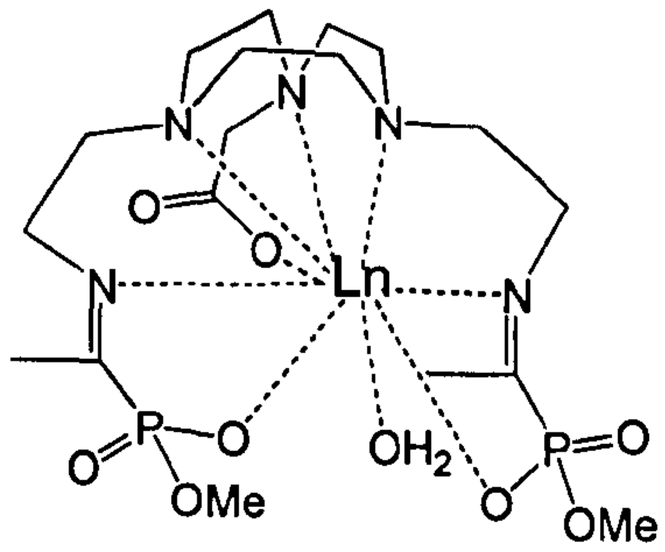

$[Ln(L^{3b})]\cdot H_2O$

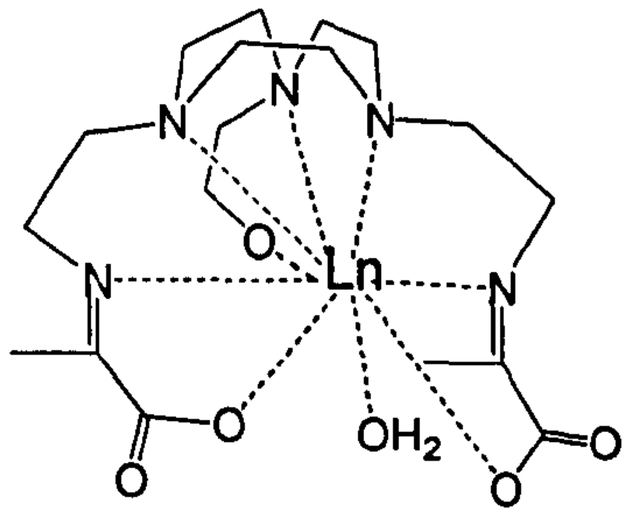

$[Ln(L^{4a})]\cdot H_2O$

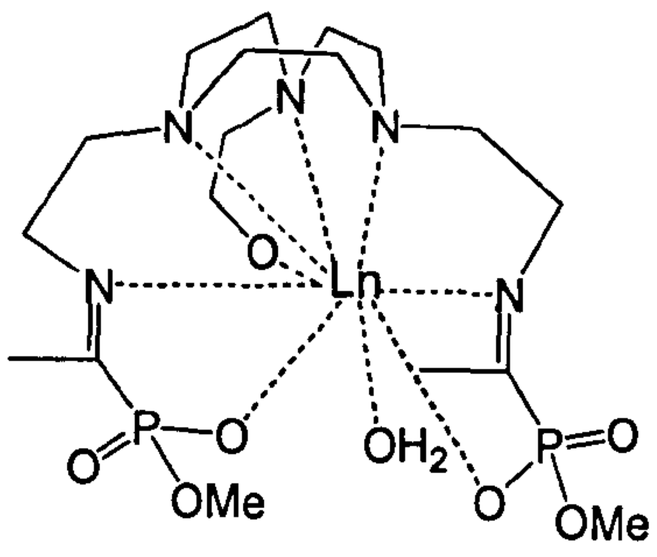

$[Ln(L^{4b})]\cdot H_2O$

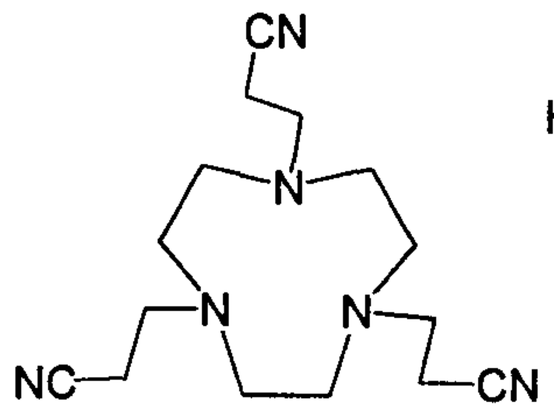

L^5

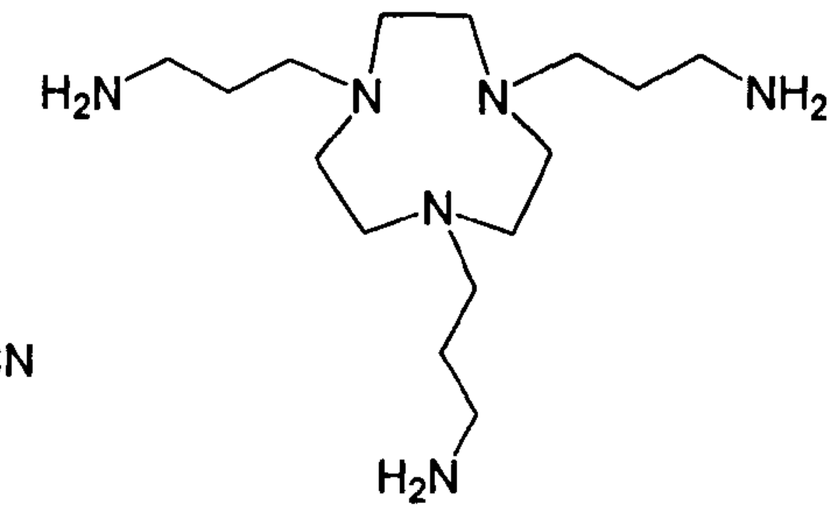

L^6

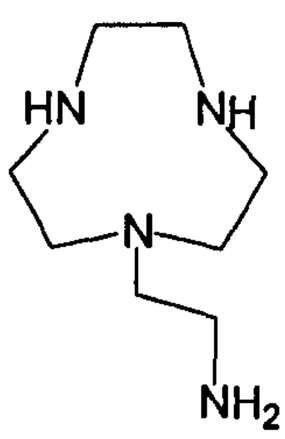

L^7

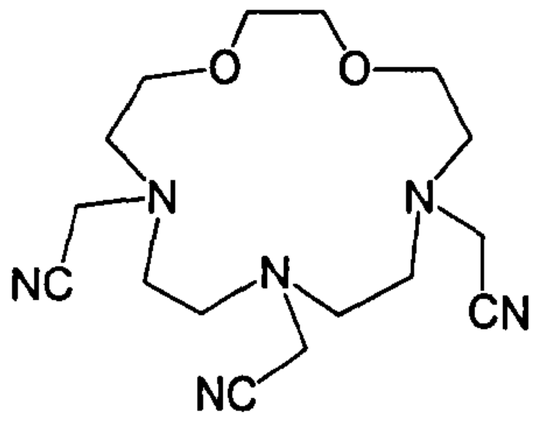

L^8

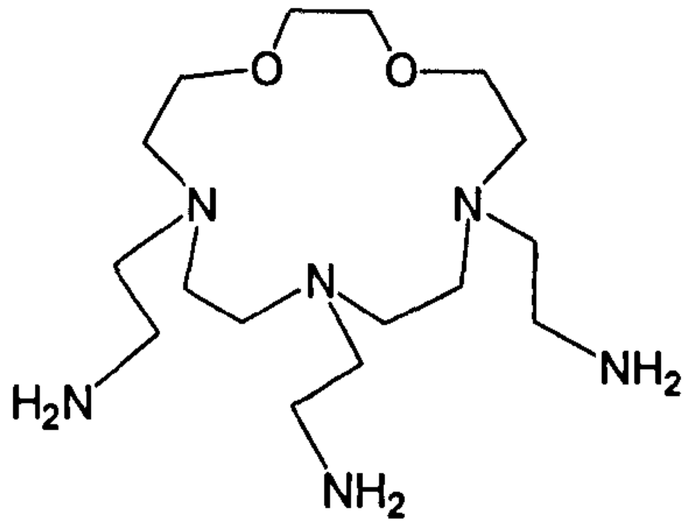

L^9

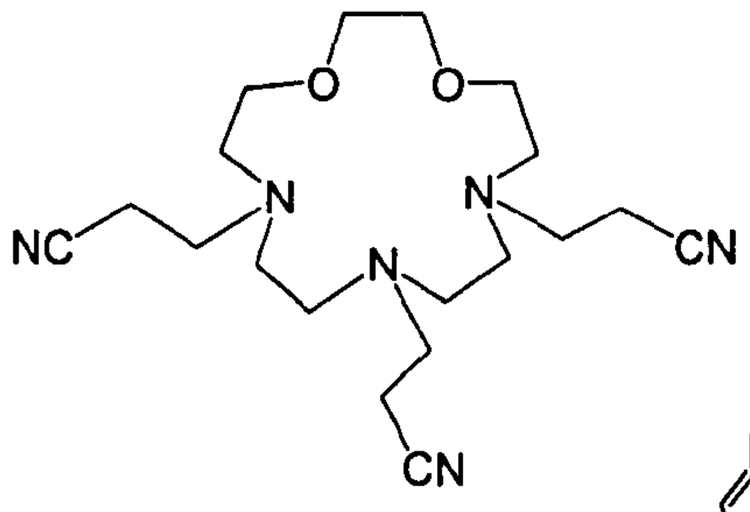

L^{10}

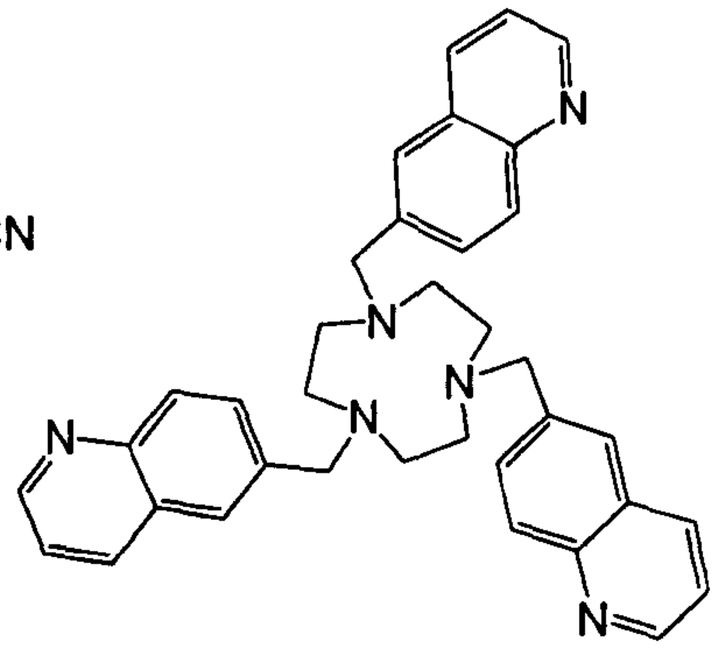

L^{11}

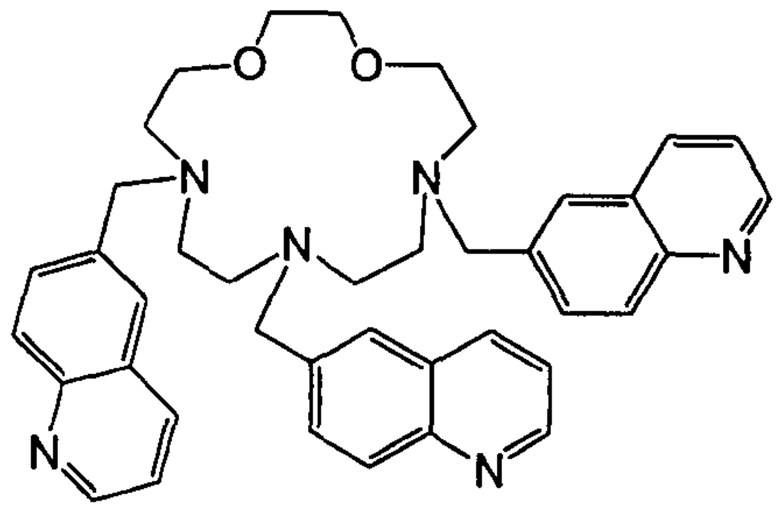

L^{12}

Chapter 1

Introduction to macrocyclic chemistry

1.1 Introduction

Before 1960, only phthalocyanines, with their strong structural resemblance to the natural porphyrin system, were a well-established category of synthetic cyclic ligands. Since then, following the discovery of the template reactions by Curtis (1960)[1,2] and of crown-ethers by Pedersen (1967),[3] a very large number of other synthetic macrocycles has been prepared, which has resulted in a great increase in interest in all aspects of the chemistry of macrocyclic systems.

After the development of highly efficient synthetic routes to large ring compounds,[4-9] attention focused on the study of their properties, in particular to the investigation of spectral, electrochemical, structural, kinetic and thermodynamic aspects of macrocyclic complex formation. Macrocyclic ligand complexes have been recognised as playing a fundamental role in many biological systems[10] such as the transport of oxygen in mammalian and other respiratory systems[11,12] and the mechanism of photosynthesis.[13] One obvious use of simple synthetic macrocycles is the synthesis of compounds with properties similar to those of biological molecules, but which possess simpler structures and so offer insights into the function of the naturally occurring species.[14-18] Such simple compounds can be structural models that reproduce spectroscopic or other features of the biological molecule, or functional models that replicate the biological and chemical reactivity.

Apart from the biological implications, aspects of the chemistry of macrocyclic ligands are of relevance to a diverse number of other areas. The clinical use of macrocyclic ligands to bind radioactive metals for chemotherapeutic applications,[19,20] or of paramagnetic complexes with lanthanides as imaging agents,[21,22] is routine in hospitals. Moreover, numerous microelectronic devices and sensors based upon the use of macrocyclic ligands for the detection, amplification or recognition of metal ions have been proposed or fabricated.[23-28]

Normally these devices undergo changes in their photochemical and electronic properties as a consequence of ion binding and release.

Macrocyclic chemistry is a rapidly expanding area and is often strongly interconnected with a larger area of the chemical science defined by Lehn as supramolecular chemistry.[9] "Supramolecular chemistry may be defined as 'chemistry beyond the molecule', bearing on the organised entities of higher complexity that result from the association of two or more chemical species held together by intermolecular forces".[29] These forces may be hydrogen-bonding, hydrophobic interactions, π-π stacking and specific co-ordination properties of metal cations or metal complexes. Therefore, supramolecular chemistry considers the binding not only of metal ions by inorganic and organic ligands but also of all kinds of cationic, anionic or neutral substrates whether inorganic, organic or biological in nature.[30]

1.2 Basic concepts in macrocyclic chemistry

As usually defined, macrocyclic ligands contain at least three donor atoms with the macrocyclic ring consisting of a minimum of nine atoms (including heteroatoms).[31] A macrocyclic ligand is defined by various structural factors such as the number and type of donor atoms, cavity size, shape, conformation, topology and rigidity.[31] All these characteristics have a strong influence in the thermodynamic and kinetic properties of metal complexes as described in the following sections.

1.2.1 Some representative macrocyclic systems

As the definition of macrocycle is very general, the number of possible macrocycles that can be designed is, in effect, unlimited. Therefore, by varying the donor atoms a great variety of macrocycles have been synthesised and their co-

ordination chemistry studied: these include macrocyclic polyethers (crown ethers),[3,32,33] polyamines,[31,34,35] polythioether (thioether crowns),[36] macrocycles with P-,[37] As-,[38] Se-,[39] Te-[40] donor atoms and mixed donor polydentate macrocycles.[31,41,42] This variety is even greater when we consider that the organic backbone can be either saturated or unsaturated, that the linkers between donor atoms can be of different lengths and that the donor atoms can be part of an heteroaromatic unit such as pyridine,[31,43,44] thiophene,[45] phenol,[46] benzene,[47] bipyridine[48] or phenanthroline.[49,50]

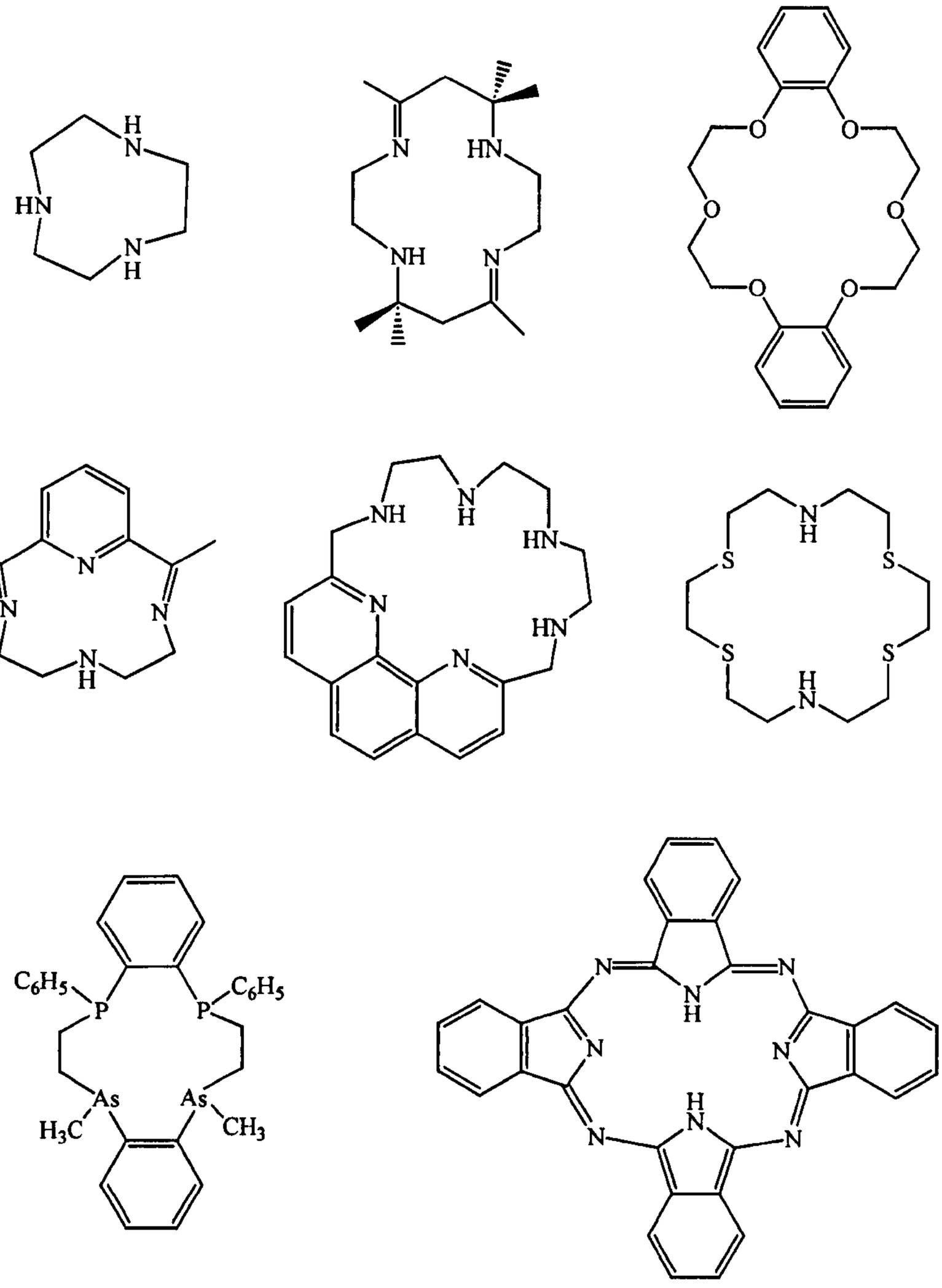

Figure 1.1 Some representative macrocyclic systems.

The study of more complicated systems, which exhibit ever-increasing structural diversity and selectivity for a particular substrate, has led to the development of new and more efficient receptors. In Section 1.3 the systems related to monocyclic rings that contain appended side chains (pendant arms) incorporating additional donor functions will be described in greater detail. Figure 1.2 shows some other examples of macrocyclic receptors: calixarenes (a),[51,52] catenands (b),[53,54] cryptands (c),[8,55] dinucleating macrocycles (d)[31,46] and linked macrocyclic ligands (e).[31]

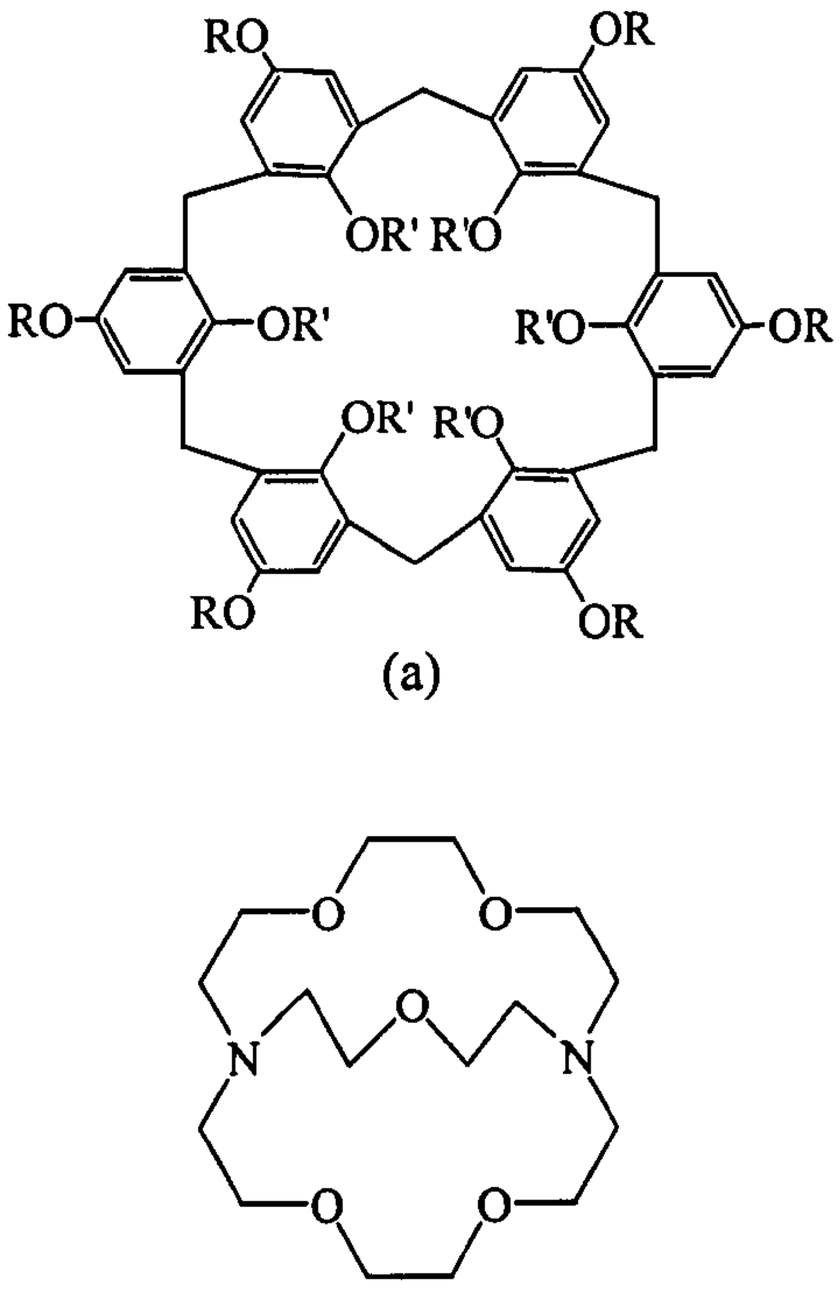

(a)

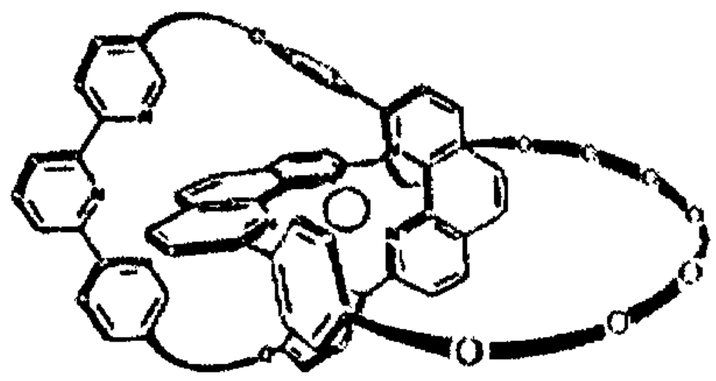

(b)

(c)

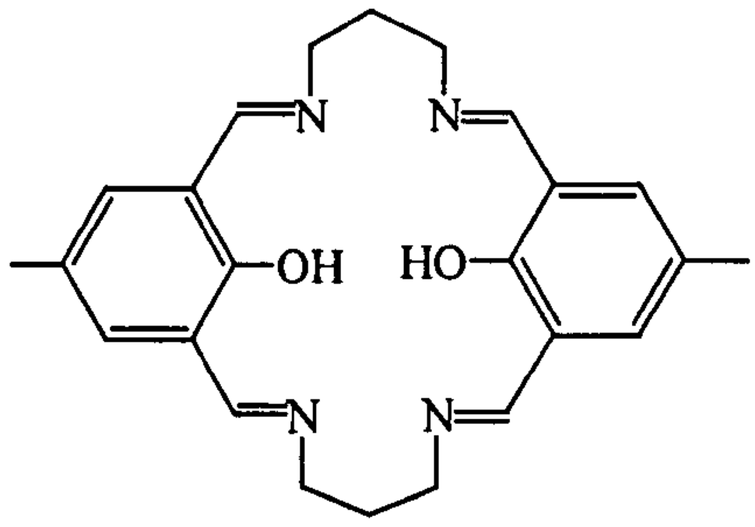

(d)

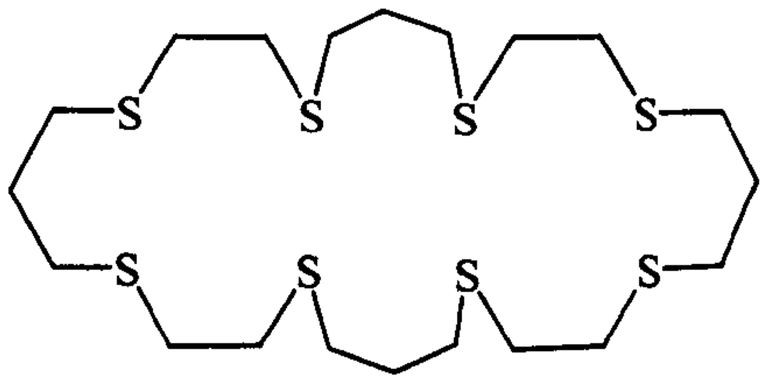

(d)

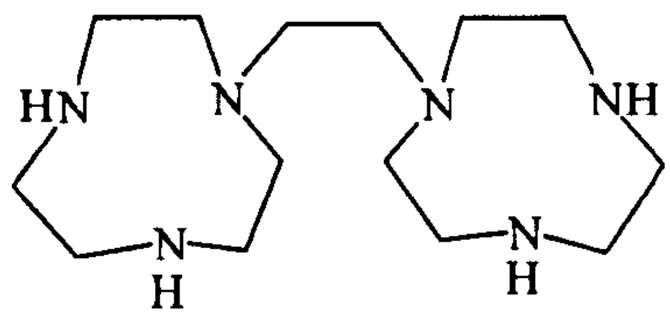

(e)

Figure 1.2 Other examples of macrocyclic receptors.

Considering this structural diversity, macrocyclic systems offer the opportunity to design artificial receptors having appropriate structural features that will confer stability and selectivity in the binding of a desired substrate.

1.2.2 Thermodynamic and kinetic considerations

Polydentate ligands have always been of particular interest because their metal complexes show enhanced thermodynamic stability over those of monodentate ligands.[56,57] The following equilibrium exemplifies this *chelate effect*:

$$[Ni(NH_3)_6]^{2+}_{(aq)} + 3\ en_{(aq)} \rightleftharpoons [Ni(en)_3]^{2+}_{(aq)} + 6\ NH_{3\ (aq)}$$

The formation of $[Ni(en)_3]^{2+}$ is entropically favoured because six molecules of ammonia are released into the solution upon co-ordination of three molecules of ethylendiamine (en) to the metal centre.[56] However, thermodynamic phenomena such as the chelate effect require the consideration of both entropic and enthalpic factors.[57]

Macrocyclic complexes are characterised by high thermodynamic stability and marked kinetic inertness with respect to formation and dissociation, respectively. The *macrocyclic effect* is the term used to describe the observation that macrocyclic complexes are more stable than their open-chain analogues.[58] The kinetic and thermodynamic origins of the macrocyclic effect can be considered separately although these two aspects are strongly inter-related.

The thermodynamic origins of the macrocyclic effect are not yet very well defined because the entropic and enthalpic contributes are sometimes ambiguous and vary between systems. The entropic term can be partly explained by the pre-organisation to co-ordination of the donor atoms in the macrocycle which therefore undergoes much less geometrical change on co-ordination than its open-chain analogue.[59,60] This is called *configurational entropy* (Figure 1.3) and is a

favourable term in the overall thermodynamic stability. Less easily predictable but also important, are the entropy changes associated with solvation.

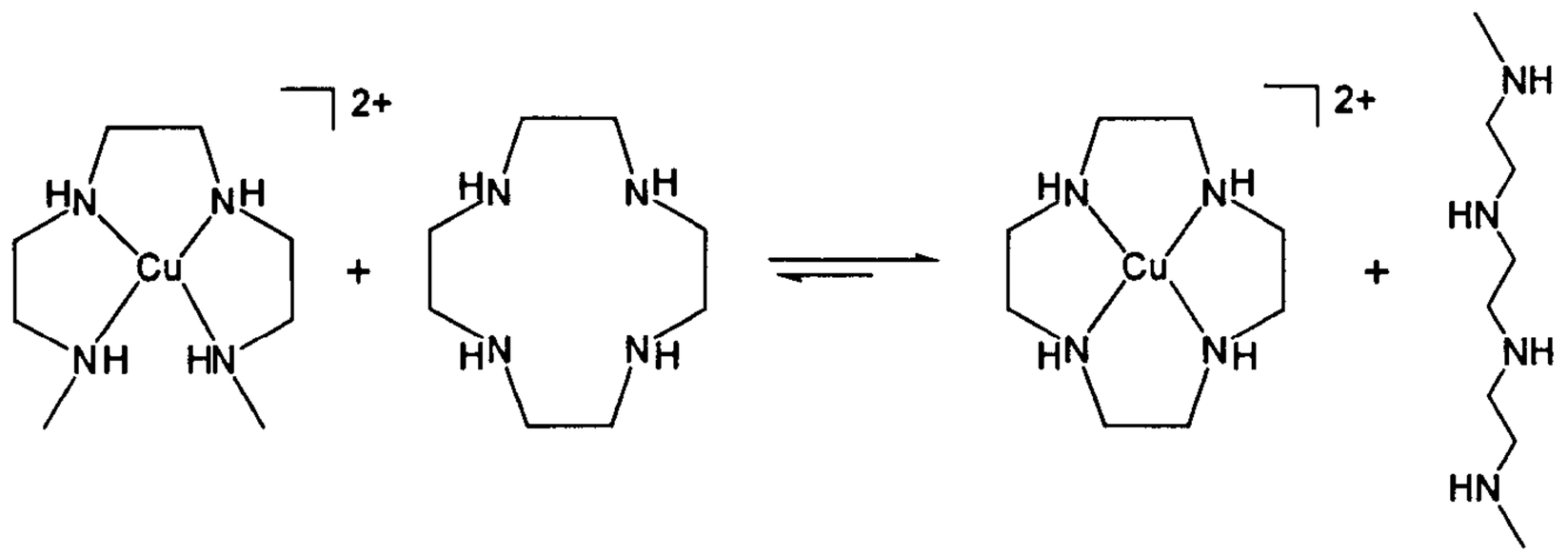

Figure 1.3 Metathetic reaction illustrating the configurational entropy gain in the macrocyclic effect.

The enthalpic contribution to the macrocyclic effect depends on various factors that are strongly dependent on the system under study and on the experimental conditions employed.[57,61-63] The macrocyclic effect can be considered in terms of the decrease in Gibbs free energy ($\Delta G=\Delta H-T\Delta S$) for the methatetic reaction shown in Figure 1.3. Table 1.1 presents thermodynamic data for a series of metathetic reactions between tetraaza macrocyclic ligands and the Cu^{II} complexes of their open-chain analogues.[63]

A clear macrocyclic effect is observed, but the enthalpic and entropic contributions vary significantly. The tetraazamacrocyclic ligands have been compared to the related N-methylated open-chain ligands because their behaviour towards both protonation and metal complexation resembles more closely the behaviour of the macrocyclic systems than the open-chain ligands containing two primary amines.[62,63] From the results shown in Table 1.1, a clear trend cannot be discerned. Other factors such as the ligand reorganisation prior to complexation,[60,64] the nature of the solvent used, the match of the macrocyclic cavity to the metal ion size[59] and the affinity of the donor atoms for the metal[65] also contribute to the enthalpic term and therefore to the macrocyclic effect.

Table 1.1 Thermodynamic parameters for the methatetic reaction of the tetraazamacrocycles L^2, L^4, L^6 and L^8 with the Cu^{II} complexes of their open-chain analogues (L^1 L^3 $L^5$and L^7).[62,63]

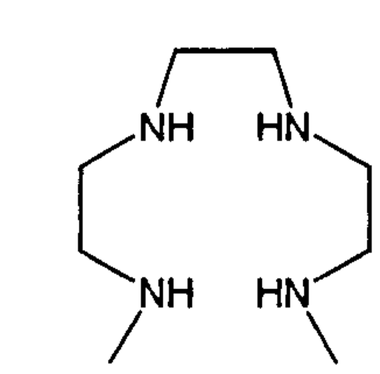

L^1

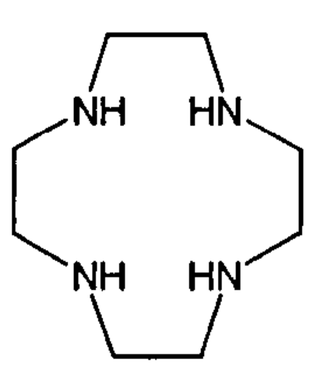

L^2

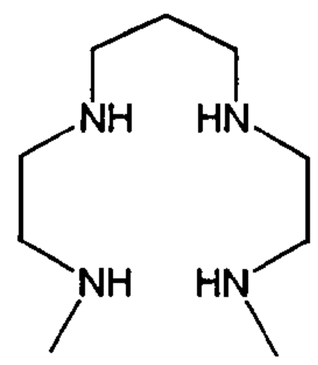

L^3

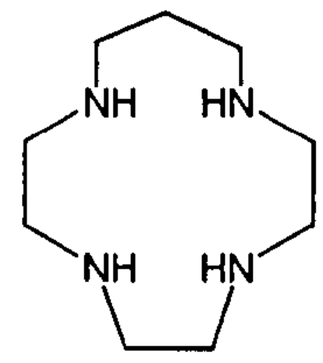

L^4

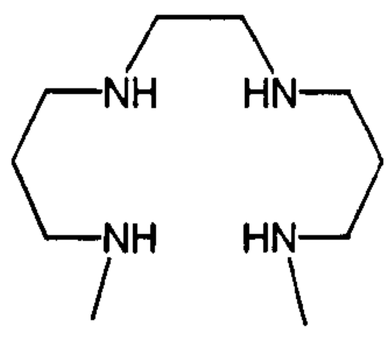

L^5

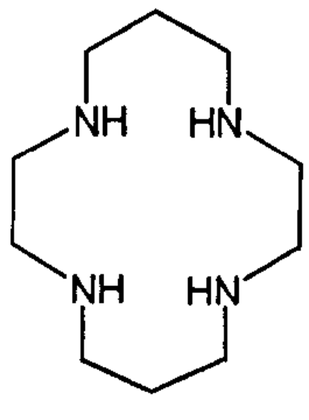

L^6

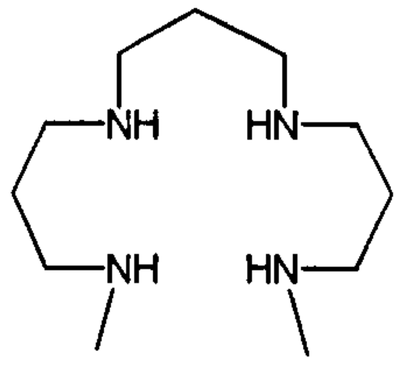

L^7

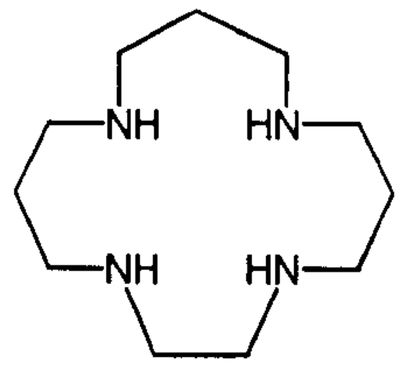

L^8

$$[Cu(L_o)]^{2+} + L_m \rightleftharpoons [Cu(L_m)]^{2+} + L_o$$

L_o/L_m[a]	$-\Delta G/kJ\cdot mol^{-1}$	$\Delta H/kJ\cdot mol^{-1}$	$T\Delta S/kJ\cdot mol^{-1}$
L^1/L^2	22.2	-6.7	15.5
L^3/L^4	41.1	1.3	42.3
L^5/L^6	49.6	-42.5	7.1
L^7/L^8	55.8	-48.6	6.8

[a] m = macrocycle, o = open-chain

The study of the macrocyclic effect is more straightforward in the case of crown ethers and their complexation towards alkali and alkaline earth metal ions since there is no competing protonation equilibrium involved. Pedersen and co-workers have observed an increase in stability of about 10^4 for the formation of the K^+ complex with [18]aneO_6 compared to its open-chain analogue in MeOH as illustrated in Figure 1.4.[66]

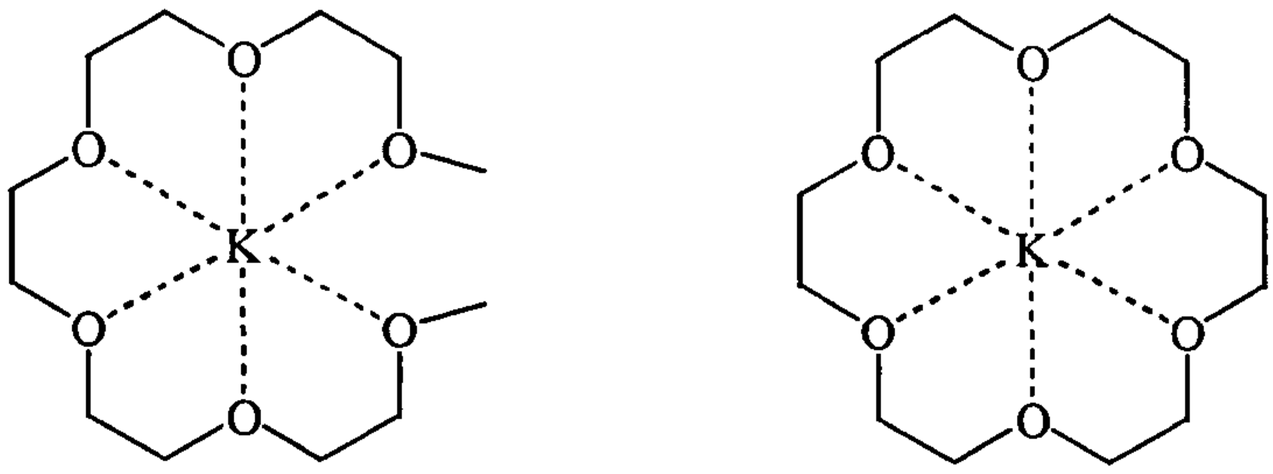

LogK = 2.27 LogK = 6.05

Figure 1.4 Differing thermodynamic stabilities for the K^+ complexes of [18]aneO_6 and its open-chain analogue. [66]

A macrocyclic system is characterised by a very slow kinetic rate of dissociation compared to the corresponding open-chain complexes.[31] This behaviour reflects the fact that stepwise removal of a cyclic ligand from the co-ordination sphere of a metal is less favourable than for its open-chain analogue. Normally, the co-ordinated cyclic ligand requires unfavourable rearrangement, such as folding, within the co-ordination sphere before dissociation can occur (Figure 1.5). Although the formation rate constant (k_f) is generally lower for

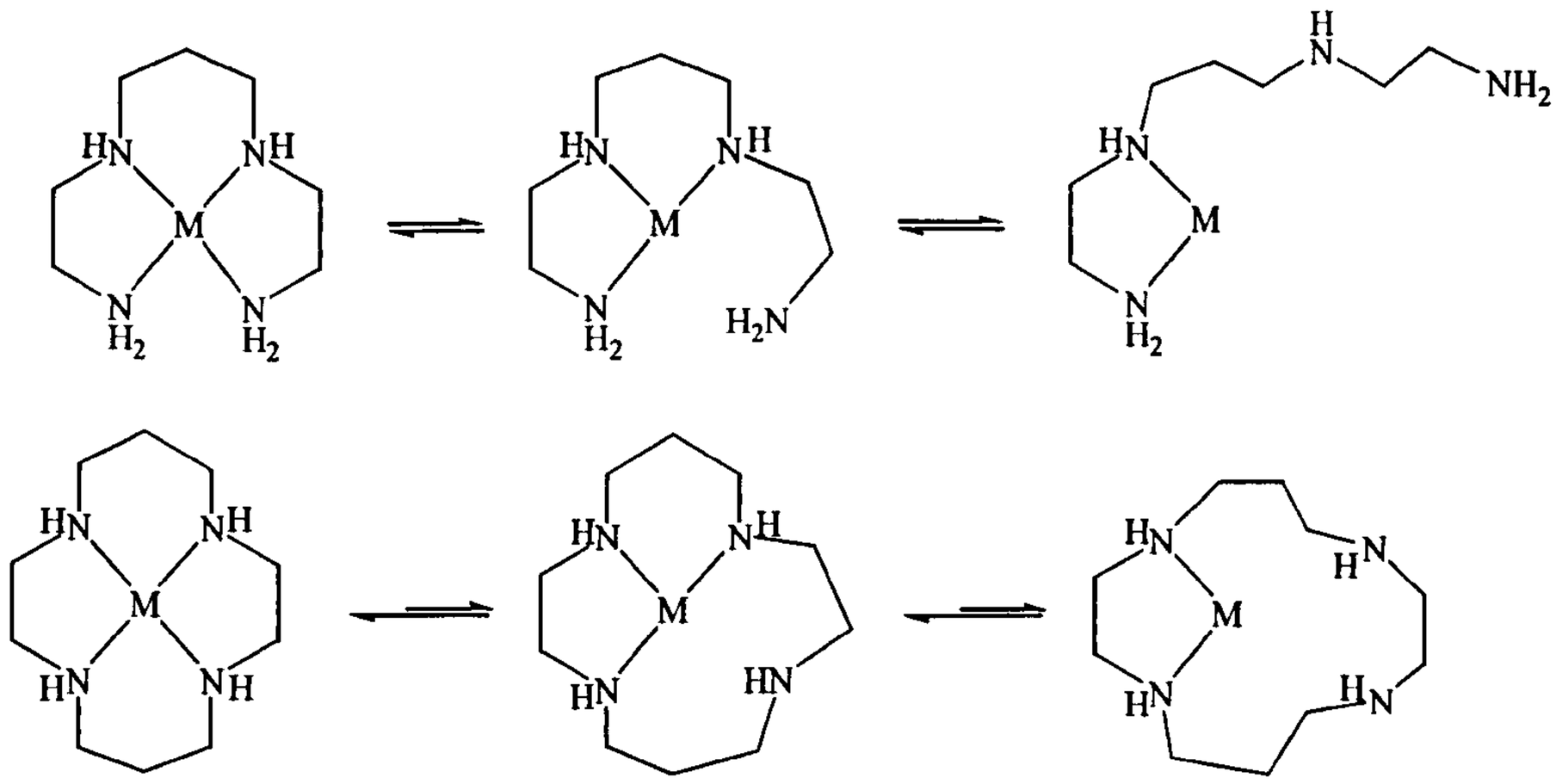

Figure 1.5 Stepwise dissociation of a generic [14]aneN_4 metal complex and of its open-chain analogue.

macrocyclic complexes compared to the open-chain analogues, the dissociation rate constant (k_d) is much smaller, therefore the overall thermodynamic stability constant ($K=k_f/k_d$) is greatly enhanced for macrocyclic systems (macrocyclic effect).[31,57,60]

1.2.3 Structural characteristics of macrocycles

The co-ordination chemistry of macrocycles depends upon many different factors such as the nature, number and arrangement of donor atoms, and also upon structural factors such as cavity size and conformational flexibility of the ligand molecule. The combination of these factors leads to the important ability of macrocycles to selectively bind certain metal ions. The HSAB theory (Hard and Soft Acids and Bases)[67] can provide a preliminary guide for donor atom selection considering, for example, that ethereal O-donors (crown-ethers) tend to form very stable complexes with alkali and alkaline-earth metal ions or that N-donors form the most stable complexes with transition metal cations. However, other more important factors must be considered in the context of ligand design.[31,41,68]

Figure 1.6 shows the effect of increasing the macrocyclic ring size from [12]aneN_4 to [16]aneN_4 on the stability constants of the Ni^{II}, Cu^{II}, Zn^{II} and Cd^{II} complexes.[69,70] While an increase of the ring size leads to a large decrease in complex stability for the complexes of large metal ions such as Cd^{II}, for smaller cations such as Ni^{II} and Cu^{II} a very similar trend in the stability constants is observed and the maximum stability occurs for the 14 membered macrocycle (cyclam). This trend has been explained in terms of both macrocyclic hole-size and chelate ring size.[68] From the 12- to the 16-membered macrocycles the chelate rings pass from four 5-membered to four 6-membered rings. The lowest strain energy for the five and six-membered chelate rings, calculated using molecular mechanics, shows that the larger chelate ring is preferred by smaller cations that can form shorter M-L bonds and N-M-N angles close to 109.5º. The 5-membered

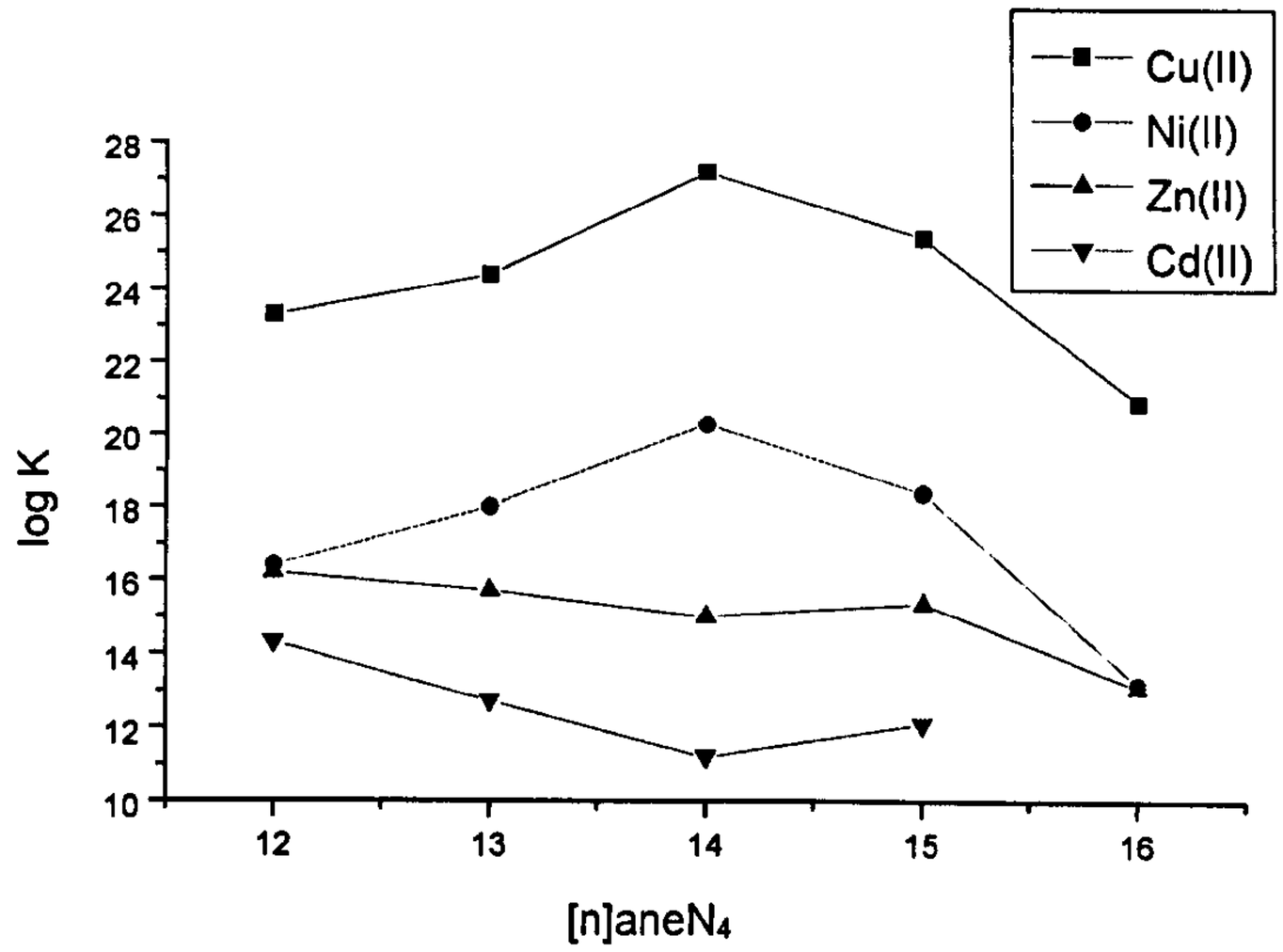

Figure 1.6 Trend of the stability constants of Cu^{II}, Ni^{II}, Zn^{II} and Cd^{II} complexes of tetraazamacrocyclic ligands with increasing the ring size. [69,70]

ring allows bond lengths up to 2.5 Å and angles around 69º and therefore is preferred by larger metal ions (Figure 1.7).[71]

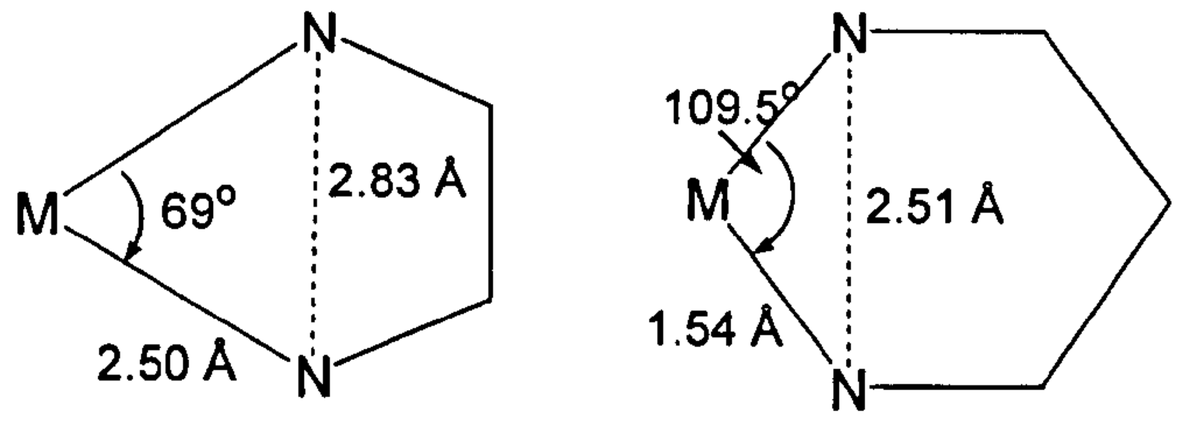

Figure 1.7 Lowest strain energy geometries calculated by using molecular mechanics for the five and six-membered chelate rings. [71]

The macrocyclic cavity size has been calculated for the planar *trans*-III conformer and for other possible conformers using molecular mechanics[72]. Figure 1.8 shows the *trans*-III conformer and also the particularly important planar *trans*-I and the folded *cis*-V conformers of complexes of [12]aneN$_4$. These calculations show that for these complexes the *trans*-III conformer is very unlikely to form

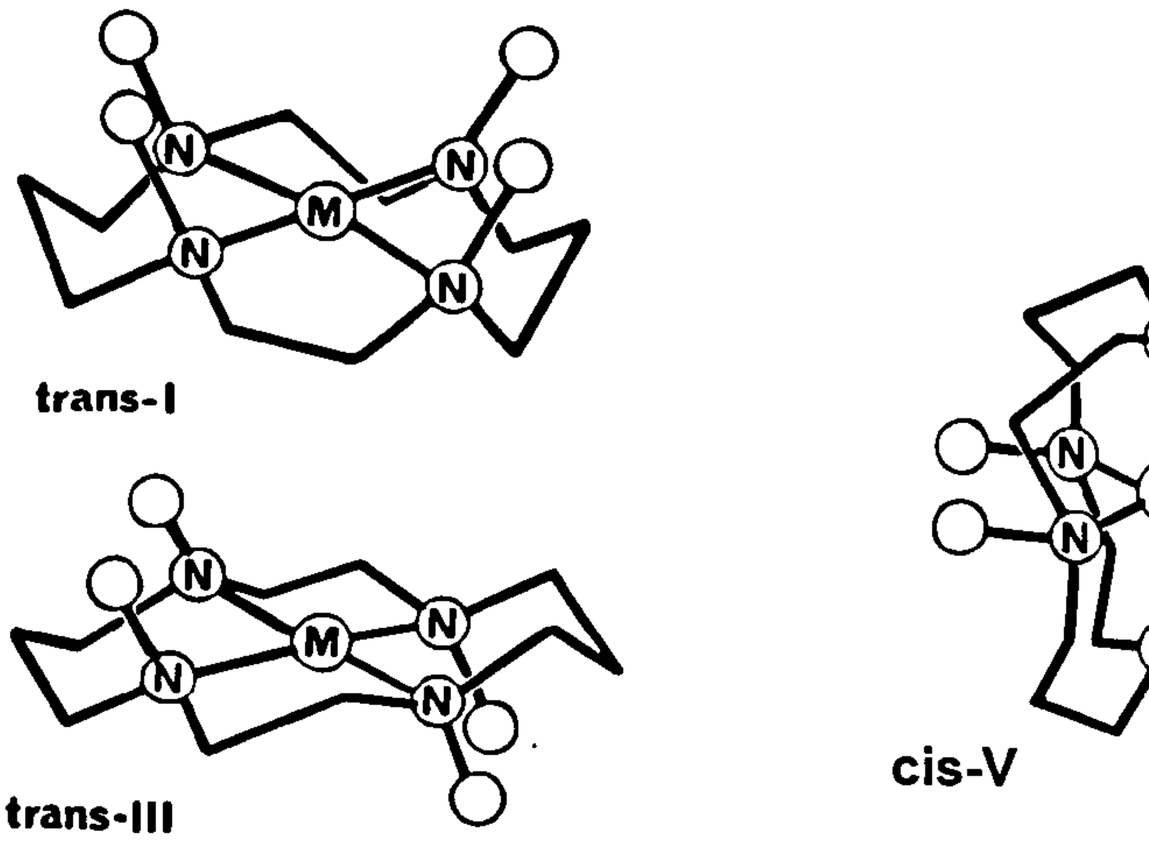

Figure 1.8 Conformers of cyclam complexes. The open circles represent amine hydrogen atoms.

because it has a very large strain energy.[73] From the data reported in Table 1.2, it can be noticed that the complexes of [12]aneN_4 present the most remarkable difference in the best-fit M-N bond lengths between the *trans*-I and the *trans*-III conformers: 2.11 Å against 1.81 Å. Given that larger metal ions such as Cd^{II} or Pb^{II} tend to form M-N bond lengths higher than 2.2-2.3 Å, they should have a preference for the *trans*-I conformer of the macrocycle [12]aneN_4. Moreover, the *trans*-I conformer is preferred by large cations because they can be co-ordinated while lying out of the plane of the donor atoms, which does not necessarily have any adverse strain effects.[68]

Table 1.2 Best-fit M-N bond lengths (Å) for tetraazamacrocycles and the strain energies (Kcal mol^{-1}) of the complexes at the best-fit size.

	[12]aneN_4		[13]aneN_4		[14]aneN_4	
Conformers	*Trans*-I	*Trans*-III	*Trans*-I	*Trans*-III	*Trans*-I	*Trans*-III
Best-fit M-N	2.11	1.81	2.03	1.92	2.00	2.05
Strain energy	10.8	19.7	11.5	13.5	9.4	8.1

The macrocycles [9]aneN_3[74] and [9]aneS_3[75] are more rigid and normally present only one conformer, the [333] conformer, in which the lone pairs of the three donor atoms point towards the centre of the ring cavity (only occasionally[76] has the [234] conformer been observed) (Figure 1.9). These two nine-membered macrocycles are said to adopt an *endo*-conformation that is pre-organised for facial tridentate co-ordination to a metal ion.[77] This enhanced rigidity leads to more stringent requirements for the preferred size of metal ion for co-ordination to the three donor atoms. Molecular mechanics calculations indicate that metal ions with M-N bond length of 2.08 Å will fit best in *bis*-[9]aneN_3 sandwich complexes formed by this triaza macrocycle.[74]

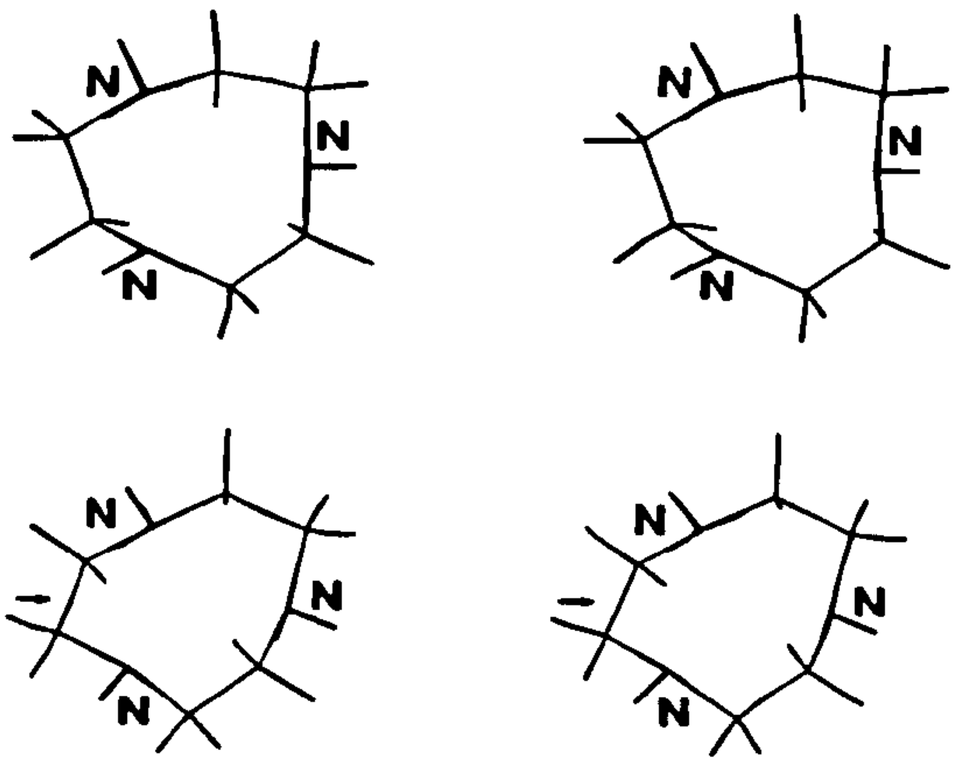

Figure 1.9 Stereoviews of the two conformations observed for the macrocycles of the [9]aneX_3 type. The arrows indicate the ethylene bridge which is oriented in an opposite fashion to that in the more symmetrical [333] conformer. [68]

Similar considerations of macrocycle flexibility and size-match selectivity can be made for crown ethers (O-donors). In conclusion, it can be observed that the degree of flexibility of macrocycles confers the ability to adopt a wide range of conformers of fairly similar energy. Thus, metal ions can adopt a range of best-fit

M-L bond lengths and can form strong complexes while lying co-ordinated out of the macrocyclic cavity thereby escaping from the size-match selectivity patterns.[68]

Macrocyclic ligands show modest levels of pre-organisation due to their flexibility, but the increased rigidity of cryptands and particularly in spherands gives them a high degree of pre-organisation.[30,31,55] This pre-organisation can lead to high selectivity providing that the metal ions and macrocyclic hole sizes are compatible. In spherands, phenol groups are incorporated within the macrocyclic framework, and conformational changes are thus inhibited, forcing the donor atoms into the centre of the ring ready for binding metal ions. Figure 1.10 shows two examples of spherands together with their selectivity factors (K_{M1}/K_{M2}) for alkali metal ions adjacent to each other in the periodic table. The size of the cavity and also the fact that water molecules are excluded from it are fundamental factors for the high stability and selectivity of these ligands.[55,78]

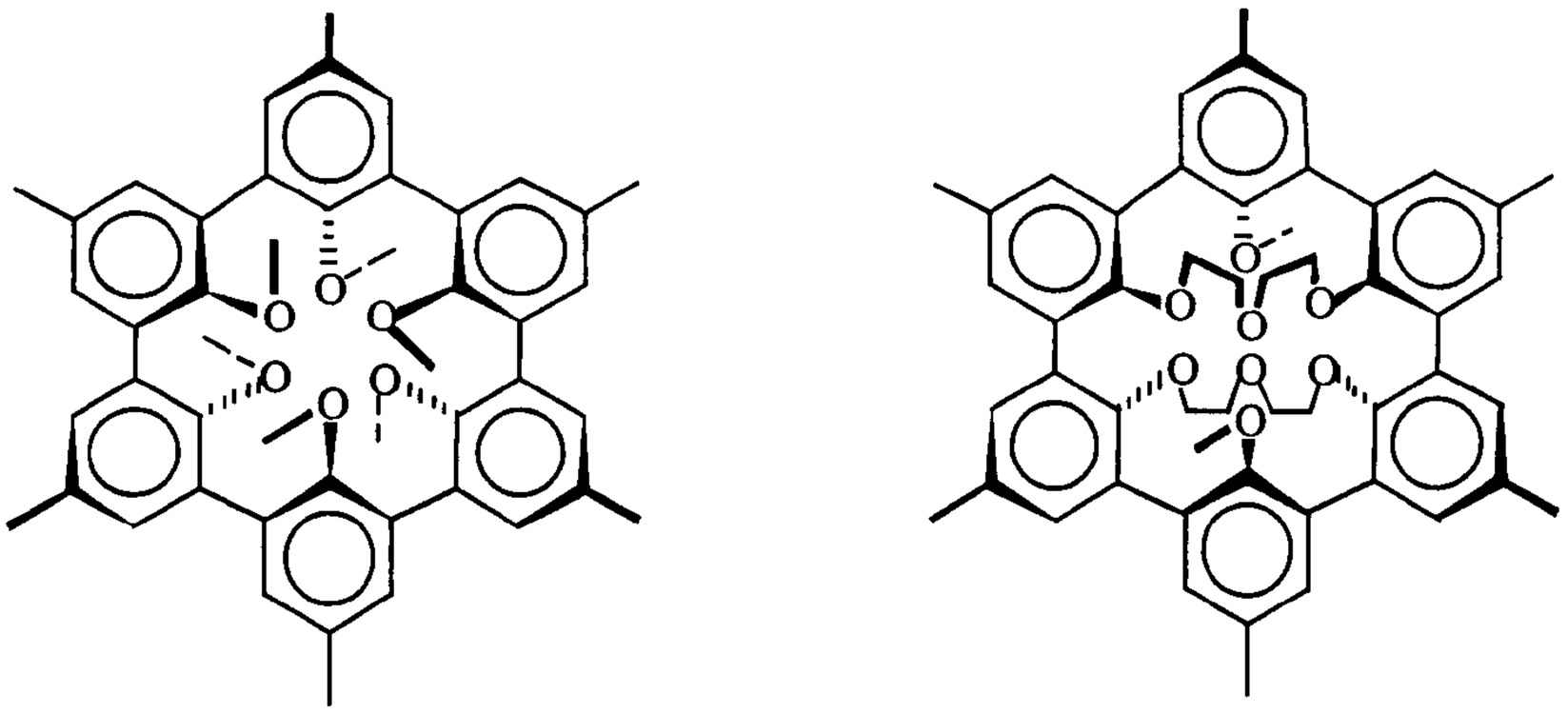

K_{Li^+}/K_{Na^+}: > 600 K_{Na^+}/K_{K^+}: 10^{10} K_{Na^+}/K_{Li^+}: 125 K_{Na^+}/K_{K^+}: 10^9

Figure 1.10 Structural recognition by two types of spherands measured by K_{M1}/K_{M2} values for alkali metal picrates.

1.3 Macrocycles with pendant functional groups

In the search for new ligands with unusual and specific characteristics, macrocycles with additional donor groups attached to their periphery have

received great interest since the late 1970's.[41,79-82] These ligands have been synthesised in large number because they have proved useful for a great variety of different chemical applications. Some selected examples will be discussed in Section 1.4, and Chapter 2 will be devoted entirely to the description of the use of lanthanide complexes of functionalised macrocycles in medicinal inorganic chemistry.

In these functionalised macrocyclic ligands, the macrocycle provides a non-labile set of donor atoms that normally serve to immobilise a metal ion and the arms with variable length and functional groups are attached in order to design a receptor with the desired characteristics. Probably the most important characteristic of these ligands is the selectivity they show towards different metal ions.[41,68] This has been exploited for different purposes, such as for making non toxic and effective drugs,[19-22] for extracting the metal ions from waste material[83,84] and for creating functional devices. [23-26]

In order to explain how the binding characteristics of these ligands can be different to that of the free macrocycles, two examples are considered in thermodynamic terms. DOTA (1,4,7,10-tetraazacyclododecane-1,4,7,10-tetraacetate) was first synthesised by Stetter and Frank in 1976[85] and, since then, it has been one of the most widely reported macrocycle containing pendant arms (Figure 1.11). [12]aneN_4, the parent macrocycle of DOTA, forms very stable complexes with transition metal ions, but it has low affinity for large cations such

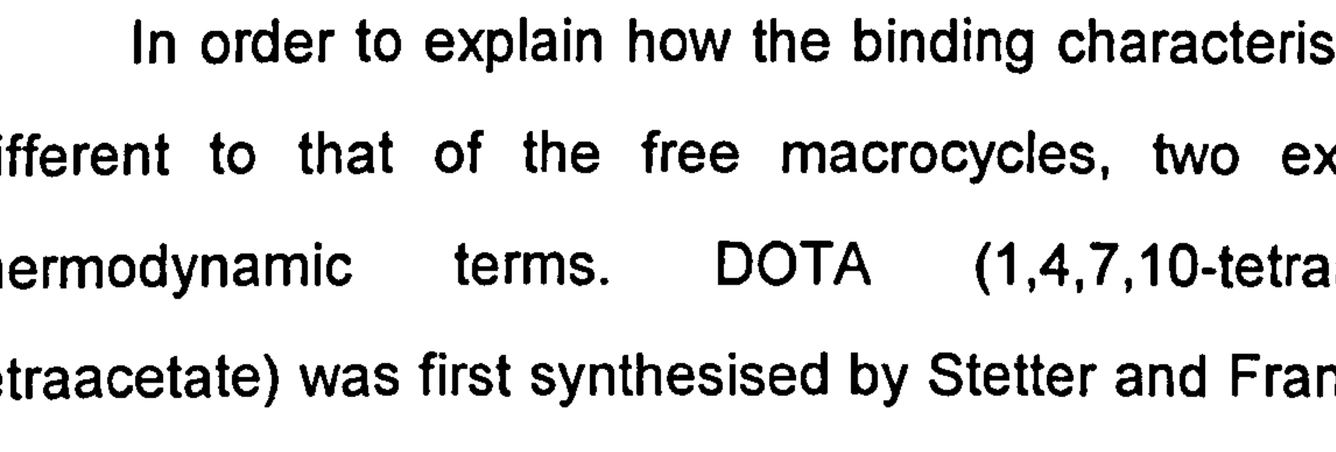

Figure 1.11 [DOTA]$^{4-}$ (left) and [NOTA]$^{3-}$ (right).

as Ca^{II} or lanthanides (Table 1.3). When the carboxylate arms are attached, the ligand has eight potential donor atoms and only a small change in the stability constants is observed for metal ions such as Cu^{II}, Ni^{II}, Zn^{II} that cannot expand their co-ordination number to eight. However, DOTA forms very stable adducts with large cations that have higher co-ordination numbers and form ionic complexes (Table 1.3).[86-88] Thus, the Ca^{II} complex of DOTA is the most stable complex of Ca^{II} with a log K of approximately 16.5 compared to log K of 3.1 with [12]aneN_4.[89] Moreover, trivalent lanthanide complexes show extremely high stability and kinetic inertness, characteristics which make the $[Gd(DOTA)]^-$ a useful (very low toxicity) contrast agent for magnetic resonance imaging (MRI).[22]

Table 1.3 Stability constants (log K) for DOTA, NOTA complexes and for the same complexes of their parent macrocycles.

Metal ion	Cu^{II}	Ni^{II}	Zn^{II}	Cd^{II}	Ca^{II}	Gd^{III}
Ionic radius (Å)	0.57	0.69	0.74	0.95	1.00	1.11
[12]aneN_4	23.3	16.4	16.2	14.3	3.1	~ 8
DOTA	20.3	18.7	20.0	19.0	16.5	25.3
Δ log K	-3.0	+1.7	+3.8	+4.7	+13.4	~ 17
[9]aneN_3	15.5	16.2	11.6	9.5		
NOTA	19.5	28.3	18.3	16.8	8.0	13.7
Δ log K	+4.0	+12.1	+6.7	+7.3		

Given that [9]aneN_3 is a more rigid ligand than [12]aneN_4 (Section 1.2.3), the ligand with three carboxylate arms attached on the triaza ring (NOTA, Figure 1.11) [74,90,91] should form complexes with remarkable metal ion selectivity. The ligand NOTA is potentially hexadentate and has a preference for small metal ions with M-L bond lengths in the vicinity of 2.00 Å. In Table 1.3 quite a remarkable

selectivity of this ligand for the six co-ordinate Ni^{II} over Cu^{II}, Zn^{II} and Cd^{II} can be observed.[68]

The two ligands DOTA and NOTA have shown quite clearly how selectivity patterns can break away from those found in the parent macrocycles by the addition of pendant donor groups. Although the effect of other pendant arms on the stability constants is not so remarkable as with carboxylates, there is always a clear change in the binding characteristics in comparison to the free macrocycles. Functionalised macrocyclic ligands normally exhibit spectroscopic, electrochemical or magnetic properties which are remarkably different from those of the free macrocycle.

1.4 Some applications

1.4.1 Enzyme modelling and catalysis

Macrocyclic ligands based upon the porphyrin ring system and close structural analogues such as corrins are widespread in biological systems.[10] Iron complexes of these ligands are involved in processes as divergent as electron transport (ferredoxins),[17] dioxygen transport and storage (hemoglobin and myoglobin, respectively)[11,12] and enzymatic catalytic processes (cytochrome P_{450}).[15] An elaborate model of cytochrome P_{450} based on an iron porphyrin with an attached alkanethiolate arm that can form a hydrogen-bonded dioxygen adduct has been recently reported by Naruta and co-workers.[92] In this model there is a hydrophobic cavity surrounded by bulky residues on each side of the heme plane. In one of the cavities the alkanethiolate group co-ordinates axially to the central ion and is sterically protected from aerobic oxidation. On the other side, two hydroxy groups oriented toward the centre of the cavity above the heme form a hydrogen bond with the bound dioxygen. The hydrogen bond stabilises this adduct (Figure

1.12a) and has significance for dioxygen binding and activation in cytochrome P_{450}.

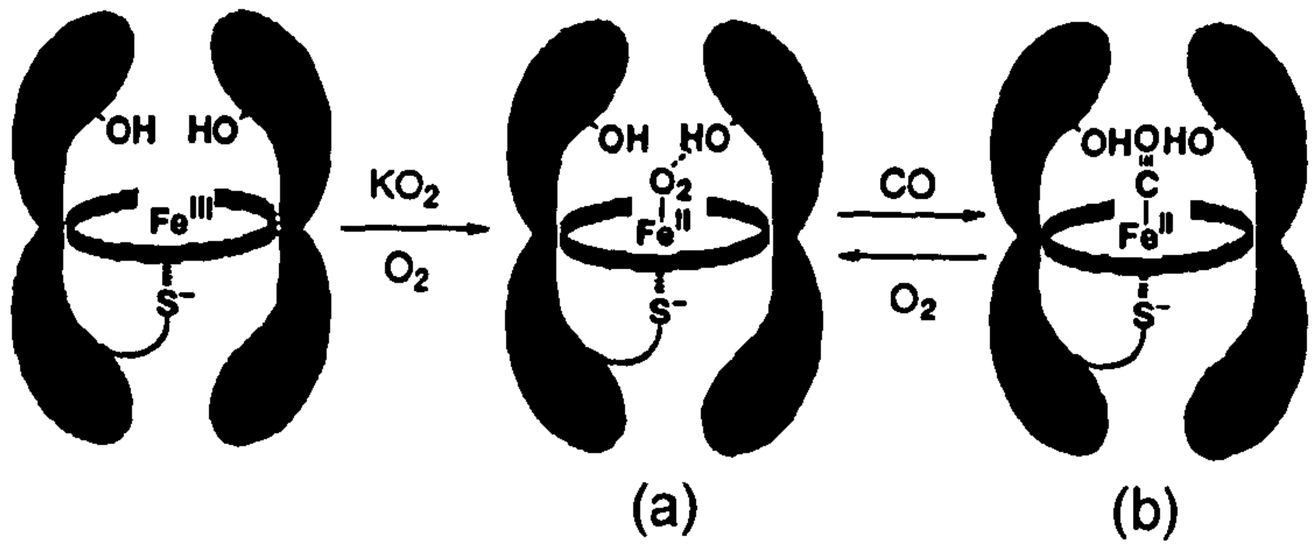

Figure 1.12 Scheme for the formation of (a) the hydrogen-bonded adduct and (b) the non-hydrogen bonded CO adduct.[92]

Macrocyclic complexes have been widely used as models for the active site of metalloenzymes because they can provide a similar co-ordination geometry and therefore analogous spectroscopic, electrochemical and, in multinuclear systems, magnetic properties of the metallobiosite. The objective is often not only the reproduction of the chemical environment (a structural model) but also the synthesis of a low molecular weight model, which has catalytic function similar to the enzyme (a functional model). The active site of alkaline phosphatase contains two Zn^{II} ions with different co-ordination environments and separated from each other by about 4 Å.[93] This enzyme hydrolyses phosphate monoesters by using two co-operative Zn^{II} ions and a serine group near the active centre. The phosphate ester, co-ordinated by Zn^{II} ions, is initially attacked by the deprotonated serine, which therefore plays an important role in the hydrolytic process.[94] A large macrocyclic ligand with an attached hydroxyethyl pendant arm that can act as the vicinal serine group has recently been used as a model of this enzyme.[95] This ligand forms a binuclear Zn^{II} complex with the alkoxy pendant arm bridging two five co-ordinate Zn^{II} ions separated by 3.54 Å (Figure 1.13). At slightly alkaline pH the

complex contains both a Zn^{II}-bound alkoxide and a Zn-OH nucleophilic function and promotes the hydrolysis of phosphate monoesters with high rate constants.[95]

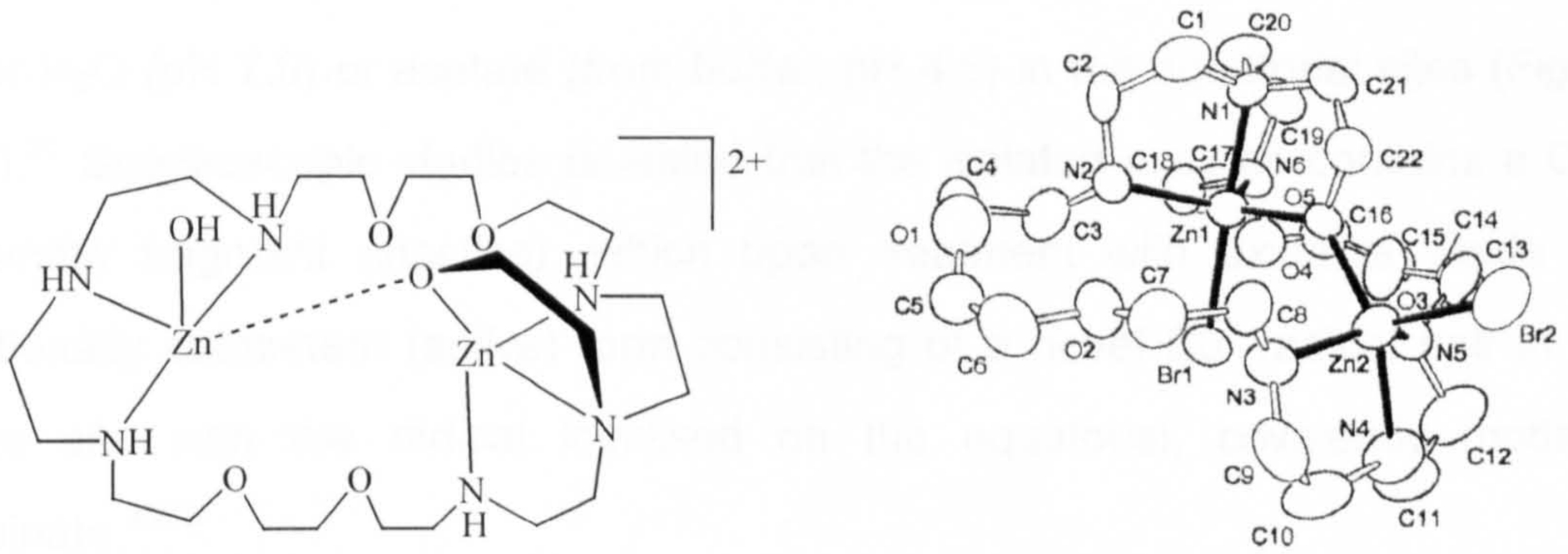

Figure 1.13 Active form of the di-zinc^{II} complex of [30]aneN_6O_4 bearing a hydroxyethyl pendant arm (L) and crystal structure of the $[Zn_2(L)Br_2]^+$ cation.[95]

Another enzyme successfully modelled by using macrocyclic ligands is *galactose oxidase*, a fungal enzyme containing a mononuclear copper active site

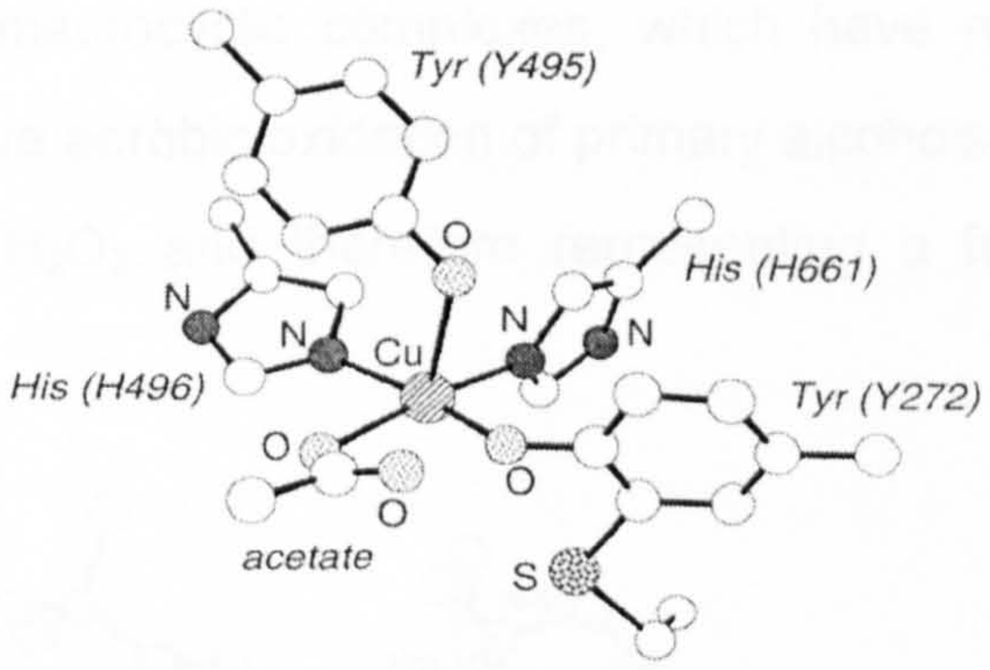

(a)

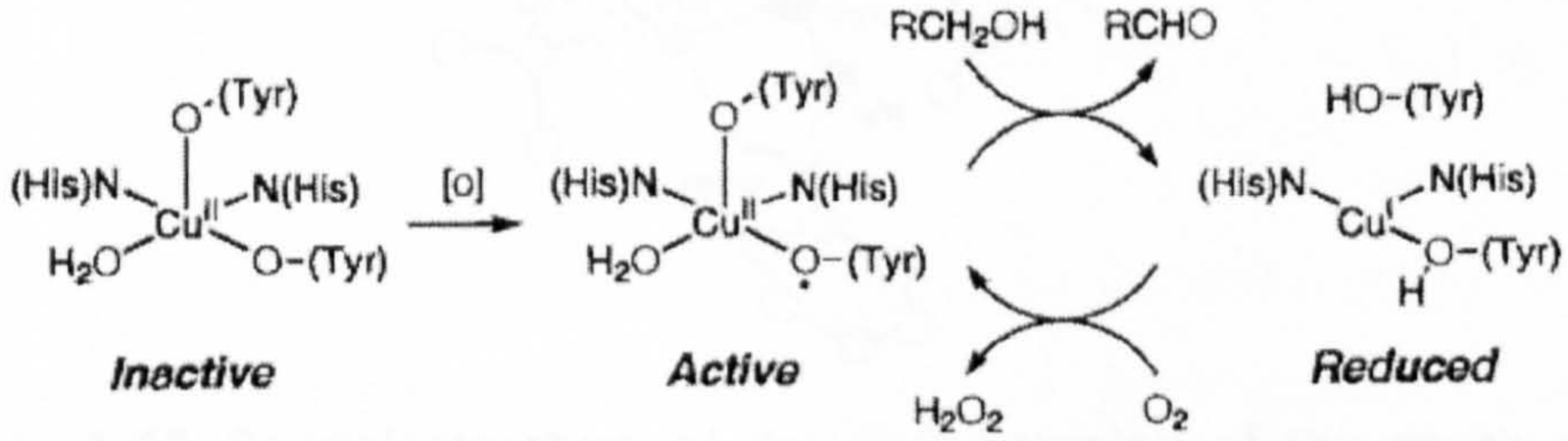

(b)

Figure 1.14 (a) The active site of galactose oxidase at pH 4.5 as determined by X-ray crystallography[97] and (b) the postulated catalytic mechanism.

that effects the two-electron oxidation of primary alcohols to aldehydes.[96] In the active site the Cu^{II} is square pyramidal with a tyrosinate (or tyrosine) ligand weakly bound in the axial position and two histidine imidazoles, a second tyrosinate and either H_2O (pH 7.0) or acetate (from buffer, pH 4.5) in the equatorial sites (Figure 1.14).[97] Spectroscopic studies revealed that the isolated enzyme contains a Cu^{II}-tyrosinate fragment (inactive), which upon treatment with oxidants yields the functionally competent (active) form consisting of a novel Cu^{II}-radical pair in the active site with the radical localised on the equatorial, covalently modified tyrosinate.[96,98]

Several Cu^{II} complexes of [9]aneN_3 derivatives with one and two phenolate arms have been synthesised as models of galactose oxidase and also several complexes with the Cu^{II}-phenoxyl radical analogous to the active enzyme have been prepared *via* electrochemical and chemical means.[99-101] These have shown the ability to oxidise primary alcohols to aldehydes but without the production of H_2O_2, thereby failing to give a complete catalytic cycle.[99] More success has been obtained with non-macrocyclic complexes, which have recently been shown to catalyse the selective aerobic oxidation of primary alcohols yielding aldehydes and one equivalent of H_2O_2 and therefore representing a functional model of the enzyme.[102]

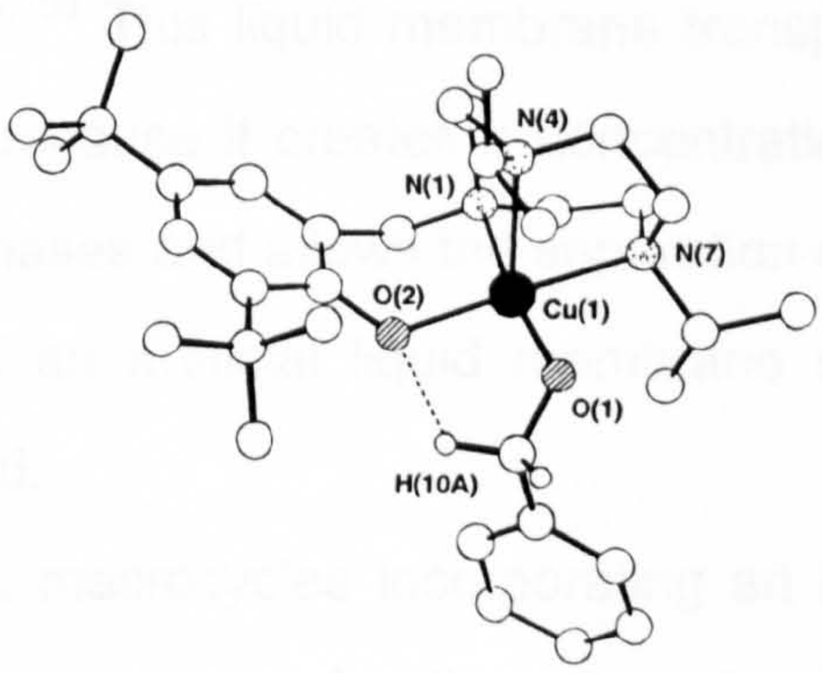

Figure 1.15 Crystal structure of the Cu^{II} complex of the mono-phenolato derivative of [9]aneN_3 showing a possible transition state in the catalytic process.[100]

Macrocyclic complexes can also be used as heterogeneous catalysts as has been shown for the Mn^{II} complex of a [9]aneN_3 pendant arm derivative immobilised on an amorphous SiO_2 surface[103] (Figure 1.16). This heterogenised Mn oxygen-transfer catalyst displays high activity for the selective oxidation of α-olefins to epoxides with high conversion and high Mn turnovers.[103]

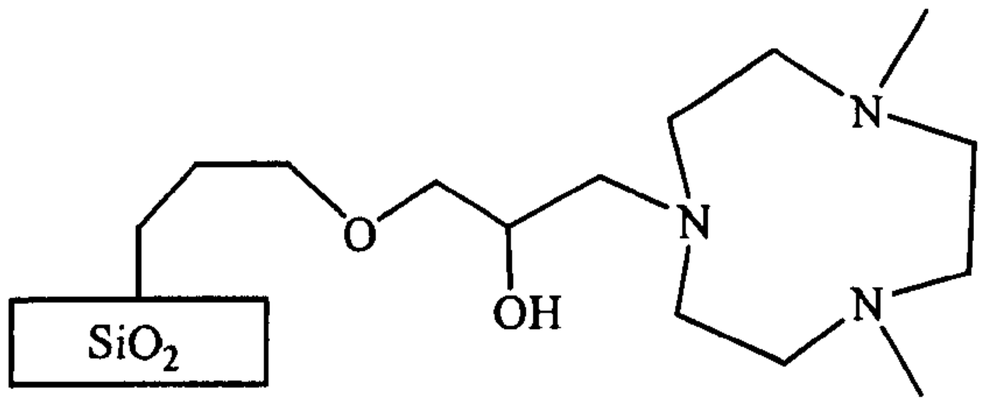

Figure 1.16 Derivative of [9]aneN_3 whose Mn^{II} complex has been used for selective alkene oxidation with H_2O_2.[103]

1.4.2 Ionophores and sensors

The ability of macrocycles to bind specifically to one cation in preference to others makes them ideal for the isolation of chemical species that are otherwise difficult to separate.[31,65] When a macrocycle is selective for a specific cation, it can be employed for separation of the metal ion, either by solvent extraction into organic phases or by membrane transport from an aqueous source phase through an organic membrane phase containing the macrocyclic ligand into an aqueous receiving phase.[104,105] This liquid membrane transport is a very good method for cation separation because it creates a concentration gradient of cationic species across the liquid phases and allows the separation of specific metal ions. In Figure 1.17 a scheme of an artificial liquid membrane system for active transport of cations is presented.

In particular, macrocycles incorporating an ionizable group as a side arm allow the rapid incorporation of cations from the basic aqueous phase into the organic phase and their rapid release to the acidic aqueous phase.[105] Moreover,

the presence of the pendant arm can enhance the selectivity by formation of a three dimensional cavity where the cation can be encapsulated.[106] At the interface between the basic aqueous phase and the organic membrane, the ligand forms a complex with a specific cation; this cation is then released into the acidic aqueous phase by protonation of the ionizable site. In this way, while the metal ions are transported through the liquid phases, a back gradient of protons that provides the necessary energy for the process is created.

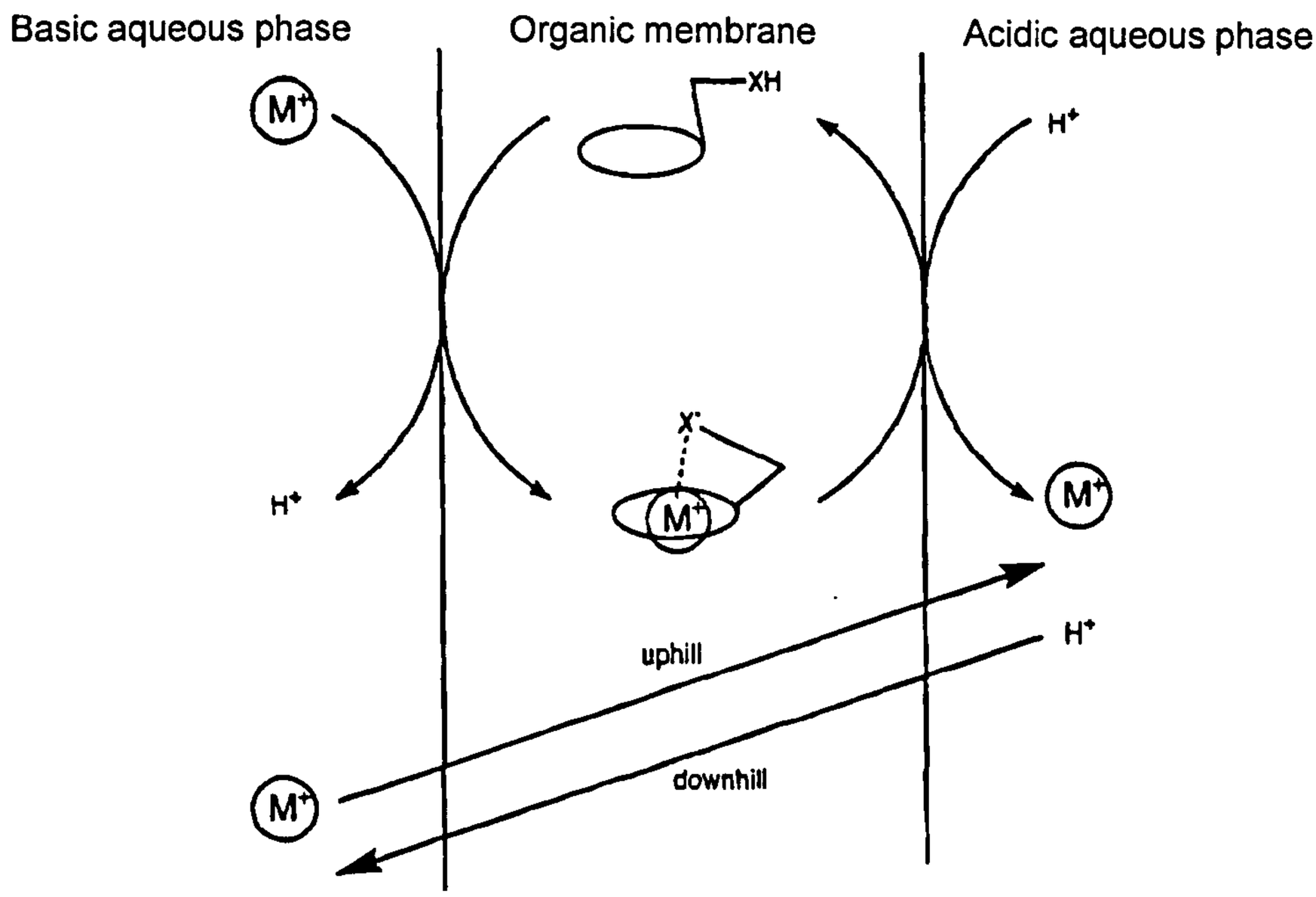

Figure 1.17 Liquid membrane system for active transport. XH is an ionizable group.[105]

Crown ether derivatives have been widely used for this membrane transport and, when a carboxylic or alkylphosphoric side arm has been attached to the macrocycle, they have proven to be particularly effective as selective carriers.[105,106] Also, when the side arm is not an ionizable group, the transport of the metal cation can be performed by providing a lipophilic counter ion (for example, hexadecanoic acid) in the organic phase which, after proton loss to the aqueous source phase, allows neutralisation of the metal cationic charge. In this

manner the need for uptake of lipophobic counter anions into the organic phase can be avoided.[107] Figure 1.18 shows two examples of ionophores studied for the transport through a liquid membrane system: one crown ether bearing an ionizable group[106] and a mixed oxa-aza macrocycle with a pyridylmethyl pendant arm attached.[107]

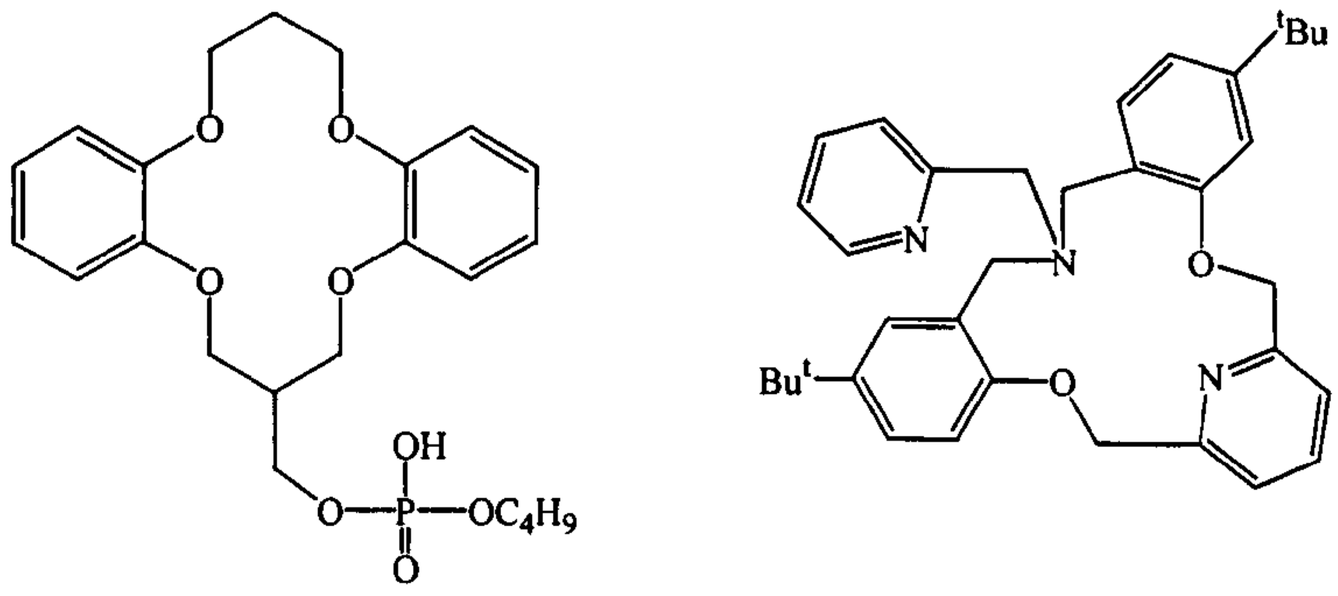

Figure 1.18. Two examples of macrocycles bearing a pendant functional group used in transport through a liquid membrane system.[106,107]

Industrially, the separation of metal ions using macrocyclic ligands can be achieved by covalently attaching the ligand to solid polymeric matrices which can be packed into chromatographic columns.[83,104] The actual separation is achieved by passing the aqueous metal ion solution through the column containing the supported ligand. In this respect, crown ethers with a silica-bound pendant arm or silica-bound mixed O/S macrocycles with selectivity towards specific metal ions have been successfully used in the separation of Hg^{II}, Cd^{II}, Zn^{II}, Pb^{II}, Ag^{I} from aqueous solutions, thereby providing a useful tool in treating heavy metal poisoning in the environment.[83,84]

Macrocycles bearing the appropriate pendant arm can also be used as sensors: these systems undergo structural changes resulting in a physically or chemically detectable response upon recognition of a specific substrate or upon the influence of an external stimulus (change in pH, light or electrons). [23-28] Many examples of these responsive systems have been recently developed and one of

them has been synthesised by Nagano and co-workers for the detection of Zn^{II} ions in living cells.[108] For biological applications it is important that the signalling functional group has an excitation wavelength in the visible range, because UV wavelengths may cause cell damage. In this system a substituted fluorescein group is attached to a macrocyclic polyamine (Figure 1.19), which strongly

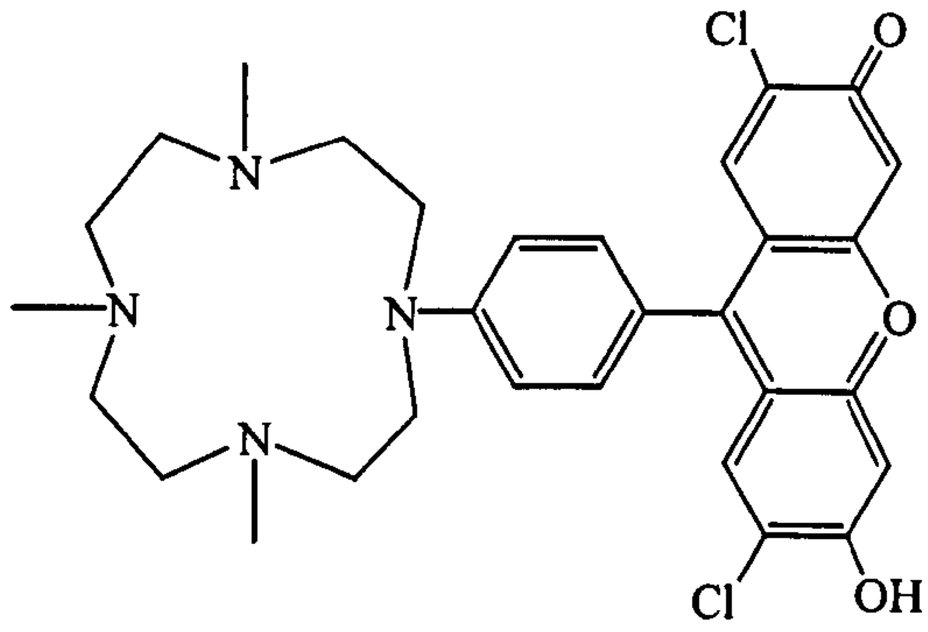

Figure 1.19 Macrocyclic ligand with a fluorescein pendant group used as sensor selective for Zn^{II} ions.[108]

complexes transition metal ions such as Zn^{II} and Cu^{II}. When an amino group is attached to the phthalic ring of fluorescein, the fluorescence is quenched. Upon complexation of Zn^{II} by the macrocyclic N-donors, the fluorescent intensity of the ligand is increased 26-fold. Remarkably, this behaviour is observed only with Zn^{II} because other cations such as K^{I} and Ca^{II} found at high concentration in cells do not form stable complexes with the macrocyclic ligand, while cations such as Cu^{II} or Fe^{II}, which do form more stable complexes with cyclic polyamines, do not fluoresce possibly because of a quencing mechanism.[108]

This device, like many others containing macrocyclic frameworks, has been designed to operate as a fluorescence switch through photoinduced electron transfer (PET) upon host-guest interaction.[109] Two switch processes can be envisaged: the "on-off" switch where the binding of the target substrate to the receptor may induce an electron transfer from the fluorophore to the receptor

compartment with a subsequent quenching of the fluorescence. And an "off-on" switch that, as in the example just described, gives an enhancement of the fluorescence upon interaction between the host and the guest, due to the inhibition of the electron transfer from the fluorophore to the receptor. Figure 1.20 shows a schematic mechanism for each of these types of switch.[109]

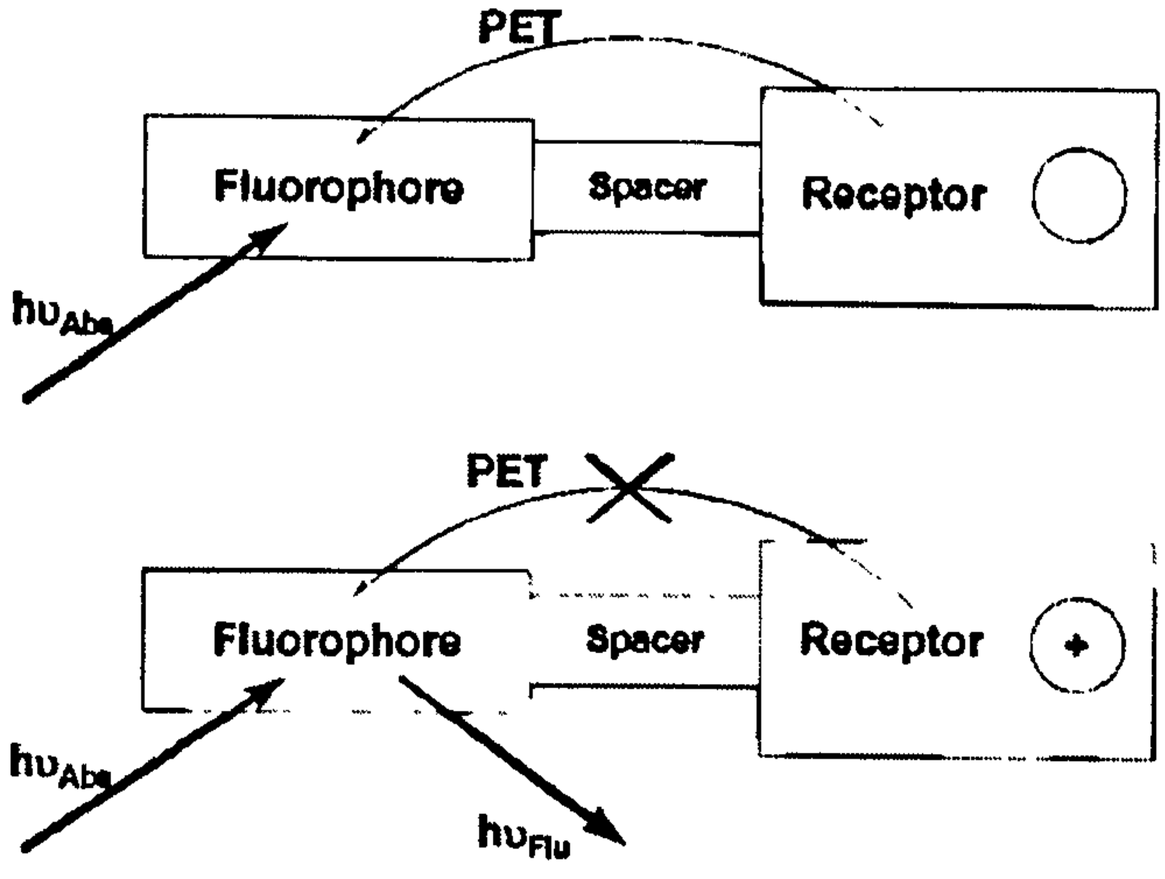

Figure 1.20 Schematic mechanism for the switch device: the system is off (above) and on (below).

Many sensors such as the one reported by Nagano and co-workers[108] have been built by assembling at molecular level the appropriate receptor and signalling group and trying to make them selective for a particular molecule or metal ion.[110] Considering the numerous applications of these molecular devices in many different areas (medicine, biology, material science) this is a growing field that will bring interesting results in future.

Chapter 2

Lanthanides and medicinal chemistry

2.1 Introduction

The lanthanide series formally comprises fourteen metallic elements from ^{58}Ce to ^{71}Lu, with electrons progressively filling the 4f orbital, but normally ^{39}Y and ^{57}La are also considered lanthanides due to their similar characteristics. The elements exhibit similar physical properties throughout the series, with changes tending to occur gradually. One of the most common features of the lanthanides is the "lanthanide contraction", a decrease in ionic radius of the +3 metal ion from La^{III} to Lu^{III}. The explanation of this contraction is that, while 4f electrons are inner electrons and therefore shielded from the surroundings of the lanthanide ion, the 5s and 5p orbitals penetrate the 4f subshell and are thus not shielded from the increasing nuclear charge, contracting as the lanthanide series is traversed from left to right.[56] Moreover, as lanthanides have very small crystal-field effects, the co-ordination polyhedra formed are largely determined by steric effects and the bonds are not directional. Thus, co-ordination numbers between 8 and 10 are common in lanthanide chemistry.[111] Ln^{III} ions behave like typical hard acids: they interact preferentially with hard bases such as fluoride or oxygen rather than with softer bases such as nitrogen, sulphur or phosphorus and they form bonds which are essentially ionic in character. Due to charge neutralisation in the complexation process, the lanthanides prefer carboxylate or phosphonate donor atoms rather than ethereal or alcoholic oxygens.[111] Looking at the thermodynamic stability of lanthanide complexes, Martell and co-workers[68] considered the effect of chelate ring size on the stability of metal complexes as already mentioned in Chapter 1, Section 1.2.3. Five-membered chelate rings are clearly preferred by large metal ions such as lanthanides over six membered ones, and this has been confirmed by simply looking at the differences in stability of the complexes with DOTA and TETA, which have the same number and type of donor atom, the same basicity but different chelate ring sizes (Table 2.1).[112]

Table 2.1 Comparison of the stability constants (log K) of DOTA and TETA complexes with small and large metal ions.[112]

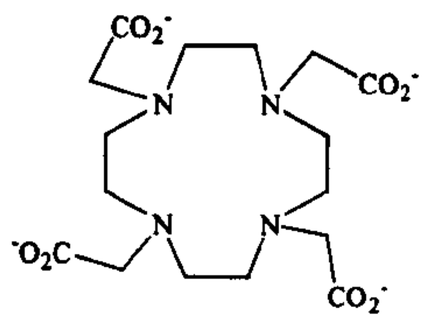

$(DOTA)^{4-}$

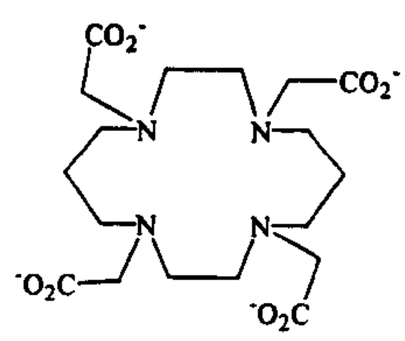

$(TETA)^{4-}$

	Cu^{II}	Ni^{II}	Ca^{II}	Sm^{III}	Gd^{III}	Yb^{III}
Ionic radius (Å)	0.57	0.69	1.00	1.13	1.11	1.03
DOTA	22.21	20.03	17.23	23.04	24.67	25.00
TETA	21.60	19.91	8.32	14.97	15.75	16.55

Certain spectroscopic and magnetic properties of lanthanides make them very useful for a wide range of biochemical and medical applications.[111,113,114] For example, not only has their high paramagnetism been exploited in the design of contrast agents in magnetic resonance imaging (MRI),[21,22] and the high luminescence of Eu^{III} and Tb^{III} complexes used for making fluorescent labels for immunoassay,[115-120] but they have also been studied in photodynamic therapy,[121,122] for the labelling of DNA,[123,124] as radiopharmaceuticals (both as diagnostic and therapeutic agents)[19,113,125] and as chemical shift reagents for determining Na^+ or K^+ ion concentrations in cells and tissues.[126-128]

2.2 Magnetic resonance imaging (MRI)

MRI technique is a very important diagnostic tool in modern medical imaging: it relies upon the observation of the ^1H nucleus of *in vivo* water molecules utilising a radiofrequency pulsed technique not very different from that employed in laboratory NMR spectrometers. MRI instruments employ a gradient magnetic field, allowing ^1H NMR signals to be acquired as a function of three dimensional space, with the final image consisting of a computer-reconstructed signal intensity map of

the spatially encoded ^1H_2O NMR signals. Differentiation between biological tissues is the primary objective for imaging use in clinical diagnosis, and depends on the fact that the ^1H signal intensities vary according to the type of tissue.[111,129,130]

Most human soft tissues contain approximately the same amount of water and therefore cannot be differentiated on the basis of water content.[129] However, the T_1 (longitudinal or spin-lattice) and T_2 (transverse or spin-spin) relaxation times of water protons vary markedly with tissue type, and, therefore, may be used as the source of contrast in MR images.[129,130] Unfortunately, these relaxation times are relatively slow, with $T_1 \sim 0.3$ seconds in normal tissue and ~ 0.7 seconds in diseased tissue, and this slowness increases the time required to obtain clinically useful images and degrades the quality of the image.

A great improvement in contrast between healthy and diseased regions in MRI images can be obtained using paramagnetic metal complexes (contrast agents), which effectively shorten the T_1 and T_2 of water protons in tissues.[22,127] Currently, about 35% of the MRI examinations are performed with the use of these contrast agents that, unlike other contrast agents used in X-ray or other clinical imaging studies, are not visualised directly on the NMR image but are detected indirectly by virtue of changes in the proton relaxation behaviour.

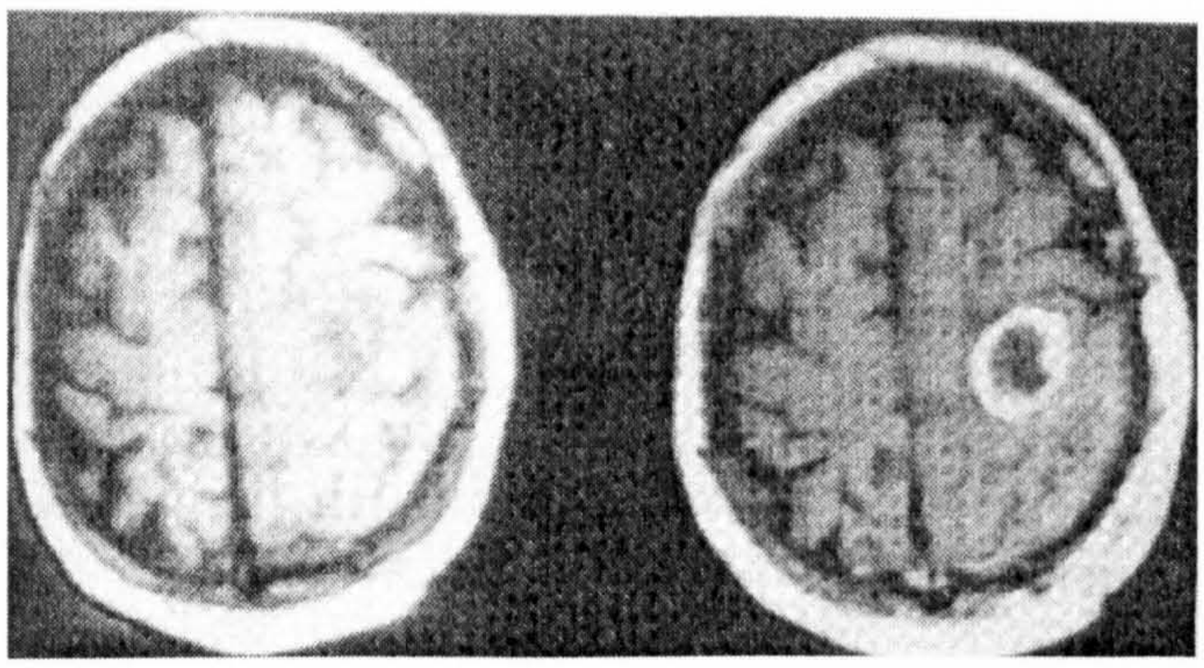

Figure 2.1 Transverse MRI images through a brain of a patient before (left) and 3 minutes after (right) intravenous injection of $[Gd(DTPA)(H_2O)]^{2-}$ showing a tumour.

2.2.1 Gadolinium (III) contrast agents

The lanthanide ion Gd^{III} is by far the most frequently chosen metal ion for MRI contrast agents because it has a symmetric ^8S ground state electronic structure coupled with a large magnetic moment with a long electron spin relaxation time (T_{1e} ~ 10^{-9} s at the magnetic field strengths of interest for MRI applications), two properties that ensure an optimum efficiency for nuclear spin relaxation of the interacting nuclei.[127]

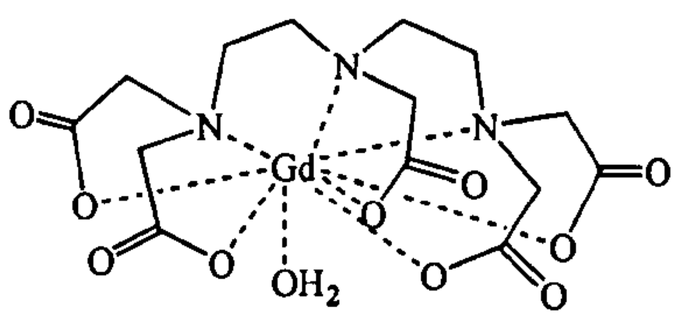

$[Gd(DTPA)(H_2O)]^{2-}$ (Magnevist™)

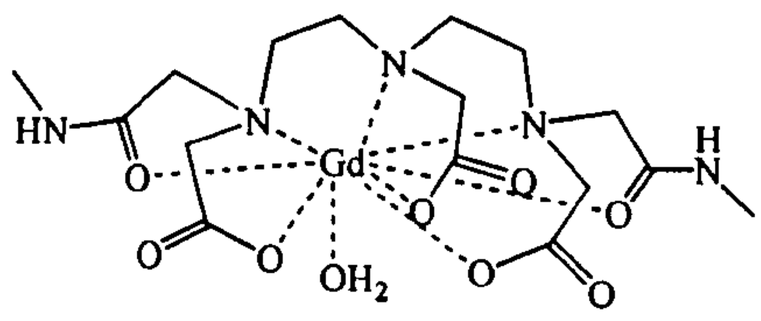

$[Gd(DTPA\text{-}BMA)(H_2O)]$ (Omniscan™)

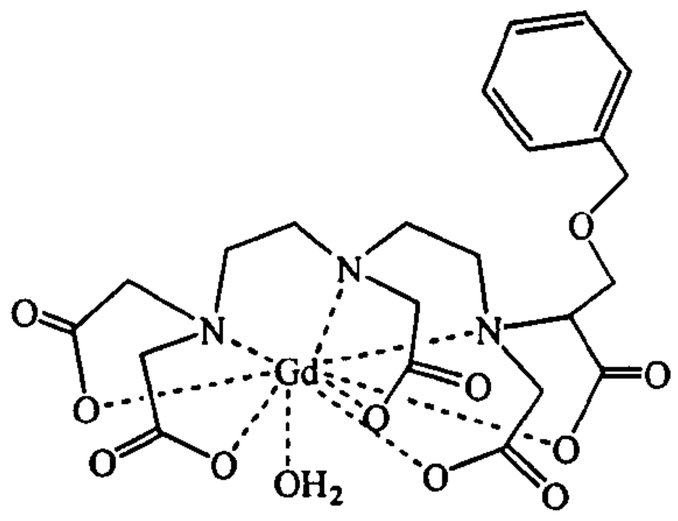

$[Gd(BOPTA)(H_2O)]^{2-}$ (Multihance™)

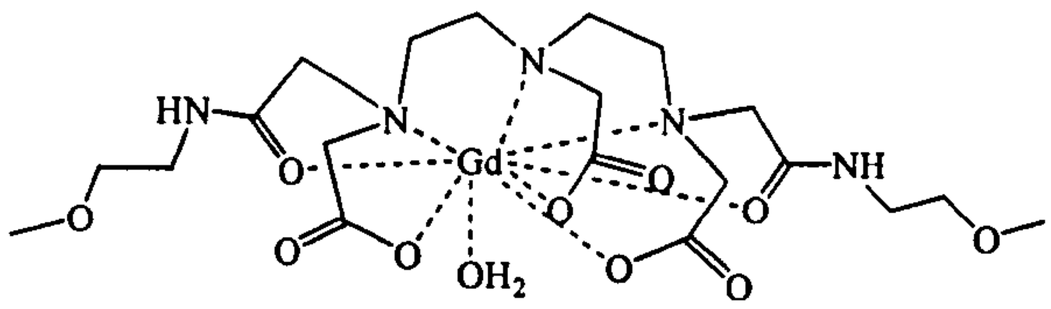

$[Gd(DTPA\text{-}BMEA)(H_2O)]$ (OptiMARK™)

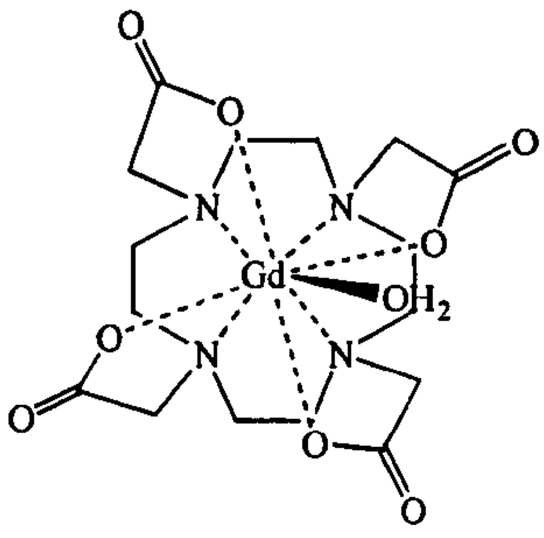

$[Gd(DOTA)(H_2O)]^-$ (Dotarem™)

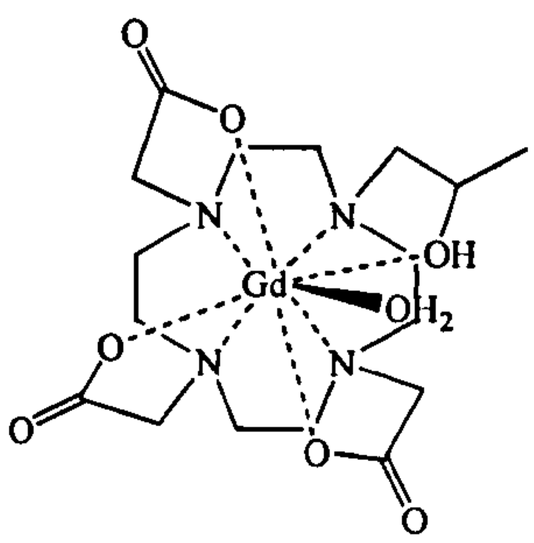

$[Gd(HP\text{-}DO3A)(H_2O)]$ (ProHance™)

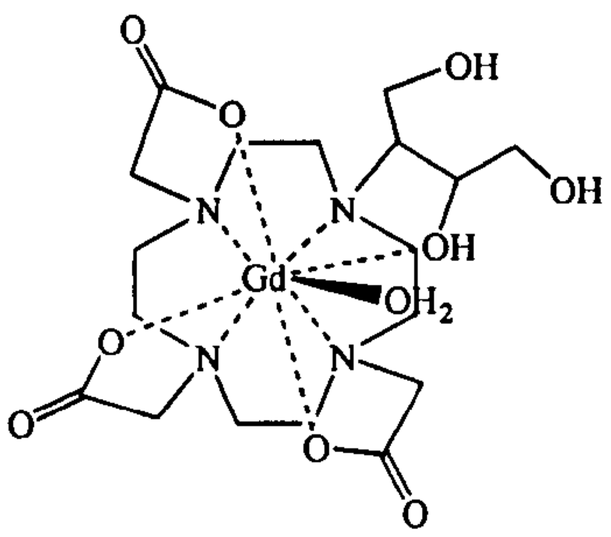

$[Gd(DO3A\text{-}butrol)(H_2O)]$ (Gadovist™)

Figure 2.2 Clinically approved Gd^{III} contrast agents.

Since the free metal ion is very toxic, it must be co-ordinated by a strongly binding ligand that occupies most of the available co-ordination sites. Figure 2.2 shows the clinically approved Gd^{III} contrast agents: all are nine-co-ordinate complexes with eight of the co-ordination sites occupied by the ligand donor atoms and the ninth occupied by a solvent water molecule.[22] The design requirements for a practical, efficient MRI contrast agent can be summarised as follows:[21,22,127]

- *High thermodynamic and kinetic stability* to avoid the release of harmful Gd^{III} ions in the body.
- *Good water solubility*. The solutions used have to be very concentrated.
- *Preferably neutral complexes.* The low osmolality associated with solutions of neutral complexes solutions lessens the discomfort of the injections.
- *High relaxivity*. The relaxivity is an intrinsic property of a paramagnetic complex that characterises its ability to enhance the nuclear magnetic relaxation rates of nearby protons. The relaxivities (r_{1p}) of selected Gd^{III} complexes are reported in Table 2.2.

Administration of Gd-based contrast agents has reached the routine in hospitals and is particularly useful in assessing organ perfusion and any abnormalities in the blood-brain barrier or in kidney clearance. Several other applications, primarily in the field of angiography and tumour targeting, are currently under intense study with the promise of soon being available in clinical practice.[125,131]

2.2.2 Thermodynamic stability and kinetic inertness

Because of the large local concentration of the contrast agent (~ 0.5 mM, roughly 0.5 – 5 g of compound) needed to obtain a 50% increase in the image contrast, strong complexation of the metal by the parent ligand is required to obtain the very low *in vivo* toxicity.[132] Both thermodynamic and kinetic factors are relevant in understanding the release of Gd^{III} from the complex *in vivo*.

Table 2.2 Toxicity, thermodynamic, kinetic and relaxivity data for selected Gd^{III} complexes.[22]

Ligand	LD_{50}[a]	$logK_{GdL}$	$logK^*_{GdL}$[b]	$logK_{sel}$[c] (pH 7.4)	k_{obs} (10^3 s^{-1})	r_{1p}[d] (mM^{-1} s^{-1})
DTPA	5.6	22.46	17.70	7.04	1.2	4.3
DTPA-BMA	14.8	16.85	14.90	9.04	>20	4.4
DTPA-BP	2.8	16.83		5.32		
DOTA	11	25.3	18.33	8.30	0.021	4.2
DO3A	7-9	21.0	14.97	4.13	2.37	4.8
HP-DO3A	12	23.8	17.21	6.95	0.064	3.7

[a] Intravenous LD_{50} in mice, mmol kg^{-1}.

[b] $K^*_{ML} = K_{ML} / (1 + K_1[H^+] + K_1K_2[H^+]^2 + \ldots + K_1K_2K_n[H^+]^n)$, where K_1, K_2, K_n are the stepwise protonation constants of the ligand.

[c] $K_{sel} = K_{ML} / (\alpha_H + K_{CaL}[Ca^{II}] + K_{ZnL}[Zn^{II}] + K_{CuL}[Cu^{II}])$, where $\alpha_H = 1 + K_1[H^+] + K_1K_2[H^+]^2 + \ldots + K_1K_2K_n[H^+]^n$ and $[Ca^{II}] = 2.5$ mM, $[Zn^{II}] = 50\mu M$, $[Cu^{II}] = 1\mu M$ and $[H^+] = 10^{-7.4}$ M (*in vivo* concentrations)

[d] Relaxivities measured at 20 MHz and 25°C (at 40°C for DO3A and HP-DO3A).

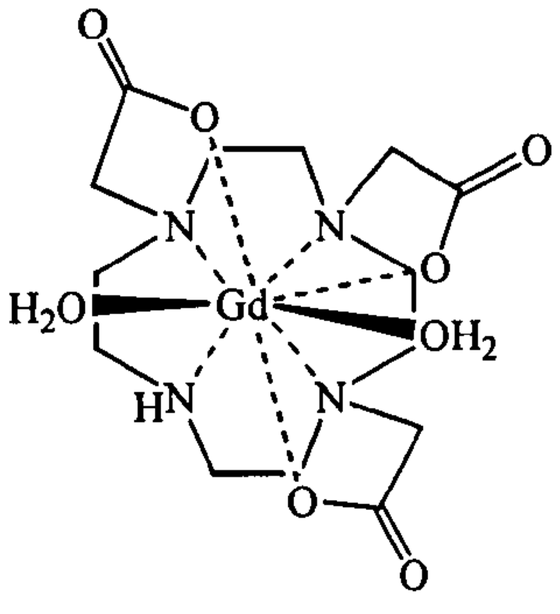

[Gd(DO3A)(H_2O)$_2$]

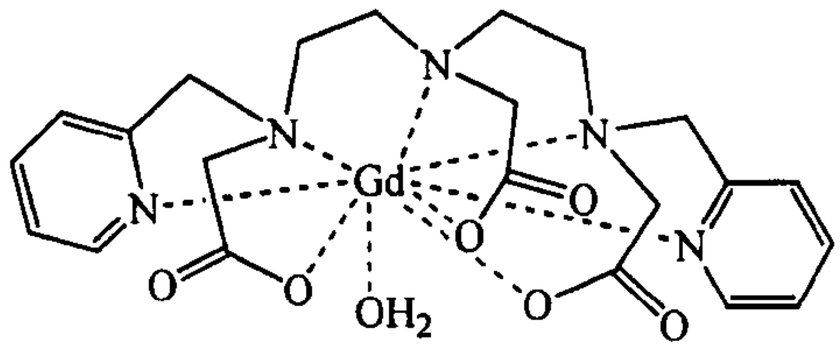

[Gd(DTPA-BP)(H_2O)]

Figure 2.3 Other selected Gd^{III} complexes studied as contrast agents (not clinically approved).

It is widely accepted that at least four parameters should be considered for determining the *in vivo* stability of a Gd^{III} contrast agent:[22,133-135]

- *The thermodynamic stability constant* (K_{GdL}) which is a measure of the presence of free Gd^{3+} or free ligand at equilibrium.
- *The conditional (or pH dependent) stability constant* (K^*_{GdL}) that considers the protonation constants of the ligands and is used to compare the relative thermodynamic stability of different Gd^{III} complexes at the physiological pH of 7.4.[136]
- *The selectivity constant* (K_{sel}) that measures the *in vitro* relative stability in the presence of endogenously available ions such as Ca^{2+}, Cu^{2+}, Zn^{2+} and H^+. At equilibrium, a ligand with a high selectivity factor will bind Gd^{III} strongly even in the presence of the competing metal ions Ca^{II}, Cu^{II} and Zn^{II}.[137]
- *The kinetic lability* (k_{obs}). Acid-catalysed dissociation rates are used as a predictor of *in vivo* loss of Gd^{III}.[136]

Table 2.2 presents all these parameters for selected ligands shown in Figures 2.2 and 2.3 together with the relaxivities and LD_{50} values that are a measure of the *in vivo* toxicity of the Gd^{III} complexes (LD_{50} is the interpolated dose at which 50% of the animals would die).

The thermodynamic and kinetic data can be rationalised by considering the usual factors of the nature and number of donor atoms, the basicity of the ligand, the size of the chelate ring and the pre-organisation and conformation of the ligand. Therefore, macrocyclic complexes are both thermodynamically and kinetically more stable than the corresponding complexes with acyclic polyaminocarboxylates ligands; however, this is not sufficient to explain *in vivo* stability trends.

Comparing the selectivity factors to the LD_{50} values, a good match between high selectivity for Gd^{III} and low toxicity can be found, but in some cases, for example for DTPA-BMA, this contradicts the values obtained for the dissociation rates under acidic conditions.[136,138] It has been observed that the thermodynamic selectivity index can be considered only for those complexes that have sufficiently

fast dissociation and substitution kinetics such that transmetallation occurs during the time in which the Gd^{III} complex remains *in vivo*.[22] Consequently, for the kinetically inert macrocyclic polyaminocarboxylate complexes, the *in vivo* toxicity, although very low, has to be explained by different mechanisms such as physiological changes due to the difference in osmolality between the injected contrast agent and that of the body.[139]

2.2.3 Relaxivity: contribution and parameters

One of the most important terms to evaluate the efficiency of a Gd^{III} complex as a contrast agent is the relaxivity parameter r_{1p} (mM^{-1} s^{-1}), the net increment in the water proton longitudinal relaxation rate per millimolar concentration of the paramagnetic compound.[21] The mechanism of relaxation enhancement involves efficient dipolar magnetic coupling between the proton nuclear spins and the unpaired electrons of the Gd^{III} ions,[140,141] and is described by a model that considers three contributions (Figure 2.4):[142-144] *inner sphere* (is) due to water molecules (*q*) directly bound to the Gd^{III} centre; *outer sphere* (os), which involves all the solvent molecules diffusing by the complex and *second co-ordination sphere* (2^{nd}) due to H_2O molecules hydrogen bonded to polar groups of the ligand:

$$r_1^{obs} = r_{1p}^{is} + r_{1p}^{os} + r_{1p}^{2nd} + r_1^{w}$$

Where r_1^{obs} is the measured relaxation rate and r_1^{w} is the relaxation rate of the solvent in the absence of the paramagnetic complex. Whereas r_{1p}^{os} is rather constant for small-sized Gd^{III} complexes (ca. 2.0-2.5 mM^{-1} s^{-1}), r_{1p}^{is} and r_{1p}^{2nd} are strongly dependent upon the molecular structure and dynamics.[144]

Inner sphere. This term represents the most important contribution to relaxivity and many studies have provided a good understanding of the role played by different relaxation parameters and of their dependence on the structural features of the complexes.[127,143,145-147] High relaxivities at the imaging fields (0.5-1.5 T) may

be obtained in the presence of long reorientational (τ_R) and electronic correlation times (τ_S) and a short exchange lifetime (τ_M) of the co-ordinated water molecule(s). Whereas the modulation of τ_S appears difficult to pursue, long molecular reorientation times may be obtained by decreasing molecular tumbling through increasing the size of the paramagnetic complex.[148,149]

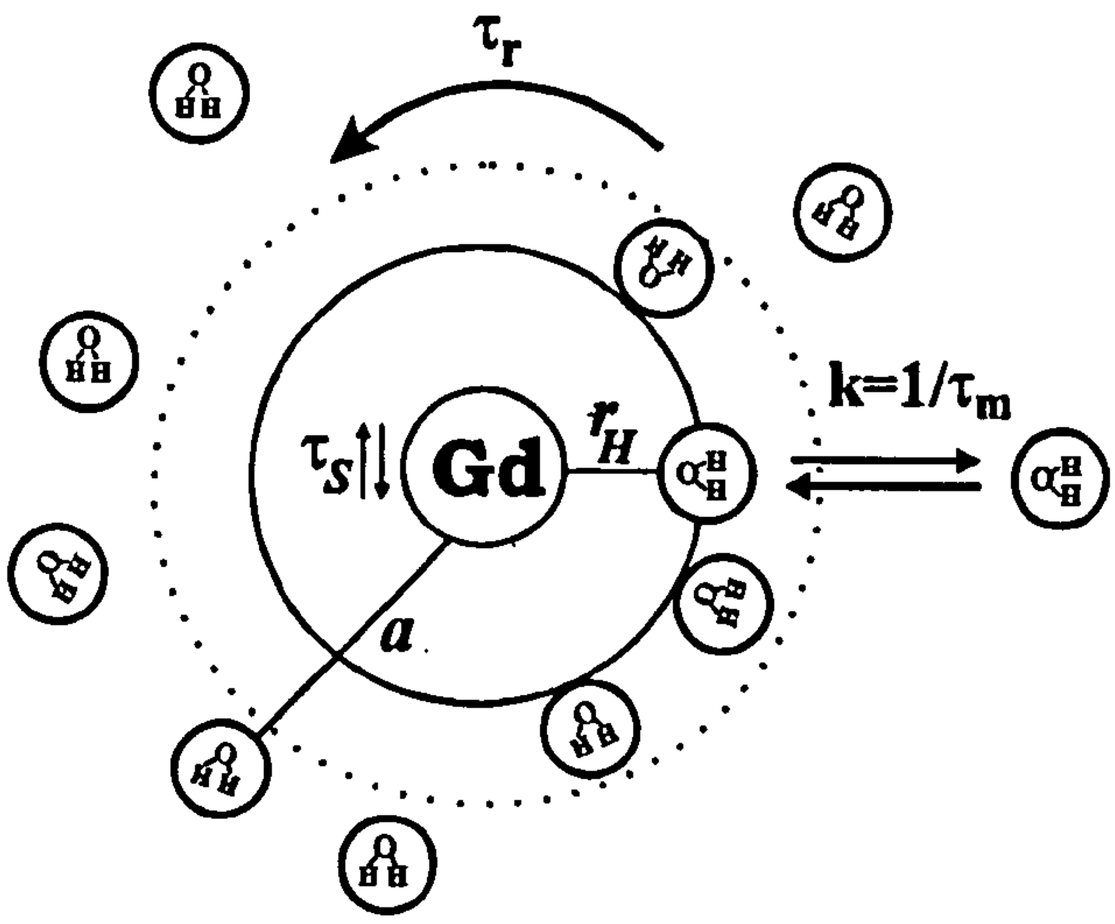

Figure 2.4 Schematic representation of the three types of hydration layers around a Gd^{III} complex and the most relevant parameters of paramagnetic relaxation.

Outer sphere. This contribution accounts for about 40% of the relaxivity of monoaquo Gd^{III} complexes at the imaging fields used, and arises from the modulation of the dipolar interaction by diffusion of the solvent molecules next to the paramagnetic centre. It depends primarily on the distance of closest approach of solute and solvent (*a*) and on the relative diffusion coefficient of solute and solvent (*D*).[141,142]

Second co-ordination sphere. Since the water molecules in the second co-ordination sphere interact with the paramagnetic complex via hydrogen-bonding,

their residence time there can be assumed to be of the order of nanoseconds. This term can then be treated in the same manner as the inner sphere term, and therefore it depends on the number and the distance of the hydrogen-bonded water molecules (q^{2nd} and r) and on the three correlation times (τ_R, τ_M^{2nd} and τ_S).[144,150]

Botta and co-workers[142,151] have recently shown that in $[Gd(DTPA)(H_2O)]^{2-}$ the contribution of the second sphere term is about 10% of the total relaxivity. Figure 2.6 shows the crystal structure of $K_2[Yb(DTPA)(H_2O)]$ where additional water molecules have been localised and assigned to either the outer or the second hydration sphere of the metal ion. In particular, a water molecule is localised at a distance of r_H = 3.28 Å from Yb^{III} strongly hydrogen-bonded to the carboxylate oxygen atoms.[151] With accurate ligand design and by exploiting strong interactions with suitable substrates, Botta and co-workers have achieved a 10-fold increase in relaxivity due only to this second co-ordination sphere contribution.[142,152-154]

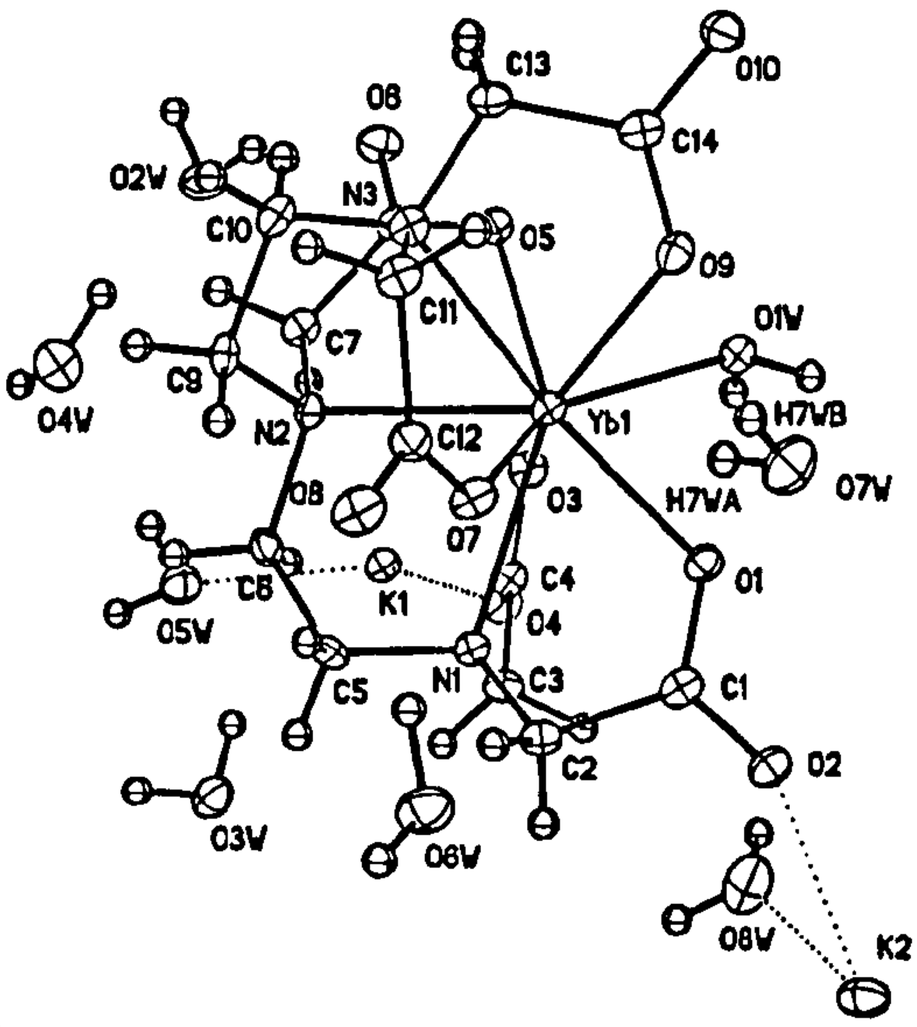

(a)

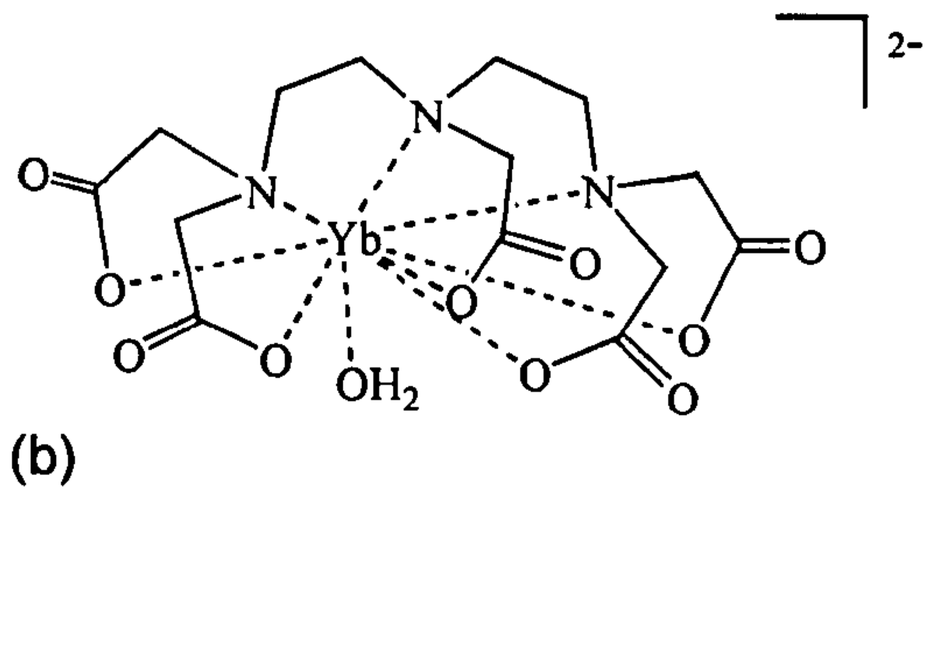

(b)

Figure 2.6 (a) Solid state structure of $K_2[Yb(DTPA)(H_2O)]$ and (b) schematic draw of $[Yb(DTPA)(H_2O)]^{2-}$.

2.2.4 Relaxivity optimisation and targeting specific areas

Current research is directed towards a second generation of Gd^{III} contrast agents, which couple higher relaxivities with an improved ability to target specific regions in the body. The achievement of higher water proton relaxation rates may be pursued through an increase of two parameters: the number of water molecules bound to the paramagnetic centre *q* and the molecular reorientational time τ_R.[22]

Increasing the hydration number offers a large increase in relaxivity, but the obvious drawback is the loss in thermodynamic stability. Notable examples of thermodynamically stable/kinetically inert complexes with $q = 3$ are the Gd^{III} complexes of the three ligands presented in Figure 2.6.[121,155,156]

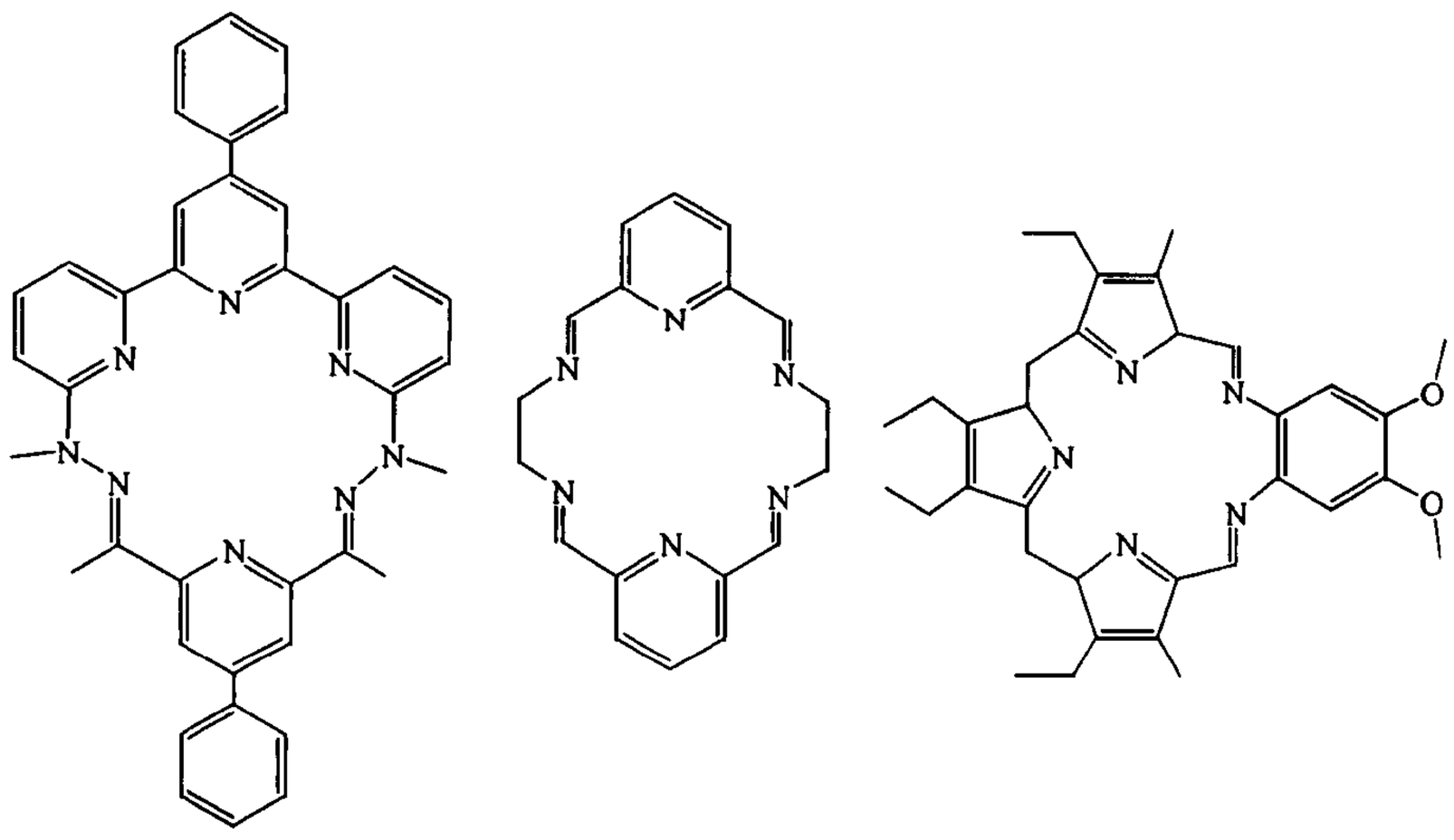

Figure 2.6 Ligands that form Gd^{III} complexes with $q = 3$. From left to right: N6-L1, HAM and texaphyrin.[121,155,156]

In all three cases the metal ion lies in the plane formed by the conjugated ligand with counterions and solvent molecules that complete its co-ordination sphere disposed on either side of this plane. Figure 2.7 shows the crystal structure of the Dy^{III}-texaphyrin complex $\{Dy(Tx)[(C_6H_5)_2PO_4]_2\}$ where the axial co-ordination sites are occupied by two bulky diphenyl phosphate anions (for clarity only the co-ordinated oxygen atoms are shown).[157] The $[Gd^{III}(texaphyrin)]^{2+}$ system has shown

high *in vivo* stability and high relaxivity (r_{1p} = 16.9 $mM^{-1}s^{-1}$ at 25°C and 50MHz), which potentially makes this complex a very efficient contrast agent.[158]

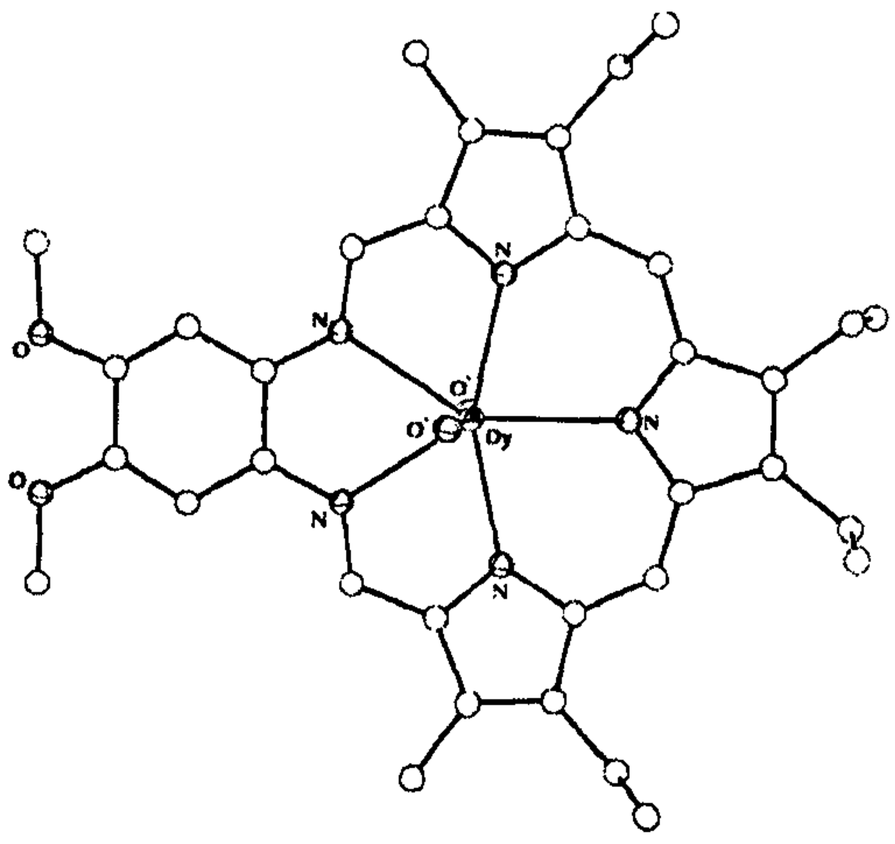

Figure 2.7 Crystal structure of $\{Dy(Tx)[(C_6H_5)_2PO_4]_2\}$. Two diphenyl phosphate oxygens occupy axial co-ordination sites in the complex.[157]

This complex is currently under clinical trials as a radiation sensitizer for brain cancer, an application that exploits the highly delocalised ring structure, not the presence of the metal ion. However, the latter has a secondary benefit: the Gd^{III} ion in the agent also creates an enhanced MRI image of the tumours.[122,159]

The increase in τ_R can be achieved by increasing the molecular weight of the Gd^{III} complexes and this has been pursued in many different ways. One of the most common approaches involves conjugation of functionalised ligands to give polymers,[160,161] dendrimers[162-165] or biological molecules.[166-168] There are several reports of these macromolecular conjugates, but they all exhibit far less than the relaxivity gain expected from the increase in molecular size. This low relaxivity is due to internal flexibility for polymers and to slow water exchange (τ_M) for the more rigid dendrimers.[22,127] An example of a contrast agent covalently attached to a polymer that has also interesting pH dependent characteristics is shown in Figure 2.8.[169]

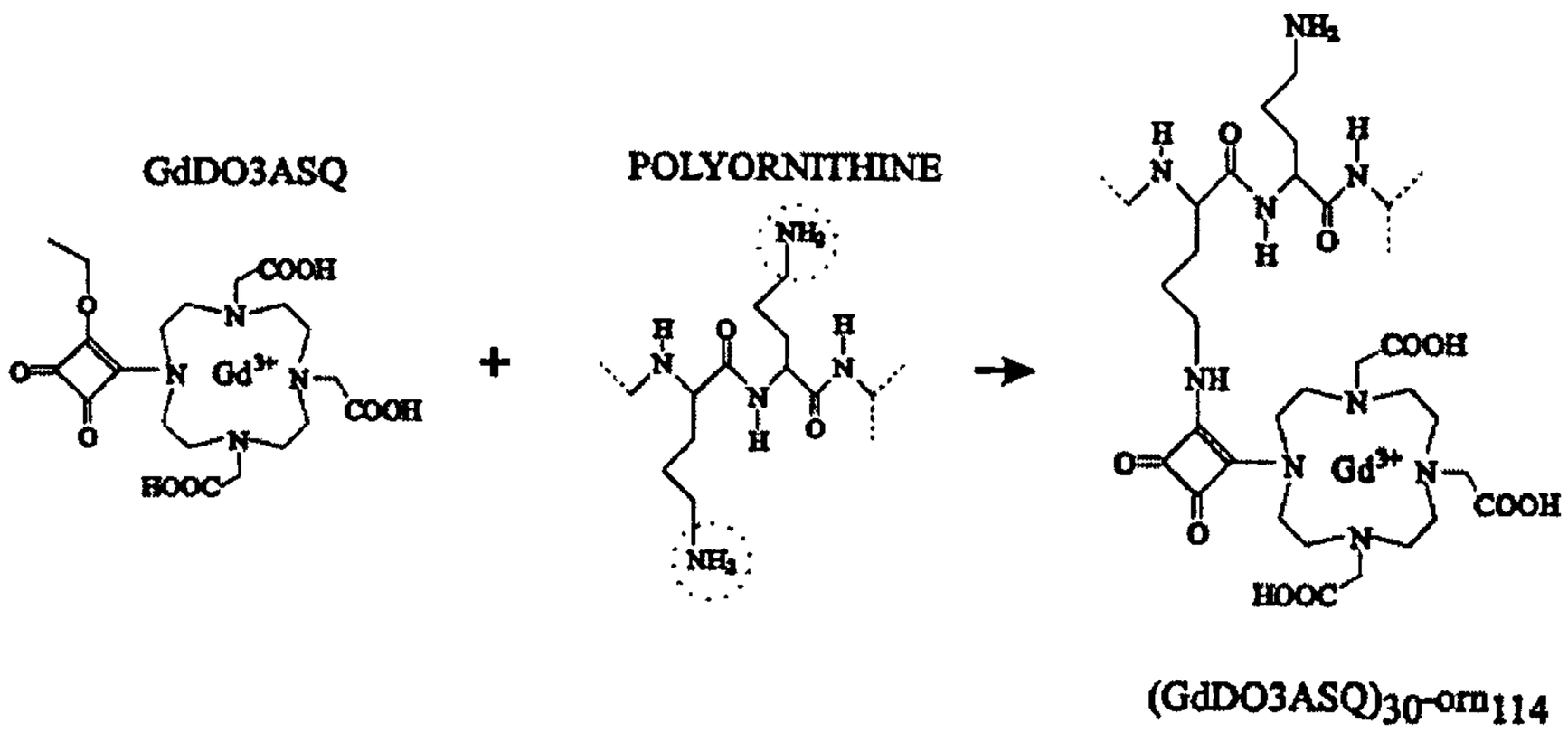

Figure 2.8 Macrocyclic Gd^{III} complex covalently attached to a polyornithine. [169]

This is a macromolecular system containing 30 Gd^{III} chelates bound to a poly(amino acid) chain made of 114 ornithine residues. At pH < 4 the relaxivity has a constant value of 23 mM^{-1} s^{-1} and increasing the pH the solution causes a linear increase of r_{1p} up to 32 $mM^{-1}s^{-1}$ (at pH ≥ 8). At low pH, the highly protonated and hydrated unreacted amino groups give high degree of mobility to the macromolecule, thereby decreasing τ_R and the relaxivity. At alkaline pH a "rigidification effect" occurs due to the formation of intramolecular hydrogen bonds between adjacent peptidic linkages. PH-sensitive Gd^{III} chelates appear particularly interesting since it is known that extracellular regions of certain tumours have quite low pH[170] and therefore these complexes can be used as contrast agents to target specific carcinogenic regions and to report pH changes *in vivo*.[169,171,172]

An alternative and more rewarding route for increasing τ_R may be pursued by forming host-guest non-covalent interactions between suitably functionalised complexes and slowly tumbling substrates (Figure 2.9). This binding causes an increased concentration and retention of the Gd^{III} complex in the area of the receptor molecule allowing it to target the specific region where this protein is

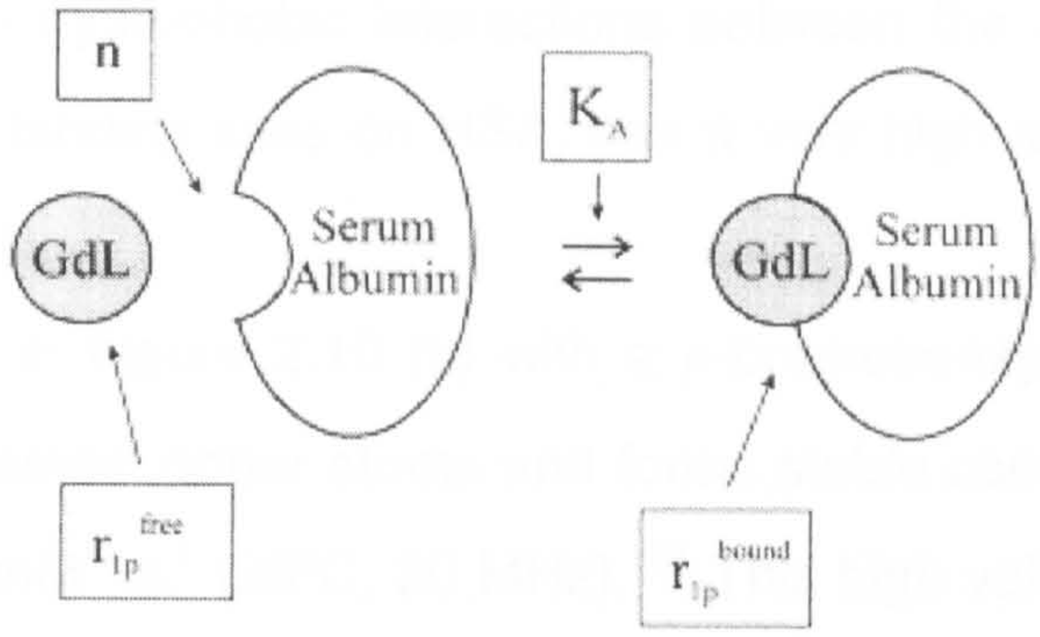

Figure 2.9 Schematic representation of the non-covalent interaction between a Gd(III) chelate $[Gd(L)]^{x+}$ and serum albumin (n is the number of interaction sites, K_A is the association equilibrium constant and r_{1p}^{free} and r_{1p}^{bound} refer to the relaxivity of the free and bound chelate, respectively).

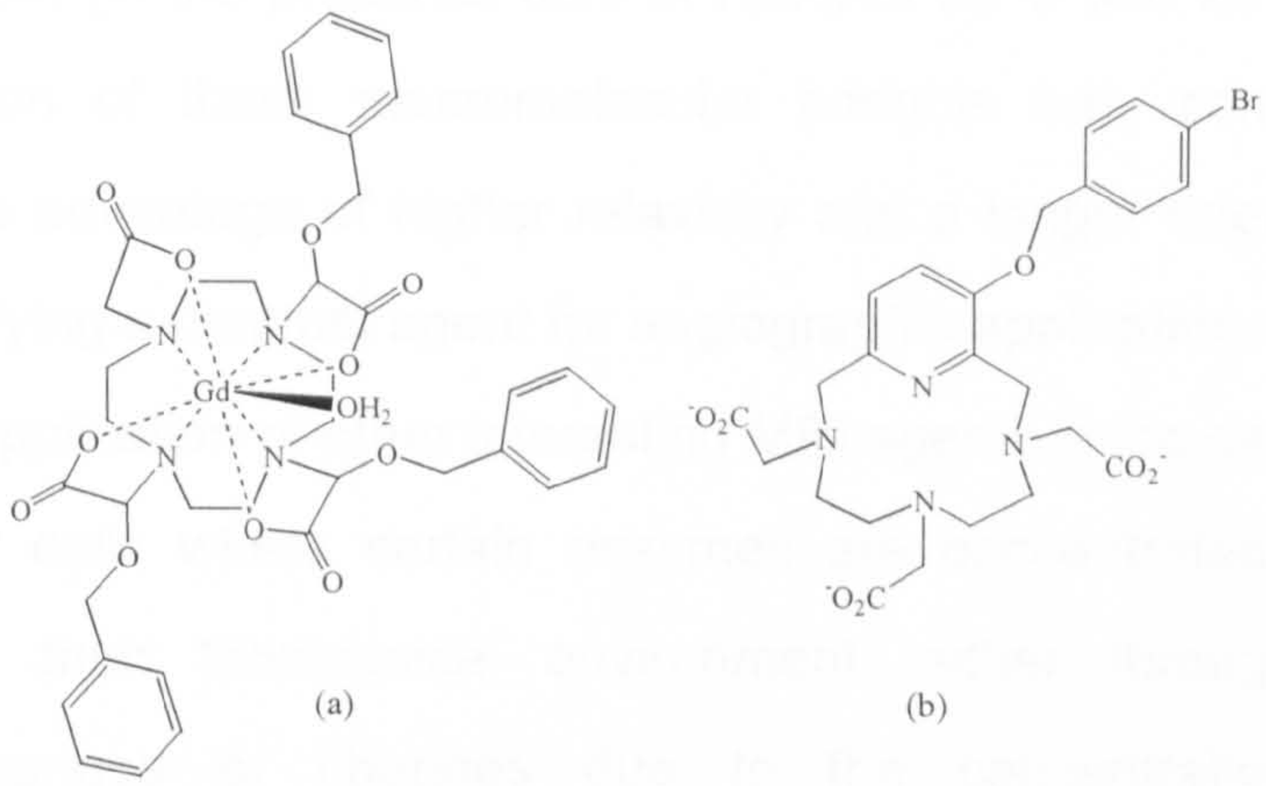

Figure 2.10 (a) $\{Gd[DOTA(BOM)_3\}^{-}$ and (b) 12-membered macrocyclic triacetate ligand with a *p*-bromobenzyloxy substituent on the pyridine ring.

localised.[144,145,148,153,173-175] Also important in this context, are the number of binding sites and the relative binding constant between the protein and the complex. The Gd^{III} complex of a DOTA-like ligand bearing three β-benzyloxy-α-propionic substituents (Figure 2.10 (a), $[DOTA(BOM)_3]^{4-}$)[176] forms quite a stable ($K = 1.7x10^3\ M^{-1}$) adduct with HSA (Human Serum Albumine), a protein present in high concentrations in the blood (~0.67 mM). This macromolecular adduct,

resulting from the hydrophobic interactions between the aromatic groups of the complex and two binding sites on HSA, has a very high relaxivity (56 mM^{-1} s^{-1} at 39ºC and 20 MHz).

The ligand in Figure 2.10 (b) with a *p*-bromobenzyloxy substituent on the pyridine ring has seven donor atoms and forms stable complexes with Gd^{III} with a relaxivity of 8.25 mM^{-1} s^{-1} (25ºC, 20 MHz).[177] This high value is direct evidence of two water molecules co-ordinated to the Gd^{III} centre, but the most interesting result is the formation of an inclusion complex with poly-β-cyclodextrin and the four-fold increase in relaxivity of this adduct. The average binding strength for the paramagnetic inclusion compound is $K = 1.1x10^3$ M^{-1} and the relaxivity measured in blood serum (in the presence also of HSA) at 25ºC and 20 MHz is 32 $mM^{-1}s^{-1}$. The formation of these macromolecular adducts has, compared to the free complex, the advantage of higher relaxivity and a longer retention in blood, both effects qualifying a contrast agent for angiographic applications.[177]

The application of other interesting MRI agents is the detection of regions in the body or cells where certain enzymes are concentrated. Such agents are sensitive to their biochemical environment, either through enzyme-induced relaxivity changes or changes due to the concentration of a particular substance.[22,145,178-180] Meade and co-workers[181] synthesised a Gd^{III} complex

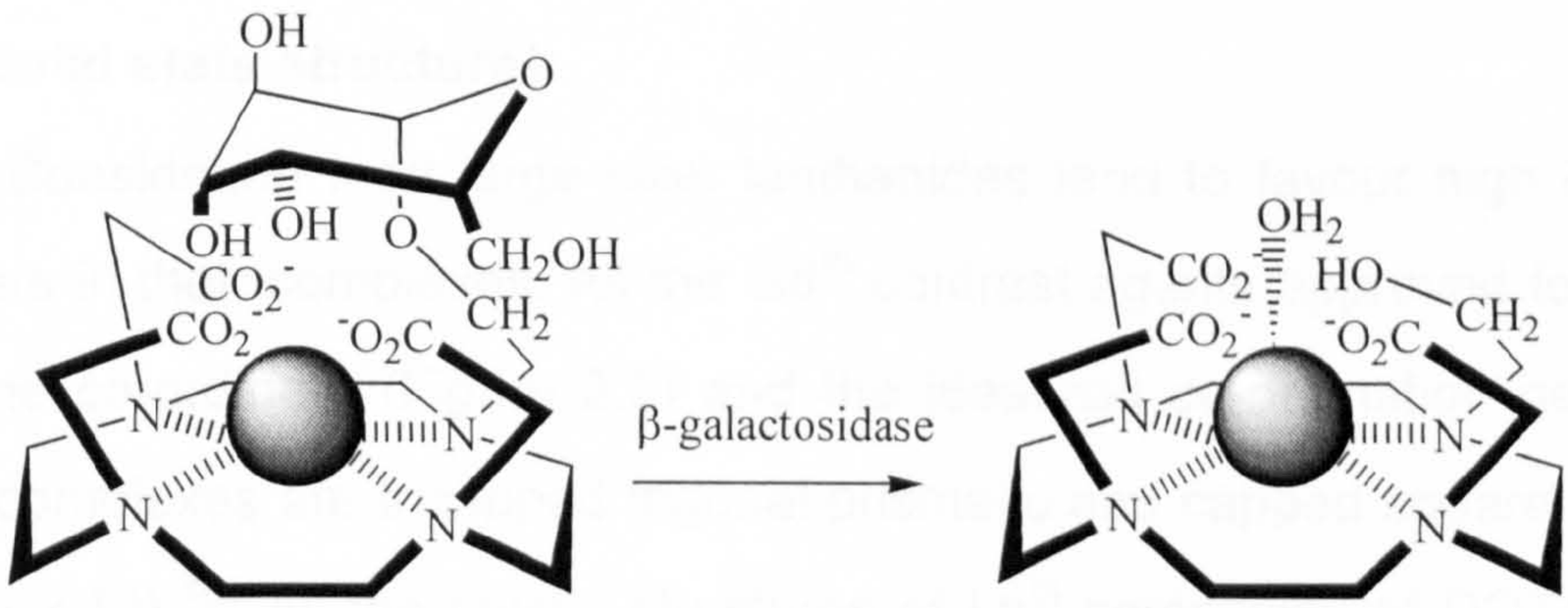

Figure 2.11 MRI contrast agent with two distinct weak (left) and strong relaxivity states (without the galactopyranose side arm, right).

covalently-bound to a galactopyranose residue (Figure 2.11), so that the access of water to the paramagnetic centre is sterically blocked and the relaxivity is low. The presence of the enzyme β-galactosidase cleaves the galactopyranose group increasing *q* from 0.7 to 1.2 and increasing the relaxivity by 20%.

Another example of these bioactivated agents is a Gd-DTPA agent with a sulfonamide group attached (Figure 2.12).[182] Sulfonamides bind quite strongly with carbonic anydrase, which is a zinc enzyme present in various tissues in variable amounts. When the concentration of this enzyme is over 0.5 mM a 1:1 adduct with a binding constant of 1.5×10^4 M^{-1} is formed and the relaxivity increases from 3.5 $mM^{-1}s^{-1}$ to about 25 $mM^{-1}s^{-1}$ (25°C, 0.02 MHz).

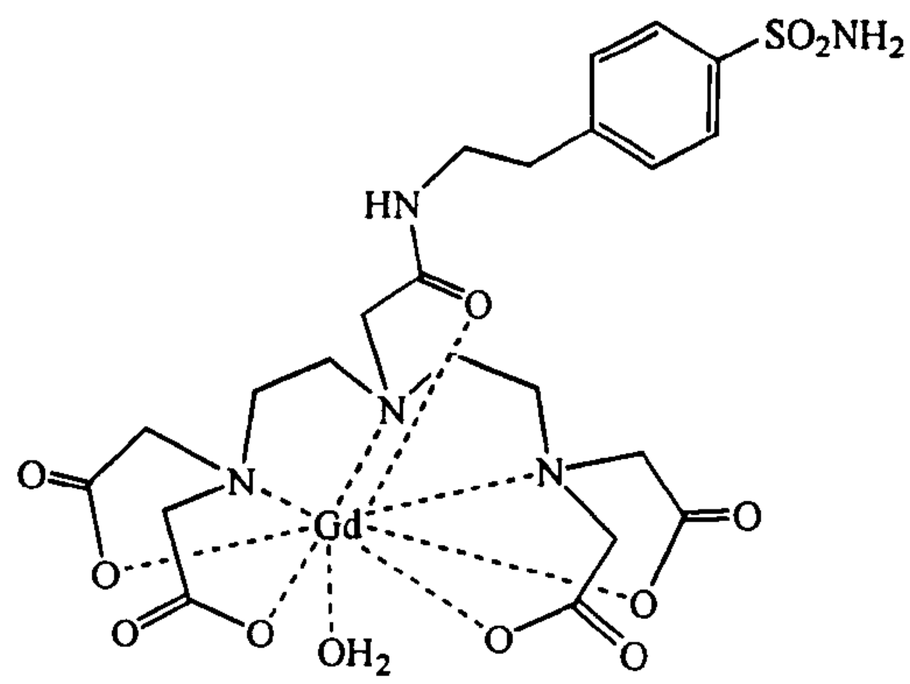

Figure 2.12 [Gd(DTPA-SA)]$^-$, the sulfonamide group strongly interacts with carbonic anydrase.

2.2.5 Solid state structures

Considering their large size, lanthanides tend to favour high co-ordination numbers in their complexes. All the Gd^{III} contrast agents approved for use in MRI are nine co-ordinate (Figure 2.3) and the idealized co-ordination geometries for these complexes are tricapped trigonal prismatic and capped square antiprismatic (Figure 2.13).[183] All the crystal structures of Ln^{III} complexes of DOTA derivatives assume a monocapped square antiprismatic geometry with the macrocyclic ring nitrogens always occupying the basal plane.[22] The water molecule takes the

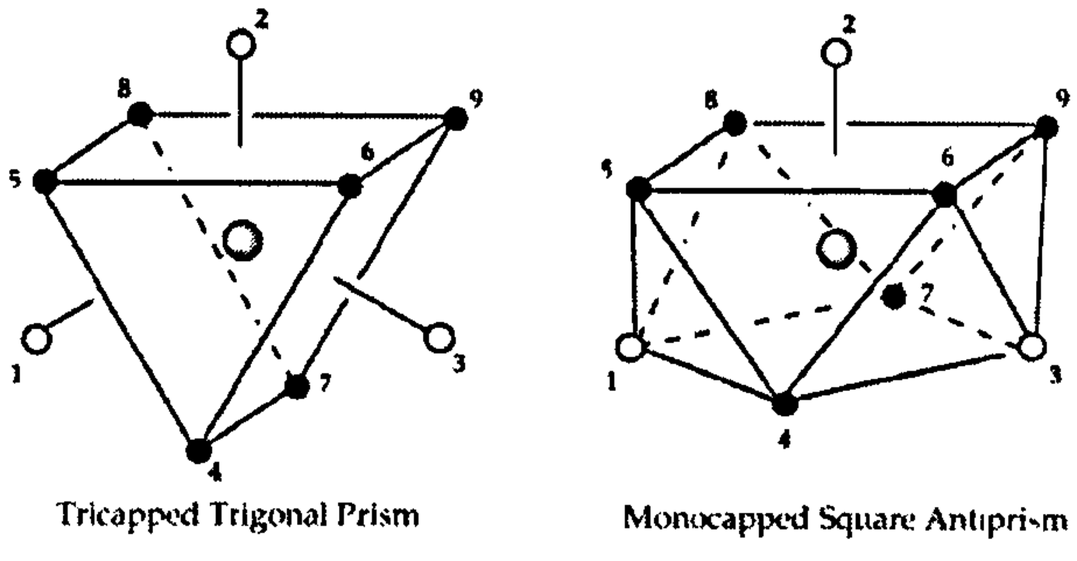

Figure 2.13 Tricapped trigonal prismatic and monocapped square antiprismatic geometries.

capping position while the capped face is surrounded by the other four oxygen donor (carboxylate, amides, etc.). However, the tricapped trigonal prismatic geometry has been identified as the most favourable for a ML_9 co-ordination complex.[184] Indeed, all the Ln^{III} complexes of DTPA-like ligands assume this geometry, albeit in a distorted form. As examples, the crystal structures of $[Gd(BOPTA)(H_2O)]^{2-}$[185] and of $[Eu(DOTA)(H_2O)]^{-}$[186] are presented in Figure 2.14.

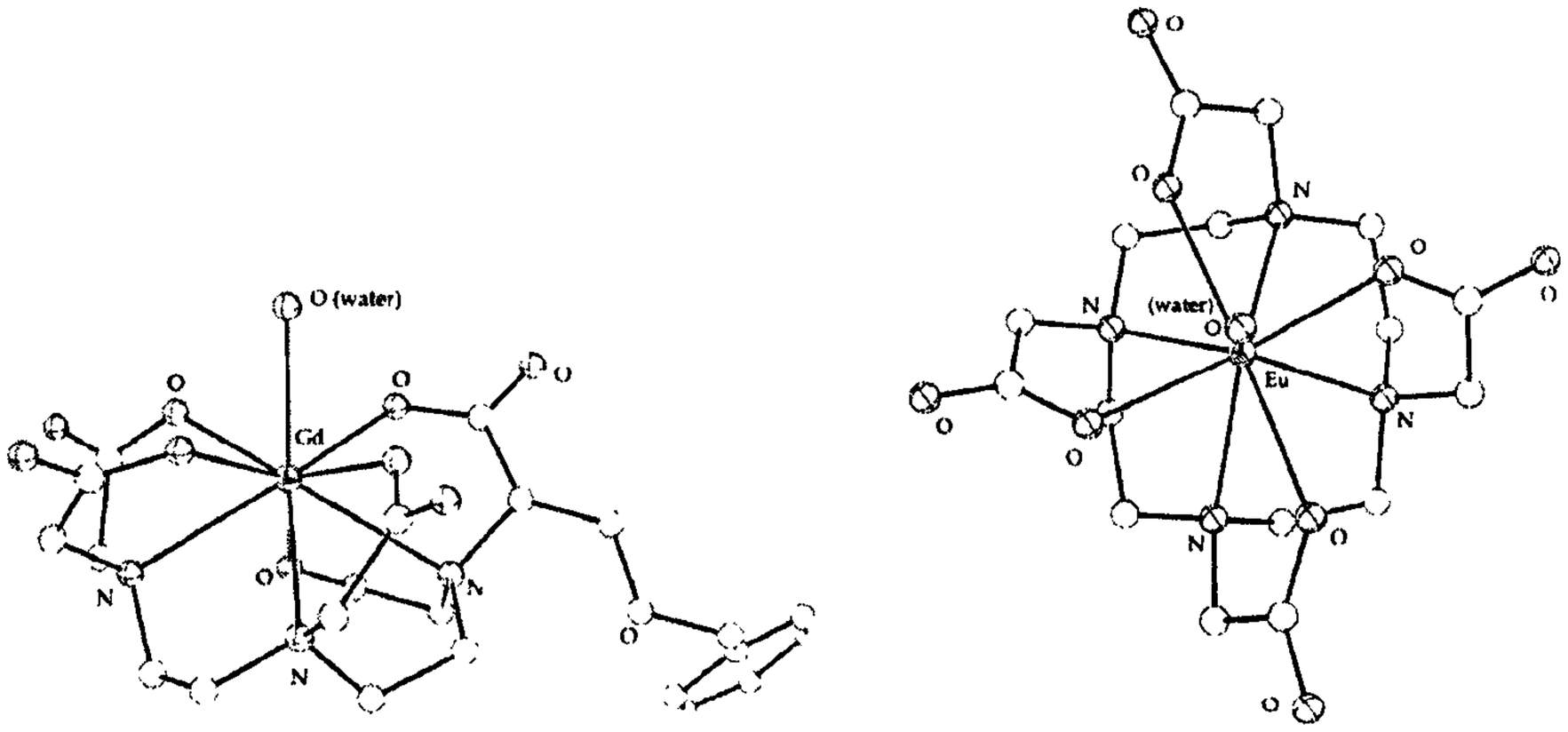

Figure 2.14 Crystal structures of $[Gd(BOPTA)(H_2O)]^{2-}$ (left) and $[Eu(DOTA)(H_2O)]^{-}$ (right).

2.3 Radiopharmaceuticals

Radiopharmaceuticals are drugs containing a radionuclide and are used routinely in nuclear medicine for the diagnosis or therapy of various diseases.[19,125] Diagnostic radiopharmaceuticals require a nuclide that emits γ radiation with a

specific energy and sufficiently long half-life to permit the preparation of the labelled radiopharmaceutical and the detection of the emitted γ-rays (γ-scintigraphy).[125] ^{99m}Tc is the radionuclide most widely used in nuclear medicine, with a great variety of radiopharmaceuticals already approved for determining organ function or assessing disease status by imaging methods,[187,188] but ^{67}Cu, ^{67}Ga and ^{111}In are also important nuclides for diagnostic imaging.[125] Among the lanthanides, ^{169}Yb is the only γ-emitting isotope proposed as a diagnostic agent[189] and ^{86}Y has been studied as positron-emitting (β^+) nuclide for application in PET imaging (Positron Emission Tomography).[190,191]

Radionuclides that decay by β-particle (electron) emission are used most extensively for radiotherapeutic applications because β-particles only travel a short distance in biological tissue and can be delivered to specific tumours causing cell death.[19] Among the lanthanides ^{90}Y, ^{153}Sm and ^{177}Lu are β-emitting isotopes widely used in radiotherapy.[192-194] ^{153}Sm-EDTMP (Figure 2.15) has been successfully used for bone cancer treatment thanks to its high and preferential localisation in bone cancer lesions and its rapid excretion *via* the kidneys.[195-197]

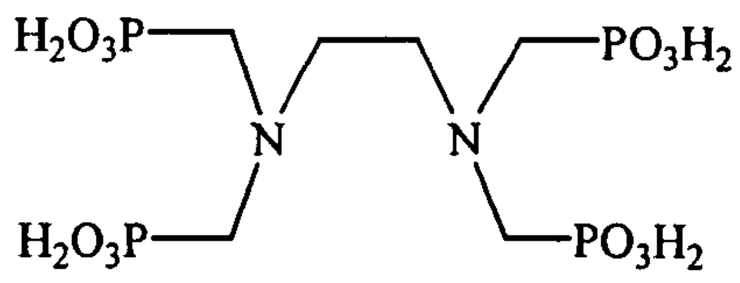

Figure 2.15 Etylenediaminotetramethylenephosphonic acid (EDTMP).

The current research in lanthanide-based radiopharmaceuticals (comprising also ^{111}In and ^{67}Ga radiopharmaceuticals for diagnostic applications) is concentrated on the improvement of bi-functional chelating agents (BFCAs).[19,198,199] The BFCA is made up of two parts: a chelating agent (often DOTA) which tightly binds to the radiometal, and an additional functional group that attaches to a biomolecule.[200] This biomolecule serves as a delivery system for

the radionuclide, allowing a specific localisation of the radioactivity. Two of the most interesting and promising biomolecules used as part of these bi-functional chelating agents are: monoclonal antibodies (biological moieties engineered to bind particular antigens found on the surface of many types of tumours)[19,201] and smaller molecules such as peptides.[19,198,202-204] The macrocyclic ligand DOTA is often employed in nuclear medicine for its ability to form complexes with lanthanides which are both kinetically and thermodynamically highly stable: this prevents the release of the radiometal *in vivo*, which would cause damage to healthy tissue. Interestingly, these BFCAs can be labelled with a variety of radiometals that are useful in different areas of diagnostic or therapeutic nuclear oncology (not only ^{90}Y or ^{177}Lu, but also ^{111}In and ^{67}Ga).[19,125,198,201]

In an example of a BFCA, DOTA can be attached to a peptide (DOTATOC) that is a somatostatin analogue (a hormone containing 14 amino acids) as shown in Figure 2.16.[205] In many human tumours, somatostatin receptors are found in large numbers, therefore targeting these receptors with a radionuclide-labelled somatostatin analogue can improve the image ([^{67}Ga-DOTATOC] for diagnosis) or efficiently treat tumours ([^{90}Y-DOTATOC] for therapy).[205-208]

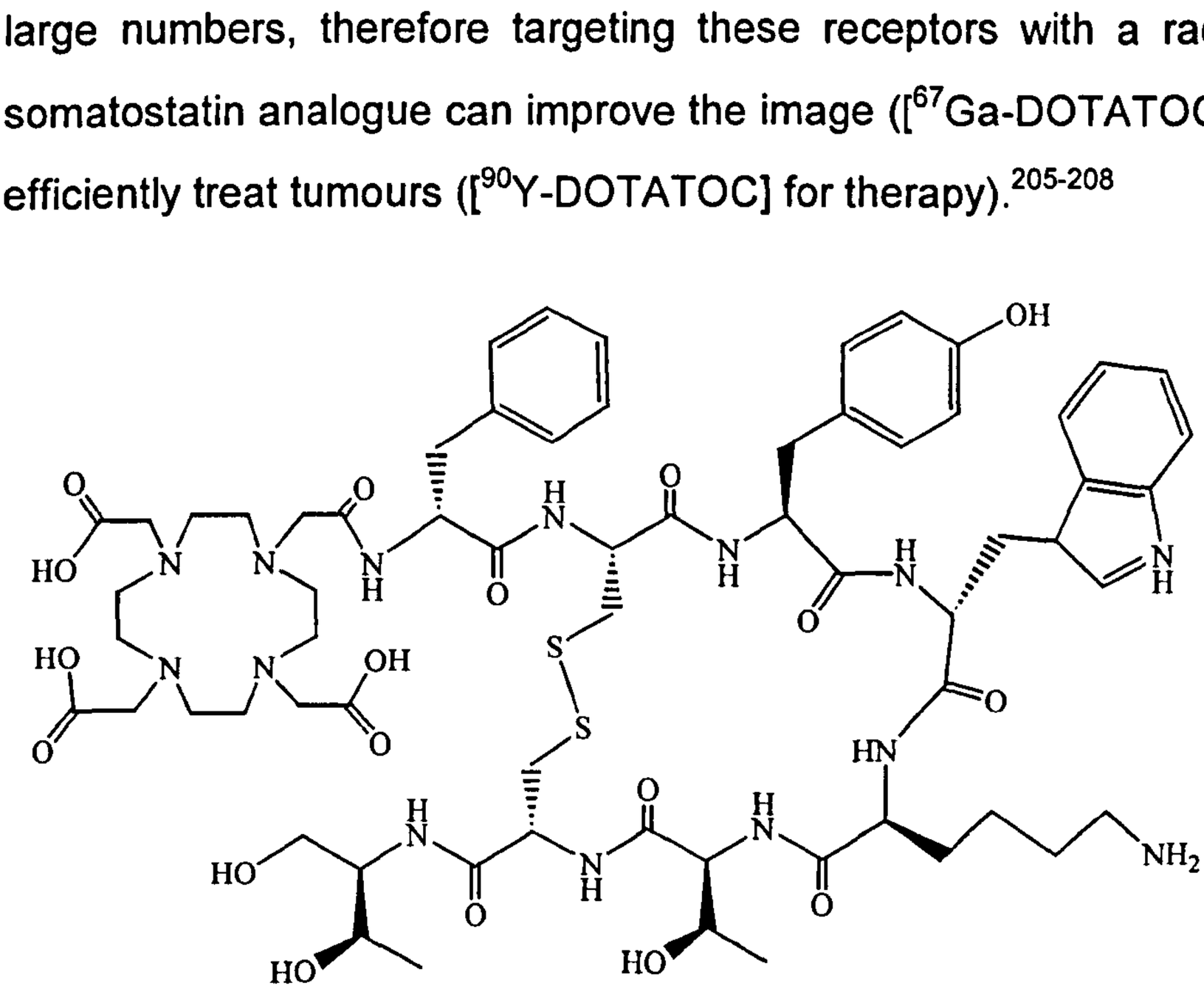

Figure 2.16 Structural formula of DOTA^0-D-Phe^1-Tyr^3-octreotide (DOTATOC).

Bifunctional chelating agents containing monoclonal antibodies (mAbs) have been extensively studied over the past ten years. MAbs are normally attached to a chelating agent by conjugation of an aryl isothiocyanate group on the DOTA-like ligand (Figure 2.17) to free NH_2 groups on the mAb forming the thiourea linkage.[19,198] These labelled mAbs have the problem of long biological half-life and this results in undesired accumulation of radioactivity in healthy tissues.[198] The inclusion of metabolizable spacer groups between the chelating agent and the protein[209-211] is one approach used to accelerate clearance from the body, and tumour pretargeting[203,212,213] is another approach in efforts to improve the efficiency of radiotherapeutic agents.

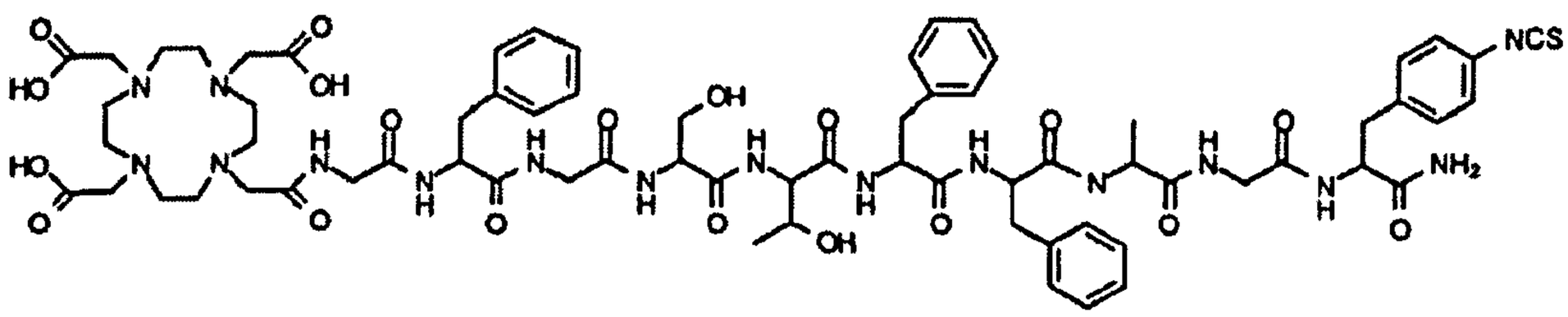

Figure 2.17 Bi-functional chelating agent derivative of DOTA.[211] The polypeptidic chain is the metabolizable linker between the radiolabel and the tumour-targeting moiety (aryl isothiocyanate group).

2.4 Luminescent probes

Under favourable conditions, many of the lanthanide(III) ions are able to exhibit long-lived luminescence following excitation into higher electronic states.[111] Of special interest is the use of lanthanide complexes as luminescent labels for analyses in biological media, in particular as an alternative to radioimmuno assay.[115-119] They are used particularly for the clinical investigation of biological molecules that are in very low concentrations and for which chemical methods are not sufficiently specific or sensitive.

The advantages of lanthanides, especially Eu^{III} and Tb^{III}, are long luminescence lifetimes which overcome the problem of the short-lived background

fluorescence of biological materials present in the body, and emission spectra with very narrow bands which are also remarkably insensitive to environmental changes. A time-resolved detection procedure has been employed, whereby a delay is set between the excitation pulse and the measurement of the lanthanide luminescence during which time the background fluorescence and scattered light decay to negligible levels. [115,118]

However, the application of these lanthanide probes to fluoroimmuno assay has encountered some problems. First of all, the absorbance bands are normally very weak; higher sensitivity has therefore been achieved by designing strongly luminiscent complexes based on the antenna effect. The concept here is that the ligand should incorporate a chromophore which absorbs strongly at a suitable

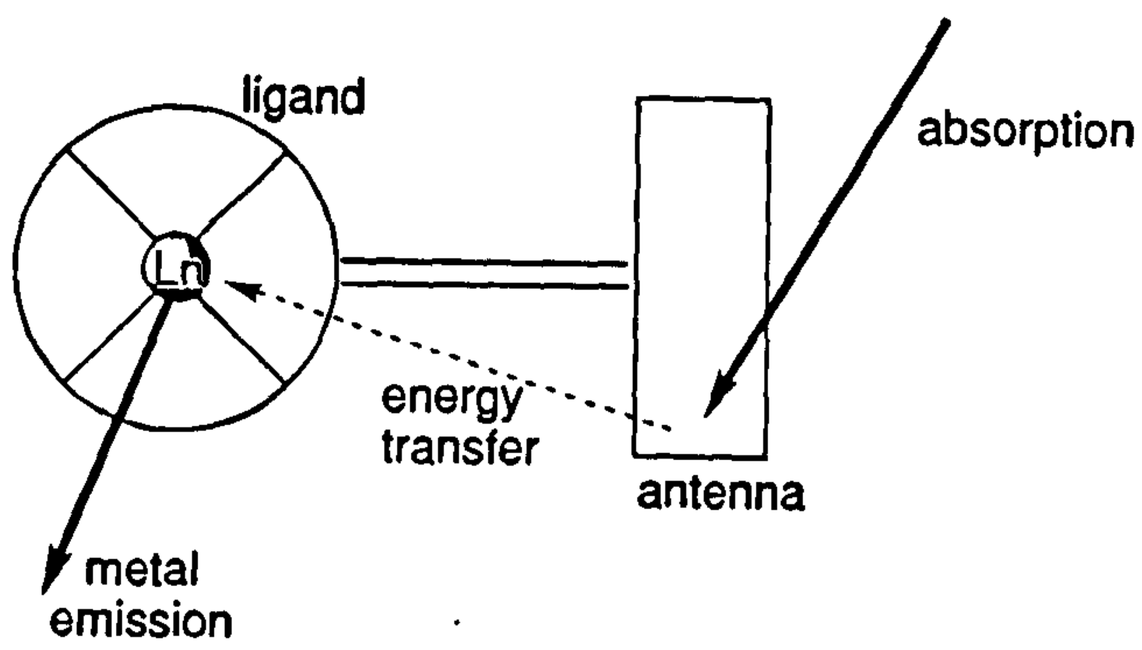

Figure 2.18 Schematic representation of the antenna effect.

wavelength and transfers its excitation energy to the metal which, in accepting this energy, becomes excited to the emissive state.[115,118] Substituted aryl or heterocyclic groups have usually been used as chromophores, including 2,2-bipyridyls and 1,10-phenanthrolines,[115,116] substituted phenyl groups,[214,215] aryl ketones,[216] benzimidazoles[217,218] and phenanthridins.[119,120,219]

Other problems encountered are the deactivation of the metal emissive states by vibrational energy transfer normally involving the solvent water molecules[220] and the stability of the complex with respect to metal ion dissociation. Therefore, in the design of luminescent lanthanide complexes, it is necessary to form kinetically and thermodynamically stable complexes where the metal is shielded as efficiently as possible from the solvent water molecules.[118]

Interestingly, the two examples shown in Figure 2.19 show changes in lanthanide emission intensity as a function of pH. In the case of the ligand with a phenanthridin unit,[119] the protonation on the nitrogen of the chromophore causes a sharp increase in the absorbance band around 370 nm. Therefore, excitation at this wavelength, when the pH is less than 5, gives rise to luminescence emission from the Eu^{III} centre, while at higher pH the chromophore is not protonated and no luminescence emission can be measured. In contrast, the ligand with a toluensulfonyl group (Figure 2.19) has a luminescence switch on passing from acidic pH to pH > 6.[221] In this case, the switch is caused by the co-ordination of the nitrogen of the sulfonamide to the metal centre on deprotonation. When the sulfonamide is bound, the number of water molecules co-ordinated to the Eu^{III} decreases from two to zero and the toluensulfonyl chromophore is closer to the metal centre; all these factors cause a strong increase in luminescence emission from the Eu^{III} at high pH.

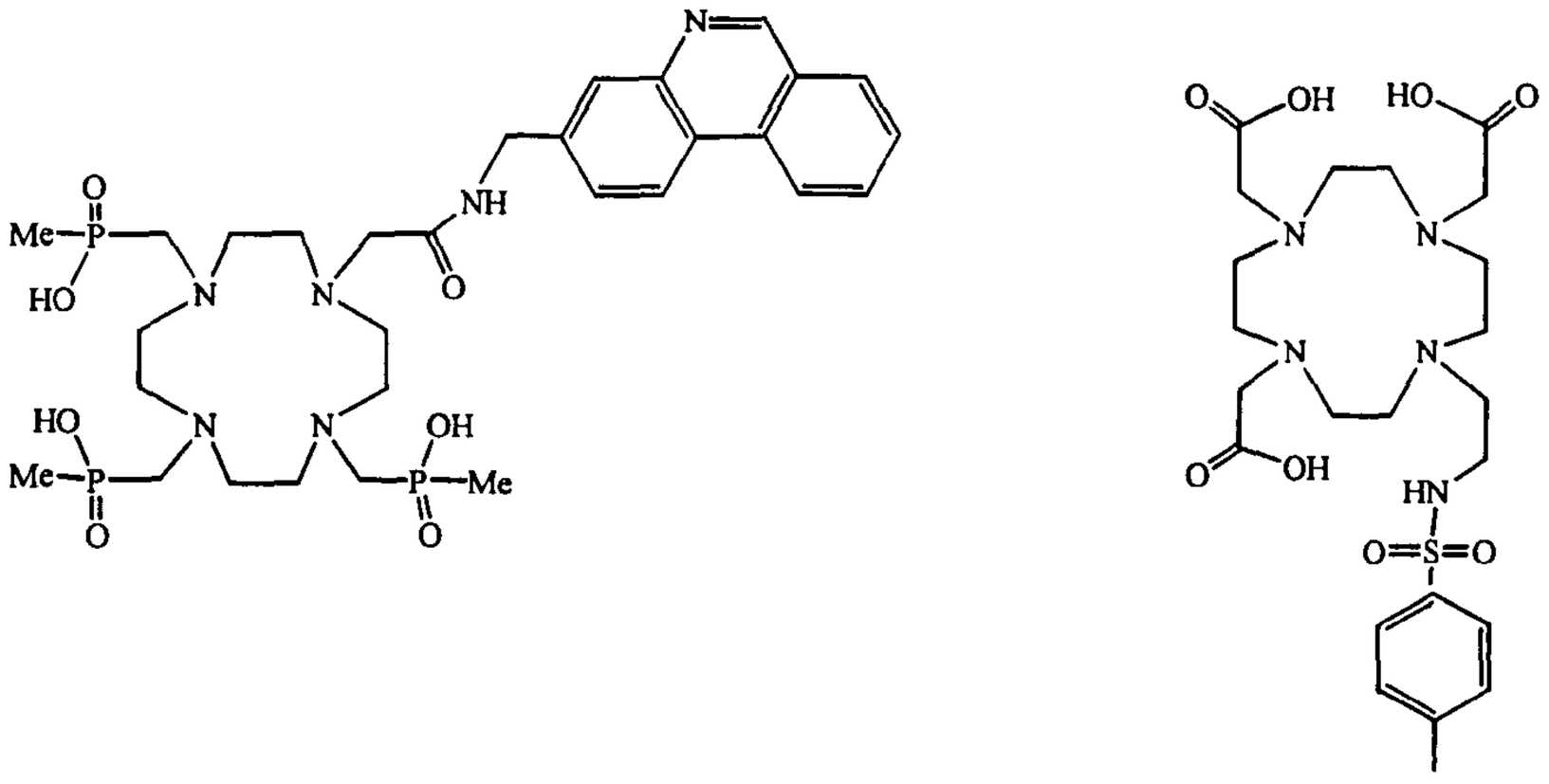

Figure 2.19 Two examples of luminescent sensors, with a phenanthridin unit[119] (left) and with a toluensulfonyl group[221] (right).

Chapter 3

Lanthanide complexes of imino-carboxylate derivatives of [9]aneN$_3$

3.1 Introduction to the co-ordination chemistry of [9]aneN$_3$ and of its symmetric derivatives

There are an enormous number of aza macrocycles reported in the literature involving different ring sizes, degrees of unsaturation and number of N-donors, and 1,4,7-triazacyclononane ([9]aneN$_3$) is one of the most studied. The co-ordination chemistry of [9]aneN$_3$ and of its derivatives bearing pendant co-ordinating groups attached to the nitrogen atoms have been comprehensively reviewed.[77,80,82,222,223]

3.1.1 [9]aneN$_3$: synthesis and co-ordination chemistry

The synthesis of [9]aneN$_3$ was first reported by Koyama and Yoshino in 1972,[224] but only when its synthesis was improved by a highly efficient method published in 1974 by Richman and Atkins[5] could the co-ordination chemistry of this 9-membered macrocycle be extensively studied. Figure 3.1 illustrates the synthetic route to [9]aneN$_3$ via a modification of the Richman-Atkins method.[225] The secondary amines of [9]aneN$_3$ are pure σ-donors and co-ordinate strongly to main

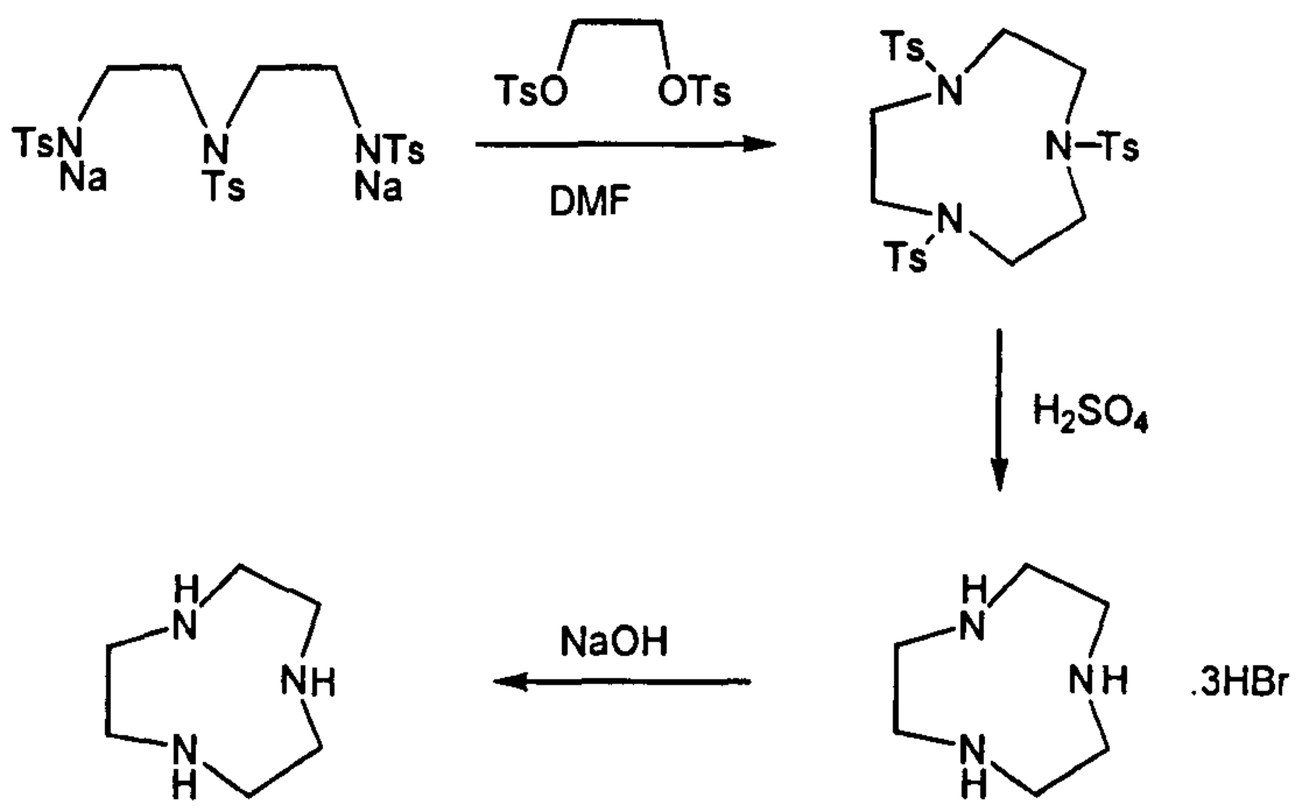

Figure 3.1 Modified Richman-Atkins synthesis of [9]aneN$_3$.

group and transition metal ions occupying in most cases a triangular face of the metal ion co-ordination sphere. [9]aneN$_3$ forms sandwich complexes of general formula [M([9]aneN$_3$)$_2$]$^{n+}$ (n=1,2,3) with a wide range of transition metal ions and these complexes exhibit very high thermodynamic stability and kinetic inertness.[77] In the presence of bridging ligands such as acetate, carbonate and azide a great variety of polynuclear species have been formed with the macrocycle behaving as a face-capping ligand and allowing variation of the donor array at one face of an octahedrally co-ordinated metal.[77]

3.1.2 Symmetric functionalised derivatives of [9]aneN$_3$: synthesis and co-ordination chemistry

The term symmetric functionalisation refers to the derivatisation of all three secondary nitrogen atoms of the macrocycle with the same functional group: this N-functionalisation can be achieved *via* a small number of general synthetic methods.[80,82] The most common one involves nucleophilic attack by the macrocyclic N–H groups onto an alkyl or aryl halide.[77,80,82,222,223] This method is very effective for a large variety of systems (see Figure 3.2 for examples), the only disadvantage being the possible quaternisation of the nitrogen atoms, observed for example in the reaction of [9]aneN$_3$ with methyl iodide.

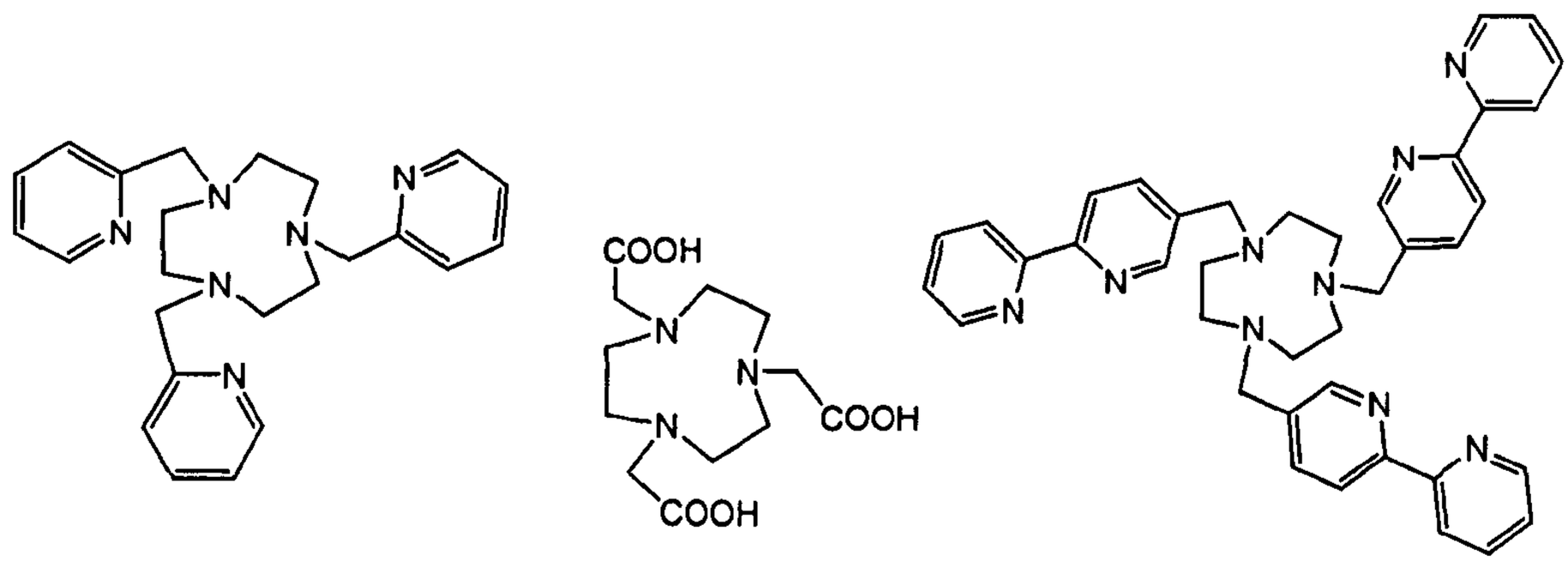

Figure 3.2 Examples of symmetrically functionalised [9]aneN$_3$.

Nucleophilic attack can also take place upon epoxides[226-230] and thiiranes[231,232] to give pendant alcohol and thiol ligands, respectively (Figure 3.3). Other

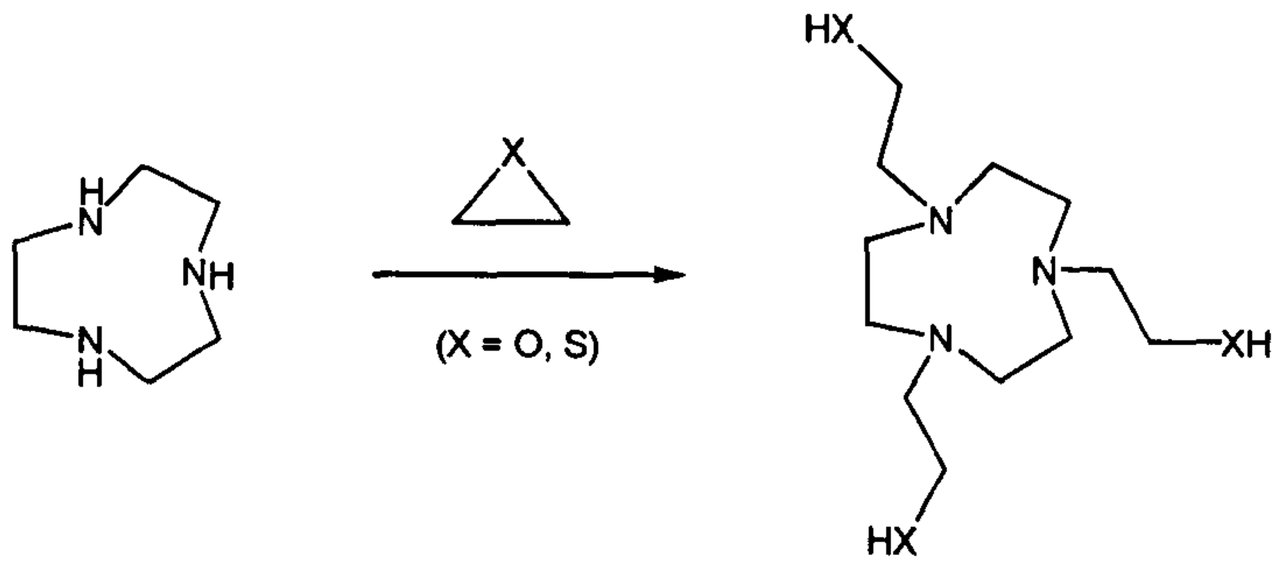

Figure 3.3 Reaction of ethylene oxide or sulphide with [9]aneN$_3$.

electrophiles used, which involve another step before obtaining the desired ligand, are shown in Figure 3.4. Reaction of [9]aneN$_3$ with an acyl chloride[233-238] or the Michael addition to unsaturated substrates [239-241](in the example shown the lone pair of the N-atoms attacks the least hindered olefinic site of acrylonitrile[239]) necessitate the reduction of the amide or nitrile groups, respectively, to form the correspondent amine and thereby the hexadentate ligand.

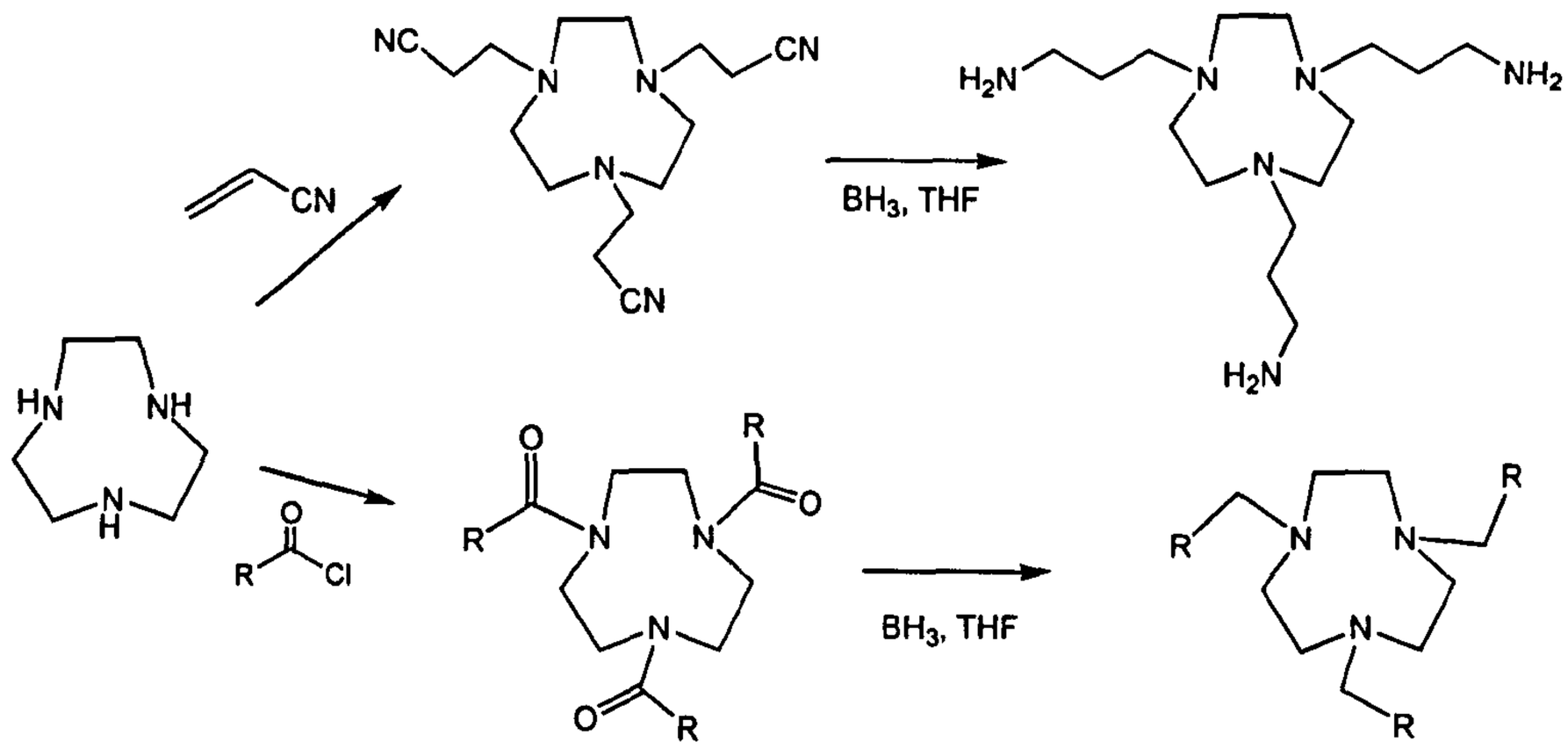

Figure 3.4 Two step synthesis of triple pendant arm derivatives of [9]aneN$_3$.

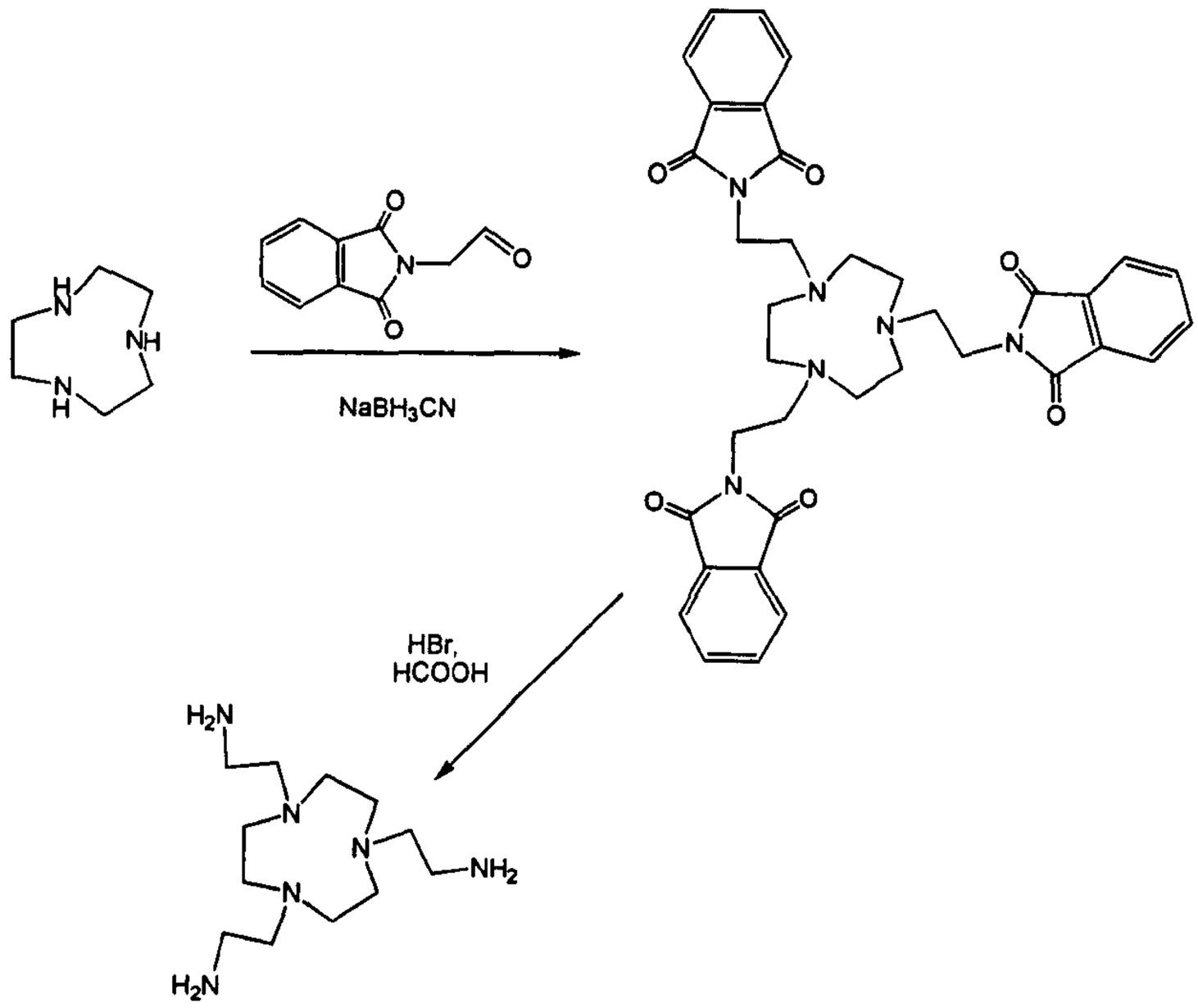

Figure 3.5 Synthesis of 1,4,7-*tris*(2-aminoethyl)-1,4,7-triazacyclononane.

1,4,7-*Tris*(2-aminoethyl)-1,4,7-triazacyclononane was synthesised by Sargeson and co-workers[242,243] by reaction of [9]aneN$_3$ with phthalimidoacetaldehyde in presence of $NaBH_3CN$. Thus, *in situ* reduction of the imminium ion formed by reaction of the aldehyde with the secondary amines of the macrocycle occurs and acid hydrolysis of the recovered product removes the protecting phthaloyl groups to give the hexaamino ligand. The first reaction step had to be performed under anhydrous conditions in acetonitrile using phthalimidoacetaldehyde previously dehydrated by azeotropic removal of water with benzene and the product could only be partially purified by chromatography. In the present chapter, a new and more efficient synthetic method to obtain this [9]aneN$_3$ derivative will be introduced.[244]

The co-ordination chemistry of these potentially six co-ordinate ligands has been extensively studied for a wide range of applications.[77,80,82,222,223] Some of these applications have already been discussed in Chapter 1 and 2 and embrace enzyme[99,100,245,246] or siderophore simulation,[247-250] ^{67}Ga and ^{111}In complexes as

radiopharmaceuticals[251-258] and selective extraction of metal ions.[259] These hexadentate macrocyclic ligands form endocyclic mononuclear complexes with transition metals in a variety of oxidation states, even more kinetically and thermodynamically stable than the complexes of the parent macrocycle [9]aneN$_3$.[77] These ligands present two groups of facial donors: the macrocyclic N-atoms and the pendant donors. In some cases not all three pendant donors co-ordinate and, especially with Cu^{II}, five co-ordinate complexes are often formed.[82]

Although many examples involving functionalised [9]aneN$_3$ have already been reported in Chapter 1, two other interesting ligands will be discussed in this section. The ligand in Figure 3.6(a) forms remarkably stable complexes with Fe^{III}, $Ga^{III}$and In^{III} and has been investigated as a chelating agent for the radionuclides ^{67}Ga and ^{111}In and as mimicry of the natural siderophores.[247,248,260,261] Siderophores are macrocyclic compounds produced by iron-deficient bacteria to sequester iron from the environment.[262] For example, *enterobactin* is a siderophore that consists of a central [12]aneO$_3$ cyclic unit and three catechol-based pendant arms (Figure 3.6b) which shows very high selectivity towards Fe^{III} with a stability constant of 10^{52}. The ligand in Figure 3.6(a), with the cyclic moiety of [9]aneN$_3$ and three phenolate pendant arms, forms an iron(III) complex with a

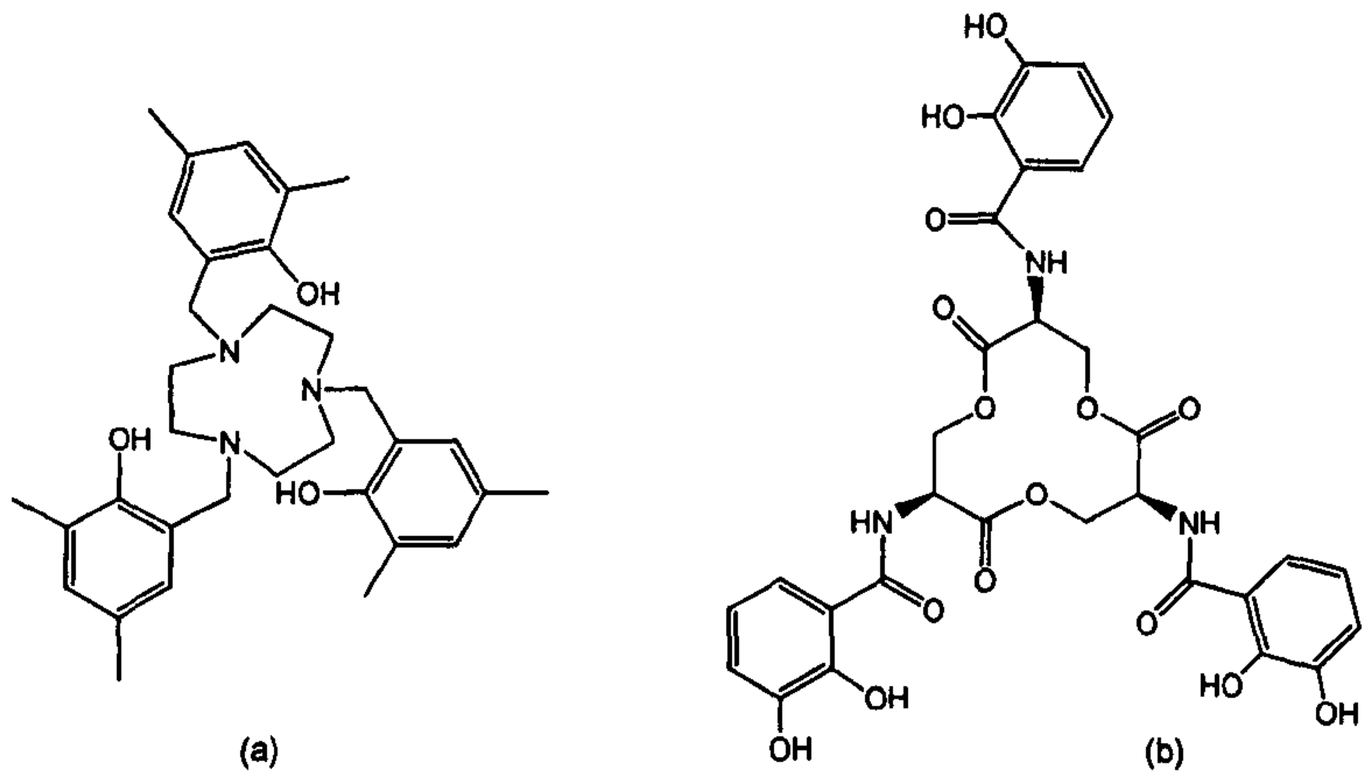

Figure 3.6 (a) [9]aneN$_3$ derivative selective for Fe^{III} and (b) the siderophore *enterobactin*.

stability constant of $10^{51.3}$, the highest known stability constant for a synthetic Fe^{III} complex,[250] and has been considered to be a promising drug for the treatment of iron overload (thalassaemia).[263] This and other related ligands with ortho-substituted benzyl groups (phenolate, thiophenolate and benzylamine) attached to the [9]aneN$_3$ have been comprehensively investigated by Wieghardt and co-workers for a large variety of purposes by means of electrochemical, EPR, NMR, UV and potentiometric methods.[245,264-269]

Another interesting ligand with three carboxybenzyl pendant arms (Figure 3.7) has been designed to be selective for uranyl ions (UO_2^{2+}).[259] While the protonated triaza macrocycle and the ethereal oxygens interact with the uranyl oxo groups, the carboxylate groups co-ordinate the metal centre, which therefore is bound only by the pendant arms. The lipophilicity of the ligand permits the quantitative and efficient extraction of uranyl ions from aqueous solutions into chloroform.[259]

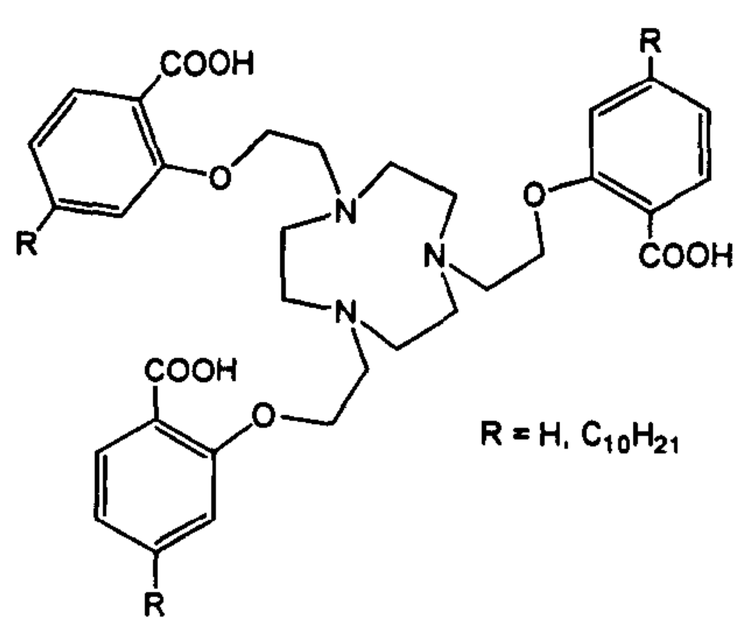

Figure 3.7 A symmetric [9]aneN$_3$ derivative for the extraction of uranyl ions.

3.2 Introduction to tripodal Schiff-base ligands for the co-ordination of lanthanide ions

Schiff-base ligands have played an important role in the search for new and more effective lanthanide complexes for the applications discussed in Chapter 2. The ability of the Ln^{III} metal ions to promote the Schiff-base condensation of the

appropriate diamine and dicarbonyl precursors has permitted the synthesis of a large variety of macrocylcic lanthanide complexes.[270-273] Most examples feature conjugation of the imine moieties with aromatic rings, which helps to stabilise the complexes against hydrolysis. Podand-type acyclic receptors have also been synthesised, often from the Schiff-base condensation of the tripodal *tris*(2-aminoethyl)amine (tren) with a large variety of ketones and aldehydes.[274,275] The reaction of tren with acetylacetone,[276,277] salicylaldehyde[278-281] and hydroxyacetophenone[276,277] derivatives as well as with sodium pyruvate,[282,283] dehydroacetic acid[284] and 2,6-diformylphenol derivatives[285-287] has led to a large number of tripodal Schiff-base ligands, normally heptadentate, which display significant affinities for lanthanide ions. These ligands always have a donor set based on four nitrogen atoms (three imines and one tertiary amine) and three or more oxygens (alcohols, phenols or carboxylates), but the co-ordination behaviour towards lanthanide ions is very variable depending on the starting materials and the conditions used.

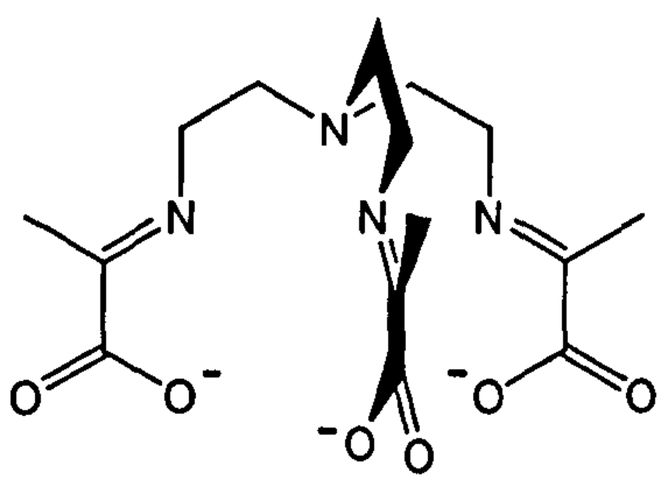

(1)

(a)

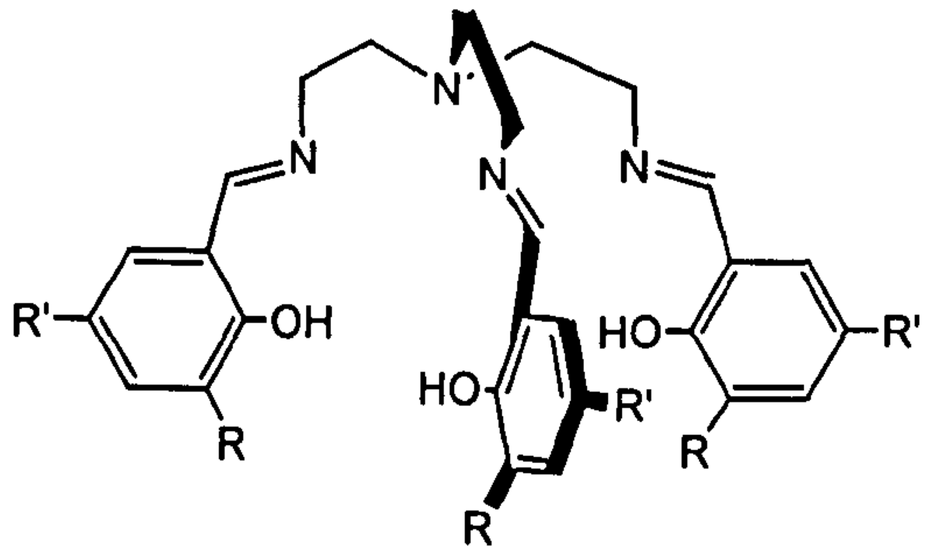

(b) **2**) R=CH(OMe)$_2$, R' = Me
3) R=CHO, R' = Cl
4) R=OMe, R' = H

Figure 3.8 Ligands obtained by Schiff-base condensation between tren and sodium pyruvate (**1**), 2,6-diformyl-4-methylphenol (**2**), 2,6-diformyl-4-chlorophenol (**3**) and 3-methoxysalicylaldehyde (**4**).

Since lanthanide ions are usually eight or nine co-ordinate with heptadentate ligands additional donor atoms are often bound to the Ln^{III} centres. For example, the ligand shown in Figure 3.8a (**1**) forms polynuclear complexes with one carboxylate group from each ligand bridging to the next metal centre[282] (Figure 3.9a) or with Na^+ cations joined to carboxylate oxygens linking together two or more units.[283] However, crystallisation of these polymeric materials from water affords monomers with two water molecules bound to the metal centre and the metal ion encapsulated inside the ligand cavity (Figure 3.9b).[282]

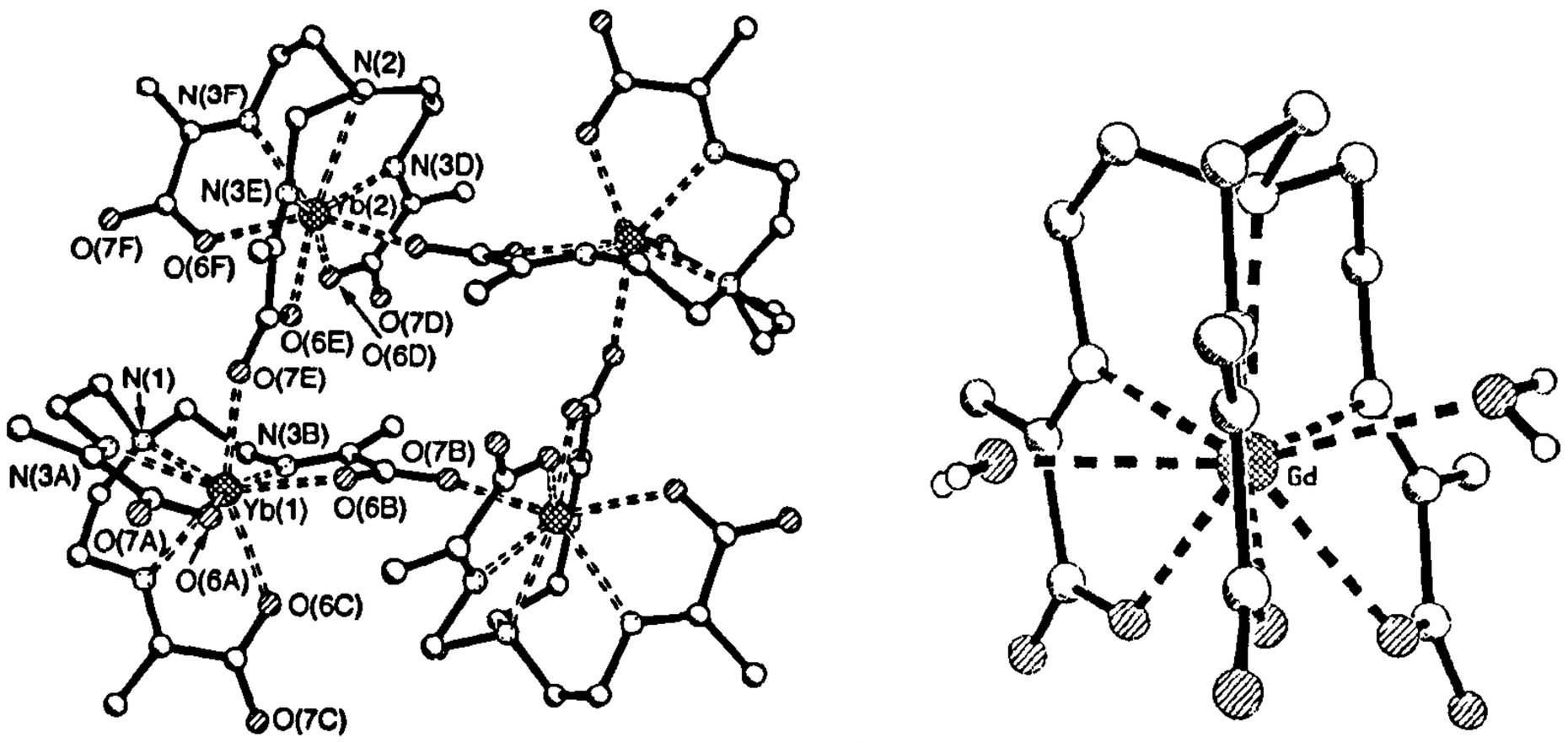

(a) (b)

Figure 3.9 (a) Yb^{III} complex of the ligand **1** crystallised from MeOH and (b) Gd^{III} complex crystallised from H_2O.

As an example of the variety of lanthanide complexes obtained with these tripodal ligands, three similar ligands obtained from the Schiff-base condensation of tren with 2,6-diformylphenol derivatives[285-287] (**2** and **3**) and with 3-methoxysalicylaldehyde[280] (**4**) are considered. In the reaction of tren with 2,6-diformyl-4-methylphenol, MeOH solvent reacts with one aldehydic functionality forming acetal groups and the X-ray structure of the Pr^{III} complex shows that the cation is deca-coordinated by six acetal and three phenolic oxygens in addition to a water molecule (Figure 3.10a).[285-287] Using 2,6-diformyl-4-chlorophenol and

anhydrous acetonitrile, the expected ligand and binuclear complexes are obtained.[287] Figure 3.10 (b) shows crystal structure of the La^{III} complex where the metal ion is nine co-ordinated to the seven donors of the N_4O_3 inner chamber, to a dimethylformamide molecule and to an aldehydic oxygen from the symmetry related ligand.[287] In the third example, the podand **4** can react with two different Ln^{III} ions forming a heterodimetallic lanthanide complex.[280] Figure 3.10(c) illustrates the crystal structure of this dinuclear complex where the Yb^{III} ion is encapsulated into the tren cavity and the La^{III} ion is bound outside it to six oxygens of the ligand (three phenolate and three acetal groups) and to two bidentate nitrate anions.[280]

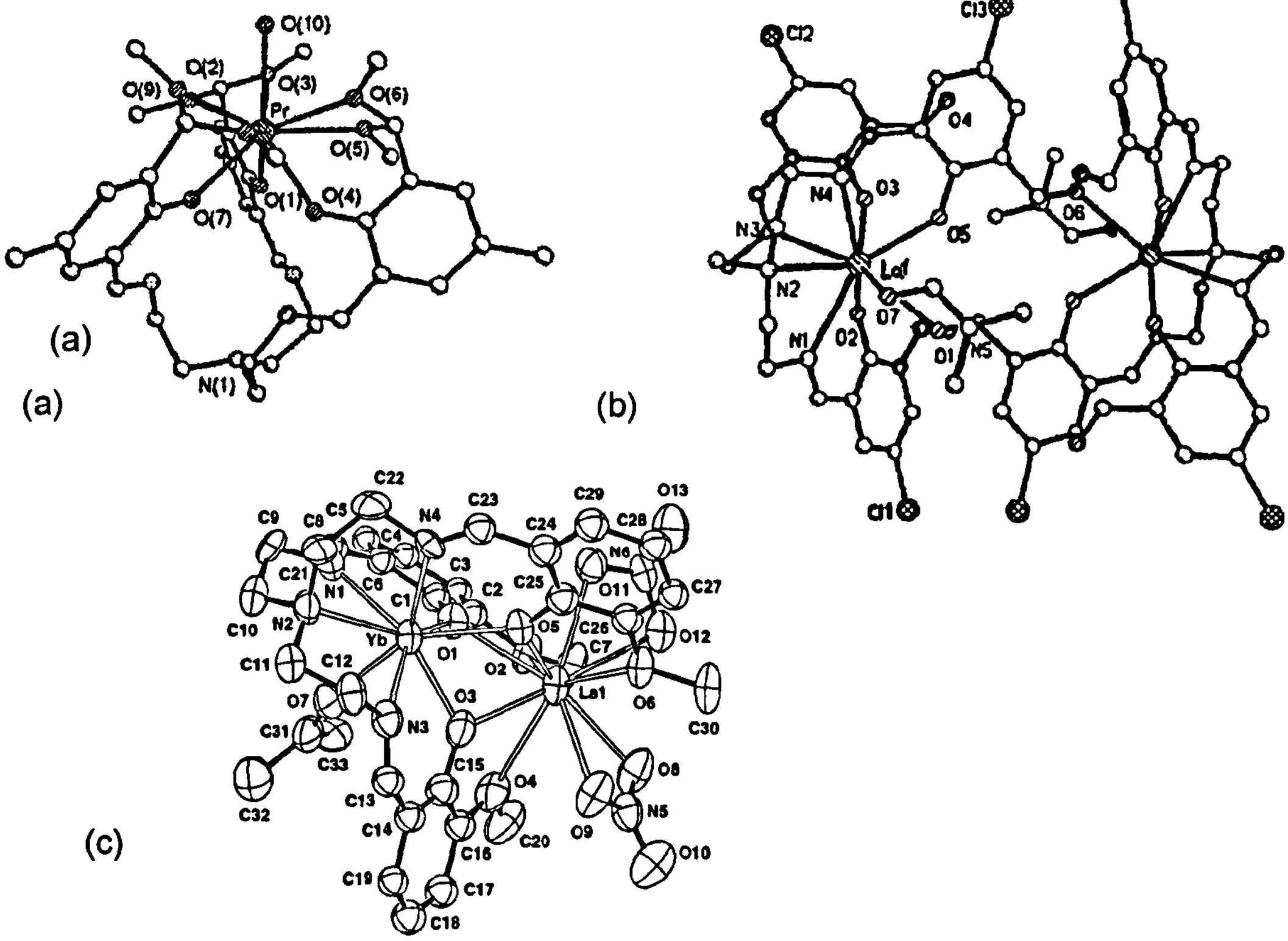

Figure 3.10 Ln^{III} crystal structures of the ligands shown in Figure 3.9b. (a) Pr^{II} complex with **2**, (b) dinuclear La^{III} complex with **3**, and (c) Yb^{III}-La^{III} dinuclea complex with **4**.

3.3 Results and discussion

The work described in this chapter was aimed at synthesising a novel tripodal ligand based on 1,4,7-triazacyclononane and capable of forming stable complexes with lanthanide ions. Such a ligand should exploit the properties of a macrocyclic ligand with extended pendant arms, thus forming stable and rigid complexes with Ln^{III} ions.

In the following sections, Ln^{III} complexes of the ligand obtained by Schiff-base condensation of 1,4,7-*tris*(2-aminoethyl)-1,4,7-triazacyclononane (L) with three molar equivalents of sodium pyruvate will be studied by X-ray diffraction and NMR spectroscopy in order to obtain a complete characterisation. Moreover, properties such as the relaxivity of the Gd^{III} complex and Dysprosium Induced Shift (DIS) will be discussed.

3.3.1 Synthesis of 1,4,7-*tris*(2-aminoethyl)-1,4,7-triazacyclononane (L)

The established route to the synthesis of 1,4,7-*tris*(2-aminoethyl)-1,4,7-triazacyclononane (L) was described in Section 3.1.2.[242,243] In the present Section, a new sequence of reactions that affords L is introduced (Figure 3.11).[244] The first is the addition of chloroacetonitrile to [9]aneN$_3$·3HBr in EtOH in the presence of an excess of Et_3N. The oil obtained after evaporation of the solvent was dissolved in chloroform and washed with water, and the product L^1 was obtained as a solid without further purification. L^1 was characterised satisfactorily by ^1H and ^{13}C NMR, IR spectroscopy and elemental analysis. The EI mass spectrum shows peaks due to the product having lost two and three nitrile arms.

The reduction of the nitrile groups in L^1 using 1M BH_3 solution in THF followed by hydrolysis of the borane complexes in refluxing concentrated HCl solution yielded the hydrochloride salt of 1,4,7-*tris*(2-aminoethyl)-1,4,7-triazacyclononane (L). The free amine was obtained by passing an aqueous

solution of this salt through a Dowex column. The NMR spectra (^{1}H and ^{13}C) show all the expected peaks with satisfactory elemental analytical data obtained. The EI mass spectrum of L shows peaks due to the product having lost two arms, two arms and an NH_2 group, and all three arms.

3.3.2 Synthesis of the complexes [Ln(L^a)]

The synthesis of the complexes [Ln(L^a)] (Ln^{III} = Y^{III}, Sm^{III}, Gd^{III}, Dy^{III}, Eu^{III}, Yb^{III}, La^{III}) was achieved by Schiff-base condensation of the triamine (L) with sodium pyruvate using the Ln^{III} ion as templating agent (Figure 3.11). Thus, refluxing one equivalent of L and of LnX_3 (X = Cl^-, NO_3^-or TfO^-) and three equivalents of sodium pyruvate in MeOH for 2 hours followed by precipitation of the product by addition of Et_2O afford the desired complexes [Ln(L^a)] as white

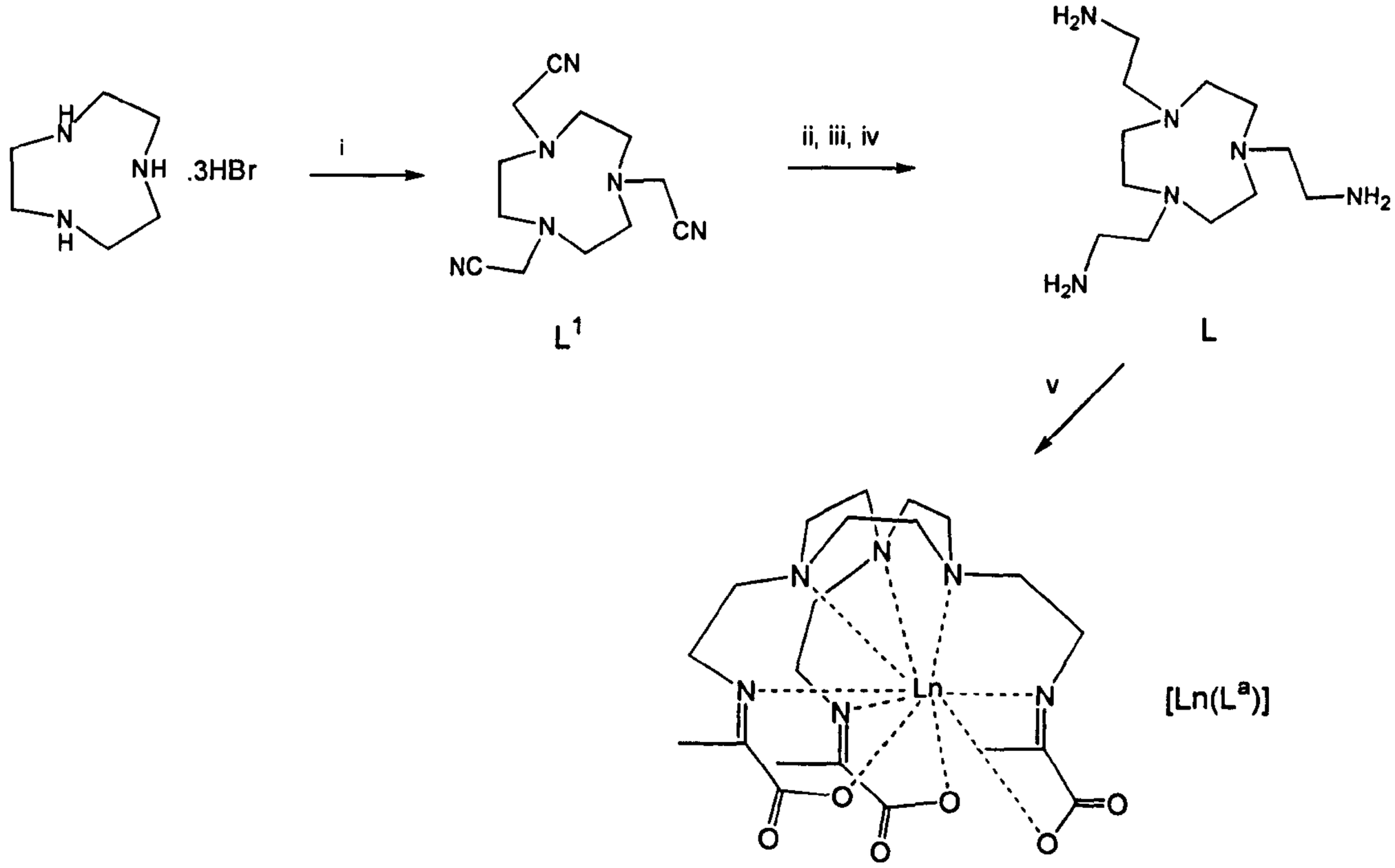

Figure 3.11 Synthesis scheme for the ligands L^1 and L and for [Ln(L^a)] complexes (i: $ClCH_2CN$, NEt_3, EtOH, 18h; ii: BH_3·THF 1 M, 48 h; iii: HCl 6 M, 24 h; iv: Dowex; v: 3 $CH_3COCOONa$, LnX, MeOH, 2 h).

solids. A template procedure is employed because the ligand L^a, which was synthesised in an analogous reaction without the Ln^{III} ion as templating agent, is highly hygroscopic and therefore difficult to handle. The complexes [Ln(L^a)] were also synthesised by simply stirring the ligand L^a with the corresponding Ln^{III} salt resulting in the same product as that obtained *via* the template method.

It is worth noting that only in the case of [Y(L^a)] it was necessary to remove the $NaNO_3$ formed with the complex by passing a solution of the complex in MeOH through a Sephadex column. In the other cases (with Cl^- or TfO^- anions) the sodium salts formed did not interfere with the isolation of the complex. Elemental analysis and mass spectra for the ligand L^a and for all the complexes are consistent with the formulation (L^a)$Na_3 \cdot 3H_2O$ and [Ln(L^a)], respectively. When the sample for elemental analysis consists of crystals of Ln^{III} complexes, results are consistent with the formulation [Ln(L^a)] with a variable number of MeOH or H_2O molecules but when the sample consists of bulk solid, the elemental analysis also reveals the presence of three equivalents of NaCl.

3.3.3 Single crystal X-ray diffraction analyses of [Ln(L^a)]

Single crystals of [Ln(L^a)] (Ln^{III} = Y^{III}, Sm^{III}, Gd^{III} and La^{III}) were obtained by diffusion of Et_2O vapour into a solution of the complexes in MeOH at room temperature. Single crystal X-ray diffraction studies show that all these complexes are isostructural. In each, the lanthanide centre is nine-coordinate, using all nine donor atoms of the ligand, namely the three amino N-donors of the macrocycle, the three imino N-donors and the three carboxylate O-donors. Bond lengths are in the range 2.622(4)-2.717(3)Å for the bonds between the Ln^{III} and the macrocyclic N-donors, in the range of 2.534(4)-2.643(3)Å for the bonds to the N-donors of the imine moieties and in the range 2.331(3)-2.441(3)Å for those to the carboxylate O-donors. The trend of the bond lengths moving from La to Y shows, as expected, a

general shortening due to the lanthanide contraction (Table 3.1). Two different views of the crystal structure of [La(L^a)] are shown in Figure 3.12 and 3.13.

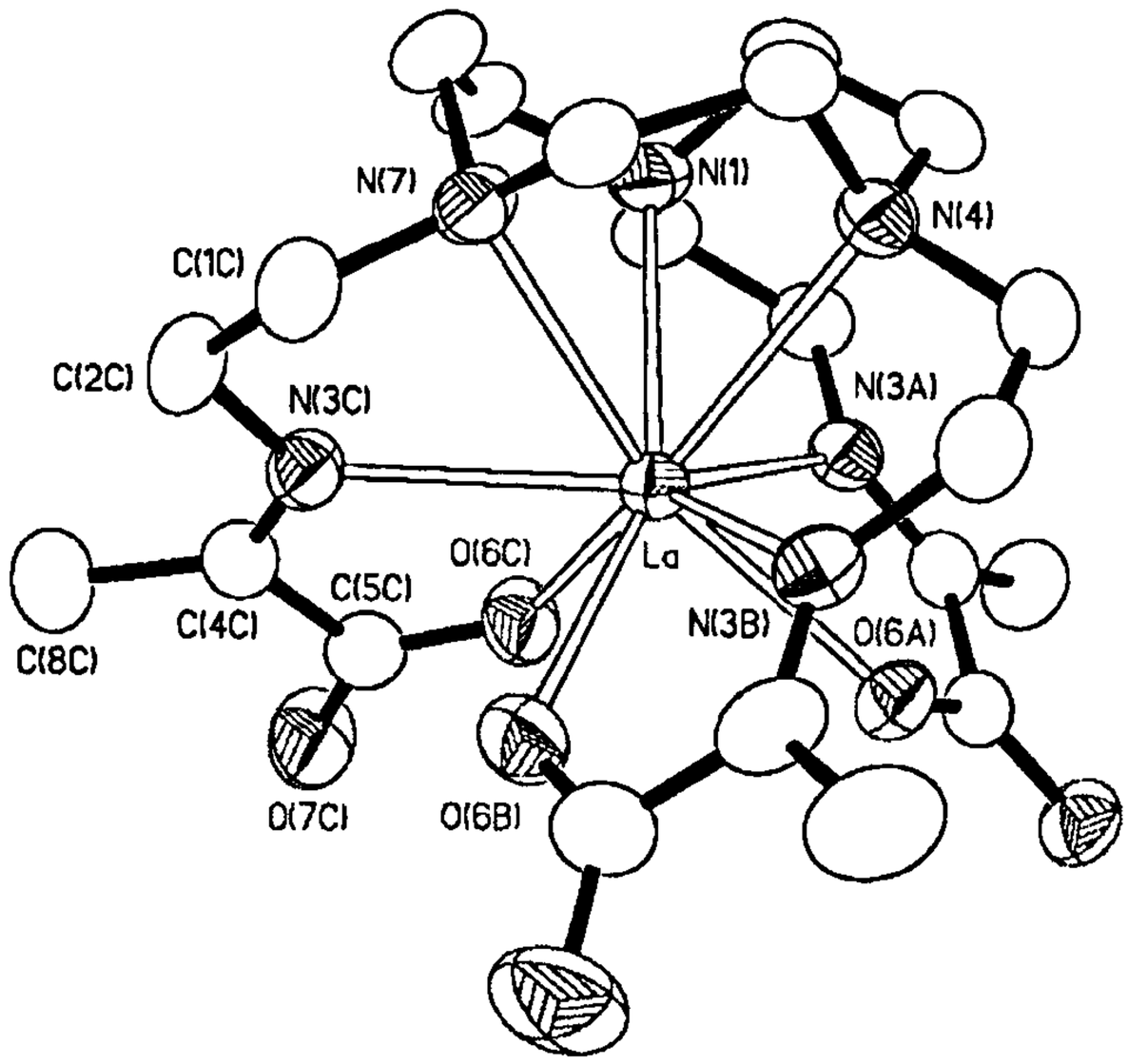

Figure 3.12 Ellipsoid plot of [La(L^a)] with numbering scheme adopted. Hydrogen atoms and MeOH solvent molecules have been omitted for clarity. Displacement ellipsoids are drawn at 50% probability.

There is a high degree of planarity in the fragments C(2)-C(8) of the pendant arms in all the structures due to conjugation between the imine and carboxylate groups, with the mean deviation from the least-squares mean plane through these seven atoms being only 0.003-0.045Å. It is interesting to note the difference in the opening of the three arms by examining the pitch angle between the plane of the macrocycle and the plane of each pyruvate. The average of the three pitch angles decreases from 52.2° for [La(L^a)], to 51.0° for [Sm(L^a)], to 50.6° for [Gd(L^a)] and to 49.6° for [Y(L^a)]. This variation is due to the different effective ionic radii for the four metal ions: 1.22Å for La^{3+}, 1.13Å for Sm^{3+}, 1.11Å for Gd^{3+} and 1.07Å for Y^{3+} (values are for nine co-ordinate ions).[288]

Table 3.1 Selected bond lengths (Å) in [Y(L^a)]·2CH$_3$OH·½H$_2$O, [Gd(L^a)]·2.75CH$_3$OH·0.75H$_2$O, [Sm(L^a)]·3CH$_3$OH·½H$_2$O and [La(L^a)]·3CH$_3$OH·H$_2$O.

	[Y(L^a)]	[Gd(L^a)]	[Sm(L^a)]	[La(L^a)]
Ln-N(1)	2.627 (4)	2.668(5)	2.669 (4)	2.717 (3)
Ln-N(4)	2.640 (4)	2.648 (5)	2.677 (4)	2.717 (3)
Ln-N(7)	2.622 (4)	2.641 (5)	2.690 (4)	2.707 (3)
Ln-N(3A)	2.552 (4)	2.561 (5)	2.602 (4)	2.643 (3)
Ln-N(3B)	2.534 (4)	2.565 (5)	2.588 (4)	2.620 (3)
Ln-N(3C)	2.544 (4)	2.574 (5)	2.579 (4)	2.630 (3)
Ln-O(6A)	2.346 (3)	2.373 (4)	2.403 (3)	2.441 (3)
Ln-O(6B)	2.331 (3)	2.378 (4)	2.391 (4)	2.436 (3)
Ln-O(6C)	2.332 (3)	2.388 (4)	2.391 (4)	2.430 (3)

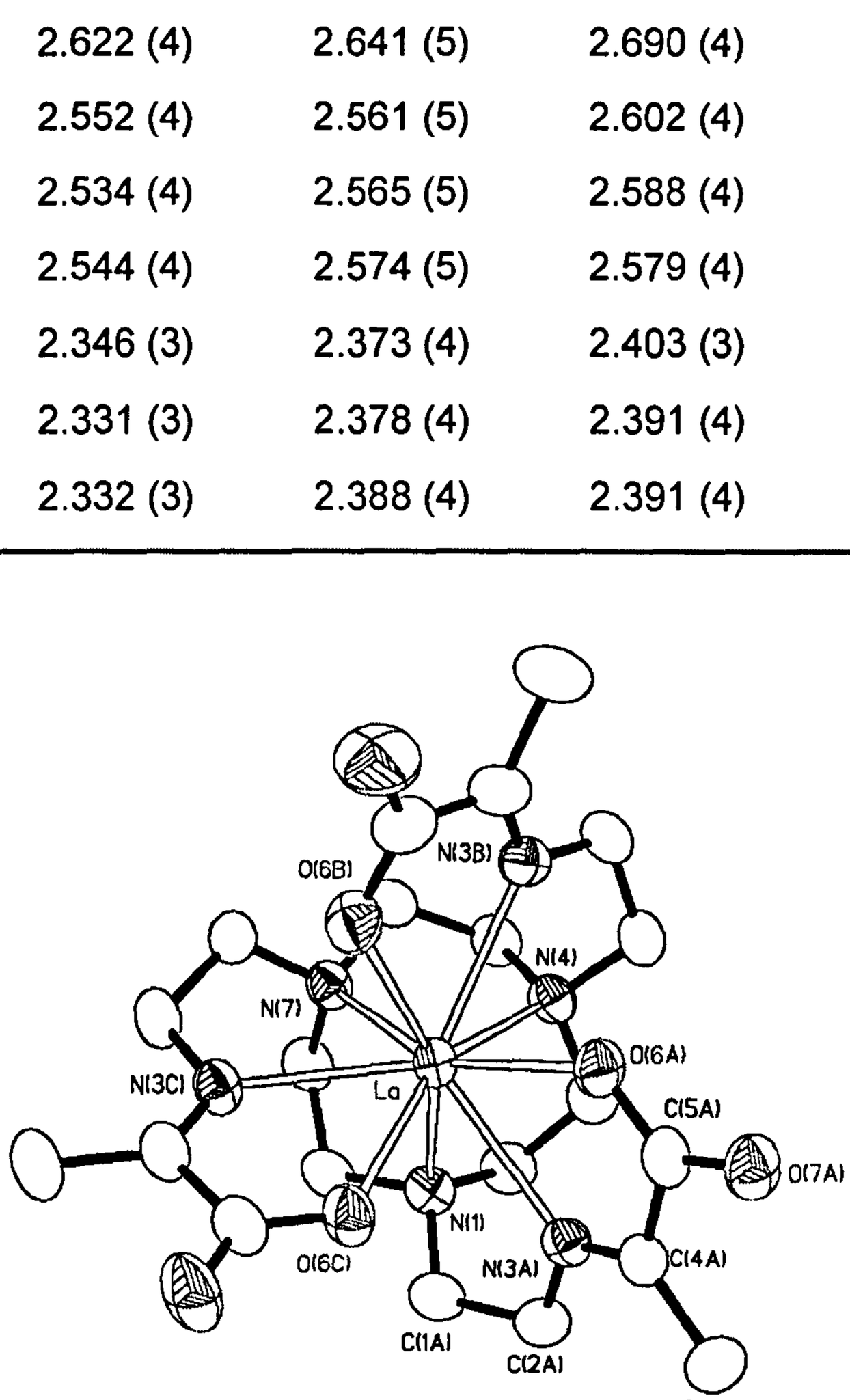

Figure 3.13 Ellipsoid plot of [La(L^a)] along the non-crystallographic 3-fold axis. Displacement ellipsoids are drawn at 50% probability.

The co-ordination geometry about the lanthanide centre is slightly distorted tricapped trigonal prismatic (Figure 3.14a). It has been already pointed out in Section 2.2.5 that the two most common geometries for nine co-ordinate complexes are capped square antiprismatic and tricapped trigonal prismatic.[183] The presence of 1,4,7-triazacyclononane as the capping system forces the Ln^{III} ion to assume a trigonal prismatic structure as the macrocyclic nitrogen donors impose the first triangular face. The other triangular face of the prism is formed by the carboxylate oxygens with the imine nitrogens capping the three rectangular faces of the prism. The upper and lower triangular faces of the prism are essentially equilateral (angle range 58.2-61.6º) and parallel (the angle between the plane defined by the triangle of the three oxygen donors and that defined by the three nitrogen donors is never more than 3.3º), but the oxygen triangular faces are always slightly twisted around the 3-fold axis compared to the nitrogen triangular face. The twist between the two triangular faces is illustrated in Figure 3.14(b) and can be quantified looking at the torsion angles formed by the four atoms of every

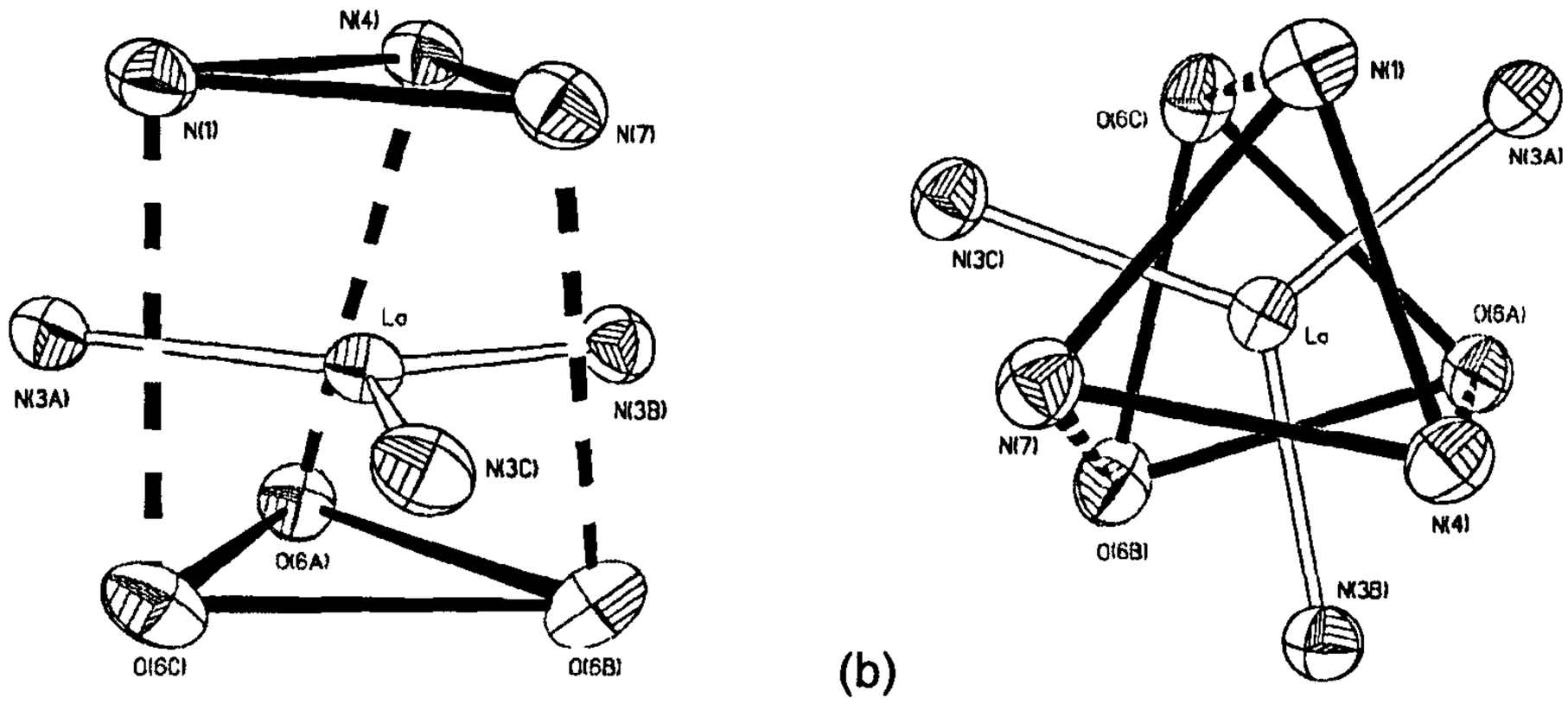

Figure 3.14 (a) Co-ordination geometry about the metal centre in [La(L^a)]. (b) View of the co-ordination geometry in [La(L^a)] down the non-crystallographic 3-fold axis.

rectangular face of the prism. In [La(L^a)] the average of the three torsion angles (one for every triangular side) is 27.0°, in [Sm(L^a)] is 22.9°, in [Gd(L^a)] is 21.4° and in [Y(L^a)] is 20.2°. Consequently, it can be observed that the distortion from the trigonal prismatic geometry is more evident as the dimension of the encapsulated ion increases. The presence of this distortion from a regular trigonal prismatic geometry can also explain why, although the crystal structures of [Ln(L^a)] are in the *R*-3 space group, they do not have a crystallographic three-fold axis.

Comparing this co-ordination geometry with the polyhedra observed for related DOTA complexes, it can be observed that in the latter, with a tetradentate macrocycle as capping system, the nine co-ordinate complexes assume a square antiprismatic conformation with the macrocyclic nitrogens forming one square face.[186,289] Nevertheless, the complexes with DOTA and its derivatives [22,186,289,290] are very similar to the complexes obtained with L^a in that their structures are monomeric with all the donor atoms involved in the co-ordination. The difference is that in DOTA examples the Ln^{III} ions are eight co-ordinate having one co-ordination site available for occupation by a solvent molecule (usually water in these examples[186,289]) while in complexes with L^a the ligand can completely fulfil the co-ordination requirements of the Ln^{III} ion, leaving no space for co-ordination of a solvent molecule. It is interesting to note that using *tris*(2-aminoethyl)amine (tren) as the tripodal triamine and the same sodium pyruvate as the ketone for the Schiff-base condensation, polymeric structures have been obtained from MeOH solutions (Section 3.2).[282,283] The complexes with L^a, like those of DOTA, form only monomeric structures because the Ln^{III} ion has a complete co-ordination sphere. When the tripodal ligand has only seven donor atoms, the lanthanide ion can complete its co-ordination sphere using donor atoms from adjacent complexes thereby forming polymeric structures.

3.3.4 ^{1}H and ^{13}C NMR spectra of complexes [Ln(L^{a})]

NMR spectroscopic studies on the diamagnetic complexes [Y(L^{a})] and [La(L^{a})] and on paramagnetic [Yb(L^{a})] and [Sm(L^{a})] were carried out and compared to the similar studies reported for [Ln(DOTA)]$^{-}$ complexes.[291-294] The ^{1}H NMR spectrum of [Y(L^{a})] (300 MHz, 298K, CD_3OD) shows a complex series of multiplets and doublets of doublets (Figure 3.15). A 2D-COSY experiment combined with a ^{1}H-^{13}C coupling 2D experiment allowed an accurate assignment of the resonances (See Figure 3.16 for labelling scheme).

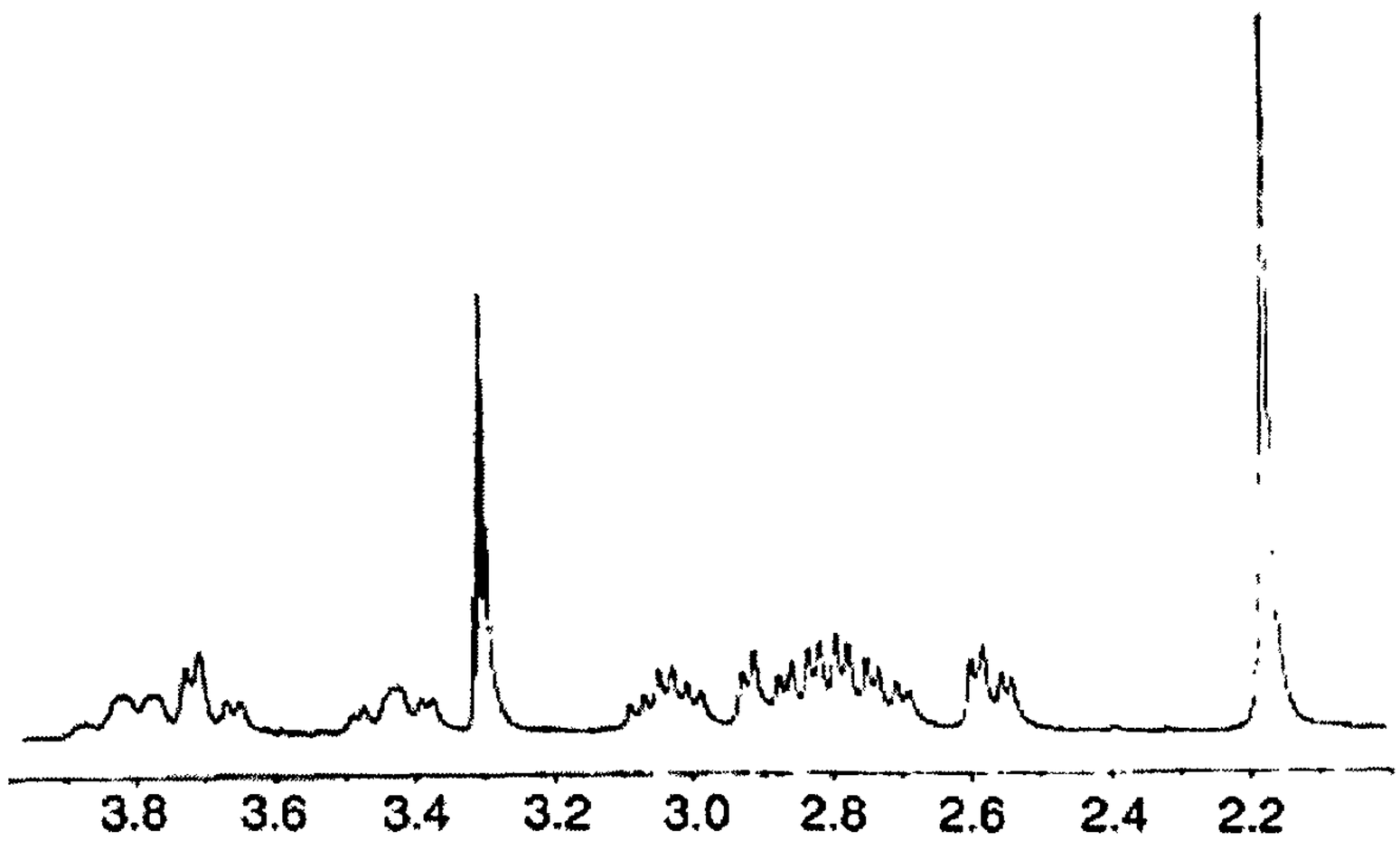

Figure 3.15 ^{1}H NMR spectra of diamagnetic [Y(L^{a})] in CD_3OD at 298 K.

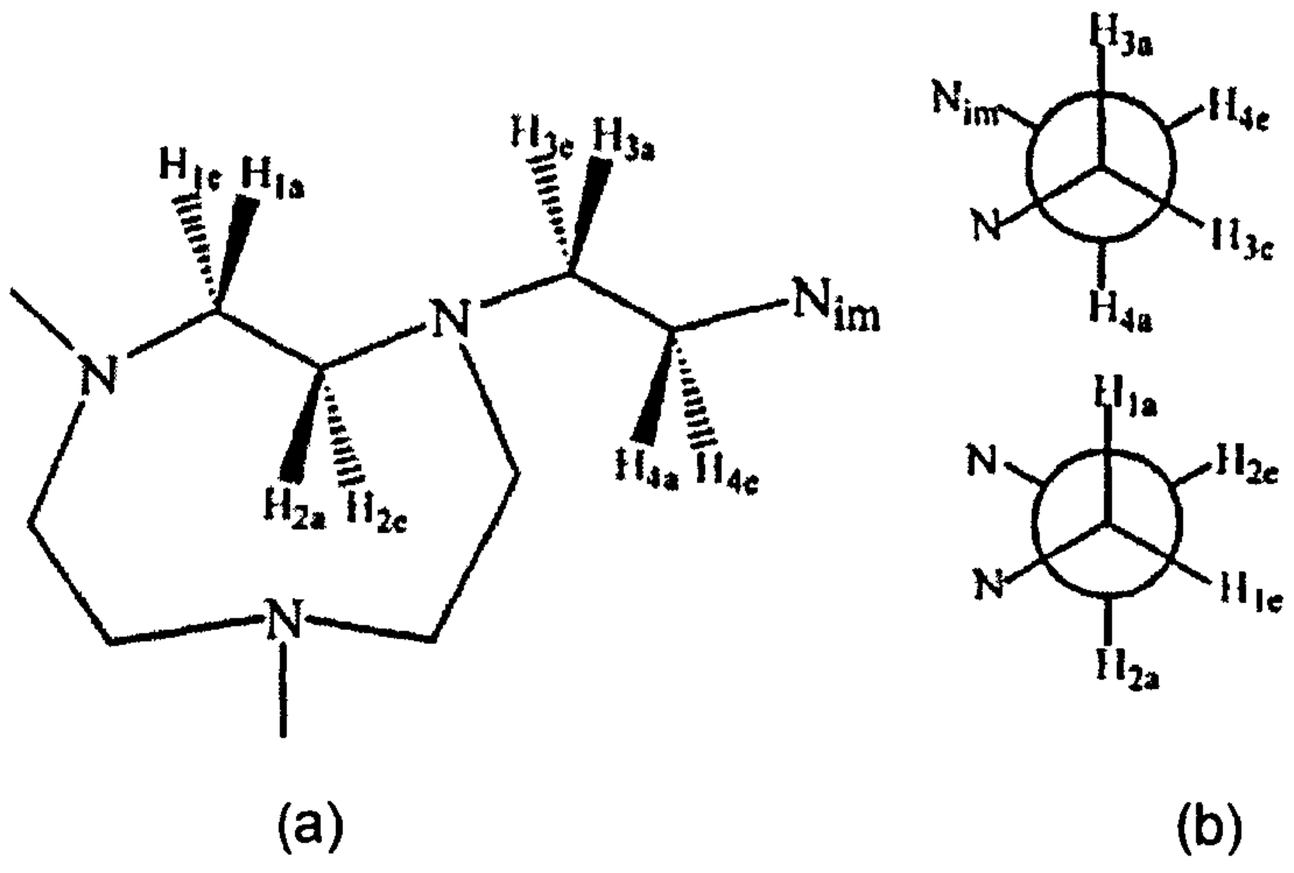

(a) (b)

Figure 3.16 (a) Labelling scheme for the CH_2CH_2 linkers of the macrocycle and the arms and (b) their Newman projections.

This splitting pattern is explained by considering that the coupling between axial protons and geminal equatorial protons is of the same magnitude as that between axial protons of adjacent CH_2 units. Consequently, every axial proton sees two equivalent protons, thereby splitting into a triplet; the smaller *trans* coupling with the equatorial proton of an adjacent CH_2 leads to the observed triplets of doublets. In contrast, equatorial protons couple strongly with geminal axial protons and only weakly with vicinal ones, thereby giving the observed doublets of doublets.

The protons of the methyl group of the pyruvate appear as a singlet at 2.18 ppm; the axial protons of the CH_2CH_2 moiety of each arm appear as a pair of complex triplets due to vicinal and geminal coupling [a broad triplet at 3.81 ppm for the axial proton of the CH_2 close to the imine nitrogen (H_{4a}) and a triplet of doublets at 3.03 ppm for the axial proton of the CH_2 close to the macrocycle (H_{3a})]; the equatorial protons appear as a pair of doublet of doublets (3.68 ppm for H_{4e} and 2.80 ppm for H_{3e}). J_{gem} is 17.2 Hz for H_{4e} and 12.3 Hz for H_{3e} while J_{trans}, due to the coupling between equatorial and axial protons of different CH_2, are 5.7 and 5.1 Hz respectively. The CH_2CH_2 groups of the macrocycle form a series of multiplets that can be assigned as follows: the axial protons afford a pair of multiplets at 3.42 ppm and 2.74 ppm while the equatorial protons afford a pair of doublets of doublets at 2.89 ppm and 2.56 ppm. The 2D-COSY experiment allowed us to establish that the equatorial proton at 2.56 ppm is geminal to the axial protons resonating at 2.74 ppm (and H_{eq} at 2.89 to H_{ax} at 3.42 ppm). The geminal couplings are 12.9 and 16.1 Hz and the *trans* (eq-ax) couplings are 4.8 and 5.3 Hz. The ^{13}C NMR spectrum of [Y(L^a)] shows one peak less than expected, but with the help of the ^1H-^{13}C coupling experiment it has been determined that the "missing" peak is overlapped by the solvent peak (CD_3OD) and consequently all the peaks reported in Table 3.2 could be assigned.

Table 3.2 ^{13}C NMR chemical shifts (ppm) for [Y(L^a)].

CH_3 (pyruvate)	CH_2-N (imine)	CH_2-N (arm)	N-CH_2-CH_2-N	N-CH_2-CH_2-N	C=N	COO^-
16.0	47.4	59.1	52.6	59.2	171.5	172.7

The ^{1}H NMR spectrum of [La(L^a)] was also recorded (300 MHz, 298 K, D_2O) and shows the same splitting pattern already described for [Y(L^a)] (Figure 3.17). The peaks were assigned and are reported in Table 3.3. The coupling constants are: 13.91 Hz for J_{gem} of H_4 (J_{trans} is 4.83 Hz), 12.77 Hz for J_{gem} of H_3 (J_{trans} is 5.33 Hz), 14.16 and 11.51 Hz for J_{gem} of H_2 and H_1 (J_{trans} are 6.11 and 5.57 Hz). The equatorial proton at 2.80 ppm is geminal to the axial protons resonating at 3.29 ppm and H_{eq} at 2.54 ppm to H_{ax} at 2.58 ppm.

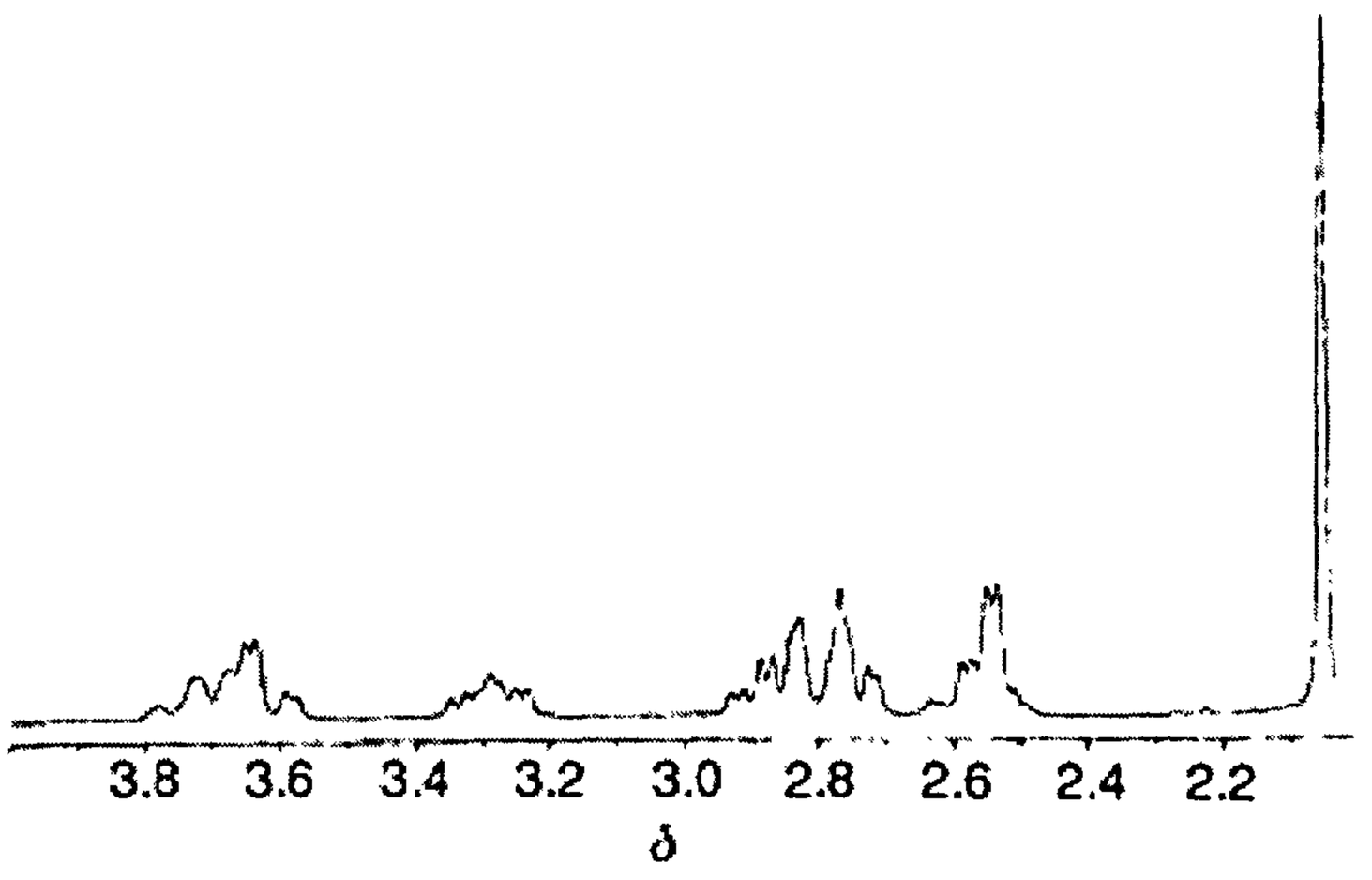

Figure 3.17 ^{1}H NMR spectrum of [La(L^a)] in D_2O at 298 K.

Proton NMR spectra for paramagnetic lanthanide complexes are shifted over an expanded spectral region.[295-298] The induced shift ($\Delta\nu/\nu$) of Ln^{III} ions is essentially dipolar (pseudo-contact) in origin and for an axially symmetric complex is given by:

$$\Delta\nu/\nu = -D(3\cos\theta - 1) / r^3$$

where D is the magnetic susceptibility term that depends upon the Ln^{III} ion and can be either positive or negative, r is the distance between the Ln^{III} centre and the proton nucleus under consideration and θ is the angle between the symmetry axis and the line which intersects the Ln^{III} centre and the proton nucleus. Thus, the proton chemical shifts can be directly correlated to the structural features of the complex.[295-298]

Table 3.3 ^{1}H NMR chemical shifts for [La(L^a)] and [Sm(L^a)].

	Multiplicity	[La(L^a)]	[Sm(L^a)]
H_{4a}	t	3.73	2.37 (overlapping)
H_{4e}	d	3.61	3.09
H_{3a}	t	2.88	5.20
H_{3e}	d	2.75	3.24
H_{ax}	t	3.29	2.95
H_{eq}	d	2.80	2.39 (overlapping)
H_{ax}	t	2.58	0.83
H_{eq}	d	2.54	2.25
$H_{pyruv.}$	s	2.05	1.88

The ^{1}H NMR spectrum of [Yb(L^a)] (300 MHz, 298 K, D_2O) shows nine resonances in the range between 36.4 ppm to –29.0 ppm (Figure 3.18) due to nine different protons (H_{pyr}, four axial and four equatorial protons). All the resonances were assigned with the help of a 2D COSY experiment (Table 3.4). The paramagnetic shift observed in the ^{1}H NMR spectrum of [Sm(L^a)] is much smaller and all the resonances lie between 0.83 ppm and 5.20 ppm (Figure 3.18), and a coupling pattern similar to that for [Y(L^a)] and for [La(L^a)] is observed. Resonances were assigned on the basis of 2D COSY experiments and are given in Table 3.3. The coupling constants are 10.14 Hz for J_{gem} of H_4, 13.05 Hz for J_{gem} of H_3, 14.03 and 11.94 Hz for J_{gem} of H_2 and H_1. The equatorial proton at 2.39 ppm is geminal to the axial protons resonating at 2.95 ppm and H_{eq} at 2.25 ppm to

H_{ax} at 0.83 ppm. It is interesting to note that in no ^{1}H NMR spectrum of a paramagnetic [Ln(DOTA)]$^-$ has a coupling pattern been detected.[292]

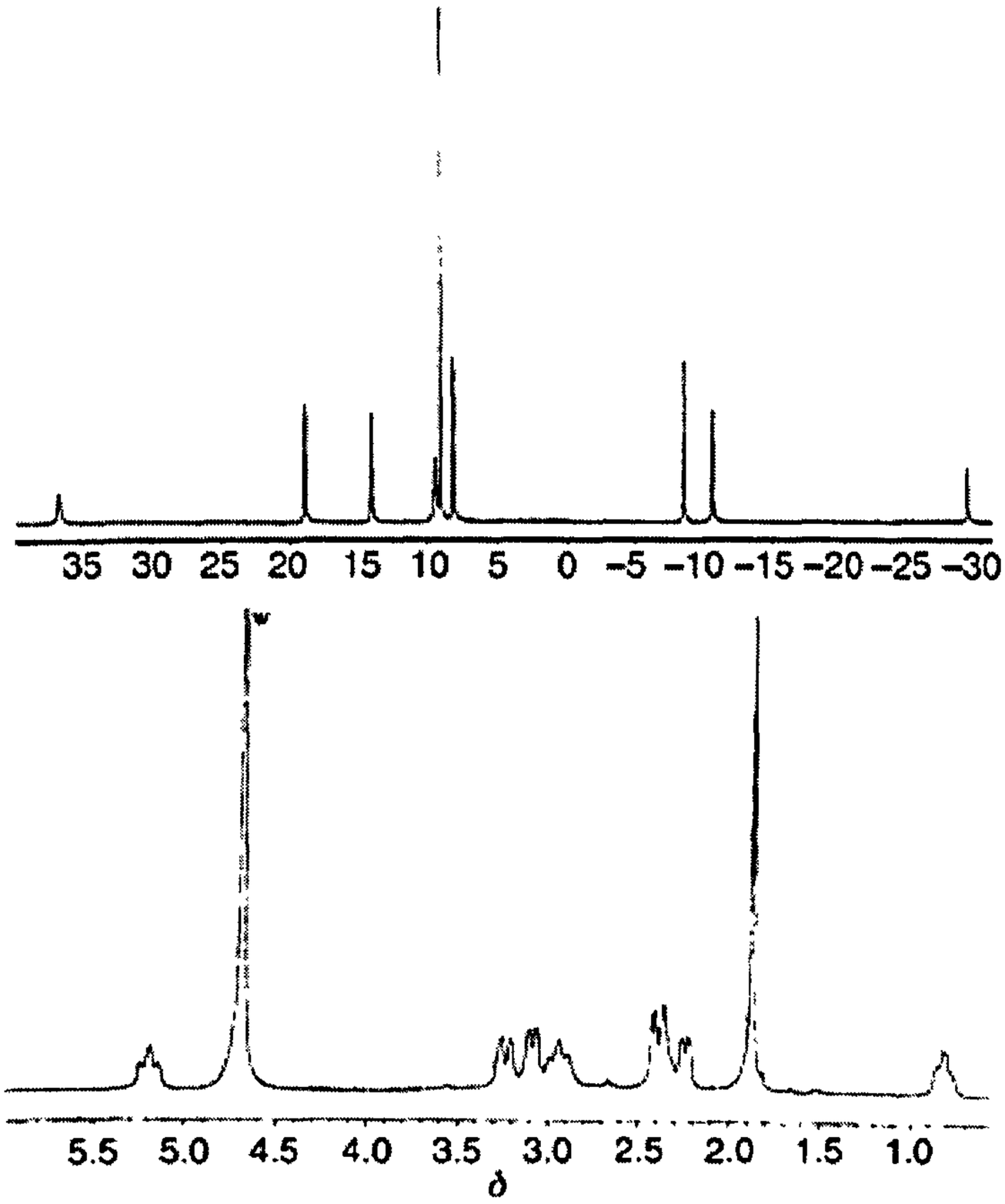

Figure 3.18 ^{1}H NMR spectra of paramagnetic [Yb(L^a)] (above) and [Sm(L^a)] (below) in D_2O at 298 K.

Table 3.4 Variable temperature ^{1}H NMR chemical shift (ppm) for paramagnetic [Yb(L^a)].

	278 K	298 K	323 K	343 K
H_{3a}	40.7	36.4	32.0	28.1
H_{4e}	20.8	18.8	16.8	15.1
H_{4a}	15.3	14.0	14.2	11.6
H_{1a}	10.0	9.4	8.8	8.4
$H_{pyruv.}$	9.7	9.0	8.3	7.7
H_{3e}	8.6	8.1	7.6	7.2
H_{1e}	-10.4	-8.6	-6.7	-5.0
H_{2e}	-12.6	-10.7	-8.5	-6.7
H_{2a}	-33.6	-29.0	-24.1	-19.9

3.3.5 Variable temperature ^{1}H NMR experiments

The solution behaviour of various lanthanide poly(amino)carboxylate complexes has been studied by variable temperature ^{1}H NMR and reported in the literature. The spectra of complexes of DTPA (Section 2.2.2) with La^{III}, Pr^{III}, Eu^{III} and Yb^{III} in D_2O[299,300] all show coalescence as the temperature is raised. In addition, the lanthanide complexes of the macrocyclic ligand DOTA show this coalescence behaviour above about 45°C in D_2O.[292,301]

The variable temperature ^{1}H NMR behaviour of [Y(L^a)] and [Yb(L^a)] was therefore investigated. Significantly, the ^{1}H NMR spectra of [Y(L^a)] in CD_3OD recorded between 223 K and 333 K show an almost unchanged splitting pattern within this temperature range. This behaviour is indicative of the highly rigid cage formed by the ligand and it is particularly interesting in respect to the dynamic process involving the CH_2CH_2 moieties of the macrocycle observed in DOTA complexes at high temperature.[291,292,301] The dynamic behaviour of DOTA and DTPA lanthanide complexes has been attributed to a rotation about the metal ion involving a "shuffling" of co-ordinated acetates along with a backbone "ethylenic flips"[292,300,301] or "wagging"[302,303] motions. None of these dynamic processes are observed for [Y(L^a)], suggesting not only that the metal ion is rigidly encapsulated by the three arms, but also that the macrocyclic framework remains bound and rigid even at high temperatures.

The temperature dependence of paramagnetic NMR shift for Ln^{III} complexes is quite complex.[295-298] The large shift observed in many paramagnetic lanthanide complexes of macrocyclic derivatives has recently suggested the use of these complexes as NMR temperature sensors.[304-308] Non-invasive temperature measurement is an interesting target that could help in the detection and localisation of regions of abnormal metabolic activity. The best chemical shift per degree temperature change ratio of almost 1 ppm $^oC^{-1}$ for ^{1}H NMR and of

more than 2 ppm $^oC^{-1}$ for ^{31}P NMR was found for $[Tm(DOTP)]^{5-}$. However, this is a highly charged complex with quite inconvenient osmolality problems.[307]

When the temperature is varied between 5°C and 70°C, the nine peaks observed in the ^1H NMR spectrum of $[Yb(L^a)]$ are all shifted (Table 3.4), the extent depending on how much the paramagnetic Yb^{III} influences the protons. The plot of the variation in chemical shift with temperature gives straight lines for almost all the H-atoms, but the steepest slopes were observed for H_{3a} and H_{2a}, which are most shifted by the paramagnetic metal ion (Figure 3.19). The change in chemical shift with temperature for these two atoms is 0.209(4) ppm $^oC^{-1}$ for H_{3a} and 0.191(5) ppm $^oC^{-1}$ for H_{2a}, with the difference that H_{3a} is shifted upfield and H_{2a} downfield. The absence of coalescence or dynamic processes upon variation of temperature, which were observed in the case of variable temperature ^1H NMR spectra of $[Pr(DOTA)]^-$,[292,301] is again indicative of the high rigidity of the cage.

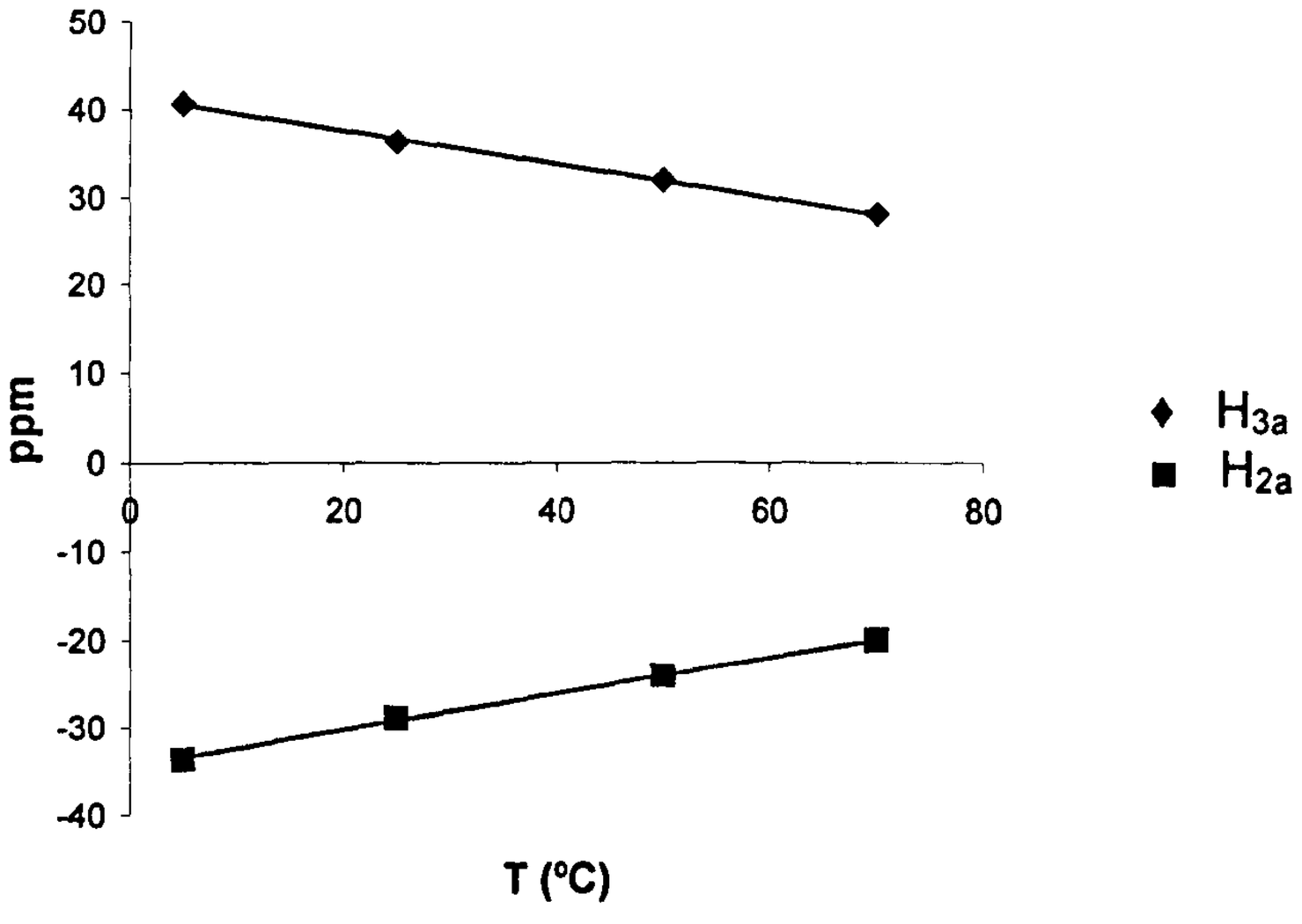

Figure 3.19 Temperature dependence of H_{3a} and H_{2a}, the protons most influenced by the paramagnetic Yb^{III} ion.

3.3.6 Hydrolysis experiments

Previous work at the University of Nottingham studied the possibility of using lanthanide complexes of the ligand obtained by Schiff-base condensation of tren with sodium pyruvate (**1**, Section 3.2) in the targeting of *in vivo* regions of low pH.[283,309] The complex suitable for this kind of medical application should have the following characteristics:

1. high solubility in H_2O to permit mobility in the blood stream;
2. electroneutrality to allow the crossing of cell membranes;
3. high stability in H_2O at pH 7 but low stability at pH 4.5 where the complex can undergo an irreversible change.

Such a complex can be used for labelling polymorphonuclear leucocytes (PMN's, the most numerous class of white blood cells). These cells contain lysosomes (intracellular packets of hydrolytic enzymes surrounded by lipid membrane), which have an internal pH of 4.5. Since the vast majority of other blood cells do not contain lysosomes, PMN's can potentially be labelled *in vivo* by such a complex without separating blood components. Moreover, as PMN's are known to concentrate at infected or inflammed sites *in vivo*, the labelling of these cells can be used for diagnostic imaging of these regions (using radionuclides such as ^{67}Ga, ^{111}In, ^{86}Y or ^{169}Yb, see Section 2.3).[283,309]

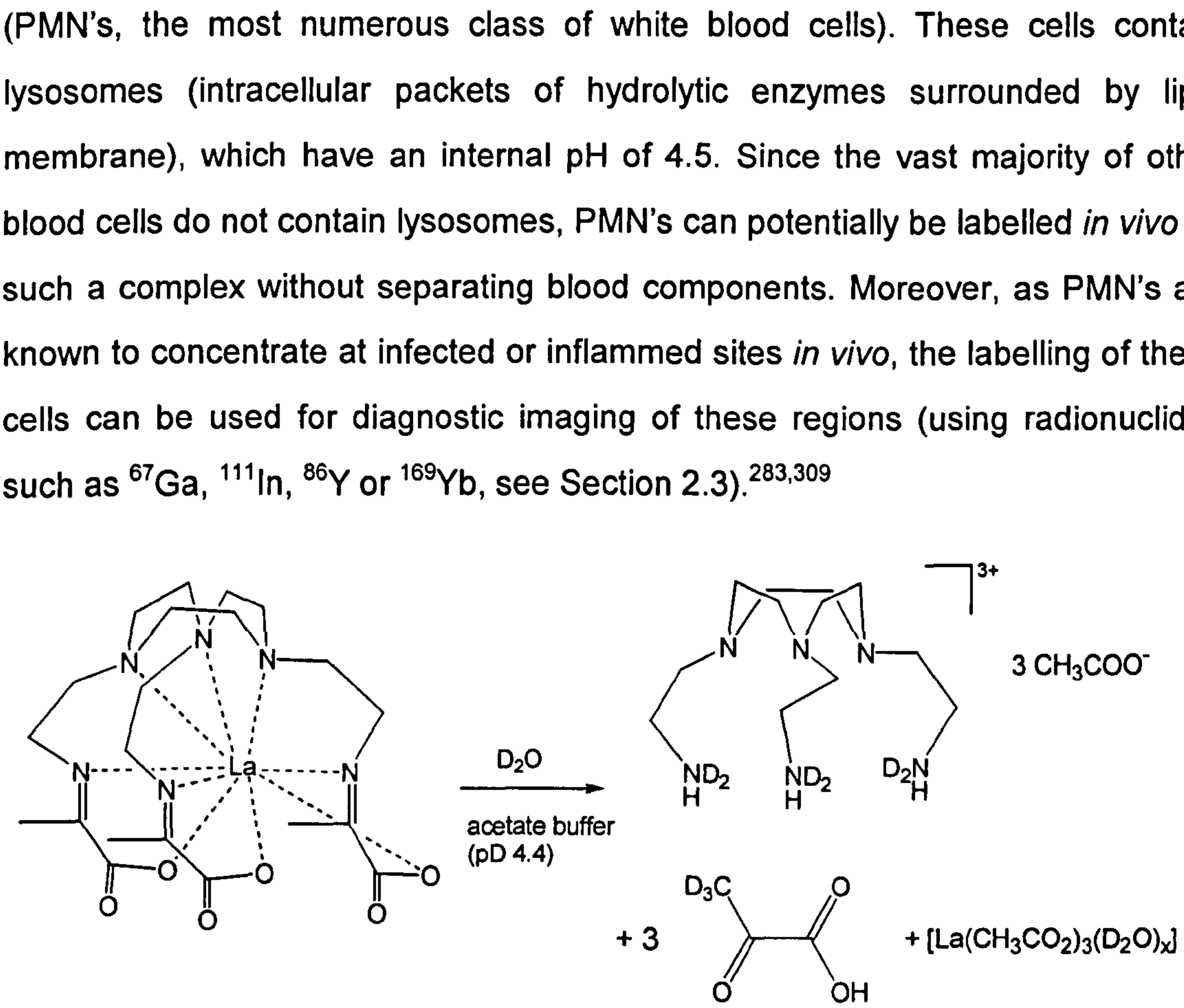

Figure 3.20 Scheme showing the hydrolysis of [La(L^a)] in D_2O at pD 4.4.

In this context, the lanthanide complexes discussed in this Chapter are highly relevant because they are soluble in water, neutral and experiments were performed on the [La(L^a)] complex in D_2O at pH 4.4 (acetate very stable in H_2O at pH 7. In order to determine the stability at pH 4.5, hydrolysis buffer). The ^{1}H NMR spectrum of [La(L^a)] was acquired at different time intervals and are shown in Figure 3.21. The first spectrum was acquired after just five minutes. All the peaks

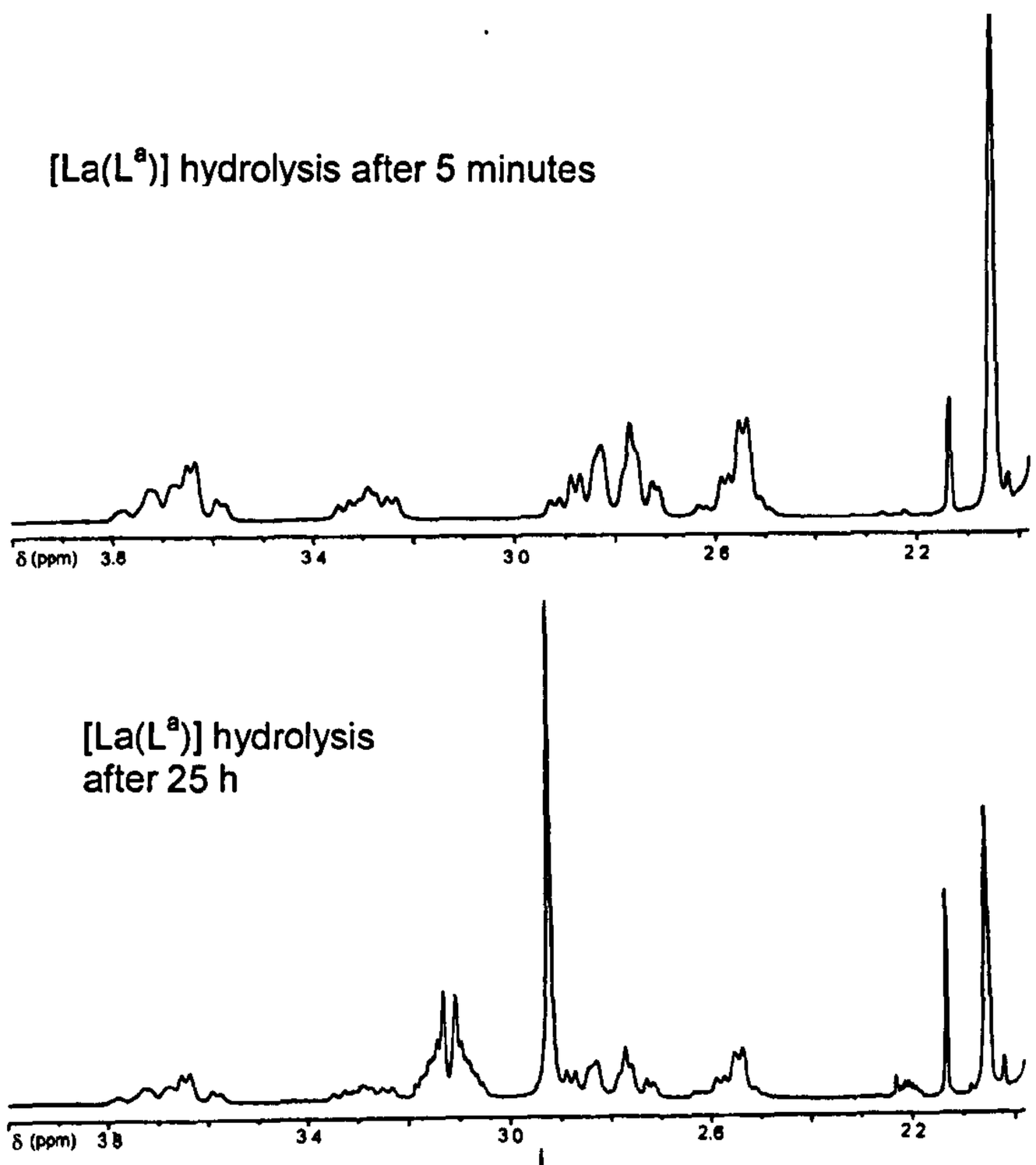

Figure 3.21 ^{1}H NMR spectra of [La(L^a)] in D_2O (pD = 4.4) acquired at the time intervals shown after the dissolution of the sample.

can be assigned as already discussed in Section 3.3.1, along with the peak at 2.14 ppm (present in all the spectra) which is a side band of the acetate peak from the acetate buffer. The integral of the peaks corresponding to [La(L^a)] decreases and that of the peaks from the hydrolysis products increases with time.

The hydrolysis of the three pyruvate groups leads to the formation of a-ketobutyric acid where the protons of the methyl group have been exchanged with deuterium and are not detected in the 1H NMR spectrum. Lanthanide amine complexes are unstable in aqueous solution (most of all in acidic conditions), hence the final products are likely to be the free metal ion and the protonated hexaamine ligand (clearly in acetic buffer the counterions would be acetate as shown in Figure 3.20). The 1H NMR spectra of the hydrolysis products show a multiplet (3.06-3.14 ppm) due to the ethylenic moiety of the arms and a singlet at 2.92 ppm due to the macrocyclic protons.

In analogous studies carried out on the YIII complex of the ligand **1**[283,309] the imine bonds hydrolyse very quickly compared to [La(L^a)]. While [Y(**1**)] hydrolyses completely after six hours at pD 5.5,[283,309] the half life of [La(L^a)] is

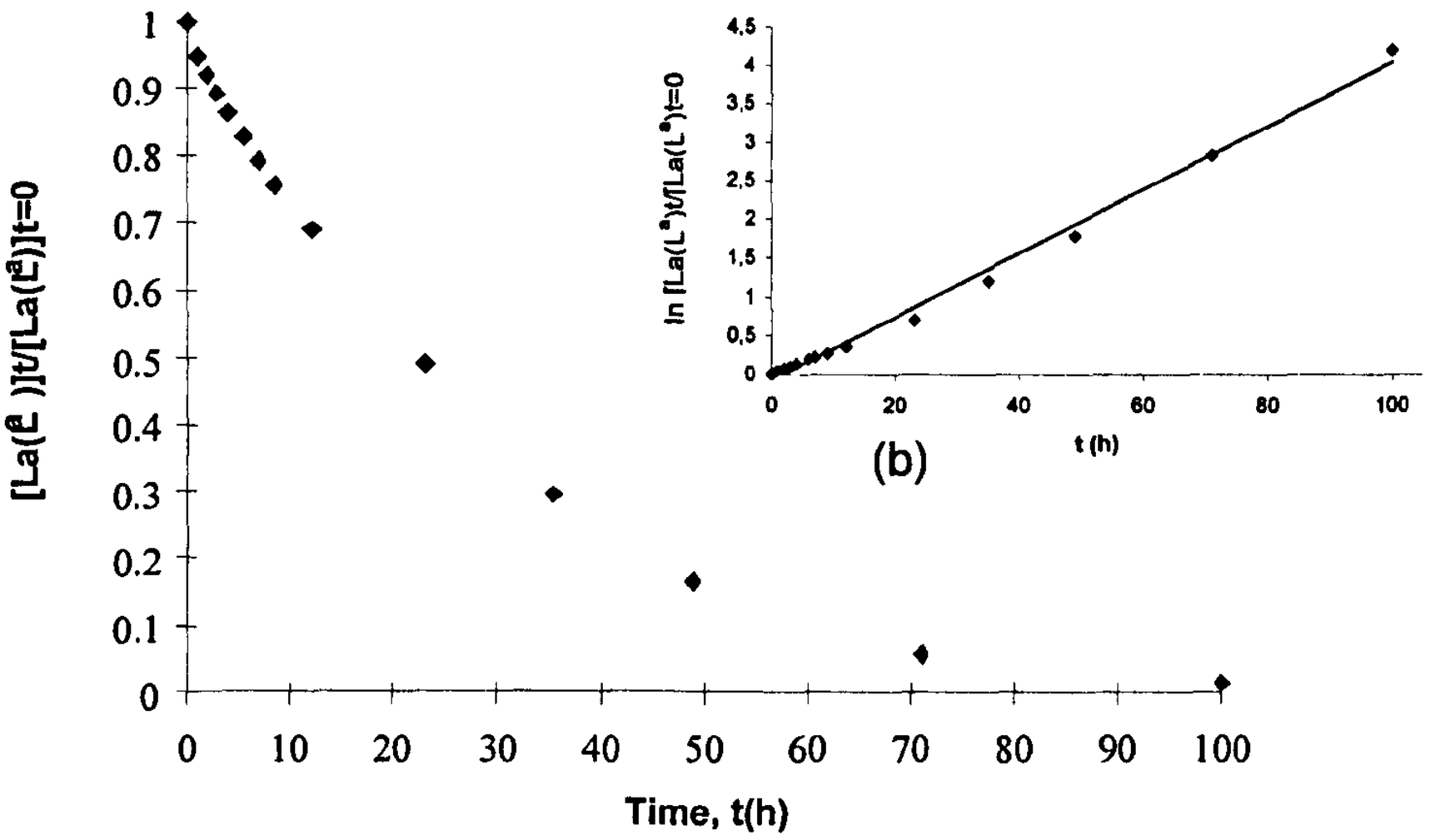

Figure 3.22 Acid-catalysed hydrolysis of [La(L^a)]: (a) asymptotic curve and (b) kinetic trace.

almost 24 hours at pD 4.4 and only after 4 days have the peaks corresponding to the complex completely disappeared (Table 3.5 in section 3.4.7). The acid catalysed hydrolysis of [La(L^a)] follows an asymptotic curve as shown in Figure 3.22(a). Preliminary considerations of the kinetics of this hydrolysis reaction suggest a second order reaction depending on the concentrations of [La(L^a)] and H^+. By taking a pseudo-first order integrated rate equation with [H^+] constant (reaction buffered at pH 4), the rate of hydrolysis can be determined as 0.114 $s^{-1}M^{-1}$. Clearly, these results are not conclusive, as further hydrolyses at different complex concentrations and pH must be carried out to obtain more definitive results.

3.3.7 Relaxivity of [Gd(L^a)]

Relaxivity (r_1) is a quantitative measure of the efficiency with which a paramagnetic complex (usually a Gd^{III} complex) enhances the water proton longitudinal relaxation rate (T_1^{-1}).[21] Relaxivity has been comprehensively introduced in Section 2.2.3 and details of the experimental procedure used to determine relaxivity are given in Section 3.5.7. The relaxivity of [Gd(L^a)] at 300 MHz and 37°C was measured as 1.26 ± 0.05 $mM^{-1}s^{-1}$.

It is important to note that relaxivity has a strong dependence upon the applied magnetic field strength and by analysis of this dependence several important structural and dynamic parameters may be obtained.[22,127] Experimentally, this is performed by measuring solvent longitudinal relaxation rates over a wide range of magnetic fields corresponding to proton Larmour frequencies of 0.01-50 MHz.[21] Data points represent the so-called nuclear magnetic relaxation dispersion (NMRD) profile that can be adequately fitted to yield the values of the relaxation parameters. In Figure 3.23 the NMRD profiles of $[Gd(DOTA)]^-$ and $[Gd(DTPA)]^{2-}$ are reported.[127]

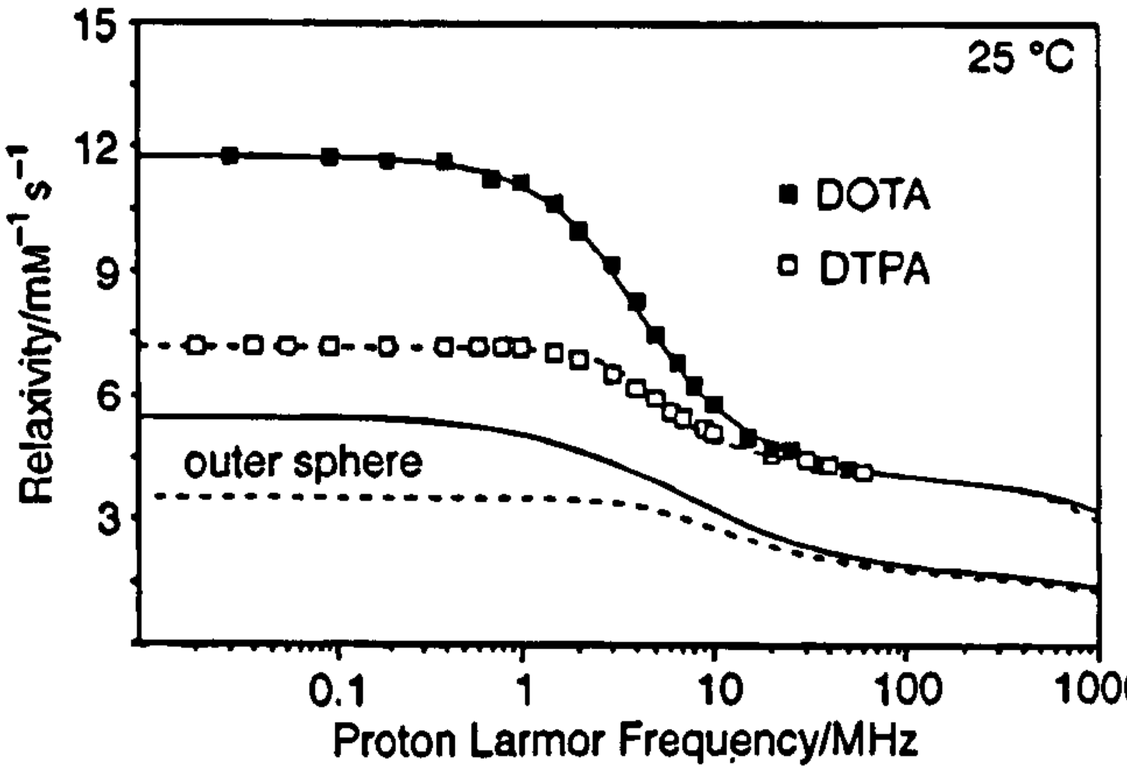

Figure 3.23 NMRD profiles of $[Gd(DOTA)]^-$ and $[Gd(DTPA)]^{2-}$

Moreover, since MRI experiments are carried out at magnetic field strengths between 0.5 and 1.5 T (21-64.5 MHz), almost all the relaxivity data on MRI contrast agents are determined at 20MHz.[22] Therefore, the value determined at 300 MHz cannot be easily compared with other Gd^{III} complexes reported in literature. A relaxivity of 4.7(4) $mM^{-1}s^{-1}$ (300 MHz, 37°C) was determined for the Gd^{III} complex of **1**.[283] In this complex two water molecules are co-ordinated to the Gd^{III} ion, thereby increasing the relaxivity (Figure 3.9b in Section 3.2).[283] In the solid state it has been found that $[Gd(L^a)]$ has no water molecule co-ordinated to the paramagnetic metal centre (Section 3.3.3) and this type of structure is likely to be maintained in solution. Without H_2O molecules bound to the Gd^{III} centre, only the second sphere and outer sphere terms contribute to the increment of the relaxivity. A value of 1.26(5) $mM^{-1}s^{-1}$ at 300 MHz is indicative of no water molecules directly bound to the Gd^{III} centre (q = 0), since the outer sphere term at 20 MHz has been determined as a constant contribution of ca. 2.0-2.5 $mM^{-1}s^{-1}$.[142] Relaxivity also changes with temperature and is normally higher at 25°C than at 37°C. The value of 1.26(5) $mM^{-1}s^{-1}$ was determined at the body temperature of 37°C, but a single preliminary measure at 25°C gave a relaxivity of 2.26 $mM^{-1}s^{-1}$.

3.3.8 Dy^{III}-induced ^{17}O NMR water shift experiments

Addition of Dy^{III} complexes to water results in a shift of the water ^{17}O NMR signal to lower frequencies. The dysprosium induced shift of water (DIS) has been exploited to estimate quantitatively the number of bound water molecules associated with various lanthanide complexes.[310-313] The reason of this is that, for paramagnetic Ln^{III} ions, the contact contribution to the Ln^{III}-induced shift of a ^{17}O nucleus bound to a lanthanide ion is almost independent of the nature of the ligand in question and also of the other ligands co-ordinated to the Ln^{III}.[314-316] Therefore, the Ln^{III}-induced ^{17}O shifts can be utilised to establish the co-ordination sites of the ligand and to determine the stoichiometry of the complex. Dy^{III} has been chosen in preference to other lanthanides because the induced ^{17}O shift is dominated by the contact shift which contributes more than 85% of the total shift and a laborious dissection of the observed induced shift into the contact and pseudo-contact contributions is not needed.[314-316]

The DIS of water is measured at varying dysprosium concentrations and the plot of DIS versus [Dy^{III}] should be proportional to the number of bound water molecules associated with the complex (*q*). The plot of DIS versus [Dy^{III}] obtained

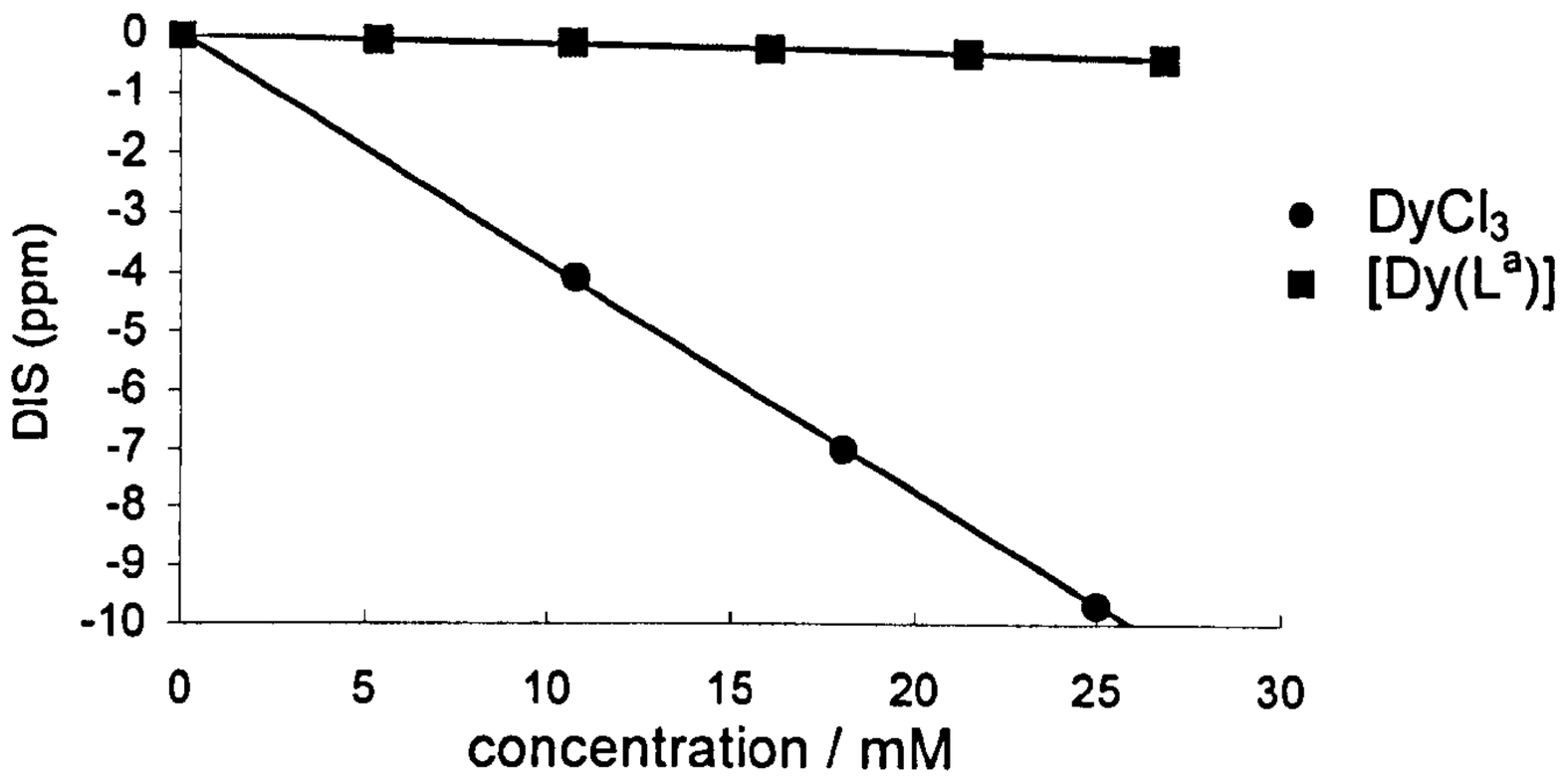

Figure 3.24 Plots showing the variation of the dysprosium induced shift (DIS, -$\Delta\delta$) with concentration of $DyCl_3$ and [$Dy(L^a)$].

by varying the concentration of $DyCl_3$ gives the graph shown in Figure 3.24 with a slope of 387 ± 1 ppm/M. There has been controversy over the number of water molecules associated with a Dy^{III} ion:[317] hydration numbers of eight and nine have been proposed. Merbach and co-workers[318,319] have concluded from neutron-scattering difference studies that the co-ordination number of Dy^{III} is eight for 0.3 and 1 mol dm^{-3} solutions of $DyCl_3$ and $Dy(ClO_4)_3$ in D_2O. On the other hand, Brücher *et al.*[320] have shown that the hydration number of Lu^{III} increases upon dilution up to values ≥9. Therefore, considering the low dysprosium concentrations used in aqueous systems, in the present work a hydration number of nine for Dy^{III} is assumed. Consequently, a slope of 387/9=43 is indicative of one bound water molecule (q = 1) and q can be determined dividing by 43 the slope of the plot of DIS versus the concentration of [Dy(L^a)].

Figure 3.24 shows the plot of DIS versus the concentration of [Dy(L^a)] with a gradient of 14.3 ± 0.3 ppm/M. This value is indicative of about 0.3 water molecules associated with [Dy(L^a)]. Fractional values of q are normally found by this method,[312] perhaps due to a small contribution by the outer and/or second sphere water molecules, but it can be assumed that in [Dy(L^a)] no water molecules are directly bound to the Dy^{III} centre.

3.4 Experimental

Spectra were recorded on a Bruker DPX 300 spectrometer (^{1}H and ^{13}C NMR), on a Perkin-Elmer 1600 spectrometer (FTIR, KBr discs). Elemental analytical data were obtained by the Microanalytical Service (Perkin-Elmer 240B analyser) at the University of Nottingham and EI (electron impact) mass spectra were measured using a V6 Autospec V67070E spectrometer. FAB (Fast Atom Bombardment) and Electrospray (ES) mass spectra were obtained by the EPSRC National Mass Spectrometry Service at the University of Swansea.

3.4.1 Synthesis of 1,4,7-*tris*(cyanomethyl)-1,4,7 triazacyclononane (L^1)

[9]aneN_3·3HBr (3.0g, 8.07mmol), chloroacetonitrile (1.9g, 25.2mmol), and Et_3N (10g, 0.099mol) in EtOH (150 cm^3) were refluxed under N_2 for 24 h. After cooling, the solvent was removed by rotary evaporation to yield a red oil which was dissolved in $CHCl_3$ (100 cm^3) and washed with H_2O (3 x 100 cm^3). The organic phase was collected and dried with $MgSO_4$, filtered, and dried by rotary evaporation. The resulting yellow oil was dried *in vacuo* to yield a pale yellow solid (1.052g, 4.27 mmol, yield 53%). ^{1}H NMR: $\delta(CDCl_3)$ 2.85 (12 H, s, NCH_2), 3.59 (6 H, s, NCH_2CN) ppm. ^{13}C NMR: δ ($CDCl_3$) 54.12 (NCH_2), 46.49 (NCHCN), 116.14 (*C*N) ppm. EI mass spectrum: m/z found 163.2, 138.1, 124.1 for 166.2 [M^+-2CH_2CN], 140.2 [M^+-2CH_2CN-CN] and 126.1 [M^+-3CH_2CN] respectively. Elemental analysis: found (calc. for $C_{12}H_{18}N_6$): C, 58.23 (58.51); H, 7.56 (7.37); N, 34.02% (34.12%). IR (KBr disk), cm^{-1}: 2937m, 2840m, 2227m (CN stretch), 1455m, 1132w, 1099w, 887w, 844w.

3.4.2 Synthesis of 1,4,7-*tris*(aminoethyl)-1,4,7-triazacyclononane (L)

1,4,7-*tris*(cyanomethyl)-1,4,7-triazacyclononane (L^1) (0.320g, 1.23 mmol) and BH_3·THF (40 cm^3, 1M solution in THF) were refluxed under N_2 for 48 h. After cooling, excess borane was destroyed by adding water (5 cm^3), then the solution

was dried *in vacuo*. The white solid obtained was dissolved in 6M HCl (50 cm^3) and heated under reflux for 24 h. After cooling, the solution was dried *in vacuo* to yield a white solid. The solid was dissolved in the minimum amount of water and the solution obtained was passed through a Dowex 1x8-200 column (10 g) activated with 1M sodium hydroxide. The solvent was removed under reduced pressure to yield a colourless oil (0.270g, 1.045 mmol, yield 85%). ^{1}H NMR: δ ($CDCl_3$) 2.76 (12 H, s, NC*H*$_2$), 2.75 (6 H, t, CH_2CH_2N), 2.59 (6 H, t, CH_2CH_2N), 1.63 (6 H, broad, N*H*$_2$) ppm. ^{13}C NMR spectrum: δ ($CDCl_3$) 56.90 (NCH_2), 62.21 ($NCH_2CH_2NH_2$), 40.26 ($NCH_2CH_2NH_2$) ppm EI mass spectrum: m/z found 213.2, 199.2, 185.2 and 159.2 for 214.3 [M^+-$CH_2CH_2NH_2$], 198.3 [M^+-$CH_2CH_2NH_2$ - NH_2], 184.3 [M^+-$CH_2CH_2NH_2$ -CH_2NH_2], 154.2 [M^+-2$CH_2CH_2NH_2$] respectively. Elemental analysis: found (calc. for $C_{12}H_{30}N_6$): C, 55.53 (55.78); H, 11.87 (11.70); N, 32.34% (32.52%).

3.4.3 Synthesis of [Y(L^a)]·2CH_3OH *via* template procedure

1,4,7-*tris*(aminoethyl)-1,4,7-triazacyclononane (L) (39.8 mg, 0.154 mmol), sodium pyruvate (50.9 mg, 0.462 mmol) and $Y(NO_3)_3$ (56.2 mg, 0.154 mmol) were heated under reflux in MeOH (30 cm^3) for 2h. After cooling, the solvent volume was reduced, Et_2O was added and a pale yellow solid was obtained. The solid was filtered off and dried under reduced pressure. $NaNO_3$ was removed from the yttrium complex by passing a concentrated methanolic solution of the solid through a LH-20 Sephadex column. Addition of Et_2O yielded a white solid (61.2 mg, 0.11 mmol, yield 71.4%). Single crystals suitable for X-ray structural analysis were obtained by diffusion of Et_2O vapour into a MeOH solution of the complex at room temperature. Mass spectrum (Electrospray) m/z = 577 (M^+ [$C_{21}H_{33}N_6O_6Y$ + Na^+]). Elemental analysis: found (calc. for $C_{21}H_{33}N_6O_6Y$

·2CH_3OH): C, 44.51 (44.66); H, 6.60 (6.68); N, 13.45% (13.56%). IR (KBr disk), cm^{-1}: 2920w, 2854w, 1654s and 1617s ($\nu_{C=N, C=O}$), 1384m, 1206m, 1110w.

3.4.3 Synthesis of $(L^a)Na_3·2H_2O$ and $[Y(L^a)]·3NaCl·2H_2O$ (non template)

1,4,7-*tris*(aminoethyl)-1,4,7-triazacyclononane (L) (50 mg, 0.193 mmol), sodium pyruvate (63.8 mg, 0.580 mmol) were heated under reflux in MeOH (40 cm^3) for 2h. After cooling, the solvent volume was reduced, Et_2O was added and a white solid was obtained. The solid was filtered off, washed thoroughly with Et_2O and dried under reduced pressure (the product is very hygroscopic and tends to become an oil on contact with air) (85.5 mg, 0.16 mmol, yield 82.9%). Elemental analysis: found (calc. for $C_{21}H_{33}N_6O_6Na_3·2H_2O$): C, 44.41 (44.21); H, 6.60 (6.54); N, 14.49% (14.73%). IR (KBr disk), cm^{-1}: 2934w, 2874w, 1603s ($\nu_{C=N, C=O}$), 1394m, 1196m, 1090w.

$(L^a)Na_3·2H_2O$ (34.2 mg, 0.06 mmol) and $YCl_3·6H_2O$ (18.2 mg, 0.06 mmol) were dissolved in MeOH (20 cm^3) and stirred at room temperature for 1h. Then the solvent volume was reduced, Et_2O was added and a white solid was obtained. The solid was filtered off and dried *in vacuo* (35.4 mg, 0.046 mmol, yield 77%). Mass spectrum (Electrospray) m/z = 577 (M^+ [$C_{21}H_{33}N_6O_6Y$ + Na^+]). Elemental analysis: found (calc. for $C_{21}H_{33}N_6O_6Y·3NaCl·2H_2O$): C, 32.81 (32.94); H, 4.68 (4.87); N, 10.65% (10.97%). IR (KBr disk), cm^{-1}: 2925w, 2864w, 1619s ($\nu_{C=N, C=O}$), 1384m, 1201m, 1110w.

3.4.5 Synthesis of Gd^{III}, Sm^{III} and La^{III} complexes with L^a

1,4,7-*tris*(aminoethyl)-1,4,7-triazacyclononane (L) (0.15-0.20 mmol), sodium pyruvate (3 equivalents) and the appropriate Ln^{III} salt (1 equivalent) were heated under reflux in methanol (30 cm^3) for 2h. After cooling, the solvent volume was reduced, Et_2O was added and a white solid was obtained. The solid was

filtered off and dried *in vacuo*. Single crystals suitable for X-ray structural analysis were obtained by diffusion of Et_2O vapour into a MeOH solution of the complex at room temperature.

[Sm(L^a)]·2CH$_3$OH·H$_2$O. Yield 72.7%. Mass spectrum (FAB, 3-NOBA matrix) m/z = 640 (M^+ [$C_{21}H_{33}N_6O_6Sm$ + Na^+]) Elemental analysis: found (calc. for $C_{21}H_{33}N_6O_6Sm·2CH_3OH·H_2O$): C, 39.81 (39.58); H, 6.40 (6.21); N, 12.21% (12.04%). IR (KBr disk), cm^{-1}: 2924w, 2851w, 1653s and 1616s ($\nu_{C=N,\ C=O}$), 1387m, 1204s, 1110m, 1030w.

[Gd(L^a)]·3NaCl·3H$_2$O. Yield 75.1%. Mass spectrum (FAB, 3-NOBA matrix) m/z = 645 (M^+ [$C_{21}H_{33}N_6O_6Gd$ + Na^+]) Elemental analysis: found (calc. for $C_{21}H_{33}N_6O_6Gd·3NaCl·3H_2O$): C, 29.83 (29.60); H, 4.46 (4.61); N, 10.10% (9.86%). IR (KBr disk), cm^{-1}: 2925w, 2869w, 1617s ($\nu_{C=N,\ C=O}$), 1388m, 1205s, 1109m, 1032w, 939w.

[La(L^a)]·2CH$_3$OH. Yield 70.3%. Mass spectrum (FAB, 3-NOBA matrix) m/z = 627 (M^+ [$C_{21}H_{33}N_6O_6La$ + Na^+]) Elemental analysis: found (calc. for $C_{21}H_{33}N_6O_6La·2CH_3OH$): C, 41.04 (41.32); H, 6.02 (6.18); N, 12.39% (12.57%). IR (KBr disk), cm^{-1}: 2914w, 2849w, 1653s and 1610s ($\nu_{C=N,\ C=O}$), 1384m, 1364m, 1274s, 1201s, 1134m, 1111m, 1031m, 641m, 573w, 518w.

3.4.6 Synthesis of Eu^{III}, Dy^{III} and Yb^{III} complexes with L^a

1,4,7-*tris*(aminoethyl)-1,4,7-triazacyclononane (L) (0.15-0.20 mmol), sodium pyruvate (3 equivalents) and the appropriate Ln^{III} salt were heated under reflux in MeOH (30 cm^3) for 2h. After cooling, the solvent volume was reduced, Et_2O was added and a pale yellow solid was obtained. The solid was filtered off and dried *in vacuo*.

[Eu(L^a)]·3NaCl·3H$_2$O. Yield 68.7%. Mass spectrum (FAB, 3-NOBA matrix) m/z = 641 (M^+ [$C_{21}H_{33}N_6O_6Eu$ + Na^+]) Elemental analysis: found (calc. for

$C_{21}H_{33}N_6O_6Eu{\cdot}3NaCl{\cdot}3H_2O$): C, 29.91 (29.78); H, 4.47 (4.64); N, 10.11% (9.92%). IR (KBr disk), cm^{-1}: 2962w, 2916w, 2848w, 1614s ($\nu_{C=N,\ C=O}$), 1383m, 1229s, 1173m, 1024w, 809w.

[Dy(L^a)]·3NaCl·2H$_2$O. Yield 72.5%. Mass spectrum (FAB, 3-NOBA matrix) m/z = 652 (M^+ [$C_{21}H_{33}N_6O_6Dy$ + Na^+]) Elemental analysis: found (calc. for $C_{21}H_{33}N_6O_6Dy{\cdot}3NaCl{\cdot}2H_2O$): C, 29.93 (30.05); H, 4.34 (4.44); N, 9.89% (10.01%). IR (KBr disk), cm^{-1}: 2991w, 2966w, 2878w, 1617s ($\nu_{C=N,\ C=O}$), 1387m, 1206s, 1110m, 1033w, 941w.

[Yb(L^a)]·CH$_3$OH·H$_2$O. Yield 60.7%. Mass spectrum (FAB, 3-NOBA matrix) m/z = 662.3 (M^+ [$C_{21}H_{33}N_6O_6Yb$ + Na^+]) Elemental analysis: found (calc. for $C_{21}H_{33}N_6O_6Yb{\cdot}CH_3OH{\cdot}H_2O$): C, 38.05 (38.37); H, 5.63 (5.71); N, 12.14% (12.20%). IR (KBr disk), cm^{-1}: 2915w, 2845w, 1653s and 1617s ($\nu_{C=N,\ C=O}$), 1387m, 1209m, 1109m.

3.4.7 Hydrolysis experiments

Acidic pH buffer: Potassium acetate (0.10 g) and acetic acid (0.32 cm^3) were dissolved in D_2O (5 cm^3): pH = 4. The pH of the buffer solution was measured, and the pD was calculated using the formula $pD = pH_{measured} + 0.4$.[29]

Table 3.5 Acid catalysed hydrolysis of [La(L^a)].

Time, t(h)	$[La(L^a)]_t/[La(L^a)]_{t=0}$	Time, t(h)	$[La(L^a)]_t/[La(L^a)]_{t=0}$
1	0.9476	12	0.6909
2	0.9201	23	0.4931
3	0.8942	35	0.2966
4	0.8645	49	0.1655
6	0.8218	71	0.0583
7	0.7928	100	0.0149
9	0.7569		

[La(L^a)]·2CH$_3$OH (0.01g) was dissolved in the acidic buffer solution (0.6 cm^3). The resulting clear solution was transferred to an NMR tube and the ^{1}H NMR spectra were acquired at time intervals [t(h)]. The proportion of [La(L^a)]·2CH$_3$OH remaining unhydrolysed ([La(L^a)]$_t$/[La(L^a)]$_{t=0}$) was calculated from this formula: [La(L^a)]$_t$/[La(L^a)]$_{t=0}$ = I[La(L^a)] / (I[La(L^a)] + I[L]), where I[La(L^a)] is the sum of the integrals of peaks corresponding to the protons on [La(L^a)] and I[L] is the sum of the integrals of peaks corresponding to the protons of L.

3.4.8 Relaxivity of [Gd(L^a)]·3NaCl·3H$_2$O

Six samples of [Gd(L^a)]·3NaCl·3H$_2$O were weighed (Table 3.6) and dissolved in D$_2$O (0.70 cm^3) before being transferred to an NMR tube. The transverse relaxation times (T_1) of the HDO peak at 4.707 ppm were measured using a 180-τ-90 pulse sequence at 37°C using a Bruker 300 MHz NMR spectrometer. The results are reported in Table 3.6.

Table 3.6 Variation in T_1^{-1} of the HDO peak with concentration of [Gd(L^a)].

Mass [Gd(L^a)]·3NaCl·3H$_2$O (mg)	Concentration of [Gd(L^a)] (mM)	T_1 (s)	T_1^{-1} (s^{-1})
1.0	1.68	0.3496	2.86
2.1	3.52	0.2281	4.38
2.8	4.69	0.1698	5.89
3.8	6.37	0.1324	7.55
5.0	8.38	0.0951	10.51
6.2	10.39	0.0729	13.72

Plot of T_1^{-1} (s^{-1}) against concentration of [Gd(L^a)] (mM) gives an appropriate straight line (correlation coefficient = 0.996, Figure 3.25). The intercept with the y axis is the relaxation rate (T_1^{-1} = 0.058 s^{-1}) of the HDO peak

without the presence of the paramagnetic metal complex ([conc] = 0). The relaxivity was calculated from the gradient of this graph as 1.26 ± 0.05 $s^{-1}mM^{-1}$.

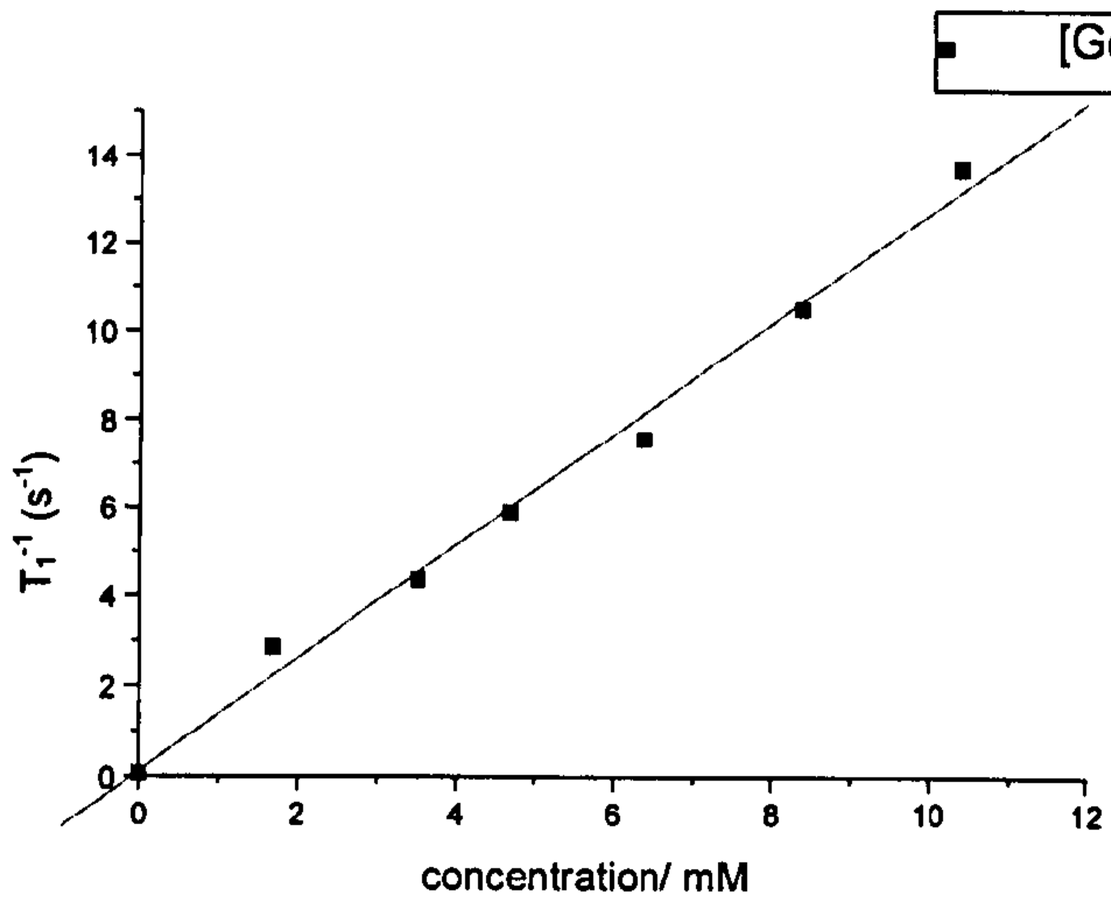

Figure 3.25 Graph showing the variation of T_1^{-1} of the HDO peak with concentration of [Gd(L^a)].

3.4.9 ^{17}O NMR measurements on [Dy(L^a)]

The natural abundance ^{17}O NMR experiments were run at 40.686 MHz on a Bruker DPX 300 spectrometer, using a 10 mm sample tube. Five samples of [Dy(L^a)]·3NaCl·2H_2O were weighed and the first dissolved in deionized water containing 20% D_2O (1.6 cm^3 of H_2O and 0.4 cm^3 of D_2O). The successive samples were dissolved in the same solution, thereby increasing the concentration of the complex. The ^{17}O shifts were measured using the ^{17}O shift of the water/D_2O as external reference (δ = -28.81). In Tables 3.7 and 3.8 the data for the ^{17}O NMR experiments on $DyCl_3$ and [Dy(L^a)], respectively, are reported. Plots of –DIS (dysprosium induced shift) (ppm) against concentration of $DyCl_3$ and of [Dy(L^a)] (mM) give appropriate straight lines (correlation coefficients = 0.999 and 0.996, respectively, Figure 3.23).

Table 3.7 Variation of the dysprosium induced shift (DIS) with concentration of $DyCl_3$.

Mass of $DyCl_3$ (mg)	Concentration of [$DyCl_a$] (mM)	δ (ppm)	-Δδ (DIS)(ppm)
8.1	10.74	-31.85	4.04
13.6	18.04	-34.77	6.96
18.8	24.94	-37.45	9.64
37.4	49.61	-46.95	19.14

Table 3.8 Variation of the dysprosium induced shift (DIS) with concentration of [$Dy(L^a)$].

Mass of [$Dy(L^a)$]·3NaCl·2H_2O (mg)	Concentration of [$Dy(L^a)$] (mM)	δ (ppm)	-Δδ (DIS)(ppm)
9.0	5.36	-27.89	0.08
17.9	10.66	-27.95	0.14
27.0	16.08	-28.04	0.23
36.0	21.44	-28.12	0.31
45.0	26.81	-28.19	0.38

3.4.10 Crystallography

Crystal data, data collection and refinement parameters for compounds [$Ln(L^a)$] (Ln = Y^{III}, Sm^{III}, Gd^{III} and La^{III}) are given in Tables 3.9 and 3.10, with selected bond lengths in Table 3.1. Data for [$Y(L^a)$]·2CH_3OH·0.5H_2O, [$Sm(L^a)$]·3CH_3OH ·0.5H_2O and [$La(L^a)$]·3CH_3OH·H_2O were collected on a Stoe IPDS diffractometer equipped with a imaging plate area detector and a rotating anode generator, using graphite-monochromated Mo-K_α radiation (λ=0.71073Å). Semi-empirical absorption corrections based on the program HABITUS[321] were applied for all compounds. Data for [$Gd(L^a)$]·2.75CH_3OH·0.75H_2O were collected on a Bruker SMART1000 CCD area detector equipped with a low temperature

device, using graphite-monochromated Mo-K_α radiation (λ=0.71073Å). Multi-scan absorption corrections were applied.

All the structures were solved by direct methods[322] and completed by iterative cycles of Δ*F* syntheses and full-matrix least squares refinement. All the non-H atoms, except for those in disordered groups, were refined anisotropically. The H atoms on water and disordered methanol molecules were not located, all the others were placed in calculated positions and refined using a riding model.[323] In [Gd(L^a)] the H atoms on two MeOH molecules were placed from Δ*F* syntheses and refined as a rigid rotating group. In all the structures disorder was identified in methanol molecules and it was modelled as follows: in [Y(L^a)] one disordered MeOH molecule was modelled using partial occupancy models over one site for the C atoms (occupancy factors of 0.50) and over three sites for the O atoms (occupancy factors of 0.167). In [La(L^a)] the two disordered MeOH molecules were modelled using partial occupancy models over three sites for both C and O atoms for one molecule and only for the O atoms in the other molecule (occupancy factors of 0.33). In [Sm(L^a)] the two disordered MeOH molecules were modelled using partial occupancy models over two sites for both C and O atoms in one molecule and only for the O atoms for the other. Finally, in [Gd(L^a)], two disordered H_2O molecules and a MeOH molecule were modelled using partial occupancy models over one site for the two water molecules (occupancy factors 0.50 and 0.25) and over two sites for the O atom (occupancy factors 0.50 and 0.25) and over three site for the C atom (occupancy factors 0.30, 0.25 and 0.20) in the MeOH molecule. Appropriate restraints to bond distances were applied in all the disordered molecules. In [Gd(L^a)] the largest residual electron density features lay near the Gd atom and in the other structures near the disordered MeOH molecules.

Table 3.9 Selected crystallographic data for the single crystal structures of $[Y(L^a)]\cdot 2CH_3OH\cdot 0.5H_2O$ and of $[Sm(L^a)]\cdot 3CH_3OH\cdot 0.5H_2O$

Compound	$[Y(L^a)]\cdot 2CH_3OH\cdot 0.5H_2O$	$[Sm(L^a)]\cdot 3CH_3OH\cdot 0.5H_2O$
Crystal Data		
Formula	$C_{21}H_{33}N_6O_6Y\cdot 2CH_3OH\cdot 0.5H_2O$	$C_{21}H_{33}N_6O_6Sm\cdot 3CH_3OH\cdot 0.5H_2O$
M / gmol^{-1}	627.03	721.02
Crystal size / mm	0.50 x 0.12 x 0.06	0.40 x 0.12 x 0.06
Crystal system	Trigonal	Trigonal
Space group	*R*-3	*R*-3
a/ Å	28.215(4)	28.337(4)
c / Å	23.170(5)	23.405(5)
U / Å^3	15974(5)	16276(5)
Reflections at ±ω to refine cell	not recorded	not recorded
2θ range / °	2.5 to 25	2.5 to 25
Z	18	18
D_c / gcm^{-3}	1.173	1.324
μ / mm^{-1}	1.688	1.673
F(000)	5913	6660
T / K	203(2)	193(2)
Data Collection		
Diffractometer	Stoe IPDS image plate	Stoe IPDS image plate
Radiation, wavelength	MoK_α , 0.71073 Å	MoK_α , 0.71073 Å
θ_{max} / °	25.98	28.04
Range of h	-34 → 31	-36 → 14
Range of k	-34 → 34	-23 → 37
Range of l	-27 → 23	-27 → 27
Measured reflections	18258	15155
Unique reflections, R_{int}	6634, 0.0543	8051, 0.0475
Observed reflections	5393 [$F_O \geq 4\sigma(F_O)$]	6483 [$F_O \geq 4\sigma(F_O)$]
Absorption correction	Habitus	Habitus
$TF_{max, min}$	not recorded	not recorded
Solution		
Method	Direct methods	Direct methods
Using	SHELXS-97	SHELXS-97
Refinement		
Full matrix least squares on	F^2	F^2
Using	SHELXL-97	SHELXL-97
Weighting scheme x, y[a]	0.097, 123.107	0.104, 11.271
Parameters refined	346	350
R_1, wR_2[b]	0.0662, 0.1876	0.0489, 0.1369
Goodness-of-fit (S)	1.071	1.004
$(\Delta/\sigma)_{max}$	0.007	0.112
$\Delta\rho_{max, min}$ / eÅ^{-3}	+1.07, -0.86	+0.92, -1.48

[a] $w^{-1} = [\sigma^2(F_o) + (xP)^2 + yP]$, $P = [MAX(F_o, 0) + 2F_C^2\}/3$
[b] $[F_O \geq 4\sigma(F_O)]$

Table 3.10 Selected crystallographic data for the single crystal structures of [Gd(L^a)]·2.75CH_3OH·0.75H_2O and of [La(L^a)]·3CH_3OH·H_2O.

Compound	[Gd(L^a)]·2.75CH_3OH·0.75H_2O	[La(L^a)]·3CH_3OH·H_2O
Crystal Data		
Formula	$C_{21}H_{33}N_6O_6Gd$·2.75CH_3OH·0.75H_2O	$C_{21}H_{33}N_6O_6La$·3CH_3OH·H_2O
M / gmol^{-1}	723.40	718.59
Crystal size / mm	0.32 x 0.06 x 0.06	0.42 x 0.04 x 0.03
Crystal system	Rhombohedral	Trigonal
Space group	R-3	R-3
a / Å	28.0190(12)	28.215(4)
c / Å	23.1774(13)	23.170(5)
U / Å^3	15758.0(13)	15974(5)
Reflections at ±ω to refine cell	6625	not recorded
2θ range / °	2.85 to 27.14	2.5 to 25
Z	18	18
D_c / gcm^{-3}	1.372	1.345
μ / mm^{-1}	1.945	1.256
F(000)	6642	6660
T / K	150(2)	203(2)
Data Collection		
Diffractometer	Bruker SMART CCD area detector	Stoe IPDS image plate
Radiation, wavelength	MoK_α , 0.71073 Å	MoK_α , 0.71073 Å
θ_{max} / °	28.81	28.62
Range of *h*	-29 → 37	-37 → 37
Range of *k*	-37 → 37	-37 → 27
Range of *l*	-31 → 29	-27 → 27
Measured reflections	33270	31695
Unique reflections, R_{int}	8371, 0.090	8390, 0.096
Observed reflections	5400 [$F_O \geq 4\sigma(F_O)$]	6714 [$F_O \geq 4\sigma(F_O)$]
Absorption correction	Semi-empirical	'Habitus'
$TF_{max, min}$	0.813,0.657	not recorded
Solution		
Method	Direct methods	Direct methods
Using	SHELXS-97	SHELXS-97
Refinement		
Full matrix least squares on	F^2	F^2
Using	SHELXL-97	SHELXL-97
Weighting scheme *x*, *y*[a]	0.066, 48.184	0.080, 10.669
Parameters refined	367	366
R_1, wR_2[b]	0.0548, 0.1203	0.0434, 0.1190
Goodness-of-fit (*S*)	1.024	1.001
$(\Delta/\sigma)_{max}$	0.037	0.012
$\Delta\rho_{max, min}$ / eÅ^{-3}	+1.29, -1.12	+0.96, -1.03

[a] $w^{-1} = [\sigma^2(F_O) + (xP)^2 + yP]$, $P = [MAX(F_O, 0) + 2F_C^2\}/3$
[b] $[F_O \geq 4\sigma(F_O)]$

Chapter 4

Lanthanide complexes of imino-phosphonate derivatives of [9]aneN$_3$

4.1 Introduction to lanthanide complexes of ligands containing phosphonyl groups

In the search for new and more effective ligands for complexation of lanthanide ions, the attachment of phosphonyl pendant arms to macrocycles such as [9]aneN$_3$[324-329] or [12]aneN$_4$[154,219,293,308,326,330-345] has received much attention over recent years. As shown in Figure 4.1, three different moieties such as phosphonate, phosphinate and phosphonate monoester can characterise the donor group of the pendant arm. These ligands have been studied not only as analogues of the amino-carboxylate ligands for the application in MRI and in nuclear medicine, but their Ln^{III} complexes have also proved to be useful as paramagnetic shift reagents for the study of biological cations having NMR-active nuclei.[127,338,346-350] Moreover, the presence of phosphorus in these ligands allows the measurement by ^{31}P NMR spectroscopy of the intracellular concentration of metal cations such as Mg^{II}.[228,328,335,351,352]

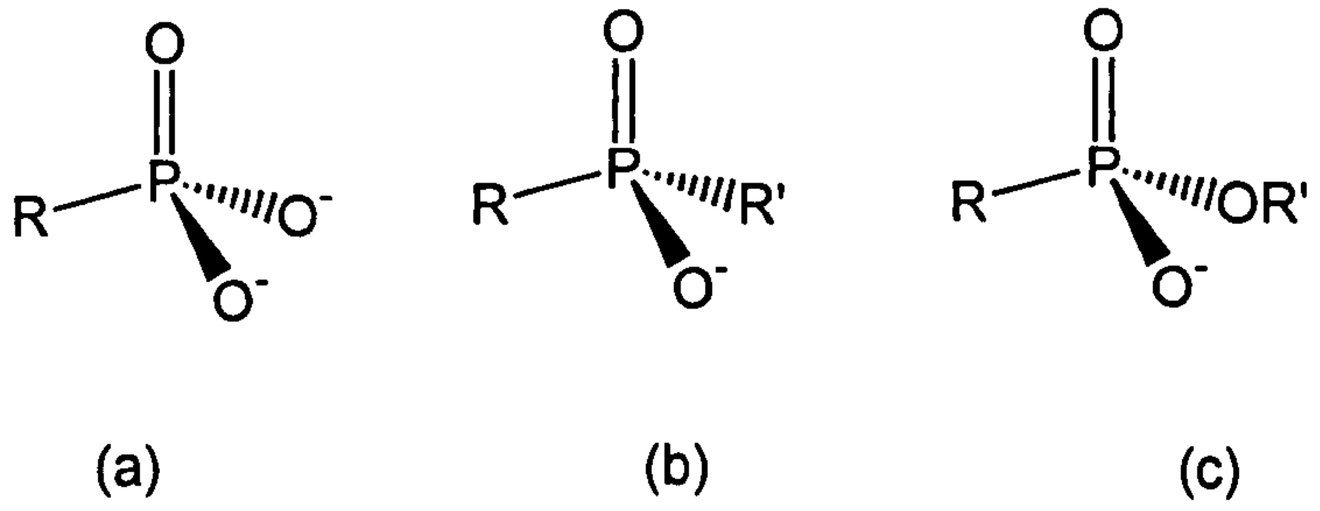

Figure 4.1 (a) Phosphonate, (b) phosphinate and (c) phosphonate monoester moieties.

Since the –P(=O)OH moiety has a substantially lower pK_a than the carboxylate moiety,[353] complexes of such ligands should exhibit greater stability at low pH than their amino-carboxylate analogues. Indeed, it has been shown that phosphinate derivatives of the tetraazacyclododecane ring system have high thermodynamic stability and kinetic inertness; in particular, they are very stable in

acidic conditions and prove to be more inert to acid dissociation than the amino-carboxylate derivatives.[22,336]

4.1.1 Amino-phosphonate ligands

The complexation properties of 1,4,7-*tris*(methylenephosphonate)-1,4,7-triazacyclononane (NOTP) (Figure 4.2a) with metal ions have been examined in some detail.[325,327] Although the phosphonate derivative appears to form more stable complexes with the lanthanides than does the carboxylate N-functionalised ligand NOTA (for example log K of $[La(NOTP)]^{3-}$ is 14.3 while log K of [La(NOTA)] is 13.5),[324,325] the highly charged $[Ln(NOTP)]^{3-}$ complexes form protonated species at physiological pH values and tend to aggregate in solution by some yet undetermined mechanism.[327]

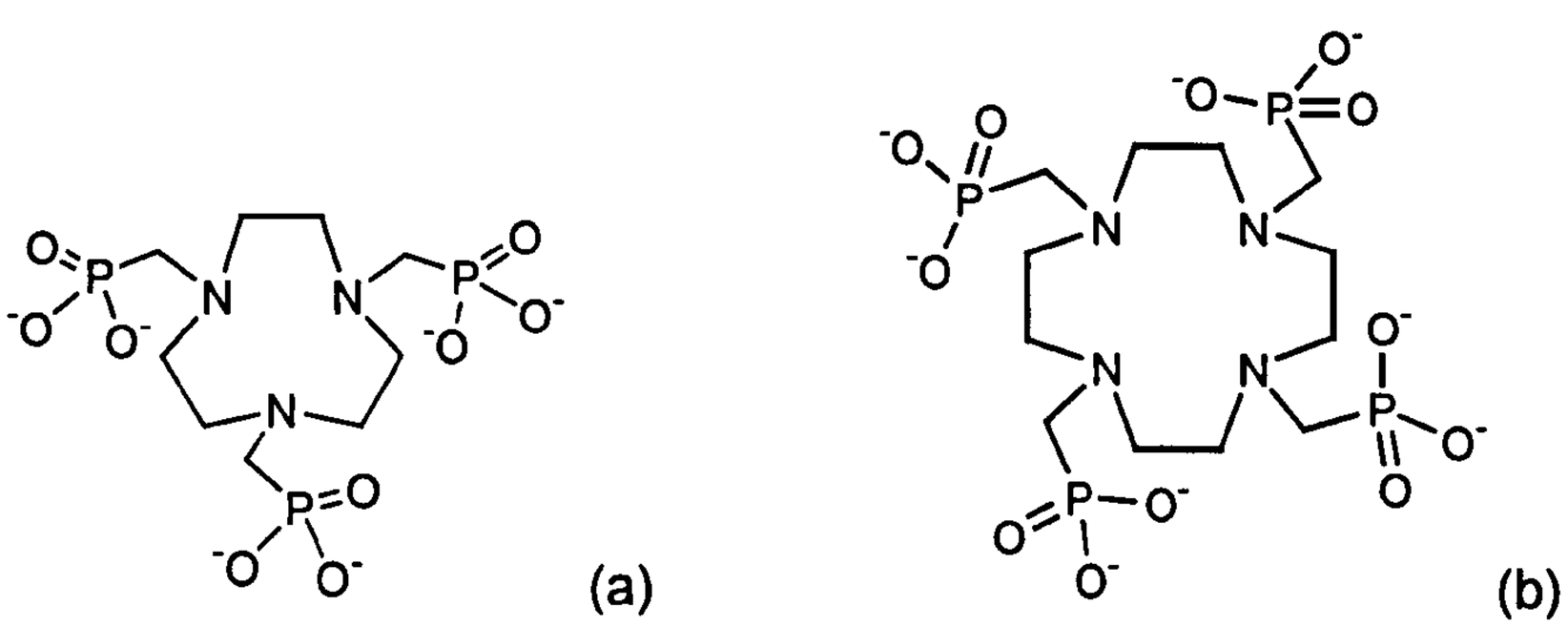

Figure 4.2 (a) $[NOTP]^{6-}$ and (b) $[DOTP]^{8-}$.

The tetrasubstituted methylenephosphonate derivative of cyclen (DOTP, Figure 4.2b) and its lanthanide complexes have been found to be very useful for a large variety of applications. DOTP forms very stable Ln^{III} complexes (log K_{ML} varies from 27.5 to 29.5 for La^{III} to Lu^{III} complexes) that can accept four protons between pH 8 and 4 without dissociation from the chelated lanthanide ion.[330,338] The average ionic form of these complexes at pH 7.4 is $[Ln(HDOTP)]^{4-}$. These highly charged, symmetrical complexes form tight ion-paired complexes with other

aqueous cations with varying stoichiometry. For example, Na^+ and other alkali ions can form complexes with stoichiometry of up to 3:1.[338] The thulium and the dysprosium complexes, $[Tm(HDOTP)]^{4-}$ and $[Dy(DOTP)]^{5-}$, have proven particularly useful as paramagnetic shift reagents for resolving intra- and extra-cellular sodium resonances *in vivo* in rat kidney, liver, heart and skeletal muscle by ^{23}Na NMR (Figure 4.3).[127,330,349]

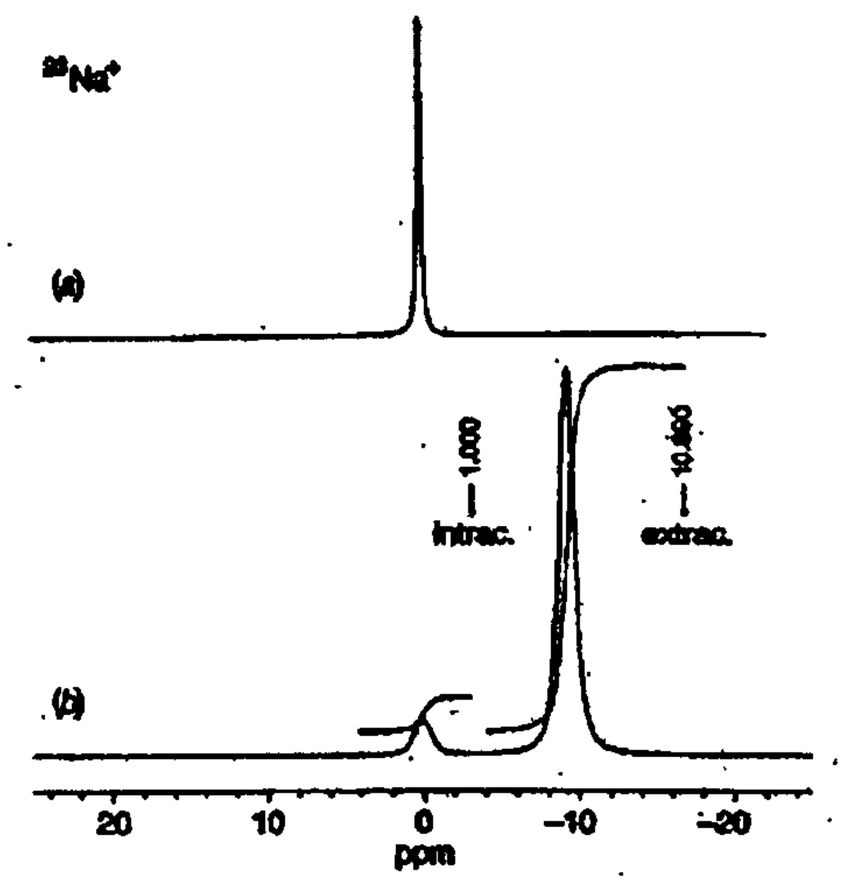

Figure 4.3 ^{23}Na NMR spectra (39 °C, 2.1 T) of human blood (a) before and (b) after the addition of a 5 mM solution of $[Dy(DOTP)]^{5-}$.

The highly charged Ln^{III} complexes of DOTP have also been studied as pH indicators by ^1H NMR spectroscopy.[127,354] In the ^1H NMR spectrum of $[Yb(DOTP)]^{5-}$, the stepwise addition of H^+ ions causes large changes in the chemical shift of all the resonances whose values then become reporters of the pH of the solution.[127,354]

Botta and co-workers have also improved the relaxivity of $[Gd(DOTP)]^{5-}$ by forming a non-covalent ternary complex between $[Gd(DOTP)]^{5-}$, a polyammonium macrocycle and β-cyclodextrin (Figure 4.4).[142,152] $[Gd(DOTP)]^{5-}$ has a relaxivity of 4.7 $mM^{-1}s^{-1}$, due only to the second hydration sphere present around the complex, because no water molecule is directly bound to the metal centre (q = 0). This non-

covalent ternary complex presents a remarkably high relaxivity of 18 $mM^{-1}s^{-1}$ at 20 MHz and 25°C, which is entirely attributable to an optimised contribution of the second hydration sphere (section 2.2.3).[142,152]

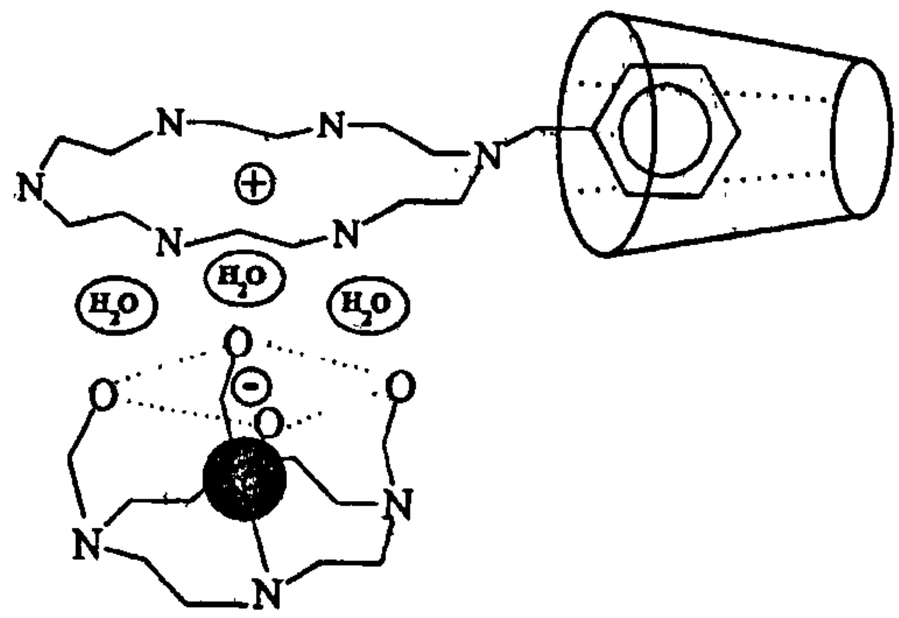

Figure 4.4 Schematic view of the non-covalent ternary complex between $[Gd(DOTP)]^{5-}$, a polyammonium macrocycle and β-cyclodextrin.

Gd^{III} complexes containing phosphonate pendant groups on their external surface have also been synthesised.[144,180] With the ligand shown in Figure 4.5a, these groups can promote the interaction with positively charged groups of polyamino acid chains of ornithine and arginine, thereby enhancing the relaxivity.[144] Considering that polyamino acids bind selectively to tumours, this system may provide a new method for their placement.[144] Phosphonates on the external surface of a Gd^{III} complex of the ligand shown in Figure 4.5b can also

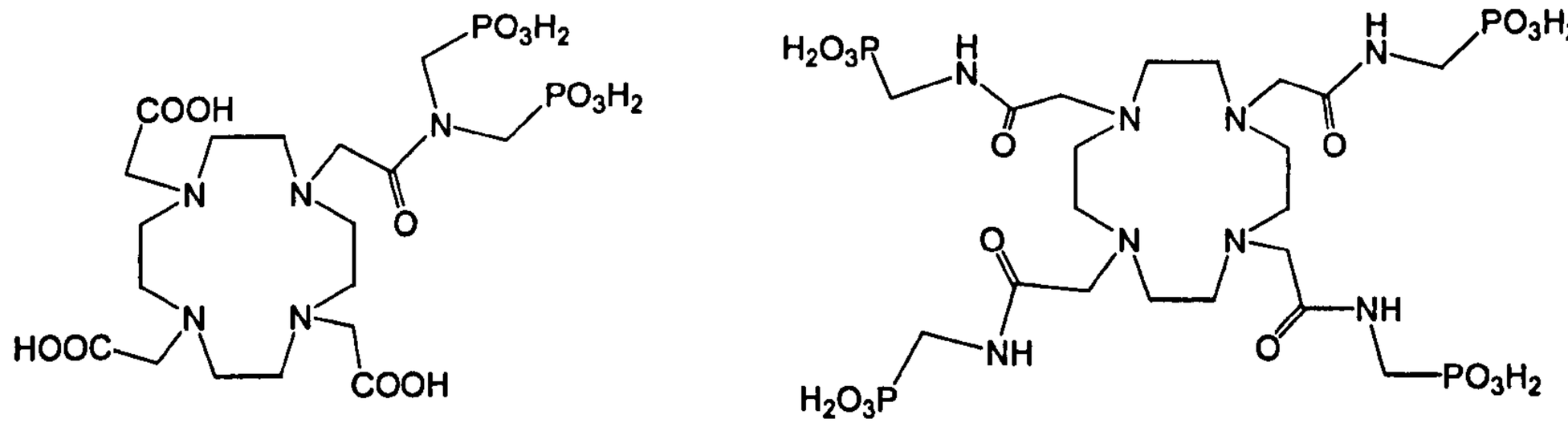

(a) (b)

Figure 4.5 Ligands containing non co-ordinating phosphonate pendant groups.

cause pH dependence of the relaxivity and produce MRI contrast exquisitely sensitive to pH.[180]

4.1.2 Amino phosphinate and phosphonate monoester ligands

Phosphinate and phosphonate monoester donors have the advantage of a possible structural variation by changing the –R or –OR group on the phosphorus, and this can facilitate variations of lipophilicity of the complexes.[330,335,336] However, the introduction of an alkyl or alkoxy functionality on the phosphorus causes the formation of chiral centres in the lanthanide complexes.[330] Nevertheless, the lanthanide complexes formed with the tetrabenzyl phosphinate ligand (DOTBP, Figure 4.6a) exist in solution as one predominant isomer with no inner sphere water molecule in the Gd^{III} complex.[293,334,355] Interestingly, X-ray crystallographic studies have demonstrated that there is a change across the series and the earlier lanthanides and La^{III} have a co-ordinated water molecule, while later lanthanides do not (Figure 4.7).[293,334] However, ligands consisting of three alkyl phosphinate groups and one carboxyamide group (Figure 4.6b) form Gd^{III} complexes with a water molecule bound to the metal centre, and therefore exhibit an enhanced relaxivity relative to the tetraalkylphosphinate Gd^{III} complex.[219,336] Such complexes

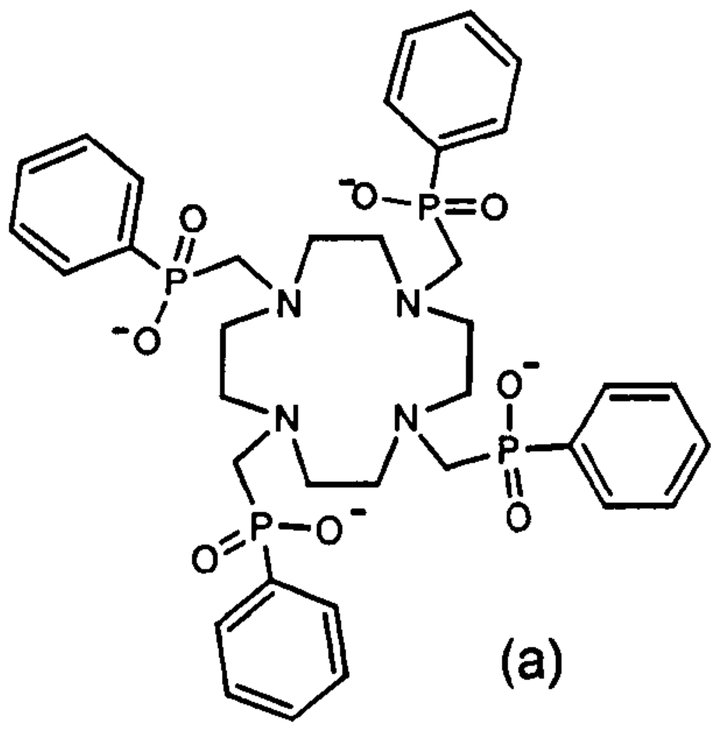

(a)

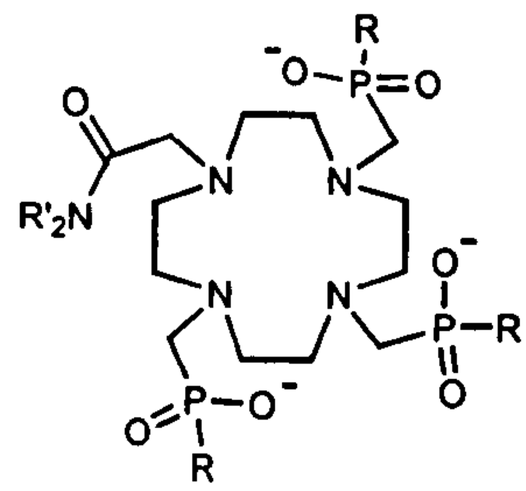

(b)

R = Me, Bu, Ph; R' = Me, Bu, Ph

Figure 4.6 (a) $[DOTPB]^{4-}$ and (b) series of ligands with three alkyl phosphinate and one carboxyamide groups.

have been found to be the most resistant to acid dissociation, with very low dissociation rates even at pH 1.0.[336,343]

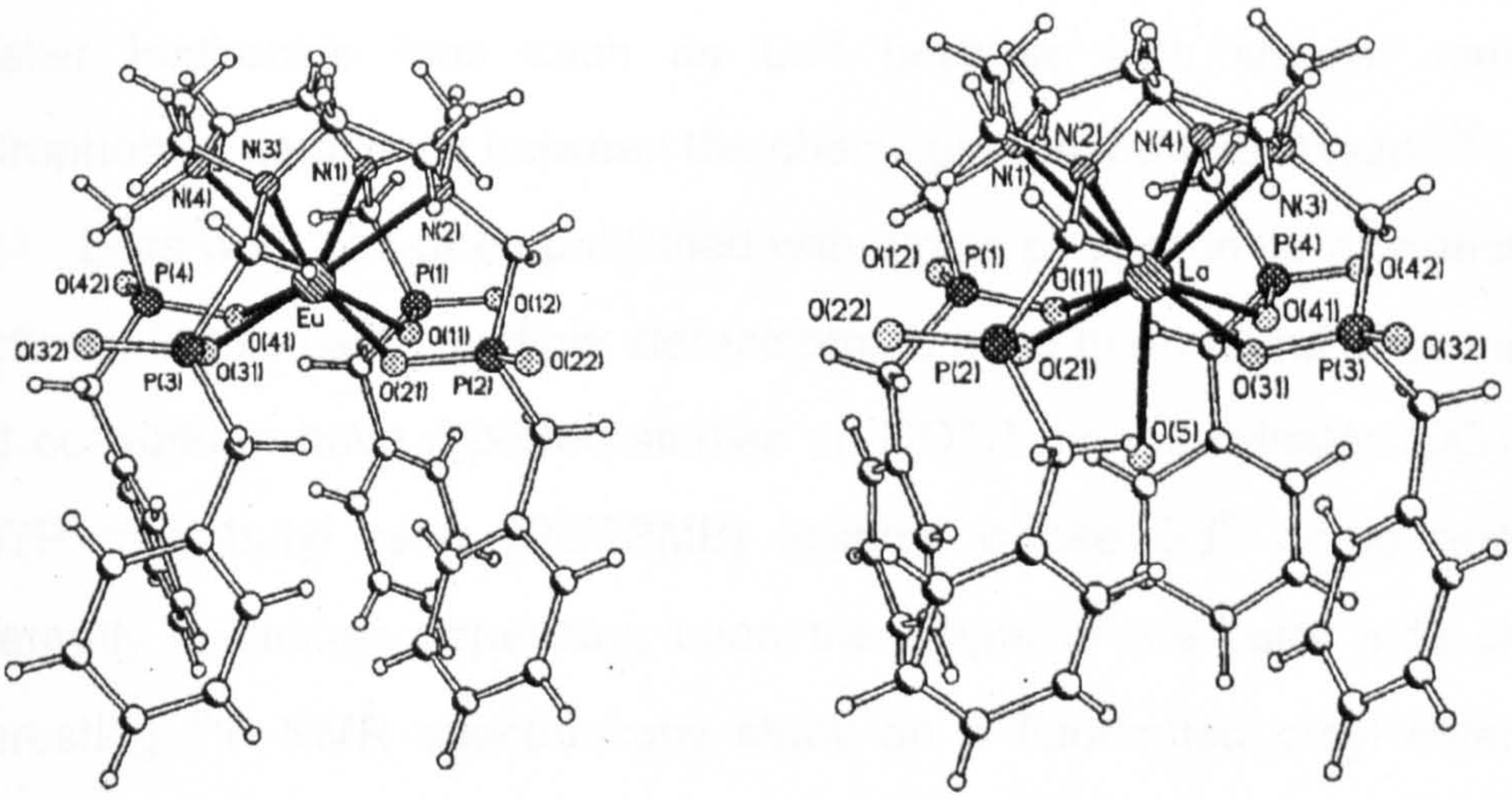

Figure 4.7 Crystal structures of $[Eu(DOTPB)]^-$ (left) and $[La(DOTPB)]^-$ (right).

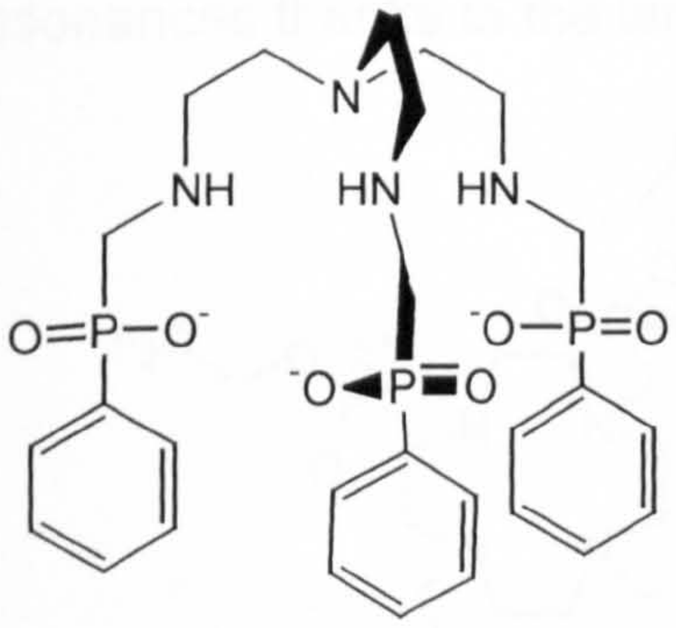

(a)

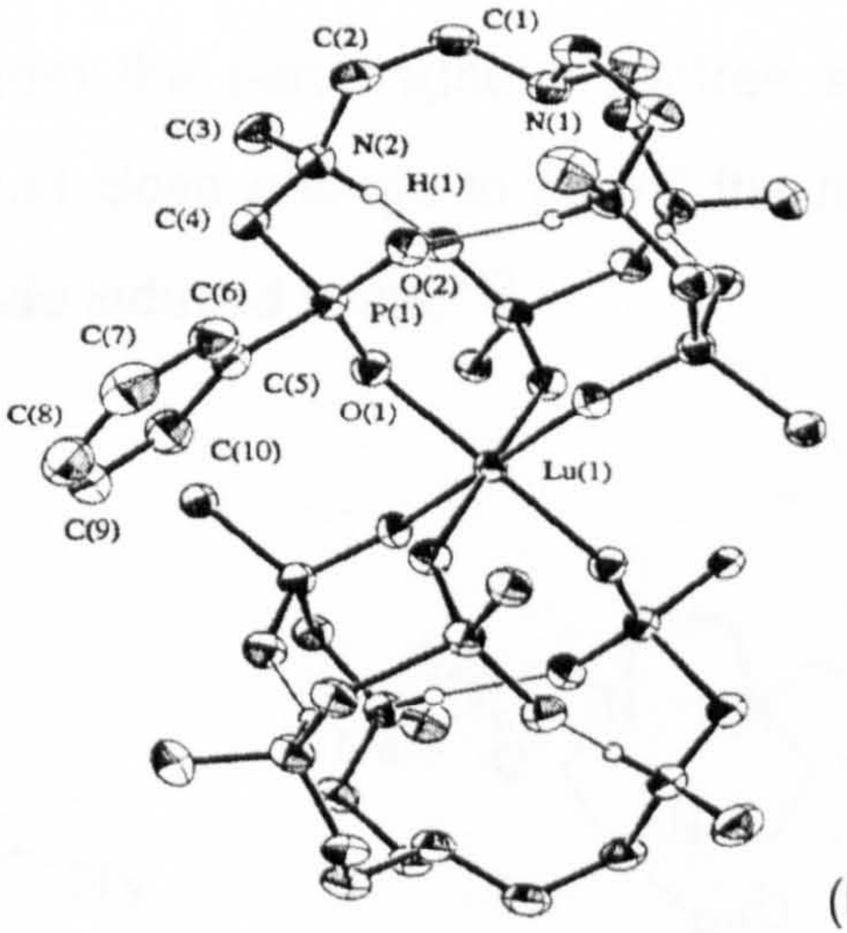

(b)

Figure 4.8 (a) $[ppma]^{3-}$ and (b) crystal structure of $[Lu(H_3ppma)]_2^{3+}$

Orvig and co-workers have investigated the lanthanide and Group 13 metal complexes of $(ppma)^{3-}$, a tripodal amino phenyl phosphinate ligand (Figure 4.8a).[356,357] Only at acidic pH (≤2) can 1:2 metal to ligand adducts such as

$[Lu(H_3ppma)]_2^{3+}$ (Figure 4.8b) be synthesised. The metal centre is octahedrally co-ordinated by six phosphinate oxygens with the nitrogen donors protonated and not participating into the co-ordination. The stability of these complexes is higher for smaller lanthanide ions such as Lu^{III} because with smaller metal cations hydrophobic interactions between the phenyl groups are maximised.[356]

Less work has been published with amino phosphonate monoester ligands, because, in this case, multiple stereoisomers have been found in solution. Sherry and co-workers have reported studies on DOTP monoethylester (DOTPME) and DOTP monobutyl ester (DOTPMB) ligands, whose Gd^{III} complexes distribute differently in tissues depending upon the length of the ester side chain.[333] An interesting ^{19}F NMR spectroscopy study on a fluorinated ethyl ester analogue (Figure 4.9a) has shown that all six possible co-ordination stereoisomers are nearly equally populated.[345] The fluorine atoms in the Ln^{III} complexes of this ligand are situated far enough away from the paramagnetic centres so that the line broadening effects are minimal and close enough to permit the resolution of the resonances thanks to the lanthanide induced shifts.[345]

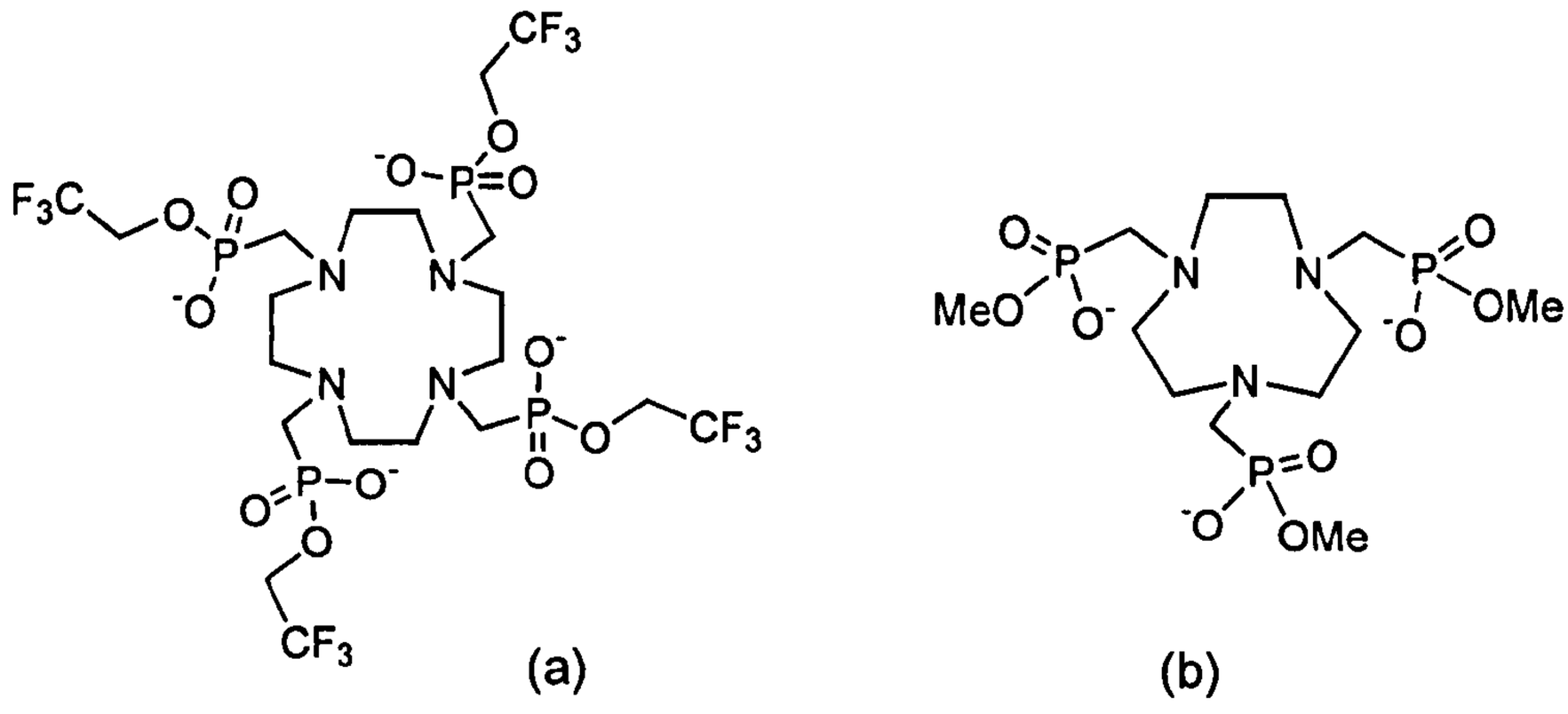

(a) (b)

Figure 4.9 (a) Fluorinated ethyl ester analogue of DOTP and (b) $[NOTPME]^{3-}$.

Sherry and co-workers have also demonstrated that the trisubstituted phosphonate monoester derivative of [9]aneN$_3$ (NOTPME, Figure 4.9b) can be

useful for monitoring the concentration of free Mg^{II} in isolated cells, although the complexes are less stable than the triphosphonate analogue [Ln(NOTP)] (log K for [La(NOTPME)] is 8.7 and for [La(NOTP)] is 14.3).[228,324] Ln^{III} complexes of NOTPME tend to form multiple species in solution at concentrations above 0.1 mM and this has been ascribed to the formation of multiple oligomeric species as already reported also for Ln^{III} complexes of NOTP (Section 4.1.1).[324,333]

4.1.3 Schiff-Base Condensation of Phosphonate Monoesters

Preliminary investigations into the co-ordination chemistry of imino-phosphonate monoesters have been carried out at the University of Nottingham.[283] The Schiff-base condensation of tren with three molar equivalents of methyl sodium acetyl phosphonate around a Ln^{III} template affords [Ln(**5**)] (Ln^{III} = Y^{III} or Gd^{III}) in good yield (Figure 4.10).

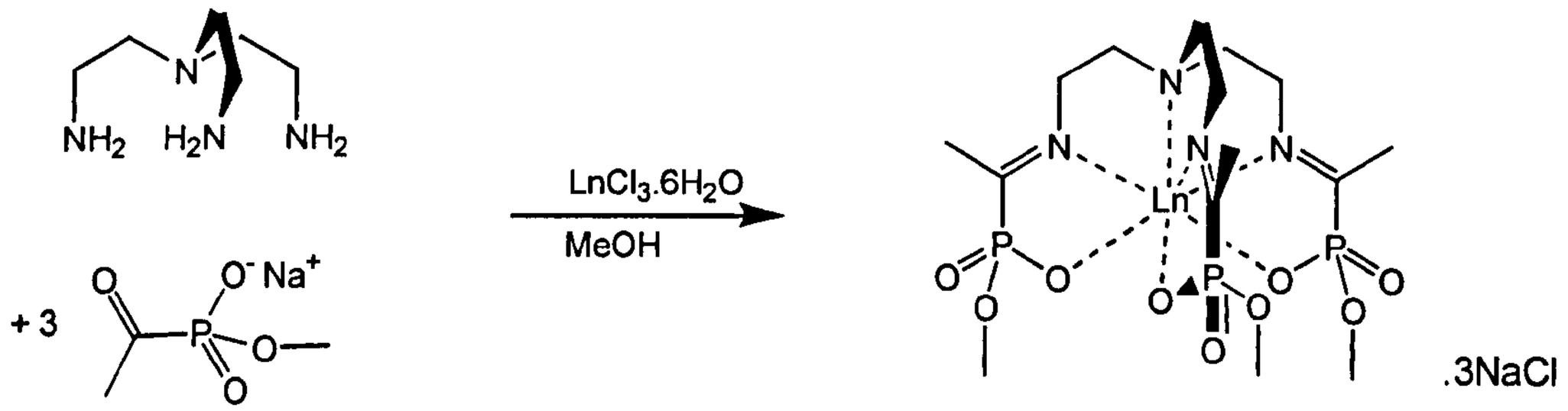

Figure 4.10 Diagram showing the synthesis of [Ln(**5**)].

The crystal structure of the Y^{III} complex with **5** has been found to be a heptanuclear cluster containing four Y^{III} and three Na^+ centres. Each Y^{III} is bound by three phosphonate oxygen donors, three imine nitrogen donors and the bridgehead nitrogen donor: the four [Y(**5**)] complexes are arranged in a chain with each Y^{III} centre bound to one phosphonate oxygen donor from each neighbouring [Y(**5**)] complex, thereby reaching a co-ordination number of eight. In Figure 4.11 the asymmetric unit with two eight co-ordinate Y^{III} centres is shown. The

tetranuclear chain [Y(**5**)]$_4$ twists around a core of three Na^+ cations, which are bound by the phosphonate oxygen donors of [Y(**5**)] and solvent MeOH and H_2O molecules.[283]

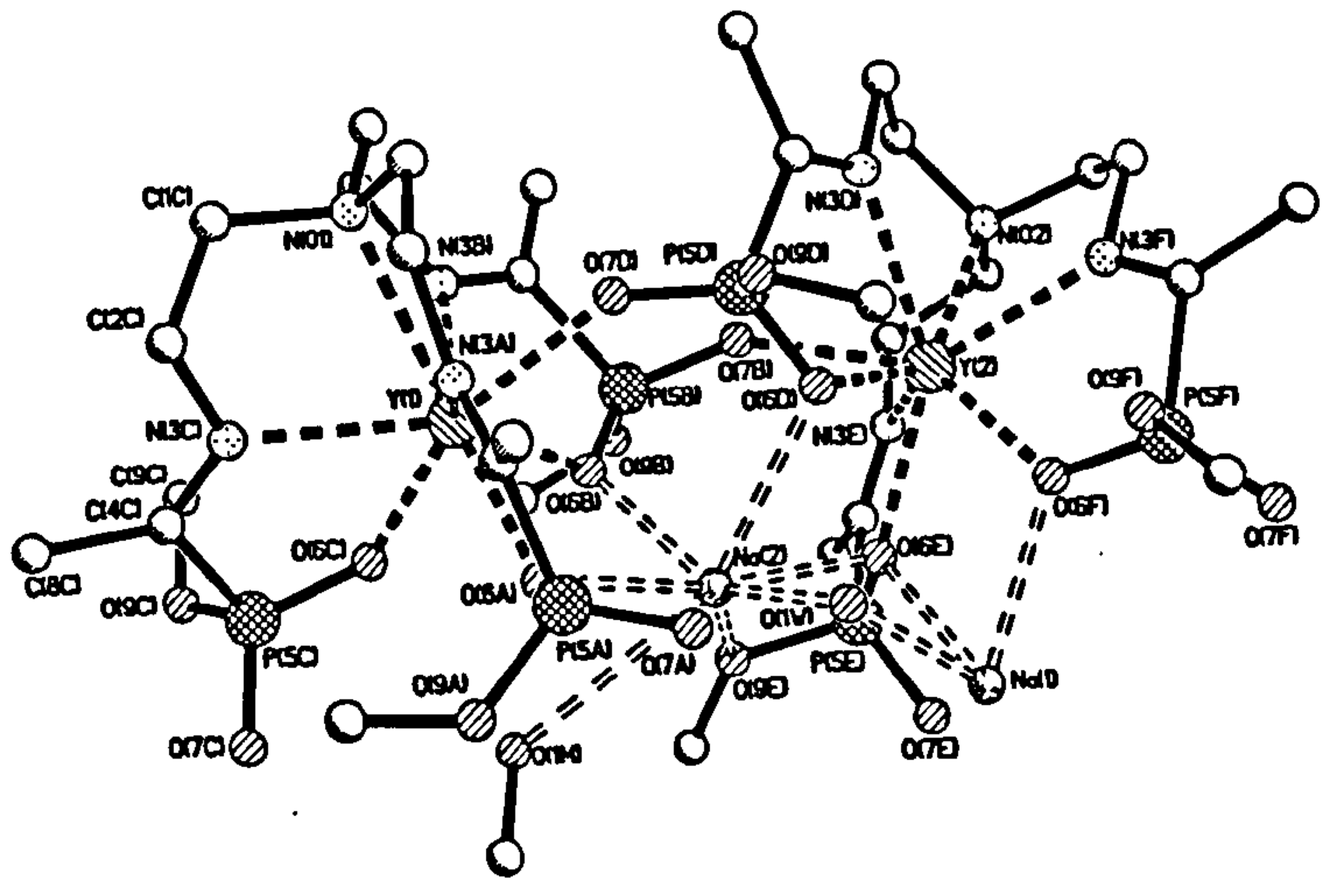

Figure 4.11 Asymmetric unit of {[Y(**5**)]$_4$Na$_3$(H_2O)$_2$($MeOH$)$_{1.2}$}(NO_3)$_3$·2H_2O·5.6MeOH.

4.2 Results and discussion

After the study on the nine co-ordinate complexes [Ln(L^a)] discussed in Chapter 3, the change of the ketone employed for the Schiff-base condensation with the triamine L was considered. Two different acetylphosphonate monoesters have been used in order to form novel nine co-ordinate Ln^{III} complexes, which have been studied by X-ray crystallography and NMR spectroscopy.

4.2.1 Synthesis of Sodium Acetylphosphonates

Sodium acetylphosphonates were synthesised *via* a modified procedure first described by Karaman *et al.*[358] (Figure 4.12). Dimethyl acetylphosphonate was synthesised by slow addition of trimethyl phosphite to the relevant acid chloride and purified by distillation under reduced pressure. Reaction of the dimethyl phosphonate in dry acetone with NaI affords the mono-sodium salt as an insoluble precipitate in good yield and high purity.

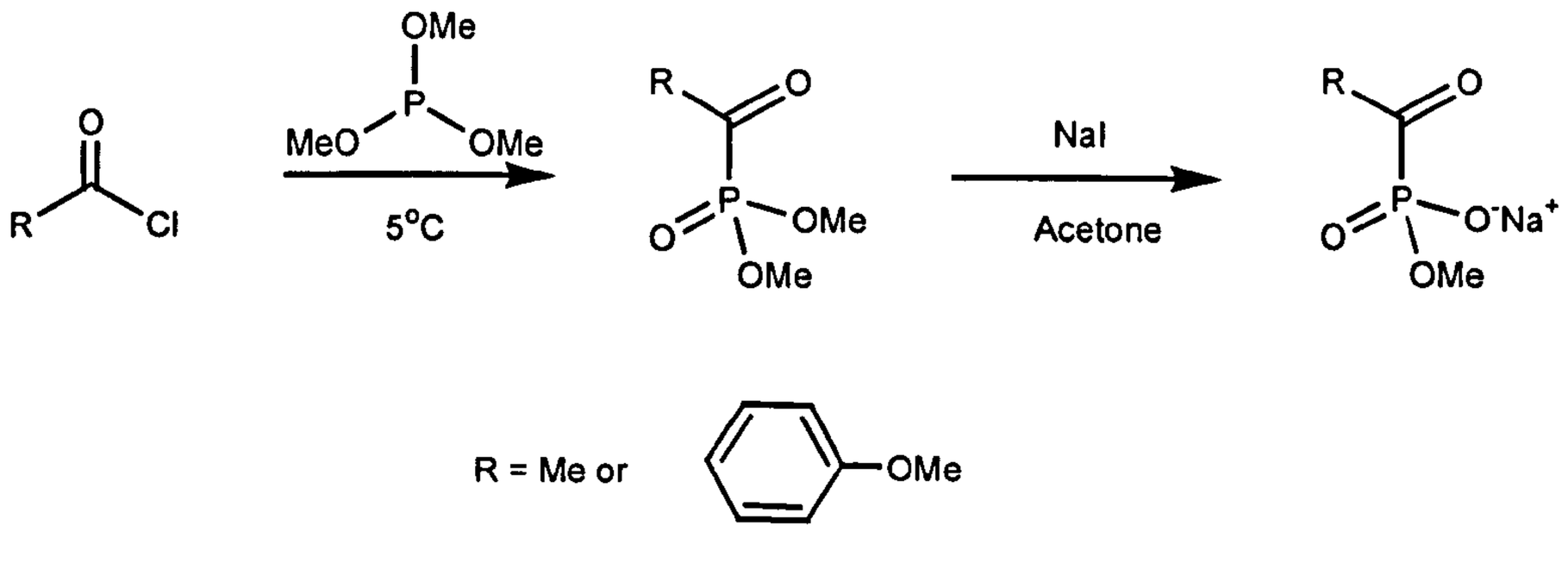

Figure 4.12 Synthesis of sodium phosphonate monoesters.

The synthetic scheme shown in Figure 4.12 was employed for two different acid chlorides, where R = methyl and methoxyphenyl. Slight modification of the preparative scheme was employed for the synthesis of methoxyphenyl sodium acetyl phosphonate due to the melting points of the starting materials (Sections 4.3.1 and 4.3.5).

4.2.2 Synthesis of Ln^{III} complexes with L^b and L^c

The synthesis of the complexes [Ln(L^b)] (Ln^{III} = Y^{III}, Gd^{III}, Yb^{III}, La^{III}) and [Ln(L^c)] (Ln^{III} = Y^{III}, Gd^{III}, Eu^{III}) is achieved by Schiff-base condensation of the triamine (L) with methyl sodium acetyl phosphonate and methoxybenzyl sodium

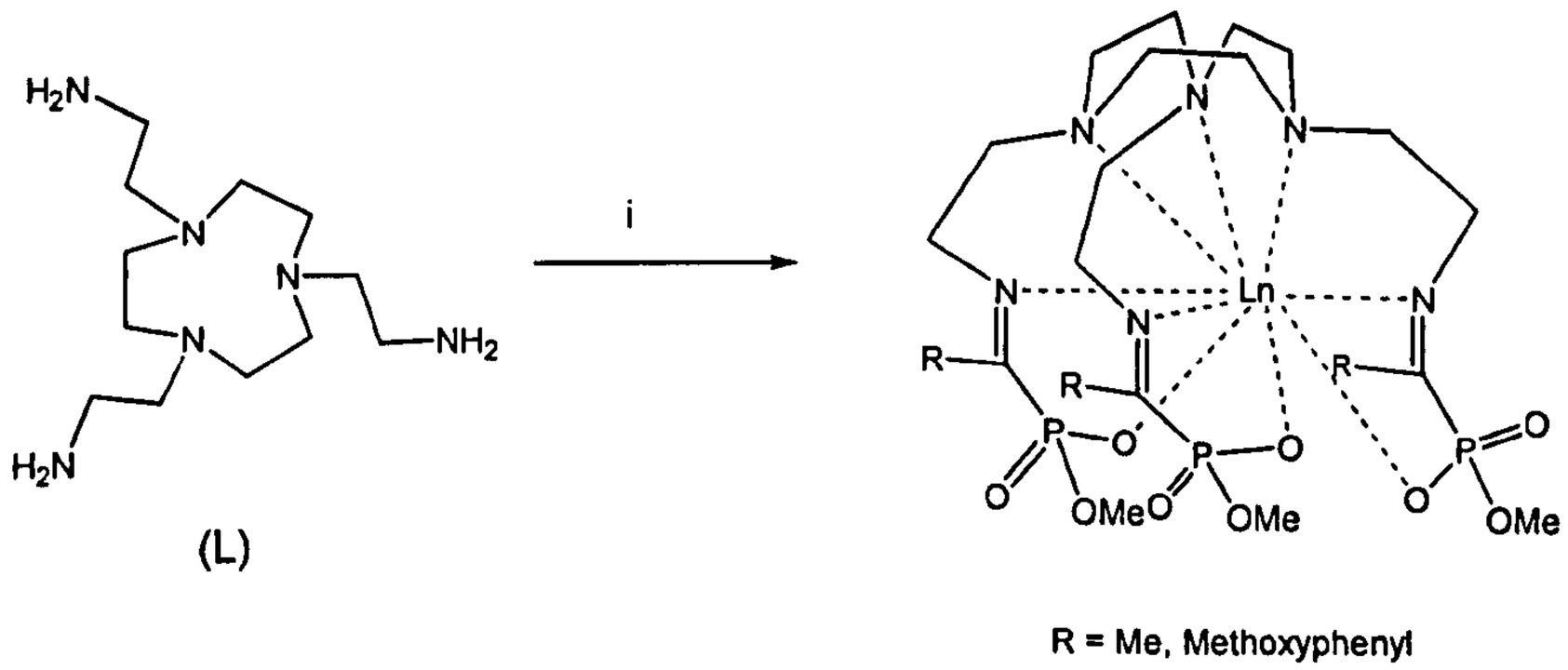

Figure 4.13 Synthetic scheme for the preparation of complexes [Ln(L^b)] and [Ln(L^c)] [i: 3 RCOP(OMe)OONa, LnX, MeOH, 2 h; (R = Methyl or methoxyphenyl)].

acetyl phosphonate, respectively, using the Ln^{III} ion as templating agent (Figure 4.13). Reaction of one equivalent of L and of the Ln^{III} salt with three equivalents of the appropriate sodium phosphonate monoester in MeOH for 2 hours followed by precipitation of the product by addition of Et_2O affords the desired complexes [Ln(L^b)] and [Ln(L^c)] as white solids. Elemental analysis and mass spectra for all the complexes are consistent with the formulation [Ln(L^b)]·3NaCl·nH_2O and [Ln(L^b)]·3NaCl·nH_2O (n = 1,2 or 3).

4.2.3 Single crystal X-ray diffraction analyses of [Ln(L^b)]

Single-crystals of [Ln(L^b)] (Ln^{III} = Y^{III} and Gd^{III}) were obtained by adding a ten-fold excess of Et_2O into a solution of the complexes in MeOH at room temperature. The cloudy solution formed was left to stand for two days and single crystals were obtained. Single crystal X-ray diffraction studies confirm these complexes to be isostructural. In each, the lanthanide metal is nine-coordinate, using all nine donor atoms of the ligand, namely the three amino N-donors of the macrocycle, the three imino N-donors and the three phosphonate O-donors. Bond lengths are in the ranges 2.659(3)-2.698(5)Å for the bonds between the metal and the macrocyclic N-donors, 2.591(3)-2.684(5)Å for the bonds to the N-donors of the imine moieties and 2.289(3)-2.357(4)Å to the phosphonate O-donors. The bond lengths between Y^{III} and the donor atoms are shorter than the Gd^{III}-N and Gd^{III}-O bond lengths, as expected, given the different effective ionic radii for the two ions: 1.11Å for Gd^{3+} and 1.07Å for Y^{3+} (values are for the nine co-ordinate ions).[288] (Table 4.1). Two different views of the crystal structure of [Gd(L^b)], as examples of the isostructural [Ln(L^b)] complexes, are shown in Figure 4.14 and 4.15.

There is a high degree of planarity in the fragments C(2)-O(7) of the pendant arms in the two structures due to the conjugation between the imine and phosphonate groups, with the mean deviation from the least squares mean plane being only 0.009-0.049Å. As already observed for the imino-carboxylate

complexes [Ln(L^a)], the difference in the opening of the three arms can be seen by looking at the pitch angle between the plane of the macrocycle and the plane of each phosphonate. The average of the three pitch angles is 41.3° for [Y(L^b)] and

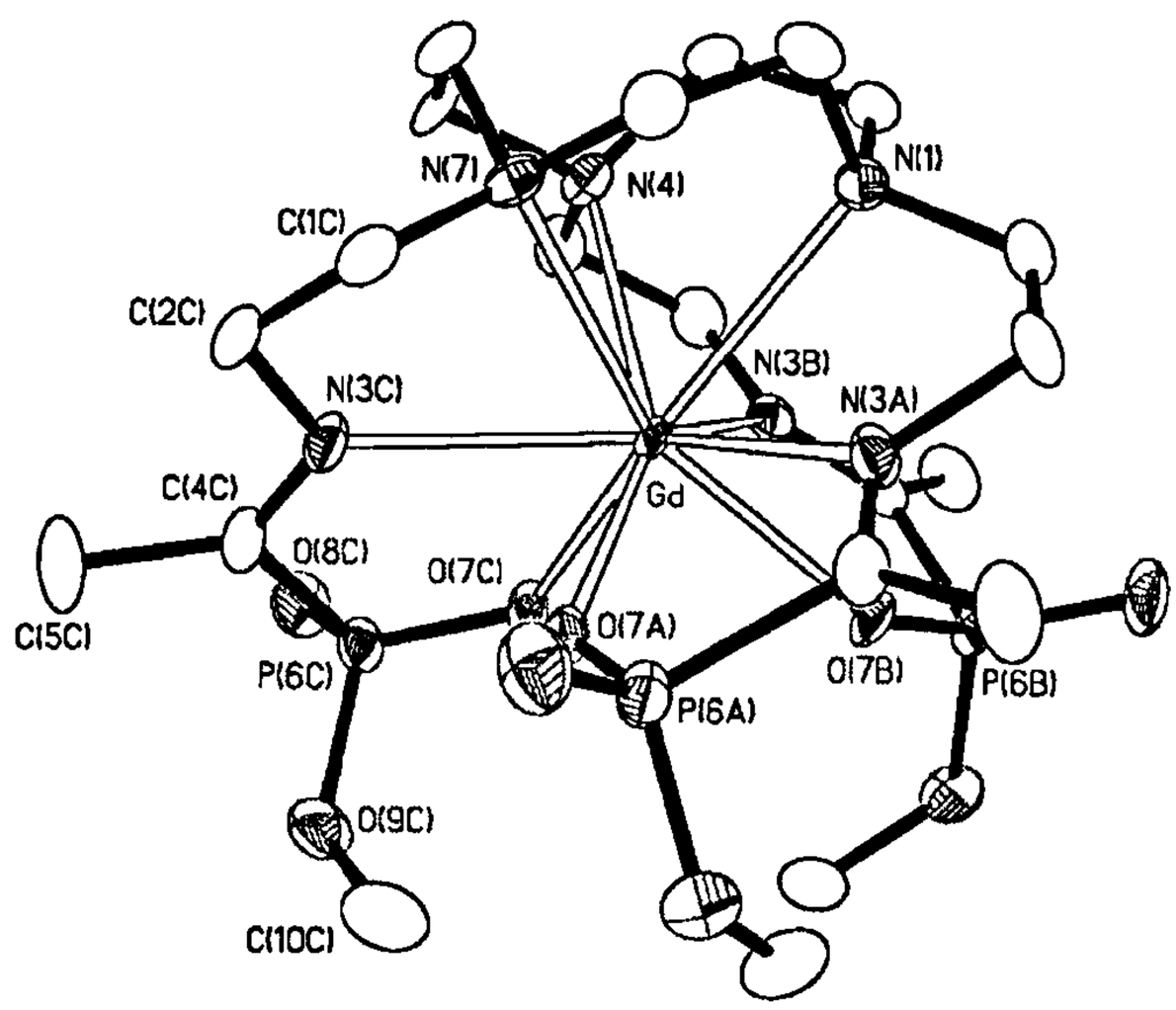

Figure 4.14 Ellipsoid plot of [Gd(L^b)] with numbering scheme adopted. Hydrogen atoms and solvent molecules have been omitted for clarity. Displacement ellipsoids are drawn at 50% probability.

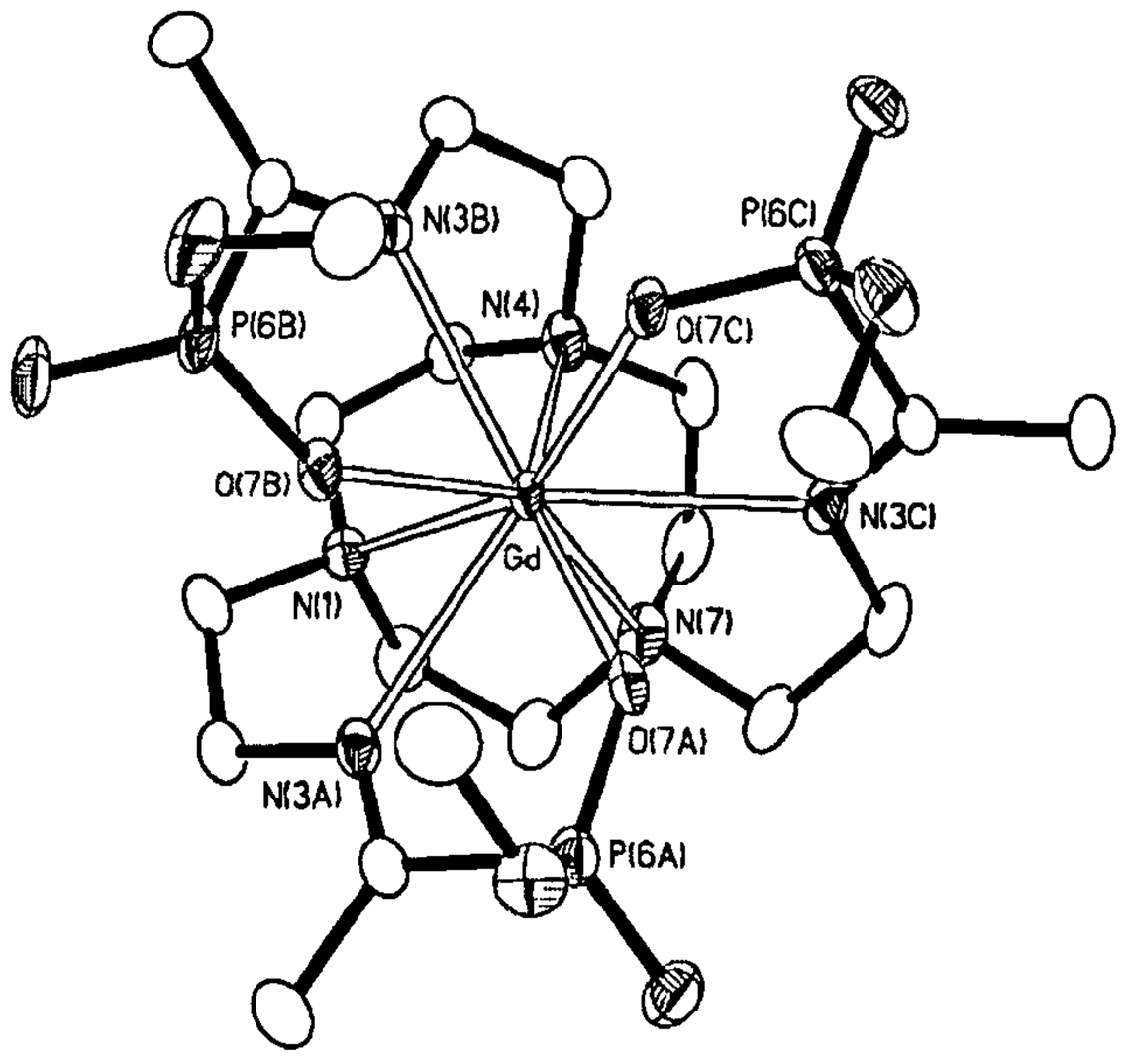

Figure 4.15 View of the crystal structure of [Gd(L^b)] along the non-crystallographic 3-fold axis.

43.0° for [Gd(L^b)], values that are smaller than those observed for the [Ln(L^a)] complexes (*i.e.* 50.6° for [Gd(L^a)] and 49.6° for [Y(L^a)]).

Table 4.1 Selected Bond Lengths (Å) in the crystal structures of [Y(L^b)]·CH_3OH and [Gd(L^b)]·1.5CH_3OH·H_2O.

	[Y(L^b)]	[Gd(L^b)]
Ln-N(1)	2.659 (3)	2.680 (5)
Ln-N(4)	2.667 (3)	2.698 (5)
Ln-N(7)	2.680 (3)	2.669 (5)
Ln-N(3A)	2.591 (3)	2.684 (5)
Ln-N(3B)	2.618 (3)	2.663 (5)
Ln-N(3C)	2.656 (3)	2.684 (5)
Ln-O(7A)	2.292 (2)	2.336 (4)
Ln-O(7B)	2.289 (3)	2.336 (4)
Ln-O(7C)	2.292 (3)	2.357 (4)

The co-ordination geometry about the lanthanide centre is a slightly distorted tricapped trigonal prism (Figure 4.16) as already observed for the complexes [Ln(L^a)]. The macrocyclic nitrogen donors and the phosphonate oxygens impose the two triangular faces with the imine nitrogens capping the three rectangular faces of the prism. The upper and lower triangular faces of the prism are essentially equilateral (angle range 57.4-61.8°) and parallel (the angle between the plane defined by the triangle of three oxygen donors and the one defined by the three nitrogen donors is never greater than 3.4°), but the oxygen triangular faces are always slightly twisted around the 3-fold axis compared to the nitrogen triangular faces. The twist between the two triangular faces can be quantified by looking at the torsion angles formed by the four atoms of every rectangular face of the prism. In [Y(L^b)] the average of the three torsion angles (one for every

triangular side) is 16.9° and in [Gd(L^b)] it is 18.4°; the distortion from the trigonal prismatic geometry is therefore more evident as the dimension of the encapsulated ion increases. The distortion observed for the [Ln(L^a)] complexes was more pronounced with values for the Y^{III} and Gd^{III} complexes of 20.2° and 21.4°, respectively.

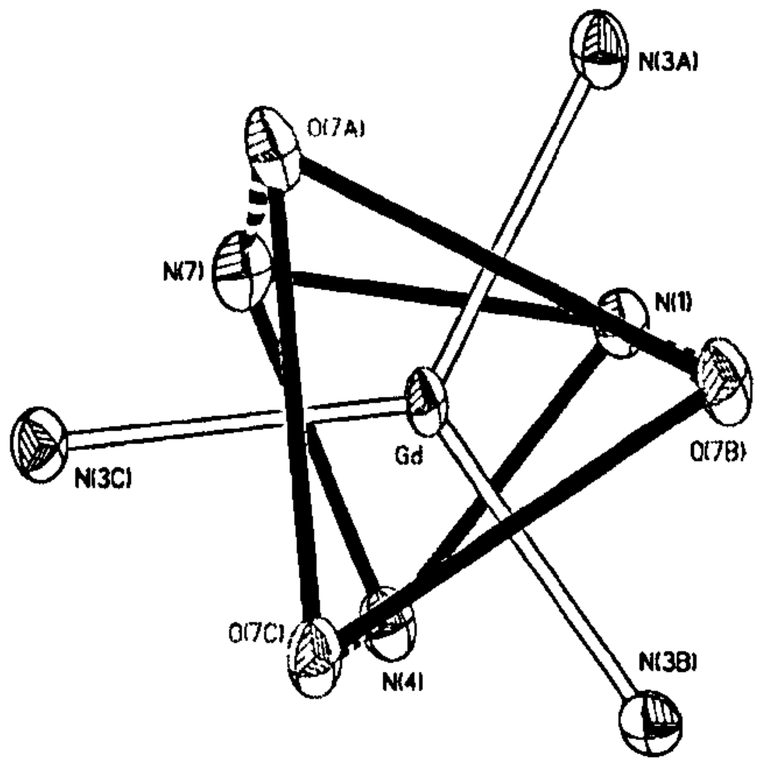

Figure 4.16 Co-ordination geometry about the metal centre in [Gd(L^b)].

4.2.4 Single crystal X-ray diffraction analysis of [Gd(L^c)]·½CH_3OH

Single crystals of [Gd(L^c)]·CH_3OH were obtained using the same method employed for [Ln(L^b)] (previous section). Single crystal X-ray diffraction studies show that the Gd^{III} is nine-coordinate, using all nine donor atoms of the ligand, namely the three amino N-donors of the macrocycle, the three imino N-donors and the three phosphonate O-donors. Bond lengths are in the ranges 2.641(13)-2.696(13)Å for the bonds between the Gd^{III} and the macrocyclic N-donors, 2.619(14)-2.701(13)Å for the bonds to the N-donors of the imine moieties and 2.303(11)-2.350(13)Å for those to the phosphonate O-donors.

In [Gd(L^c)]·CH_3OH the fragments C(2)-O(6) and C(10) are almost planar due to the conjugation between the imine and phosphonate groups, with the mean deviation from the least squares mean plane being only 0.020Å - 0.067Å. The pitch angles between the plane of the macrocycle and the plane of each

phosphonate characterise the opening of the three arms. The average of the three pitch angles for [Gd(L^c)] is 43.7º, very similar to that observed in [Gd(L^b)]. Also the methoxybenzene fragments are planar (mean deviation of 0.018-0.047Å) and almost perpendicular to the plane formed by the imino-phosphonate fragments (79.6-106.8º).

Table 4.2 Selected bond lengths (Å) for [Gd(L^c)]·½CH_3OH.

	[Gd(L^c)]
Gd-N(1)	2.643 (14)
Gd-N(4)	2.696 (13)
Gd-N(7)	2.641 (13)
Gd-N(3A)	2.619 (14)
Gd-N(3B)	2.701 (13)
Gd-N(3C)	2.652 (13)
Gd-O(6A)	2.303 (11)
Gd-O(6B)	2.350 (13)
Gd-O(6C)	2.334 (11)

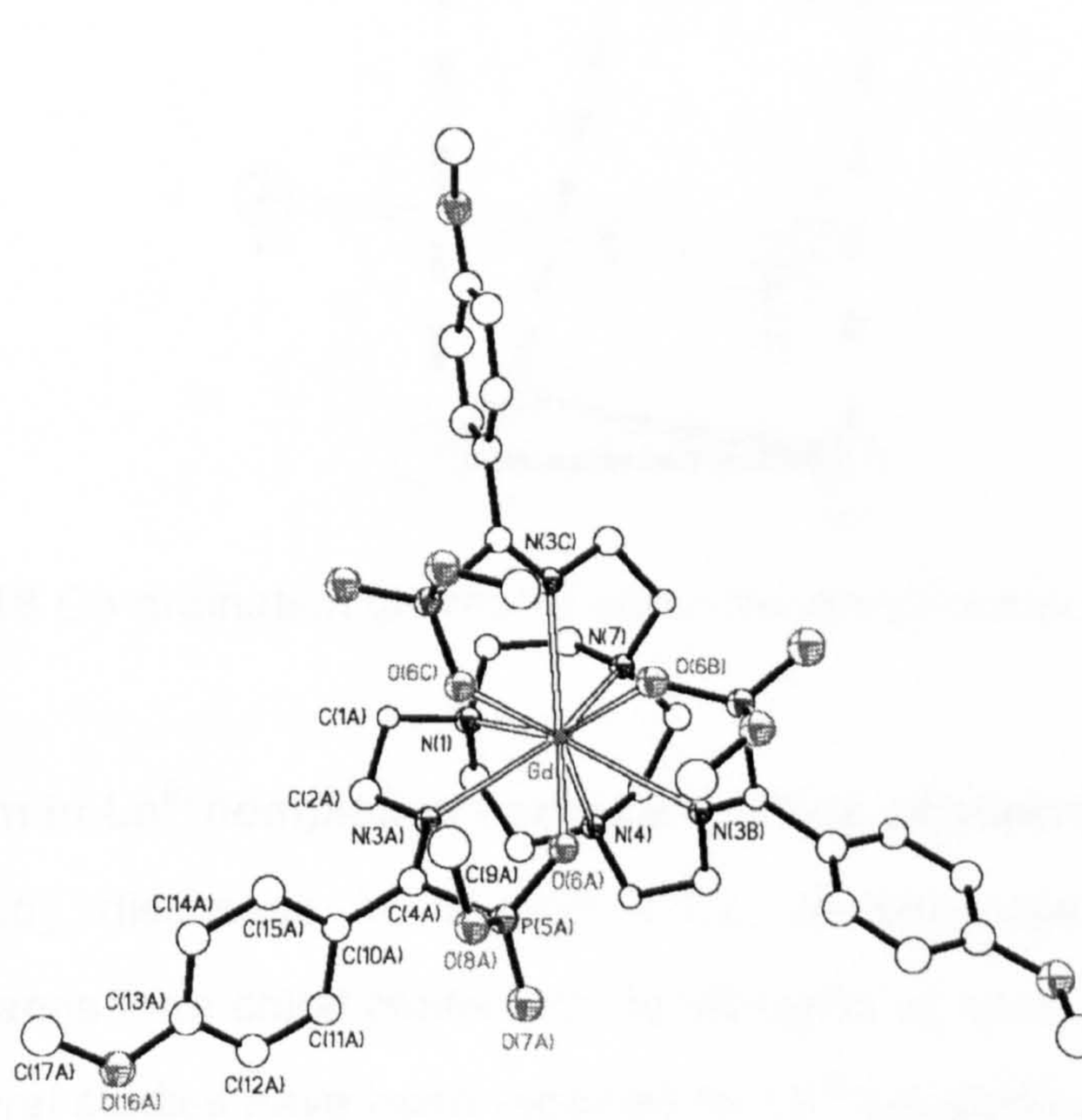

Figure 4.17 Crystal structure of [Gd(L^c)]·½CH_3OH with numbering scheme adopted. Hydrogen atoms and solvating CH_3OH molecules have been omitted for clarity.

The co-ordination geometry about the Gd^{III} centre is again slightly distorted tricapped trigonal prismatic (Figure 4.18). The macrocyclic nitrogen donors and the phosphonate oxygens impose the two triangular faces and the imine nitrogens cap the three rectangular faces of the prism. The upper and lower triangular faces of the prism are essentially equilateral (angle range 59.0-60.6º) and parallel (the angle between the plane defined by the triangle of three oxygen donors and the one defined by the three nitrogen donors is 1º), but the nitrogen triangular face is slightly twisted around the 3-fold axis relative to the oxygen triangular face. Looking at the torsion angles formed by the four atoms of every rectangular face of the prism, it is possible to quantify the twist between the two triangular faces. In this structure the average of the three torsion angles (one for every triangular side) is 17.5º; a similar distortion is observed in [Gd(L^b)].

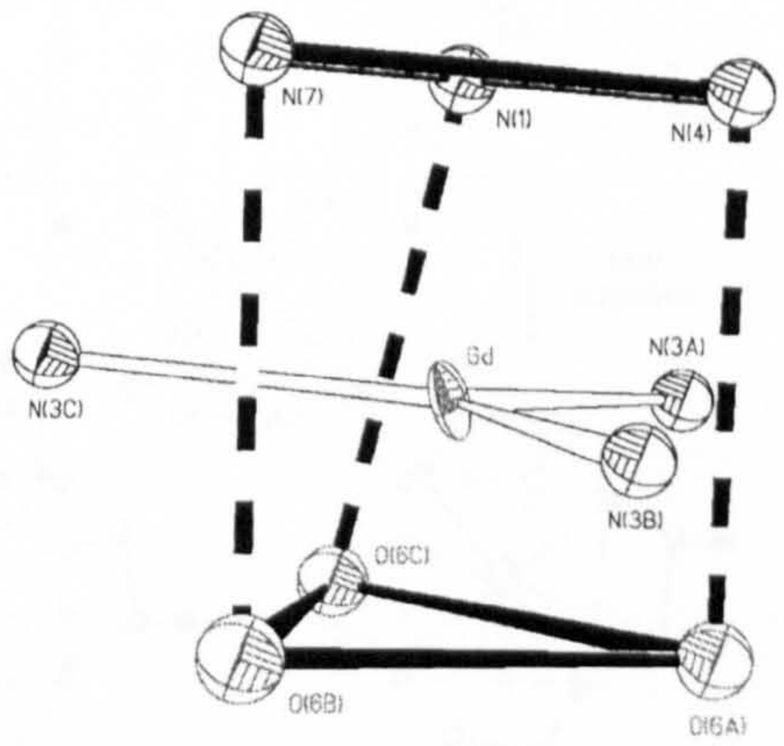

Figure 4.18 Co-ordination geometry about the metal centre in [Gd(L^c)].

4.2.5 Isomerism in Ln^{III} complexes containing chiral phosphorus centres

As already discussed in Section 4.1.2, phosphonate monoester and phosphinate ligands form chiral centres at the phosphorus upon co-ordination to a metal ion. Several studies have been reported on Ln^{III} complexes containing chiral phosphorus centres and NMR spectra with multiple resonances have been discussed.[22,341,345]

It is important to remark that Ln^{III} complexes of all cyclen derivatives show the presence of two slowly interconverting diastereomers in solution due to clockwise (Δ) and counter-clockwise (Λ) rotation of the cyclododecane ring conformation as well as rotation of the methylene groups in the pendant arms (λ and δ).[291-293,359,360] The two diastereomeric conformations (monocapped square antiprismatic (CSAP) and twisted CSAP) for lanthanide complexes of DOTA are illustrated in Figure 4.20. Pairs of enantiomers interconverting by ring inversion or arm rotation exist for the major isomer [$\Delta(\lambda\lambda\lambda\lambda)$ and $\Lambda(\delta\delta\delta\delta)$] and for the minor isomer [$\Delta(\delta\delta\delta\delta)$ and $\Lambda(\lambda\lambda\lambda\lambda)$] of [Ln(DOTA)]$^-$.

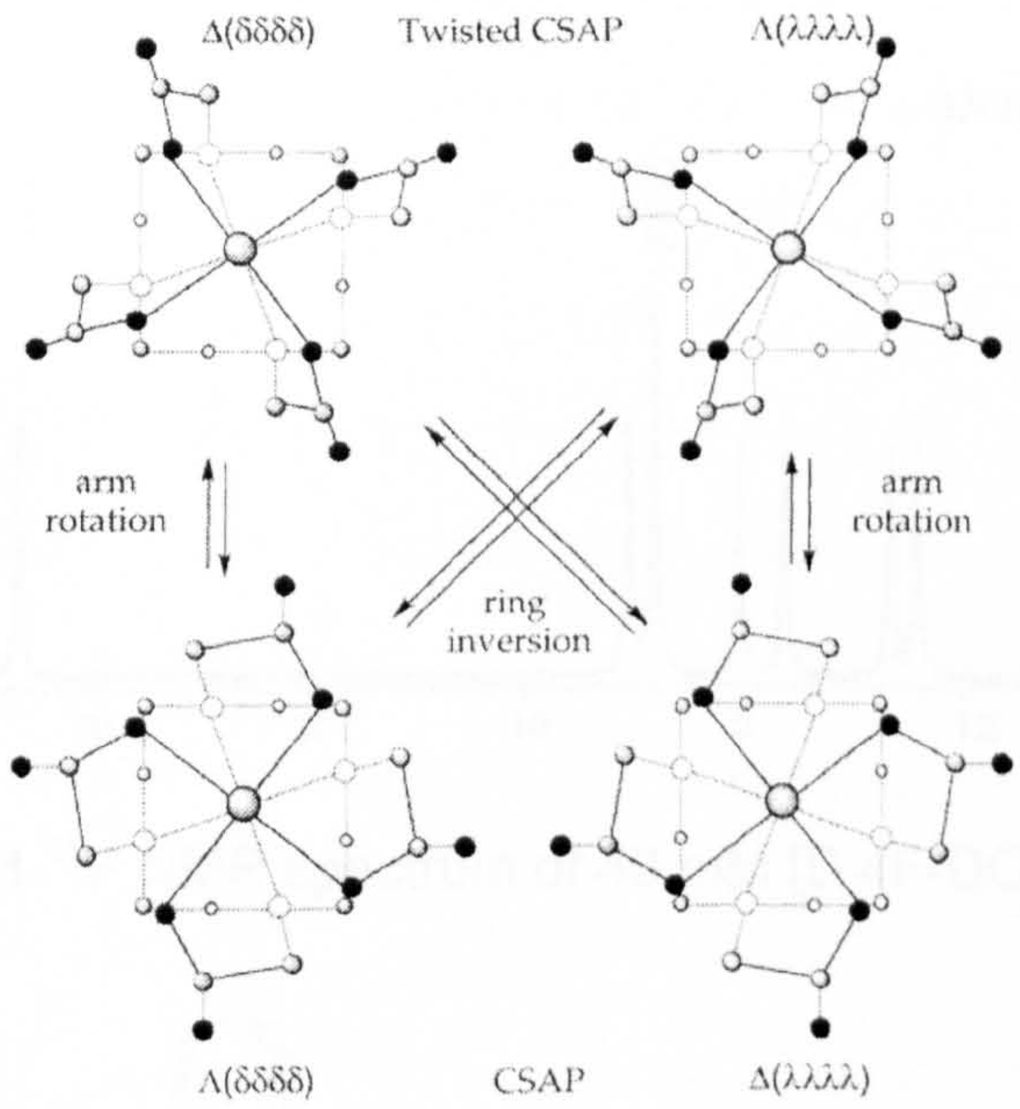

Figure 4.20 Diastereomeric conformations (CSAP and twisted CSAP) for lanthanide complexes of DOTA.

In addition to this isomerism, phosphinate and phosphonate ester lanthanide complexes have an asymmetric centre at each phosphorus with possible *R* or *S* orientation (if the orientation of each group is independent of the orientation of the others). In Section 4.1.2 the use of ^{19}F NMR spectra on a

fluorinated ester analogue of DOTP (Figure 4.9a) was discussed. Sherry and co-workers have observed the sixteen possible ^{19}F resonances in the spectra of paramagnetic complexes due to six different diastereomers [Δ(*RRRR*), Δ(*RRRS*), Δ(*RRSS*), Δ(*RSRS*), Δ(*RSSS*) and Δ(*SSSS*)] (Figure 4.21).[345] They considered only the clockwise (Δ) isomers, therefore Δ(*RRRR*) refers to the enantiomeric pair Δ(*RRRR*)/Λ(*SSSS*) different from the Δ(*SSSS*)/Λ(*RRRR*) pair. Statistically, diastereomeric complexes are not equally abundant since, for example, Δ(*RRRR*) occurs only once among the 16 possibilities while Δ(*RRRS*) occurs four times. Therefore, while only one peak correspondent to the Δ(*RRRR*) diastereomer is observed, four peaks of equal intensities are observed for the Δ(*RRRS*)

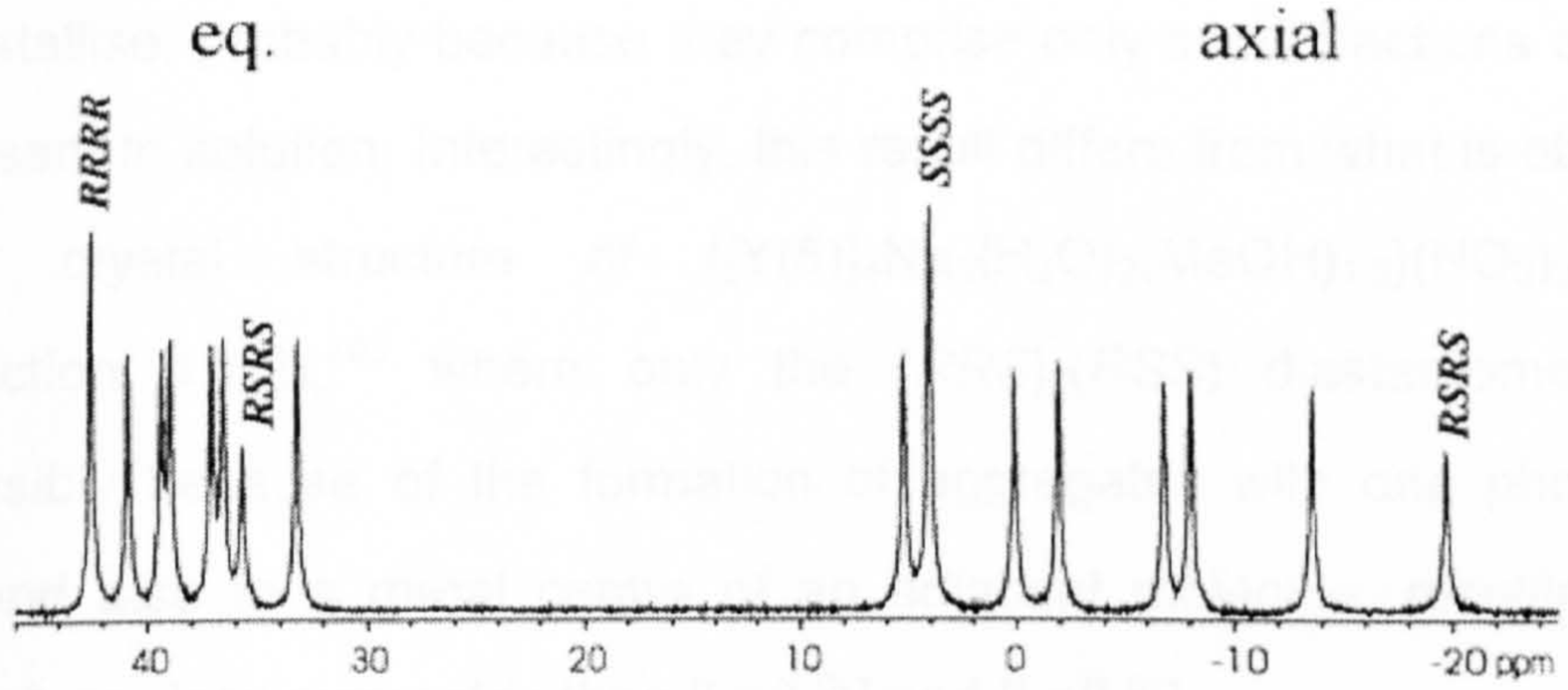

Figure 4.21 ^{19}F NMR spectrum of 40 mM [Dy(F-DOTPME)]$^-$ at 25 °C.

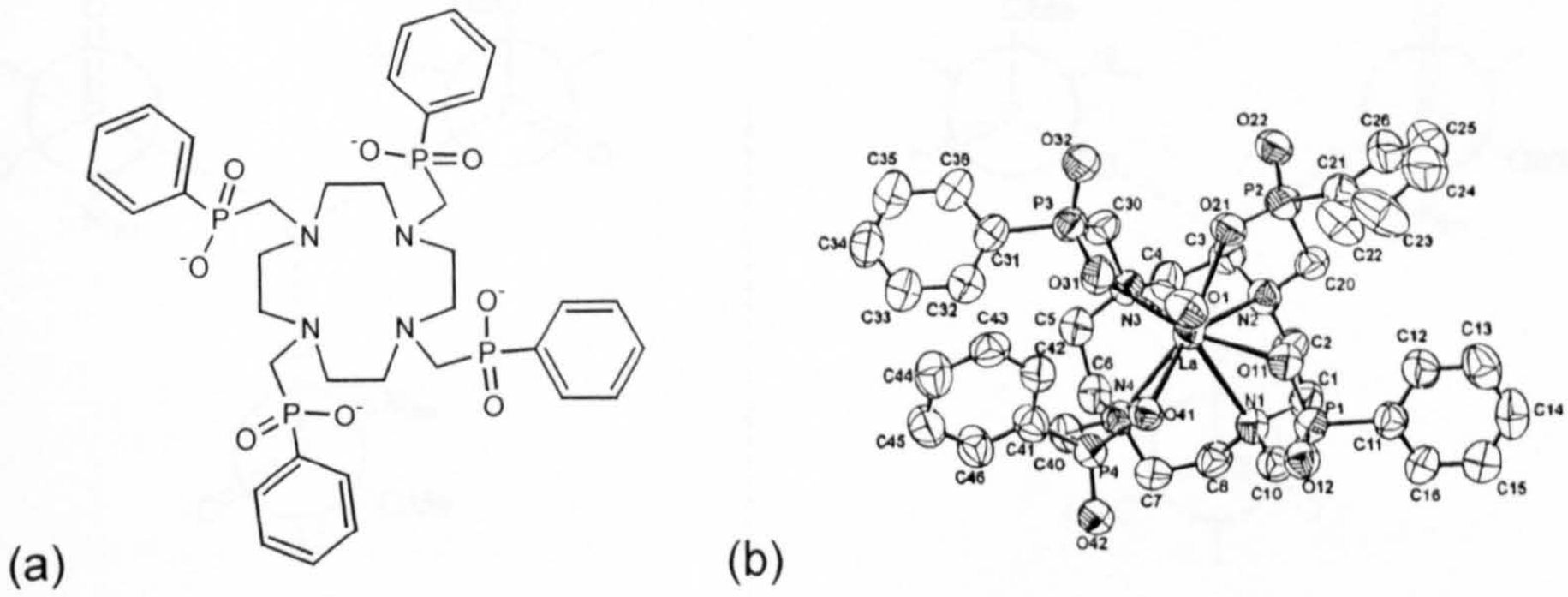

Figure 4.22 (a) Tetra(phenyl)phosphinic acid derivative of cyclen (DOTPP)^4; (b) crystal structure of Li[La(DOTPP)].

diastereomer.[345] An analogous study has been reported by Lukes and co-workers on the tetra(phenyl)phosphinic acid derivative of cyclen (DOTPP, Figure 4.22).[341] In this case the orientation of the phosphinic groups in the solid state is (*RSRS*), but the ^{31}P NMR spectrum of the Lu^{III} complex in solution again shows sixteen resonances due to the six diastereomers mentioned above.[341]

Since the nine co-ordinate lanthanide complexes such as [Ln(L^b)] and [Ln(L^c)] contain three chiral phosphorus centres, four possible diastereomers, each of them with two enantiomers, can be distinguished. The three crystal structures [Y(L^b)]·CH$_3$OH, [Gd(L^b)]·1.5CH$_3$OH·H$_2$O and [Gd(L^c)]·0.5CH$_3$OH show the presence of only one diastereomer, the (*RRR*)-(*SSS*) (Figure 4.23). The other three diastereomers, (*RRS*)-(*RSS*), (*RSS*)-(*RRS*) and (*RSR*)-(*SRS*), do not crystallise, probably because they comprise only small fractions of the complexes present in solution. Interestingly, this result differs from what is observed in the X-ray crystal structure of {[Y(**5**)]$_4$Na$_3$(H$_2$O)$_2$(MeOH)$_{1.2}$}(NO$_3$)$_3$·2H$_2$O·5.6MeOH (Section 4.1.2),[283] where only the (*RRS*)-(*RSS*) diastereomer was present, possibly because of the formation of aggregates with one phosphonate group bound also to a metal centre of an adjacent molecule, resulting in complexes which are less symmetric than [Ln(L^b)] and [Ln(L^c)].

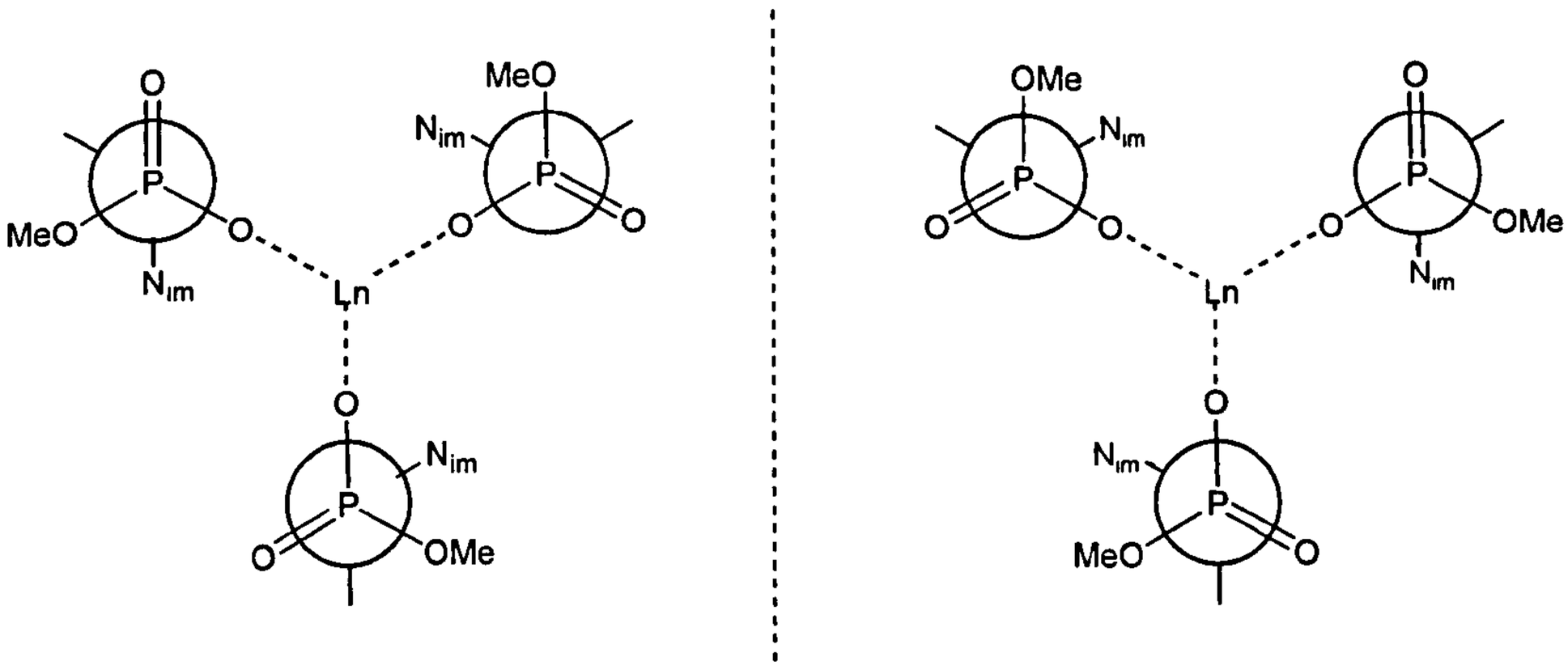

Figure 4.23 (*RRR*)-(*SSS*) pair of enantiomers in [Ln(L^b)] and [Ln(L^c)] complexes.

NMR spectroscopic studies were carried out in order to determine whether the four different diastereomers present in solution could be distinguished. The ^{1}H NMR spectrum of [Yb(L^b)] (300 MHz, 298 K, D_2O) has turned out to be particularly useful because the peaks are shifted over an expanded spectral region due to the paramagnetic shift allowing minor isomers to be detected. The ^{1}H NMR spectrum of [Yb(L^b)], shown in Figure 4.24, shows ten resonances shifted in a range between 43.4 ppm and -37.7 ppm corresponding to the major isomer, each of them surrounded by three smaller peaks in a ratio of about 70:10:10:10. The resonances of the major isomeric form were assigned with the help of a 2D COSY experiment and are reported in Table 4.3. Since all the single crystals obtained from solution of [Ln(L^b)] and [Ln(L^c)] complexes show the presence of only the (*RRR*)-(*SSS*) diastereomer, there is a strong possibility that the major component in solution, which gives the highest peaks in the ^{1}H NMR spectrum, is the (*RRR*)-(*SSS*) diastereomer.

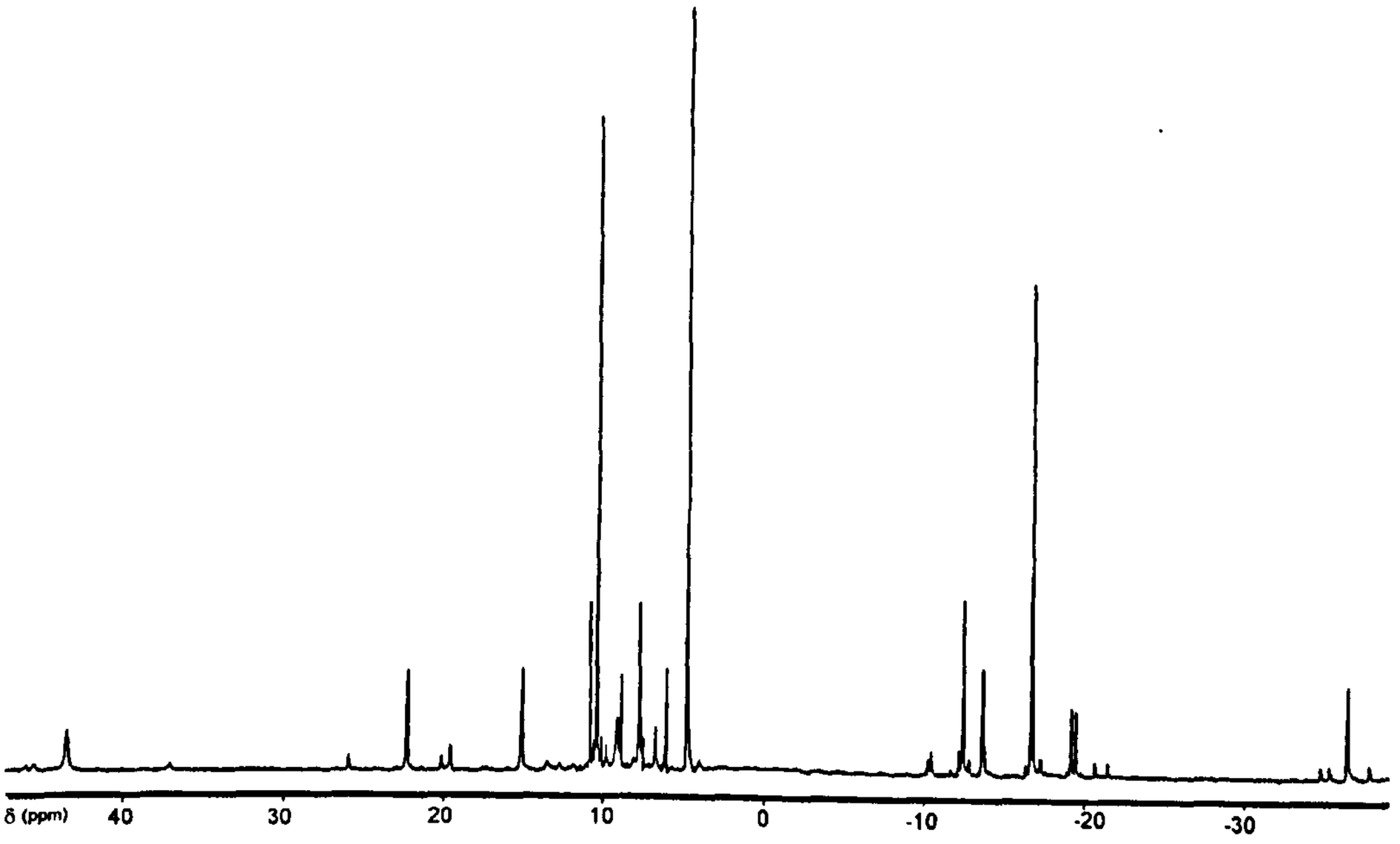

Figure 4.24 ^{1}H NMR spectra of paramagnetic [Yb(L^a)] in D_2O at 298 K.

Interestingly, the 2D COSY experiment shows that each resonance of a species is correlated with the corresponding signals of the other diastereomers and this fact indicates the occurrence of an exchange between the four diastereomers as a consequence of an isomerisation process that is quite fast at room temperature.

Table 4.3 ^{1}H NMR chemical shift (ppm) for the major isomer in the paramagnetic [Yb(L^b)] complex.

	δ (ppm)
H_{3a}	43.4
H_{4e}	22.3
H_{4a}	15.1
H_{Me1}	10.4
H_{1a}	9.1
H_{3e}	7.6
H_{1e}	-12.4
H_{2e}	-13.6
H_{Me2}	-16.7
H_{2a}	-37.7

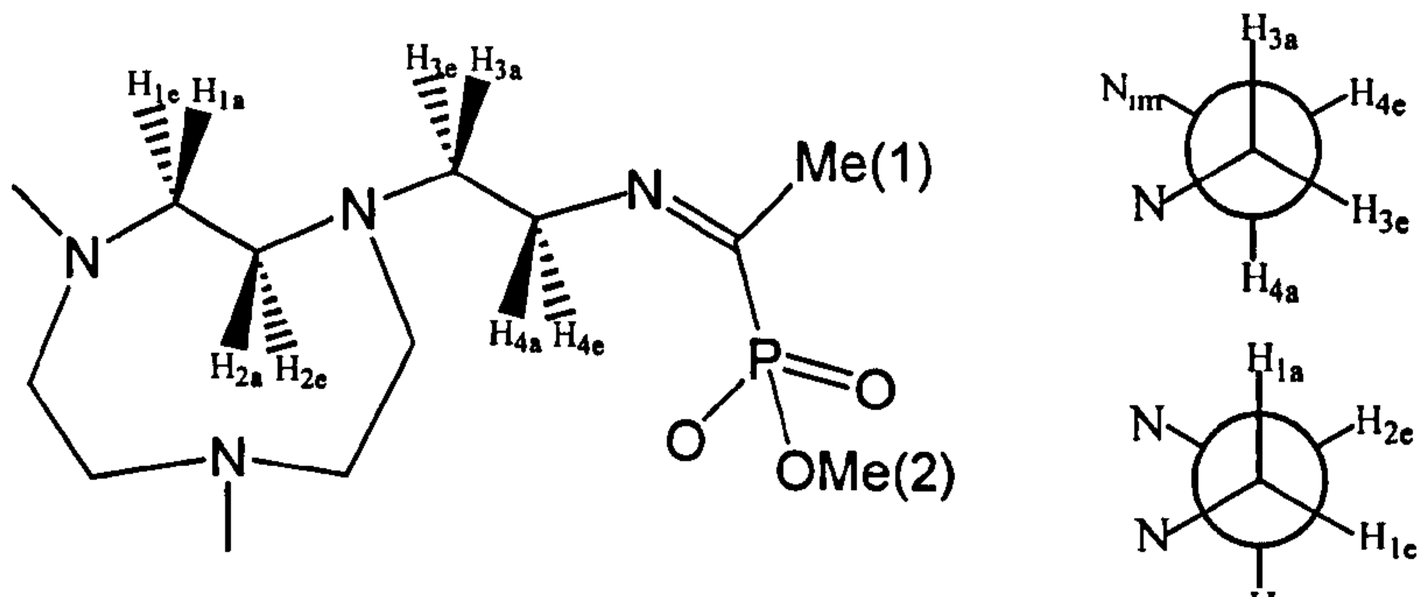

(a) (b)

Figure 4.25 (a) Labelling scheme for the phosphonate group, for the CH_2CH_2 linkers of the macrocycle and the arms and (b) their Newman projections.

4.2.6 ^{1}H, ^{13}C and ^{31}P NMR spectra of diamagnetic [Ln(L^b)] and [Ln(L^c)] complexes

Further NMR spectroscopic studies were performed on Y^{III} complexes of L^b and L^c and on [La(L^b)] and compared with the studies reported in Section 3.4.1 for the [Ln(L^a)] complexes. ^{1}H NMR spectra of [Y(L^b)] and [La(L^b)] show a very similar splitting pattern (Figure 4.26) with a complex series of multiplets and doublets of doublets. A 2D-COSY experiment combined with a ^{1}H-^{13}C coupling 2D experiment allowed accurate assignment of the resonances (Table 4.4, see Figure 4.25 for labelling scheme). The signals are broader than those observed for the ^{1}H NMR spectra of [Ln(L^a)] complexes and the coupling constants could be determined only for the macrocyclic protons and for the methyl groups coupled to the phosphorus

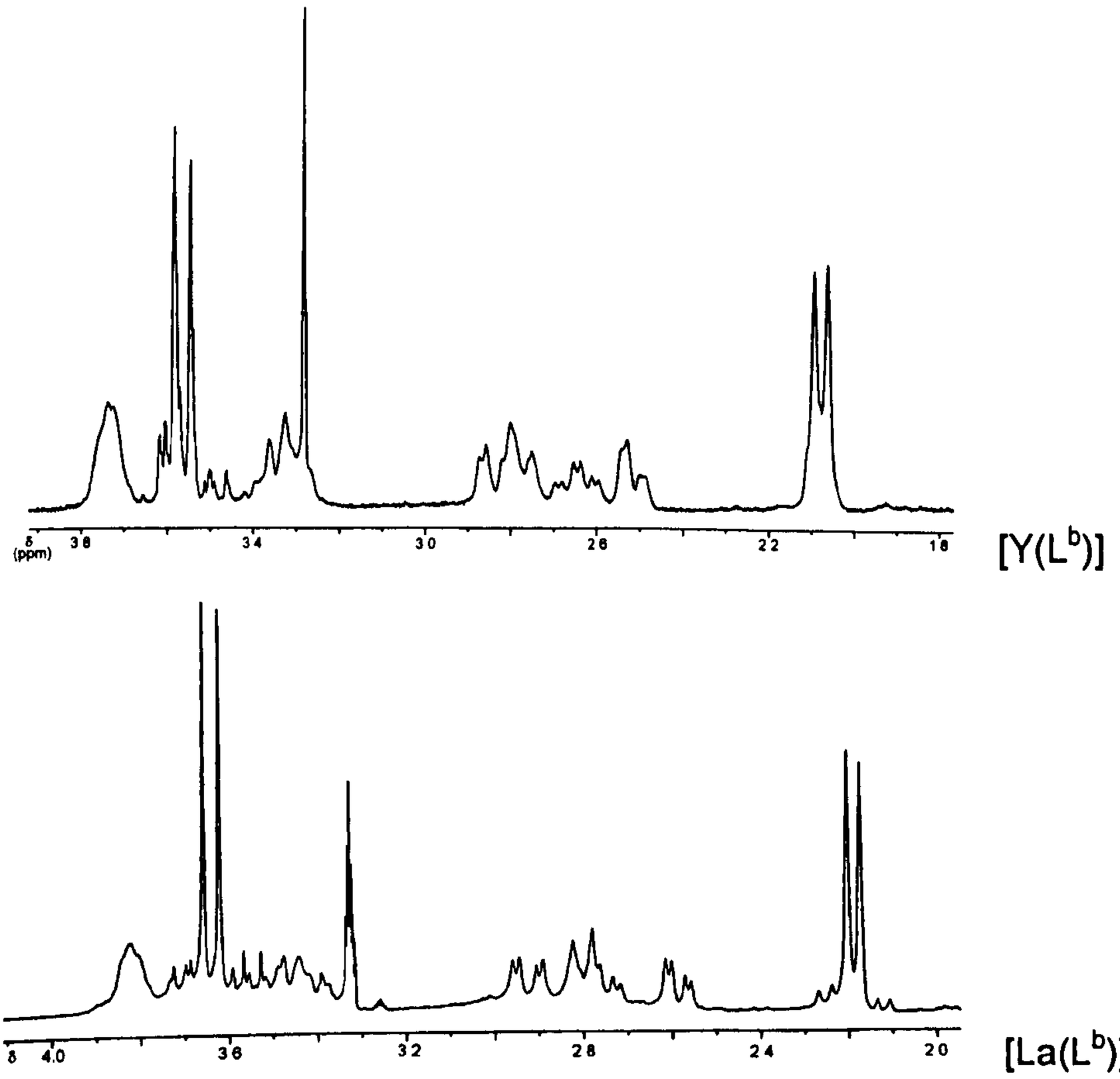

Figure 4.26 ^{1}H NMR spectra of [Y(L^b)] (above) and [La(L^b)] (below) at 298 K in D_2O and CD_3OD, respectively.

atoms. The ethylenic moiety of the macrocycle forms a series of multiplets and the 2D-COSY experiment allowed us to assign the equatorial proton at 2.53 ppm as geminal to the axial proton at 2.66 ppm (and H_{eq} at 2.88 to H_{ax} at 3.33). Only one geminal coupling could be detected (13.0 Hz) and the *trans* coupling constants are 4.6 Hz and 4.8 Hz. The H-P coupling constants are 9.1 Hz (8.6 Hz for [La(L^b)]) for the methyl group next to the imine bond (H_{Me1}) and 9.7 Hz (11.1 Hz for [La(L^b)]) for the methyl of the methoxy group (H_{Me2}). In the ^{1}H NMR spectrum of [La(L^b)] (recorded in CD_3OD), the equatorial proton at 2.58 ppm belonging to the ethylenic moiety of the macrocycle is geminal to the axial proton at 2.77 ppm (J_{gem} = 13.1 Hz) and H_{eq} at 2.92 to H_{ax} at 3.44 ppm (J_{gem} = 16.3 Hz). The *trans* (eq-ax) coupling constants are 4.1 Hz and 4.6 Hz, respectively.

Table 4.4 ^{1}H NMR chemical shift (ppm) for diamagnetic [Y(L^b)] and [La(L^b)].

	[Y(L^b)]	[La(L^b)]
H_{Me1}	2.08	2.19
H_{1e}	2.53	2.58
H_{1a}	2.66	2.77
H_{3a}	2.80	2.78
H_{2e}	2.88	2.92
H_{2a}	3.33	3.44
H_{3e}	3.36	3.48
H_{Me2}	3.56	3.64
H_4 (ax. and eq.)	3.75	3.82

While the ^{1}H NMR spectrum of [Y(L^b)] does not clearly show the presence of different isomers, in the ^{1}H NMR spectrum of [La(L^b)] two minor isomers can be observed near the doublet at 2.19 ppm corresponding to H_{Me1} (Figure 4.26). In contrast, only in the ^{31}P NMR spectrum of [Y(L^b)] can more than one peak corresponding to the other diastereomers be seen, while the ^{31}P NMR spectrum of [La(L^b)] shows only one large singlet at 14.5 ppm. The ^{31}P NMR spectrum of [Y(L^b)] (Figure 4.27) shows one dominant doublet at 14.67 ppm which results from

the coupling between ^{89}Y and ^{31}P (J_{YP} = 8.8 Hz) and three minor doublets (one of them overlapped at 14.74) at 14.51 and 13.75 ppm (J_{YP} = 8.9 and 8.6 Hz, respectively) corresponding to the three minor diastereomers.

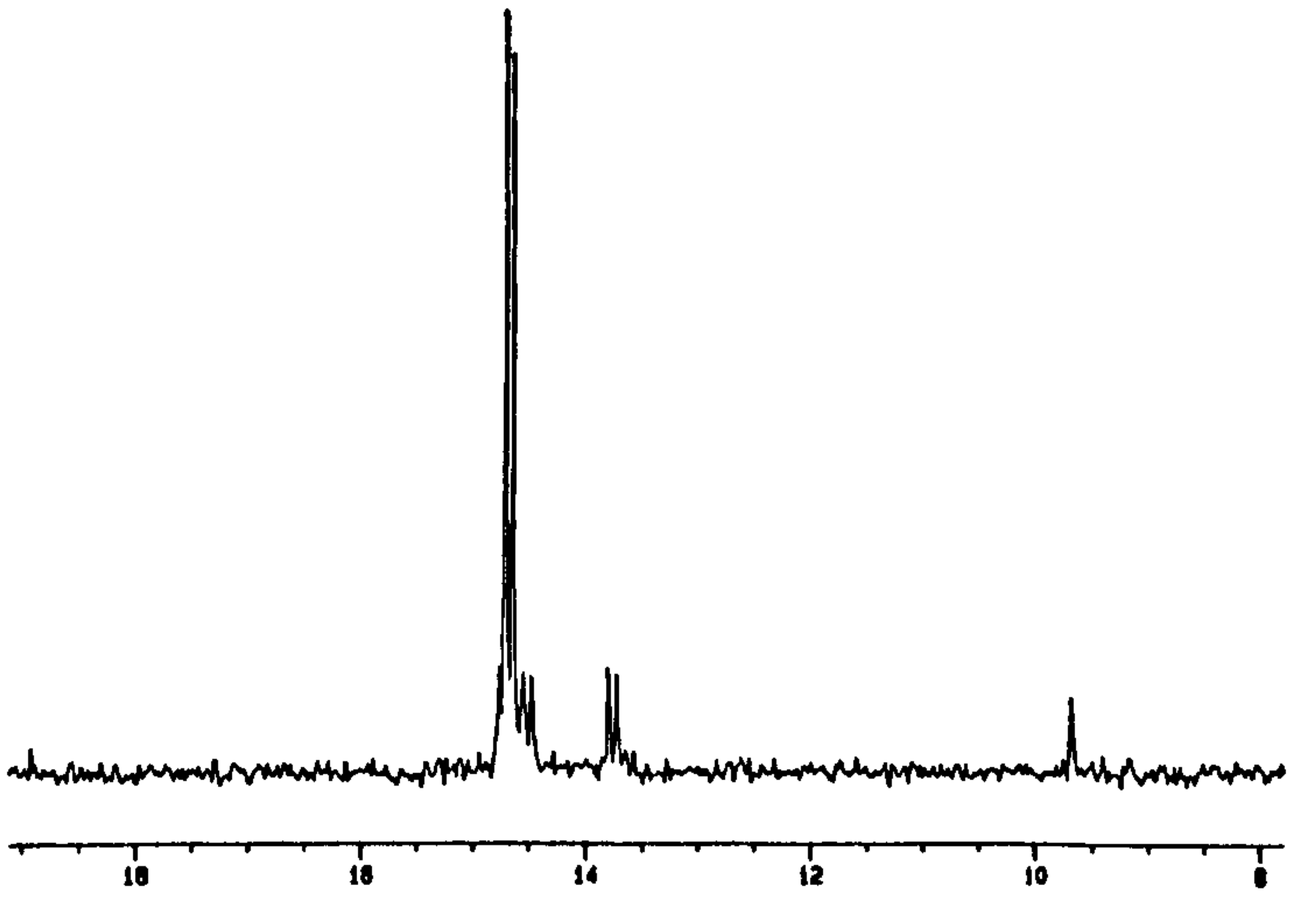

Figure 4.27 ^{31}P NMR spectrum of [Y(L^b)] in D_2O at 298 K.

The ^{13}C NMR spectrum of [Y(L^b)] (75.5 MHz, 298 K, D_2O) shows the expected signals assigned with the help of a ^{1}H-^{13}C coupling experiment and reported in Table 4.5. Interestingly, the coupling between ^{13}C and ^{31}P observed in this spectrum presents quite large coupling constants: the carbon at 175.2 ppm, assigned to the imine carbon, appear as a doublet with J_{CP} of 187.4 Hz and the carbons of the two methyl groups, one next to the imine carbon and the other one of the methoxy group, appear as two doublets with J_{CP} of 23.4 and 22.9 Hz, respectively.

The ^{1}H NMR spectrum of [Y(L^c)] (300 MHz, 298 K, D_2O) is not as clear as the spectra described so far, all the CH_2 groups next to the N-atoms giving a broad multiplet between 2.73 and 3.88 ppm; the methyl group of the methoxybenzene unit gives a singlet at 3.91 ppm and the methoxy group on the phosphorus forms a doublet at 3.57 ppm (J_{HP} = 12.0 Hz). The proton on the benzene ring gives two doublets at 7.17 and 7.51 ppm (J_{HH} = 8.5 and 8.6 Hz, respectively). The expected

resonances of the ^{13}C NMR spectrum of [Y(L^c)] are reported in Table 4.5. The ^{31}P NMR spectrum of the same complex shows again a coupling between ^{89}Y and ^{31}P, a major isomer at 11.7 ppm (J_{YP} = 9.1 Hz) and the other three isomers at 11.5, 10.7 and 9.7 ppm with coupling constants of 8.9, 8.5 and 8.8 Hz, respectively.

Table 4.5 ^{13}C NMR chemical shift (ppm) for [Y(L^b)] and [Y(L^c)].

	[Y(L^b)]	[Y(L^c)]
CH_3C=N	16.7	--
CH_2N=C	51.1	36.1
NCH_2 (arm)	52.9	50.8
NCH_2 (ring)	57.6	49.5
CH_3OP	48.2	55.5
CH_3OAr	--	54.0
C(Ar)	--	113.6, 114.4, 114.7, 127.8, 131.0, 132.3
C=N	175.2	160.7

4.2.7 Hydrolysis experiments

Previous work at the University of Nottingham investigated the hydrolysis of [Y(**5**)] (section 4.1.3) in two separately buffered solutions, the first one at pD = 5.5, and the second one at pD = 7.8.[283] The rate of hydrolysis at pD = 7.8 was found to be relatively slow and, in fact, it was slower than the hydrolysis of the analogous carboxylate complex [Y(**1**)] (section 3.4.2). In contrast, the hydrolysis at pD = 5.5 of [Y(**5**)] was complete before the first NMR spectrum could be recorded (under 5 minutes).[283]

As already seen for the complexes [Ln(L^a)], [Y(L^b)] was found to be stable in D_2O. Hydrolysis experiments were carried out at acidic pH to determine the hydrolysis rate of the imine bonds in this complex. The hydrolysis of [Y(L^b)] was investigated in two separately buffered solutions at pD = 4.4 and pD = 5.5 (acetate buffer). In both cases the hydrolysis was complete in less than two hours. Therefore it appears that [Y(L^b)] is much less stable under acidic conditions than

[La(L^a)] (Section 3.4.3). The product of the hydrolysis of [Y(L^b)] should be the protonated ligand $[H_3L]^{3+}$, $[Y(D_2O)_x]^{3+}$ and only one phosphorus containing product (presumably the methyl acetylphosphonic acid) as confirmed by ^{31}P NMR spectroscopy (Figure 4.28).

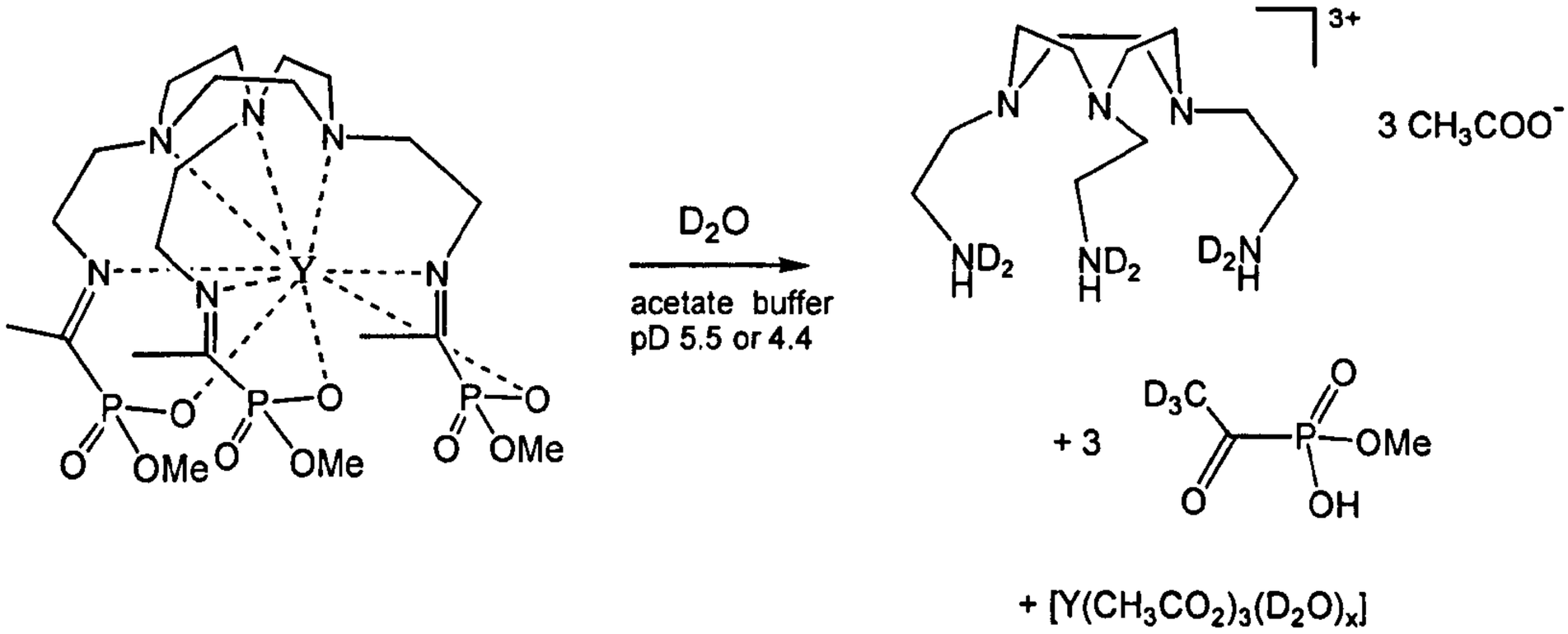

Figure 4.28 Scheme showing the hydrolysis of [Y(L^b)] in D_2O at pD 5.5 and 4.4.

As already pointed out for [Y(**5**)], the low stability in acidic conditions of these phosphonate monoester complexes may be due to ineffective conjugation between the imine and the phosphonate group in [Y(L^b)] compared to the imine and carboxylate groups in [La(L^a)]. This explanation is supported by quantum mechanical calculations on dimethyl-benzoylphosphonate (Figure 4.29) which show a very low energy barrier to rotation about the C-P bond.[358]

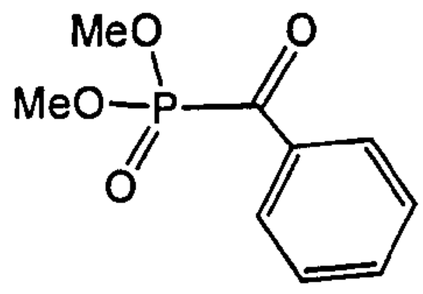

Figure 4.29 Dimethyl-benzoylphosphonate.

Confirmation of the low stability of phosphonate monoester complexes comes from the complex [Y(L^c)] which was found to be unstable in D_2O at neutral pH and at room temperature. The imine bond hydrolyses completely within five

days and the course of the hydrolysis could not be followed by ^{1}H or ^{31}P NMR because of their complexity. Indeed, the products of the hydrolysis are not only the amine L, the free lanthanide ion and the starting methoxybenzoylphosphonate, but also another product present in both the ^{1}H and ^{31}P NMR spectra, which could be identified as the methoxy benzylphosphonate co-ordinated to the Y^{III}.

4.2.8 Relaxivity of [Gd(L^{b})]·3NaCl·3H$_2$O and [Gd(L^{c})]·3NaCl·3H$_2$O

Relaxivities of [Gd(L^{b})]·3NaCl·3H$_2$O and of [Gd(L^{c})]·3NaCl·3H$_2$O at 300 MHz and 37°C were measured as 1.64 ± 0.08 and 1.54 ± 0.08 $mM^{-1}s^{-1}$, respectively. These values, only slightly higher than the value of 1.26 (5) $mM^{-1}s^{-1}$ observed for the imino-carboxylate analogue [Gd(L^{a})], suggest that no H_2O molecules are bound to the Gd^{III} centres and only the second sphere and outer sphere terms contribute to the relaxivity. Also the X-ray crystal structure determination confirmed that [Gd(L^{b})] and [Gd(L^{c})] have no water molecule co-ordinated to the paramagnetic metal centre (Section 4.2.2) and this type of structure is likely to be maintained in solution.

4.5 Experimental

4.5.1 Synthesis of Methyl sodium acetylphosphonate

Methyl sodium acetyl phosphonate was synthesised using a modified procedure to that reported by Karaman *et al.*[358] Thus trimethyl phosphite (5.52 g, 44.5 mmol) was added dropwise to acetyl chloride (3.50 g, 44.6 mmol) over 1.25h at 5°C to produce a colourless solution. The cooling bath was removed and the solution was left to stir at ambient temperature for 18 h to give a colourless oil which was purified by vacuum distillation to yield dimethyl sodium acetyl phosphonate (2.37 g, 15.6 mmol, 35%). Due to its toxicity, this compound was not characterised: instead, the data obtained by Karaman *et al.*[358] is quoted: b.p.

65°C/1.5 mmHg. IR (neat): 1695s, 1260s, 1025s cm^{-1}. ^{1}H NMR ($CDCl_3$): δ = 2.40 (3H, d, *J* 5.1 Hz), 3.95 (6H, d, *J* 11Hz) ppm. ^{31}P NMR: δ = -2.93 (sept) ppm. Sodium iodide (2.34 g, 15.6 mmol) in dry acetone (14 cm^3) was added to a solution of dimethyl sodium acetylphosphonate (2.37 g, 15.6 mmol) in dry acetone (20 cm^3). This solution was left to stir for 24 h to produce a white precipitate which was filtered, washed with dry acetone and dried under vacuum to yield the product as a white solid (Yield: 1.07 g, 6.7 mmol, 43%). ^{1}H NMR (D_2O): δ = 2.35 (3H, d, -COC*H*$_3$), 3.56 (3H, d, -OC*H*$_3$) ppm. Mass spectrum (FAB): m/z = 161 (*M*$^+$ [($C_3H_6O_4PNa$) + 1]$^+$), 183 [($C_3H_6O_4PNa$) + Na]$^+$. Elemental analysis: found (calc. for $C_3H_6O_4PNa$): C, 22.09 (22.51), H, 3.66 (3.78), N, 0.00% (0.00%). IR (KBr disc): 2950s, 2847s, 1675s, 1244s, 1096s, 1039s cm^{-1}.

4.5.2 Synthesis of [Y(L^b)] and [Gd(L^b)]

1,4,7-*tris*(aminoethyl)-1,4,7-triazacyclononane (L) (22.2 mg, 0.086 mmol) dissolved in MeOH (10 cm^3) was added to a solution of methyl sodium acetylphosphonate (41.3 mg, 0.258 mmol) and the appropriate Ln^{III} chloride in MeOH (30 cm^3). The resulting colourless solution was heated under reflux for 2h. After cooling, the solvent volume was reduced, Et_2O was added and a white solid was obtained. The solid was filtered and dried under reduced pressure. Single crystals suitable for X-ray structural analysis were obtained from a Et_2O/MeOH (10/1) solution of the complex at room temperature.

[Y(L^b)]·2CH$_3$OH. Obtained 46.8 mg, 0.066 mmol, yield 77.2%. Mass spectrum (FAB, Glycerol/MeOH/H_2O matrix) m/z = 727 (*M*$^+$ [$C_{21}H_{42}N_6O_9P_3Y$ + Na$^+$]). Elemental analysis: found (calc. for $C_{21}H_{42}N_6O_9P_3Y$·2CH_3OH): C, 36.07 (35.95); H, 6.64 (6.56); N, 10.68% (10.94%). IR (KBr disk), cm^{-1}: 2940w, 2854w, 1637s ($\nu_{C=N, C=O}$), 1458w, 1212m, 1075m, 785m, 553m.

[Gd(L^b)]·3NaCl·3H$_2$O. Obtained 47.2 mg, 0.061 mmol, yield 71.0%. Mass spectrum (FAB, Glycerol/MeOH/H$_2$O matrix) m/z = 796 (M^+ [$C_{21}H_{42}N_6O_9P_3Gd$ + Na^+]) Elemental analysis: found (calc. for $C_{21}H_{42}N_6O_9P_3Gd$·3NaCl·3H$_2$O) C, 25.32 (25.17); H, 4.95 (4.83); N, 8.48% (8.39%). IR (KBr disk), cm^{-1}: 2949w, 2852m, 1629s ($\nu_{C=N, C=O}$), 1473w, 1359w, 1208s, 1110m, 1071s, 783m, 588m.

4.5.3 Synthesis of [Yb(L^b)] and [La(L^b)]

A solution of 1,4,7-*tris*(aminoethyl)-1,4,7-triazacyclononane (L) (0.15-0.20 mmol) in MeOH (10 cm^3) was added to 3 molar equivalents of methyl sodium acetylphosphonate and the appropriate $LnCl_3$ dissolved in MeOH (30 cm^3). The resulting colourless solution was heated under reflux for 2h. After cooling, the solvent volume was reduced, Et_2O was added and a white solid was obtained. The solid was filtered off and dried *in vacuo*.

[Yb(L^b)]·3NaCl·3H$_2$O. Yield 68.9%. Mass spectrum (FAB, Glycerol/MeOH/H$_2$O matrix) m/z = 812 (M^+ [$C_{21}H_{42}N_6O_9P_3Yb$ + Na^+]). Elemental analysis: found (calc. for $C_{21}H_{33}N_6O_9P_3Yb$·3NaCl·3H$_2$O): C, 24.88 (24.78); H, 4.91 (4.75); N, 8.40% (8.26%). IR (KBr disk), cm^{-1}: 2952w, 2918w, 2852w, 1634s ($\nu_{C=N, C=O}$), 1475w, 1360w, 1216s, 1111m, 1076s, 784m, 763m, 551m.

[La(L^b)]·3NaCl·3H$_2$O. Yield 70.8%. Mass spectrum (FAB, 3-NOBA matrix) m/z = 777 (M^+ [$C_{21}H_{33}N_6O_9P_3La$ + Na^+]) Elemental analysis: found (calc. for $C_{21}H_{33}N_6O_9P_3La$·3NaCl·3H$_2$O): C, 25.81 (25.64); H, 4.90 (4.92); N, 8.41% (8.54%). IR (KBr disk), cm^{-1}: 2959m, 2928m, 2857w, 1628s ($\nu_{C=N, C=O}$), 1465m, 1382m, 1285s, 1226m, 1068m, 1033m, 793m, 640m.

4.5.4 Synthesis of Methyl Sodium 4-Methoxy Benzoylphosphonate

Methyl sodium 4-methoxybenzoylphosphonate was synthesised using a modified procedure of that described by Karaman *et al.*[358] Thus trimethyl phosphite

(12.79 g, 0.1 mol) was added dropwise to *p*-anisoyl chloride (17.23 g, 0.1 mol) at 25°C. During the addition of trimethyl phosphite, the mixture was cooled to 5°C with an ice bath. After this addition, the cooling bath was removed and the solution was left to stir at ambient temperature for 12 h affording a pale yellow solution which was purified by vacuum distillation to produce dimethyl 4-methoxy benzoylphosphonate (10.05 g, 47.6 mmol, yield 48%). ^{1}H NMR ($CDCl_3$): δ = 3.84 (6H, t, P(OC*H*$_3$)$_2$), 3.87 (3H, d, 4-C*H*$_3$O), 6.92 (2H, d, (C*H*)$_2$C=O), 8.21 (2H, d, (C*H*)$_2$COMe) ppm. ^{13}P NMR ($CDCl_3$): δ = 0.21 (sept) ppm. ^{13}C NMR ($CDCl_3$): δ = 54.04 (P(OCH_3)$_2$), 55.65 (CH_3C), 114.28 ((C*H*)$_2$CC=O), 129.48 (*C*C=O), 132.51 (MeOC(*C*H)$_2$), 165.14 (*C*-OMe), 195.88 (*C*=O) ppm. A solution of sodium iodide (7.14 g, 47.6 mmol) in dry acetone (32 cm^3) was added to a solution of dimethyl 4-methoxybenzoylphosphonate (10.05 g, 47.6 mmol) in dry acetone (50 cm^3). The solution was left to stir for 12 h to produce a milky solution, which was filtered, washed with dry acetone and dried under vacuum to produce the desired product as an off-white solid (6.59 g, 55%). ^{1}H NMR (D_2O): δ = 3.65 (3H, d, -POC*H*$_3$), 3.88 (3H, s, -COC*H*$_3$), 7.06 (2H, d, C(C*H*)$_2$), 8.17 (2H, d, MeOC(C*H*)$_2$) ppm. ^{31}P NMR (D_2O): δ = 2.81 (s) ppm. ^{13}C NMR (D_2O): δ = 53.17 (P(OCH_3)), 55.87 (CH_3C), 114.44 ((*C*H)$_2$CC=O), 129.43 (*C*C=O), 132.31 (MeOC(*C*H)$_2$), 164.49 (*C*-OMe), 206.02 (*C*=O) ppm Mass spectrum (FAB, 3-NOBA matrix): m/z = 275 (M^+ [($C_9H_{10}O_5PNa$) + Na]$^+$), 526 [($C_9H_{10}O_5PNa$)$_2$ + Na]$^+$, 778 [($C_9H_{10}O_5PNa$)$_3$ + Na]$^+$, 1031 [($C_9H_{10}O_5PNa$)$_4$ + Na]$^+$. IR (KBr disc): 2947w, 1602s, 1256s, 1089s, 1060s, 834m, 762w, 557m cm^{-1}.

4.5.5 Synthesis of [Y(L^c)], [Gd(L^c)] and [Eu(L^c)]

1,4,7-*tris*(aminoethyl)-1,4,7-triazacyclononane (L) (0.15-0.20 mmol) dissolved in MeOH (10 cm^3) was added to a solution of methyl sodium 4-methoxy benzoylphosphonate (3 molar equivalents) and the appropriate $LnCl_3$ in MeOH (30

cm^3). The resulting colourless solution was heated under reflux for 2h. After cooling, the solvent volume was reduced and, by addition of Et_2O, a white solid was obtained. The solid was filtered and dried *in vacuo*.

[Y(L^c)]·3NaCl·3H$_2$O. Yield 67.8%. Mass spectrum (FAB, 3-NOBA matrix) m/z = 1004 (M^+ [$C_{39}H_{54}N_6O_{12}P_3Y$ + Na^+]). Elemental analysis: found (calc. for $C_{39}H_{54}N_6O_{12}P_3Y$·3NaCl·3$H_2O$): C, 38.44 (38.71); H, 5.16 (5.00); N, 7.08% (6.95%). IR (KBr disk), cm^{-1}: 2954w, 2848w, 1606s ($\nu_{C=N,\ C=O}$), 1509s, 1456m, 1418w, 1299m, 1253m, 1211s, 1082s, 1052s, 785m, 560m.

[Gd(L^c)]·3NaCl·3H$_2$O. Yield 74.5%. Single crystals suitable for X-ray structural analysis were obtained from a Et_2O/MeOH (10/1) solution of the complex at room temperature. Mass spectrum (FAB, 3-NOBA matrix) m/z = 1072 (M^+ [$C_{39}H_{54}N_6O_{12}P_3Gd$ + Na^+]) Elemental analysis: found (calc. for $C_{39}H_{54}N_6O_{12}P_3Gd$·3NaCl·3$H_2O$): C, 37.05 (36.64); H, 4.85 (4.73); N, 6.81% (6.57%). IR (KBr disk), cm^{-1}: 2953w, 2850m, 1634s ($\nu_{C=N,\ C=O}$), 1505m, 1370w, 1255s, 1213m, 1090m, 1052s, 779m, 561m.

[Eu(L^c)]·3NaCl·4H$_2$O. Yield 69.9%. Mass spectrum (FAB, 3-NOBA matrix) m/z = 1064 (M^+ [$C_{39}H_{54}N_6O_{12}P_3Eu$ + Na^+]). Elemental analysis: found (calc. for $C_{39}H_{54}N_6O_{12}P_3Eu$·3NaCl·4$H_2O$): C, 36.48 (36.28); H, 4.69 (4.84); N, 6.33% (6.51%). IR (KBr disk), cm^{-1}: 2957w, 2852w, 1616s ($\nu_{C=N,\ C=O}$), 1509s, 1466m, 1297m, 1251m, 1208s, 1084s, 1050s, 785m, 565m.

4.5.6 Hydrolysis experiments

Buffer solutions at pD 5.5 was formulated using the general procedure described in section 3.4.7 for the acidic buffer at pH 4. Potassium acetate (0.10g) and acetic acid (0.28 cm^3) were dissolved in D_2O (5 cm^3): pD = 5.5.

Two samples of [Y(L^b)]·2CH_3OH (5.6 and 5.2 mg, respectively) were dissolved in the two acidic buffer solutions at pD 4.4 and 5.5 (0.6 cm^3). The

resulting clear solutions were transferred into an NMR tube and the ^{1}H NMR spectra were acquired at time intervals [t(h)]. Both the hydrolyses occurred in less than two hours and no quantitative measurement on the integrals was carried out.

[Y(L^c)]·3NaCl·3H$_2$O (5.0 mg) was dissolved in D$_2$O (0.6 cm^3) and the resulting clear solution was transferred into an NMR tube and the ^{1}H NMR spectra were acquired at time intervals [t(h)]. In this case the course of the hydrolysis could not be followed easily because of the complexity of the ^{1}H NMR spectra.

4.5.7 Relaxivity of [Gd(L^b)] and [Gd(L^c)]

Five samples of [Gd(L^b)]·3NaCl·3H$_2$O and of [Gd(L^c)]·3NaCl·3H$_2$O were weighed (Table 4.6 and 4.7) and dissolved in 0.70 cm^3 of D$_2$O before transferring into an NMR tube. The transverse relaxation times (T_1) of the HDO peak at 4.707 ppm were measured using a 180-τ-90 pulse sequence at 37°C using a Bruker 300 MHz NMR spectrometer. For [Gd(L^c)], which was found to hydrolyse slowly in D$_2$O (section 4.5.5), the delay between dissolving the sample in D$_2$O and completing the T_1 measurement was less than 15 minutes, a time interval over which hydrolysis of the complex is thought to be minimal. The results are reported in Tables 4.6 and 4.7.

Table 4.6 Variation of T_1^{-1} (s^{-1}) of the HDO peak with concentration of [Gd(L^b)].

Mass [Gd(L^b)]·3NaCl·2H$_2$O (mg)	Concentration of [Gd(L^b)] (mM)	T_1 (s)	T_1^{-1} (s^{-1})
0.9	1.31	0.2985	3.35
2.1	3.05	0.1840	5.43
2.9	4.21	0.1453	6.88
3.6	5.23	0.1099	9.10
4.7	6.82	0.0971	10.94
5.8	8.42	0.0676	14.78

Plots of T_1^{-1} (s^{-1}) against concentration of [Gd(L^b)] and of [Gd(L^c)] (mM) give appropriate straight lines (Figure 4.30 and 4.31, respectively) with correlation coefficients of 0.994 and 0.995, respectively. The intercept with the y axis is again the relaxation rate (T_1^{-1} = 0.058 s^{-1}) of the HDO peak without the presence of the paramagnetic metal complex ([conc] = 0) (section 3.5.7). The relaxivities for the two complexes were calculated from the gradient of the two graphs as (1.64 ± 0.08) s^{-1} mM^{-1} for [Gd(L^b)] and (1.54 ± 0.08) s^{-1} mM^{-1} for [Gd(L^c)].

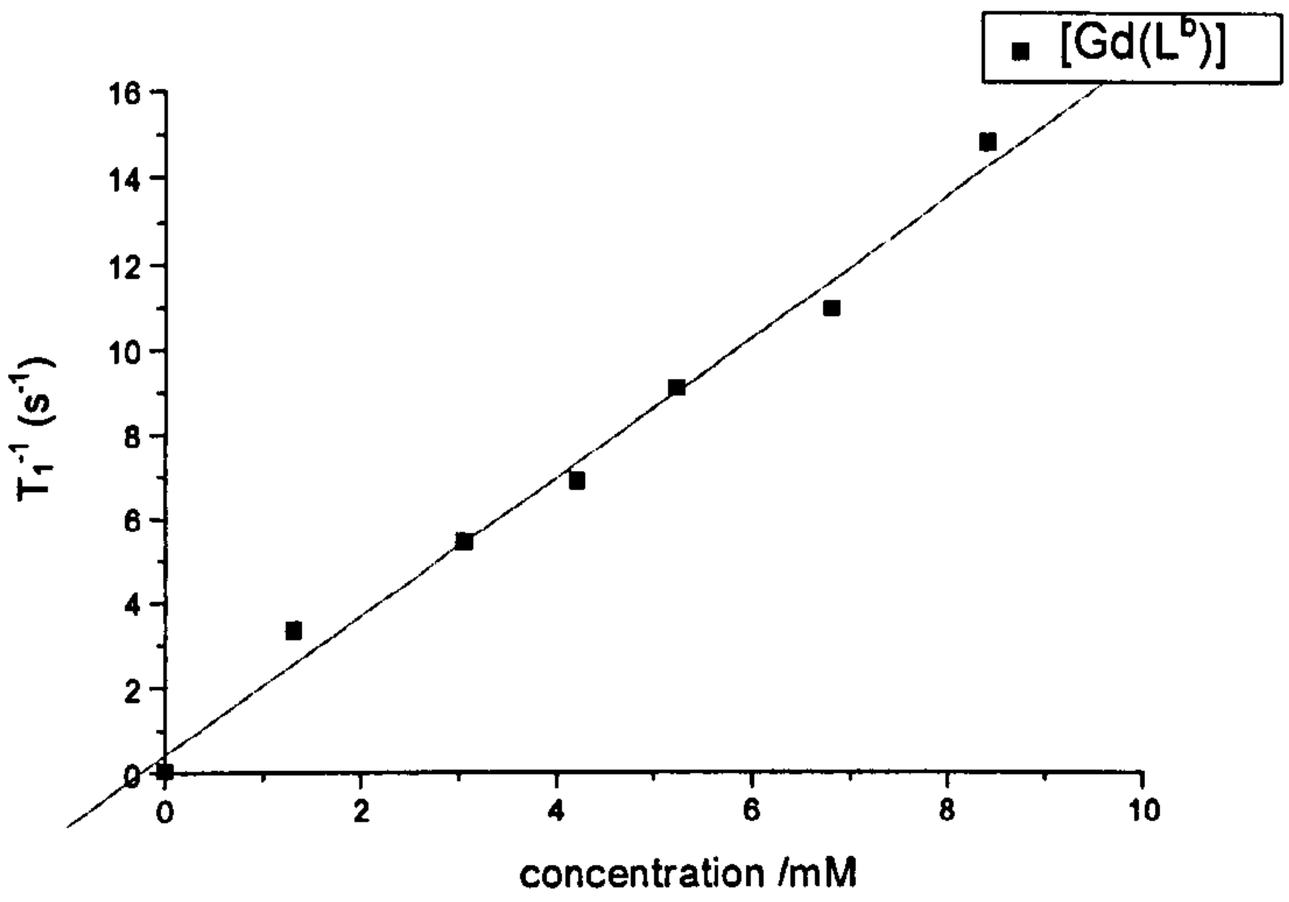

Figure 4.30 Graph showing the variation of T_1^{-1} (s^{-1}) of the HDO peak with concentration of [Gd(L^b)].

Table 4.7 Variation of T_1^{-1} (s^{-1}) of the HDO peak with concentration of [Gd(L^c)].

Mass [Gd(L^c)]·3NaCl·3H_2O (mg)	Concentration of [Gd(L^c)] (mM)	T_1 (s)	T_1^{-1} (s^{-1})
0.5	0.56	0.7807	1.28
1.0	1.12	0.5126	1.95
1.4	1.56	0.3483	2.87
2.0	2.23	0.2709	3.69
2.4	2.68	0.2360	4.24

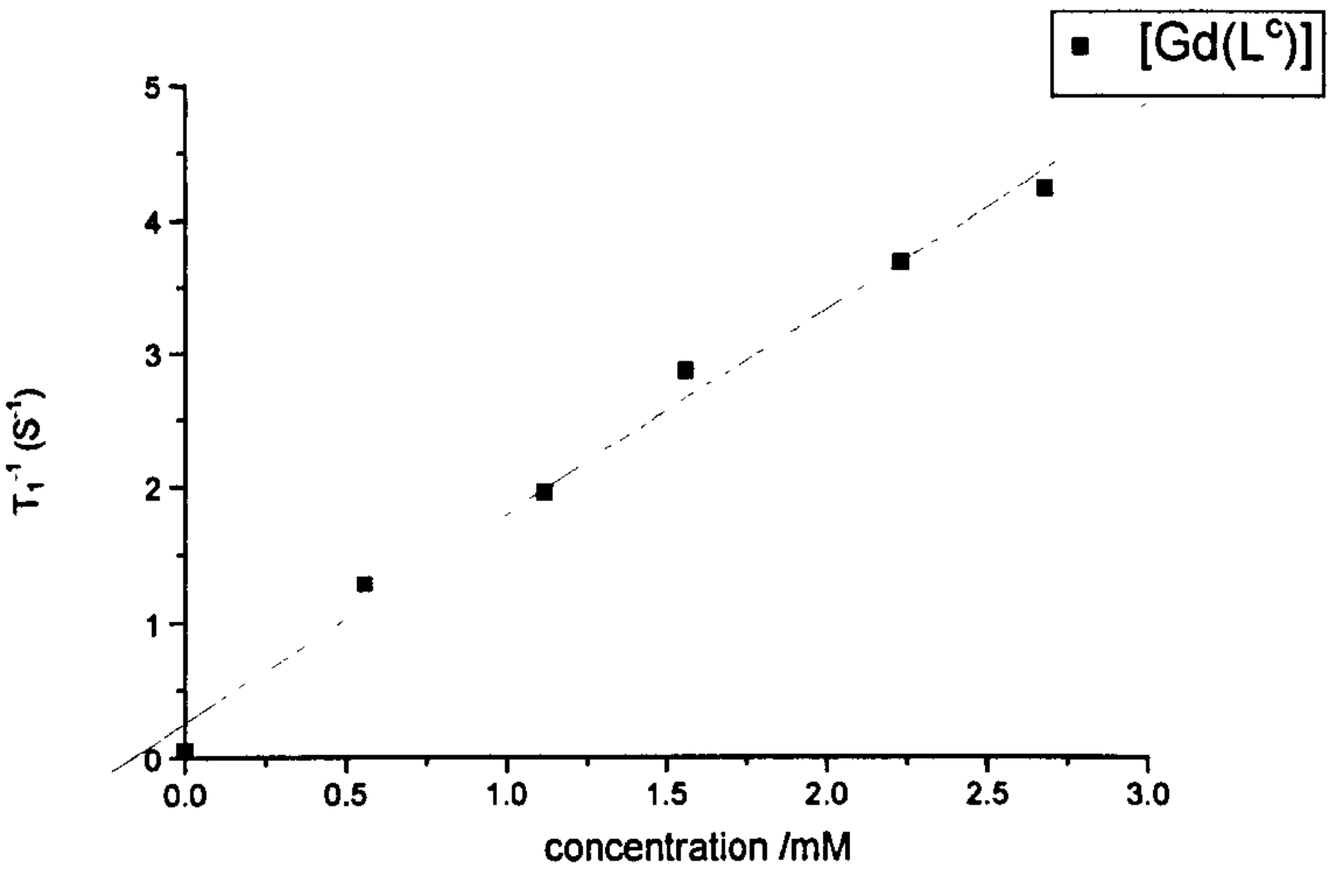

Figure 4.31 Plot of variation (T_1^{-1}) of the HDO peak with the concentration of [Gd(L^c)].

4.5.10 Crystal structure determinations

Crystal data, data collection and refinement details for compounds [Ln(L^b)] (Ln = Y^{III} and Gd^{III}) and [Gd(L^c)] are given in Table 4.8, selected bond lengths in Table 4.1 and 4.2. Data for [Y(L^b)]·CH_3OH and [Gd(L^b)]·1.5CH_3OH·H_2O and [Gd(L^c)]·0.5CH_3OH were collected on a Bruker SMART1000 CCD area detector diffractometer equipped with a low temperature device, using graphite-monochromated Mo-K_α radiation (λ=0.71073Å). Multi-scan absorption corrections were applied. For [Gd(L^b)]·1.5CH_3OH·H_2O data were also corrected for absorption using the program XABS.[361]

All the structures were solved by direct methods,[322] apart from [Gd(L^b)]·1.5CH_3OH·H_2O which was solved using the heavy atom method, and completed by iterative cycles of ΔF syntheses and full-matrix least squares refinement. All the non-H atoms, except those in disordered groups, were refined anisotropically. The crystal structure of [Gd(L^c)]·0.5CH_3OH was not completed as a fully anisotropic model; only the Gd atom was refined anisotropically and all the

other atoms were left isotropic. In all the structures, the H atoms on MeOH molecules were placed from ΔF syntheses and refined as part of a rigid rotating group. All the other H atoms were placed in calculated positions and refined using a riding model.[323] In [Gd(L^b)]·1.5CH$_3$OH·H$_2$O, the H$_2$O molecule and one MeOH molecule were disordered, hence the H atoms on them were omitted. These disordered molecules were modelled using partial occupancy models over two sites (occupancy factors 0.70 and 0.30) for H$_2$O and over one site for the MeOH (occupancy factor 0.50). Appropriate restraints to bond distances were applied in all the disordered molecules. In all the structures the largest residual electron density features lay near the heavy atom.

Table 3.9 Selected crystallographic data for the single crystal structures of [Y(L^b)]·CH_3OH, of [Gd(L^b)]·1.5CH_3OH·H_2O and of [Gd(L^c)]·0.5CH_3OH.

Compound	[Y(L^b)]·CH_3OH	[Gd(L^b)]·1.5CH_3OH·H_2O	[Gd(L^c)]·0.5CH_3OH
Crystal Data			
Formula	$C_{21}H_{42}N_6O_9P_3Y$ ·CH_3OH	$C_{21}H_{42}N_6O_9P_3Gd$ ·1.5CH_3OH·H_2O	$C_{21}H_{42}N_6O_9P_3Gd$ ·0.5CH_3OH
M / gmol^{-1}	736.47	838.84	1065.06
Crystal size / mm	0.48 x 0.06 x 0.05	0.52 x 0.19 x 0.08	0.20 x 0.18 x 0.15
Crystal system	Orthorhombic	Monoclinic	Monoclinic
Space group	*Pna*2$_1$	*P*2$_1$/*n*	*P*2$_1$/*c*
a / Å	13.590(2)	16.129(2)	22.570(3)
b / Å	13.071(2)	10.9177(14)	11.0602(13)
c / Å	17.506(3)	20.047(3)	19.798(2)
α / °	90	90	90
β/ °	90	106.462(2)	111.791(2)
γ / °	90	90	90
U / Å^3	3109.7(8)	3385(4)	4505 (2)
Reflections at ±ω to refine cell	3640	4882	7038
2θ range / °	2.45 to 25.31	2.63 to 28.28	2.21 to 28.65
Z	4	4	4
D_c / gcm^{-3}	1.573	1.646	1.570
μ / mm^{-1}	2.091	2.164	1.646
F(000)	1536	1712	2176
T / K	150(2)	150(2)	150(2)
Data Collection			
Diffractometer	Bruker SMART1000 CCD area detector	Bruker SMART1000 CCD area detector	Bruker SMART1000 CCD area detector
Radiation, wavelength	MoK_α , 0.71073 Å	MoK_α , 0.71073 Å	MoK_α , 0.71073 Å
θ_{max} / °	29.01	25.00	25.00
Range of *h*	-17 → 18	-20 → 20	-27 → 30
Range of *k*	-14 → 17	-14 → 14	-9 → 14
Range of *l*	-22 → 23	-26 → 26	-22 → 25
Measured reflections	19962	20527	21219
Unique reflections, R_{int}	7072, 0.068	5910, 0.0760	7726, 0.078
Observed reflections	4514 [$F_O \geq 4\sigma(F_O)$]	4747 [$F_O \geq 4\sigma(F_O)$]	5923 [$F_O \geq 4\sigma(F_O)$]
Absorption correction	Semi-empirical	Semi-empirical	Semi-empirical
$TF_{max, min}$	0.802, 0.643	0.522, 0.148	0.807, 0.476
Solution			
Method	Direct methods	Heavy atom methods	Direct methods
Using	SHELXS-97	SHELXS-97	SHELXS-97
Refinement			
Full matrix least squares on	F^2	F^2	F^2
Using	SHELXL-97	SHELXL-97	SHELXL-97
Weighting scheme *x*, *y*[a]	0.020, 0.00	0.045, 19.768	0.00, 256.10
Parameters refined	388	403	272
R_1, wR_2[b]	0.0395, 0.0565	0.0383, 0.0896	0.1109, 0.2340
Goodness-of-fit (S)	0.838	1.150	1.322
Absolute Struct. Parameter	0.007(4)	--	--
$(\Delta/\sigma)_{max}$	0.002	0.040	0.140
$\Delta\rho_{max, min}$ / eÅ^{-3}	+0.59, -0.56	+1.53, -1.07	+3.69, -3.56

[a] $w^{-1} = [\sigma^2(F_O) + (xP)^2 + yP]$, $P = [MAX(F_O, 0) + 2F_C^2\}/3$

[b] $[F_O \geq 4\sigma(F_O)]$

Chapter 5

Lanthanide complexes of asymmetric derivatives of [9]aneN_3

5.1 Asymmetric functionalisation of 1,4,7-triazacyclononane

Derivatives of [9]aneN$_3$ with pendant donor groups attached onto only one or two of the nitrogen atoms of the ring, or with three different pendant arms on the macrocycle, normally require multistep syntheses involving the masking, protection and deprotection of functionalities. The dearth of papers concerning the asymmetric functionalisation of [9]aneN$_3$ in comparison to the exhaustive trifunctionalisation literature is therefore hardly surprising.

There are a number of synthetic strategies for the asymmetric derivatisation of 1,4,7-triazacyclononane. The simplest is to perform the reaction with the amine in excess and then separate the mono- and/or di-substituted macrocycle from the unconverted amine.[362-365] Other methods involve the use of protecting groups: the synthesis can start from the orthoamide[366] (Figure 5.1a) or the monotosylated[367] (Figure 5.1b) derivatives of [9]aneN$_3$, or can involve selective carbamation[368] or selective protonation of the macrocycle.[337]

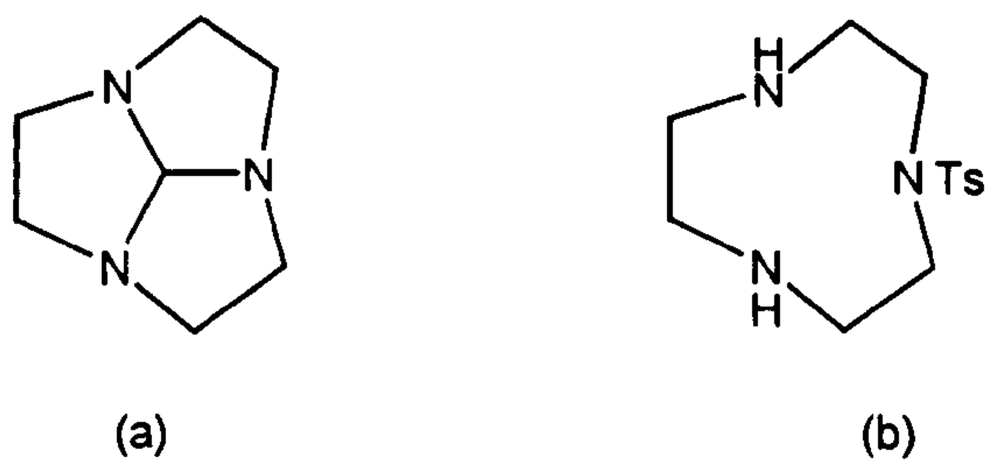

Figure 5.1 (a) Orthoamide (HC[9]aneN$_3$) [366] and (b) monotosylated[367] derivatives of [9]aneN$_3$.

5.1.1 Mono- and di-*N*-functionalisation

The attachment of only one or two pendant donor groups to the nitrogen atoms of the ring has been performed with a large number of different groups over the last twenty years.[99,100,256,362-365,369-382] These [9]aneN$_3$ derivatives can potentially form four or five co-ordinate metal complexes, which are of particular

interest as they offer the possibility of binding and activating small molecules at a co-ordinatively unsaturated metal centre, thereby providing the basis of models for the active sites of biological systems or catalytic reagents. In this context, some examples of mimicry of enzymes' active sites or of catalytic behaviour of metal complexes with such ligands have already been presented in the introductory Chapter 1. In the present chapter, the synthetic strategies for asymmetric functionalisation of 1,4,7-triazacyclononane will be introduced.

4,7-*bis*(2-aminoethyl)-1,4,7-triazacyclononane (Figure 5.2) was synthesised as a by-product of the trifunctionalised derivative because, as already mentioned in Section 3.1.2, the synthesis of 1,4,7-tris(2-aminoethyl)-1,4,7-triazacyclononane (Figure 3.5)[242,381] does not proceed cleanly to the trifunctionalised product, but affords 10-20% of the disubstituted product.

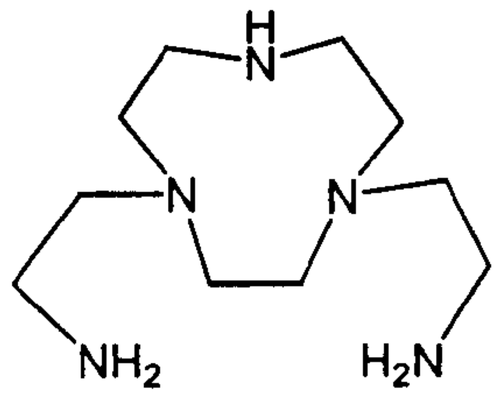

Figure 5.2 4,7-*bis*(2-aminoethyl)-1,4,7-triazacyclononane.

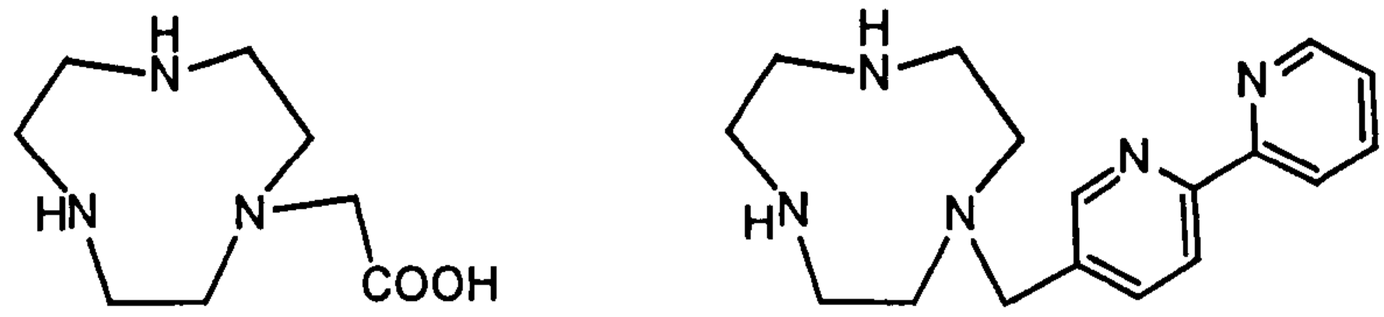

Figure 5.3 Monofunctionalised derivatives of [9]aneN$_3$.

Other ligands have been synthesised using a large excess of the macrocycle over the substrate. For example, the ligands shown in Figure 5.3 have been obtained using five molar equivalents of [9]aneN$_3$ and the unreacted macrocycle has been recovered by washing or distillation.[362-365,382] For the

synthesis of the ligand shown in Figure 5.4(a)[383] a 20-fold excess of 1,4,7-triazacyclononane has been employed. Such a ligand system (in Figure 5.4b the crystal structure of the Ni^{II} complex is shown) produces surface active complexes from non-surface active ligands upon co-ordination to a labile metal centre.[383]

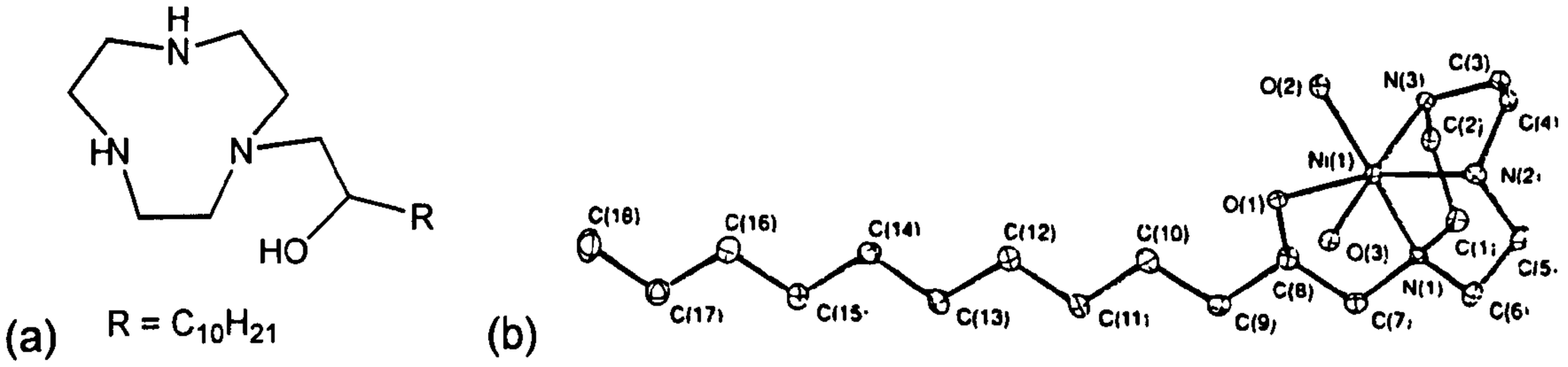

Figure 5.4 (a) [9]aneN$_3$ based ligand studied as surfactant and (b) its Ni^{II} crystal structure.[383]

Starting from the orthoamide derivative of [9]aneN$_3$ (HC[9]aneN$_3$, Figure 5.1a) various mono- and di-substituted ligands have been synthesised.[99,100,369,370,374,377] In Figure 5.5 the route to the synthesis of the mono- and bis-hydroxyalkyl-1,4,7-triazacyclononane is illustrated.[374] The reaction of an electrophile with HC[9]aneN$_3$ generally affords mono-substituted macrocycles and in Figure 5.6 some examples are shown.[371] Reaction of $PhCH_2O(CH_2)_2Br$ with HC[9]aneN$_3$ and subsequent removal of the benzyl group by hydrogenolysis with Pd/C affords the mono-hydroxyethyl macrocyclic ligand (Figure 5.5).[374] By refluxing HC[9]aneN$_3$ in hydrochloric acid the orthoamide function is ring-cleaved to the monoformyl species OHC[9]aneN$_3$.[366,384] OHC[9]aneN$_3$ has been found to be useful as a monoprotected macrocycle as the two remaining nitrogens can be substituted in the presence of the amide function before the formyl group is finally cleaved. The synthesis of 1,4-*bis*(2-hydroxy-2-dimethylethyl)-1,4,7-triazacyclononane shown in Figure 5.5 is an example of this strategy.[374]

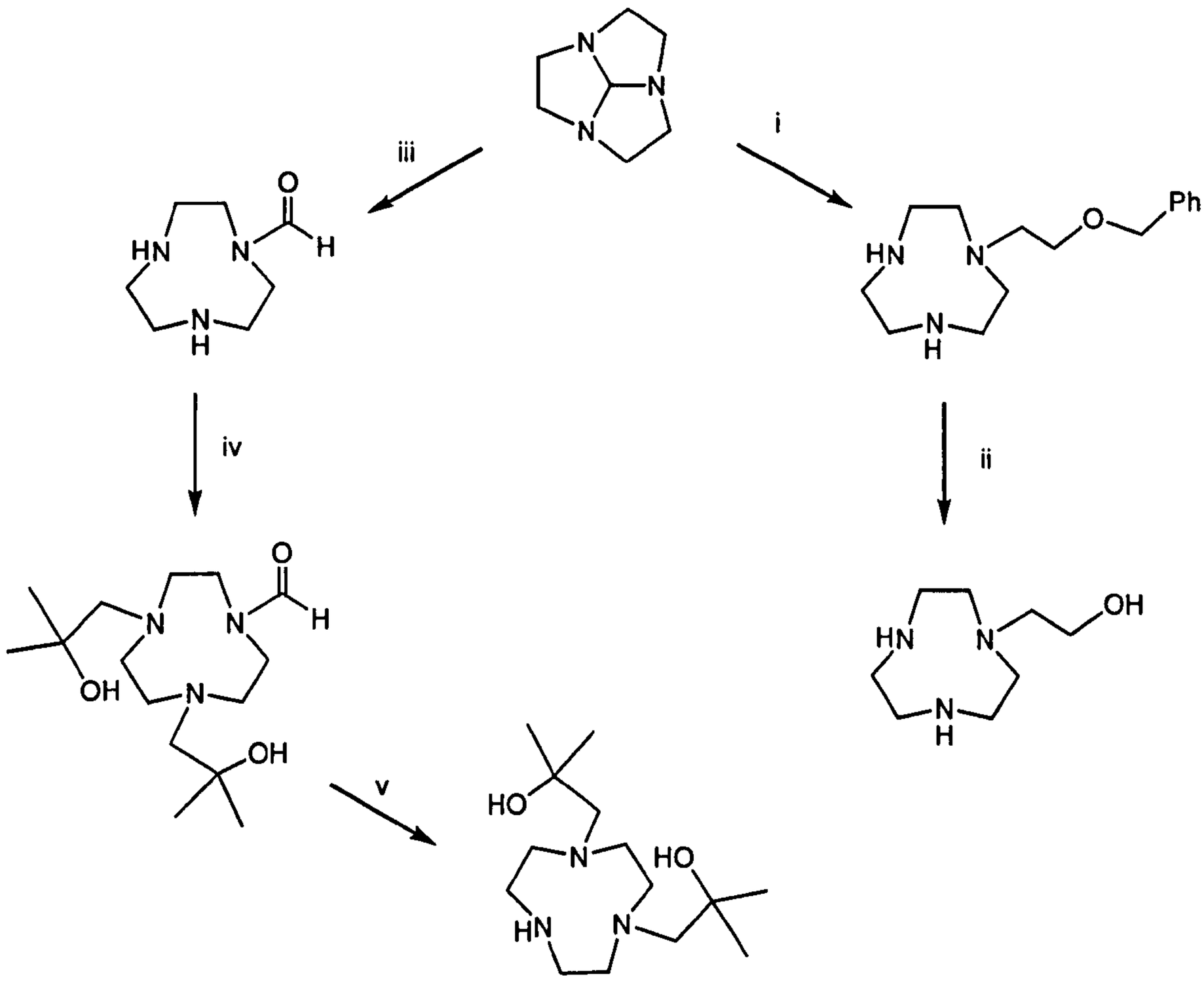

Figure 5.5 Synthesis of mono- and di-substituted [9]aneN$_3$ starting from the orthoamide derivative.[374] i: (a) $PhCH_2O(CH_2)_2Br$, Et_2O; (b) H_2O, reflux 5h; KOH-EtOH, 72h; ii: Pd/C-H_2, CH_3COOH; iii: HCl 2.8 M; iv: isobutylene oxide, EtOH; v: KOH-EtOH, reflux.

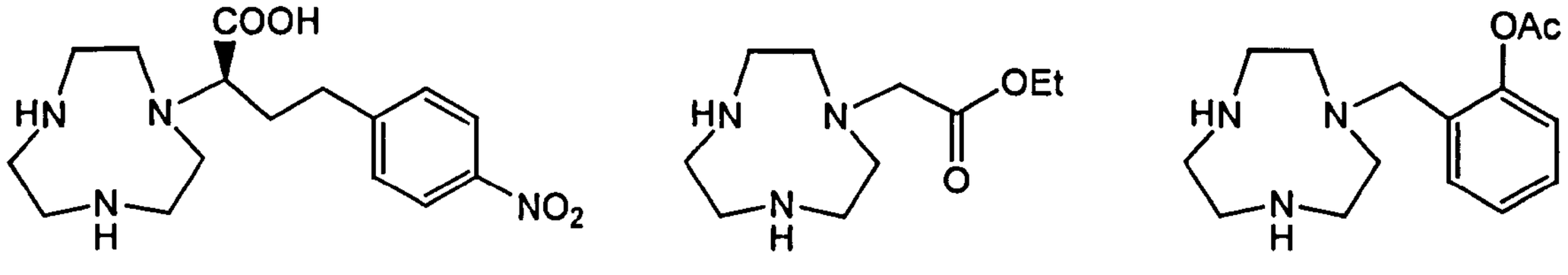

Figure 5.6 Mono-substituted derivatives of [9]aneN$_3$ starting from the orthoamide.

5.1.2 Asymmetric tri-functionalisation

The synthetic routes to this class of [9]aneN$_3$ derivatives involve two different general methods: 1) the reaction of excess [9]aneN$_3$ with the appropriate

electrophile to give mono or di-functionalised derivatives which are subsequently functionalised on the remaining free N-donor atom(s) of the ring;[103,362-365,369,372-375,383] 2) the use of different protecting groups for one or two nitrogens of the macrocycle and then their deprotection after functionalisation of the remaining free nitrogen(s).[366-368] Whichever of the two methods is chosen, further inherent synthetic difficulties can arise depending on the nature of the donor pendant arms in the target ligand. For these reasons, the synthesis of new asymmetric tri-functionalised [9]aneN$_3$ derivatives is always an interesting challenge and could lead to new synthetic strategies of general application. Furthermore, these ligands are of major interest because they can be used for the construction of multifunctional materials such as dendrimers,[385] and their complexes exhibit specific chemical properties[386] and have practical applications including radio-labelling[388] and selective cation binding.[328,351]

Two examples of asymmetric tri-functionalised ligand syntheses are illustrated in Figures 5.7 and 5.8. Wieghardt *et al.*[386] have synthesised two

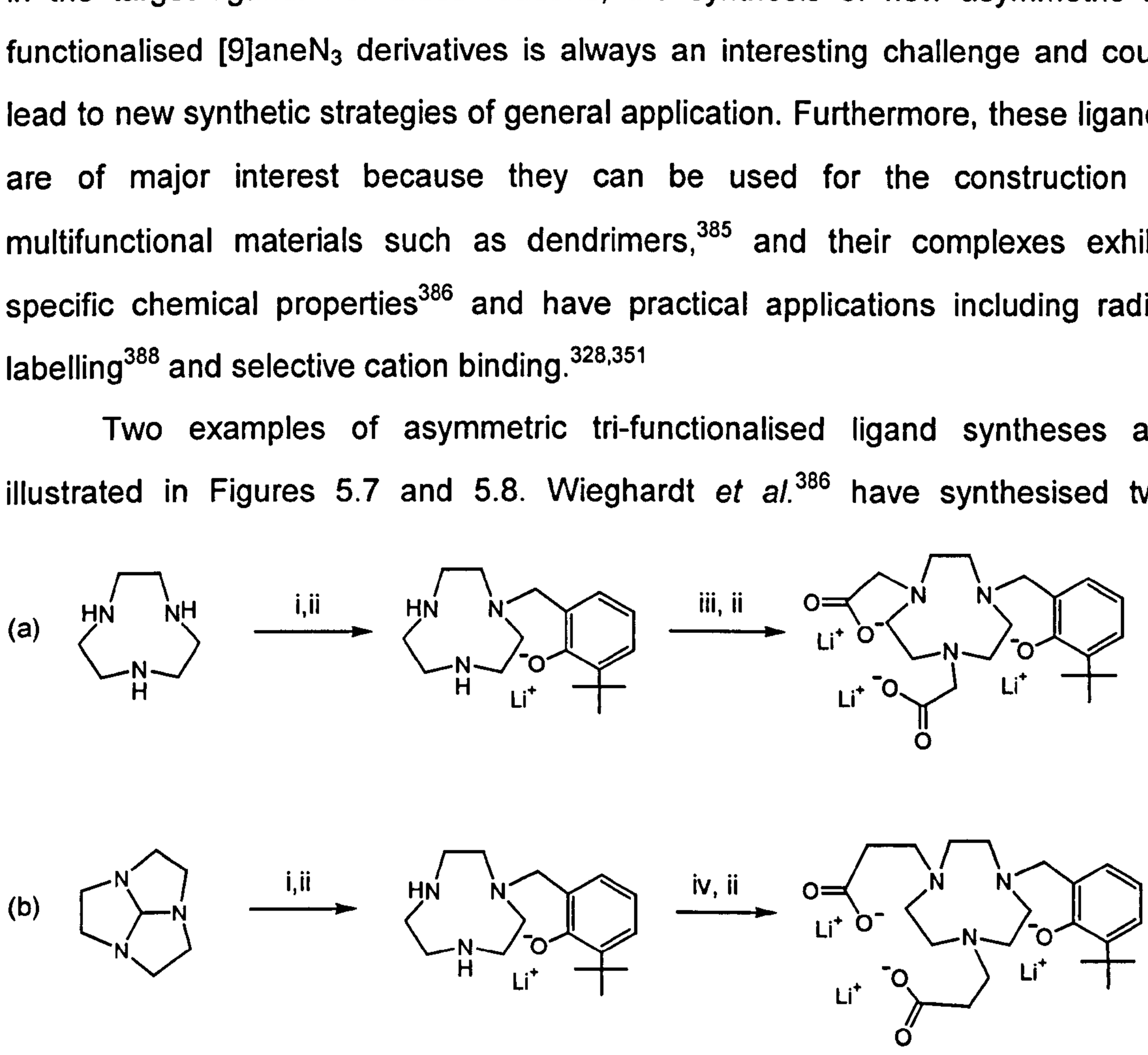

Figure 5.7 Synthesis of [9]aneN$_3$ derivatives with phenolate and carboxylate pendant arms.[386] i: 2-bromomethyl-6-*tert*-butylphenylacetate, EtOH-H_2O; ii: $LiOH \cdot H_2O$; iii: MeOH-H_2O, ethylbromoacetate (2 eq); iv: CH_3COOH conc., methylacrylate (2eq), EtOH.

asymmetric ligands by different methods (Figure 5.7): in the first, the mono-functionalisation was achieved by using a five-fold excess of macrocycle and then the two carboxylate arms were attached directly to the secondary N-atoms of the ring (Figure 5.7a). In the second, the orthoamide (HC[9]aneN$_3$) was the starting material and in two steps the desired product was synthesised (Figure 5.7b): the carboxylate arms were attached by Michael addition of methyl acrylate and then the ester groups were hydrolysed with LiOH.[386]

Mani and co-workers[387] have synthesised the [9]aneN$_3$ derivative shown in Figure 5.8 by first using an excess of the macrocycle; a carboxylic acid group then has been attached in one step to the free secondary nitrogen of the ring. The complexes of these hexadentate ligands, mainly with transition metal ions, show interesting electrochemistry and X-ray crystal structures.[386,387]

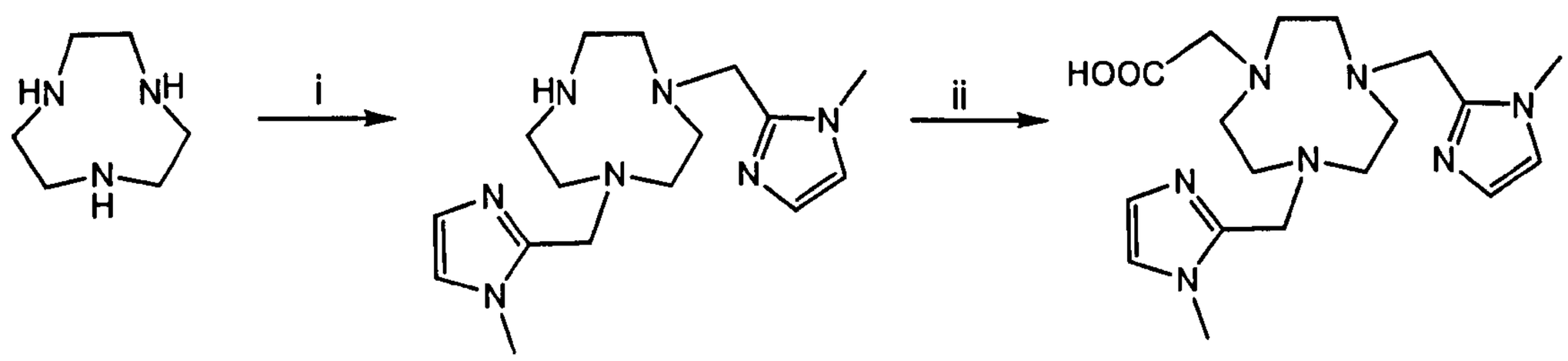

Figure 5.8 Synthesis of an asymmetric derivative of [9]aneN$_3$ with two imidazoles and one carboxylate. i: 2-chloromethyl-1-methylimidazole (2.5 eq), CH_3CN-DMF, proton sponge; ii: $BrCH_2COOK$, KOH, H_2O, pH = 11.5.[387]

Since the ligand [NOTA]$^{3-}$ (1,4,7-triazacyclononane-1,4,7-triacetate) has very strong affinity towards trivalent metal ions such as Ga^{III} and In^{III} widely used for biomedical applications, several groups have pursued the design of asymmetric bifunctional [9]aneN$_3$ derivatives containing three carboxylate functions for the complexation of the metal ion and another function designed for linking to monoclonal antibodies or other biomolecules (Section 2.3).[256,388] The two ligands shown in Figure 5.9 have been synthesised by Parker and co-workers in few steps

starting from [9]aneN$_3$, with the aim of attaching a radioactive ^{67}Ga or ^{111}In labelled complex to a monoclonal antibody.[256]

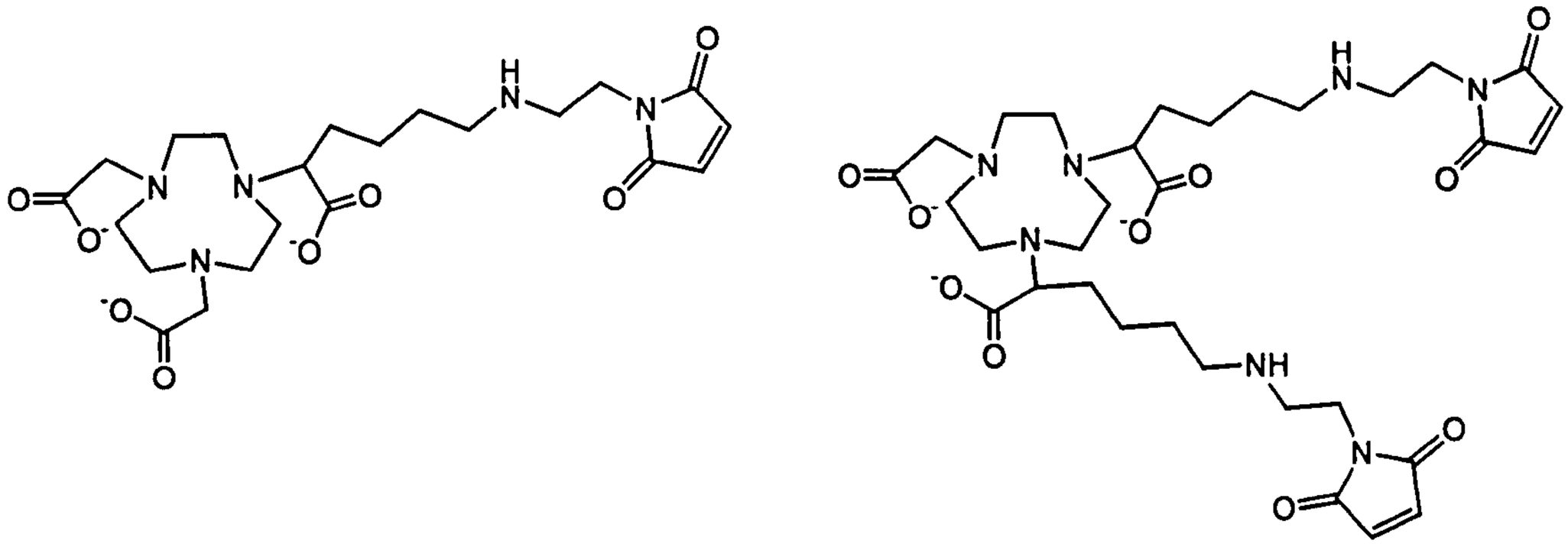

Figure 5.9 Two bifunctional chelating agents designed for co-ordination of metal ions and for coupling with monoclonal antibodies.[256]

The Ga^{III} complex of the bifunctional chelator NODASA (1,4,7-triazacyclononane-1-succinic acid-4,7-diacetic acid) has been recently synthesised by Maecke *et al.*[388] and its crystal structure is shown in Figure 5.10(a). Since the β-carboxylate remained free, while the others co-ordinated the metal centre, it was coupled to a model peptide such as *D*-phenylalanineamide (Figure 5.10b), showing the effectiveness of this bifunctional chelating agent.[388]

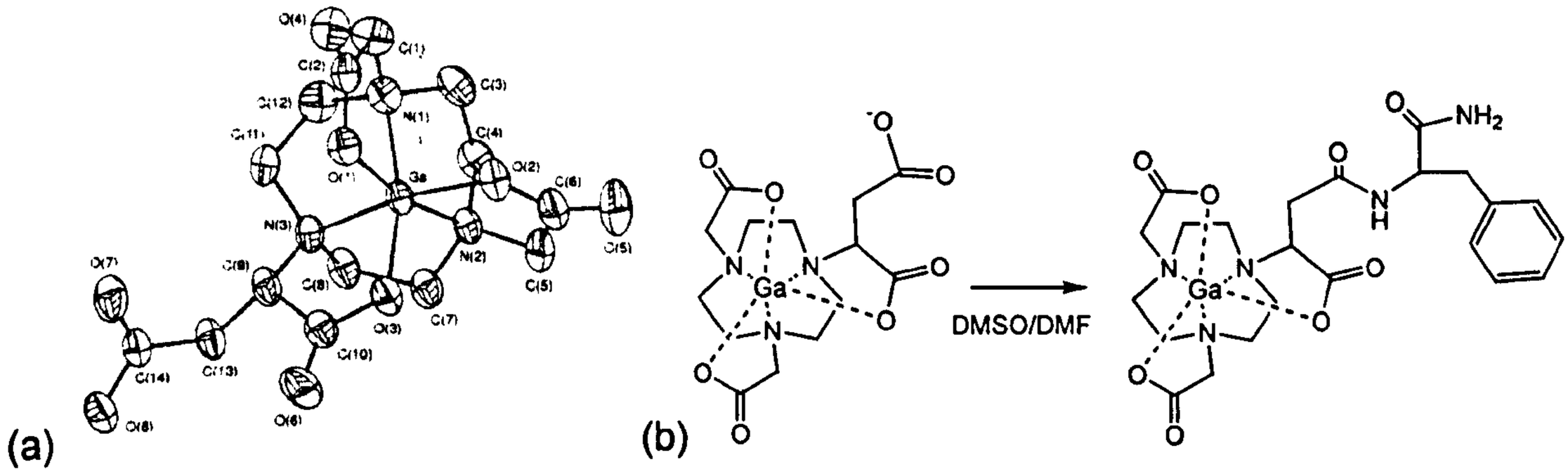

Figure 5.10 (a) Crystal structure of [Ga(NODASA)]$^-$ and (b) coupling with *D*-phenylalanineamide.[388]

Sherry and co-workers have prepared the monoprotected [9]aneN$_3$ by reacting the macrocycle with trifluoromethanesulfonic acid (TfOH) in order to obtain the monoacid salt.[369] This method, using H^+ as the "protecting group", relies on the fact that there is a large gap between the stability constants (in water) of the first and the second protonation steps of [9]aneN$_3$. In this way, using an alkylating agent such as *tert*-butylbromoacetate, the disubstituted product has been synthesised with a selectivity of 70%. The asymmetric trifunctionalised ligands

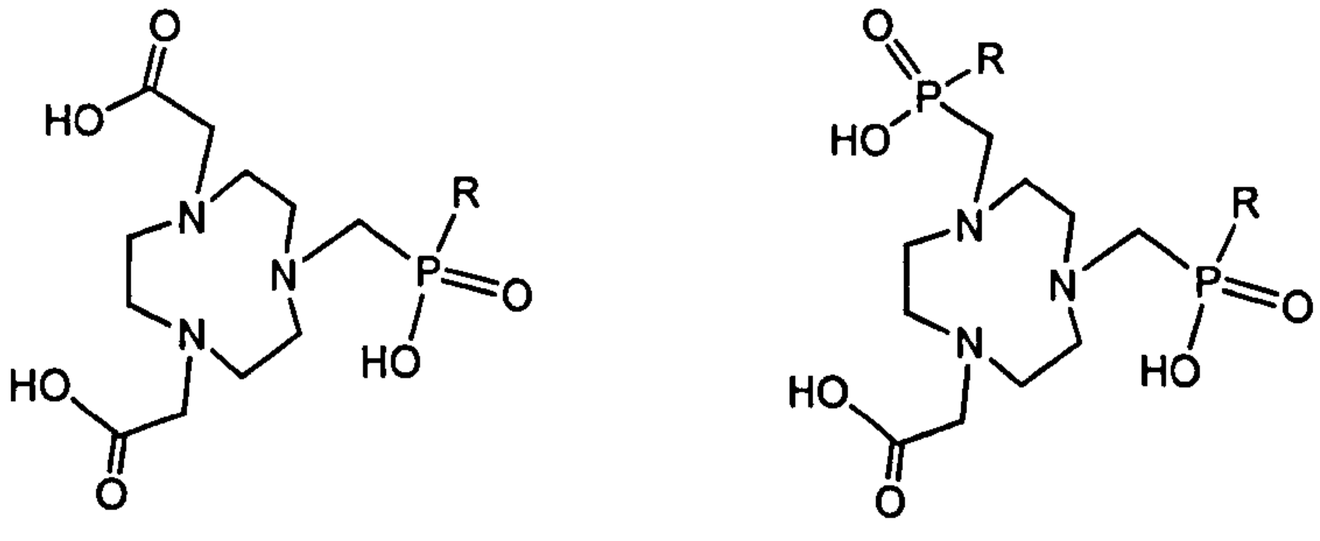

R = Me or Et

Figure 5.11 Derivatives of [9]aneN$_3$ with carboxylate and methylphosphinate pendant arms.

shown in Figure 5.11 have been synthesised by this method. It has been demonstrated that such ligands can be effectively used for monitoring by ^{31}P NMR the concentration of free Mg^{II} in isolated cells and are very promising for *in vivo* applications.[328,351]

Finally, the monotosylated derivative of [9]aneN$_3$, whose synthesis was described by Sessler *et al.* in 1990,[367] has been used recently by Beer and co-workers as starting material for the synthesis of dendrimers based on multiple [9]aneN$_3$ derivatives.[385] The two branching synthons (a and b in Figure 5.12) required for convergent and divergent syntheses of the target dendritic macrocyclic molecules have been prepared as shown in Figure 5.12. The second generation dendrimer illustrated in Figure 5.13 has been synthesised *via* successive condensation reactions and reductions between the amine and the carboxylate

groups of the nitro groups.[385] Spectrophotometric titration curves suggest that the second generation dendrimer in Figure 5.13 binds ten Cu^{II} metal cations with every Cu^{II} complexed by each triazacyclononane unit of the dendrimer.[385]

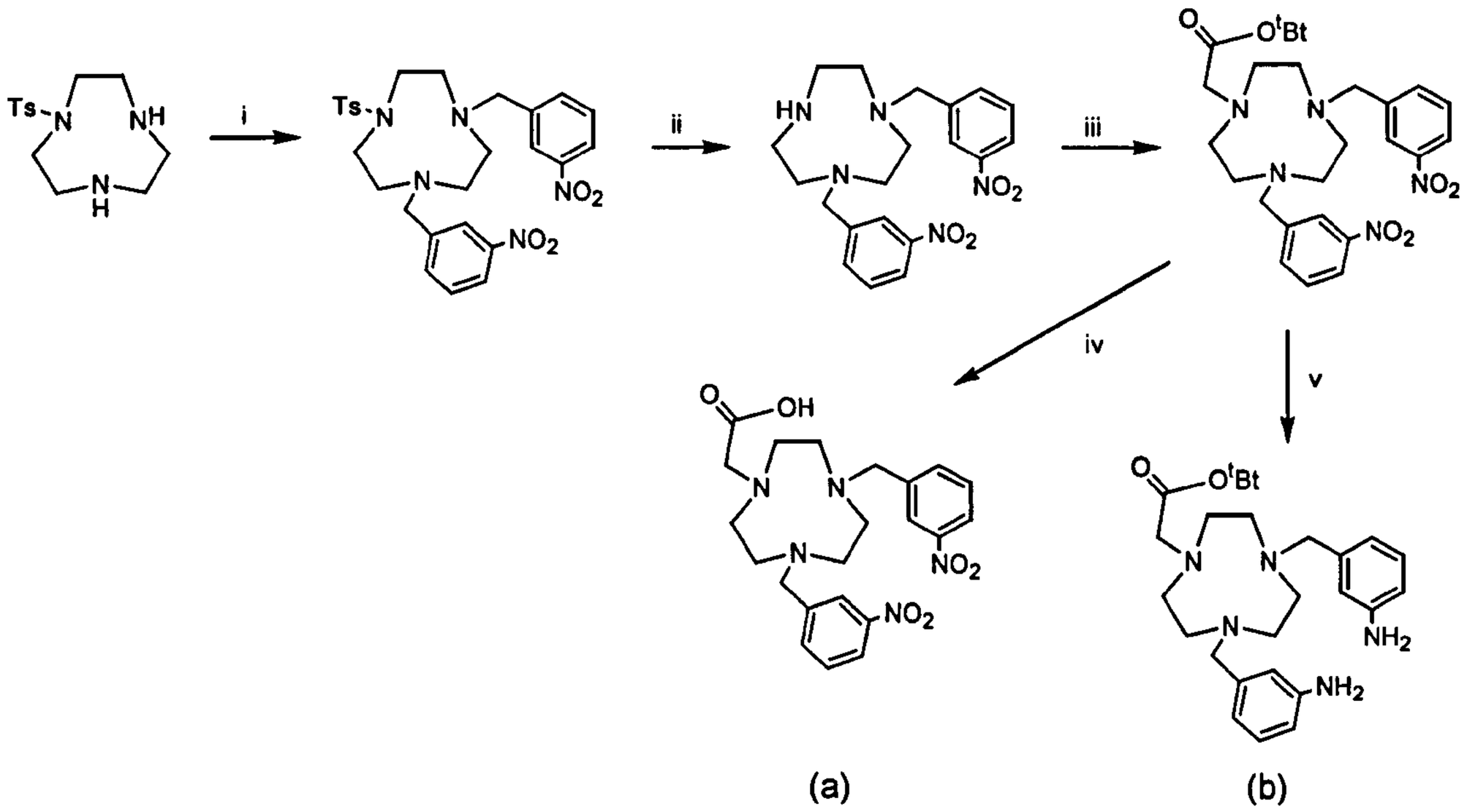

Figure 5.12 Synthesis of the two branching synthons used for the preparation of the dendrimer based on multiple [9]aneN$_3$ derivatives.[385] i: 3-nitrobenzyl chloride (2eq), K_2CO_3, CH_3CN, reflux; ii: H_2SO_4 conc., 150°C; iii: *t*-butylbromoacetate, K_2CO_3, CH_3CN, reflux; iv: formic acid, reflux; v: H_2, Ni-Raney, MeOH-THF, 55°C.

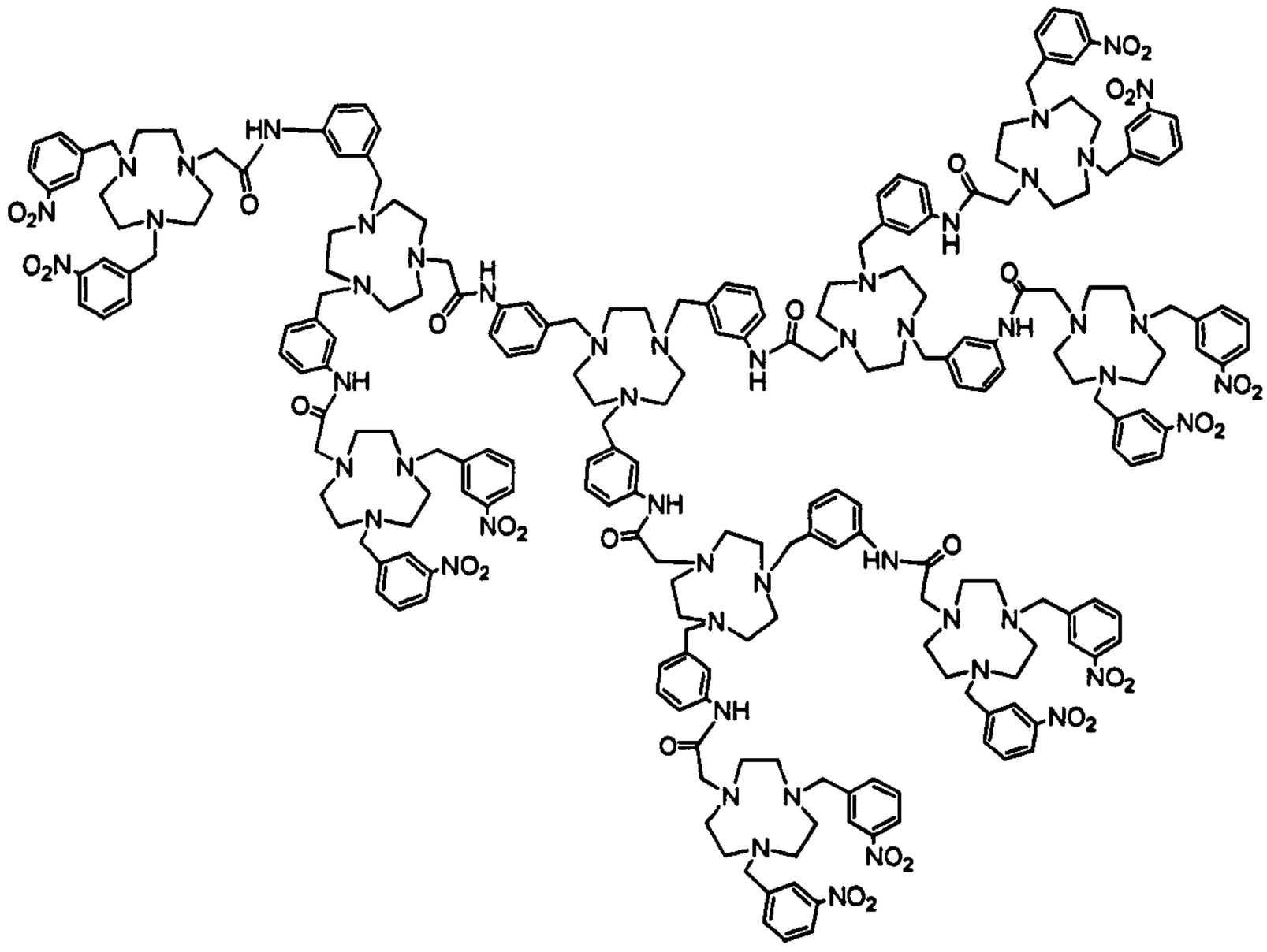

Figure 5.13 Second generation dendritic poly-1,4,7-triazacyclononane molecule.

5.2 Ln^{III} complexes with asymmetric substituted cyclen ligands

Several asymmetric derivatives of 1,4,7,10-tetraazacyclododecane have been reported in the literature and, as discussed in Chapter 2, the research is mainly proceeding towards the synthesis of asymmetric derivatives with three carboxylate arms and one different pendant arm with various possible functional groups. The reason why asymmetric Ln^{III} complexes are so interesting can be ascribed to the formation of neutral complexes (and therefore minimisation of osmolality as discussed in Section 2.2.1) and to the possible attachment of functional groups which can be used for many different purposes such as attachment to monoclonal antibodies (bifunctional chelating agents, Section 2.3) or interaction with proteins or other macromolecules (Section 2.2.4).

Remarkably, two out of three approved cyclen based contrast agents reported in Section 2.2.1 (Figure 2.2) are asymmetric, having three carboxylate arms and one hydroxyl arm (*i.e.* [Gd(HP-DO3A)(H$_2$O)] and [Gd(DO3A-butrol)(H$_2$O)]). As an example the crystal structure of [Gd(HP-DO3A)(H$_2$O)] is shown in Figure 5.14.[389]

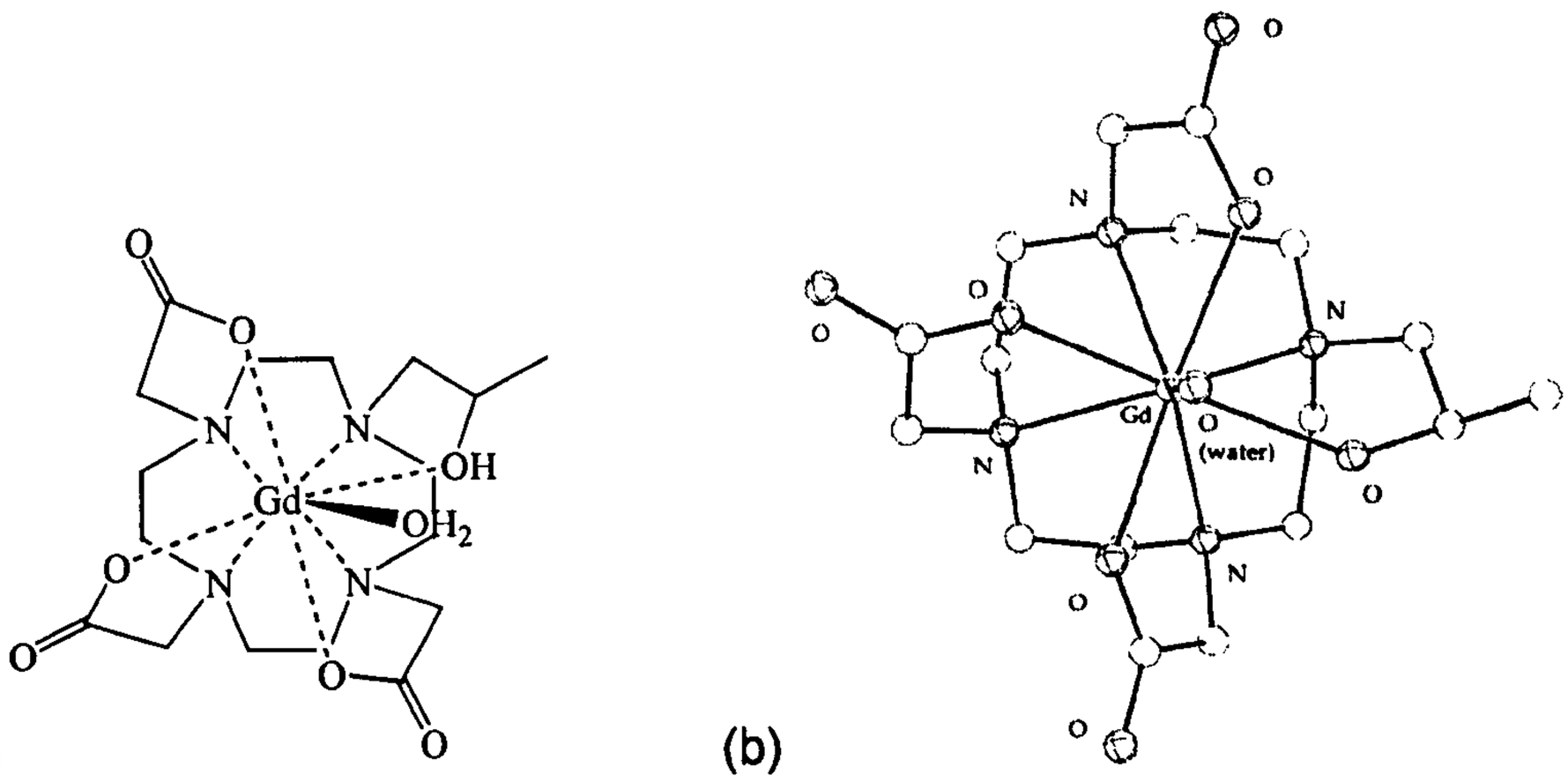

(a) (b)

Figure 5.14 (a) [Gd(HP-DO3A)(H$_2$O)] and (b) ORTEP drawing of the crystal structure of [Gd(HP-DO3A)(H2O)] as viewed looking approximately down the water-metal bond.

However, the drawback is that the synthetic procedures are always long and difficult, and the complexes formed with such ligands often present many isomeric forms. For example, the replacement of an acetate arm of DOTA with a hydroxypropyl group (HP-DO3A) gives rise to diastereomeric differentiation of the four expected isomers, depending on the ring conformations (Section 4.2.5).[390] Moreover, the presence of a chiral carbon centre in the hydroxypropyl arm doubles the number of possible stereoisomers to eight, making the study more complex.[390]

5.3 Results and discussion

Each of the ligands discussed in the two previous chapters has nine donor atoms and fulfill the co-ordination requirements of the lanthanide ions such that there is no water molecule directly co-ordinated to the metal centre and the relaxivity enhancement is not very high. The ligands discussed in the present chapter have been synthesised in order to provide a set of seven or eight donor atoms for the co-ordination of lanthanide ions, leaving one or two co-ordination sites available for the binding of water molecules. Since the ligand L (Chapters 3 and 4) is a symmetric derivative of [9]aneN$_3$ with three aminoethyl pendant arms, the next step could be the synthesis of asymmetric derivatives of [9]aneN$_3$ with two aminoethyl pendant arms and one different arm on the remaining secondary amine of the macrocycle. Therefore, the ligands L^2 with a secondary amine left on the macrocyclic ring, HL^3 with a carboxylic arm as third pendant group and HL^4 with a hydroxyl and two aminoethyl pendant arms have been synthesised (Figure 5.15).

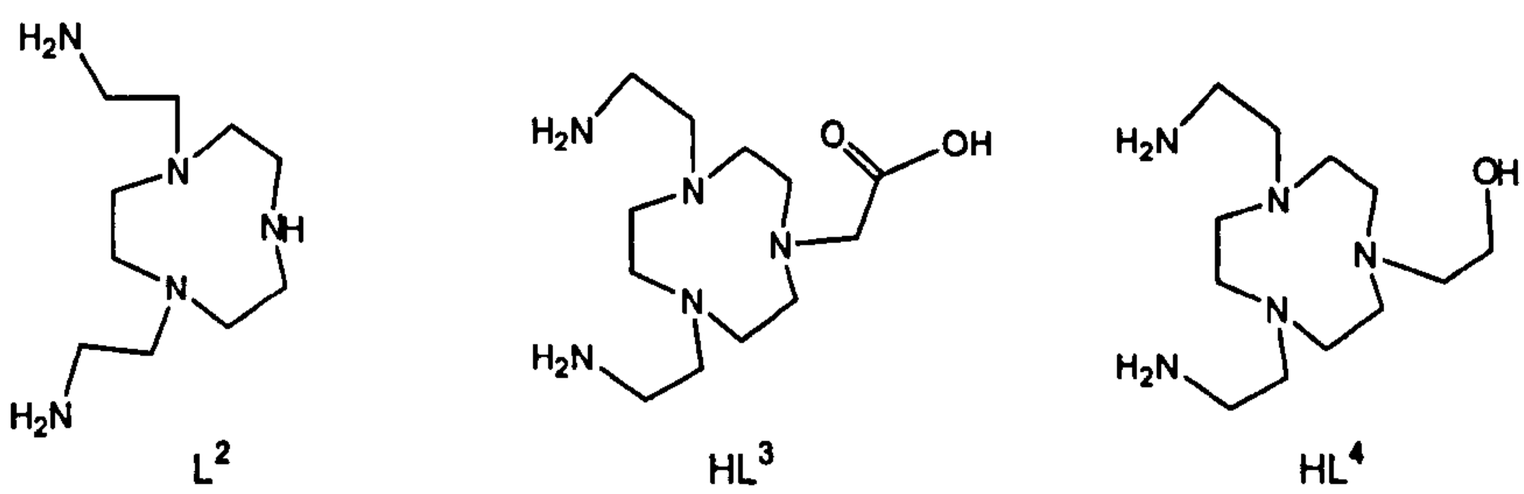

Figure 5.15 Asymmetric derivatives of [9]aneN$_3$ described in this chapter.

Reacting these ligands with two equivalents of sodium pyruvate, methyl sodium acetyl phosphonate or methoxybenzyl sodium acetyl phosphonate using the Ln^{III} ion as templating agent, seven or eight co-ordinate lanthanides complexes have been obtained (Section 5.2.2, Figures 5.17 and 5.18). These complexes have been studied to obtain information about relaxivity, number of water molecule bound to the metal centre and rate of hydrolysis of the imine bonds.

5.3.1 Synthesis of asymmetric derivatives of [9]aneN$_3$

The preparation of the asymmetric functionalised ligands is shown in Figure 5.16. The reaction of 1-(*p*-tolylsulfonyl)-1,4,7-triazacyclononane (**6**) with two equivalents of N-tosyl-aziridine in CH_3CN and under N_2 gave 1-(*p*-tolylsulfonyl)-4,7-*bis*(2-aminoethyl-N-*p*-tolylsulfonyl)-1,4,7-triazacyclononane (**7**) in 96% yield and high purity. When the two starting materials are pure the reaction goes cleanly, otherwise it is necessary to use column chromatography to purify the product. Detosylation with concentrated sulphuric acid afforded L^2 in 92% yield after passing a water solution of the sulphate salt of the amine through an Amberlite IRA 416 column activated with 1M NaOH. The ligand L^2 has been already reported in the literature,[381] but only as a by-product of the synthesis of tris(2-aminoethyl)-1,4,7-triazacyclononane (Section 5.1.1), and its co-ordination chemistry has not been studied so far.

As the ligand L^2 has one secondary and two primary amines, in order to allow selective electrophilic addition to the secondary nitrogen, the primary amino functionalities must be protected. Sosnovsky *et al.*[391] selectively protected the two NH_2 groups of diethylenetriamine using *N*-(benzyloxycarbonyloxy)succinimide. Unfortunately, the reaction of the same protective agent and L^2 under the same conditions gave the triprotected derivative (**8**, Figure 5.16), probably because the secondary amine on the [9]aneN$_3$ is still very reactive even after the formation of the two amides on the pendant arms (in diethylenetriamine the two amides are

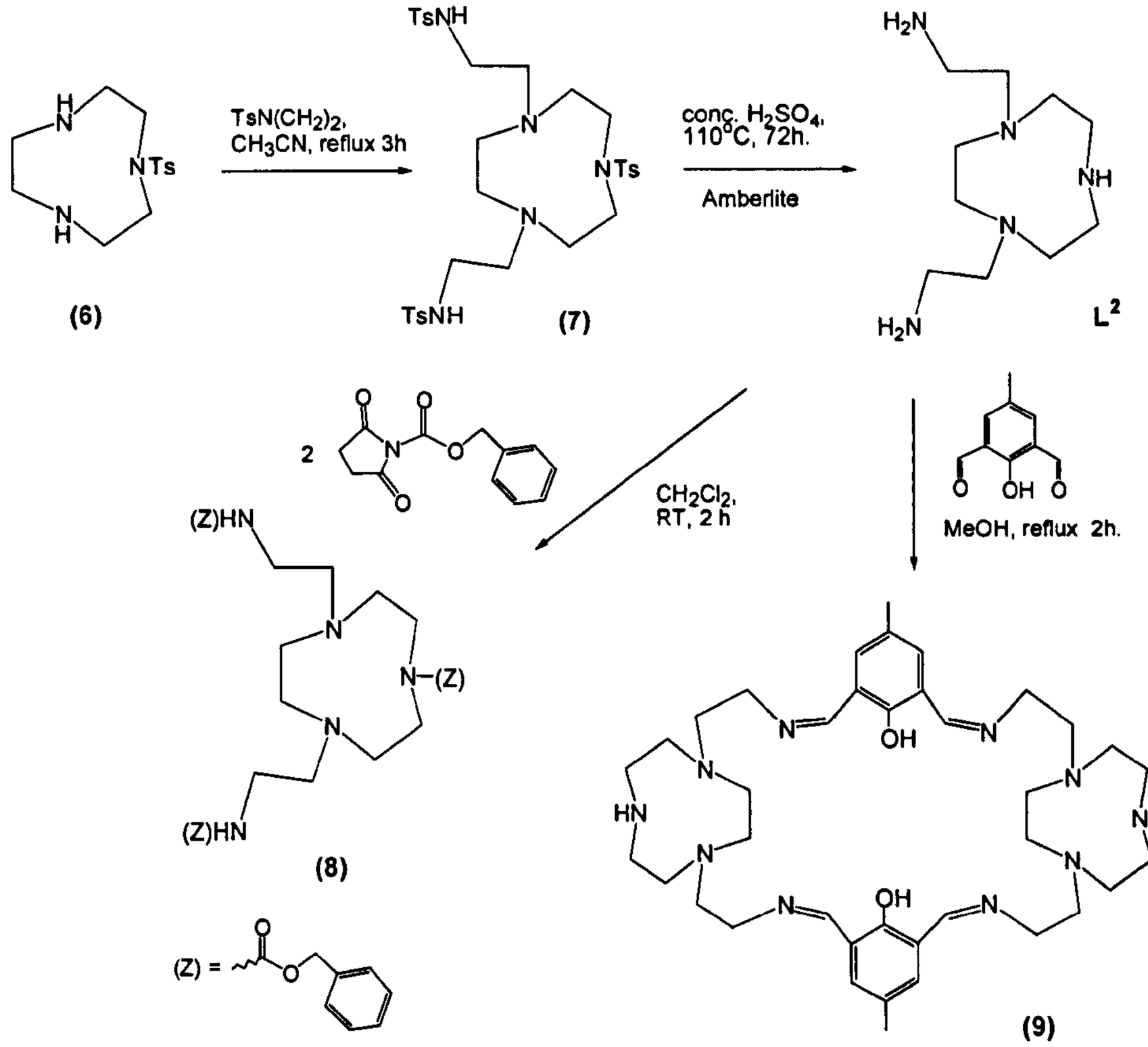

Figure 5.16 Scheme of the synthesis of L^2 and of the macrocyclic cage **9**.

closer to the secondary nitrogen and probably deactivate it). The primary amino functions were successfully selectively protected by Schiff base condensation with 4-methyl-2,6-diformylphenol. The imino bonds are not normally used as protecting groups for amines because of their low stability in water, especially under acidic conditions. The reaction of 4,7-*bis*(2-aminoethyl)-1,4,7-triazacyclononane (L^2) with one equivalent of 4-methyl-2,6-diformylphenol afforded the macrocyclic cage (**9**), as demonstrated by mass spectrum and elemental analysis, instead of the bicyclic Schiff-base product derived from a 1+1 condensation.

The reaction of **9** with two equivalents of *tert*-butyl bromoacetate or 2-bromoethanol afforded **10a** or **10b**, respectively (Figure 5.17). These two compounds were isolated as viscous orange oils, but they were not fully

characterized because of their instability. In fact, the hydrolysis of the imino bonds in **10a** and **10b** with dilute aqueous HCl afforded the hydrochloric salts of the two desired products HL^3 and L^4, respectively, in good yields. In the case of **10a**, the reaction with dilute aqueous HCl also hydrolyses the *tert*-butyl ester group to the carboxylic acid function in HL^3. The two hydrochloride salts were recrystallised by diffusing Et_2O vapour into a MeOH solution of the ligands. Reaction of HL^3 with

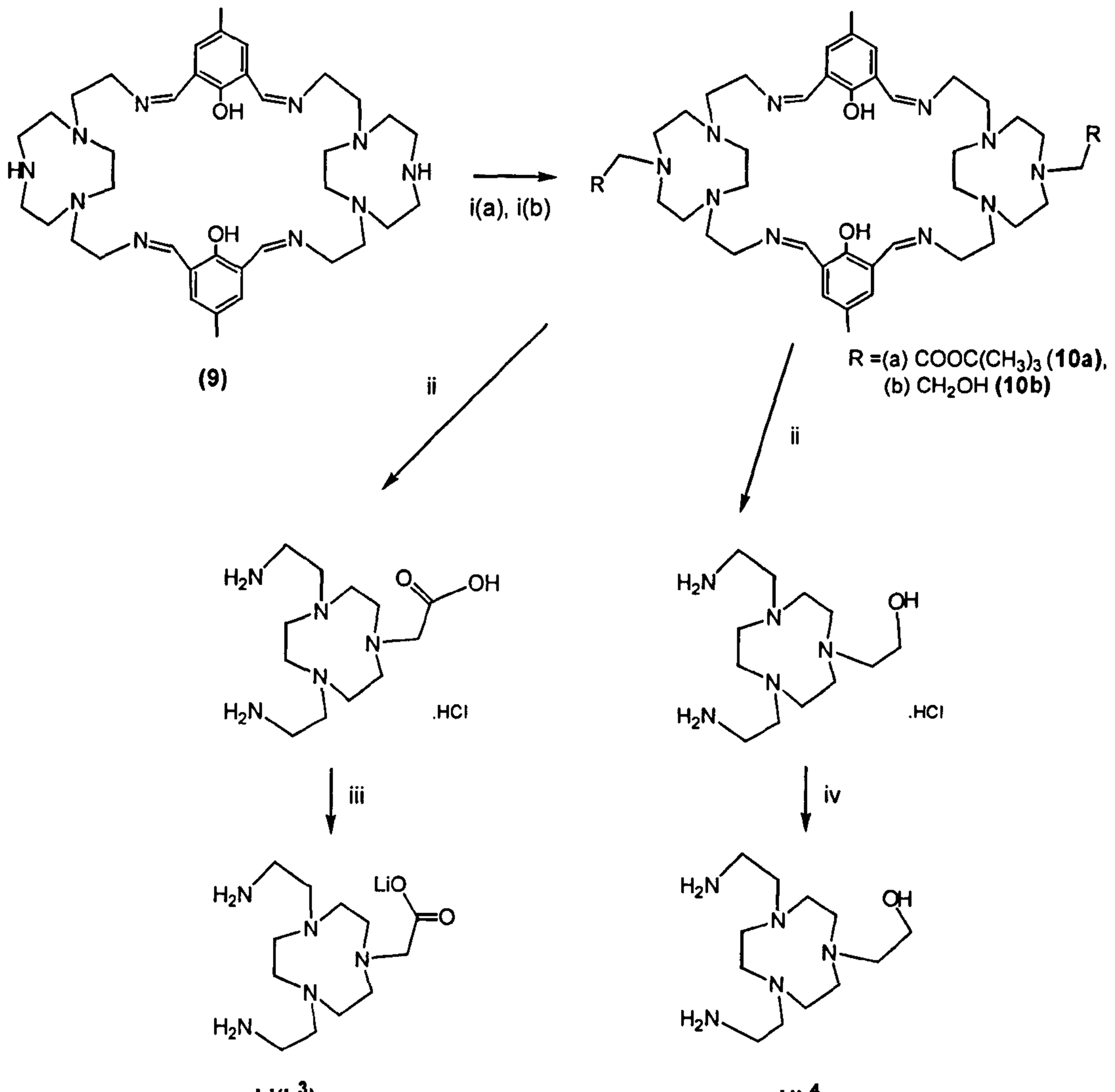

Figure 5.17 Synthesis of $Li(L^3)$ and HL^4 starting from **9**. i(a): *tert*-butylbromoacetate (2eq), diisopropylethylamine, $CHCl_3$, 12h, RT; i(b): 2-bromoethanol, EtOH, 12h, 50°C; ii: HCl 0.01M, RT, 12h; iii: LiOH, MeOH, 2h; iv: Dowex 1x8-50.

four molar equivalents of $LiOH{\cdot}H_2O$ in MeOH afforded the lithium salt of L^3, which was subsequently used for complexations. In the case of HL^4 the amines were freed by passing an aqueous solution of $HL^4{\cdot}3HCl$ through a Dowex 1x8-50 column previously activated with 1M NaOH. Satisfactory elemental analyses, mass spectra, ^1H and ^{13}C NMR spectra were obtained for the hydrochloride salts $HL^3{\cdot}3HCl$ and $HL^4{\cdot}3HCl$, but only ^1H and ^{13}C NMR spectra were obtained for $Li(L^3)$ and HL^4.

5.3.2 Synthesis of Ln^{III} complexes

The Schiff base condensation of the ligand L^2 with sodium pyruvate (a), methyl sodium acetyl phosphonate (b) and methoxybenzyl sodium acetyl phosphonate (c) using the Ln^{III} ion as templating agent (Figure 5.18) gives rise to positive charged Ln^{III} complexes: $[Ln(L^{2a})]^+$, $[Ln(L^{2b})]^+$, and $[Ln(L^{2c})]^+$, respectively (Ln^{III} = Y^{III}, Eu^{III}, Gd^{III}, Yb^{III}, La^{III}). The ligands L^{2a}, L^{2b} and L^{2c} each have seven donor atoms, so it was argued that bidentate counterions such as acetate or nitrate would complete the co-ordination sphere of the lanthanide ions.

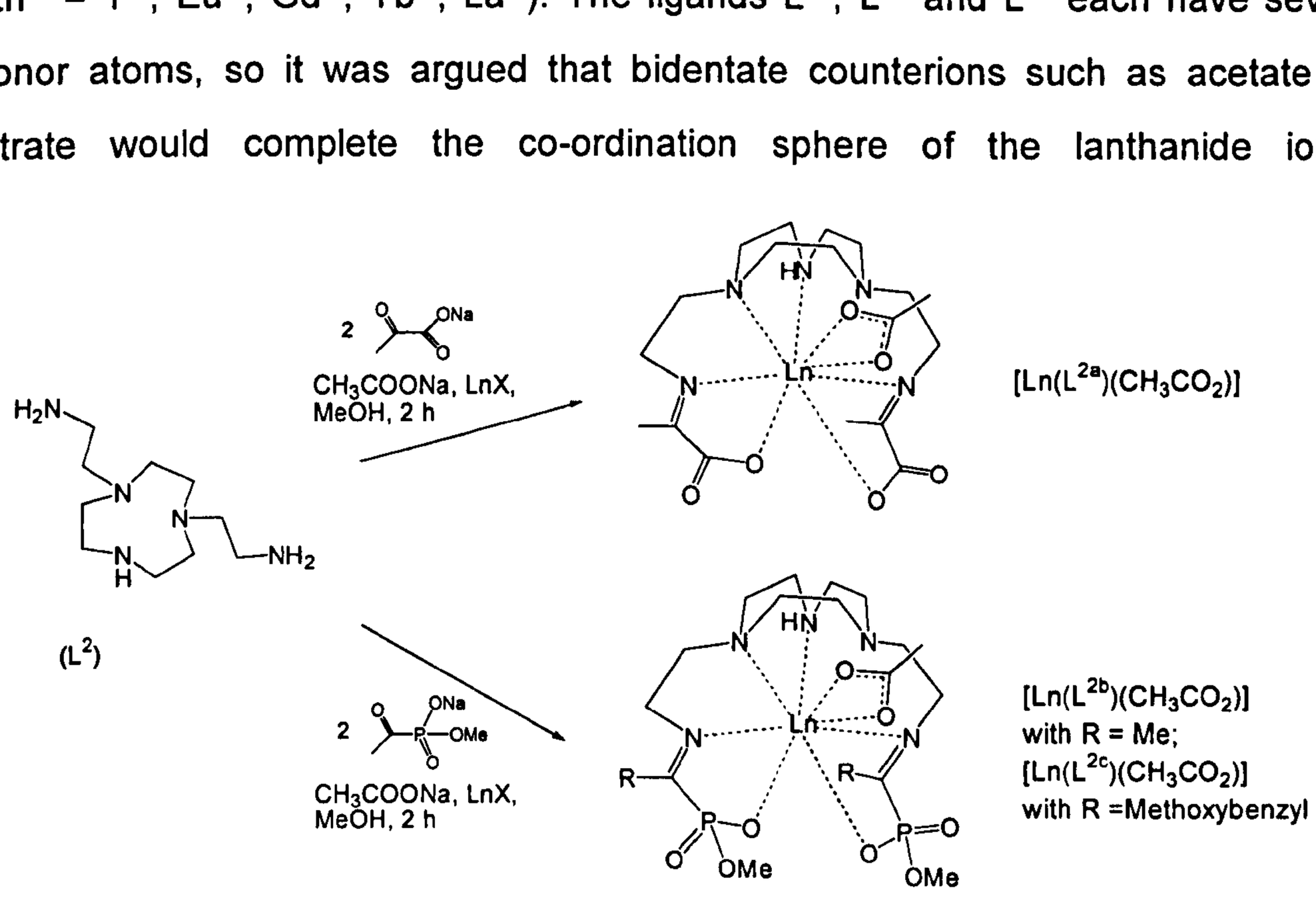

Figure 5.18 Synthesis of the complexes $[Ln(L^{2a})(CH_3CO_2)]$, $[Ln(L^{2b})(CH_3CO_2)]$ and $[Ln(L^{2c})(CH_3CO_2)]$.

Unfortunately, using $Y(NO_3)_3 \cdot 5H_2O$, the complex precipitated out from the reaction solution and was almost insoluble in MeOH. Consequently, acetate was chosen as bidentate counterion and every complex (except for $[Eu(L^{2a})Cl] \cdot 2NaCl \cdot 2H_2O$ and $[Yb(L^{2a})Cl] \cdot 2NaCl \cdot H_2O$) was synthesised *via* reaction of one molar equivalent of L^2 with one of CH_3COONa, one of the Ln^{III} salt (usually the chloride) and three of the appropriate ketone in MeOH under reflux for 2 hours (Figure 5.18).

The Schiff base condensation of the ligands $Li(L^3)$ and HL^4 with two molar equivalents of sodium pyruvate (a) or methyl sodium acetyl phosphonate (b) using the Ln^{III} ion as templating agent yielded the neutral Ln^{III} complexes $[Ln(L^{3a})]$, $[Ln(L^{3b})]$, $[Ln(L^{4a})]$ and $[Ln(L^{4b})]$ (Figure 5.19 a and b). Since the ligands L^{3a}, L^{3b}, L^{4a} and L^{4b} have eight donor atoms, the lanthanide ions could be lacking of the ninth donor atom that is probably taken by a water molecule as normally observed in other lanthanide complexes. After refluxing for 2 h, the solvent volume was reduced and precipitation of the product by addition of Et_2O afforded the desired complexes as white or slightly yellow solids. During the reaction for the formation of $[Ln(L^{3a})]$ and $[Ln(L^{3b})]$ complexes the cloudy solution formed was filtered through celite before reducing the solvent volume. The formation of insoluble precipitates is thought to be due to both the formation of polymeric products by intermolecular reaction of the primary amines with the carboxylic acid but also to formation of lanthanide hydroxides because of excess LiOH in $Li(L^3)$.

Elemental analysis and mass spectra for all the complexes are consistent with the formulations $[Ln(L^{2x})(CH_3CO_2)] \cdot 3NaCl \cdot nH_2O$ (x = a, b or c; n = 1, 2, 3) or $[Ln(L^{2a})Cl] \cdot 2NaCl \cdot nH_2O$ for Eu^{III} and Yb^{III} complexes and $[Ln(L^{3x})] \cdot 2NaCl \cdot nH_2O$ or $[Ln(L^{4x})] \cdot 2NaCl \cdot nH_2O$ (x = a or b; n = 1,2, 3 or fractional). In the case of the complexes of L^3 the elemental analyses revealed the presence of Li^+, which is probably surrounded by water molecules. In $[Ln(L^{4a})]$ and $[Ln(L^{4b})]$ it is assumed that the hydroxyl group is deprotonated, mainly because in the mass spectra the

molecular ions were the neutral complex (with the OH deprotonated) with associated Na^+ ions.

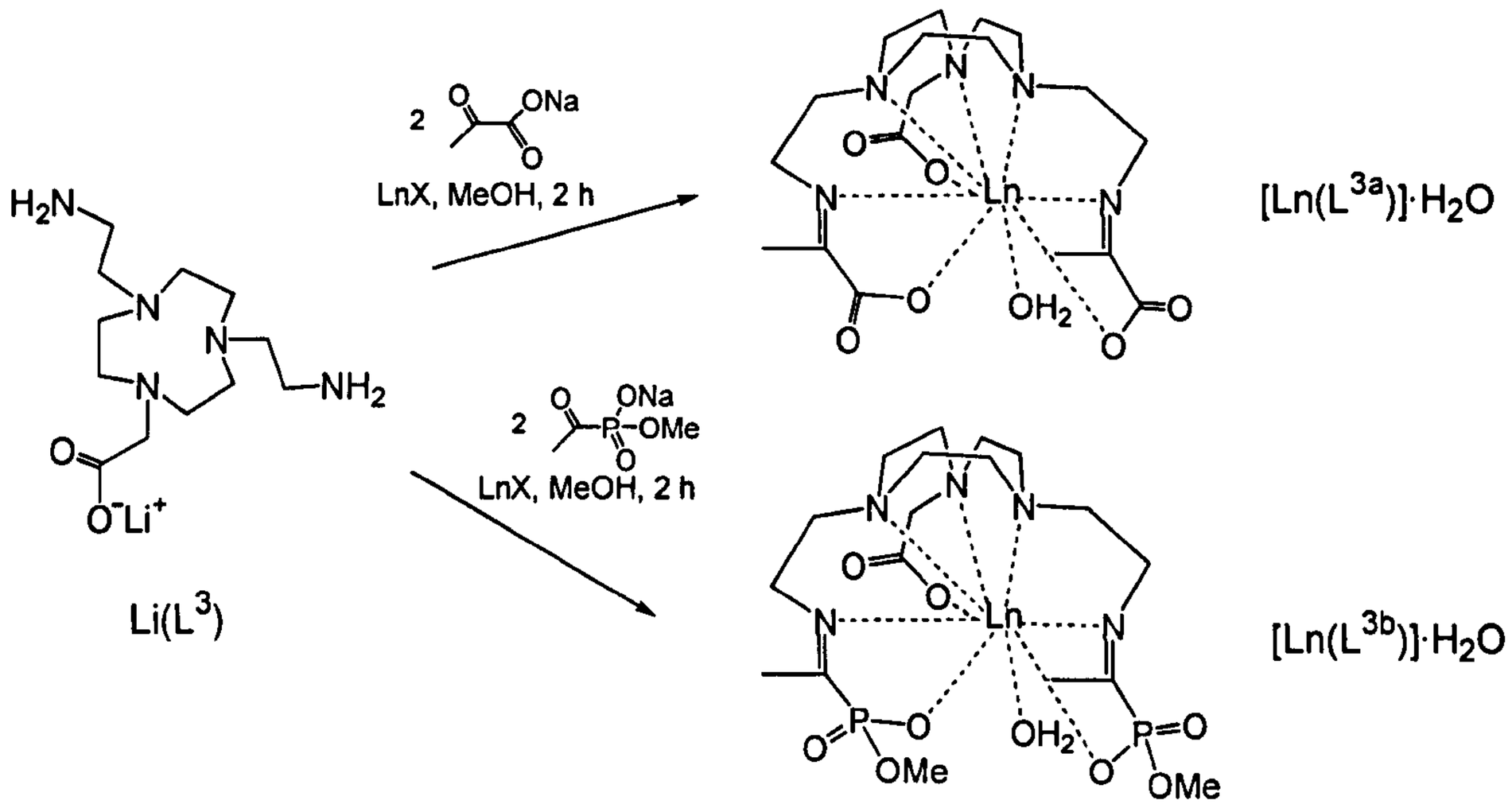

Figure 5.19a. Synthesis of the complexes [Ln(L^{3a})] and [Ln(L^{3b})].

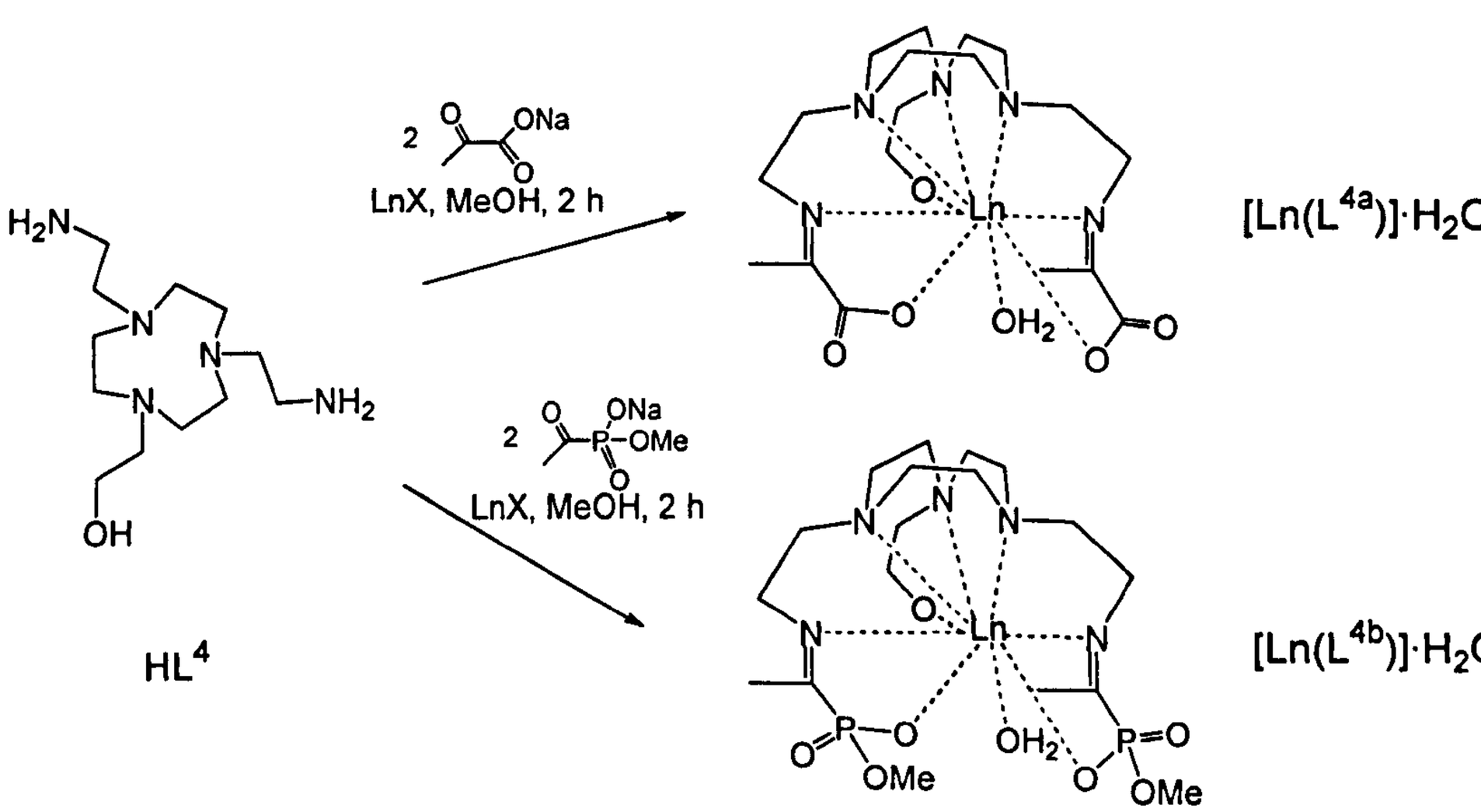

Figure 5.19b. Synthesis of the complexes [Ln(L^{4a})], and [Ln(L^{4b})].

5.2.3 Single crystal X-ray diffraction analysis of [Gd(L^{2a})(CH_3CO_2)]·CH_3OH

Single-crystals of [Gd(L^{2a})(CH_3CO_2)]·CH_3OH were obtained by adding a ten fold excess of Et_2O into a solution of the complex in MeOH at room temperature.

The cloudy solution formed was left standing for two days whereupon single crystals were obtained. Single crystal X-ray diffraction studies show the Gd^{III} centre as nine-coordinate, using all seven donor atoms of the ligand, namely the three amino N-donors of the macrocycle, the two imino N-donors and the two pyruvate O-donors. The Gd^{III} centre is further co-ordinated to a bidentate acetate anion thereby reaching the co-ordination number nine. Bond lengths are in the range 2.667(8)-2.625(9)Å for the bonds between the metal and the macrocyclic N-donors; 2.593(9) and 2.591(8)Å are the lengths for the bonds to the N-donors of the imine moieties [Gd-N(3A) and Gd-N(3B)] and 2.382(7) and 2.401(7)Å to the pyruvate O-donors [Gd-O(6A) and Gd-O(6B)]. The acetate anion is bound with bond lengths of 2.496(7) and 2.492(7) Å [Gd-O(1AC) and Gd-O(2AC), respectively].

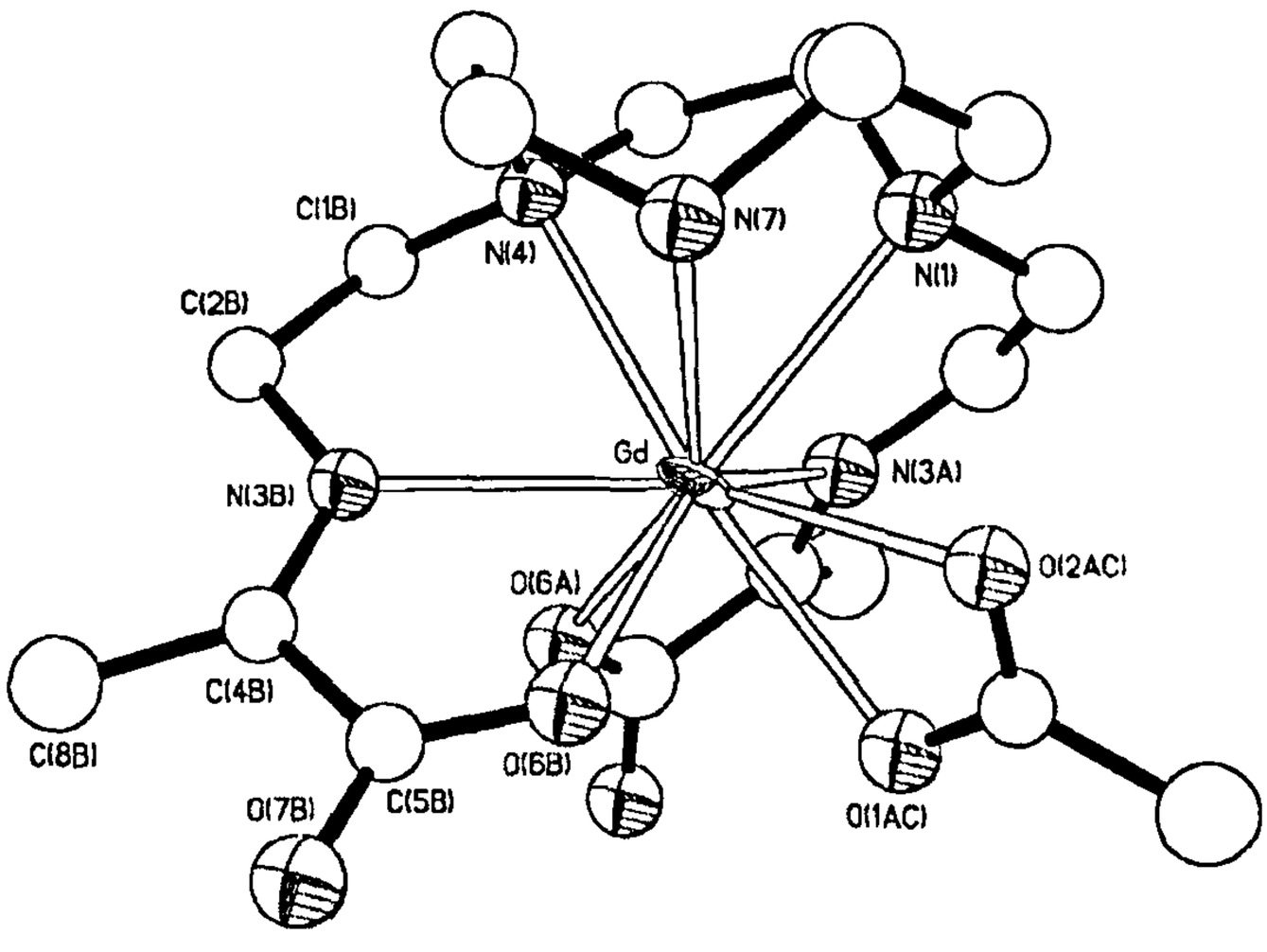

Figure 5.20 Crystal structure of [Gd(L^{2a})(CH_3CO_2)] with numbering scheme adopted. Hydrogen atoms and solvating MeOH molecules have been omitted for clarity.

In [Gd(L^{2a})(CH_3CO_2)]·CH_3OH the fragments C(2)-C(8) of the two pendant arms have a high degree of planarity with the mean deviation from the least squares mean plane of 0.048Å and 0.068Å. However, in contrast to both imino-

carboxylate and imino-phosphonate complexes discussed in Chapters 3 and 4, the pitch angles formed by the plane of the macrocycle and the plane of each pyruvate are not similar [51.4° for the fragment C(2A)-C(8A) and 44.0° for C(2B)-C(8B)]. The plane containing acetate anion is oriented with an angle of 57.1° with respect to the macrocyclic plane.

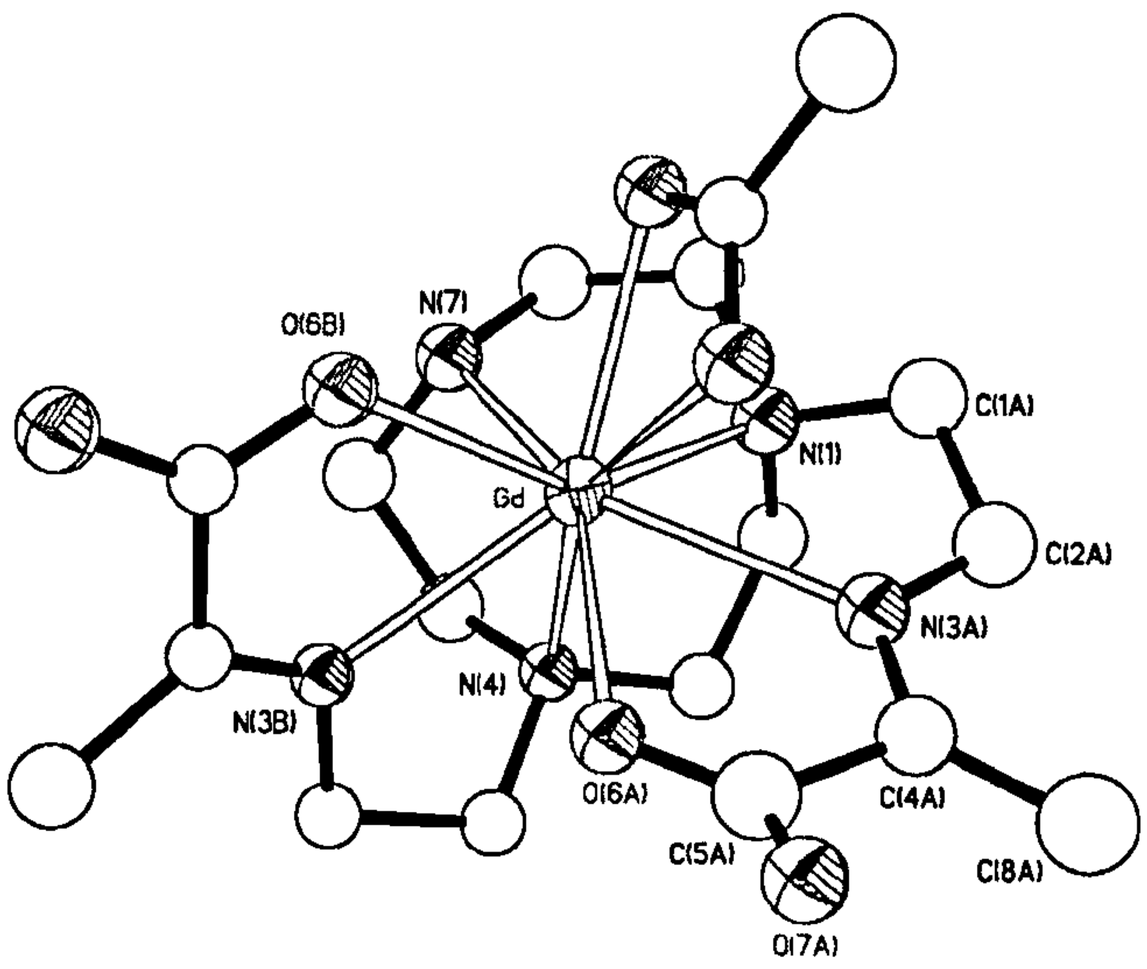

Figure 5.21 Different view of the crystal structure of [Gd(L^{2a})(CH_3CO_2)].

Table 5.1 Selected bond lengths (Å) in the crystal structure of [Gd(L^{2a})(CH_3CO_2)]·CH_3OH.

	[Gd(L^{2a})(CH_3CO_2)]·CH_3OH
Gd-N(1)	2.667 (8)
Gd-N(4)	2.664 (7)
Gd-N(7)	2.625 (9)
Gd-N(3A)	2.593 (9)
Gd-N(3B)	2.591 (8)
Gd-O(6A)	2.401 (7)
Gd-O(6B)	2.382 (7)
Gd-O(1AC)	2.496 (7)
Gd-O(2AC)	2.492 (7)

As in all the lanthanide complexes described in this thesis, the co-ordination geometry about the Gd^{III} centre is a distorted tricapped trigonal prism (Figure

5.22). This confirms that the presence of 1,4,7-triazacyclononane as a capping system forces the Ln^{III} ion to assume a trigonal prismatic structure, as the macrocyclic nitrogen donors impose the first triangular face. In this case, the other triangular face of the prism is formed by the two carboxylate oxygens and one acetate oxygen [O(1AC)], with the imine nitrogens and the other acetate oxygen capping the three rectangular faces of the prism. The upper and lower triangular faces of the prism are essentially equilateral, although the face formed by the three oxygens is more distorted (angle range 55.2-67.1º), and parallel (the angle between the plane defined by the triangle of three oxygen donors and that defined by the three nitrogen donors is 12.2º). The oxygen triangular face is slightly twisted around the three-fold axis, compared to the nitrogen triangular face with the average of the three torsion angles formed by the four atoms of every rectangular face of the prism being 19.4º. In conclusion, looking also at the crystal structures discussed in previous chapters, it can be observed that the twist between the two triangular faces of the prism is more evident in the imino-carboxylate complexes [Ln(L^a)] discussed in Chapter 3.

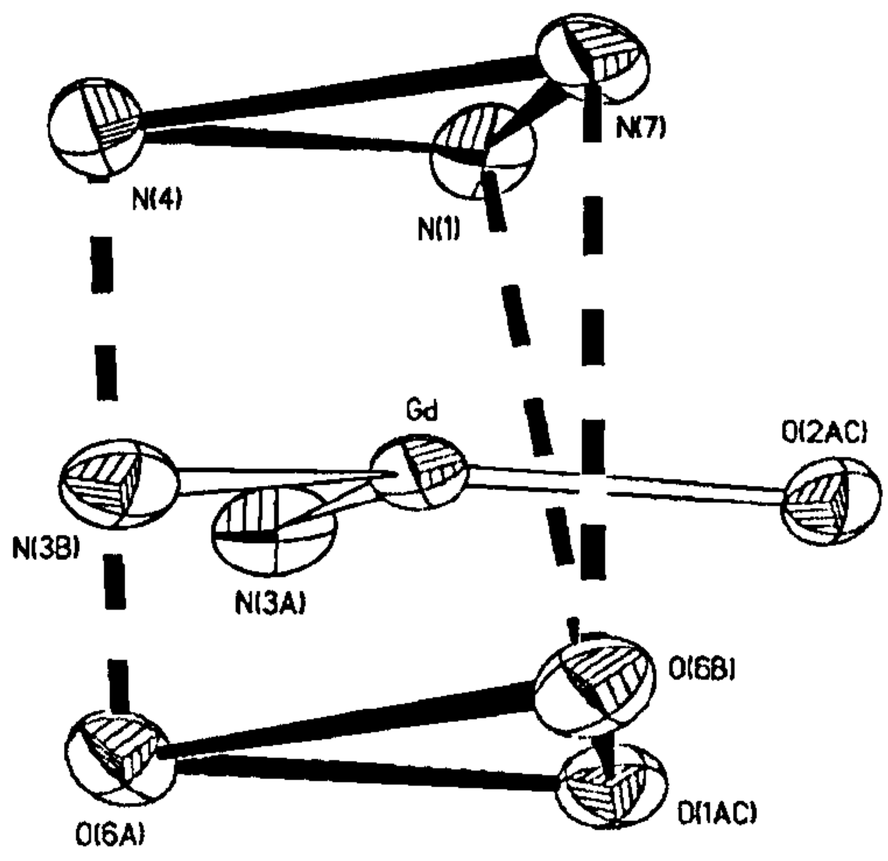

Figure 5.22 Co-ordination geometry about the metal centre in [Gd(L^{2a})(CH_3CO_2)]·CH_3OH.

5.3.4 ^{1}H and ^{13}C NMR spectra of [Y(L^{2a})X], [Y(L^{2b})X] and [Y(L^{2c})X] (X = $CH_3CO_2^-$ or Cl^-)

NMR spectroscopic studies on the Y^{III} complexes with heptadentate ligands L^{2a}, L^{2b} and L^{2c} were performed in order to characterise the complexes and compare them with the symmetric nine co-ordinate complexes [Ln(L^a)], [Ln(L^b)] and [Ln(L^c)] discussed in Chapters 3 and 4.

The ^{1}H NMR spectra of [Y(L^{2a})(CH_3CO_2)] and [Y(L^{2b})(CH_3CO_2)] recorded in D_2O at 298 K and 300 MHz and of [Y(L^{2c})(CH_3CO_2)] recorded in CD_3OD (298 K and 300 MHz) are quite similar. Figure 5.23 shows the ^{1}H NMR spectrum of [Y(L^{2b})(CH_3CO_2)], while the ^{1}H NMR spectrum of [Y(L^{2a})(CH_3CO_2)] is shown in Figure 5.25 in Section 5.3.6. The protons of the macrocyclic CH_2 groups appear as a singlet and two triplets and those of the arms form a triplet and a broad peak at lower field due to the CH_2 adjacent to the imine nitrogen. 2D COSY experiments allowed the assignment of the resonances, which are reported in Table 5.2 (see Figure 5.24 for labelling scheme). The low rigidity of these asymmetric complexes does not allow the discrimination between axial and equatorial protons, but allows the detection of triplets due to coupling between CH_2 groups. It is worth noting that

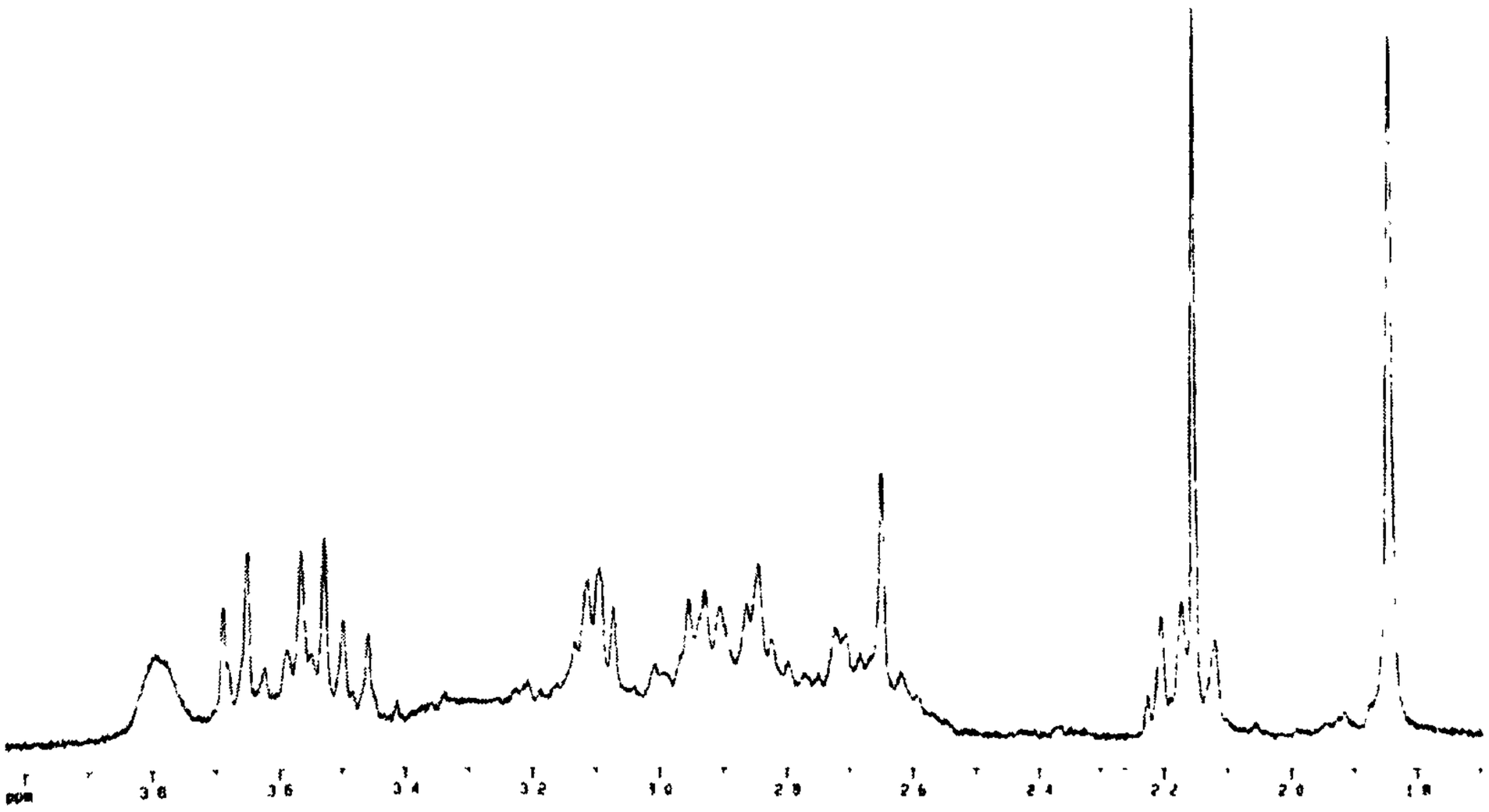

Figure 5.23 ^{1}H NMR spectrum of [Y(L^{2b})(CH_3CO_2)] (D_2O, 298 K).

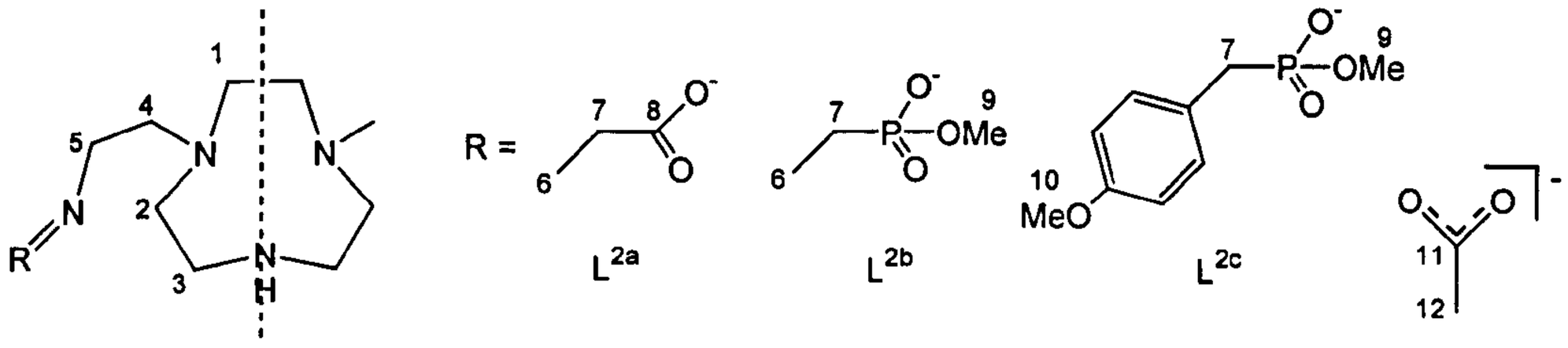

Figure 5.24 Labelling scheme for the Y^{III} complexes with ligands L^{2a}, L^{2b} and L^{2c}.

the presence of the acetate anion co-ordinated to the metal centre leads to increased rigidity in the molecule, since the ^{1}H NMR spectrum of [Y(L^{2a})Cl] in D_2O appears as a broad multiplet with only the peaks of the pyruvate and of the CH_2 adjacent to the imine nitrogen distinguishable at 2.14 and 3.77 ppm, respectively. The reason for this fluxional ^{1}H NMR spectrum could be that the eight co-ordinate complex [Y(L^{2a})Cl] has a vacant co-ordination site occupied by a water molecule and therefore is much more flexible than the nine co-ordinate [Y(L^{2a})(CH_3CO_2)].

^{13}C NMR spectra of the Y^{III} complexes of L^{2a}, L^{2b} and L^{2c} were also recorded and the assignment of the peaks is reported in Table 5.3. The coupling constants between C and P atoms, observed in the phosphonate complexes [Y(L^{2b})(CH_3CO_2)] and [Y(L^{2c})(CH_3CO_2)], are also reported in Table 5.3.

Table 5.2 ^{1}H NMR chemical shift (ppm) for diamagnetic [Y(L^{2a})(CH_3CO_2)], [Y(L^{2b})(CH_3CO_2)] and [Y(L^{2c})(CH_3CO_2)].

	Multiplicity	[Y(L^{2a})(CH_3CO_2)]	[Y(L^{2b})(CH_3CO_2)]	[Y(L^{2c})(CH_3CO_2)]
H_1	s	2.61	2.65	2.84
H_2	t	2.89 (J = 6.8 Hz)	2.93 (J = 6.6 Hz)	2.93 (J = 7.1 Hz)
H_3	t	3.05 (J = 6.8 Hz)	3.10 (J = 6.6 Hz)	3.10 (J = 7.1 Hz)
H_4	t	2.80 (J = 5.9 Hz)	2.84 (J = 5.7 Hz)	2.84 (J = 6.0 Hz)
H_5	broad	3.70	3.80	3.83
H_6	s (m for L^{2b})	2.08	2.12-2.20	--
H_9	m	--	3.46-3.69	3.46-3.62
H_{10}	s	--	--	3.83
H_{12}	s	1.82	1.85	1.85

Table 5.3 ^{1}H NMR chemical shift (ppm) for [Y(L^{2a})Cl], [Y(L^{2b})(CH_3CO_2)] and [Y(L^{2c})(CH_3CO_2)].

	[Y(L^{2a})Cl]	[Y(L^{2b})(CH_3CO_2)]	[Y(L^{2c})(CH_3CO_2)]
C_1	51.4	52.7	50.8
C_2	50.0	49.0	47.1
C_3	48.9	48.3	43.9
C_4	57.6	56.9	51.8
C_5	45.1	44.7	37.0
C_6	14.6	17.4 (J_{CP} = 25.8 Hz)	--
C_7	170.1	170.3 (J_{CP} = 113.2 Hz)	162.7 (J_{CP} = 128.3 Hz)
C_8	171.0	--	--
C_9	--	55.4 (J_{CP} = 21.2 Hz)	55.6 (J_{CP} = 15.3 Hz)
C_{10}	--	--	54.5
C (Ar)	--	--	113.6, 129.5, 130.2, 131.2
C_{11}	--	182.0	181.1
C_{12}	--	23.3	23.0

5.3.5 ^{1}H and ^{13}C NMR spectra of [Y(L^{3x})] and [Y(L^{4x})] (x = a or b)

The ^{1}H NMR spectra of [Y(L^{3a})], [Y(L^{4a})] and [Y(L^{4b})] were recorded in D_2O ([Y(L^{3b})] in CD_3OD) at 300 MHz and 298 K. They are all very broad and show a large broad multiplet assigned to the CH_2 groups adjacent to tertiary amines (belonging to both ring and arms). Only some peaks could be assigned and the partial assignment is reported in Table 5.4. As already discussed for the ^{1}H NMR spectrum of [Y(L^{2a})Cl], the ^{1}H NMR spectra of the Y^{III} complexes reported in this section are broad and fluxional possibly because of the presence of a vacant co-ordination site occupied by a water molecule, which could cause increased flexibility. ^{13}C NMR spectra of [Y(L^{3a})] and [Y(L^{4a})] were also recorded and the assignment of the peaks is reported in Table 5.5.

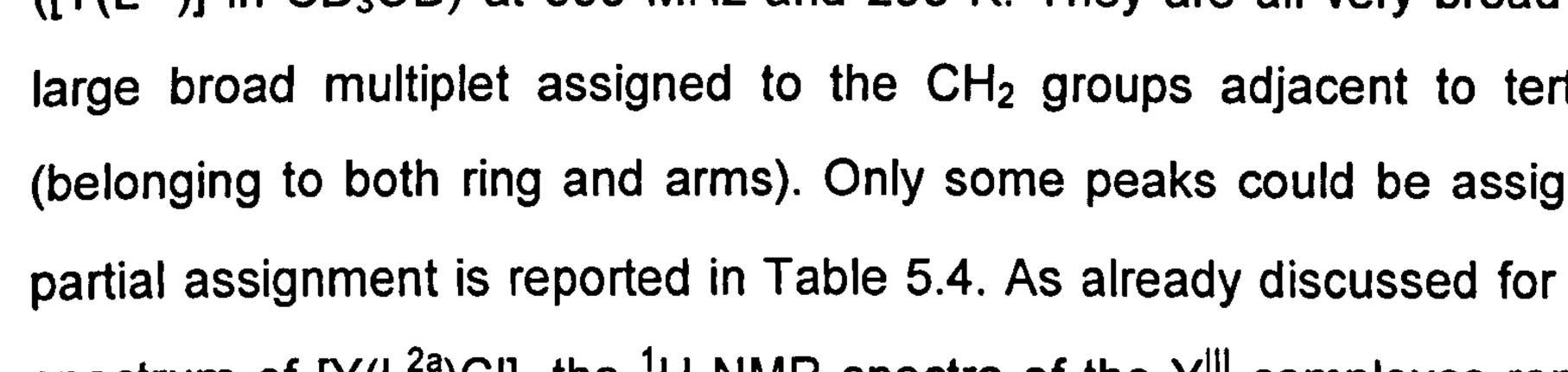

Figure 5.26 Labelling scheme for [Y(L^{3a})], [Y(L^{3b})], [Y(L^{4a})] and [Y(L^{4b})] complexes.

Table 5.4 ^{1}H NMR chemical shift (ppm) for [Y(L^{3a})], [Y(L^{3b})], [Y(L^{4a})] and [Y(L^{4b})].

	Multiplicity	[Y(L^{3a})]	[Y(L^{3b})]	[Y(L^{4a})]	[Y(L^{4b})]
H_1-H_4	m	2.44-3.24	2.75-3.26	2.54-3.38	2.60-3.42
H_5	broad	3.46	3.73	3.97	3.97
H_6	s (m for L^{4y})	3.77	3.92	3.16-3.38	3.58-3.70
H_7	s (d for L^{xb})	2.22	2.25	2.14	2.13
H_{10}	m (d for L^{4b})	--	3.47-3.63	--	3.50
H_{12}	t (broad)	--	--	3.77	3.75

Table 5.5 ^{13}C NMR chemical shift (ppm) for [Y(L^{3a})] and [Y(L^{4a})].

	[Y(L^{3a})]	[Y(L^{4a})]
C_1-C_4	54.8, 55.5, 56.4, 57.3	51.2, 56.8, 57.2, 57,7
C_5	50.9	48.2
C_6	65.6	51.9
C_7	14.8	15.8
C_8	169.9	171.8
C_9	173.3	173.4
C_{11}	177.6	--
C_{12}	--	59.5

5.3.6 Hydrolysis experiments

The symmetric Ln^{III} complexes [Ln(L^a)] and [Ln(L^b)] showed very high stability in water at pH 7.0, but lower stability at more acidic pH as discussed in Sections 3.4.3 and 4.3.5. All the Y^{III} complexes considered in this chapter exhibited a very low stability in D_2O at acidic pH, being hydrolysed in a few hours. The rapidity of these hydrolyses and often the complexity of the ^{1}H NMR spectra prevented a quantitative measure of the hydrolysis rate at pD 5.5.

However, the hydrolyses of the Y^{III} complexes with L^{2a}, L^{2b}, L^{2c}, L^{3a} and L^{4a} in D_2O monitored by ^{1}H NMR showed interesting results. The solutions of the complexes were not buffered at pH 7, but pH measurements during the course of the hydrolyses showed that, at the low concentrations used, the pH does not change considerably. For example, a 4 mM solution of [Y(L^{2c})(CH_3CO_2)]·3NaCl

·2H_2O in water has a pH of 7.14, which increases to pH 7.35 during the course of the hydrolysis.

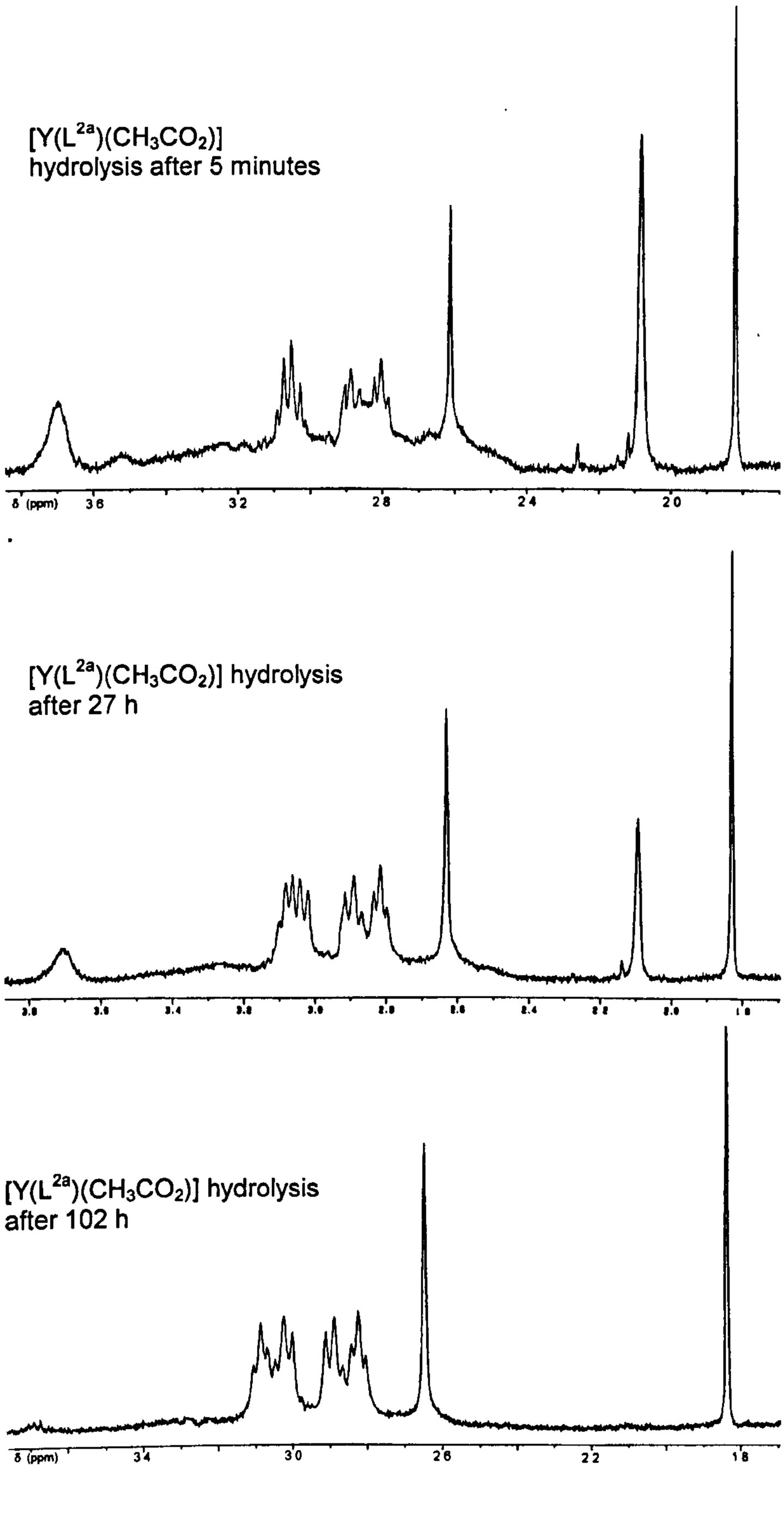

Figure 5.27 ^{1}H NMR spectra of [Y(L^{2a})(CH$_3$CO$_2$)] hydrolysis in D_2O acquired at the time intervals shown.

Figure 5.27 shows the ^{1}H NMR spectra of [Y(L^{2a})(CH_3CO_2)] in D_2O acquired at the time intervals shown. Similar spectra were recorded for the other Y^{III} complexes with L^{2b}, L^{2c}, L^{3a} and L^{4a}, but only for [Y(L^{2a})(CH_3CO_2)], [Y(L^{2b})(CH_3CO_2)] and [Y(L^{4a})] the hydrolyses could be monitored. The assignment of the ^{1}H NMR spectrum of [Y(L^{2a})(CH_3CO_2)] has already been reported in Table 5.2 (Section 5.3.4). The final ^{1}H NMR spectrum after complete hydrolysis of [Y(L^{2a})(CH_3CO_2)] (after more than 4 days) shows all the triplets due to the CH_2 groups of the macrocycle and of the arms (Table 5.2) not considerably shifted. Only the peaks assigned to the methylene group adjacent to the imine bond (at 3.70 ppm) and to the methyl group of the pyruvate (at 2.08 ppm) clearly decrease during the hydrolysis and another triplet due to the CH_2 adjacent to the primary amines of L^2 at 3.09 ppm is formed. The fact that the signals assigned to the methylene groups of the macrocycle and of the arms do not shift during the hydrolysis may suggest either that the ligand L^2 still co-ordinates the metal ion or that the amines are partly protonated. The other hydrolysis products are sodium pyruvate with the methyl group deuterated and the metal ion probably partly complexed by the ligand L^2. Similar considerations apply to the hydrolyses of [Y(L^{2b})(CH_3CO_2)] and [Y(L^{2c})(CH_3CO_2)]; also for [Y(L^{3a})] and [Y(L^{4a})] the hydrolysis reaction forms similar products, although the complexity and the broadness of the spectra prevented any definitive conclusion.

The Y^{III} complexes with ligands L^{3a} and L^{4a} are less stable in D_2O than the complexes with L^{2x} (x = a, b or c), their half-life being about 24 hours. The hydrolyses of [Y(L^{2a})(CH_3CO_2)] and [Y(L^{2b})(CH_3CO_2)] were quite slow with half-lives of about 2 and 7 days, respectively. [Y(L^{2c})(CH_3CO_2)] has an half-life of approximately 3 days in D_2O. The varying concentrations of H^+ in solution prevented calculation of the hydrolysis rate.

Considering the purpose of targeting *in vivo* regions at low pH as introduced in Section 3.4.3, the hydrolyses of the complexes discussed in this section gave

results similar to those observed for the hydrolysis of [Y(**1**)],[283,309] since the hydrolyses are very fast at low pH and have half-lives of more than one day at neutral pH. Therefore, the neutral complexes [Ln(L^{3a})] and [Ln(L^{4a})] discussed in this chapter could be effective in the targeting of *in vivo* regions at low pH. Unfortunately, the complexes with L^{2a}, L^{2b} and L^{2c} are not neutral and therefore fail to meet the condition of electroneutrality necessary to permit the crossing of cell membranes.

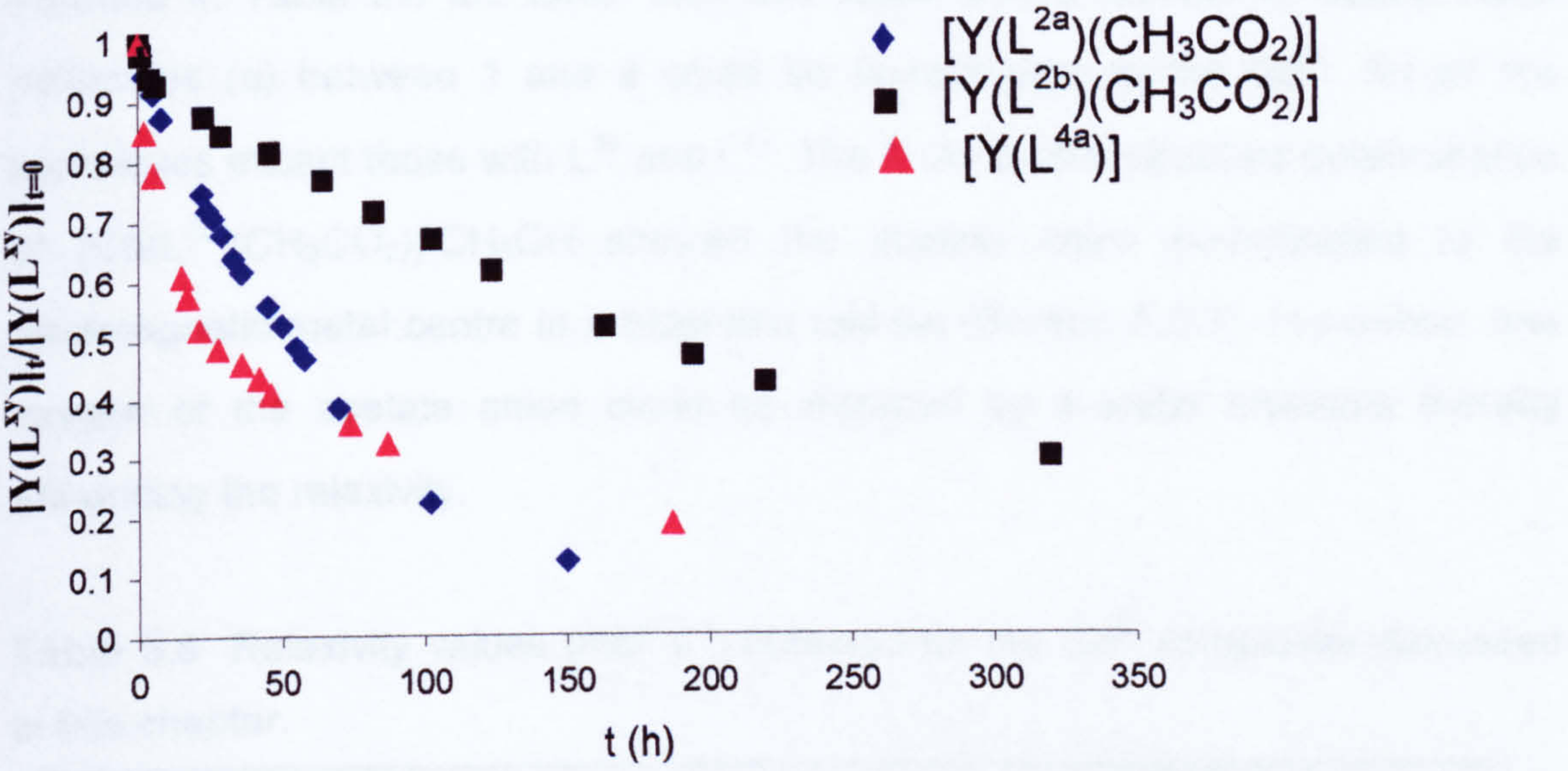

Figure 5.28 Plot of the hydrolyses in D_2O for [Y(L^{2a})(CH_3CO_2)], [Y(L^{2b})(CH_3CO_2)] and [Y(L^{4a})].

5.3.7 Relaxivity of Gd^{III} complexes

The relaxivities of [Gd(L^{2a})(CH_3CO_2)]·3NaCl·H_2O, [Gd(L^{2b})(CH_3CO_2)]·3NaCl ·2H_2O, [Gd(L^{2c})(CH_3CO_2)]·3NaCl·H_2O, [Gd(L^{3a})]·2NaCl·LiCl·4H_2O, [Gd(L^{3b})]·2NaCl ·LiCl·3H_2O, [Gd(L^{4a})]·2NaCl·2H_2O and of [Gd(L^{4b})]·2NaCl·1/2H_2O in D_2O at 300 MHz and 37°C were measured and the results reported in Table 5.6. The values obtained for these Gd^{III} complexes suggest that at least one H_2O molecule is bound to the Gd^{III} centre in almost all the complexes. The only unexpected result is

the relaxivities of only 1.11 $mM^{-1}s^{-1}$ and 1.10 $mM^{-1}s^{-1}$ observed for [Gd(L^{3a})] and [Gd(L^{3b})], which suggest that no water molecule is co-ordinated to the metal centre. Since the ligand L^{3a} has eight donor atoms, it was expected that the ninth co-ordination site on the Gd^{III} ion would be occupied by a water molecule, but this low relaxivity value suggests that the gadolinium(III) in these complexes is only eight co-ordinate. A relaxivity of 4.7(4) $mM^{-1}s^{-1}$ was determined for [Gd(**1**)][283,309] which could have two water molecules bound to the metal centre; all the values reported in Table 5.6 are lower than this value, and a number of bound water molecules (q) between 1 and 2 could be co-ordinated to the Gd^{III} for all the complexes except those with L^{3a} and L^{3b}. The X-ray crystal structure determination of [Gd(L^{2a})(CH_3CO_2)]·CH_3OH showed the acetate anion co-ordinated to the paramagnetic metal centre in a bidentate fashion (Section 5.3.3). In solution, one oxygen of the acetate anion could be replaced by a water molecule thereby enhancing the relaxivity.

Table 5.6 Relaxivity values ($mM^{-1}s^{-1}$) obtained for the Gd^{III} complexes discussed in this chapter.

Complex	r_1 ($mM^{-1}s^{-1}$)
[Gd(L^{2a})(CH_3CO_2)]·3NaCl·H_2O	3.02 ± 0.13
[Gd(L^{2b})(CH_3CO_2)]·3NaCl·2H_2O	3.80 ± 0.13
[Gd(L^{2c})(CH_3CO_2)]·3NaCl·H_2O	4.32 ± 0.17
[Gd(L^{3a})]·2NaCl·LiCl·4H_2O	1.11 ± 0.04
[Gd(L^{3b})]·2NaCl·LiCl·3H_2O	1.10 ± 0.11
[Gd(L^{4a})]·2NaCl·2H_2O	3.12 ± 0.14
[Gd(L^{4b})]·2NaCl·1/2H_2O	3.80 ± 0.22

5.3.8 Dysprosium induced shift experiments

Figure 5.29 shows the plot of DIS (Dysprosium Induced Shift) versus the concentration of [Dy(L^{2a})(CH_3CO_2)], [Dy(L^{3a})] and [Dy(L^{4a})] together with the plot already reported of the DIS of $DyCl_3$. The gradients of the three lines are 63 ± 4,

33 ± 2 and 55 ± 3 ppm/M. Considering that a slope of 43 is indicative of one bound water molecule (q = 1) and each multiple of 43 corresponds to one water (Section 3.3.8), these values are indicative of 1.5 water molecules associated with [Dy(L^{2a})(CH_3CO_2)], 0.8 with [Dy(L^{3a})] and 1.3 with [Dy(L^{4a})]. Fractional values of q are normally found by this method, perhaps due to a small contribution from the outer and/or second sphere water molecules. The value of q = 0.8 for [Dy(L^{3a})] confirms that in the complexes with the ligand L^{3a} the metal ion is only partially co-ordinated to a water molecule, not reaching q = 1. While it was expected that [Dy(L^{4a})] would have one water molecule directly bound to the Dy^{III} centre, the number of water molecules co-ordinated to the metal centre in [Dy(L^{2a})(CH_3CO_2)] was expected to be around two, but, as hypothesised in the discussion of the relaxivity of the analogous Gd^{III} complex, the acetate anion could be still partially bound to the metal centre in fast exchange with a water molecule, giving thereby q = 1.5.

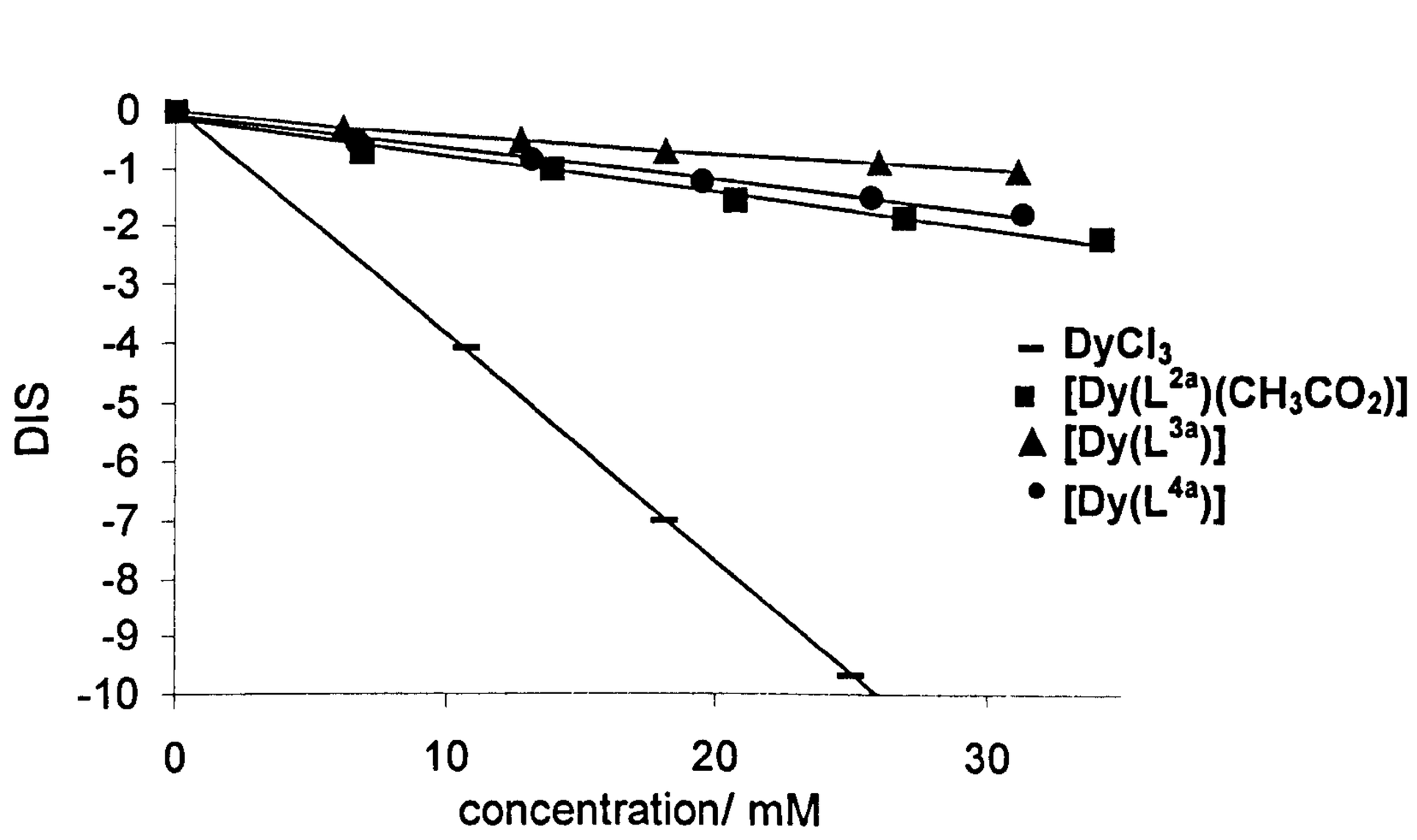

Figure 5.29 Plots showing the variation of the dysprosium induced shift (DIS, $\Delta\delta$) with concentration of $DyCl_3$, [Dy(L^{2a})(CH_3CO_2)], [Dy(L^{3a})] and [Dy(L^{4a})].

5.3.9 Luminescence of [Eu(L^{2a})Cl]

It has already been mentioned in Section 2.4 that lanthanides are able to exhibit luminescence emission with long lifetimes after excitation into higher electronic states. Following excitation at a suitable wavelength, the intensity of the luminescence decay with an exponential curve characterized by k_{obs}, the observed rate constant for deactivation of the emissive state.[115,118] The lifetime (τ) of the emission is simply the reciprocal of k_{obs}. Since water molecules quench the luminescence emission by energy transfer into O-H stretching vibrations and energy transfer into O-D vibration is much less efficient, the quenching effect of the water is not observed using D_2O as a solvent. Therefore, the number of water molecules (q) associated with the metal ion can be determined with the equation:

$$q = A_{Ln}(\tau_{H2O}^{-1} - \tau_{D2O}^{-1})$$

with τ that is the luminescence lifetime and A_{Ln} a proportionality constant specific to a given Ln^{III} ion.[115,118] The empirical proportionality constant for Eu^{III} complexes have been determined by Horrocks and Sudnick as 1.05 (with τ in ms).[392,393]

Upon excitation at the charge transfer band, [Eu(L^{2a})Cl] exhibits a low-intensity structured emission in the visible region. The detector used did not allow us to register any emission above 650 nm. For that reason, only bands at 595 and 620 nm could be registered. According to literature data, they were assigned to $^5D_0 \rightarrow {}^7F_J$ with J = 1 (595 nm) and J =2 (620 nm). The transition to J = 0, expected at 585 nm, was registered as a low intensity shoulder on the high-energy side of the J = 1 transition. Excitation spectra recorded at 620 and 595 nm (Figure 5.30) match absorption spectra in the region 200-350 nm. However, a new band at 390nm appears in the excitation spectra while there is no sign of it in the absorption spectra. The position of this band corresponds to the intra f-shell Eu^{III} transition. It reveals that the emission observed indeed arises from the intra-metal excited states, and that in case of the compound studied energy-transfer is not

very efficient. The last observation can be explained by a competitive non-radiative deactivation of the charge-transfer state through photo-induced electron transfer from chromophore to the metal.

Upon excitation into the 390 nm absorption band, the same emission spectrum was registered, and the same emission lifetime seen at 595 and 620 nm was obtained. Rate constants of emission decay for [Eu(L^{2a})Cl] in D_2O and in H_2O are 2.2±0.2 and 3.5±0.2 ms^{-1}, respectively. Consequently, the number of water molecules coordinated to the metal centre can be determined as 1.5, the same value obtained with the DIS method. The value obtained confirms the hypothesis that the acetate anion and a water molecule are both partially co-ordinated to the metal centre and in equilibrium with each other.

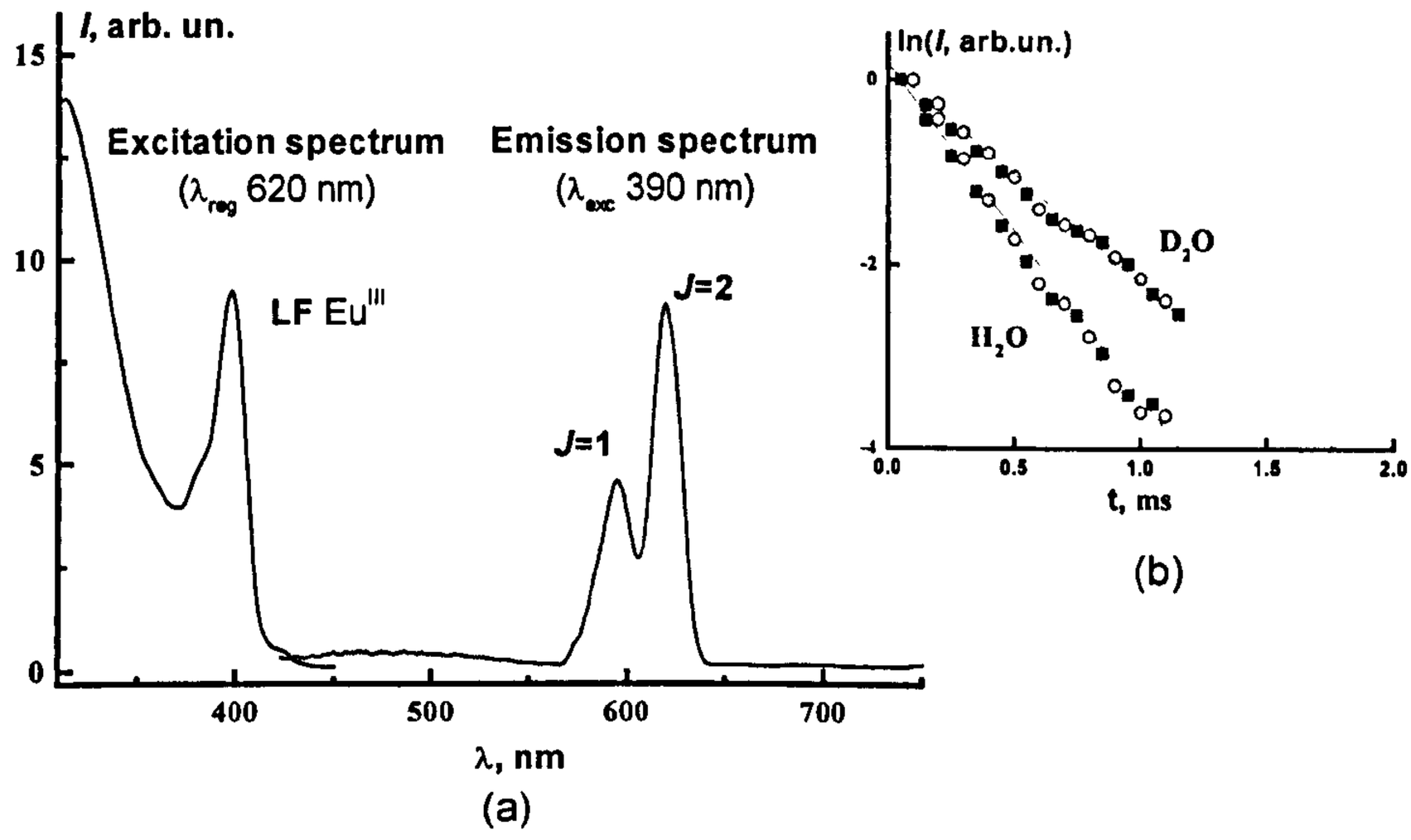

Figure 5.30 (a) Excitation and emission spectra in D_2O for [Eu(L^{2a})Cl] and (b) kinetic traces at 620 nm for the luminescence decay of [Eu(L^{2a})Cl] in H_2O and D_2O.

5.4 Experimental

1-(*p*-Tolylsulfonyl)-1,4,7-triazacyclononane[367] (**6**), N-(*p*-tolylsulfonyl)-aziridine[394] and 2,6-diformyl-4-methylphenol[395] were prepared as described in literature.

5.4.1 Synthesis of 1-(*p*-tolylsulfonyl)-4,7-bis(2-aminoethyl-N-*p*-tolylsulfonyl)-1,4,7- triazacyclononane (7)

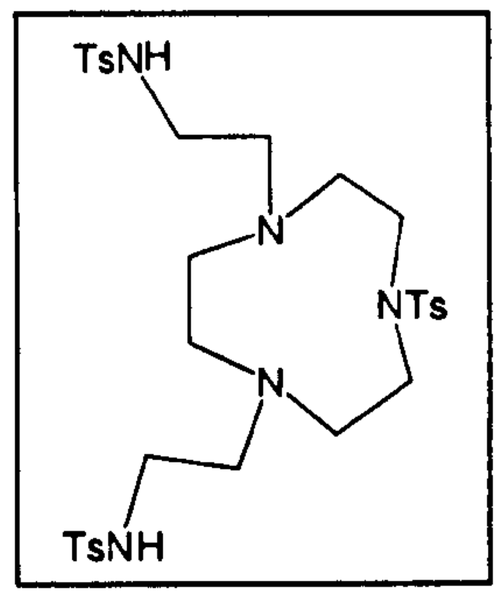

1-(*p*-Tolylsulfonyl)-1,4,7-triazacyclononane (**6**) (2.36g, 8.7mmol) was dissolved in CH_3CN (100 cm^3) and heated to reflux under N_2. A solution of N-(*p*-tolylsulfonyl)-aziridine (3.46g, 17.5mmol) in CH_3CN (50 cm^3) was added in 2h. The resulting solution was heated under reflux for further 3h. The course of the reaction was monitored by TLC ($CHCl_3$ with 5% MeOH; R_f = 0.36). After cooling, the solvent was removed by rotary evaporation to yield a pale yellow solid which was dried *in vacuo* (5.67g, 8.36 mmol, yield 96.1%). ^{1}H NMR: δ ($CDCl_3$, 298 K, 300 MHz) 2.40 (ArC*H*$_3$, 6H, s), 2.44 (ArC*H*$_3$, 3H, s), 2.68 (NC*H*$_2$ ring, 4H, s) 2.69 (NC*H*$_2$ arms, 4H, t, overlapped), 2.85 (NC*H*$_2$ ring, 4H, br) 2.96 (ArNHC*H*$_2$ arms, 4H, t, J = 5.67 Hz) 3.17 (NC*H*$_2$ ring, 4H, br), 7.65 (Ar*H*, 2 H, d, J = 8.21 Hz) 7.31 (Ar*H*, 2 H, d, J = 8.21 Hz), 7.77 (Ar*H*, 4 H, d, J = 7.86 Hz) 7.27 (Ar*H*, 4 H, d, J = 7.86 Hz) ppm. ^{13}C NMR: δ 21.48(Ar*C*H$_3$), 41.48 (TsNHCH$_2$ arms), 54.25, 55.99 and 56.23 (NCH$_2$ ring), 57.01(NCH$_2$ arms), 127.24 and 129.71 (*C*H, benzene ring), 136.91 and 144.24 (*C*, benzene ring) ppm. FAB mass spectrum (3-NOBA matrix): m/z, found: 700.3 and 678.3 for 700.9 [*M* + Na$^+$] and 677.9 [*M*], respectively. Elemental analysis: found (calc. for $C_{31}H_{43}N_5O_6S_3$) C, 54.64(54.92); H, 6.23 (6.39); N, 10.14% (10.33%).

5.4.2 Synthesis of 4,7-*bis*(2-aminoethyl)-1,4,7-triazacyclononane (L^2)

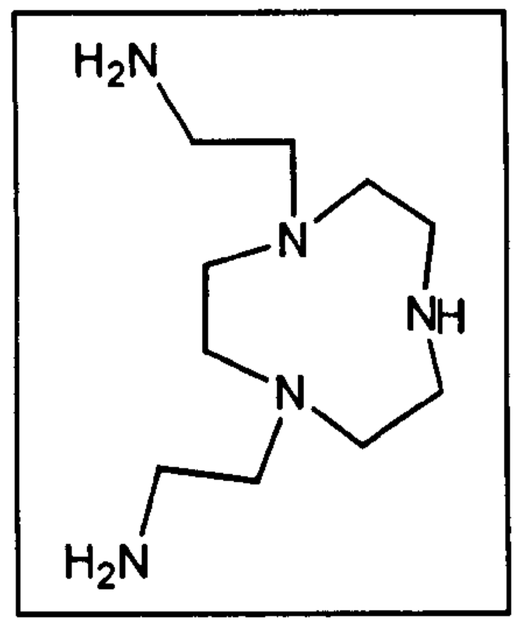

1-(*p*-Tolylsulfonyl)-4,7-bis(2-aminoethyl-N-*p*-tolylsulfonyl)-1,4,7-triazacyclononane (**7**) (3.20g, 4.72 mmol) was dissolved in concentrated H_2SO_4 (40 cm^3) and heated to 110 °C under N_2 atmosphere for 72 h. After cooling, the dark solution was added in 1 h to a mixture of Et_2O and EtOH (400 cm^3, v/v 1:1). The solid formed was filtered, washed with Et_2O and dissolved in H_2O. The water solution was then passed through a Amberlite IRA 416 column (30 g) activated with a solution 1M of NaOH. The solvent was removed under reduced pressure to yield a colourless oil (1.01g, 4.33 mmol, yield 91.7%). ^{1}H NMR: δ ($CDCl_3$, 298 K, 300 MHz) 2.08 (N*H*$_2$, 4H, br) 2.57 (NC*H*$_2$ ring, 4 H, s) 2.58 - 2.67 (NC*H*$_2$, 12 H, m), 2.74 (C*H*$_2$NH$_2$, 4 H, t, J = 5.83 Hz) ppm. ^{13}C NMR: δ 40.34 ($NCH_2CH_2NH_2$), 46.78 (CH_2HNCH_2), 52.21, 53.72 (NCH_2 ring), 61.29 ($NCH_2CH_2NH_2$) ppm. EI mass spectrum: m/z found 185.2, 168.2, 142.1 and 128.1 for 185.3 [*M*$^+$-CH_2NH_2], 169.2 [*M*$^+$- CH_2NH_2 - NH_2], 141.1 [*M*$^+$-$CH_2CH_2NH_2$-CH_2NH_2], 127.1 [*M*$^+$-2$CH_2CH_2NH_2$] respectively. Elemental analysis: found (calc. for $C_{10}H_{25}N_5 \cdot H_2O$) C, 51.41 (51.47); H, 11.55 (11.66); N, 29.82% (30.01%).

5.4.3 Synthesis of 8

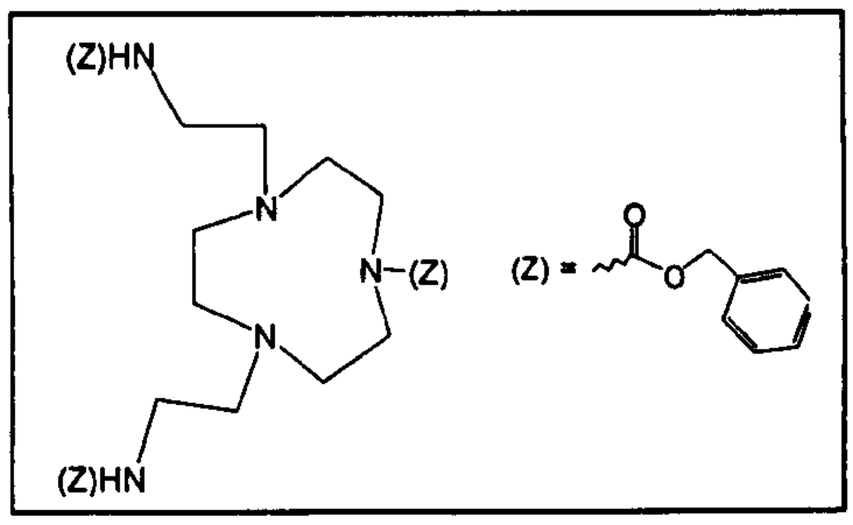

N-(benzyloxycarbonyloxy)succinimide (0.241 g, 0.96 mmol) in CH_2Cl_2 (10 cm^3) was added to a solution of L^2 (0.104 g, 0.46 mmol) in CH_2Cl_2 (15 cm^3) at 5 °C over a period of 30 minutes. The solution was then stirred at this temperature for 2 h. The reaction was monitored by TLC ($CHCl_3$ with 5% of MeOH; R_f = 0.30) and stopped when only one product was observed. The solution was washed with water (3 x 40 cm^3), dried with

$MgSO_4$ and filtered. Removal of the solvent at the rotary evaporator yielded a viscous slighly yellow oil that was dried under reduced pressure (0.136 g, 0.22 mmol, yield 23%). ^{1}H NMR: δ ($CDCl_3$, 298 K, 300 MHz) 2.46, 2.58, 2.71, 2.83 (NCH_2, 10 H, broad singlets), 3.18, 3.31 (CH_2NCO_2, 8 H, broad singlets), 5.08, 5.09, 5.12 (ArCH_2, 6 H, s), 5.51, 6.03 (N*H*CO, 2 H, broad), 7.32 (Ar*H*, 15 H, s) ppm. ^{13}C NMR: δ 39.37, 52.17, 54.12, 54.83, 57.26 (NCH_2), 66.70, 67.12 ($ArCH_2$), 128.29 (*Ar*H), 136.93 (*Ar*), 156.41 (NHC=O) ppm. FAB mass spectrum (3-NOBA matrix) *m/z*: 640 and 618 [*M* + Na^+] and [*M*], respectively.

5.4.4 Synthesis of 9

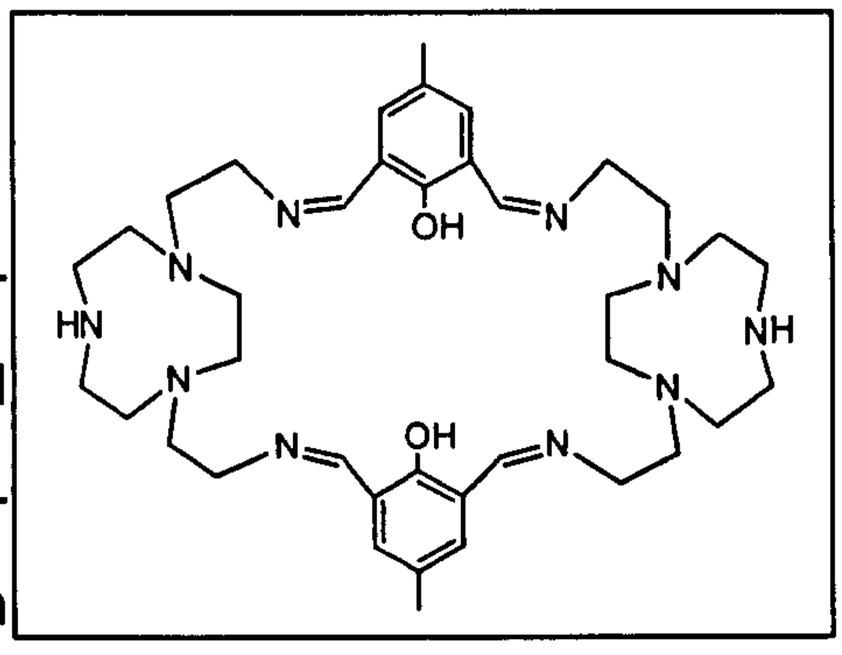

A solution of 4,7-bis (2-aminoethyl)-1,4,7-triazacyclononane (L^2) (0.15 g, 0.64 mmol) in MeOH (10 cm^3) was added dropwise to a solution of 2,6-diformyl-4-methylphenol (0.105 g, 0.64 mmol) in MeOH (20 cm^3). The resulting solution was heated under reflux for 2h. After cooling, the solvent volume was reduced, petroleum ether (40-60 °C) was added and an orange solid, which was filtered off and dried under reduced pressure, was obtained (0.182 g, 0.265 mmol, yield 82.8%). ^{1}H NMR: δ ($CDCl_3$, 298 K, 300 MHz) 2.30 (ArCH_3, 6 H, s) 2.55 – 2.72 (NCH_2, 32 H, m), 3.47 (CH_2N=C, 8 H, m), 7.36 (Ar*H*, 4 H, s), 8.36 (N=C*H*, 4 H, s) ppm. ^{13}C NMR: δ 20.36, 47.18, 51.99, 53.95, 57.40, 58.40, 118.44, 125.40, 126.98, 130.75, 131.72, 157.09 and 165.59 ppm. FAB mass spectrum (3-NOBA matrix) m/z, found: 709, 687 for [*M* + Na^+] and [*M*], respectively. IR (KBr disk), cm^{-1}: 2925s, 2852s, 1637s and 1600s ($\nu_{C=N}$), 1458s, 1384s, 1260m, 1101m, 1033m and 804m. Elemental analysis: found (calc. for $C_{38}H_{58}N_{10}O_2$): C, 66.15 (66.44); H, 8.39 (8.51); N, 20.24% (20.39%).

5.4.5 Synthesis of the lithium salt of 1-(carboxymethyl)-4,7-*bis*(2-aminoethyl)-1,4,7-triazacyclononane Li(L^3)·

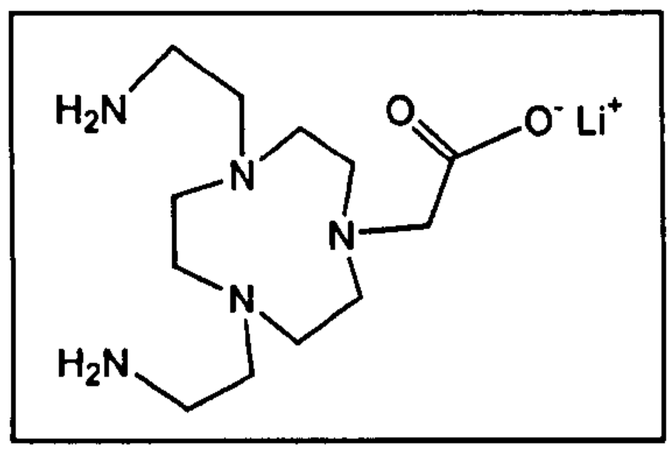

tert-Butyl-bromoacetate (114.3 mg, 0.586 mmol) in $CHCl_3$ (5 cm^3) was added dropwise to a solution of (**9**) (201.2 mg, 0.293 mmol) and diisopropylethylamine (2 cm^3) in $CHCl_3$ (30 cm^3). The resulting solution was stirred 12 h at room temperature. The solvent was then removed and the resulting oil was dissolved in $CHCl_3$ and washed with water (3 x 20 cm^3). The organic solution was dried with $MgSO_4$ and filtered and the solvent was removed under reduced pressure. The yellow oil obtained was dissolved in HCl 0.01 M and stirred at room temperature for 12 h. Filtration and removal of the solvent on a rotary evaporator yielded a pale brown solid which was re-crystallised from MeOH/Et_2O. The pale yellow solid obtained was filtered and dried *in vacuo*. The *tris*-hydrochloride salt of 1-(carboxymethyl)-4,7-*bis*(2-aminoethyl)-1,4,7-triazacyclononane ($HL^3 \cdot 3HCl \cdot 2H_2O$) was obtained. (153.8 mg, 0.402 mmol, yield 68.6%). ^{1}H NMR: δ (D_2O, 298 K, 300 MHz) 2.77 (C*H*$_2$ ring, 4H, s) 2.92 (NC*H*$_2$ ring, 4 H, t, J = 5.76 Hz), 3.03 (NC*H*$_2$ arms, 4 H, t, J = 6.42 Hz), 3.15 (C*H*$_2$NH$_2$, 4 H, t, J = 6.42 Hz), 3.25 (NC*H*$_2$ ring, 4 H, br) and 3.89 (C*H*$_2$COOH, 2 H, s) ppm. ^{13}C NMR: δ 37.17 ($NCH_2CH_2NH_2$), 46.78 (NCH_2 ring), 51.07 (NCH_2 ring), 53.45 (NCH_2 ring), 53.81 ($NCH_2CH_2NH_2$) and 58.10 (CH_2COOH) ppm. FAB mass spectrum (Glycerol/H_2O/MeOH matrix) m/z = 274 [*M*+ H^+]. Elemental analysis: found (calc. for $C_{12}H_{30}Cl_3N_5O_2 \cdot 2H_2O$): C, 34.48 (34.42); H, 8.03 (8.18); N, 16.81% (16.72%).

$LiOH \cdot H_2O$ (67.6 mg, 1.61 mmol) in MeOH (10 cm^3) was added to a solution of $HL^3 \cdot 3HCl \cdot 2H_2O$ (153.8 mg, 0.402 mmol) in MeOH (10 cm^3) and the solution stirred for 2 h until complete dissolution of the LiOH. The solvent volume was then reduced, Et_2O was added and a slightly yellow precipitate was obtained (110.2 mg, 0.39 mmol, yield 98.1%). ^{1}H NMR: δ (CD_3OD, 298 K, 300 MHz) 2.52 - 2.87 (C*H*$_2$,

20 H, m) and 3.24 (C*H*$_2$COOH, 2 H, s) ppm. ^{13}C NMR: δ 38.89 (NCH$_2$CH$_2$NH$_2$), 52.29 (NCH$_2$ ring), 52.79 (NCH$_2$ ring), 53.19 (NCH$_2$ ring), 60.22 (NCH$_2$CH$_2$NH$_2$) 62.59 (*C*H$_2$COOH), 179.33 (*C*OOH) ppm.

5.4.6 Synthesis of 1-(2-hydroxyethyl)-4,7-*bis*(2-aminoethyl)-1,4,7-triazacyclononane (HL^4)

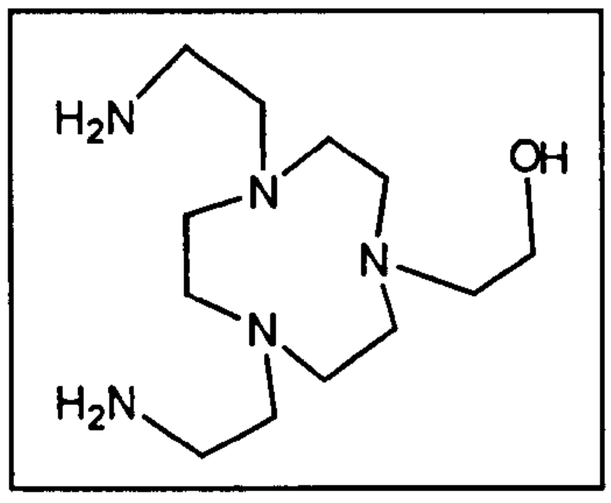

2-Bromoethanol (107 mg, 0.836 mmol) in EtOH (5 cm^3) was added dropwise to a suspension of (**9**) (287.2 mg, 0.418 mmol) and K_2CO_3 (0.7 g, 5.1 mmol) in EtOH (50 cm^3). This mixture was heated to 50 °C and stirred for 16 h. The solvent was then removed and the resulting oil was taken up with $CHCl_3$ and filtered. The yellow oil obtained after evaporation was dissolved in HCl 0.01 M and stirred overnight at room temperature. Filtration and removal of the solvent on a rotary evaporator yielded an orange solid which was recrystallised from MeOH/Et$_2$O. The pale yellow solid obtained was filtered and dried *in vacuo*. The *tris*-hydrochloric salt of 1-(hydroxyethyl)-4,7-*bis*(2-aminoethyl)-1,4,7-triazacyclononane was obtained (HL^4·3HCl·H$_2$O). (217.2 mg, 0.59 mmol, yield 70.6%). ^{1}H NMR: δ (D$_2$O, 298 K, 300 MHz) 2.78 (C*H*$_2$ ring, 4H, s) 2.95-3.08 (NC*H*$_2$ arms and ring, 8 H, m), 3.17 (C*H*$_2$NH$_3^+$, 4 H, t, J = 6.98 Hz), 3.34 (NC*H*$_2$ ring, 4 H, t, J = 5.84 Hz), 3.40 (NC*H*$_2$CH$_2$OH, 2 H, t, J = 5.10 Hz) and 3.87 (C*H*$_2$OH, 2 H, t, J = 5.10 Hz) ppm. ^{13}C NMR: δ 36.19 (NCH$_2$CH$_2$NH$_2$), 46.26 (NCH$_2$ ring), 49.57 (NCH$_2$ ring), 51.18 (NCH$_2$ ring), 52.45 (NCH$_2$CH$_2$NH$_2$) 54.94 (CH$_2$CH$_2$OH) and 57.06 (CH$_2$OH) ppm. FAB mass spectrum (Glycerol/H$_2$O/MeOH matrix) m/z = 260 [*M*+ H$^+$]. Elemental analysis: found (calc. for C$_{12}$H$_{32}$Cl$_3$N$_5$O·H$_2$O): C, 37.10 (37.26); H, 8,76 (8.86); N, 18.02% (18.11%).

The free amine HL^4 was obtained by passing a water solution of HL^4·3HCl through a Dowex 1x8-50 column previously activated with a solution 1M of NaOH.

Removal of the solvent from the collected water solution afforded a slightly yellow oil (142.7 mg, 0.55 mmol, yield 92.3%). ^{1}H NMR: δ ($CDCl_3$, 298 K, 300 MHz) 2.55 - 2.74 (NC*H*$_2$ arms and ring, 16 H, m) and 3.55 (C*H*$_2$OH, 2 H, t, J = 5.12 Hz) ppm. ^{13}C NMR: δ 40.12 ($NCH_2CH_2NH_2$), 56.14 (NCH_2 ring), 56.61 (NCH_2 ring), 57.95 (NCH_2 ring), 58.12 ($NCH_2CH_2NH_2$), 59.68 (CH_2CH_2OH) and 62.59 (CH_2OH) ppm.

5.4.7 Synthesis of [Y(L^{2a})X] (X = Cl$^-$, $CH_3CO_2^-$, NO_3^-)

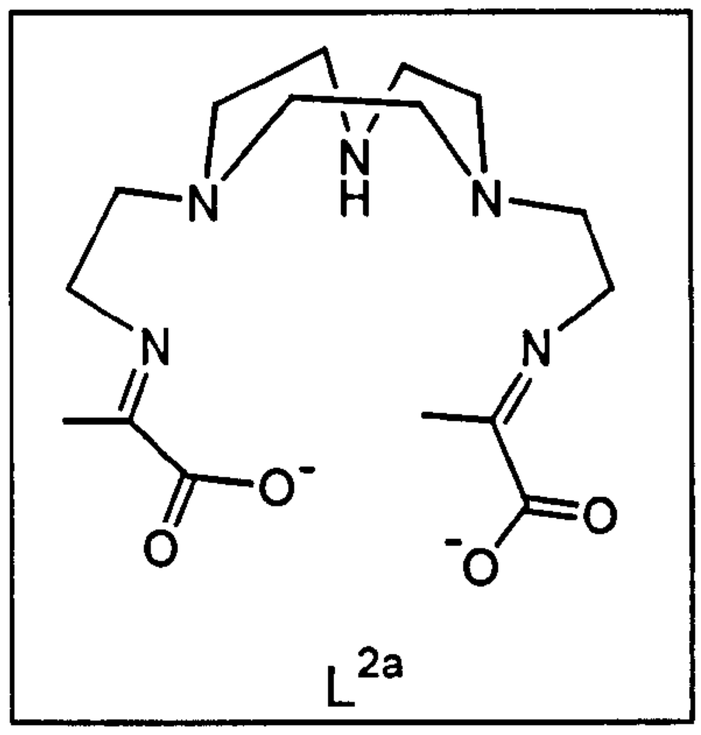

A solution of 4,7-*bis*(2-aminoethyl)-1,4,7-triazacyclononane (L^2) (20.0 mg, 0.085 mmol) in MeOH (5 cm^3) was added dropwise to a solution of sodium pyruvate (18.8 mg, 0.170 mmol) and $YCl_3 \cdot 6H_2O$ (25.8 mg, 0.085 mmol) in MeOH (25 cm^3). The resulting solution was heated under reflux for 2h. After cooling, the solvent volume was reduced, Et_2O was added and a white solid was obtained. The solid was filtered off and dried *in vacuo*. (44.1 mg, 0.072 mmol, yield 84.7%). Mass spectrum (FAB, 3-NOBA matrix): m/z = 442 (*M*$^+$ $[C_{16}H_{27}N_5O_4Y]^+$). Elemental analysis: found (calc. for $C_{16}H_{27}N_5O_4YCl \cdot 2NaCl \cdot H_2O$): C, 31.81 (31.37); H, 4.96 (4.77); N, 11.68 % (11.43 %) (KBr disk), cm^{-1}: 2964w, 1636s ($\nu_{C=N,\ C=O}$), 1384m, 1262m, 1207w, 1098m, 1026m, 803m.

[Y(L^{2a})(NO_3)]. The same procedure as for [Y(L^{2a})Cl]·2NaCl·H_2O was used. 30.6 mg (0.085 mmol) of $Y(NO_3)_3 \cdot 5H_2O$ were used. (40.2 mg, 0.055 mmol, yield 64.7%). Mass spectrum (FAB, 3-NOBA matrix): m/z = 442 (*M*$^+$ $[C_{16}H_{27}N_5O_4Y]^+$). IR (KBr disk), cm^{-1}: 2954w, 1634s ($\nu_{C=N,\ C=O}$), 1381m, 1262m, 1197w, 1092m, 803m.

[Y(L^{2a})(CH_3CO_2)]·3NaCl·H_2O. CH_3COONa (7.0 mg, 0.085 mmol) was added to a solution of sodium pyruvate and $YCl_3 \cdot 6H_2O$ and the reaction was carried out as for [Y(L^{2a})Cl]·2NaCl·H_2O. (49.3 mg, 0.071 mmol, yield 83.5%) Mass spectrum (FAB, 3-NOBA matrix): m/z = 524 (*M*$^+$ $[C_{18}H_{30}N_5O_6Y + Na^+]$, 501 [*M*$^+$ - Na$^+$] and 442 [*M*$^+$ -

CH_3COONa]). Elemental analysis: found (calc. for $C_{18}H_{30}N_5O_6Y \cdot 3NaCl \cdot H_2O$): C, 31.52 (31.12); H, 4.37 (4.64); N, 10.33% (10.08%). IR (KBr disk), cm^{-1}: 2958w, 2925m, 2853w, 1634s ($\nu_{C=N, C=O}$), 1558m, 1456m, 1262m, 1206w, 1041m, 803m.

5.4.8 Synthesis of $[Ln(L^{2a})Cl] \cdot 2NaCl \cdot H_2O$ (Ln^{III} = Eu^{III} and Yb^{III})

4,7-*bis*(2-Aminoethyl)-1,4,7-triazacyclononane (L^2) (30.0 mg, 0.128 mmol) dissolved in MeOH (5 cm^3) was added to a solution of sodium pyruvate (28.2 mg, 0.256 mmol) and $LnCl_3 \cdot 6H_2O$ (1 molar equivalent) in MeOH (30 cm^3). The resulting solution was heated under reflux for 2h. After cooling, the solvent volume was reduced, Et_2O was added and a white solid was obtained. The solid was filtered off and dried *in vacuo*.

$[Eu(L^{2a})Cl] \cdot 2NaCl \cdot 2H_2O$. (71.5 mg, 0.103 mmol, yield 80.5%) Mass spectrum (FAB, 3-NOBA matrix) m/z = 506 (M^+ $[C_{16}H_{27}N_5O_4Eu]^+$). Elemental analysis: found (calc. for $C_{18}H_{30}N_5O_6Eu \cdot 2NaCl \cdot 2H_2O$): C, 28.06 (27.70); H, 4.76 (4.50); N, 10.41% (10.09%). IR (KBr disk), cm^{-1}: 2919w, 2858w, 1637s ($\nu_{C=N, C=O}$), 1383m, 1263w, 1204m, 1109m, 963w, 805m, 666m.

$[Yb(L^{2a})Cl] \cdot 2NaCl \cdot H_2O$. (63.4 mg, 0.091 mmol, yield 71.1%) Mass spectrum (FAB, 3-NOBA matrix) m/z = 527 (M^+ $[C_{16}H_{27}N_5O_4Yb]^+$). Elemental analysis: found (calc. for $C_{18}H_{30}N_5O_6Yb \cdot 2NaCl \cdot H_2O$): C, 27.81 (27.58); H, 4.36 (4.19); N, 9.81% (10.05%). IR (KBr disk), cm^{-1}: 2961w, 2922w, 1642s ($\nu_{C=N, C=O}$), 1464w, 1384m, 1260s, 1228m, 1170m, 1032s, 642s.

5.4.9 Synthesis of $[Ln(L^{2a})(CH_3CO_2)] \cdot 3NaCl \cdot H_2O$ (Ln^{III} = Gd^{III}, Dy^{III} and La^{III})

4,7-*bis*(2-Aminoethyl)-1,4,7-triazacyclononane (L^2) (30.0 mg, 0.128 mmol) dissolved in MeOH (5 cm^3) was added to a solution of sodium pyruvate (28.2 mg, 0.256 mmol), $LnCl_3 \cdot 6H_2O$ (1 molar equivalent) and CH_3COONa (10.5 mg, 0.128 mmol) in MeOH (30 cm^3). The resulting colourless solution was heated under

reflux for 2h. After cooling, the solvent volume was reduced, Et_2O was added and a white solid was obtained. The solid was filtered off and dried *in vacuo*.

[Gd(L^{2a})(CH$_3$CO$_2$)]·3NaCl·H$_2$O. (76.3 mg, 0.10 mmol, yield 78.3%) Mass spectrum (FAB, 3-NOBA matrix) m/z = 511 (M^+ $[C_{16}H_{27}N_5O_4Gd]^+$). Elemental analysis: found (calc. for $C_{18}H_{30}N_5O_6Gd·3NaCl·H_2O$): C, 28.58 (28.33); H, 4.11 (4.23); N, 9.04% (9.18%). IR (KBr disk), cm^{-1}: 2963w, 2922w, 2852w, 1635s ($\nu_{C=N,\ C=O}$), 1384m, 1261m, 1205s, 1039m, 802m. Single crystals suitable for X-ray structural analysis were obtained from a Et_2O/MeOH (10/1) solution of the complex at room temperature.

[Dy(L^{2a})(CH$_3$CO$_2$)]·3NaCl·H$_2$O. (74.5 mg, 0.097 mmol, yield 75.6%) Mass spectrum (FAB, 3-NOBA matrix) m/z = 517 (M^+ $[C_{16}H_{27}N_5O_4Dy]^+$). Elemental analysis: found (calc. for $C_{18}H_{30}N_5O_6Dy·3NaCl·H_2O$): C, 28.01 (28.14); H, 4.40 (4.20); N, 9.34% (9.12%). IR (KBr disk), cm^{-1}: 2923w, 2861w, 1636s ($\nu_{C=N,\ C=O}$), 1384s, 1263s, 1207w, 1162m, 935s, 808m, 651m.

[La(L^{2a})(CH$_3$CO$_2$)]. (72.5 mg, 0.095 mmol, yield 74.3%) Mass spectrum (FAB, 3-NOBA matrix) m/z = 492 (M^+ $[C_{16}H_{27}N_5O_4La]^+$). IR (KBr disk), cm^{-1}: 2961w, 2824w, 1636s ($\nu_{C=N,\ C=O}$), 1384s, 1262s, 1229w, 1172m, 1033s, 808m, 641m.

5.4.10 Synthesis of [Ln(L^{2b})(CH$_3$CO$_2$)]·3NaCl·2H$_2$O (Ln^{III} = Y^{III}, Gd^{III} and La^{III})

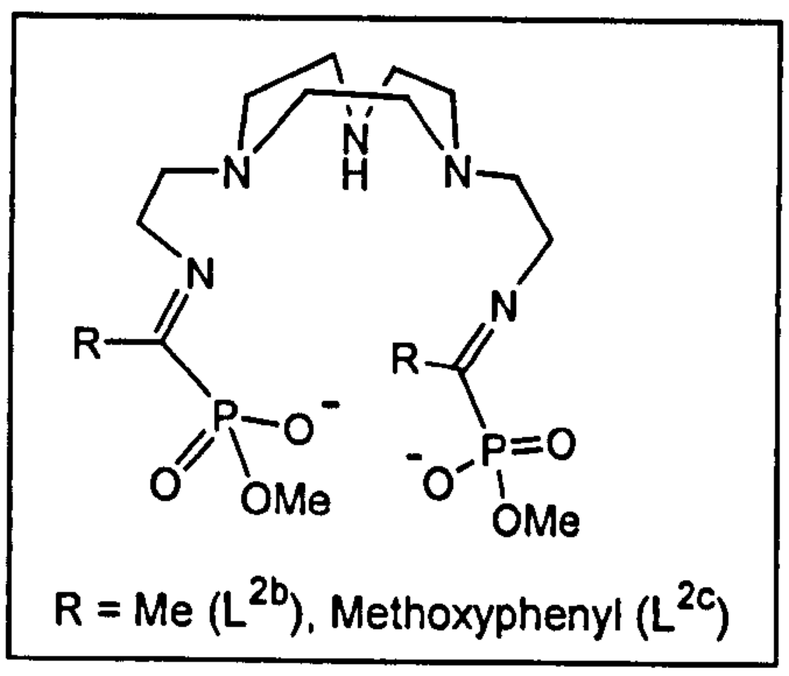

R = Me (L^{2b}), Methoxyphenyl (L^{2c})

Methyl sodium acetylphosphonate (23.8 mg, 0.15 mmol), the appropriate Ln^{III} salt (0.075 mmol) and CH_3COONa (6.5 mg, 0.075 mmol) were heated in MeOH (30 cm^3) and a solution of 4,7-*bis*(2-aminoethyl)-1,4,7-triazacyclononane (L^2) (16.0 mg, 0.075 mmol) in MeOH (5 cm^3) was added dropwise before reaching the reflux point. The colourless solution was refluxed for 2h. After cooling, the solvent volume was reduced, Et_2O was added until a white solid precipitated. The solid was filtered and dried under reduced pressure.

[Y(L^{2b})(CH$_3$CO$_2$)]·3NaCl·2H$_2$O. (47.1 mg, 0.058 mmol, yield 77.3%) Mass spectrum (FAB, 3-NOBA matrix) m/z = 542 (M^+ [$C_{16}H_{33}N_5O_6P_2Y$]$^+$). Elemental analysis: found (calc for $C_{18}H_{36}N_5O_8P_2Y$·3NaCl·2H$_2$O): C, 26.09 (26.60); H, 4.61 (4.96); N, 8.78% (8.62%). IR (KBr disk), cm^{-1}: 2956m, 1633m ($\nu_{C=N,\ C=O}$), 1379s, 1192s, 1049s.

[Gd(L^{2b})(CH$_3$CO$_2$)]·3NaCl·2H$_2$O. (53.7 mg, 0.061 mmol, yield 81.0%) Mass spectrum (FAB, 3-NOBA matrix) m/z = 611 (M^+ [$C_{16}H_{33}N_5O_6P_2Gd$]$^+$). Elemental analysis: found (calc for $C_{18}H_{36}N_5O_8P_2Gd$·3NaCl·H$_2$O): C, 25.32 (25.05); H, 4.25 (4.44); N, 8.38% (8.11%). IR (KBr disk), cm^{-1}: 2954m, 1635m ($\nu_{C=N,\ C=O}$), 1384s, 1193s, 1048s.

[La(L^{2b})(CH$_3$CO$_2$)]·3NaCl·3H$_2$O]. (48.4 mg, 0.055 mmol, yield 73.5%) Mass spectrum (FAB, 3-NOBA matrix) m/z = 592 (M^+ [$C_{16}H_{33}N_5O_6P_2La$]$^+$). Elemental analysis: found (calc for $C_{18}H_{36}N_5O_8P_2La$·3NaCl·3H$_2$O): C, 25.22 (24.55); H, 4.99 (4.81); N, 7.58% (7.95%). IR (KBr disk), cm^{-1}: 2954m, 1631m ($\nu_{C=N,\ C=O}$), 1383s, 1195s, 1053s.

5.4.11 Synthesis of [Ln(L^{2c})(CH$_3$CO$_2$)]·3NaCl·2H$_2$O (Ln^{III} = Y^{III}, Eu^{III}, Gd^{III}, La^{III})

Methyl sodium 4-methoxybenzoylphosphonate (37.3 mg, 0.15 mmol), the appropriate Ln^{III} salt (0.075 mmol) and CH$_3$COONa (6.5 mg, 0.075 mmol) were heated in MeOH (30 cm^3) and, before reaching the reflux point, a solution of 4,7-*bis* (2-aminoethyl)-1,4,7-triazacyclononane (L^2) (16.0 mg, 0.075 mmol) in MeOH (5 cm^3) was added dropwise. The colourless solution was refluxed for 2h. After cooling, the solvent volume was reduced, Et$_2$O was added and a white solid was obtained. The solid was filtered and dried *in vacuo*.

[Y(L^{2c})(CH$_3$CO$_2$)]·3NaCl·2H$_2$O. (64.8 mg, 0.065 mmol, yield 87.1%) Mass spectrum (FAB, 3-NOBA matrix) m/z = 726 (M^+ [$C_{28}H_{41}N_5O_8P_2Y$]$^+$). Elemental analysis: found (calc for $C_{30}H_{44}N_5O_{10}P_2Y$·3NaCl·2H$_2$O): C, 35.82 (36.14); H, 5.08

(4.85); N, 7.38% (7.03%). IR (KBr disk), cm^{-1}: 2954w, 2861w, 1611m ($\nu_{C=N,\ C=O}$), 1414m, 1383s, 1260s, 1195s, 1053m, 800m.

[Eu(L^{2c})(CH$_3$CO$_2$)]·3NaCl·2H$_2$O. (47.2 mg, 0.061 mmol, yield 71.0%) Mass spectrum (FAB, Glycerol/MeOH/H$_2$O matrix) m/z = 808 (M^+ [$C_{28}H_{41}N_5O_8P_2Eu$ + H_2O]$^+$) and 790 ([$C_{28}H_{41}N_5O_8P_2Eu$]$^+$). Elemental analysis: found (calc for $C_{30}H_{44}N_5O_{10}P_2Y$·3NaCl·2H$_2$O): C, 34.38 (33.99); H, 4.96 (4.56); N, 6.45% (6.61%). IR (KBr disk), cm^{-1}: 2949m, 2848m, 1605s ($\nu_{C=N,\ C=O}$), 1509s, 1462m, 1256s, 1208s, 1182s, 1056s, 774m, 580m.

[Gd(L^{2c})(CH$_3$CO$_2$)]·3NaCl·H$_2$O. (65.0 mg, 0.060 mmol, yield 79.7%) Mass spectrum (FAB, Glycerol/MeOH/H$_2$O matrix) m/z = 813 (M^+ [$C_{28}H_{41}N_5O_8P_2Gd$ + H_2O]$^+$) and 794 ([$C_{28}H_{41}N_5O_8P_2Gd$]$^+$). Elemental analysis: found (calc for $C_{30}H_{44}N_5O_{10}P_2Gd$·3NaCl·H$_2$O): C, 33.84 (34.41); H, 4.11 (4.43); N, 6.97% (6.69%). IR (KBr disk), cm^{-1}: 2999w, 2853w, 1617s ($\nu_{C=N,\ C=O}$), 1465m, 1208m, 1175s, 1093s.

[La(L^{2c})(CH$_3$CO$_2$)]·3NaCl·2H$_2$O. Obtained 57.6 mg, 0.056 mmol, yield 75.0%. Mass spectrum (FAB, 3-NOBA matrix) m/z = 776 (M^+ [$C_{28}H_{41}N_5O_8P_2La$]$^+$). IR (KBr disk), cm^{-1}: 2951w, 2874w, 1609m ($\nu_{C=N,\ C=O}$), 1465m, 1254s, 1195s, 1081m, 803w.

5.4.12 Synthesis of [Y(L^{3a})], [Gd(L^{3a})] and [Dy(L^{3a})]

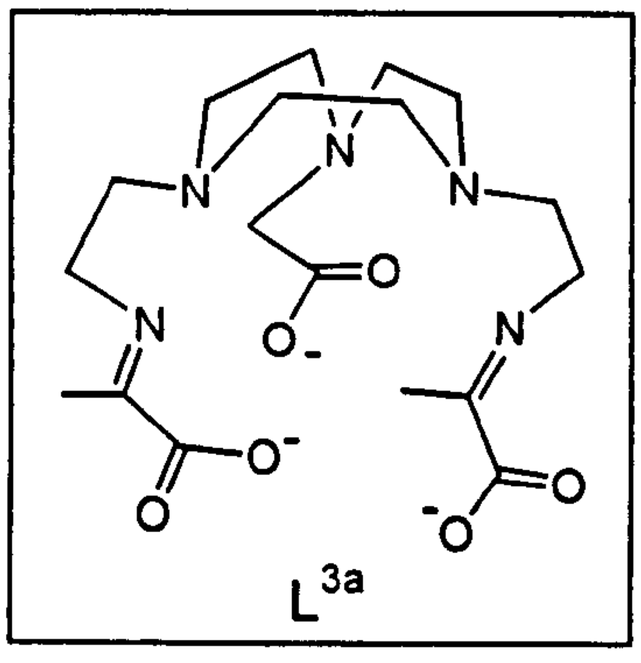

A solution of the lithium salt of 1-(carboxymethyl)-4,7-*bis*(2-aminoethyl)-1,4,7-triazacyclononane [Li(L^3)] (25.1 mg, 0.09 mmol) in MeOH (5 cm^3) was added dropwise to a warm solution of sodium pyruvate (19.8 mg, 0.18 mmol) and the appropriate $LnCl_3$ (1 molar equivalent) in MeOH (30 cm^3). The resulting colourless solution was heated under reflux for 2h. Once the reflux started the solution

became cloudy. After cooling, the solution was filtered through Celite, then the solvent volume was reduced, Et_2O was added and a white solid was obtained. The solid was filtered off, washed with Et_2O and dried *in vacuo*.

[Y(L^{3a})]·2NaCl·LiCl·2H$_2$O. (28.2 mg, 0.040 mmol, yield 44.3%) Mass spectrum (Electrospray) m/z = 522 (M^+ [$C_{18}H_{28}N_5O_6Y$ + Na^+]). Elemental analysis: found (calc. for $C_{18}H_{28}N_5O_6Y$·2NaCl·LiCl·2H_2O): C, 31.61 (31.12); H, 4.70 (4.64); N, 9.44% (10.08%). IR (KBr disk), cm^{-1}: 2960w, 2933w, 2856w, 1618s ($\nu_{C=N,\ C=O}$), 1384s, 1205w, 1122w, 1039w, 804w.

[[Gd(L^{3a})]·2NaCl·LiCl·4H$_2$O. (27.9 mg, 0.035 mmol, yield 38.8%) Mass spectrum (Electrospray) m/z = 649 (M^+ [$C_{18}H_{28}N_5O_6Gd$ + NaCl + Na^+] and 591 [$C_{18}H_{28}N_5O_6Gd$ + Na^+]) Elemental analysis: found (calc. for $C_{18}H_{28}N_5O_6Gd$·2NaCl·LiCl·4H_2O): C, 27.48 (27.06); H, 4.21 (4.54); N, 8.44% (8.76%). IR (KBr disk), cm^{-1}: 2960w, 2914w, 2863w, 1624s ($\nu_{C=N,\ C=O}$), 1415m, 1383m, 1260m, 1204s, 1096m, 800m.

[Dy(L^{3a})]·2NaCl·LiCl·3H$_2$O. (33.8 mg, 0.043 mmol, yield 47.8%) Mass spectrum (Electrospray) m/z = 597 (M^+ [$C_{18}H_{28}N_5O_6Dy$ + Na^+] and 575 [$C_{18}H_{28}N_5O_6Dy$ + H^+]). Elemental analysis: found (calc. for $C_{18}H_{28}N_5O_6Dy$·2NaCl·LiCl·3H_2O): C, 27.01 (27.50); H, 4.40 (4.36); N, 9.34% (8.91%). IR (KBr disk), cm^{-1}: 2954w, 2864w, 1635s ($\nu_{C=N,\ C=O}$), 1381s, 1265s, 1203w, 1174m, 1020s, 808m.

5.4.13 Synthesis of [Y(L^{3b})] and [Gd(L^{3b})]

A solution of the lithium salt of 1-(carboxymethyl)-4,7-*bis*(2-aminoethyl)-1,4,7-triazacyclononane [Li(L^3)] (25.1 mg, 0.09 mmol) in MeOH (5 cm^3) was added dropwise to a warm solution of methyl sodium acetylphosphonate (28.6 mg, 0.18 mmol) and $LnCl_3$·xH_2O (1 molar equivalent) in MeOH (20 cm^3). The resulting colourless solution was heated under reflux for 2h, becoming cloudy once the reflux started. After cooling, the solution was filtered through Celite, then the

solvent volume was reduced, Et_2O was added and a white solid was obtained. The solid was filtered off, washed with Et_2O and dried *in vacuo*.

[Y(L^{3b})]·2NaCl·LiCl·H$_2$O. (29.4 mg, 0.037 mmol, yield 41.2%) Mass spectrum (Electrospray) m/z = 622 (M^+ [$C_{18}H_{34}N_5O_8Y$ + Na^+]). Elemental analysis: found (calc. for $C_{18}H_{34}N_5O_8Y$·2NaCl·LiCl·H_2O): C, 29.01 (30.25); H, 4.40 (5.08); N, 10.24% (9.80%). IR (KBr disk), cm^{-1}: 2960w, 2848w, 1634s ($\nu_{C=N,\ C=O}$), 1404w, 1383s, 1260s, 1168w, 1081s, 794s.

[[Gd(L^{3b})]·2NaCl·LiCl·3H$_2$O. (31.7 mg, 0.036 mmol, yield 39.8%) Mass spectrum (Electrospray) m/z = 691 (M^+ [$C_{18}H_{34}N_5O_8Gd$ + Na^+]). Elemental analysis: found (calc. for $C_{18}H_{30}N_5O_6Gd$·2NaCl·LiCl·3H_2O): C, 26.58 (26.40); H, 5.11 (4.92); N, 9.04% (8.55%). IR (KBr disk), cm^{-1}: 2963w, 2912w, 2850w, 1635s ($\nu_{C=N,\ C=O}$), 1384m, 1260m, 1205s, 1085m, 802m.

5.4.14 Synthesis of [Y(L^{4a})], [Gd(L^{4a})] and [Dy(L^{4a})]

1-(2-hydroxyethyl)-4,7-*bis*(2-aminoethyl)-1,4,7-triazacyclononane (HL^4) (25.0 mg, 0.096 mmol), sodium pyruvate (21.2 mg, 0.193 mmol) and the appropriate Ln^{III} trichloride (1 molar equivalent) were heated under reflux in MeOH (30 cm^3) for 2h. After cooling, the solvent volume was reduced, Et_2O was added and a slightly yellow solid was obtained. The solid was filtered off and dried *in vacuo*.

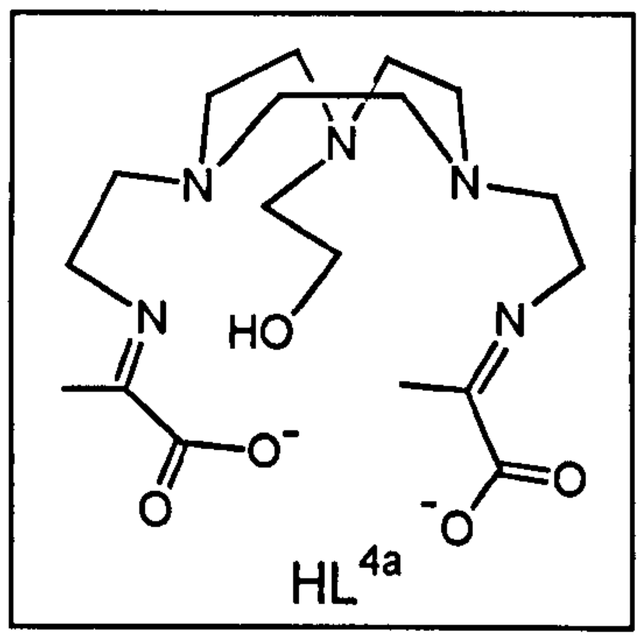

[Y(L^{4a})]·2NaCl·2H$_2$O. (49.9 mg, 0.078 mmol, yield 81.0%) Mass spectrum (Electrospray) m/z = 508 (M^+ [$C_{18}H_{30}N_5O_5Y$ + Na^+]) and 486 (M^+ [$C_{18}H_{30}N_5O_5Y$ + H^+). Elemental analysis: found (calc. for $C_{18}H_{30}N_5O_5Y$·2NaCl·2H_2O): C, 34.01 (33.87); H, 5.40 (5.37); N, 10.44% (10.97%). IR (KBr disk), cm^{-1}: 2919w, 2853w, 1634s ($\nu_{C=N,\ C=O}$), 1381m, 1261m, 1210w, 1060m, 798m.

[[Gd(L^{4a})]·2NaCl·2H$_2$O. (50.3 mg, 0.073 mmol, yield 76.0%) Mass spectrum (Electrospray) m/z = 577 (M^+ [$C_{18}H_{30}N_5O_5Gd$ + Na^+]) and 555 (M^+ [$C_{18}H_{30}N_5O_5Gd$ + H^+]). Elemental analysis: found (calc. for $C_{18}H_{30}N_5O_5Gd·2NaCl·2H_2O$): C, 30.98 (30.60); H, 5.21 (4.85); N, 10.07% (9.91%). IR (KBr disk), cm^{-1}: 2956w, 2921w, 2851w, 1634s ($\nu_{C=N, C=O}$), 1388m, 1258m, 1204m, 1094m, 1029m, 800m.

[Dy(L^{4a})]·2NaCl·3/2H$_2$O. (53.6 mg, 0.076 mmol, yield 79.4%) Mass spectrum (Electrospray) m/z = 581 (M^+ [$C_{18}H_{30}N_5O_5Dy$ + Na^+]) and 561 (M^+ [$C_{18}H_{30}N_5O_5Dy$ + H^+]). Elemental analysis: found (calc. for $C_{18}H_{30}N_5O_5Dy·2NaCl·3/2H_2O$): C, 34.99 (34.78); H, 5.70 (5.35); N, 11.04% (11.27%). IR (KBr disk), cm^{-1}: 2961w, 2854w, 1636s ($\nu_{C=N, C=O}$), 1386s, 1256s, 1203w, 1102m, 1038s, 802m.

5.4.15 Synthesis of [Y(L^{4b})] and [Gd(L^{4b})]

1-(2-Hydroxyethyl)-4,7-*bis*(2-aminoethyl)-1,4,7-triazacyclononane (HL^4) (25.0 mg, 0.096 mmol), methyl sodium acetylphosphonate (30.5 mg, 0.193 mmol) and $LnCl_3·xH_2O$ (1 molar equivalent) were heated under reflux in MeOH (25 cm^3) for 2h. After cooling, the solvent volume was reduced, Et_2O was added and a slightly yellow-orange solid was obtained. The solid was filtered, washed with Et_2O and dried *in vacuo*.

[Y(L^{4b})]. (51.2 mg, 0.071 mmol, yield 74.1%) Mass spectrum (Electrospray) m/z = 608 (M^+ [$C_{18}H_{35}N_5O_7P_2Y$ + Na^+]) and 586 (M^+ [$C_{18}H_{35}N_5O_7P_2Y$ + H^+]). IR (KBr disk), cm^{-1}: 2960w, 2853w, 1639s ($\nu_{C=N, C=O}$), 1452w, 1378w, 1255s, 1188m, 1081s, 799s.

[[Gd(L^{4b})]·2NaCl·1/2H$_2$O. (58.5 mg, 0. 075 mmol, yield 78.2%) Mass spectrum (Electrospray) m/z = 677 (M^+ [$C_{18}H_{35}N_5O_7P_2Gd$ + Na^+]) and 655 (M^+ [$C_{18}H_{35}N_5O_7P_2Gd$ + H^+]). Elemental analysis: found (calc. for $C_{18}H_{35}N_5O_7P_2Gd·2NaCl·1/2H_2O$): C, 30.48 (30.89); H, 5.41 (5.18); N, 10.24% (10.01%). IR (KBr disk), cm^{-1}: 2955w, 2914w, 2848w, 1634s ($\nu_{C=N, C=O}$), 1378m, 1258m, 1200s, 1045s, 794s.

5.4.16 Hydrolysis experiments

Table 5.7 The proportion of [Y(L^{2a})(CH_3CO_2)], [Y(L^{2b})(CH_3CO_2)] and [Y(L^{4a})] remaining unhydrolysed ([Y(L^{xy})]$_t$/[Y(L^{xy})]$_{t=0}$) at time intervals (^{1}H NMR in D_2O).

Time (h)	[Y(L^{2a})(CH_3CO_2)]	[Y(L^{2b})(CH_3CO_2)]	[Y(L^{4a})]
0	1	1	1
1	0.981	0.980	
2	0.946		0.850
4		0.941	
5	0.915		0.780
6		0.929	
8	0.873		
15			0.609
17			0.574
21.1			0.518
22	0.748		
23		0.876	
24	0.719		
26	0.706		
27.6			0.485
29	0.678	0.843	
33	0.639		
36	0.616		
36.1			0.459
42			0.434
45	0.558		
46		0.814	0.407
50	0.525		
55	0.487		
58	0.467		
64.6		0.768	
70	0.384		
74			0.356
82.6		0.714	
87			0.323
102	0.224		
103		0.669	
124		0.616	
150	0.120		
163.7		0.520	
187			0.186
194.5		0.470	
220		0.425	
320		0.296	

$[Y(L^{2a})(CH_3CO_2)]\cdot 3NaCl\cdot H_2O$ (4.8 mg), $[Y(L^{2b})(CH_3CO_2)]\cdot 3NaCl\cdot 2H_2O$ (5.6 mg), $[Y(L^{2c})(CH_3CO_2)]\cdot 3NaCl\cdot 2H_2O$ (5.2 mg), $[Y(L^{3a})]\cdot 2NaCl\cdot LiCl\cdot H_2O$ (6.0 mg) and $[Y(L^{4a})]\cdot 2NaCl\cdot 2H_2O$ (5.8 mg) were dissolved in D_2O (0.6 cm^3) and the resulting clear solutions were transferred to NMR tubes. ^{1}H NMR spectra of each sample were acquired at time intervals t(h) and the proportion of unhydrolysed complex remaining was calculated using the relative heights of peaks due to complex and hydrolysis product. Quantitative measurements of the proportion of complex remaining unhydrolysed ($[Y(L^{xy})]_t/[Y(L^{xy})]_{t=0}$) could be carried out only for $[Y(L^{2a})(CH_3CO_2)]\cdot 3NaCl\cdot H_2O$, $[Y(L^{2b})(CH_3CO_2)]\cdot 3NaCl\cdot 2H_2O$ and $[Y(L^{4a})]\cdot 2NaCl\cdot 2H_2O$. The results are shown in Table 5.7 and are plotted graphically in Figure 5.28 (Section 5.3.6).

5.4.17 Relaxivity of Gd^{III} complexes

Samples of $[Gd(L^{2a})(CH_3CO_2)]\cdot 3NaCl\cdot H_2O$, $[Gd(L^{2b})(CH_3CO_2)]\cdot 3NaCl\cdot 2H_2O$, $[Gd(L^{2c})(CH_3CO_2)]\cdot 3NaCl\cdot H_2O$, $[Gd(L^{3a})]\cdot 2NaCl\cdot LiCl\cdot 4H_2O$, $[Gd(L^{3b})]\cdot 2NaCl\cdot LiCl\cdot 3H_2O$, $[Gd(L^{4a})]\cdot 2NaCl\cdot 2H_2O$ and of $[Gd(L^{4b})]\cdot 2NaCl\cdot 1/2H_2O$ were weighed (Tables 5.8-5.14) and dissolved in 0.70 cm^3 of D_2O before transfer to NMR tubes. The transverse relaxation times (T_1) of the HDO peak at 4.707 ppm were measured using a 180-τ-90 pulse sequence at 37°C using a Bruker 300 MHz NMR spectrometer. All the complexes were found to hydrolyse slowly in D_2O (Section 5.3.5), but the delay between dissolving the sample in D_2O and completing the T_1 measurement was less than 15 minutes, a time interval over which hydrolysis of the complex is thought to be minimal. The results are reported in Tables 5.14-5.20.

Plots of T_1^{-1} (s^{-1}) against concentration of $[Gd(L^{2a})(CH_3CO_2)]$, $[Gd(L^{2b})(CH_3CO_2)]$, $[Gd(L^{2c})(CH_3CO_2)]$, $[Gd(L^{3a})]$, $[Gd(L^{3b})]$, $[Gd(L^{4a})]$ and of $[Gd(L^{4b})]$ (mM) give appropriate straight lines (Figure 5.31-5.37). The intercept with the y axis is again (see Section 3.5.7) the relaxation rate (T_1^{-1} = 0.058 s^{-1}) of the

HDO peak in the absence of the paramagnetic metal complex (concentration = 0). The relaxivities for the complexes were calculated from the gradient of the respective graph and are reported in Table 5.8-5.14.

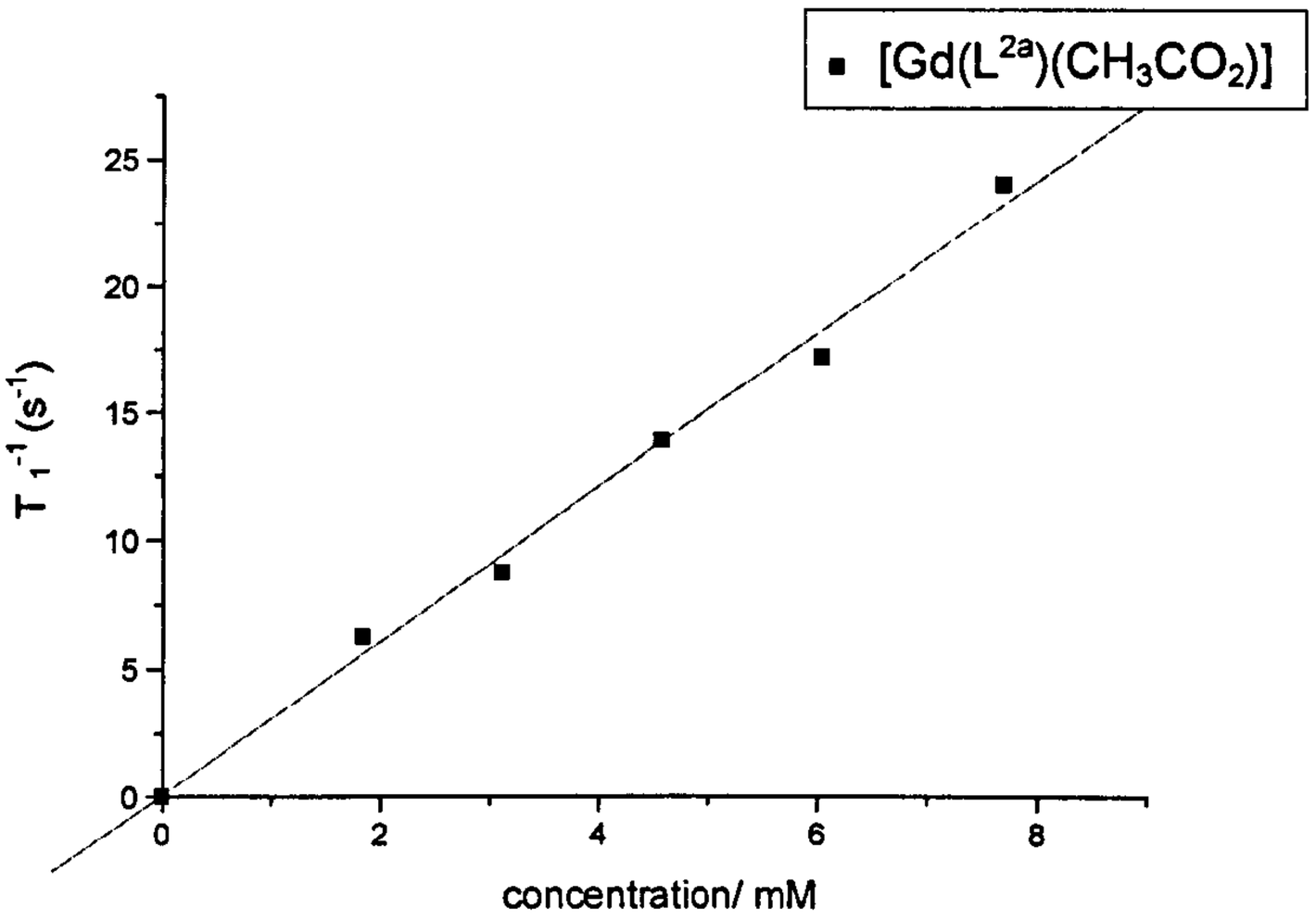

Figure 5.31 Plot of variation (T_1^{-1}) of the HDO peak with the concentration of $[Gd(L^{2a})(CH_3CO_2)]$ (correlation coefficient = 0.996).

Table 5.8 Variation of T_1^{-1} (s^{-1}) of the HDO peak with concentration of $[Gd(L^{2a})]$.

Mass of $[Gd(L^{2a})(CH_3CO_2)]\cdot 3NaCl\cdot 2H_2O$ (mg)	Concentration of $[Gd(L^{2a})(CH_3CO_2)]$ (mM)	T_1 (s)	T_1^{-1} (s^{-1})
1.0	1.83	0.1580	6.33
1.7	3.11	0.1139	8.78
2.5	4.57	0.0718	13.92
3.3	6.03	0.0580	17.23
4.2	7.68	0.0415	24.08

Table 5.9 Variation of T_1^{-1} (s^{-1}) of the HDO peak with concentration of [Gd(L^{2b})].

Mass of [Gd(L^{2b})(CH_3CO_2)]·3NaCl·H_2O (mg)	Concentration of [Gd(L^{2b})(CH_3CO_2)] (mM)	T_1 (s)	T_1^{-1} (s^{-1})
0.75	1.24	0.2015	4.96
1.5	2.48	0.0902	11.09
2.3	3.81	0.0668	14.96
3.1	5.13	0.0493	20.30
3.9	6.45	0.0408	24.49

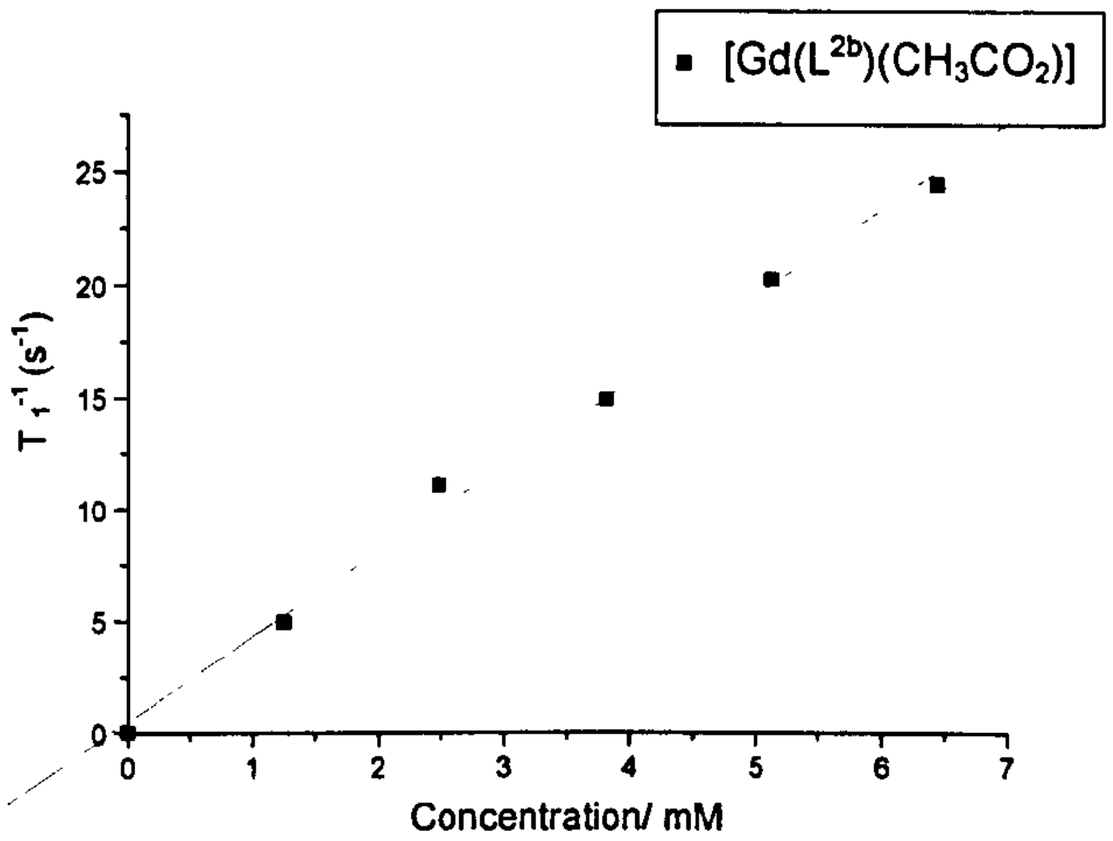

Figure 5.32 Plot of variation (T_1^{-1}) of the HDO peak with the concentration of [Gd(L^{2b})(CH_3CO_2)] (correlation coefficient = 0.998).

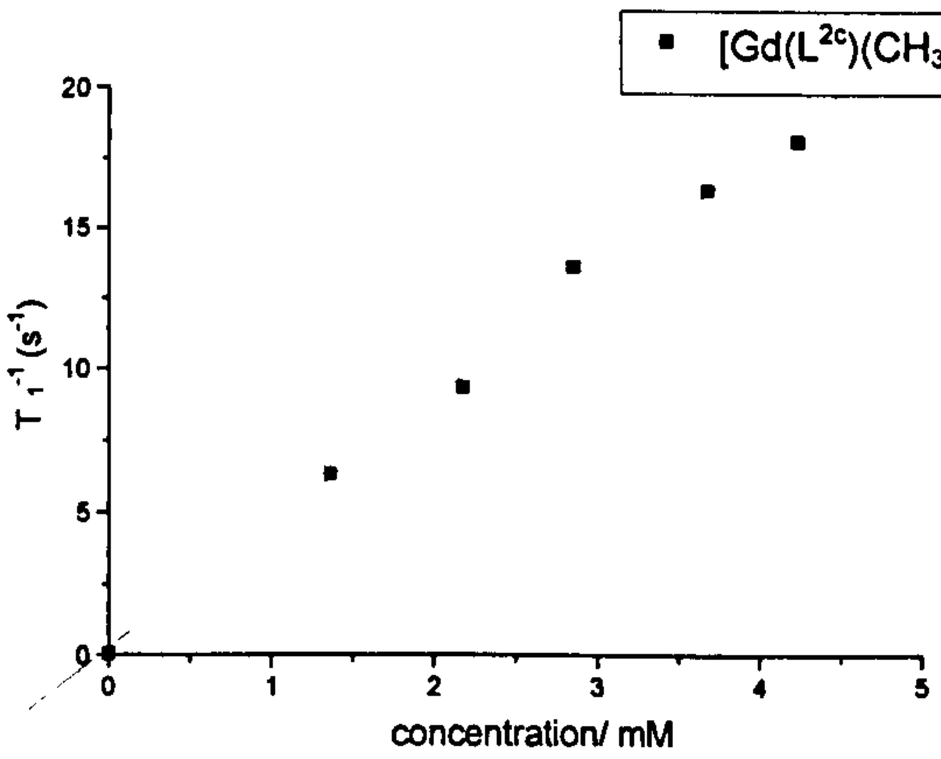

Figure 5.33 Plot of variation (T_1^{-1}) of the HDO peak with the concentration of [Gd(L^{2c})] (correlation coefficient = 0.997).

Table 5.10 Variation of T_1^{-1} (s^{-1}) of the HDO peak with concentration of [Gd(L^{2c})].

Mass of [Gd(L^{2c})(CH_3CO_2)]·3NaCl·H_2O (mg)	Concentration of [Gd(L^{2c})(CH_3CO_2)] (mM)	T_1 (s)	T_1^{-1} (s^{-1})
1.0	1.36	0.1576	6.34
1.6	2.18	0.1078	9.28
2.1	2.86	0.0738	13.55
2.7	3.68	0.0613	16.31
3.1	4.23	0.0555	18.02

Table 5.11 Variation of T_1^{-1} (s^{-1}) of the HDO peak with concentration of [Gd(L^{3a})].

Mass of [Gd(L^{3a})]·2NaCl·LiCl·$4H_2O$ (mg)	Concentration of [Gd(L^{3a})] (mM)	T_1 (s)	T_1^{-1} (s^{-1})
0.4	0.71	0.8922	1.12
1.0	1.79	0.5052	1.98
1.3	2.32	0.3762	2.66
1.5	2.68	0.3044	3.28
1.8	3.22	0.2754	3.63
2.2	3.93	0.2192	4.56

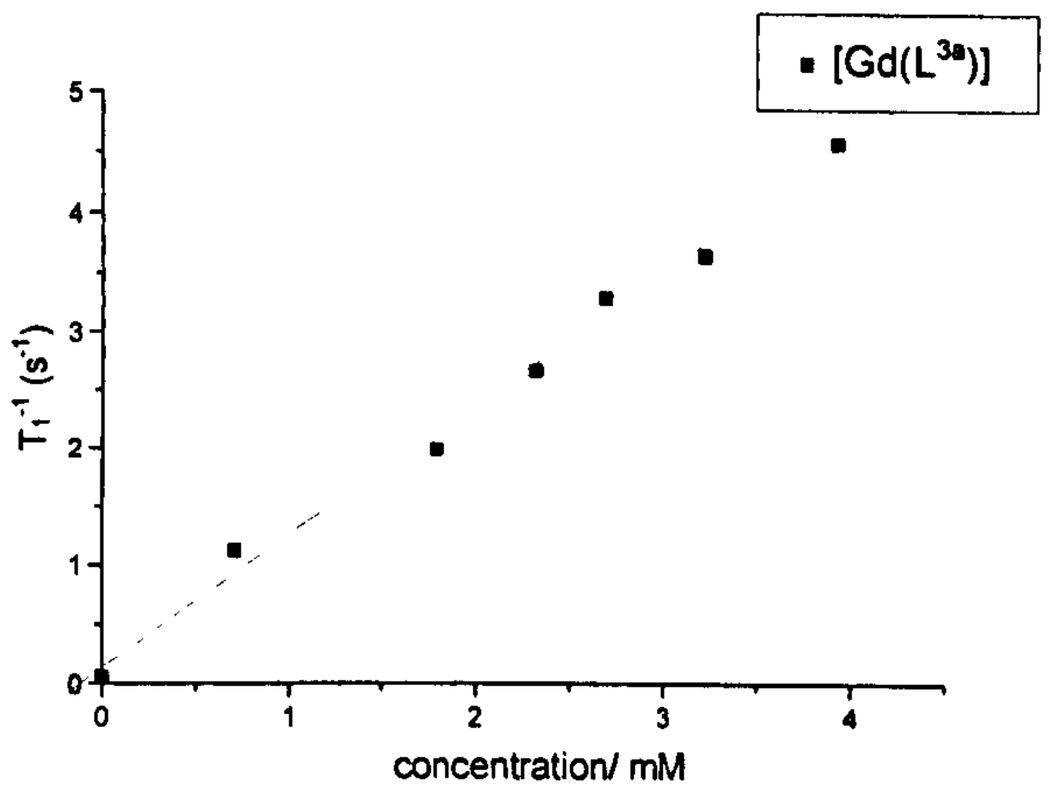

Figure 5.34 Plot of variation (T_1^{-1}) of the HDO peak with the concentration of [Gd(L^{3a})] (correlation coefficient = 0.996)

Table 5.12 Variation of T_1^{-1} (s^{-1}) of the HDO peak with concentration of [Gd(L^{3b})].

Mass of [Gd(L^{3b})]·2NaCl·LiCl·3H_2O (mg)	Concentration of [Gd(L^{3b})] (mM)	T_1 (s)	T_1^{-1} (s^{-1})
2.5	4.56	0.1991	5.02
4.3	7.84	0.1285	7.78
5.4	9.85	0.0970	10.30
6.2	11.30	0.0799	12.52

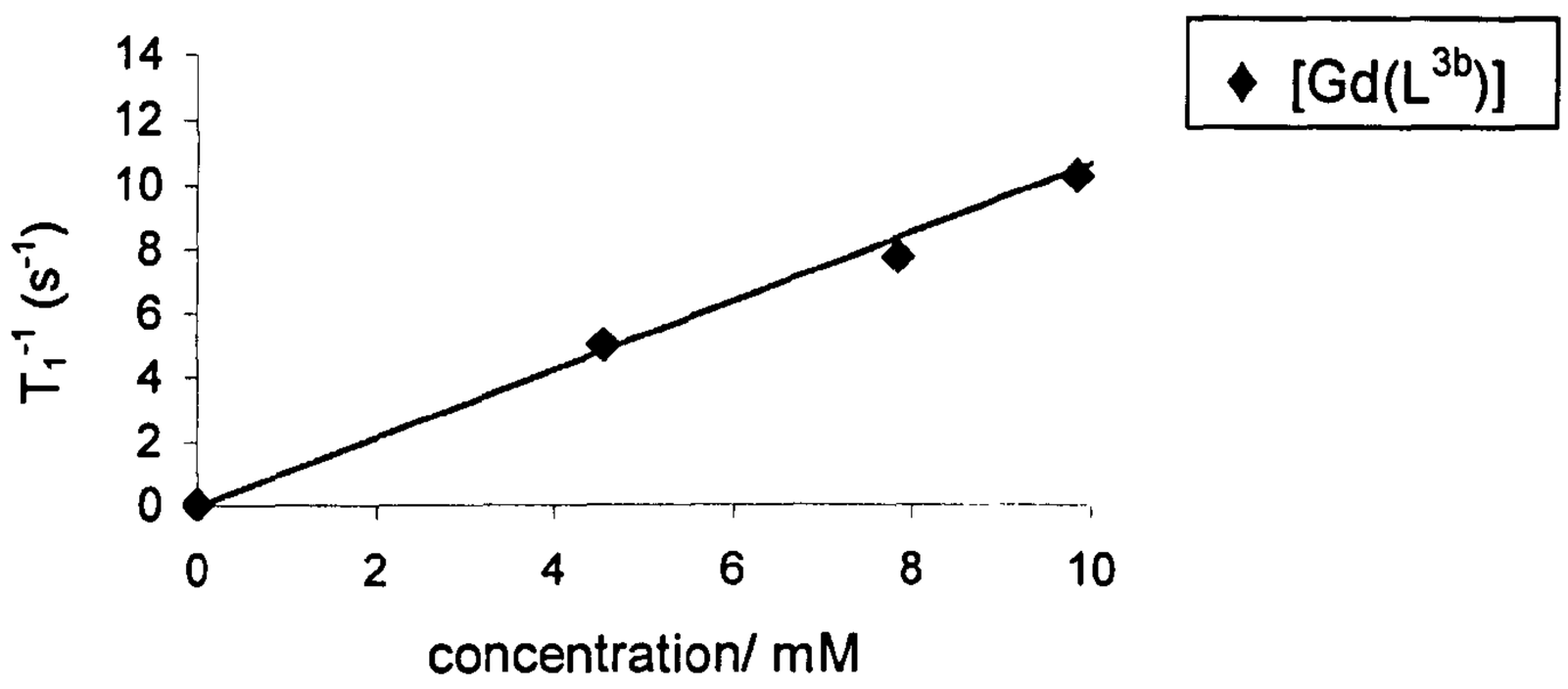

Figure 5.35 Plot of variation (T_1^{-1}) of the HDO peak with the concentration of [Gd(L^{3b})] (correlation coefficient = 0.991)

Table 5.13 Variation of T_1^{-1} (s^{-1}) of the HDO peak with concentration of [Gd(L^{4a})].

Mass of [Gd(L^{4a})]·2NaCl·2H_2O (mg)	Concentration of [Gd(L^{4a})] (mM)	T_1 (s)	T_1^{-1} (s^{-1})
0.7	1.42	0.2808	3.56
1.5	3.04	0.0988	10.12
2.1	4.26	0.0790	12.66
2.7	5.48	0.0561	17.83
3.4	6.90	0.0480	20.85

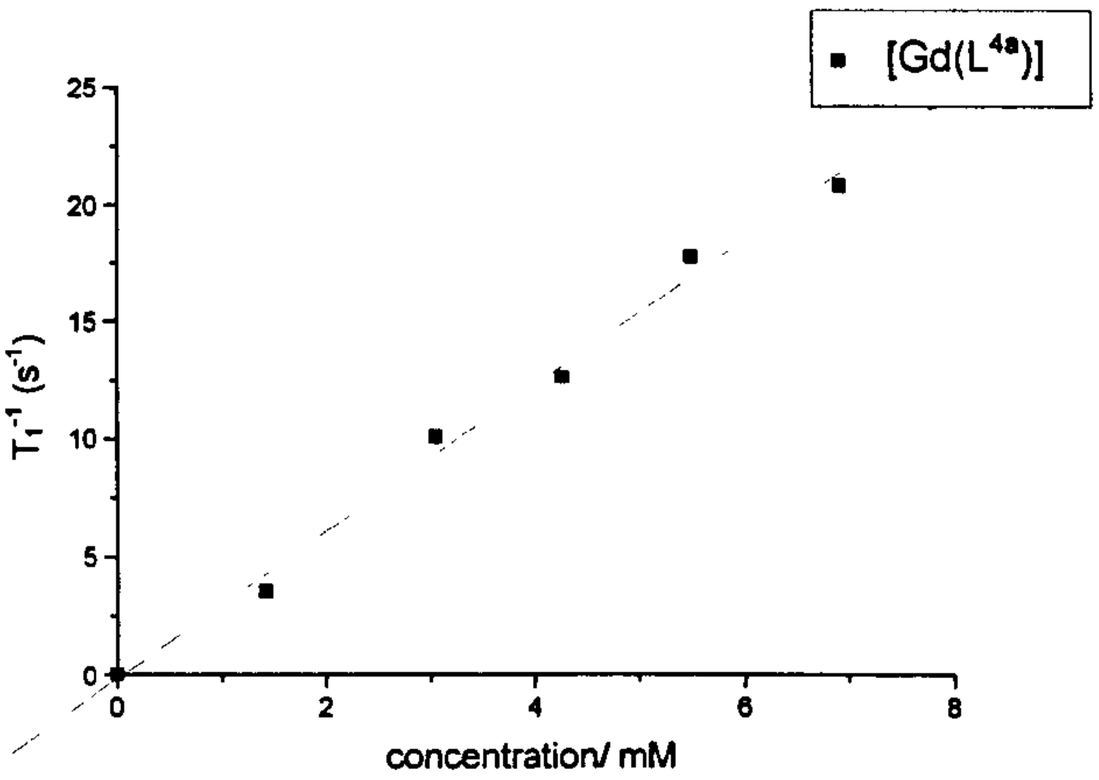

Figure 5.36 Plot of variation (T_1^{-1}) of the HDO peak with the concentration of [Gd(L^{4a})] (correlation coefficient = 0.996).

Table 5.14 Variation of T_1^{-1} (s^{-1}) of the HDO peak with concentration of [Gd(L^{4b})].

Mass of [Gd(L^{4b})]·2NaCl·1/2H_2O (mg)	Concentration of [Gd(L^{4b})] (mM)	T_1 (s)	T_1^{-1} (s^{-1})
0.8	1.47	0.1761	5.68
1.3	2.38	0.0884	11.31
2.2	4.03	0.0594	16.84
3.0	5.50	0.0433	23.09
4.1	7.51	0.0357	27.97

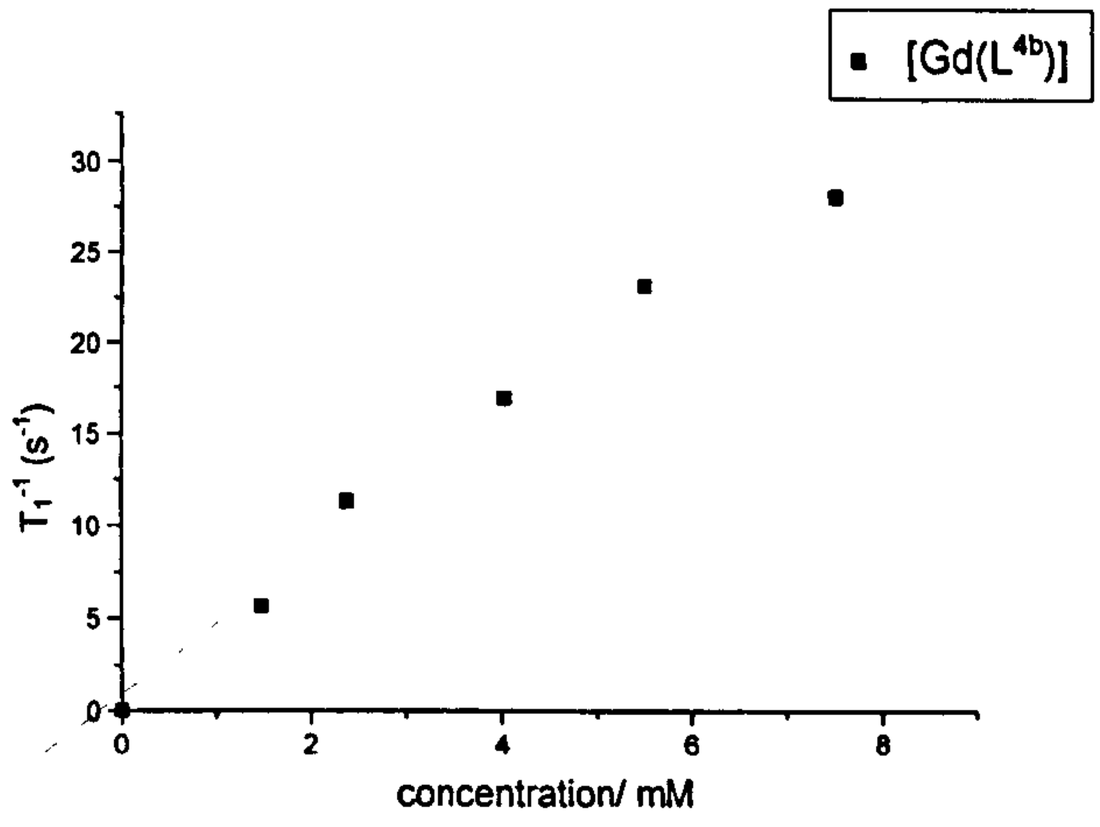

Figure 5.37 Plot of variation (T_1^{-1}) of the HDO peak with the concentration of [Gd(L^{4b})] (correlation coefficient = 0.993).

5.4.18 ^{17}O NMR measurements on [Dy(L^{2a})(CH_3CO_2)], [Dy(L^{3a})] and [Dy(L^{4a})]

Natural abundance ^{17}O NMR experiments were run at 40.686 MHz on a Bruker DPX 300 spectrometer, using 10 mm sample tube. Five samples of [Dy(L^{2a})(CH_3CO_2)]·3NaCl·H_2O, [Dy(L^{3a})]·2NaCl·LiCl·4H_2O and [Dy(L^{4a})]·2NaCl·3/2H_2O were weighed and for every complex the first sample was dissolved in a solution of deionized water containing 20% of D_2O (1.6 cm^3 of H_2O and 0.4 cm^3 of D_2O). The successive samples were dissolved in the same solution, thereby increasing the concentration of the complex. All the complexes were found to hydrolyse slowly in D_2O (Section 5.3.5), but the delay between dissolving the sample in D_2O and completing the ^{17}O measurement was less than 15 minutes, a time interval over which hydrolysis of the complex is thought to be minimal. The ^{17}O shifts were measured using the ^{17}O shift of the water/D_2O solution as external reference (δ = -28.81). In table 5.15, 5.16 and 5.17 the data for the ^{17}O NMR experiments on [Dy(L^{2a})(CH_3CO_2)], [Dy(L^{3a})] and [Dy(L^{4a})], respectively, are reported. Plots of DIS (dysprosium induced shift) (ppm) against concentration of $DyCl_3$ (data in Section 3.5.9), [Dy(L^{2a})(CH_3CO_2)], [Dy(L^{3a})] and [Dy(L^{4a})], (mM) give appropriate straight lines (Figure 5.28; correlation coefficients = 0.992, 0.993 and 0.995, respectively with slopes of 63 ± 4 ppm/M for [Dy(L^{2a})(CH_3CO_2)], 33 ± 2 ppm/M for [Dy(L^{3a})] and 55 ± 3 ppm/M for [Dy(L^{4a})].

Table 5.15 Variation of DIS with concentration of [Dy(L^{2a})(CH_3CO_2)]

Mass of [Dy(L^{2a})(CH_3CO_2)]·3NaCl·2H_2O (mg)	Concentration of [Dy(L^{2a})(CH_3CO_2)] (mM)	δ (ppm)	-$\Delta\delta$ (DIS)(ppm)
10.6	6.90	-28.51	0.70
21.4	13.93	-28.82	1.01
31.8	20.69	-29.35	1.54
41.3	26.88	-29.67	1.86
52.5	34.17	-30.02	2.21

Table 5.16 Variation of (DIS) with concentration of [Dy(L^{3a})].

Mass of [Dy(L^{3a})]·2NaCl·LiCl·3H_2O (mg)	Concentration of [Dy(L^{3a})] (mM)	δ (ppm)	-Δδ (DIS)(ppm)
9.7	6.17	-28.10	0.29
20.1	12.78	-28.33	0.52
28.5	18.12	-28.51	0.70
40.8	25.95	-28.72	0.91
48.9	31.10	-28.84	1.03

Table 5.17 Variation of DIS with concentration of [Dy(L^{4a})].

Mass of [Dy(L^{4a})]·2NaCl·3/2H_2O (mg)	Concentration of [Dy(L^{4a})] (mM)	δ (ppm)	-Δδ (DIS)(ppm)
9.4	6.68	-28.35	0.54
18.5	13.14	-28.66	0.85
27.4	19.46	-29.03	1.22
36.2	25.71	-29.30	1.49
44.0	31.25	-29.58	1.77

5.4.19 Emission measurements

Emission and excitation spectra of carefully degassed solutions of [Eu(L^{2a})Cl] in D_2O and H_2O were recorded using the phosphorescence mode of a Perkin Elmer LS50B instrument. For the emission spectra, excitation and emission slits were 15 nm, for excitation spectra excitation slit 10nm, emission slit 15 nm. The initial time delay used was not less than 0.05 ms. Emission spectra were not dependent upon either the concentration or time delay/time gate used. Emission lifetimes were obtained using the short phosphorescence decay mode of the Perkin Elmer LS50B instrument. Emission lifetimes were independent of concentration and excitation wavelength used.

5.4.20 Crystal structure determination

Crystal data, data collection and refinement parameters for $[Gd(L^{2a})(CH_3CO_2)]\cdot CH_3OH$ are given in Table 5.18, selected bond lengths in Table 5.1. Data for $[Gd(L^{2a})(CH_3CO_2)]\cdot CH_3OH$ were collected on a Bruker SMART1000 CCD area detector diffractometer equipped with a low temperature device, using graphite-monochromated Mo-K_α radiation (λ=0.71073Å). Data were corrected for absorption using multi-scan absorption corrections and the program XABS.[361]

$[Gd(L^{2a})(CH_3CO_2)]\cdot CH_3OH$ was solved by direct methods[322] and completed by iterative cycles of ΔF syntheses and full-matrix least squares refinement. All the atoms, except the Gd atom, were left isotropic because the ellipsoids of the anisotropic model were very large in one direction and very short in the other. The H atoms on methanol molecules were placed from ΔF syntheses and refined as a rigid rotating group. All the other H atoms were placed in calculated positions and refined using a riding model.[323] Since the oxygen atom of the MeOH molecule was found to be disorded its H atoms were omitted. The atom O(7A) was also found disordered and disorder was modelled using partial occupancy models over two sites for both the oxygen atoms (occupancy factors 0.65 and 0.35). Appropriate restraints to bond distances were applied. In this structure the largest residual electron density feature lies near the heavy atom.

Table 5.18 Selected crystallographic data for the single crystal structure of $[Gd(L^{2a})(CH_3CO_2)]\cdot CH_3OH$.

Compound	$[Gd(L^{2a})(CH_3CO_2)]\cdot CH_3OH$
Crystal Data	
Formula	$C_{18}H_{29}N_5O_6Gd\cdot CH_3OH$
M / gmol^{-1}	600.75
Crystal size / mm	0.27 x 0.16 x 0.04
Crystal system	Monoclinic
Space group	$P2_1/c$
a / Å	11.213(2)
b / Å	15.138(3)
c / Å	15.278(3)
α / °	90
β/ °	11.476(4)
γ / °	90
U / Å^3	2413(2)
Reflections used to refine cell	2412
2θ range / °	2.37 to 28.24
Z	4
D_c / gcm^{-3}	1.654
μ / mm^{-1}	2.795
F(000)	1208
T / K	150(2)
Data Collection	
Diffractometer	Bruker SMART1000 CCD area detector
Radiation, wavelength	MoK_α , 0.71073 Å
θ_{max} / °	25.00
Range of h	-14 → 14
Range of k	-19 → 19
Range of l	-19 → 16
Measured reflections	11249
Unique reflections, R_{int}	4229, 0.099
Observed reflections	2665 [$F_O \geq 4\sigma(F_O)$]
Absorption correction	Semi-empirical
$TF_{max, min}$	0.515, 0.180
Solution	
Method	Direct methods
Using	SHELXS-97
Refinement	
Full-matrix least squares on	F^2
Using	SHELXL-97
Weighting scheme x, y[a]	0.0335, --
Parameters refined	145
R_1, wR_2[b]	0.0628, 0.1212
Goodness-of-fit (S)	1.163
$(\Delta/\sigma)_{max}$	0.002
$\Delta\rho_{max, min}$ / eÅ^{-3}	+1.19, -1.32

[a] $w^{-1} = [\sigma^2(F_O^2) + (xP)^2 + yP]$, $P = [MAX(F_O^2, 0) + 2F_c^2\}/3$
[b] $[F_O \geq 4\sigma(F_O)]$

Chapter 6

Transition metal complexes of [9]aneN_3 derivatives

6.1 Introduction

A large number of derivatives of 1,4,7-triazacyclononane ([9]aneN$_3$), have already been discussed in the Introductions to Chapters 3 and 5. Many of these ligands have been studied for a number of different applications from the mimicry of enzymes to radiopharmaceuticals and catalysts.

The aim of this chapter is the study of the co-ordination chemistry of derivatives of [9]aneN$_3$ bearing various pendant co-ordinating groups, mainly primary aminoalkyl groups (Figure 6.1). The syntheses of many of these ligands have already been described in previous chapters, but now we wish to consider their co-ordination chemistry towards transition metal ions.

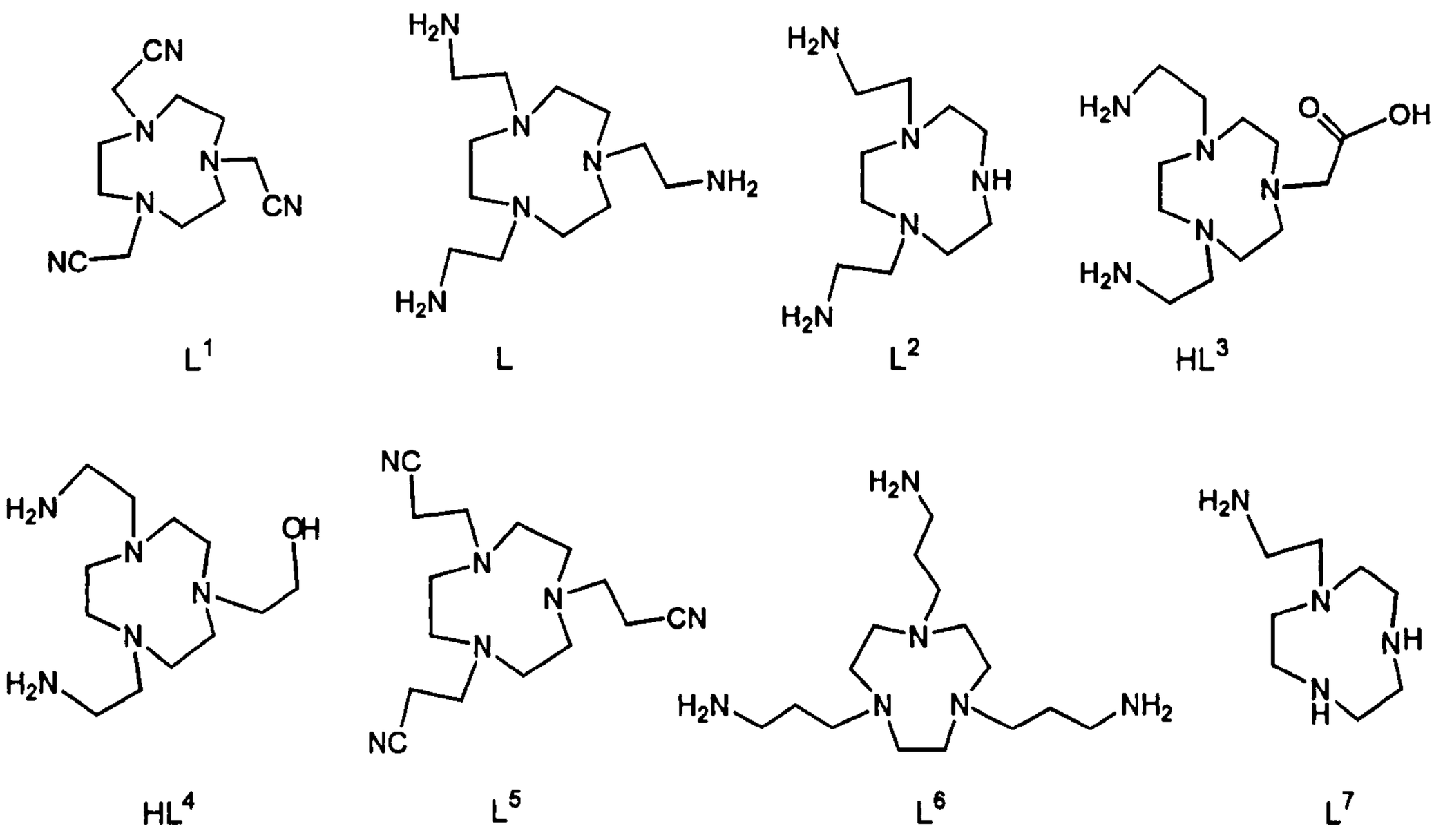

Figure 6.1 Macrocyclic ligands derived from [9]aneN$_3$ discussed in this chapter.

6.1.1 Different behaviour of the nitrile group

Nitriles, R-C≡N, which are isoelectronic with other unsaturated ligands such as dinitrogen, carbon monoxide, isocyanides and alkynes, are extensively used for the preparation of transition metal complexes from which, owing to their weak σ donor ability and π acceptor ability, they can be readily displaced

to afford novel co-ordination and organometallic complexes. Nitriles can interact with metal centres in several different ways but the most common mode of co-ordination is the terminal σ-bonded, η^1-NCR ($L_nM\leftarrow:N\equiv C\text{-}R$), which occurs by σ bonding through the nitrogen lone pair.[396-400]

Although nitrile groups have been used as precursors in the synthesis of primary amines, the co-ordination chemistry of macrocyclic ligands bearing nitrile pendant arms has not been extensively studied. In Chapter 8 the ability of such ligands to form polymeric Ag^I complexes with nitrile groups bridging two or more units in a multidimensional network will be discussed. Except for the binding of Ag^I, nitrile groups attached onto a macrocyclic ligand do not normally participate in the co-ordination of the metal ion. Chung and co-workers[401] reported the syntheses of the cyanoethyl pendant arm derivatives of the two

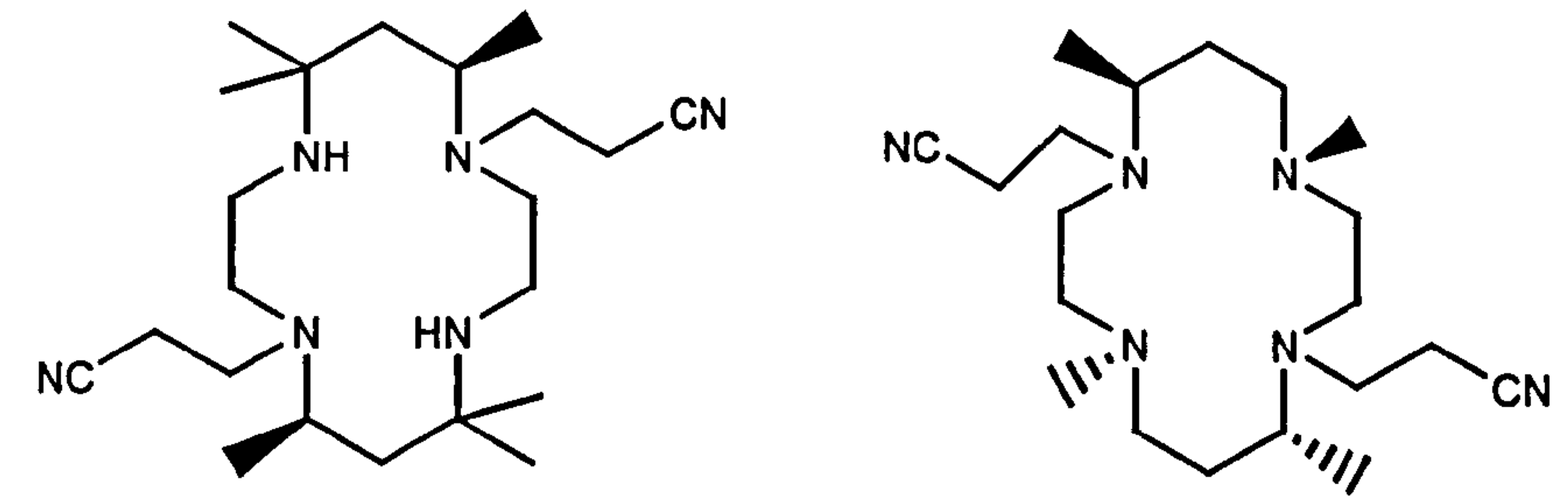

Figure 6.2 Cyanoethyl pendant arm derivatives of two tetraazamacrocycles.

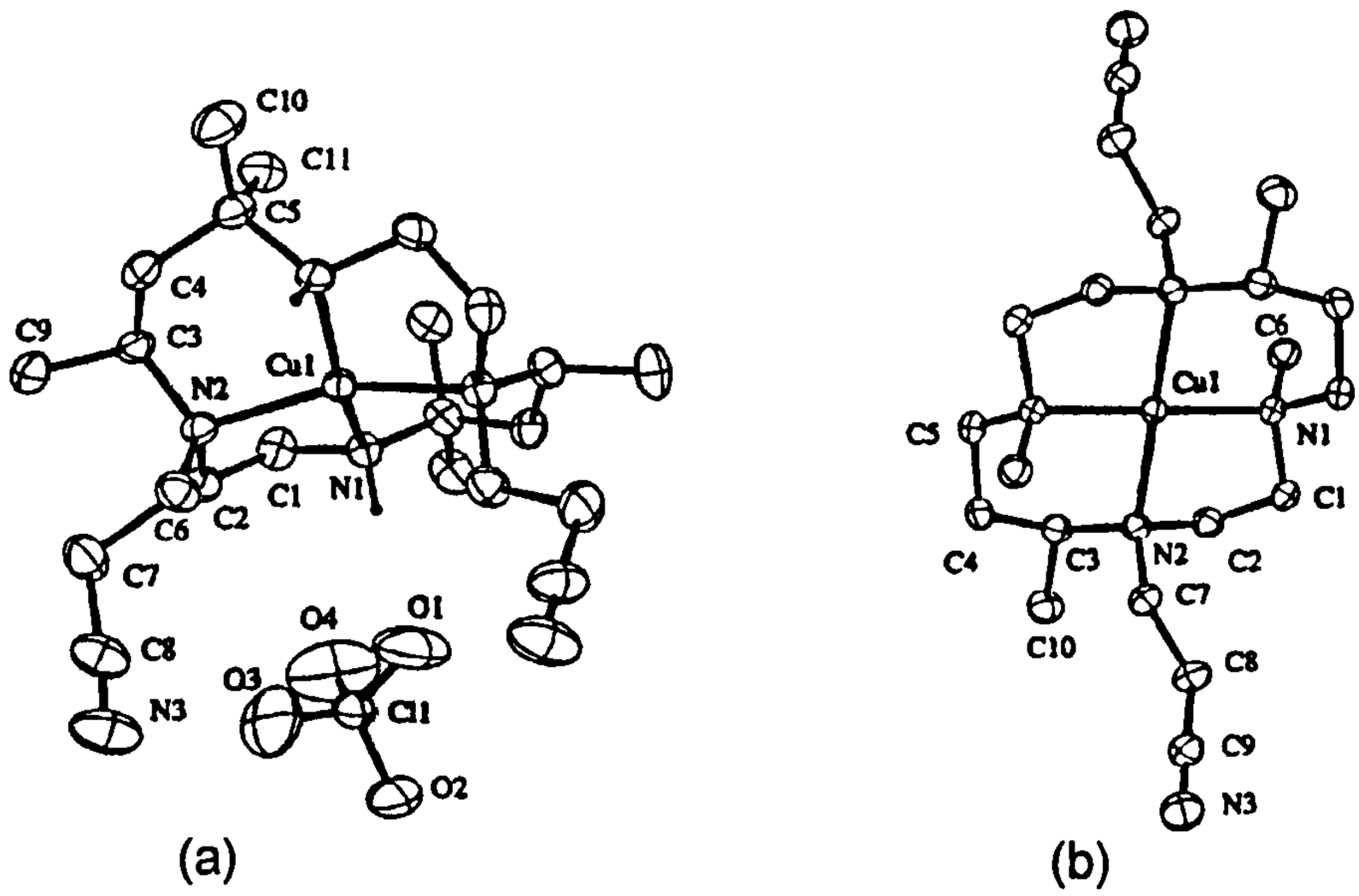

Figure 6.3 Crystal structures of Cu^{II} with the ligands shown (a) in Figure 6.2a and (b) in Figure 6.2b.

tetraaza macrocycles shown in Figure 6.2 and the crystal structures of their Cu^{II} complexes (Figure 6.3). In both molecular structures the Cu^{II} ion is co-ordinated only by the four N-atoms of the macrocycles in a distorted square-planar geometry and the nitrile pendant arms are dangling away from the metal centre. The same behaviour has been observed with the cyanoethyl derivatives of the macrocycles [9]aneN$_2$S and [9]aneNS$_2$.[402] The crystal structures of the Cu^{II} complexes reported in Figure 6.4 are quite similar and show the copper(II) centre co-ordinated to the three donors of the macrocycles and to two chloride anions in a distorted square pyramidal geometry. Even in these structures the nitrile functionalised pendant arms are dangling away from the metal centre because they are not able to bend and co-ordinate linearly to the metal ion.[402]

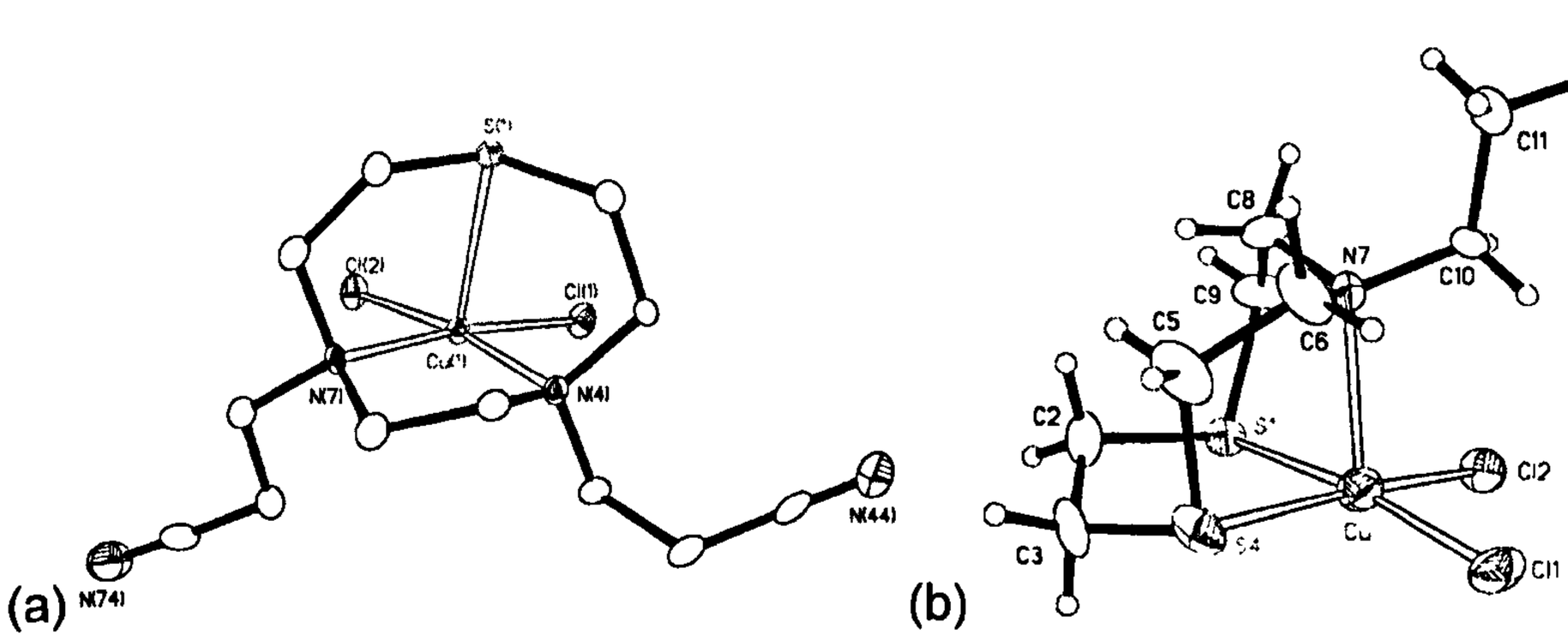

Figure 6.4 Crystal structures of the Cu^{II} complexes of the (a) [9]aneN$_2$S and (b) [9]aneNS$_2$ cyanoethyl derivatives.

Extensive studies on nitrile (R-C≡N) co-ordination have been carried out with small molecules such as acetonitrile (R = Me) or other similar molecules with R = Et, $CHCl_2$, ^tBu and CH_2Ph.[396,403-405] The ability of these nitriles to convert into other organic ligands as a consequence of chemical processes such as insertion, coupling, nucleophilic or electrophilic attack has been studied in some detail in catalytic processes, as intermediates in organic syntheses or as pharmaceutical materials.[406-409] In fact, while metal-coordinated nitriles in general are so labile that they are readily replaced by many other organic molecules, they also show higher reactivity than the free ones.[396,397] Reactions

between free nitriles and nucleophiles such as amines, alcohols and water usually require the presence of an acid or a base,[410] whereas co-ordinated nitriles react even without these.[396,397]

Hydration and alcoholysis of nitriles are normally catalysed by a metal ion which, thanks to its charge density and its stereochemistry, facilitates nucleophilic attack on the C≡N bond.[399,405,411,412] Most of all, the stereochemical role of the metal ion and the stabilisation of the product molecule through complex formation often become important in deciding the course of the reaction. Reactions based upon nucleophilic attack on co-ordinated nitriles are mainly catalysed by kinetically robust systems (Co^{III}, Rh^{III}, Ir^{III} or Ru^{III}) or less labile square-planar complexes of Pt^{II} or Pd^{II}.[404,413-418] In all these reactions the nitrile group is normally initially co-ordinated to the metal centre, as is the product of solvolysis. However, in a few cases metal ion catalysed hydrolysis of uncomplexed nitrile groups has also been found to take place.[419-422] Moreover, catalytic hydration of nitriles to the correspondent carboxyamides in high turnover has been accomplished by using some metal complexes as homogeneous catalysts.[404,423-425]

To our knowledge, solvolysis of nitrile groups catalysed by Cu^{II} ion has been reported only by Hubberstey and co-workers with the system shown in Figure 6.5.[426] The copper(II) ion forms a square planar complex only after alcoholysis of the two nitrile groups of the *bis*(2-cyanoguanidine), giving Cu-N bond lengths in the range 1.938(2)-1.958(2) Å. This reaction takes place with

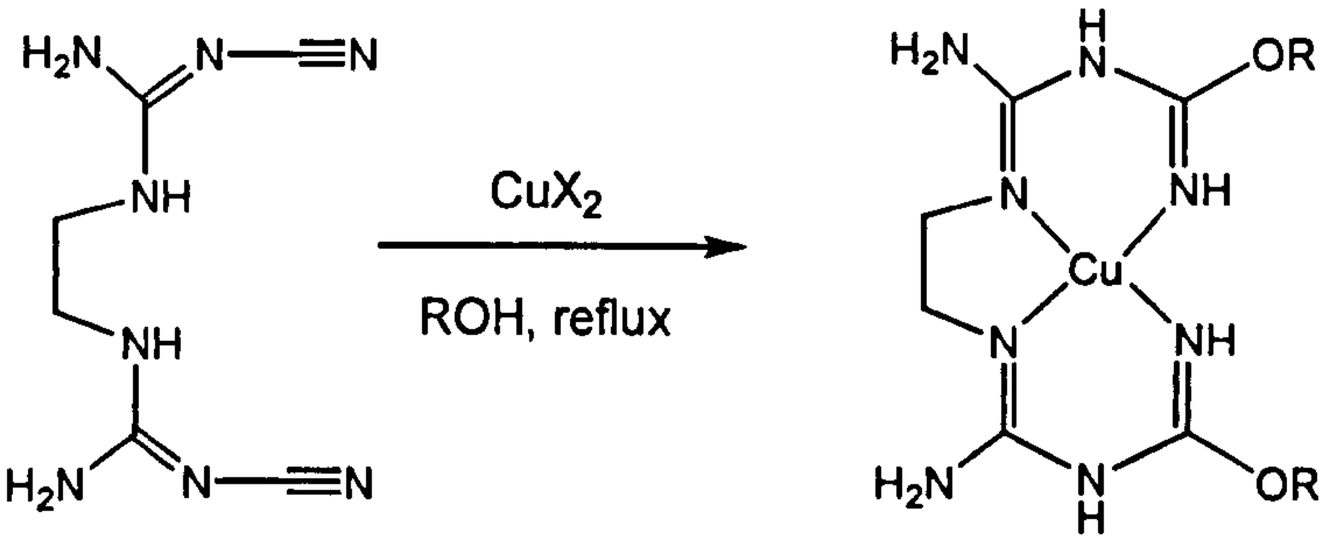

Figure 6.5 Alcoholysis, catalysed by Cu^{II}, of the two terminal nitrile groups in *bis*(2-cyanoguanidine).

either methanol or ethanol and with different Cu^{II} salts (BF_4^-, Cl^-, Br^- and SO_4^{2-}), indicating a strong stabilisation of the system with the formation of the square planar complex.[426]

6.1.2 [9]aneN$_3$ bearing alkyl and benzylamino pendant arms

Many derivatives of [9]aneN$_3$ containing four, five or six donor atoms have been synthesised and studies of their co-ordination chemistry with a wide range of transition metal ions in different oxidation states have been reported.[77,80,82,222,223] Among these ligands, those containing aminoalkyl or aminobenzyl pendant groups have attracted great interest. Sargeson and co-workers[242] synthesised the ligand L [1,4,7-*tris*(2-aminoethyl)-1,4,7-triazacyclononane], as already discussed in Section 3.1.2, but they only studied its co-ordination chemistry towards Co^{III}.[242] McAuley and co-workers reported the transition metal complexes of *mono*-, *bis*- and *tris*(3-propylamino)-1,4,7-triazacyclononane (Figure 6.6) and studied their properties in both solid state and solution.[239,427] However, separation and purification of the two asymmetric pendant arm derivatives (**11** and **12**) were achievable only by column chromatography of the Ni^{II} complexes and gave low yields.[427]

In the complex cation $[Ni(L^6)]^{2+}$ (Figure 6.7a), the metal centre is in an approximately octahedral geometry, being co-ordinated by all six N-donors of the ligand with a mean Ni-N bond length of 2.14 Å and no significant difference in the bond lengths between the Ni^{II} and primary or tertiary amino groups.[239]

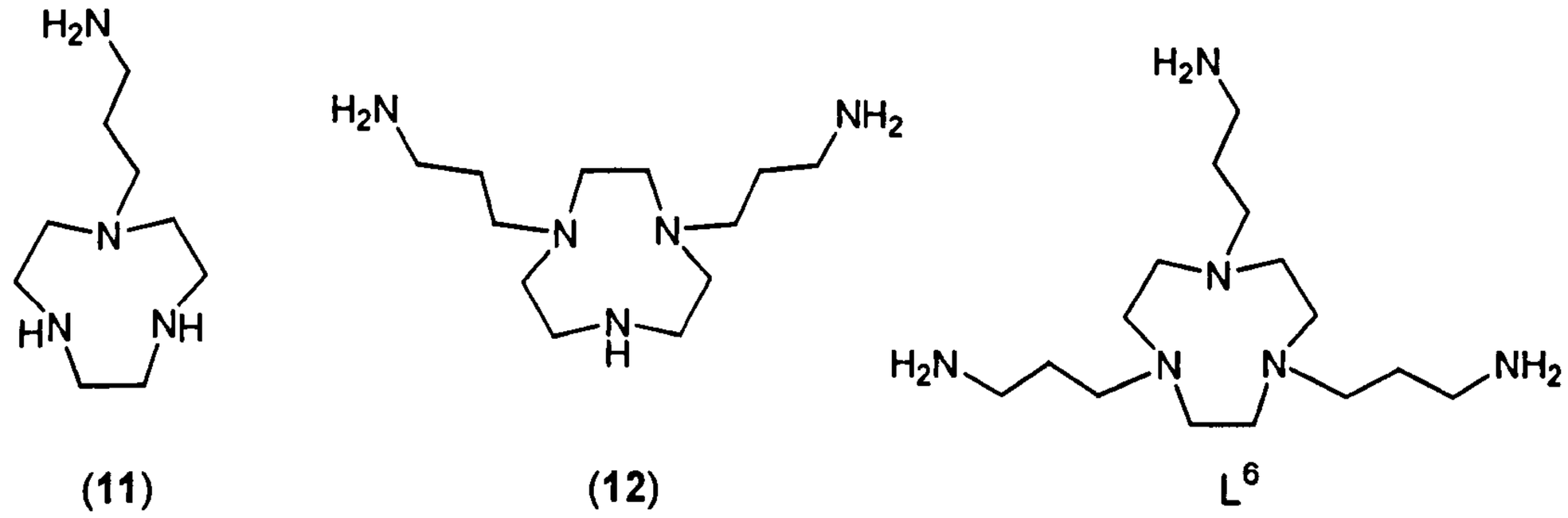

(11) **(12)** L^6

Figure 6.6 *Mono*, *bis*, and *tris*(3-propylamino) derivatives of [9]aneN$_3$.

The crystal structure of $[Cu(\mathbf{12})]^{2+}$ is shown in Figure 6.7(b) and shows the Cu^{II} ion in a distorted square pyramidal geometry, co-ordinated to the five N-donors of the ligand. The Cu-N bond lengths fall in three categories: Cu-N(basal) are at 2.026(13) Å for the bond lengths to the primary amines and 2.07(1) Å for the ones to the tertiary amines and Cu-N(apical) is at 2.251(12) Å.[427]

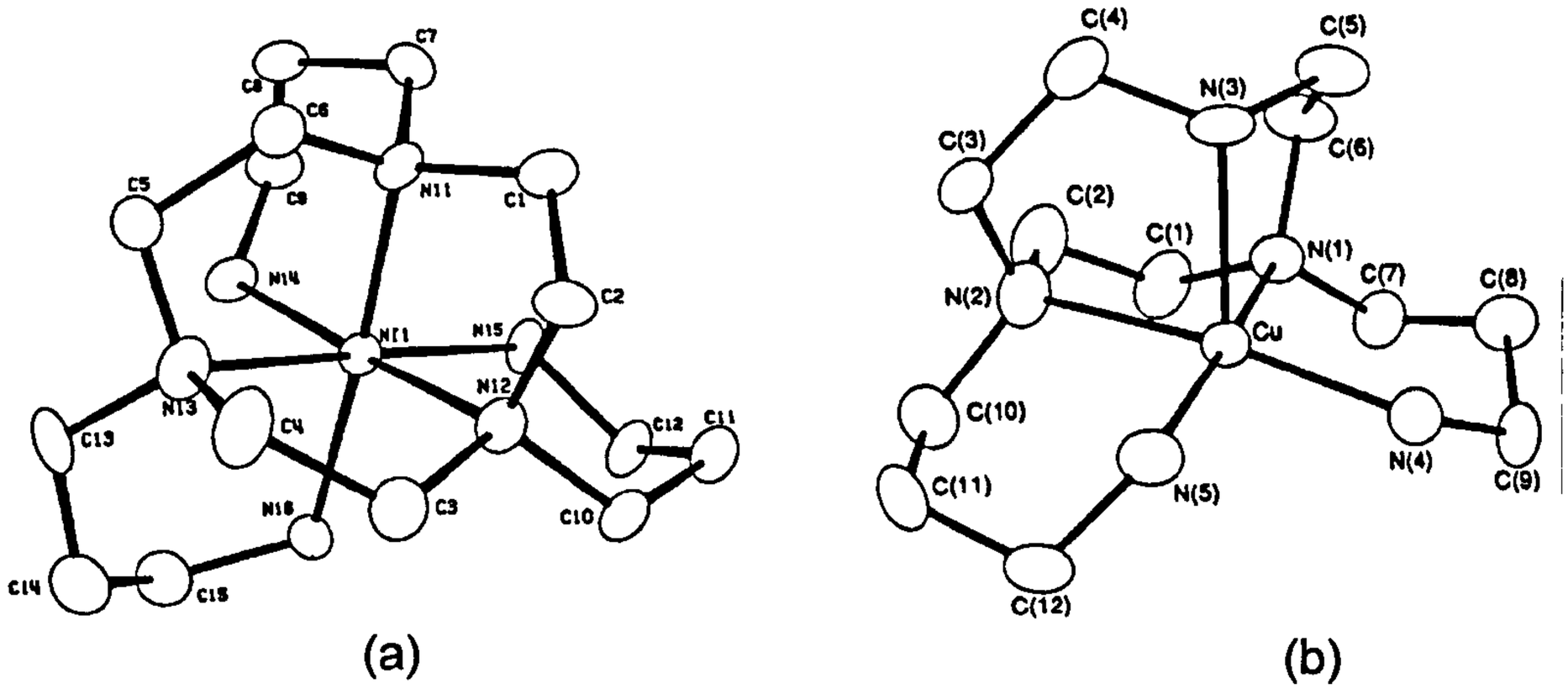

Figure 6.7 Crystal structures of the complex cations (a) $[Ni(L^6)]^{2+}$ and (b) $[Cu(\mathbf{12})]^{2+}$.

The dinuclear $[Ni_2(\mathbf{11})_2(\mu\text{-}Cl)_2][ClO_4]_2$ crystal structure shown in Figure 6.8 has the Ni^{II} ions in a distorted octahedral geometry, being linked to the four N-atoms of the ligands and two bridging chloride ions in mutually *cis* positions. The Ni-N bond lengths to the macrocyclic N-donors are 2.097(4) Å, whereas the bond to the primary amine of the pendant arm is slightly shorter at 2.080(3) Å.[427]

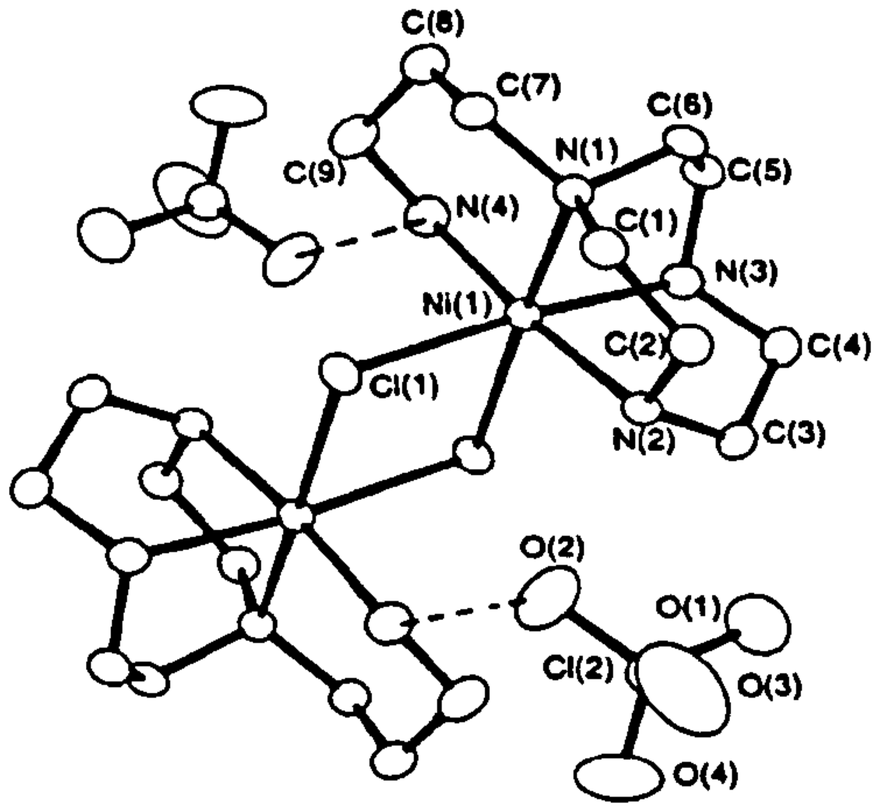

Figure 6.8 Crystal structure of $[Ni_2(\mathbf{11})_2(\mu\text{-}Cl)_2][ClO_4]_2$.

The two ligands shown in Figure 6.9 have each been synthesised in two steps starting from [9]aneN$_3$: the reaction with nitrobenzyl bromide (or nitrophenyl chloride) and the subsequent reduction of the nitro group with hydrazine afforded the aniline groups.[266,267,428] The presence of the rigid pendant arms gives rise to different co-ordination polyhedra depending on the

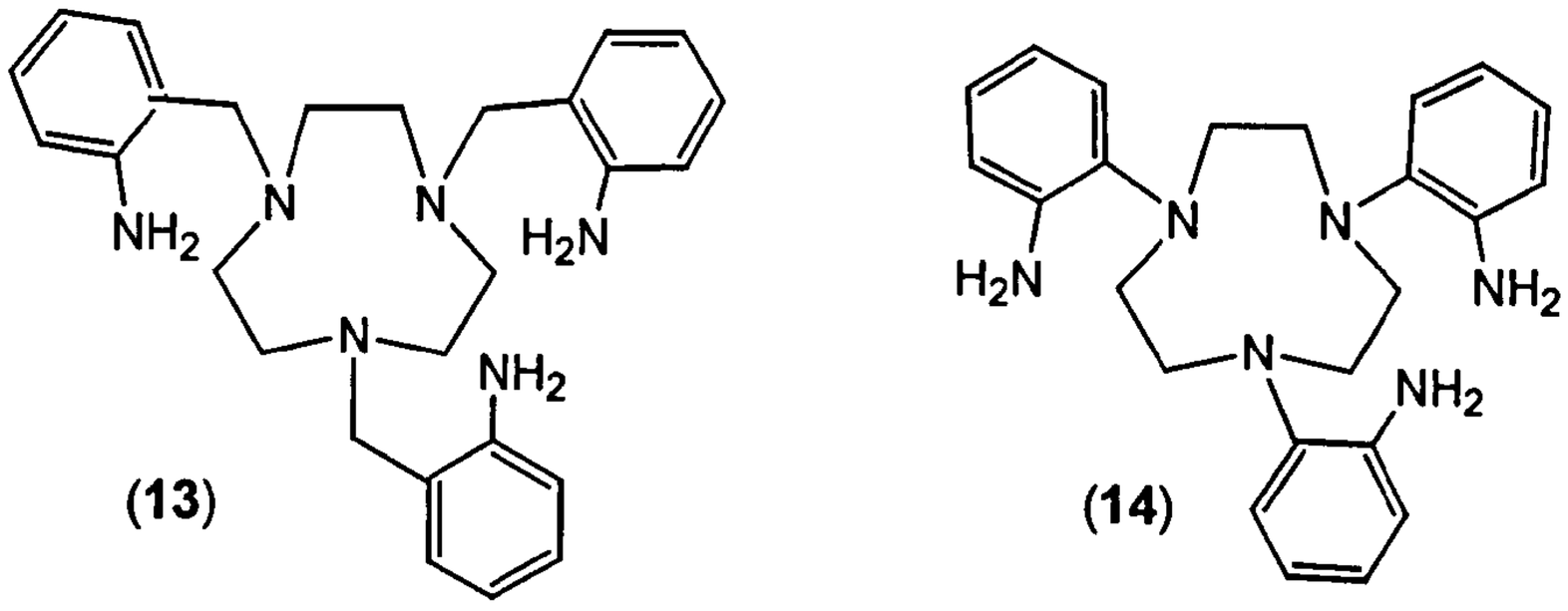

Figure 6.9 [9]aneN$_3$ bearing aminobenzyl (**13**) and aminophenyl (**14**) pendant arms.

ligand field stabilisation energy. When the latter is absent (d^{10} electronic configuration) the geometry is trigonal prismatic, being governed by the steric requirements of the ligand. This energy is at the maximum for high spin d^8 electronic configuration with a preference for an octahedral geometry; indeed, the crystal structure of the [Ni(**13**)]$^{2+}$ complex presents a slightly distorted octahedral geometry (Figure 6.10a).[267] Interestingly, the [Cu(**13**)]$^{2+}$ complex

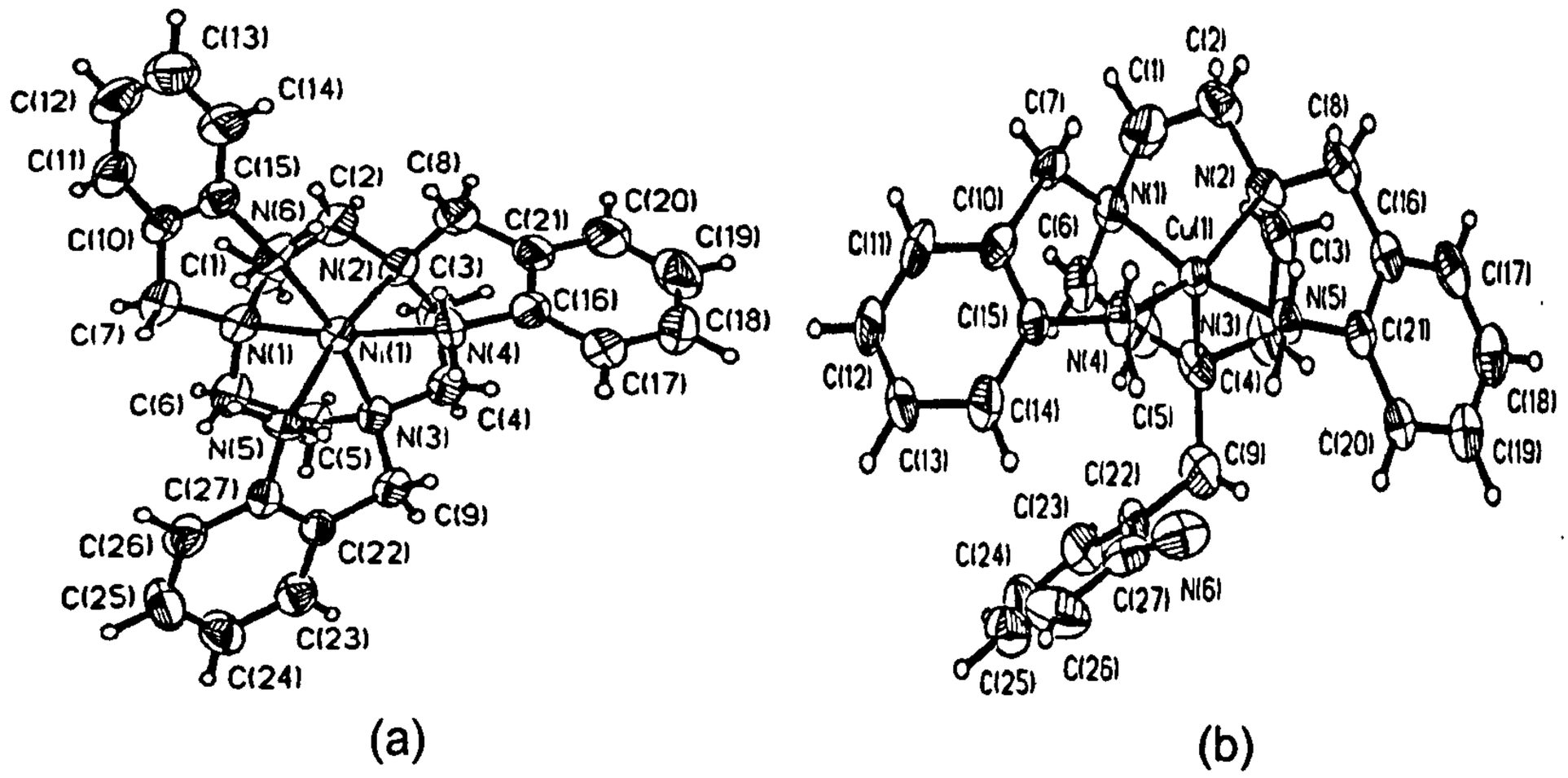

Figure 6.10 Crystal structures of (a) [Ni(**13**)]$^{2+}$ and (b) [Cu(**13**)]$^{2+}$.

cation (Figure 6.10b) shows a five co-ordinate copper (II) centre with a square-based pyramidal MN_5 polyhedron and one pendant arm dangling away from the metal centre.[267] In contrast, the crystal structure of $[Cu(\mathbf{14})]^{2+}$ shows the Cu^{II} in a six-co-ordinate geometry with three relatively short and three long metal-nitrogen distances indicating a rhombic distortion. On the other hand, the crystal structure of the Ni^{II} complex with **14** shows a six-co-ordinate metal centre with the macrocycle in its typical face-capping mode and, differently from what observed in $[Ni(\mathbf{13})]^{2+}$, a twist angle of 44° indicating a tendency towards a trigonal prismatic geometry.[428] The twist angle (θ) defines the difference between trigonal and octahedral co-ordination geometry, being 60° for an octahedron and 0° for a trigonal prism (Figure 6.11). The two crystal structures reported with the ligand L^6 are both nearly octahedral with twist angles of 59.55° for $[Co(L^6)]^{3+}$ and 56.94° and 57.36° for the two independent cations of the Ni^{II} complex.[239,427]

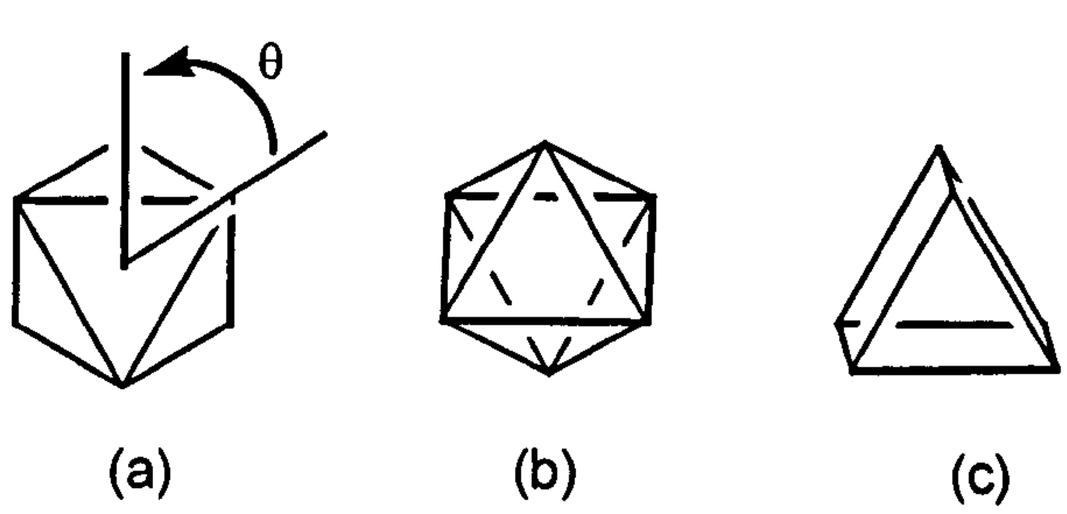

Figure 6.11. (a) Twist angle (θ) for (b) octahedral (θ = 60°) and (c) trigonal prismatic (θ = 0°) geometries.

6.2 Co-ordination behaviour of nitrile derivatives of [9]aneN$_3$

The synthetic procedures used to obtain the two nitrile derivatives of [9]aneN$_3$ L^1 and L^5 were respectively described in Chapter 3 and by McAuley and co-workers.[239] Single crystals of L^1 suitable for X-ray diffraction studies were grown by diffusion of Et_2O vapour into a CH_3CN solution of L^1. The crystal structure is shown in Figure 6.12 and shows the macrocyclic ligand with the

pendant arms directed away from the cavity. The linearity of the C≡N triple bond, with angles C1X-C2X-N3X (X = A, B and C) in the range 175.8(2)-177.9(2)°, means that the nitrile groups cannot co-ordinate linearly to a metal ion within the macrocyclic cavity *via* σ bonding (M←:N≡C-R) because they cannot bend and form endocyclic complexes. In Chapter 8, the ability of these ligands to form polymeric networks with Ag^{I} ions will be described.

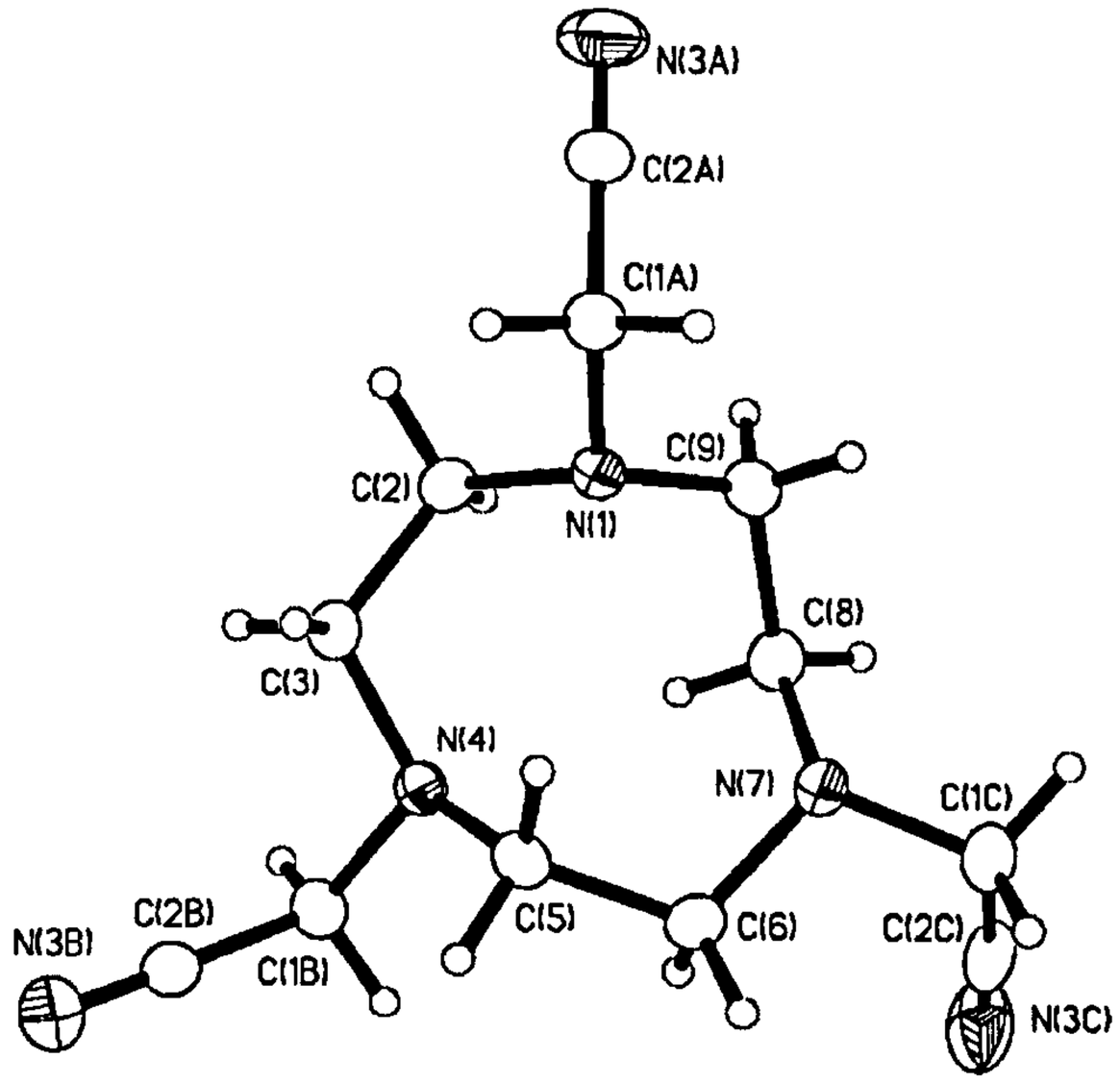

Figure 6.12. Crystal structure of the ligand L^1 with numbering scheme adopted. Displacement ellipsoids are drawn at 50% probability.

Reacting L^1 and one equivalent of $Cu(BF_4)_2{\cdot}4H_2O$ in MeOH at room temperature yielded a blue-green oil which could not be recrystallised. Presumably, the three donor atoms of the triaza macrocycle are not sufficient to fulfilling the co-ordination sphere of the Cu^{II} ion given that the BF_4^- anions do not co-ordinate strongly the metal ion. Interestingly, warming the same reaction to 65°C for two hours led to the formation of an intense blue solution from which blue single crystals suitable for diffraction studies could be grown by diffusion of Et_2O vapour into an acetonitrile solution of the complex $[Cu(\mathbf{15})]^{2+}$. The crystal structure confirms the hypothesis made on the basis of the mass spectrum and elemental analytical data: the formation of $[Cu(\mathbf{15})](BF_4)_2$ after methanolysis of two nitriles and formation of imino-ether groups.

The N–H stretching bands in the range 3120-3350 cm^{-1} and strong bands due to C=N stretching in the range 1630-1660 cm^{-1} in the IR spectrum are clearly indicative of the presence of the NH=C(OR')R moiety. The imino N-donors can co-ordinate the Cu^{II} ion, which is already bound to the N-donors of [9]aneN$_3$, to form a square-based pyramidal copper(II) centre (Figure 6.13).

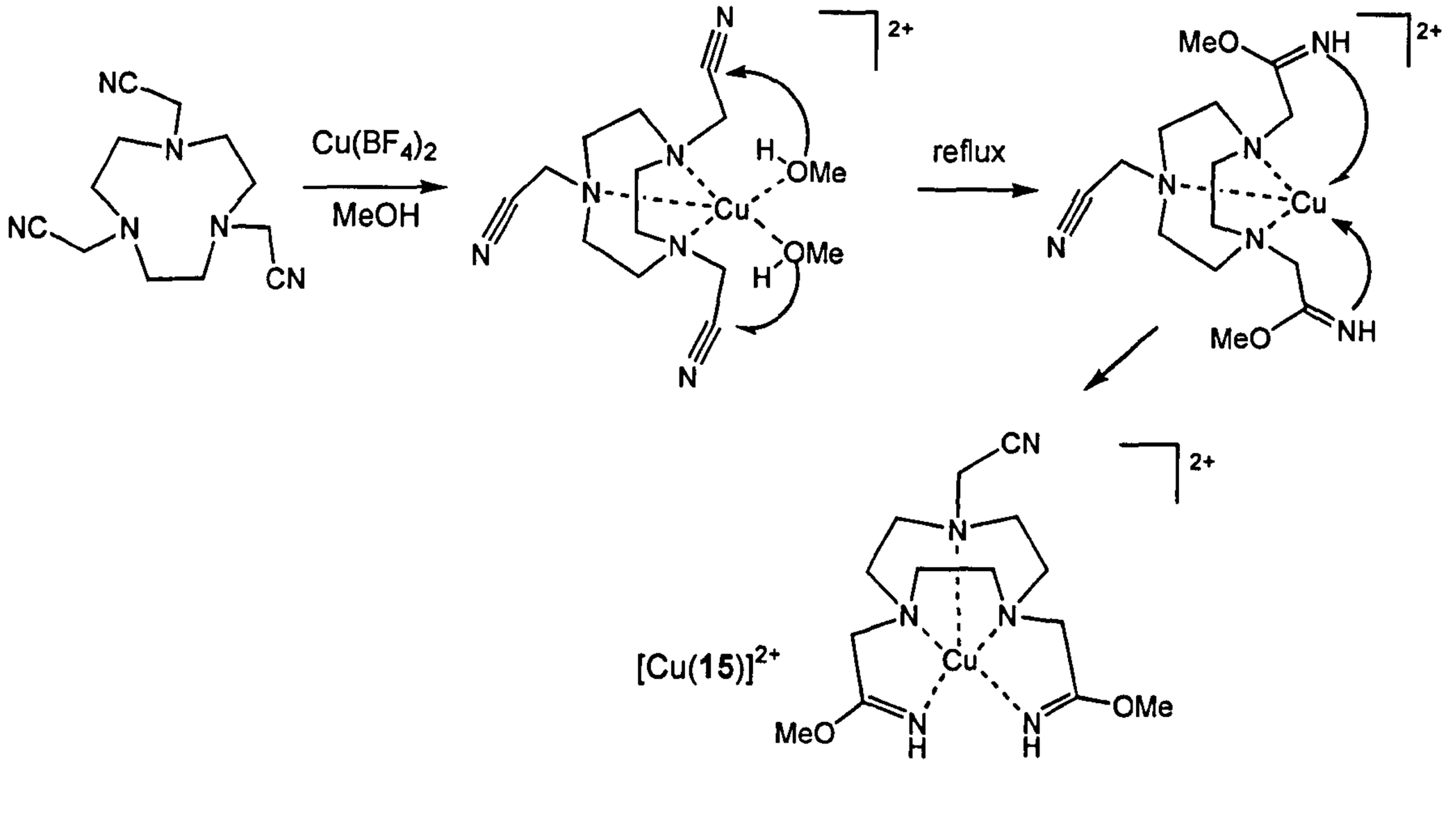

Figure 6.13. Proposed mechanism of the Cu^{II} catalysed methanolysis of two nitrile groups of L^1.

The mechanism of such a reaction starts with the co-ordination of the metal ion by the nitrogen atoms of the macrocycle; at higher temperatures the nitriles undergo nucleophilic attack by two MeOH molecules, probably weakly bound to the metal centre, allowing the co-ordination of the metal by the two imino donors and the formation of a square-based pyramidal copper(II) complex. This reaction is facilitated by the stereochemistry of the Cu^{II} ion, which catalyses the reaction and the formation of a stable square pyramidal complex. Remarkably, the third nitrile group of L^1 is not involved in this reaction, because the Cu^{II} prefers five- rather than six-co-ordination, thereby catalysing the methanolysis of only two of the three nitrile groups of the ligand.

The same reaction was carried out with L^5 to see if the behaviour was similar to that of L^1. Despite the longer pendant nitrile arms, these are still not expected to be sufficient to allow formation of endocyclic complexes which requires bending of the pendant arms to allow linear co-ordination of the nitrile

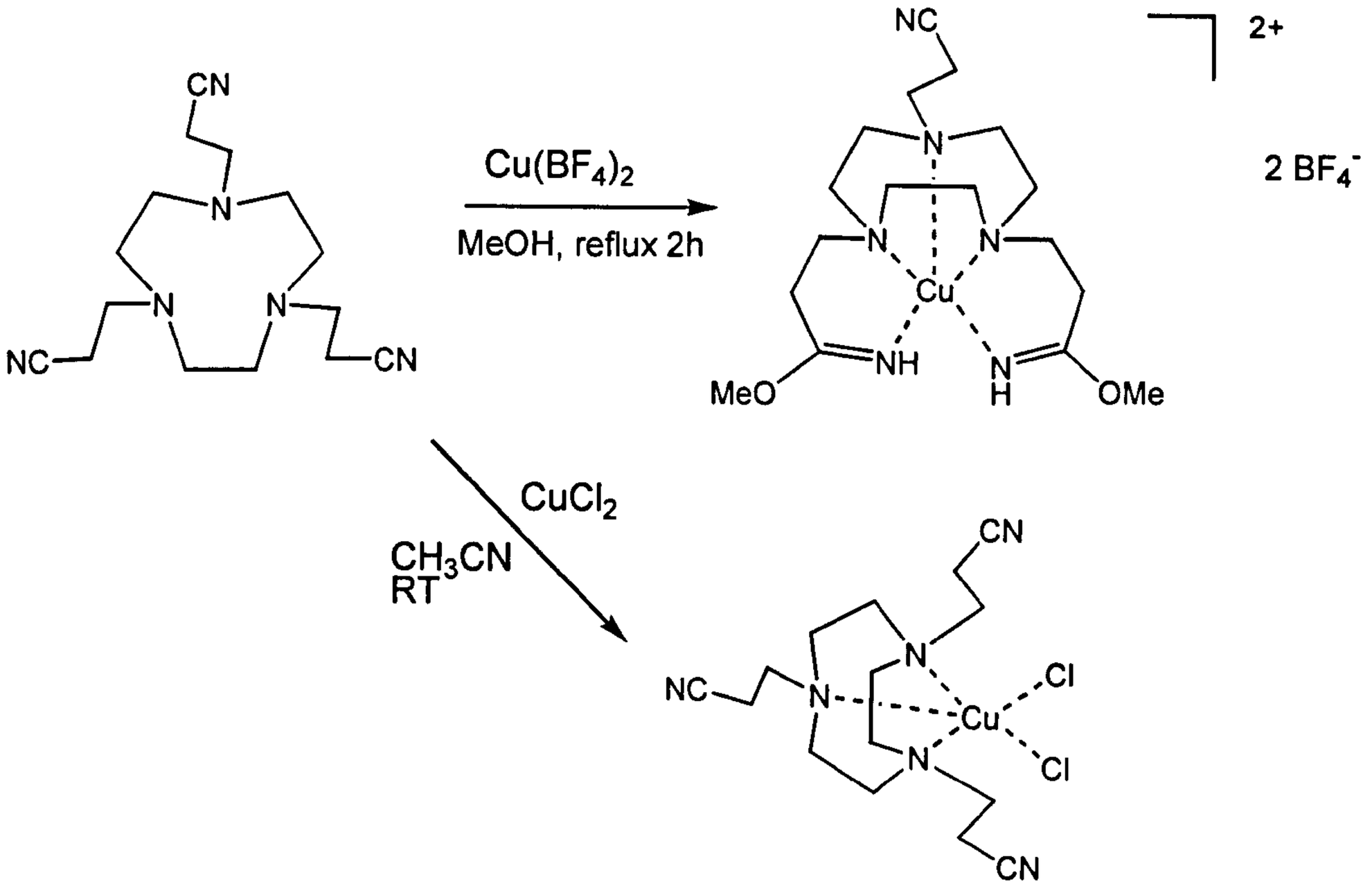

Figure 6.14 Synthesis of the two complexes [Cu(**16**)]$(BF_4)_2$·and [Cu(L^5)Cl_2] starting from L^5.

groups. Indeed, the reaction of L^5 with one equivalent of $Cu(BF_4)_2 \cdot 4H_2O$ in refluxing MeOH formed an intense blue solution from which single crystals were grown. Again, the crystal structure determination confirms the data obtained by mass spectrum and elemental analysis, with methanolysis occurring at two nitrile groups to form the square-based pyramidal copper(II) complex $[Cu(\mathbf{16})]^{2+}$. The mechanism of this reaction is the same as that described for the formation of [Cu(**15**)]$(BF_4)_2$ (Figure 6.13), involving nucleophilic attack by two methanol molecules upon two C≡N bonds. This leads to co-ordination of the Cu^{II} by imino-ether groups within a square pyramidal complex.

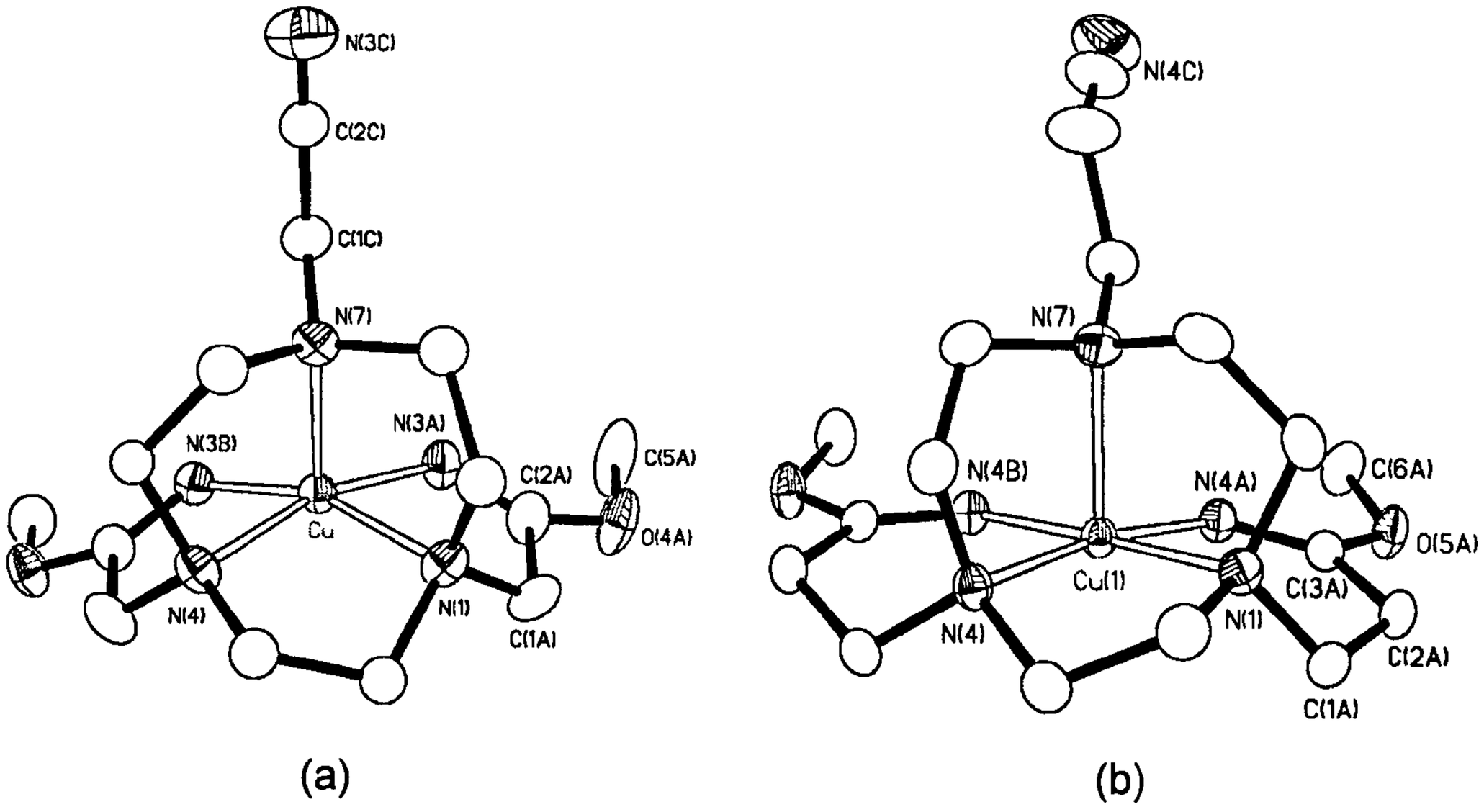

(a) (b)

Figure 6.15. Crystal structures of the complex cations (a) [Cu(**15**)]$^{2+}$ and (b) [Cu(**16**)]$^{2+}$ with numbering schemes adopted. Hydrogen atoms have been omitted for clarity. Displacement ellipsoids are drawn at 50% probability.

Bond lengths and angles for [Cu(**15**)](BF$_4$)$_2$ and [Cu(**16**)](BF$_4$)$_2$ are reported in Tables 6.1 and 6.2, respectively; Figure 6.15 shows the crystal structures of the complex cations [Cu(**15**)]$^{2+}$ (a) and [Cu(**16**)]$^{2+}$ (b). The [Cu(**16**)](BF$_4$)$_2$ crystal structure has four independent complexes in the asymmetric unit, but among them there are no significant differences in bond lengths, angles and co-ordination geometry around the metal centre, therefore only one complex cation is discussed. The donor atoms forming the base of the pyramid are two imines {N(3A) and N(3B) for [Cu(**15**)]$^{2+}$ and N(4A) and N(4B) for [Cu(**16**)]$^{2+}$} from the pendant arms and two tertiary amines [N(1) and N(4)] from the macrocyclic framework. The r.m.s. deviation of the N atoms from the N$_4$ basal planes are 0.046Å for [Cu(**15**)]$^{2+}$ and 0.063Å for [Cu(**16**)]$^{2+}$. In [Cu(**15**)](BF$_4$)$_2$ the Cu^{II} ion lies 0.242 Å from the N$_4$ plane in the direction of the apical tertiary amine [N(7)], with the Cu-N(7) apical bond forming an angle of 18.6° with the normal to the basal plane. In [Cu(**16**)](BF$_4$)$_2$ the Cu^{II} ion lies 0.082 Å from the basal plane, while the Cu-N(7) [N(7) apical donor] bond forms

an angle of 12.9° with the normal to the basal plane. Therefore, in both cases, the Cu-N(apical) bond is very near to be perpendicular to the N_4 basal planes. In [Cu(**15**)]$(BF_4)_2$ and [Cu(**16**)]$(BF_4)_2$ the basal Cu-N bond lengths lie in the range 1.942(5)-2.044(5)Å and 1.979(3)-2.050(3)Å, respectively, and apical Cu-N distances are 2.249(5)Å and 2.280(3)Å, respectively. The Cu-N(imine) bond lengths are the shortest ones in both structures [range 1.942(5)-2.003(3) Å] and are comparable to the Cu-N(imine) bond lengths reported for the Cu^{II} complex with the *bis*(amidino-*O*-alkylurea) ligand discussed in Section 6.1.1.[426] The Cu-N(macrocycle) bond distances, both Cu-N(basal) and Cu-N(apical), are comparable to those reported for other Cu^{II} complexes of pentadentate ligands derivatives of [9]aneN$_3$, for example 1-methyl-4,7-*bis*(3-aminopropyl)-1,4,7-triazacyclononane[377] or 4,7-*bis*(2-methylpyridyl)-1,4,7-triazacyclononane.[375,429,430] Also, the Cu^{II} complexes with *N*,*N*',*N*"-trimethyl-1,4,7-triazacyclononane exhibit bond lengths that are not very different from those in [Cu(**15**)]$^{2+}$ and [Cu(**16**)]$^{2+}$ [range 2.053(4)-2.119(5) Å for Cu-N(basal) and 2.230(4)-2.290(5) Å for Cu-N(apical)].[431]

Table 6.1 Selected bond lengths (Å) and angles (°) for [Cu(**15**)]$(BF_4)_2$.

Cu – N(1)	2.044(5)	N(4)-Cu-N(7)	83.1(2)
Cu – N(4)	2.030(5)	N(1)-Cu-N(3A)	82.8(2)
Cu – N(7)	2.249(5)	N(1)-Cu-N(3B)	161.3(2)
Cu – N(3A)	1.942(5)	N(4)-Cu-N(3A)	165.2(2)
Cu – N(3B)	1.947(5)	N(4)-Cu-N(3B)	83.8(2)
		N(7)-Cu-N(3A)	105.3(2)
N(1)-Cu-N(4)	86.1(2)	N(7)-Cu-N(3B)	110.7(2)
N(1)-Cu-N(7)	83.5(2)	N(3A)-Cu-N(3B)	104.1(2)

Table 6.2 Selected bond lengths (Å) and angles (°) of one out of four complex cations ([Cu(**16**)]$^{2+}$) in [Cu(**16**)]$_4(BF_4)_8 \cdot 4H_2O$.

Cu(1) – N(1)	2.050(3)	N(4)-Cu(1)-N(7)	84.2(1)
Cu(1) – N(4)	2.031(3)	N(1)-Cu(1)-N(4A)	90.7(1)
Cu(1) – N(7)	2.280(3)	N(1)-Cu(1)-N(4B)	177.6(1)
Cu(1) – N(4A)	1.979(3)	N(4)-Cu(1)-N(4A)	170.9(1)
Cu(1) – N(4B)	2.003(3)	N(4)-Cu(1)-N(4B)	92.3(1)
		N(7)-Cu(1)-N(4A)	103.5(1)
N(1)-Cu(1)-N(4)	81.6(1)	N(7)-Cu(1)-N(4B)	99.1(1)
N(1)-Cu(1)-N(7)	85.6(1)	N(4A)-Cu(1)-N(4B)	91.2(1)

In both structures the *trans*-basal angles [N(1)-Cu-N(3B) 161.3(2)° and N(4)-Cu-N(3A) 165.2(2)° in [Cu(**15**)]$^{2+}$; N(1)-Cu-N(4B) 177.6(1)° and N(4)-Cu-N(4A) 170.9(1)° in [Cu(**16**)]$^{2+}$] are in good agreement with the values expected for a square pyramidal geometry around d^9 Cu^{II} centres.[432,433] In [Cu(**15**)]$^{2+}$ the square base of the pyramid is quite regular with three five-membered chelate rings formed at the metal centre; these are very similar both in the angles at the metal centre [82.8(2)°-86.1(2)°] and in the distance between the nitrogens [2.64(1)Å-2.78(1)Å]. In [Cu(**16**)]$^{2+}$ the extended pendant arms lead to the formation of two six-membered chelate rings at the Cu^{II} centre which are slightly different from the five-membered chelate ring formed by the macrocyclic N-donors, both in the angles subtended at the metal centre and in the distance between the nitrogens [81.6(1)° and 2.77(1)Å for the five membered chelate ring and an average of 91.5° and 2.89Å for the six-membered rings].

The electronic spectra of [Cu(**15**)]$^{2+}$ and [Cu(**16**)]$^{2+}$ recorded in CH_3CN at room temperature show only one band in the visible region at 587 and 582 nm, respectively, with molar extinction coefficients of 107 and 105 dm^3 mol^{-1} cm^{-1}, respectively. These values are typical for a d_{xy}, $d_{yz} \rightarrow d_{x^2-y^2}$ transition in a Cu^{II} ion having square-based pyramidal or distorted square-based pyramidal co-ordination geometry.[377,429,430]

The X-band EPR spectra of the complexes [Cu(**15**)]$^{2+}$ and [Cu(**16**)]$^{2+}$ were recorded as frozen (77 K) MeCN/DMF (ratio 9/1, v/v) glasses. The two EPR spectra (Figure 6.16) are typical of mononuclear Cu^{II} complexes with nuclear spin 3/2 and tetragonally distorted or square-based pyramidal co-ordination geometry with a $d_{x^2-y^2}$ ground state. For [Cu(**15**)]$^{2+}$ g_{11} = 2.215, A_{11} = 181.3 G, g_{22} = 2.053 and g_{33} = 1.997 and for [Cu(**16**)]$^{2+}$ g_{11} = 2.214, A_{11} = 185.3 G, g_{22} = 2.056 and g_{33} = 1.994. The difference between the two spectra is that in the spectrum of [Cu(**16**)]$^{2+}$ (Figure 6.16b) a superhyperfine coupling to the nitrogen atoms co-ordinated to the Cu^{II} centre can be seen in the perpendicular region of the spectrum. This superhyperfine coupling seems to agree with a

total of four nitrogen atoms (probably the basal N-donors) strongly coupled to the metal centre.

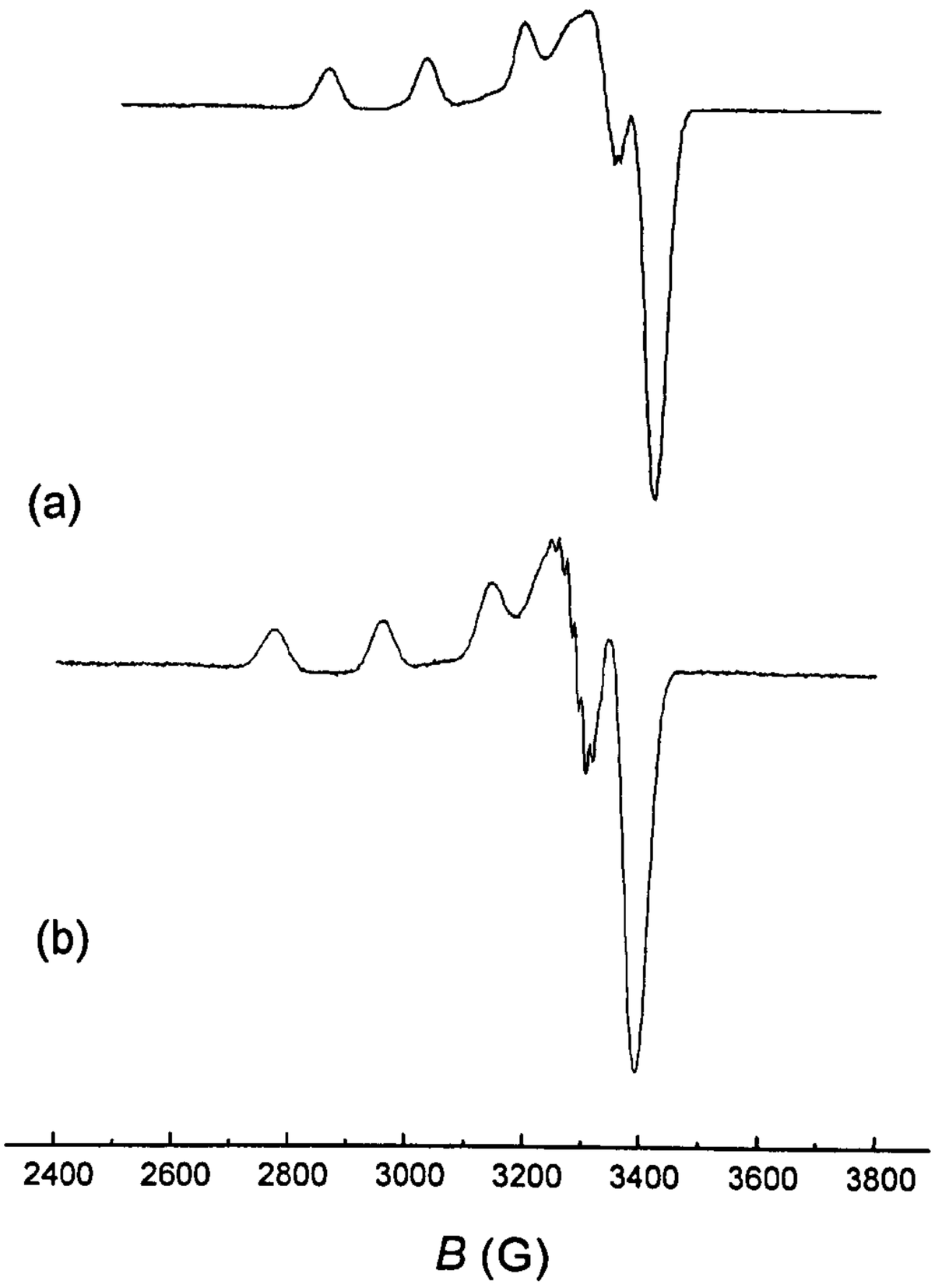

Figure 6.16 Frozen solution EPR (77 K) spectra for (a) [Cu(**15**)](BF$_4$)$_2$ and (b) [Cu(**16**)](BF$_4$)$_2$ in CH$_3$CN/DMF (9:1) solutions.

In order to evaluate the behaviour of these nitrile derivatives of [9]aneN$_3$ with different Cu^{II} salts, the reaction of L^5 with CuCl$_2$·2H$_2$O in CH$_3$CN at room temperature was carried out (Figure 6.14). Pale green single crystals suitable for X-ray diffraction studies were grown by diffusion of Et$_2$O vapour into an acetonitrile solution of the complex. The crystal structure (Figure 6.17) and the elemental analytical data confirm that this time the counterions are still co-ordinated to the metal centre to form the distorted square-based pyramidal copper(II) complex [Cu(L^5)Cl$_2$]. The presence of these co-ordinated Cl$^-$ anions explains why, in contrast to the situation in [Cu(**15**)](BF$_4$)$_2$ and [Cu(**16**)](BF$_4$)$_2$, the Cu^{II} forms a stable complex with L^5, although the nitrile pendant arms are all

pointing away from the metal centre. This behaviour is analogous to that observed with the two cyanoethyl derivatives of [9]aneN$_2$S and [9]aneNS$_2$ (Section 6.1.1, Figure 6.4) with the Cu^{II} ion co-ordinated to the three donors of the macrocycle and to two chloride anions.[402] The donor atoms forming the base of the pyramid are two tertiary amines [N(1) and N(4)] from the macrocyclic framework and the two chloride anions [Cl(1) and Cl(2)]. The Cu^{II} ion is displaced 0.166 Å from the mean plane defined by N(1), N(4), Cl(1) and Cl(2) in the direction of the apical position occupied by the remaining tertiary amine [N(7)]. The Cu-N(7) apical bond forms an angle of 16.1° with the normal to the basal plane, and the *trans*-basal angles are 176.40(5)° and 163.99(5)° [N(1)-Cu-Cl(1) and N(4)-Cu-Cl(2), respectively]. The Cu-N(basal) and the Cu-Cl bond lengths lie in the ranges 2.120(2)-2.129(2)Å and 2.262(1)-2.287(1)Å, respectively, and Cu-N(apical) is 2.237(2)Å (Table 6.3). The base of the pyramid is less regular than in the two crystal structures discussed before, with larger angles between the nitrogen atoms and the chlorides [91.46(5)° and 93.92(5)°] than between the two nitrogen donors N(1) and N(4) [83.02(6)°]. The Cu-N(basal) bond distances are significantly longer than those of [Cu(**15**)]$^{2+}$ and [Cu(**16**)]$^{2+}$, but comparable with those reported for the Cu^{II} complex with the

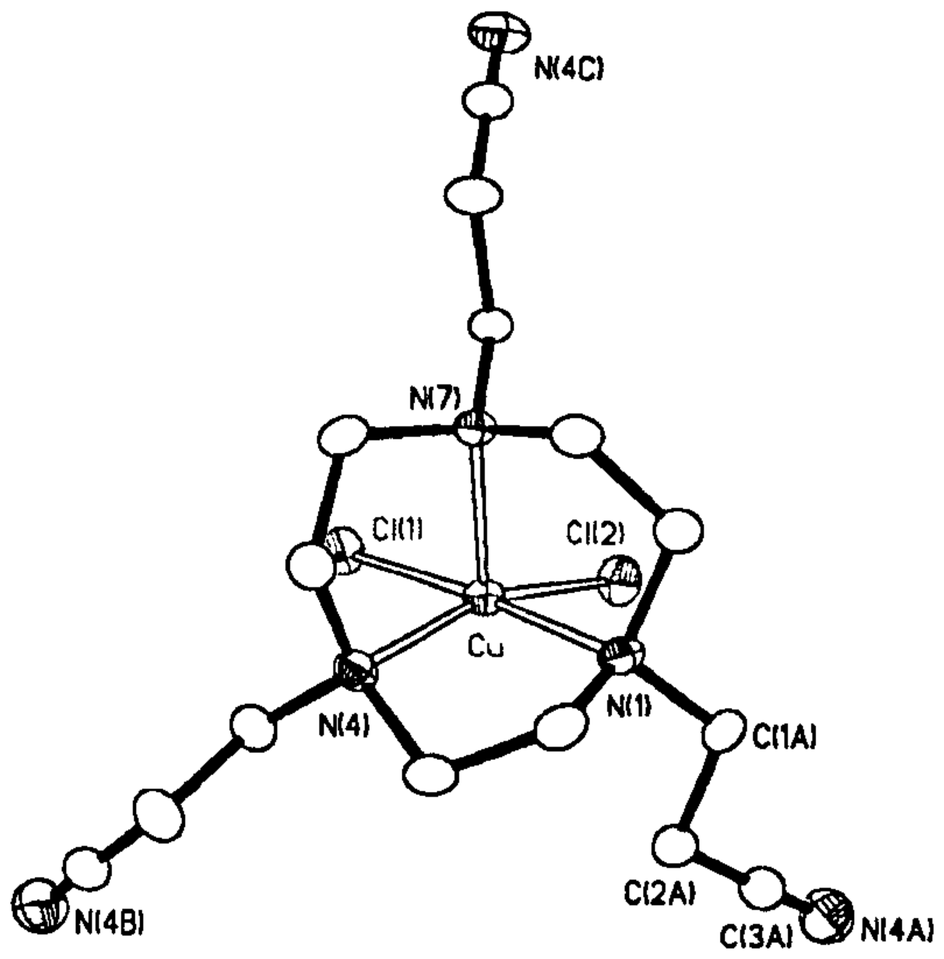

Figure 6.17. Crystal structure of [Cu(L^5)Cl$_2$] with numbering scheme adopted. Hydrogen atoms have been omitted for clarity and displacement ellipsoids are drawn at 50% probability.

bis(2-cyanoethyl) derivative of [9]aneN$_2$S (Figure 6.4a): as in [Cu(L^5)Cl$_2$], this has the basal positions occupied by the two tertiary amines of the macrocycle and by two chloride anions [range Cu-N 2.095(5)-2.132(6)Å].[402] However, the Cu-N(apical) bond length is similar to those reported for other square-based pyramidal Cu^{II} complexes with [9]aneN$_3$ derivatives.[375,377,429,430]

Table 6.3 Selected bond lengths (Å) and angles (°) for [Cu(L^5)Cl$_2$].

Cu – N(1)	2.120(2)	N(4)-Cu-N(7)	83.28(6)
Cu – N(4)	2.129(2)	N(1)-Cu-Cl(1)	176.40(5)
Cu – N(7)	2.237(2)	N(1)-Cu-Cl(2)	91.46(5)
Cu – Cl(1)	2.287(1)	N(4)-Cu-Cl(1)	93.92(5)
Cu – Cl(2)	2.262(1)	N(4)-Cu-Cl(2)	163.99(5)
		N(7)-Cu-Cl(1)	98.97(4)
N(1)-Cu-N(4)	83.02(6)	N(7)-Cu-Cl(2)	111.00(4)
N(1)-Cu-N(7)	82.59(6)	Cl(1)-Cu-Cl(2)	91.00(2)

Due to time restrictions, a complete solution study of [Cu(L^5)Cl$_2$] could not be carried out and the analogous complex with L^1 was not synthesised, although presumably it is analogous to [Cu(L^5)Cl$_2$]. Interestingly, refluxing L^5 with CuCl$_2$·2H$_2$O in MeOH for two hours caused a colour change in the solution, but attempts to crystallise the complex were unsuccessful. The reason probably lies in the formation of a mixture of products: one type of complex retains the two co-ordinated chloride anions while another reacts with methanol forming imino-ether groups.

6.3 Co-ordination chemistry of aminoalkyl derivatives of [9]aneN$_3$

6.3.1 Mono-aminoethyl derivative of [9]aneN$_3$

The preparation of the mono-aminoethyl derivative of [9]aneN$_3$ L^7 is shown in Figure 6.18. The reaction of 4,7-*bis*(*p*-tolylsulfonyl)-1,4,7-triazacyclononane (**17**) with one molar equivalent of *N*-tosyl-aziridine in CH$_3$CN and under N$_2$ gave 4,7-*bis*(*p*-tolylsulfonyl)-1-(2-aminoethyl-N-*p*-tolylsulfonyl)-

1,4,7-triazacyclononane (**18**) in 81% yield after recrystallisation from $CHCl_3$/EtOH. Single crystals suitable for X-ray diffraction studies were obtained, and the molecular structure of **18** is shown in Figure 6.19. The detosylation with concentrated sulphuric acid afforded L^7 in 78.5% yield after passing a water solution of the sulphate salt of the amine through an Amberlite IRA 416 column activated with 1M NaOH.

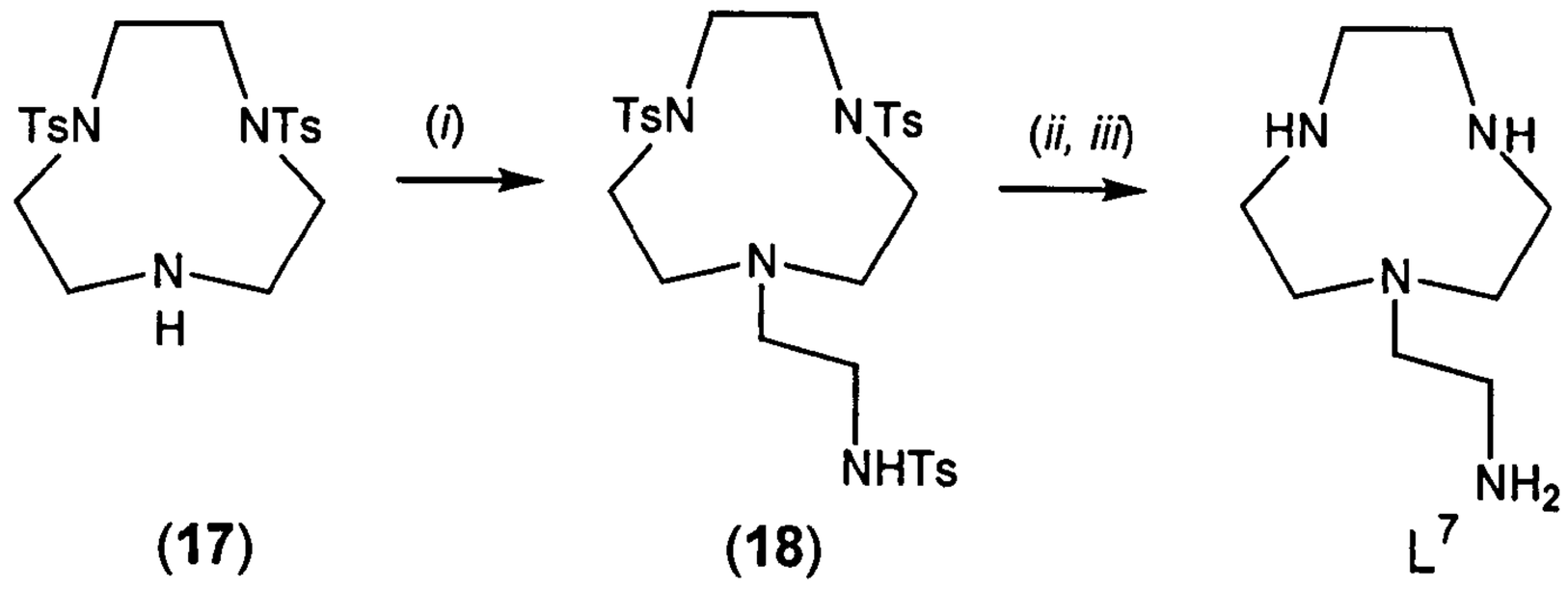

Figure 6.18 Scheme for the synthesis of L^7. *i*: Ts-aziridine, MeCN, reflux 28 h; *ii*: H_2SO_4 conc., 72 h; iii: Amberlite IRA-416.

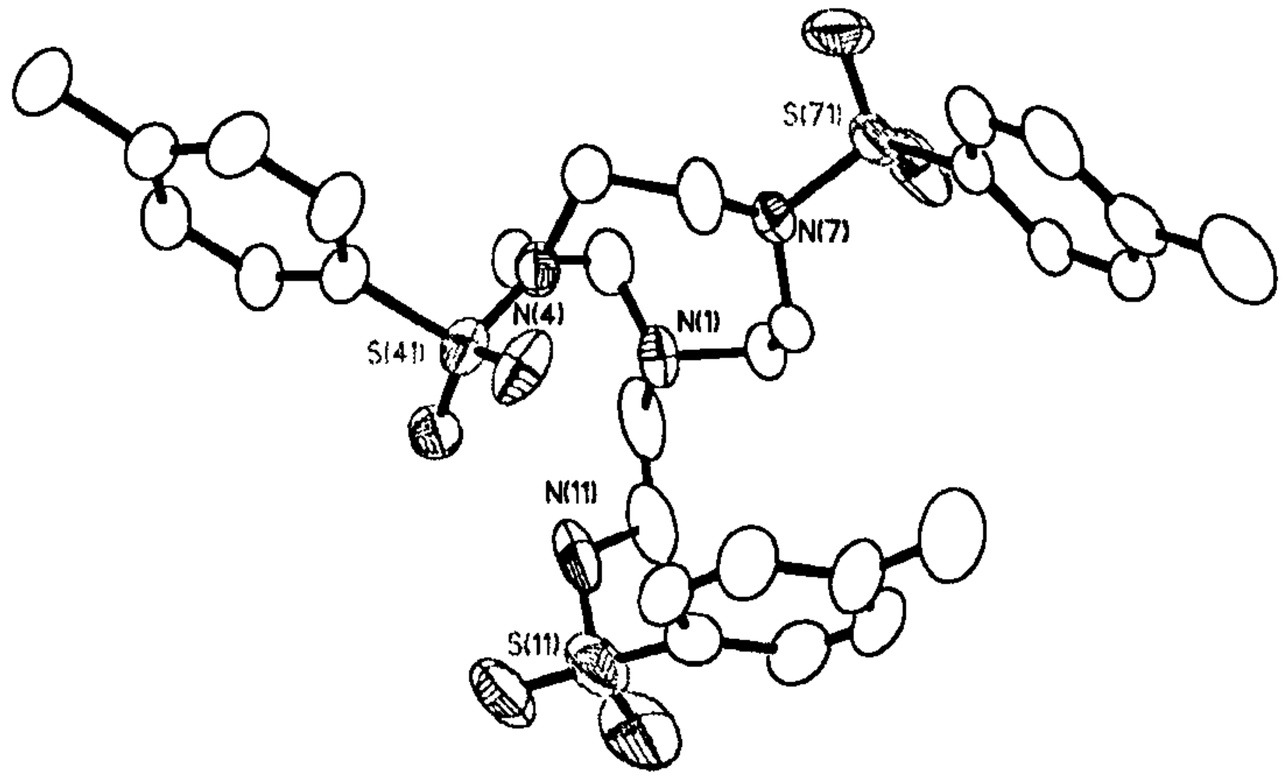

Figure 6.19. Crystal structure of **18** with numbering scheme adopted. Hydrogen atoms have been omitted for clarity. Displacement ellipsoids are drawn at 50% probability.

Reaction of L^7 with one molar equivalent of $M(BF_4)_2 \cdot xH_2O$ (M = Cu^{II} or Zn^{II}) gave only oily products. Therefore the residue was further reacted with one molar equivalent of NaBr (in the case of the Cu^{II} complex) and KSCN (for the Zn^{II} complex) yielding crystalline solids which by elemental analytical data and

mass spectra are consistent with the respective formulations $[Cu(L^7)]Br_2$ and $[Zn(L^7)(SCN)](BF_4)$.

Diffraction quality crystals of the Cu^{II} complex were obtained by slow diffusion of Et_2O vapour into a DMF solution of the complex. The molecular structure of the complex cation $[Cu(L^7)Br]^+$, shown in Figure 6.20, is best described as a distorted square pyramid, with the copper atom above the plane described by the four basal donors [N(1), N(7), N(3A) and Br(1)] and the apical

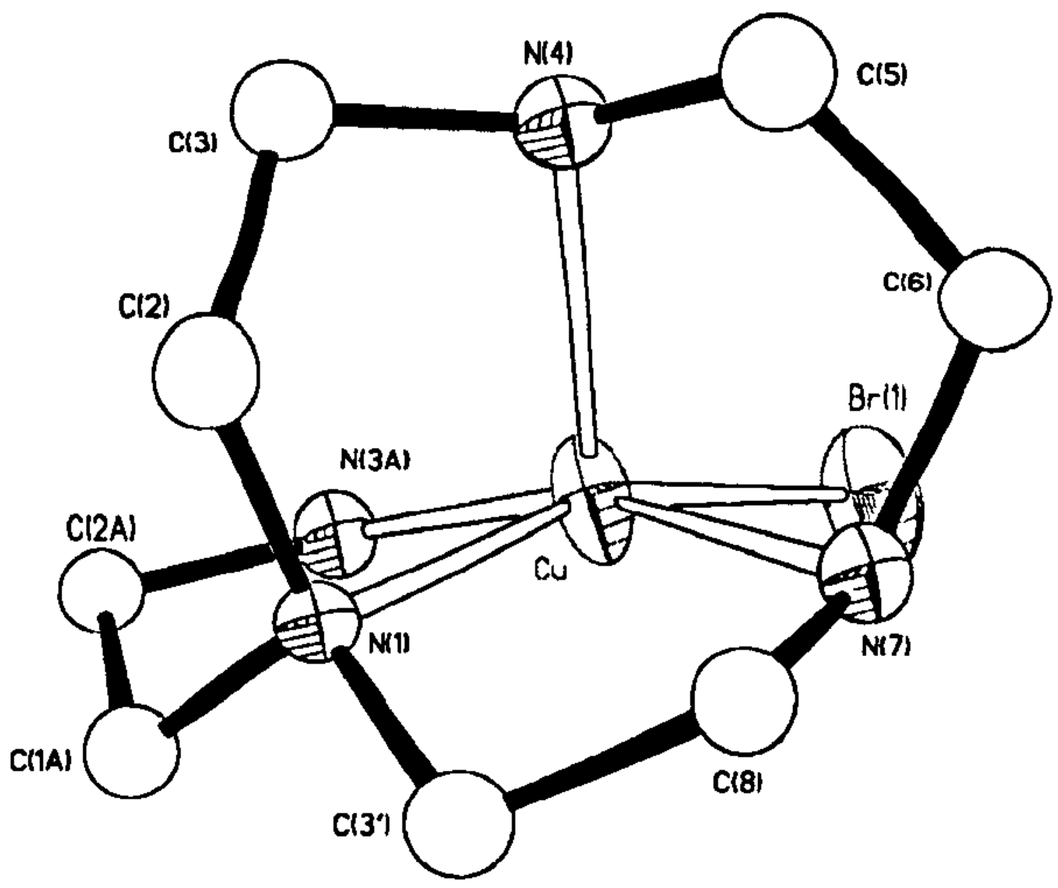

Figure 6.20. Structure of the complex cation $[Cu(L^7)Br]^+$ with the numbering scheme adopted. Hydrogen atoms have been omitted for clarity and displacements ellipsoids are drawn at 50% probability.

nitrogen [N(4)] tilted away from the position directly above the copper atom. The displacement of the Cu^{II} out of the plane is 0.30 Å towards the apical position and the angle between the N(apical)-Cu vector and the normal to the N_3Br plane is 18.7°. The latter is a result of the inability of the ligand completely to reach over and occupy the apical position. The Cu-N bond lengths are different from those observed in other square-based pyramidal Cu^{II} complexes because the Cu-N(apical) distance [2.119(10) Å] is only slightly longer than Cu-N(basal) [1.955(9)-2.100(9) Å], showing a very small Jahn-Teller distortion. The major difference lies in the bond lengths between the metal ion and primary or tertiary amino groups [Cu-N(3A) 1.955(9) Å; average Cu-N(tertiary amine)

2.099 Å] which could be due in part to the increased steric repulsion at the tertiary amines and in part to lower binding ability of tertiary compared with primary amines. The *trans*-basal angles [N(1)-Cu-Br(1) and N(7)-Cu-N(3A), respectively] are 162.9(2)° and 160.9(3)°, in good agreement with the values expected for square pyramidal geometry around d^9 Cu^{II} complexes.[432,433] The base of the pyramid is more rhomboidal than square, with longer distances between the nitrogen atoms and the bromide [N(7)-Br(1) 3.320 Å and N(3A)-Br(1) 3.215 Å] than between the N-donors [N(1)-N(3A) 2.716 Å and N(1)-N(7) 2.740 Å].

Table 6.3 Selected bond lengths (Å) and angles (°) for $[Cu(L^7)]Br_2$.

Cu – N(1)	2.100(9)	N(4)-Cu-N(7)	83.3(3)
Cu – N(4)	2.119(10)	N(1)-Cu-N(3A)	84.0(4)
Cu – N(7)	2.077(9)	N(1)-Cu-Br(1)	162.9(2)
Cu – N(3A)	1.955(9)	N(4)-Cu-N(3A)	108.4(3)
Cu – Br(1)	2.4089(14)	N(4)-Cu-Br(1)	111.5(2)
		N(7)-Cu-N(3A)	160.9(3)
N(1)-Cu-N(4)	85.0(3)	N(7)-Cu-Br(1)	95.2(2)
N(1)-Cu-N(7)	82.0(3)	N(3A)-Cu-Br(1)	94.3(3)

$[Cu(L^7)Br]^+$ can be compared to the crystal structure of the Cu^{II} complex with the derivative of [9]aneNS$_2$ having one propylamino pendant arm. In this square-based pyramidal Cu^{II} complex the base of the pyramid is formed by one S- and the N-donor of the macrocycle, the primary amine and a chloride anion and the apical position is taken up by the other S-donor from the ring. Again, the shortest Cu-donor bond length involves the primary amine [1.996(3) Å]. Triaza macrocycles bearing one primary amino pendant arm have been synthesised, but only Ni^{II} and Zn^{II} complexes have been reported.[434]

The electronic spectrum of $[Cu(L^7)Br]^+$ recorded in CH_3CN at room temperature shows only one band in the visible region at 622 nm, with molar extinction coefficient of 96 dm^3 mol^{-1} cm^{-1}, values typical of a slightly distorted square-based pyramidal Cu^{II} complex.[377,429]

The X-band EPR spectrum of $[Cu(L^7)Br]^+$ was recorded as frozen (77 K) MeCN/DMF (ratio 9/1, v/v) glass and shows four hyperfine signals typical of

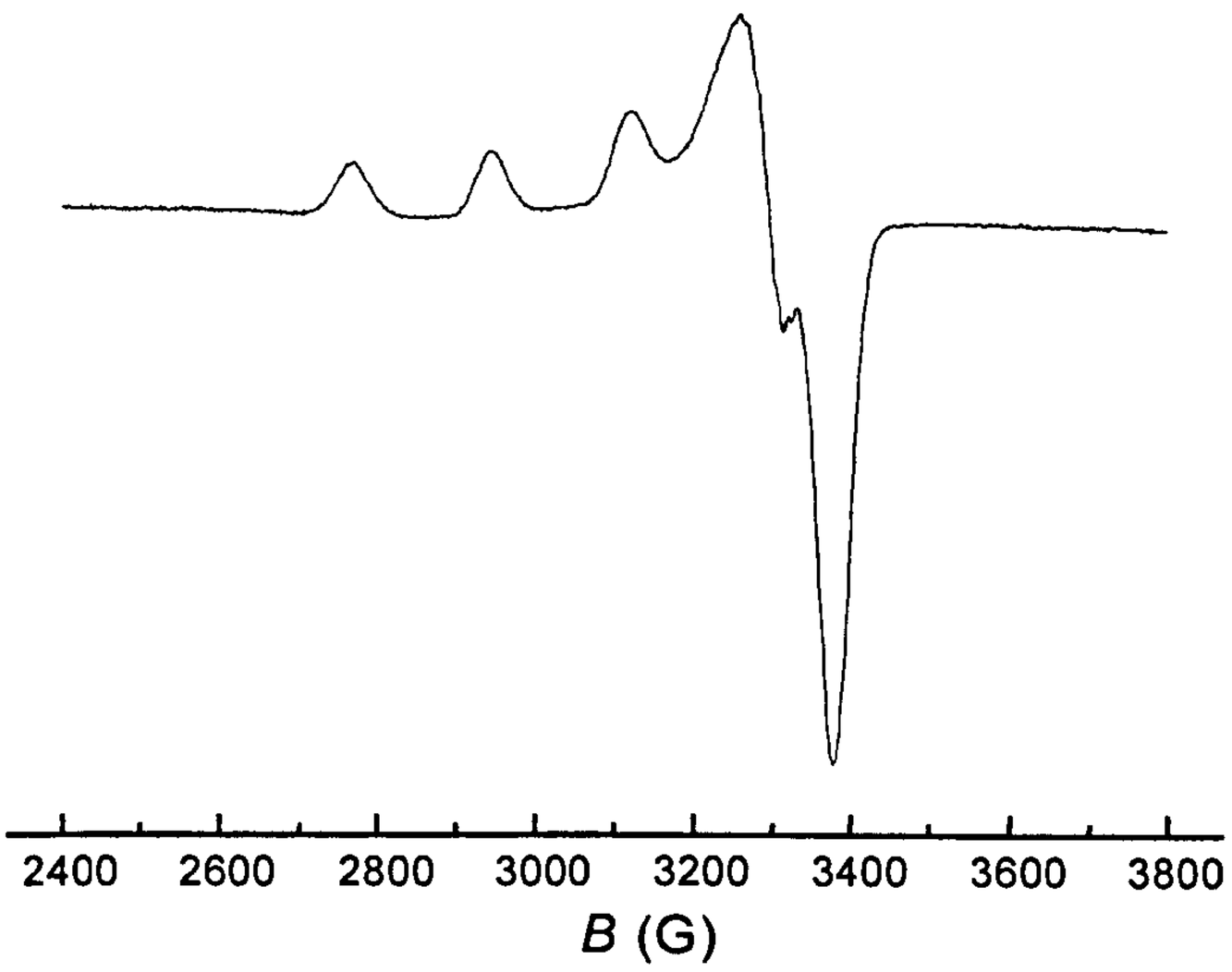

Figure 6.21. Frozen solution EPR (77 K) spectrum for $[Cu(L^7)Br]^+$ in CH_3CN/DMF (9:1) solution.

mononuclear Cu^{II} complexes with nuclear spin 3/2 and tetragonally distorted or square-based pyramidal co-ordinating geometry with $d_{x^2-y^2}$ ground state (g_{11} = 2.230, A_{11} = 175.2 G, g_{22} = 2.053 and g_{33} = 2.004). Again, although it is weak, a superhyperfine coupling to the nitrogen atoms co-ordinated to the Cu^{II} centre can be seen in the perpendicular region of the spectrum.

Single crystals of the Zn^{II} complex were not suitable for X-ray diffraction studies; ^1H and ^{13}C NMR spectroscopic studies were carried out in order to evaluate the shift of the ligand's peaks after complexation. The ^1H NMR spectrum recorded in CD_3CN at 298 K shows a complex splitting pattern with many overlapping peaks. The ^{13}C NMR spectrum (CD_3CN, 298 K) shows six peaks (Table 6.5) corresponding to five methylene carbon atoms of the complex (two from the pendant arm and three from the macrocyclic ring) and one from the SCN^- anion. With respect to the free ligand L^7, all the carbon atoms next to the nitrogen atoms are shielded, showing that in solution all the N-donors are co-ordinated to the metal ion. A more pronounced shift with respect to the peaks of L^7 is observed for the methylene carbon atoms of the pendant arms [$\Delta\delta$ =-4.68 and -2.95 ppm for C(1A) and C(2A), respectively; the numbering scheme adopted is the same in the crystal structure of the Cu^{II}

complex] than for the C(2), C(3) and C(5) carbons of the macrocycle (average $\Delta\delta$ = -2.67 ppm).

Table 6.5. ^{13}C NMR chemical shift data (δ, ppm) for L^7 and $[Zn(L^7)(SCN)](BF_4)$ (CD_3CN, 298 K).

	C(2A)	C(3) or C(5)	C(3) or C(5)	C(2)	C(1A)	SCN
L^7	40.41	46.86	47.05	53.50	60.81	--
$[Zn(L^7)(SCN)](BF_4)$	37.46	44.23	44.37	50.80	56.13	122.67

6.3.2 Bis-aminoethyl derivative of [9]aneN$_3$

The synthesis of the ligand L^2 has been already described in Section 5.3.1; herein its co-ordination properties towards transition metals are described. Reacting L^2 with one equivalent of the appropriate metal salt (MX_2 where M = Mn^{II}, Ni^{II}, Cu^{II} or Zn^{II}; X = NO_3^-, BF_4^- or ClO_4^-) in MeOH at room temperature gives the complexes $[Mn(L^2)](NO_3)_2$, $[Ni(L^2)CH_3CN](BF_4)_2$ and $[M(L^2)](ClO_4)_2$ (M = Cu^{II} and Zn^{II}). Elemental analytical data and mass spectra for all the complexes are consistent with these formulations.

Colourless columnar crystals of $[Mn(L^2)NO_3](NO_3)$ were obtained by diffusion of Et_2O vapour into a methanolic solution of the complex. A single crystal X-ray structure determination confirms the product to be a mononuclear complex (Figure 6.22) with the Mn^{II} ion co-ordinated to the five N-donors of the ligand and one oxygen from a nitrate anion. The co-ordination geometry around the Mn^{II} centre is a distorted trigonal prism, with one face taken up by the three N-donors of the triaza ring [Mn-N 2.247(2)-2.388(2) Å] and the other occupied by the two primary amines [Mn-N(3A) 2.228(2) and Mn-N(3B) 2.250(2) Å] and by the oxygen atom [Mn-O(4) 2.268(2) Å]. The two triangular faces of the prism are almost parallel, being inclined to each other by only 6.1°, and slightly twisted (average of 4.3°). Interestingly, intermolecular and intramolecular H-bonds occur between nitrate oxygens and both the primary amines and the N-H on the ring: Figure 6.22 shows two centres linked by a bridging nitrate and also the six-membered ring formed by the nitrate [N(2N), O(4) and O(5)], the metal

and N(3B). These hydrogen bonds (N–H···O) have H···O distances between 2.14 Å and 2.47 Å and N–H···O angles of 142°–154°. The Mn-N bond distances are comparable to those reported for a Mn^{II} complex of 4,7-*bis*(2-methylpyridyl)-1,4,7-triazacyclononane, a pentadentate ligand derivative of [9]aneN$_3$.[435] In this complex the Mn^{II} centre is co-ordinated by the five N-donors of the ligand and by a chloride anion in a trigonal prismatic geometry, more distorted than that in [Mn(L^2)](NO$_3$)$_2$ (twist angle of 23.4°).

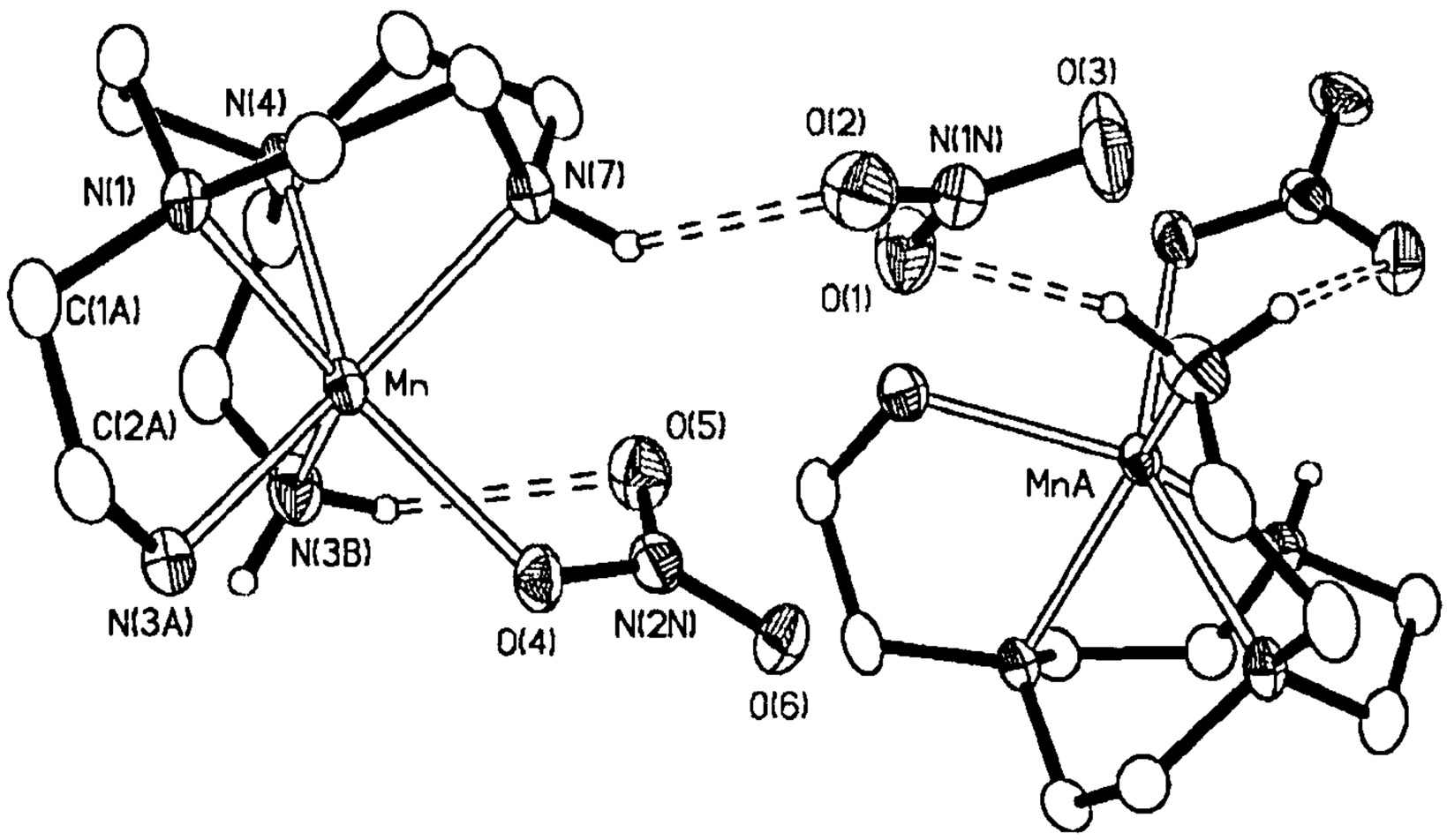

Figure 6.22 View of two complex cations connected by hydrogen-bonded bridging nitrates in [Mn(L^2)](NO$_3$)$_2$ with numbering scheme adopted. Hydrogen atoms on carbon atoms have been omitted for clarity. Symmetry operation: A =-x+1, y+1/2, -z+1/2.

The Ni^{II} complex with L^2 was re-crystallised from Et$_2$O/CH$_3$CN to give light green crystals suitable for X-ray diffraction studies, which showed the complex [Ni(L^2)CH$_3$CN](BF$_4$)$_2$ with the metal centre in a slightly distorted octahedral geometry (Figure 6.23). The six co-ordinate metal ion is co-ordinated by the five N-donors of the ligand (three tertiary and two primary amines) and one acetonitrile molecule. The donor atoms in the equatorial plane are N(4), N(7), N(3A) and N(3B) which have an r.m.s. deviation from the N$_4$ equatorial plane of 0.141 Å, while the axial positions are taken up by N(1) and N(3S), the latter from the acetonitrile molecule. The metal ion is displaced only

0.085 Å out of the N_4 equatorial plane. $[Ni(L^2)CH_3CN](BF_4)_2$ exhibits a slight trigonal elongation with the triangular face of the octahedron formed by N(7), N(3A) and N(3B) elongated in respect to the face N(1), N(4) and N(3S) (bond lengths 2.101(2)-2.144(2) Å and 2.078(2)-2.092(2) Å, respectively).

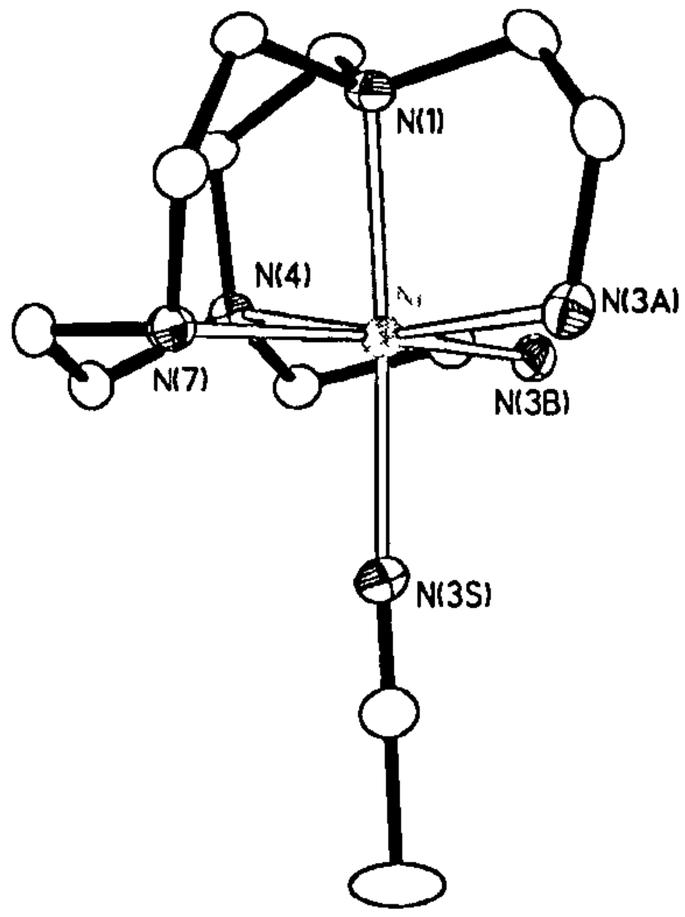

Figure 6.23 Crystal structure of the cation $[Ni(L^2)(CH_3CN)]^{2+}$ with numbering scheme adopted. Hydrogen atoms and BF_4^- anions have been omitted for clarity. Displacement ellipsoids are drawn at 50% probability.

An X-ray diffraction study on the Cu^{II} complex with L^2 was undertaken to ascertain the stereochemistry and ligation within the complex. As observed for the Cu^{II} complexes discussed in Section 6.2, the structure of the cation in $[Cu(L^2)](ClO_4)_2$ (Figure 6.24) shows the ligand encapsulating the metal ion in a distorted square-based pyramidal geometry. The basal co-ordination sites are occupied by the two primary amino groups [N(3A) and N(3B) at 2.018(3) and 2.019(3) Å] and two N-donors of the macrocycle [N(1) and N(4) at 2.054(2) and 2.033(2) Å]. The apical position is taken up by the secondary amino group of the pentadentate ligand L^2 [Cu-N(7) 2.206(2)Å]. The Cu-N_{eq} bond lengths are typical of N_4 ligands co-ordinated in planar fashion around Cu^{II}, but a slight difference in the bond distances between the metal centre and primary and tertiary N-donors can be discerned, as already observed in the Cu^{II} complex of 1-methyl-4,7-bis(3-aminopropyl)-1,4,7-triazacyclononane [Cu-N_{eq}: 2.026(6)-

2.074(5) Å].[377] This difference could be due in part to the increased steric repulsion at the tertiary amines and in part to lower binding ability of tertiary compared to primary amines. The Cu-N(apical) bond is more similar to that reported for the copper(II) complex of 4,7-bis(2-methylpyridyl)-1,4,7-triazacyclononane [2.162(8) Å][429] than to that of the Cu^{II} complex of 1-methyl-4,7-bis(3-aminopropyl)-1,4,7-triazacyclononane [2.257(6) Å],[377] probably because in the first complex the apical N-donor is a secondary amine, as in $[Cu(L^2)]^{2+}$, while in the second it is a tertiary amine. The metal ion is displaced out of the N_4 plane (r.m.s. deviation from this plane is 0.10 Å) by 0.379 Å towards the apical N-donor and the Cu-N(7) vector shows a deviation from perpendicularity with the N_4 basal plane [23.9°]. These values exceed those observed for Cu^{II} complexes with similar ligands, indicating a more pronounced distortion from regular square pyramidal geometry: this can also be seen in the *trans*-basal angles [N(1)-Cu-N(3B) 152.0(1)° and N(4)-Cu-N(3A) 163.5(1)°]. In $[Cu(L^2)]^{2+}$ the square base of the pyramid is quite regular with three five-membered chelate rings formed at the metal centre: these are very similar both in the angles at the metal centre [82.7(1)°-85.6(1)°] and in the distance between the nitrogens [2.75(1)Å-2.78(1)Å]. Moreover, hydrogen bonding interactions

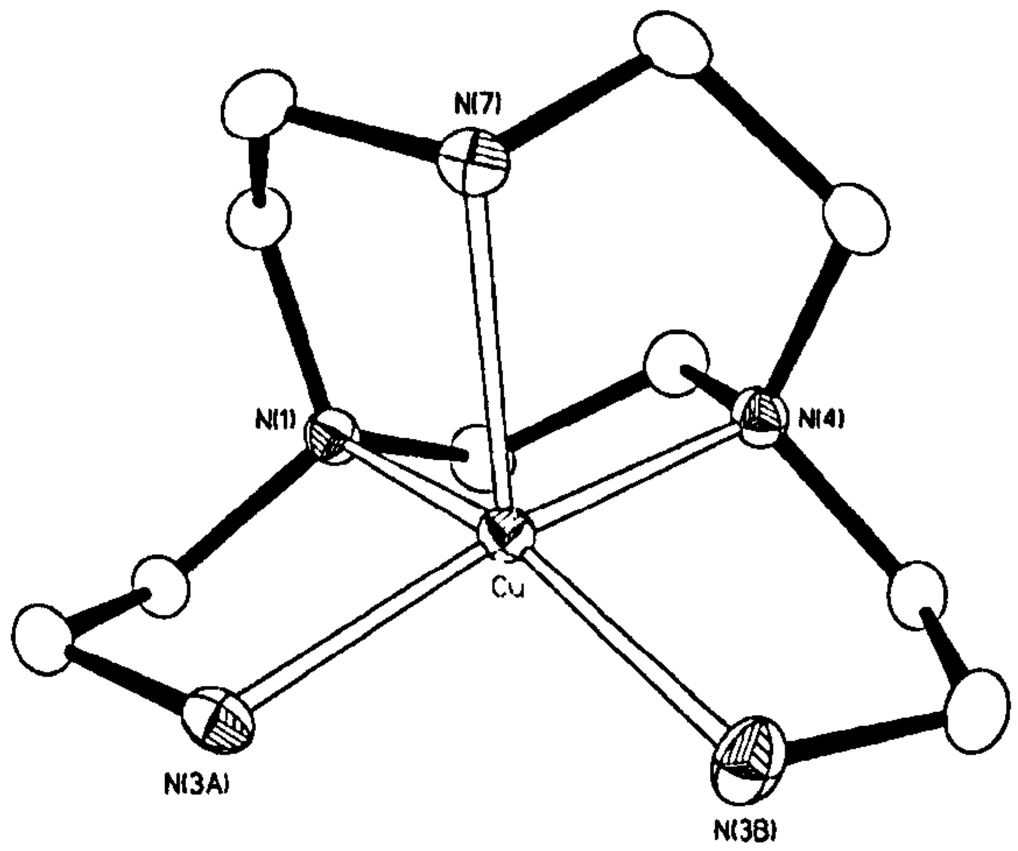

Figure 6.24 Crystal structure of $[Cu(L^2)](ClO_4)_2$ with numbering scheme adopted. Anions and hydrogen atoms have been omitted for clarity. Displacement ellipsoids are drawn at 50% probability.

between NH_2 and anion oxygens which connect more units together occur in the structure (H···O distances of 2.10 and 2.24 Å and N–H···O angles of 147° and 159°, respectively).

The electronic spectrum of $[Cu(L^2)]^{2+}$ recorded in CH_3CN at room temperature shows only one band in the visible region at 591 nm, with a molar extinction coefficient of 107 $dm^3\ mol^{-1}\ cm^{-1}$. This value is very similar to those reported for other slightly distorted square-based pyramidal Cu^{II} complexes $[Cu(\mathbf{15})]^{2+}$, $[Cu(\mathbf{16})]^{2+}$ and $[Cu(L^7)Br]^{+}$. The electronic spectrum of $[Ni(L^2)MeCN]^{2+}$ recorded in CH_3CN at room temperature shows two bands at 516 and 807 nm, with molar extinction coefficients of 26 and 37 $dm^3\ mol^{-1}\ cm^{-1}$, respectively.

Table 6.6 Selected bond lengths (Å) and angles (°) for $[Cu(L^2)](BF_4)_2$, $[Ni(L^2)(CH_3CN)](BF_4)_2$ and $[Mn(L^2)](NO_3)_2$ [X = N(3S) for the Ni^{II} and O(4) for the Mn^{II} crystal structures].

	$[Cu(L^2)](BF_4)_2$	$[Ni(L^2)(CH_3CN)](BF_4)_2$	$[Mn(L^2)](NO_3)_2$
M – N(1)	2.054(2)	2.092(2)	2.343(2)
M – N(4)	2.033(2)	2.078(2)	2.388(2)
M – N(7)	2.206(2)	2.107(2)	2.247(2)
M – N(3A)	2.018(3)	2.101(2)	2.250(2)
M – N(3B)	2.019(3)	2.144(2)	2.228(2)
M – X	--	2.081(2)	2.268(2)
N(1)-M-N(4)	85.6(1)	85.14(8)	74.33(6)
N(1)-M-N(7)	84.1(1)	83.13(8)	76.88(6)
N(4)-M-N(7)	82.7(1)	83.28(8)	75.81(6)
N(1)-M-N(3A)	85.6(1)	83.15(8)	76.08(7)
N(1)-M-N(3B)	152.0(1)	100.33(8)	131.52(7)
N(4)-M-N(3A)	163.5(1)	167.09(8)	128.55(6)
N(4)-M-N(3B)	85.5(1)	82.27(8)	76.21(7)
N(7)-M-N(3A)	110.2(1)	100.64(9)	135.17(7)
N(7)-M-N(3B)	120.9(1)	164.79(8)	130.59(7)
N(3A)-M-N(3B)	95.8(1)	94.49(8)	93.91(7)
N(1)-M-X	--	171.72(8)	133.15(6)
N(4)-M-X	--	98.67(8)	144.20(6)
N(7)-M-X	--	89.98(8)	87.94(6)
N(3A)-M-X	--	93.65(9)	85.20(6)
N(3B)-M-X	--	87.51(9)	91.73(7)

Single crystals of the Zn^{II} complex were not suitable for X-ray diffraction studies, but as the ^1H NMR spectrum recorded in CD_3CN at 298 K shows a complex splitting pattern with many peaks overlapping each other, the ^{13}C NMR spectrum was recorded in order to evaluate the shift of the ligand peaks after complexation. The ^{13}C NMR spectrum (CD_3CN, 298 K) shows five peaks (Table 6.7) corresponding to five methylene carbon atoms of the complex (a mirror plane passes through the metal and N(7) and bisects the N(1)-Zn-N(4) angle, using the numbering scheme for the Mn^{II}, Ni^{II} and Cu^{II} crystal structures). With respect to the free ligand L^2, all the carbon atoms adjacent to N-donors are shielded, showing that in solution all the nitrogen atoms are co-ordinated to the metal ion. A more pronounced shift with respect to the peaks of L^2 is observed for the methylene carbon atoms of the pendant arms ($\Delta\delta$ =-3.79 and -2.46 ppm for C(1A) and C(2A), respectively) than for the C(2), C(8) and C(9) carbons of the macrocycle (average $\Delta\delta$ = -0.96 ppm).

Table 6.7 ^{13}C NMR (298 K, CD_3CN) chemical shift data (δ, ppm) for L^2 and $[Zn(L^2)](BF_4)_2$ (X = A or B).

	C(2X)	C(8)	C(2) or C(9)	C(2) or C(9)	C(1X)
L^2	40.34	46.78	52.21	53.72	61.25
$[Zn(L^2)](BF_4)_2$	37.88	45.95	51.10	52.79	57.50

6.3.3 Complexes with 1,4,7-tris(3-aminopropyl)-1,4,7-triazacyclononane

Although this ligand (L^6, Figure 6.6) has already been described in the literature together with its complexes with Co^{III} and Ni^{II} (Section 6.1.2),[239] no study of its complexes with transition metal ions such as Mn^{II}, Cu^{II} and Zn^{II} has been reported.

Reaction of L^6 with one molar equivalent of $Mn(NO_3)_2$ in MeOH at room temperature gave colourless columnar crystals following partial removal of the solvent and diffusion of Et_2O vapour into the remaining solution. The X-ray single crystal determination shows the Mn^{II} ion co-ordinated in a distorted

octahedral geometry to the six N-donors of the ligand. The Mn-primary amine [N(4X) X = A, B and C] bond lengths are slightly shorter [2.228(6)-2.253(5)Å] than those involving Mn-tertiary amines [2.297(5)-2.306(5)Å], as expected from a consideration of the increased steric repulsion at the tertiary amines and the lower donor ability of tertiary amino groups compared to primary ones. This difference in the bond lengths between the metal ion and primary and tertiary amines leads to a trigonal elongation of the octahedron towards the triangular face formed by the macrocyclic N-donors. The N_4 equatorial plane is formed by N(4), N(7), N(4A) and N(4B) (r.m.s. deviation 0.106 Å) with the metal ion displaced out of the plane of 0.136 Å towards N(4C). The vectors Mn-N_{ax} between the metal ion and the two axial N-donors [N(1) and N(4C)] are almost perpendicular to the N_4 equatorial plane [11.7° and 2.6°, respectively]. In $[Mn(L^6)]^{2+}$, the twist angle, as defined in the introductory Section 6.1.2, is 48.7° showing a distortion from ideal octahedral towards trigonal prismatic geometry. Interestingly, intermolecular and intramolecular H-bonds were identified

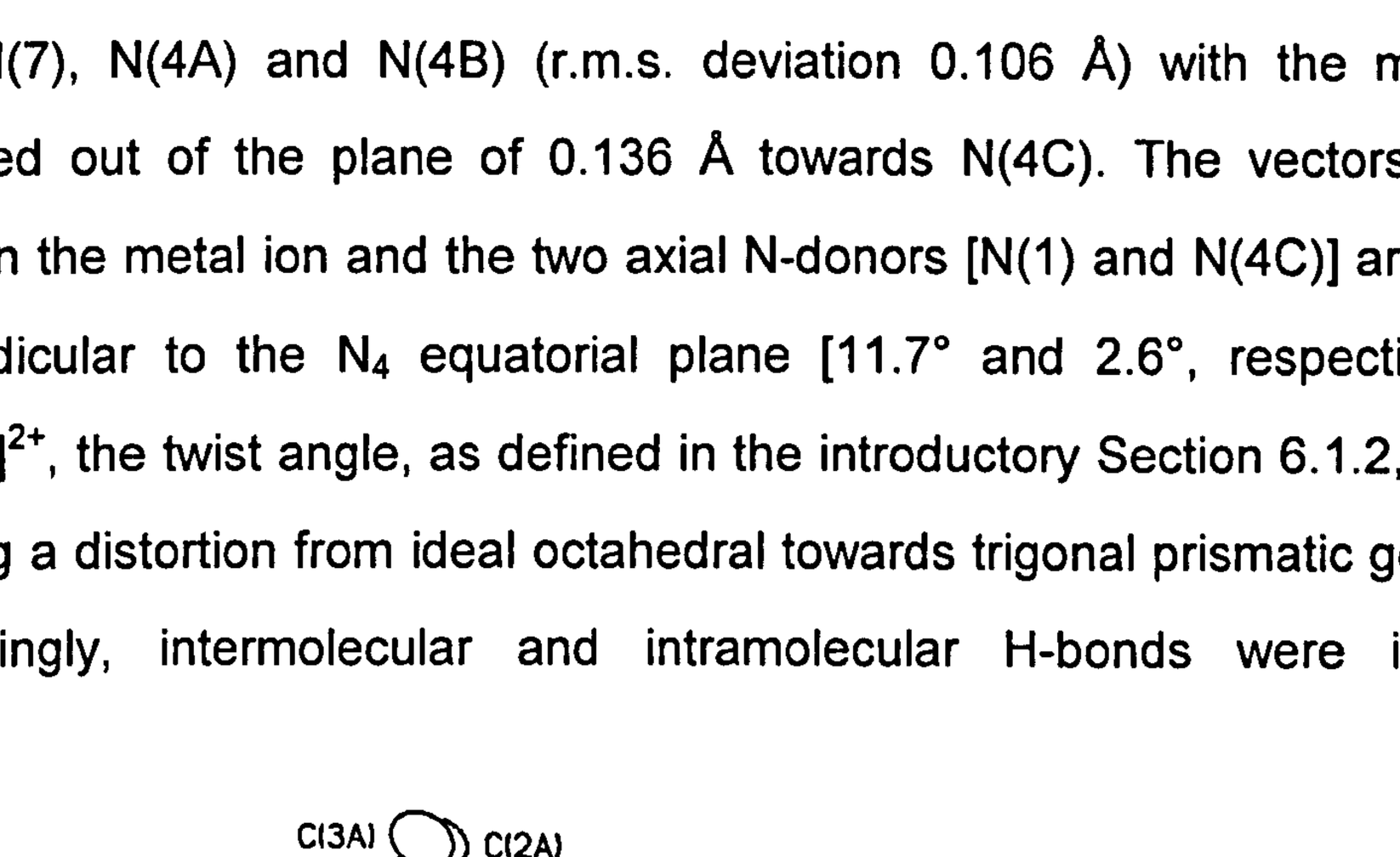

Figure 6.25 View of two complex cations connected by hydrogen-bonded bridging nitrates in $[Mn(L^6)](NO_3)_2$ with numbering scheme adopted. Hydrogen atoms on carbon atoms have been omitted for clarity. Symmetry operation: A = ¼+x, ¾-y, -¼+z.

between nitrate oxygens and the primary amines. Figure 6.25 shows two units connected by a bridging nitrate and also the eight-membered ring formed by one nitrate anion [N(2N), O(5N) and O(6N)], Mn(A) and two N-H from the symmetry related unit. In these hydrogen bonds (N–H···O) H···O distances are between 2.11 Å and 2.27 Å and N–H···O angles are between 151° and 165°.

The molecular structure of the Zn^{II} complex could be obtained by an X-ray single crystal determination of the colourless crystals grown by diffusion of Et_2O into an acetonitrile solution of the complex. The crystal structure of $[Zn(L^6)](BF_4)_2$ (Figure 6.26) shows the Zn^{II} ion encapsulated by the six N-donors of the ligand in a slightly distorted octahedral geometry (θ = 51.2°). The donor atoms in the equatorial plane [N(4), N(7), N(4A) and N(4B)] have an r.m.s. deviation from the mean N_4 equatorial plane of 0.056 Å, while the axial positions are taken up by N(1) and N(4C). The Zn-N_{ax} vectors are nearly perpendicular to the mean N_4 equatorial plane [9.0° and 2.2°] and the N(1)-Zn-N(4C) angle is 171.5(1)°. As observed for $[Mn(L^6)]^{2+}$, the Zn-primary amine N(4X) [X = A, B and C] bond lengths are slightly shorter [2.149(4)-2.165(3)Å] than the Zn-tertiary amine distances [2.219(4)-2.254(4)Å]. Therefore, $[Zn(L^6)](BF_4)_2$ shows a slight trigonal elongation from regular octahedral

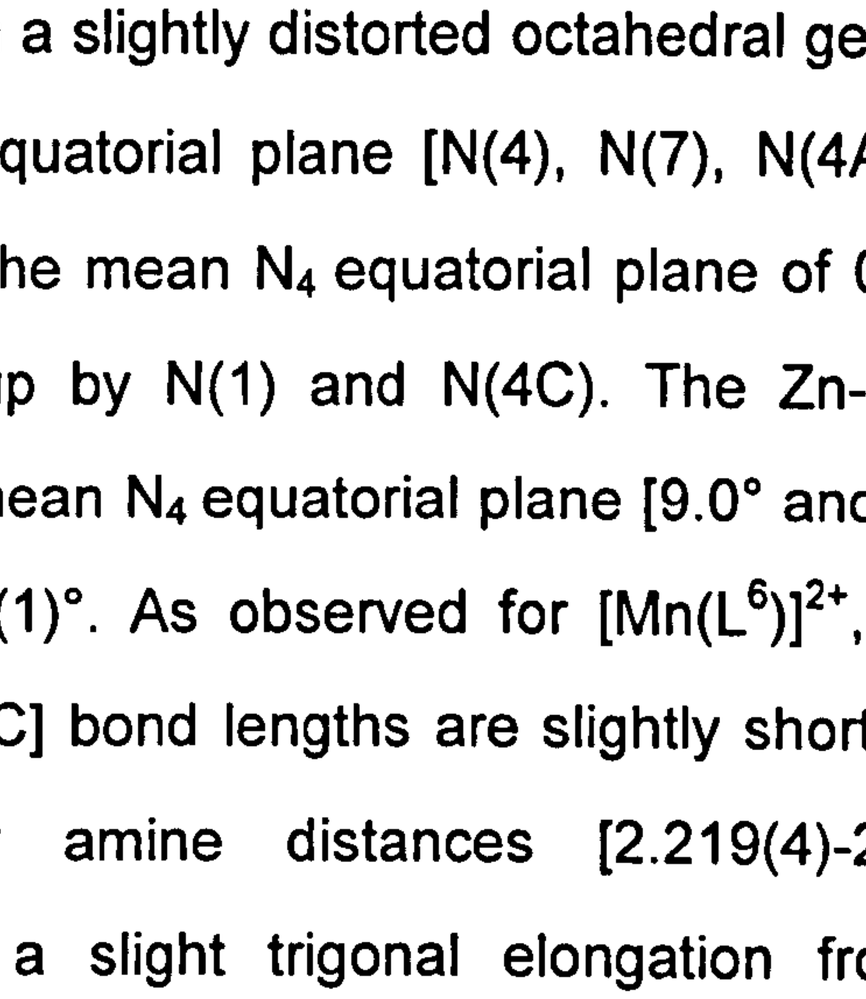

Figure 6.26 Crystal structure of $[Zn(L^6)](BF_4)_2$ with numbering scheme adopted. Hydrogen atoms and anions have been omitted for clarity. Displacement ellipsoids are drawn at 50% probability.

geometry with the triangular face of the octahedron formed by N(1), N(4) and N(7) elongated in respect to the face N(4A), N(4B) and N(4C).

Table 6.8 Selected bond lengths (Å) and angles (°) for [Cu(**12**)](BF$_4$)$_2$, [Mn(L^6)](NO$_3$)$_2$ and [Zn(L^6)](BF$_4$)$_2$

	[Cu(**12**)](BF$_4$)$_2$	[Mn(L^6)](NO$_3$)$_2$	[Zn(L^6)](BF$_4$)$_2$
M – N(1)	2.094(14)	2.304(5)	2.225(4)
M – N(4)	2.030(14)	2.297(5)	2.254(4)
M – N(7)	2.186(15)	2.306(5)	2.219(4).
M – N(4A)	2.022(13)	2.253(5)	2.165(3)
M – N(4B)	2.030(13)	2.228(5)	2.149(4)
M – N(4C)		2.228(6)	2.164(4)
N(1)-M-N(4)	86.7(6)	78.0(2)	80.48(14)
N(1)-M-N(7)	82.6(6)	78.2(2)	80.74(15)
N(4)-M-N(7)	82.9(6)	78.5(2)	81.01(14)
N(1)-M-N(4A)	88.7(5)	89.5(2)	90.86(15)
N(1)-M-N(4B)	171.3(6)	99.3(2)	95.92(15)
N(1)-M-N(4C)	--	168.7(2)	171.55(15)
N(4)-M-N(4A)	173.0(6)	167.5(2)	171.26(14)
N(4)-M-N(4B)	93.7(6)	90.5(2)	90.15(14)
N(4)-M-N(4C)	--	98.8(2)	96.34(14)
N(7)-M-N(4A)	101.8(6)	98.6(2)	96.50(13)
N(7)-M-N(4B)	106.1(6)	169.0(2)	170.94(14)
N(7)-M-N(4C)	--	90.5(2)	91.06(15)
N(4A)-M-N(4B)	90.0(6)	92.1(2)	91.95(14)
N(4A)-M-N(4C)	--	93.4(2)	92.07(15)
N(4B)-M-N(4C)	--	91.5(2)	91.89(14)

The reaction of L^6 with one equivalent of [Cu(BF$_4$)$_2$]·4H$_2$O in MeOH at room temperature yielded an interesting product. In fact, one of the three propylamino pendant arms was cleaved off and a square-based pyramidal five co-ordinate Cu^{II} complex was formed (Figure 6.28). The molecular structure of the complex cation [Cu(**12**)]$^{2+}$ has already been reported by McAuley and co-workers,[427] but it was prepared by reaction of **12** with Cu(ClO$_4$)$_2$ in H$_2$O/EtOH. In the same paper, the five co-ordinate nature of the Cu^{II} centre was noted in contrast with the corresponding Ni^{II} and Co^{III} complexes with **12** in which both metal centres are octahedral.[427] The Cu^{II} complex with L^6 is the only example involving a first row transition metal ion in which an arm is cleaved. The

cleavage is thought to be catalysed by the Cu^{II} ion which, as in all the structures reported in this chapter, prefers the penta than the octahedral co-ordination. There is a very small crystal field stabilisation energy (CFSE) difference between octahedral and square pyramidal complexes for d^9 ions, such that the difference in CFSE would not compensate for the steric strain caused by the addition of a sixth donor. Interestingly, the Cu^{II} centre is also five co-ordinate in the complex with the exodentate ligand **13** (Section 6.1.2 and Figure 6.10b), which has one aminobenzyl pendant arm directed away from the metal centre.[267]

The structure of $[Cu(\mathbf{12})]^{2+}$ is very similar to that of $[Cu(L^2)]^{2+}$ described in the previous section and only differs in having propylamino rather than ethylamino pendant arms. It is a distorted square pyramidal Cu^{II} complex with N(1), N(4), N(4A) and N(4B) as the four basal N-donors and N(7) as the apical N-donor (Figure 6.27). The Cu-N(basal) bond lengths [2.022(13)-2.094(14)] are slightly different from those reported in the literature, particularly for the Cu-N(apical) bond which is 2.186(15) Å against the reported value of 2.251(12) Å.[427] The former value is closer to the bond distances reported for a similar Cu-secondary amino group in $[Cu(L^2)]^{2+}$ and in the Cu^{II} complex of 4,7-bis(2-

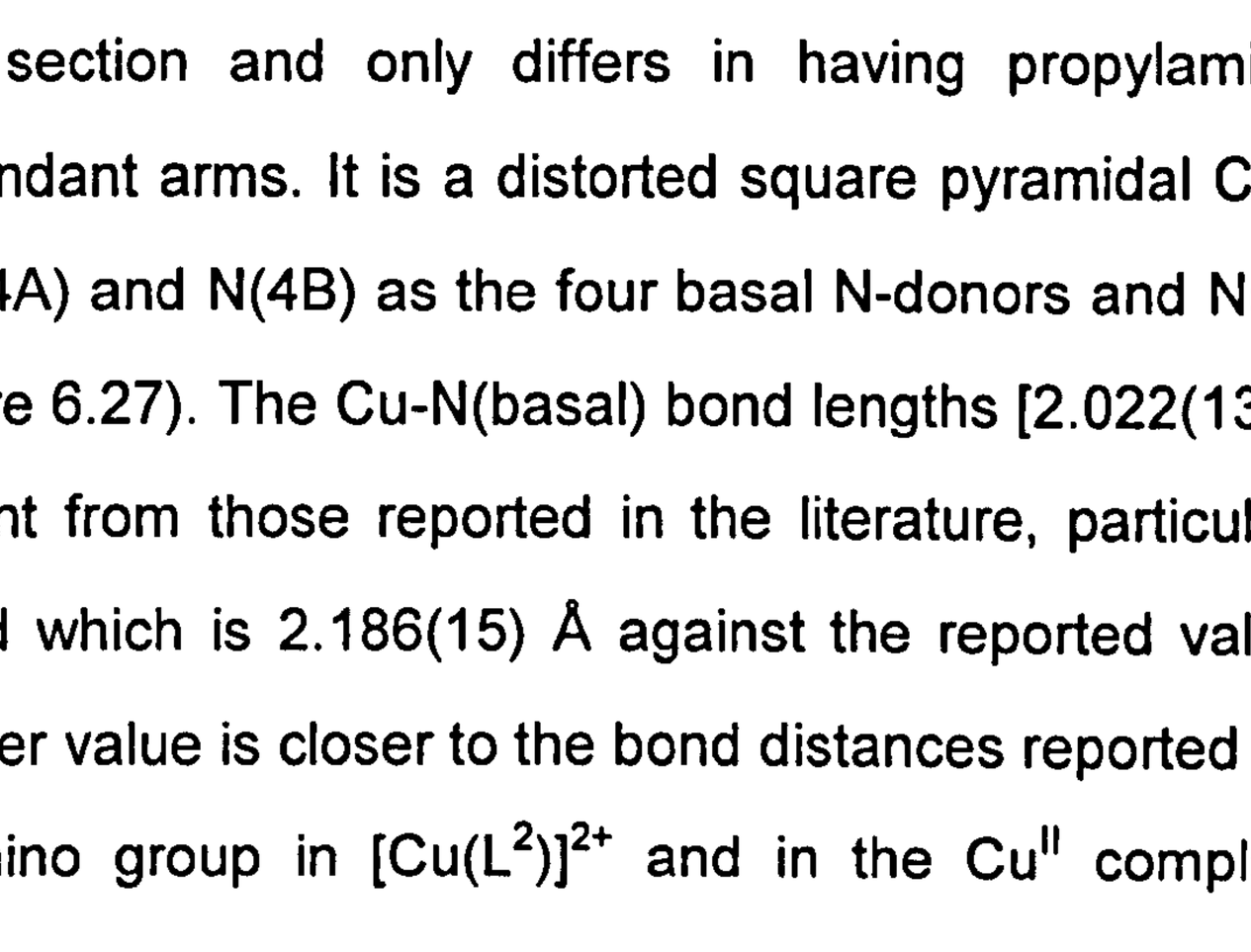

Figure 6.27 Crystal structure of $[Cu(\mathbf{12})](BF_4)_2$ with numbering scheme adopted. Hydrogen atoms and anions have been omitted for clarity. Displacement ellipsoids are drawn at 30% probability.

methylpyridyl)-1,4,7-triazacyclononane. The metal ion is displaced out of the N_4 plane (r.m.s. deviation 0.28 Å) by 0.127 Å towards the apical N-donor and the Cu-N(7) vector shows a slight deviation from perpendicularity with the N_4 basal plane [15.0°]. The *trans*-basal angles [N(1)-Cu-N(4B) 171.3(6)° and N(4)-Cu-N(4A) 173.0(6)°] are in good agreement with the values expected for a square pyramidal geometry around d^9 Cu^{II} complexes.[432,433] These values are characteristic of square pyramidal geometry and are not very different from those reported in the literature.[427]

6.4 Asymmetric derivatives of [9]aneN$_3$

While the syntheses of the ligands Li(L^3) and HL^4 have already been described in Section 5.3.1, their behaviour towards transition metal ions will be analysed herein.

Colourless crystals were obtained from the reaction of Li(L^3) and of HL^4 with one molar equivalent of $Mn(ClO_4)_2$ in MeOH. Analytical and mass spectroscopic data for the two products were consistent with the formulations $[Mn(L^3)](ClO_4)\cdot MeOH$ and $[Mn(HL^4)](ClO_4)_2$ for the two complexes. A single crystal X-ray determination for the former shows a mononuclear complex with the Mn^{II} ion co-ordinated by five N-donors and one O-donor from the ligand. The co-ordination geometry around the Mn^{II} centre is a distorted trigonal prism as found for $[Mn(L^2)(NO_3)]^+$, with one face taken up by the three N-donors of the triaza ring [Mn-N 2.300(2)-2.326(2) Å] and the other face defined by the two primary amines [Mn-N(3A) 2.227(2) Å and Mn-N(3B) 2.204(2) Å] and by the carboxylate oxygen [Mn-O(4C) 2.129(1)] (Figure 6.28). In this structure the two triangular planes of the prism are inclined by 4.1° and the two triangular faces are twisted by 12.9°. Hydrogen bonding interactions between NH_2 and anion oxygens connect more units together (H···O distances of 2.28 and 2.43 Å and N–H···O angles of 153° and 149°). In $[Mn(L^3)](ClO_4)\cdot MeOH$ a quite short H-

bond between the OH of the methanol and the carboxylate oxygen not involved in the co-ordination of the metal can also be observed with H···O distance of 2.01 Å and N–H···O angle of 156°)

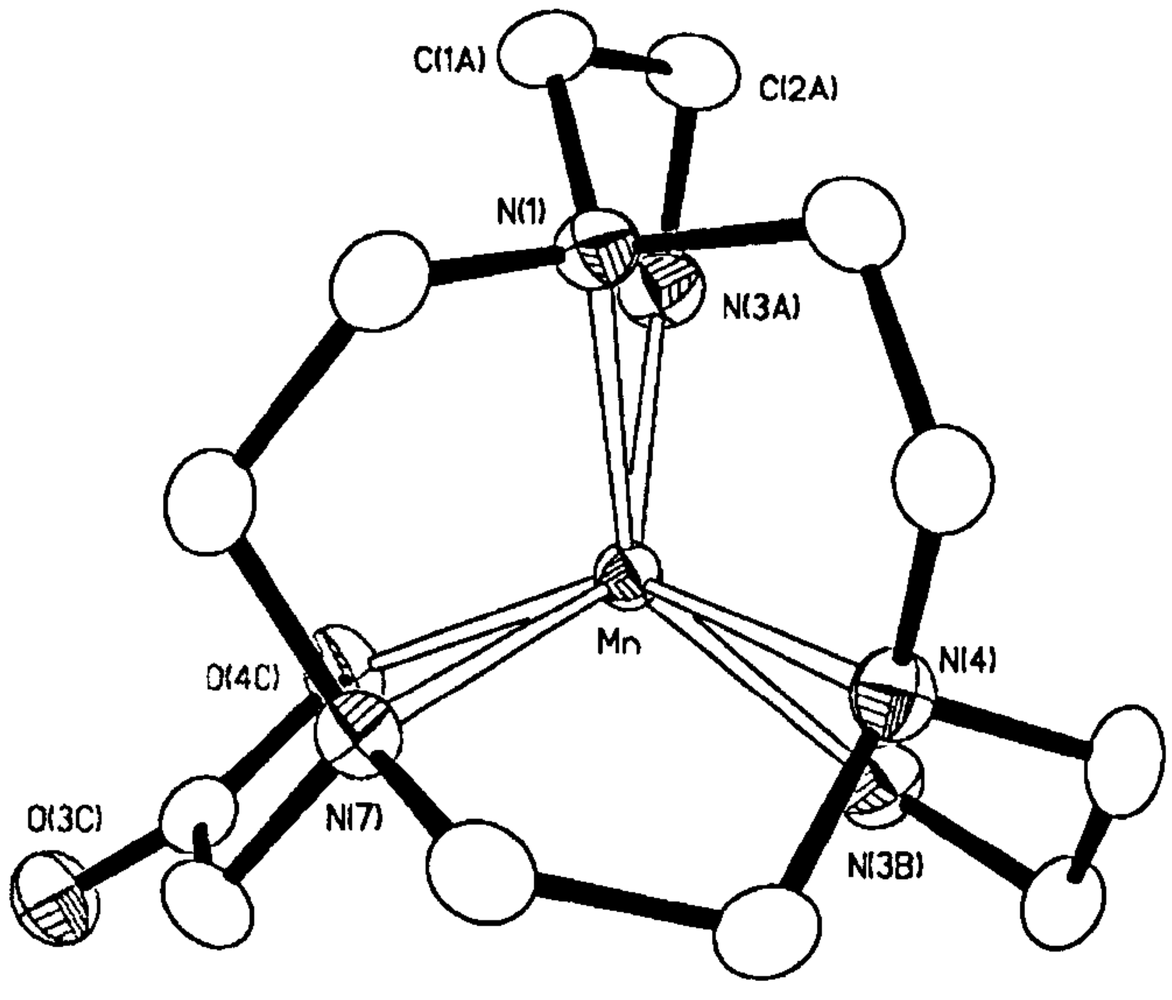

Figure 6.28 Crystal structure of the complex cation $[Mn(L^3)]^+$ with numbering scheme adopted. ClO_4^- anion and hydrogen atoms have been omitted for clarity. Displacement ellipsoids are drawn at 50% probability.

Colourless crystals were also obtained from the reaction of $Li(L^3)$ and of HL^4 with one molar equivalent of $Zn(ClO_4)_2$ in MeOH. Analytical and mass spectroscopic data for the two products were consistent with the formulations $[Zn(L^3)](ClO_4)\cdot 2H_2O$ and $[Zn(HL^4)](ClO_4)_2$ for the two complexes. A single crystal X-ray determination could be carried out only for the former. The molecular structure shows two Zn^{II} complexes in the asymmetric unit with the Zn^{II} ion always co-ordinated by five N-donors and one O-donor from the ligand. Any major difference in the metal centre co-ordination environment has been detected between the two independent Zn^{II} complexes, as can be seen in Table 6.9 where bond lengths and angles are reported for both the complexes. The only difference between the two complexes is that in one of them a Li^+ ion is co-ordinated to the oxygen of the carboxylate group not involved in the co-ordination of the metal [O(3C)] and to three water molecules in a tetrahedral

geometry [Li-O bond lengths are in the range 1.921(9)-1.978(9) Å and O-Li-O angles in the range 102.5(4)°-117.6(4)°].

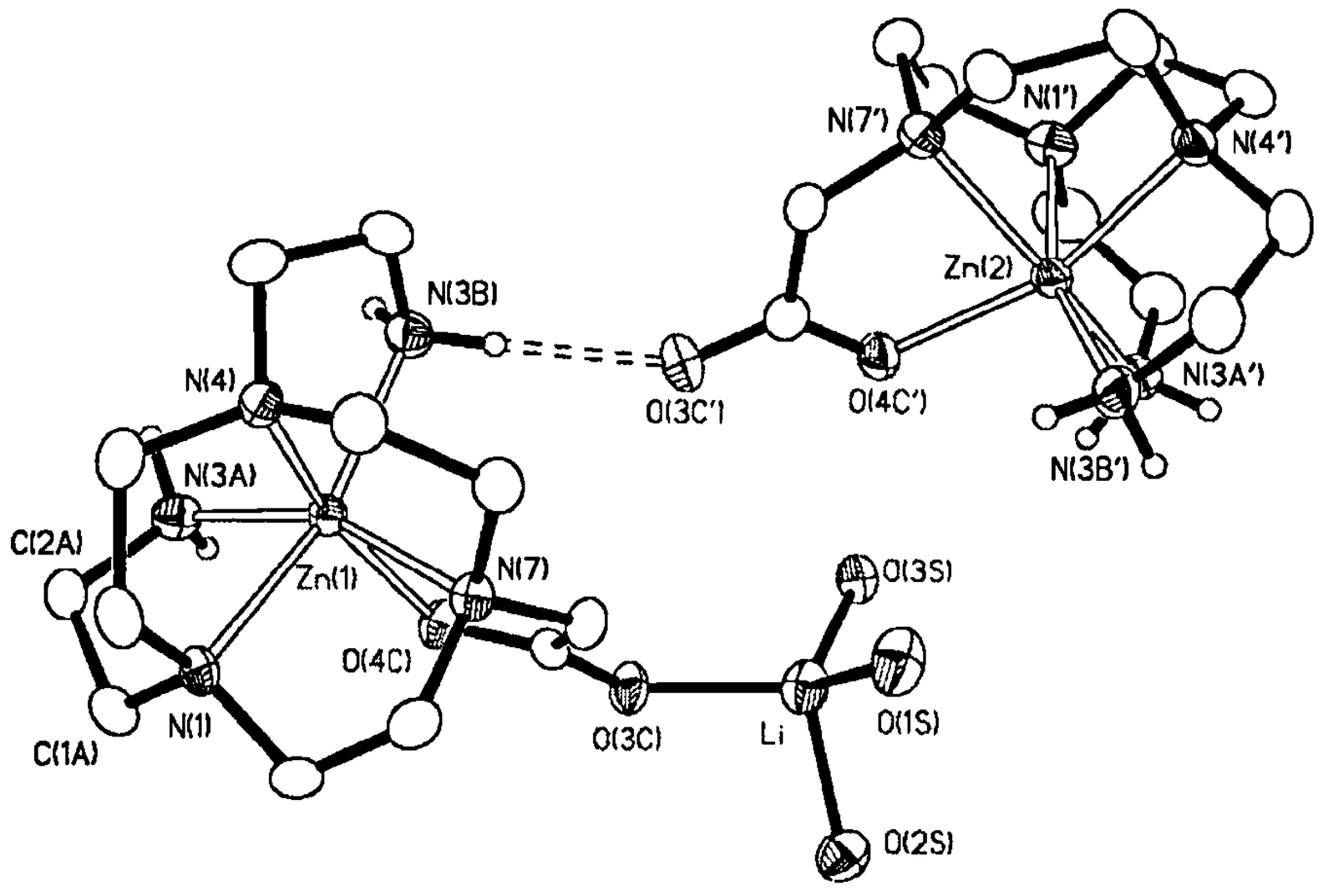

Figure 6.29. Crystal structure of $\{[Zn(L^3)]_2Li(H_2O)_3Cl(ClO_4)_2\}$ with numbering scheme adopted. Only the hydrogen atoms on primary amines are shown, the others have been omitted for clarity as have the anions. Displacement ellipsoids are drawn at 50% probability.

The hydrogen bond between one primary amine N-H [N(3B)] and the carboxylate oxygen not involved in the co-ordination of the metal and of the Li^+ ion [O(3C)'] connects the two complex cations together (H···O distance of 2.13 Å and N–H···O angle of 174°)(Figure 6.29). $[Zn(L^3)]^+$ does not adopt a specific ideal geometry around the Zn^{II} centre in either of the complex cations: twist angles between the triangular faces defined by the macrocyclic N-donors and the pendant arm donors are 37.0° and 36.6°, intermediate between an octahedron and a trigonal prism. This absence of a specific co-ordination polyhedron around the Zn^{II} ion is not surprising considering that a d^{10} metal ion does not have any electronically preferred geometry and therefore the disposition of the donor atoms is regulated only by steric factors. While the Zn-O bond lengths are 2.098(3) and 2.102(3) Å for O(4C) and O(4C)', respectively, the Zn-N(primary amine) bond lengths lie in the range 2.116(4)-2.145(4) Å,

shorter than the Zn-N(tertiary amine) bonds which are in the range 2.180(4)-2.231(4) Å. Mani and co-workers have reported[387] a comparable Zn^{II} complex with the [9]aneN$_3$ derivative containing one carboxylate and two imidazole pendant co-ordinating groups (Section 5.1.2) where the bond lengths between the metal and the macrocyclic N-donors are quite long [range 2.224(2)-2.339(2) Å] with the Zn^{II} ion shifted towards the N and O-donors of the pendant arms [range 2.074(3)-2.081(2) Å] within a distorted trigonal prismatic geometry.

Table 6.9 Selected bond lengths (Å) and angles (°) for $[Mn(L^3)](ClO_4)\cdot MeOH$ and for the two different cations (1 and 2) in $\{[Zn(L^3)]_2Li(H_2O)_3Cl(ClO_4)_2\}$.

	$[Mn(L^3)](ClO_4)\cdot MeOH$	$[Zn(L^3)]^+$ (1)	$[Zn(L^3)]^+$(2)
M – N(1)	2.300(2)	2.212(4)	2.199(4)
M – N(4)	2.326(2)	2.180(4)	2.210(4)
M – N(7)	2.308(2)	2.203(4)	2.231(4)
M – N(3A)	2.227(2)	2.145(4)	2.127(4)
M – N(3B)	2.204(2)	2.126(4)	2.116(4)
M – O(4C)	2.129(1)	2.098(3)	2.102(3)
N(1)-M-N(4)	76.16(6)	80.6(1)	80.7(1)
N(1)-M-N(7)	77.68(6)	80.8(1)	80.4(1)
N(4)-M-N(7)	75.74(6)	80.7(1)	79.4(1)
N(1)-M-N(3A)	77.71(6)	80.3(1)	80.6(2)
N(1)-M-N(3B)	140.76(6)	160.9(1)	160.4(2)
N(1)-M-O(4C)	118.60(6)	100.7(1)	99.4(1)
N(4)-M-N(3A)	127.68(6)	108.4(1)	108.5(2)
N(4)-M-N(3B)	77.31(6)	81.3(1)	81.4(1)
N(4)-M-O(4C)	142.70(6)	159.3(1)	157.5(1)
N(7)-M-N(3A)	139.51(6)	157.3(1)	157.8(2)
N(7)-M-N(3B)	122.41(7)	102.1(1)	104.3(1)
N(7)-M-O(4C)	74.82(7)	79.1(1)	78.5(1)
N(3A)-M-N(3B)	96.71(7)	99.8(1)	97.4(2)
N(3A)-M-O(4C)	89.61(6)	92.1(1)	93.6(1)
N(3B)-M-O(4C)	99.96(6)	98.4(1)	100.2(1)

The ^{13}C NMR chemical shifts for $[Li(L^3)]$, HL^4 and for their Zn^{II} complexes in CD_3CN solution at 298 K are reported in Table 6.10 (in Figure 6.30 the numbering scheme adopted for the assignment is shown). The spectra of both the Zn^{II} complexes show seven peaks indicating that in solution the complexes possess C_s symmetry with the mirror plane passing through the carboxymethyl

pendant arm for $[Zn(L^3)]^+$ (the 2-hydroxyethyl pendant arm for $[Zn(HL^4)]^{2+}$), the metal and through the C(2)-C(3) bond. With respect to the free ligands, the carbon atoms in $[Zn(HL^4)]^{2+}$ are all shifted upfield (average $\Delta\delta$ = -4.22 ppm), while in $[Zn(L^3)]^+$ one of the macrocyclic carbon atoms is deshielded ($\Delta\delta$ = 1.79 ppm) and all the others are shielded ($\Delta\delta$ = -0.72 ppm). The fact that all the peaks are shifted is an indication of the interaction between the metal ion and all the donor atoms of the ligands. As for $[Zn(L^2)]^{2+}$, the ^{1}H NMR spectra of the Zn^{II} complexes with $Li(L^3)$ and HL^4 are very complex with all the peaks overlapping, making it impossible to derive any useful information.

Table 6.10. ^{13}C NMR chemical shift data (δ, ppm) for $Li(L^3)$ and $[Zn(L^3)](ClO_4)$ and for HL^4 and $[Zn(HL^4)](ClO_4)_2$ (CD_3CN, 298 K) (X = A or B).

	C(2X)	C_{macr}	C_{macr}	C_{macr}	C(1X)	C(1C)	C(2C)
$Li(L^3)$	38.89	52.29	52.79	53.19	60.22	63.59	179.33
$[Zn(L^3)](ClO_4)$	37.18	52.03	52.65	54.98	58.77	63.23	178.95
HL^4	40.12	56.14	56.61	57.95	58.12	59.68	62.59
$[Zn(HL^4)](ClO_4)_2$	37.88	50.39	51.17	52.81	54.26	56.99	58.20

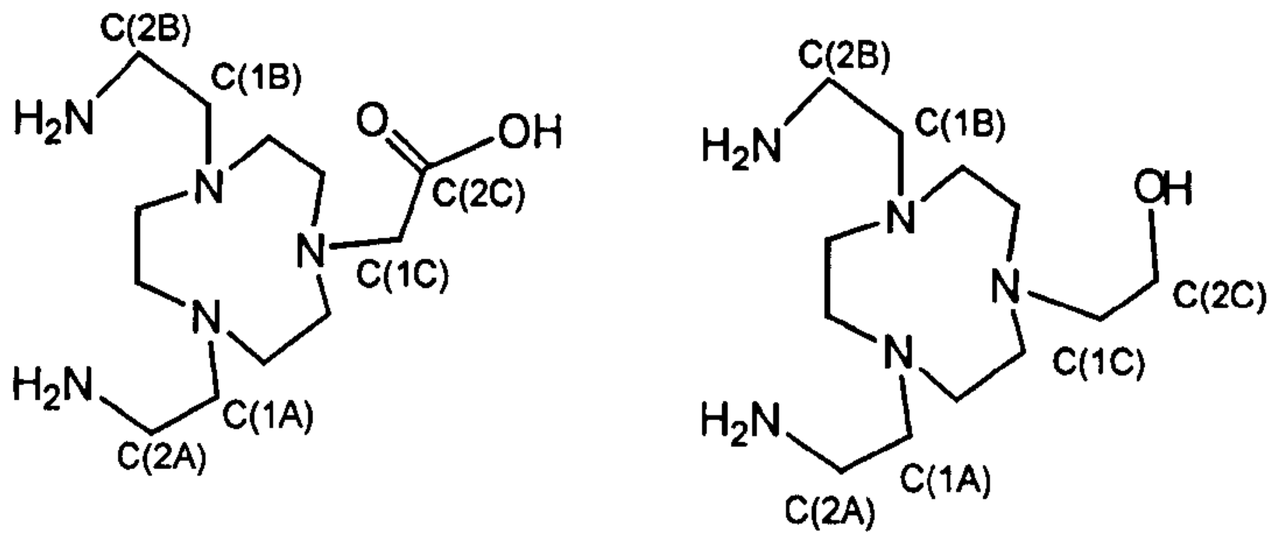

Figure 6.30. Numbering schemes used in the assignment

6.4 Experimental

4,7-bis(*p*-Tolylsulfonyl)-1,4,7-triazacyclononane[367] and *N*-(*p*-tolylsulfonyl)-aziridine[394] were prepared as described in literature. All starting materials were obtained from Aldrich Chemical Co. and used without further purification.

6.4.1 Synthesis of 1,4,7-*tris*(2-cyanoethyl)-1,4,7-triazacyclononane (L^5)

A mixture of 1,4,7-triazacyclononane (0.53 g, 4.10 mmol) and acrylonitrile (30 cm^3) was refluxed overnight under N_2. The solvent was removed under reduced pressure and the resulting yellow oil was purified by flash chromatography on silica gel using THF as eluent. On removal of the solvent from the collected fractions a pale yellow solid was obtained (1.12g, 3.89 mmol, 95% yield). ^{1}H NMR ($CDCl_3$, 300 MHz): δ 2.44 (CH_2CN, 6H, t, J = 6.67 Hz), 2.79 (12H, s, CH_2 ring), 2.86 (NCH_2CH_2CN, 6H, t, J = 6.62 Hz). ^{13}C NMR ($CDCl_3$, 75.47 MHz): δ 17.06 (CH_2CN), 54.06 (NCH_2 ring), 55.71 (NCH_2 arms), 119.26 (*C*N). EI$^+$ mass spectrum *m/z* = 248 (M^+ – CH_2CN), 234 (M^+ – CH_2CH_2CN). Elemental analysis: found (calc. for $C_{15}H_{24}N_6$): C, 61.80 (62.50); H, 8.22 (8.33); N, 28.88% (29.17%). IR spectrum (KBr disc): 2922m, 2811m, 2244s, 1455m, 1422w, 1361s, 1305w, 1133m, 1105s, 1022m, 994w, 872w, 744w cm^{-1}.

6.4.2 Synthesis of 1,4,7-*tris*(3-aminoethyl)-1,4,7-triazacyclononane (L^6)

1,4,7-*tris*(2-cyanoethyl)-1,4,7-triazacyclononane (L^5) (0.92g, 3.19 mmol) and BH_3·THF (60 cm^3, 1M solution in THF) were refluxed under N_2 for 48 h. After cooling, excess borane was destroyed by adding water (5 cm^3), and the solvent removed *in vacuo*. The white solid obtained was dissolved in 6M HCl (50 cm^3) and heated under reflux for 24 h. After cooling, the solvent was removed *in vacuo* to yield a white solid. The solid was dissolved in the minimum amount of water and the resulting solution passed through a Dowex 1x8-50 column (10 g) activated with 1M NaOH. The solvent was removed

under reduced pressure to yield a colourless oil (0.83g, 2.77 mmol, yield 86.7%). ^{1}H NMR: δ ($CDCl_3$, 298 K, 300 MHz) 1.56 ($CH_2CH_2CH_2$, 6H, q, J = 6.94 Hz), 2.49 (CH_2NH_2, 6H, t, J = 7.19 Hz) 2.70 (NCH_2, 12 H, s) 2.68 - 2.73 (NCH_2, 6 H, m) ppm. ^{13}C NMR: δ 31.95 ($NCH_2CH_2CH_2NH_2$), 40.39 (CH_2NH_2), 56.12 (NCH_2 ring), 56.57 (NCH_2 arm) ppm. EI$^+$ mass spectrum: *m/z*, found: 284.1, 255.1 and 241.1 for 284.5 [M^+-NH_2], 256.4 [M^+-$CH_2CH_2NH_2$] and 242.4 [M^+-$CH_2CH_2CH_2NH_2$], respectively. Elemental analysis: found (calc. for $C_{15}H_{36}N_6$) C, 59.53 (59.96); H, 11.80 (12.08); N, 28.23% (27.97%).

6.4.3 Synthesis of 4,7-*bis*(*p*-tolylsulfonyl)-1-(2-aminoethyl-N-*p*-tolylsulfonyl)-1,4,7- triazacyclononane (18)

4,7-(*p*-Tolylsulfonyl)-1,4,7-triazacyclononane (**17**) (0.92g, 2.1mmol) was dissolved in CH_3CN (100 cm^3) and heated to reflux under N_2. A solution of *N*-(*p*-tolylsulfonyl)-aziridine (0.415g, 2.1mmol) in CH_3CN (50 cm^3) was added in 2h. The resulting solution was heated under reflux for 28h. After cooling, the solvent was removed by rotary evaporation to yield a pale yellow solid. Colourless crystals suitable for X-ray diffraction studies were obtained by re-crystallisation from $CHCl_3$/EtOH (TLC: eluent $CHCl_3$ with 5% MeOH, R_f = 0.74)(1.08g, 1.7 mmol, yield 80.9%). ^{1}H NMR: δ ($CDCl_3$, 298 K, 300 MHz) 2.34 ($ArCH_3$, 3H, s), 2.43 ($ArCH_3$, 6H, s), 2.72 (NCH_2 arm, 2H, t, J = 5.24 Hz) 2.83 (NCH_2 ring, 4H, t, J = 4.73 Hz), 3.00 (CH_2NHTs, 2H, q, J = 5.26 Hz, J = 5.33 Hz) 3.12 (NCH_2 ring, 4H, br) 3.41 (NCH_2, 4H, s) 5.90 ($ArNHCH_2$ arm, 1H, t, J = 5.30 Hz), 7.24 (Ar*H*, 2 H, d, J = 8.15 Hz) 7.81 (Ar*H*, 2 H, d, J = 8.15 Hz), 7.64 (Ar*H*, 4 H, d, J = 8.19 Hz) 7.31 (Ar*H*, 4 H, d, J = 8.19 Hz) ppm. ^{13}C NMR: δ 21.44 ($ArCH_3$ arm), 21.55 ($ArCH_3$ ring), 41.26 ($TsNHCH_2$), 52.61, 53.36 and 55.41 (NCH_2 ring), 57.14(NCH_2 arm), 127.19, 129.71, 135.21 and 143.81 (Ts on the macrocycle), 127.31, 129.53, 137.84 and 142.82 (Ts on the pendant arm) ppm. FAB mass spectrum (3-NOBA matrix): *m/z* = 635 [M^+]. Elemental

analysis: found (calc. for $C_{29}H_{38}N_4O_6S_3$) C, 54.65 (54.87); H, 5.81 (6.03); N, 9.03% (8.83%).

6.4.4 Synthesis of 1-(2-aminoethyl)-1,4,7-triazacyclononane (L^7)

4,7-*bis*(*p*-Tolylsulfonyl)-1-(2-aminoethyl-N-*p*-tolylsulfonyl)-1,4,7-triazacyclononane (**18**) (1.08g, 1.7 mmol) was dissolved in concentrated H_2SO_4 (15 cm^3) and heated to 110°C under a nitrogen atmosphere for 72 h. After cooling, the dark solution was added over 1 h to a mixture of Et_2O/EtOH (300 cm^3, 1:1 v/v) The solid formed was filtered, washed with Et_2O and dissolved in H_2O. The aqueos solution was then passed through a Amberlite IRA 416 column (15 g) activated with 1M aqueous NaOH. The solvent was removed under reduced pressure to yield a colourless oil (0.23g, 0.133 mmol, yield 78.5%). ^{1}H NMR: δ ($CDCl_3$, 298 K, 300 MHz) 1.81 (N*H*$_2$, 2H, br) 2.50-2.56 (NC*H*$_2$, 6 H, m) 2.64 - 2.68 (NC*H*$_2$, 10 H, m) ppm. ^{13}C NMR: δ 40.41 ($NCH_2CH_2NH_2$), 46.86 and 47.05 (CH_2HNCH_2), 53.50 (NCH_2), 60.81 ($NCH_2CH_2NH_2$) ppm. EI$^+$ mass spectrum: *m/z*, found: 155.1, 142.1 and 128.1 for 156.3 [*M*$^+$-NH_2], 142.2 [*M*$^+$- CH_2NH_2] and 128.2 [M^+-$CH_2CH_2NH_2$], respectively. Elemental analysis: found (calc. for $C_8H_{20}N_4 \cdot ½H_2O$) C, 52.43 (53.00); H, 11.30 (11.67); N, 30.23% (30.90%).

6.4.5 Synthesis of [Cu(15)](BF$_4$)$_2$, [Cu(16)](BF$_4$)$_2$ and [Cu(L^5)Cl$_2$]

[Cu(15)](BF$_4$)$_2$. A mixture of 1,4,7-*tris*(cyanomethyl)-1,4,7-triazacyclononane (L^1) (20.0 mg, 0.081 mmol) and $Cu(BF_4)_2 \cdot 4H_2O$ (25.0 mg, 0.081 mmol) in MeOH (30 cm^3) was stirred at 65°C for 2 h until an intense blue colour appeared. The solvent was removed under reduced pressure and the residue dissolved in the minimum amount of MeCN and deep blue crystals of diffraction quality were obtained by slow diffusion of Et_2O vapour (28.0 mg, 0.051 mmol, 63.0% yield). FAB mass spectrum (3-NOBA matrix): *m/z* = 460 (*M*$^+$ [Cu(**15**)(BF$_4$)]$^+$) and 373 (*M*$^{2+}$ [Cu(**15**)]$^{2+}$). Electronic spectrum: (MeCN) λ_{max} =

587 nm (ε_{max} = 107 dm^3 mol^{-1} cm^{-1}). Elemental analysis: found (Calc. for $C_{14}H_{26}B_2CuF_8N_6O_2$): C, 31.10 (30.71); H, 4.88 (4.79); N, 15.58% (15.35%). IR spectrum (KBr disc): 3353s, 3332s, 3125s, 2930m, 2877m, 2242w, 1655s, 1639s, 1458m, 1409m, 1314m, 1217m, 1084s, 879m cm^{-1}.

[Cu(16)](BF$_4$)$_2$. A mixture of 1,4,7-*tris*(cyanoethyl)-1,4,7-triazacyclononane (L^5) (20.0 mg, 0.069 mmol) and Cu(BF$_4$)$_2$·4H$_2$O (21.3 mg, 0.069 mmol) in MeOH (30 cm^3) was stirred under reflux for 2 h until an intense blue colour appeared. The solvent was removed under reduced pressure and the residue dissolved in MeCN. Blue crystals of diffraction quality were obtained by slow diffusion of Et$_2$O vapour into this solution of the complex (26.5 mg, 0.045 mmol, 65.2% yield). FAB mass spectrum (3-NOBA matrix): *m/z* = 502 (M^+ [Cu(**16**)(BF$_4$)]$^+$) and 415 (M^{2+} [Cu(**16**)]$^{2+}$). Electronic spectrum: (MeCN) λ_{max} = 582 nm (ε_{max} = 105 dm^3 mol^{-1} cm^{-1}). Elemental analysis: found (Calc. for $C_{17}H_{32}B_2CuF_8N_6O_2$): C, 34.08 (34.63); H, 5.27 (5.47); N, 14.14% (14.25%). IR spectrum (KBr disc): 3349s, 3328s, 3125s, 2955m, 2868m, 2249w, 1637s, 1466m, 1414m, 1221m, 1084s, 1035s, 841m, 772m cm^{-1}.

[Cu(L^5)Cl$_2$]. 1,4,7-*tris*(cyanoethyl)-1,4,7-triazacyclononane (L^1) (20.0 mg, 0.069 mmol) and CuCl$_2$·2H$_2$O (11.8 mg, 0.069 mmol) were stirred in MeCN (30 cm^3) at room temperature for 3 h. The solvent volume was reduced and green blocky crystals of diffraction quality were obtained by slow diffusion of Et$_2$O vapour (21.2 mg, 0.050 mmol, 72.7% yield). Elemental analysis: found (Calc. for $C_{15}H_{24}Cl_2CuN_6$): C, 42.91 (42.59); H, 6.10 (5.72); N, 20.03% (19.87%). IR spectrum (KBr disc): 2978w, 2930w, 2880w, 2238m, 1448s, 1409m, 1345m, 1304s, 1210m, 1084s, 1030s, 980s, 731m cm^{-1}.

6.4.6 Complexes with 1-(2-aminoethyl)-1,4,7-triazacyclononane (L^7)

[Cu(L^7)Br]Br. 1-(2-aminoethyl)-1,4,7-triazacyclononane (L^7) (25 mg, 0.145 mmol) and Cu(BF$_4$)$_2$·4H$_2$O (44.8 mg, 0.145 mmol) were stirred in MeOH (30 cm^3) at room temperature for 3 h. The solvent was removed under reduced pressure and the residue dissolved in MeCN. Since re-crystallisation yielded

only oils, the residue was further reacted with one molar equivalent of NaBr (14.8mg, 0.145 mmol) and blue crystals of diffraction quality were obtained by slow diffusion of Et_2O vapour into a DMF solution of the complex (41.3 mg, 0.104 mmol, 72.0% yield). FAB mass spectrum (3-NOBA matrix): *m/z* = 315 (M^+ $[Cu(L^7)Br]^+$) and 236 (M^{2+} $[Cu(L^7)]^{2+}$). Electronic spectrum: (MeCN) λ_{max} = 622 nm (ε_{max} = 96 dm^3 mol^{-1} cm^{-1}). Elemental analysis: found (Calc. for $C_8H_{20}Br_2CuN_4$): C, 24.10 (24.29); H, 5.48 (5.10); N, 14.28 % (14.16%). IR spectrum (KBr disc): 3310m, 3242m, 3150m, 2931w, 2863w, 1654w, 1637w, 1460w, 1383m, 1123m, 1084s, 1031m, 818w cm^{-1}.

[Zn(L^7)(NCS)](BF$_4$). 1-(2-aminoethyl)-1,4,7-triazacyclononane (L^7) (24.3 mg, 0.141 mmol) and $Zn(BF_4)_2 \cdot 6H_2O$ (48.9 mg, 0.141 mmol) were stirred in MeOH (25 cm^3) at room temperature for 3 h. The solvent was removed under reduced pressure and the residue dissolved in MeCN. Since only a white powder could be obtained by re-crystallisation, the residue was further reacted with one molar equivalent of KNCS (13.7mg, 0.141 mmol) and colourless crystals were obtained by slow diffusion of Et_2O vapour into a MeCN solution of the complex (36.8 mg, 0.096 mmol, 68.2% yield). FAB mass spectrum (3-NOBA matrix): *m/z* = 294 (M^+ $[Zn(L^7)(NCS)]^+$). Elemental analysis: found (Calc. for $C_9H_{20}BF_4N_5SZn$): C, 28.08 (28.26); H, 5.80 (5.27); N, 18.07% (18.31%). IR spectrum (KBr disc): 3278m, 3057m, 3004w, 2969w, 2868w, 2079s, 1647w, 1476m, 1427m, 1383w, 1099m, 1034m, 940w, 743s, 715s cm^{-1}.

6.4.7 Complexes with 4,7-*bis*(2-aminoethyl)-1,4,7-triazacyclononane (L^2)

[Mn(L^2)(NO$_3$)](NO$_3$). A mixture of 4,7-*bis*(2-aminoethyl)-1,4,7-triazacyclononane (L^2) (25 mg, 0.107 mmol) and $Mn(NO_3)_2 \cdot 6H_2O$ (30.7 mg, 0.107 mmol) in MeOH (25 cm^3) was stirred at room temperature for 4 h. Crystals of diffraction quality were obtained by slow diffusion of Et_2O vapour in to a concentrated solution of the complex in MeOH (34.7 mg, 0.088 mmol, 82.0% yield). FAB mass spectrum (3-NOBA matrix): *m/z* = 332 (M^+ $[Mn(L^2)(NO_3)]^+$). Elemental analysis: found (calc. for $C_{10}H_{25}MnN_7O_6$): C, 30.57 (30.46); H, 6.55 (6.39); N, 25.04% (24.87%).IR

spectrum (KBr disc): ν 3318m, 3264m, 2920m, 2851m, 1472m, 1384s, 1006w, 802w cm^{-1}.

$[Ni(L^2)(CH_3CN)](BF_4)_2$. 4,7-*bis*(2-aminoethyl)-1,4,7-triazacyclononane (L^2) (21.2 mg, 0.091 mmol) and $Ni(BF_4)_2 \cdot xH_2O$ (21.1 mg, 0.091 mmol) were stirred in MeOH (30 cm^3) at room temperature for 3 h. Single crystals suitable for X-ray diffraction were obtained by slow diffusion of Et_2O vapour into a solution of the complex in MeCN (29.7 mg, 0.062 mmol, 68.1% yield). FAB mass spectrum (3-NOBA matrix): *m/z* = 360 (M^+ $[Ni(L^2)(BF_4)]^+$) and 272 (M^{2+} $[Ni(L^2)]^{2+}$). Electronic spectrum: (MeCN) λ_{max} = 516 and 807 nm (ε_{max} = 26 and 36 $dm^3\ mol^{-1}\ cm^{-1}$, respectively). Elemental analysis: found (calc. for $C_{10}H_{25}B_2F_8N_5Ni \cdot CH_3CN$): C, 27.57 (27.72); H, 6.35 (5.92); N, 17.44% (17.63%). IR spectrum (KBr disc): ν 3339s, 3290m, 3248m, 2920w, 2890w, 2860w, 2249w, 1489w, 1456w, 1121s, 1091s, 626s cm^{-1}.

$[Cu(L^2)](ClO_4)_2$. A mixture of 4,7-*bis*(2-aminoethyl)-1,4,7-triazacyclononane (L^2) (25 mg, 0.107 mmol) and $Cu(ClO_4)_2 \cdot 6H_2O$ (39.6 mg, 0.107 mmol) in MeOH (25 cm^3) was stirred at room temperature for 4 h. Deep blue crystals of diffraction quality were obtained by slow diffusion of Et_2O vapour into a concentrated solution of the complex in MeCN (44.5 mg, 0.093 mmol, 87.0% yield). FAB mass spectrum (3-NOBA matrix): *m/z* = 377 (M^+ $[Cu(L^2)(ClO_4)]^+$ and 278 (M^{2+} $[Cu(L^2)]^{2+}$). Electronic spectrum: (MeCN) λ_{max} = 591 nm (ε_{max} = 107 $dm^3\ mol^{-1}\ cm^{-1}$). Elemental analysis: found (calc. for $C_{10}H_{25}Cl_2CuN_5O_8$): C, 25.44 (25.14); H, 5.45 (5.27); N, 15.04% (14.66%). IR spectrum (KBr disc): ν 3270m, 2924w, 2879w, 1458w, 1384s, 1121s, 1092s, 795m, 628s cm^{-1}.

$[Zn(L^2)](ClO_4)_2$. A mixture of 4,7-*bis*(2-aminoethyl)-1,4,7-triazacyclononane (L^2) (19.6 mg, 0.084 mmol) and $Zn(ClO_4)_2 \cdot 6H_2O$ (31.3 mg, 0.084 mmol) was stirred in MeOH (30 cm^3) at room temperature for 3 h. Small colourless crystals were obtained by slow diffusion of Et_2O vapour into a concentrated solution of the complex in MeOH (27.1 mg, 0.053 mmol, 63.0% yield). FAB mass spectrum (3-NOBA matrix): *m/z* = 378 (M^+ $[Zn(L^2)(ClO_4)]^+$) and 278 (M^{2+} $[Zn(L^2)]^{2+}$). Elemental

analysis: found (calc. for $C_{10}H_{25}Cl_2ZnN_5O_8$): C, 26.23 (25.82); H, 5.21 (5.71); N, 13.26% (13.69%). IR spectrum (KBr disc): ν 3320w, 2930m, 2859m, 1460m, 1384s, 1120s, 1090s, 799m, 627s cm^{-1}.

6.4.8 Complexes with 1,4,7-*tris*(3-aminopropyl)-1,4,7-triazacyclononane (L^6)

[Mn(L^6)](NO_3)$_2$ A solution of $Mn(NO_3)_2 \cdot 6H_2O$ (30.4 mg, 0.106 mmol) in MeOH (10 cm^3) was added to a solution of 1,4,7-*tris*(3-aminopropyl)-1,4,7-triazacyclononane (L^6, 31.9 mg, 0.106 mmol) in MeOH (15 cm^3). The mixture was stirred for 3h at room temperature, after which the volume was reduced to 5 cm^3 and colourless single crystals of good quality were obtained by diffusion of Et_2O vapour. (33.9mg, 0.086 mmol, 81.2% yield) FAB mass spectrum (3-NOBA matrix): *m/z* = 415 (M^+ [Mn(L^6)(NO_3)]$^+$). Elemental analysis: found (calc. for $C_{15}H_{36}MnN_8O_6$): C, 37.12 (37.58); H, 7.54 (7.57); N, 22.97% (23.37%). IR spectrum (KBr disc): ν 3284m, 3225m, 3133m, 2922m, 2870m, 1477m, 1384s, 1157m, 1098m, 1021m, 924m cm^{-1}.

[Cu(8)](BF_4)$_2$ A solution of $Cu(BF_4)_2 \cdot 4H_2O$ (25.7 mg, 0.083 mmol) and 1,4,7-*tris*(3-aminopropyl)-1,4,7-triazacyclononane (L^6, 25.0 mg, 0.083 mmol) in MeOH (25 cm^3) was stirred overnight at room temperature. The solvent was removed under reduced pressure and the residue dissolved in MeCN. Blue crystals of diffraction quality were obtained by diffusion of Et_2O vapour. (20.8mg, 0.043 mmol, 52.0% yield). FAB mass spectrum (3-NOBA matrix): *m/z* = 306 (M^{2+} [Cu(8)]$^+$). Elemental analysis: found (calc. for $C_{12}H_{29}B_2F_8CuN_5$): C, 30.57 (29.99); H, 6.33 (6.08); N, 14.81% (14.57%). IR spectrum (KBr disc): ν 3278m, 3134m, 2923w, 2871w, 1472m, 1384s, 1120s, 1093s, 626s cm^{-1}.

[Zn(L^6)](ClO_4)$_2$ A solution of $Zn(BF_4)_2 \cdot xH_2O$ (23.9 mg, 0.10 mmol) in MeOH (10 cm^3) was added to a solution of 1,4,7-*tris*(3-aminopropyl)-1,4,7-triazacyclononane (L^6, 30.0 mg, 0.10 mmol) in MeOH (15 cm^3). The mixture was stirred for 3h at room temperature, then the volume was reduced to 5 cm^3

and colourless crystals of diffraction quality were obtained by diffusion of Et_2O vapour (40.3mg, 0.075 mmol, 75.0% yield). FAB mass spectrum (3-NOBA matrix): *m/z* = 451 (M^+ $[Zn(L^6)(BF_4)]^+$) and 365 (M^{2+} $[Zn(L^6)]^{2+}$). Elemental analysis: found (calc. for $C_{15}H_{36}B_2F_8ZnN_6$): C, 33.27 (33.52); H, 6.55 (6.38); N, 15.31% (15.64%). IR spectrum (KBr disc): ν 3288m, 3224m, 3130m, 2920m, 2862m, 1472m, 1384s, 1084s, 1035m, 880m cm^{-1}.

6.4.9 Complexes with the lithium salt of 1-carboxymethyl-4,7-*bis*(2-aminoethyl)-1,4,7-triazacyclononane [Li(L^3)]

[Mn(L^3)](ClO_4)·MeOH. $Mn(ClO_4)_2·6H_2O$ (31.8 mg, 0.088 mmol) was dissolved MeOH (10 cm^3) and a solution of Li(L^3) (24.6 mg, 0.088 mmol) in MeOH (10 cm^3) was added dropwise. The solution was stirred for 3h at room temperature. Single crystals suitable for X-ray structural analysis were obtained by diffusion of Et_2O vapour into a solution of the complex in MeOH (24.6 mg, 0.054 mmol, 61% yield). FAB mass spectrum (3-NOBA matrix) *m/z* = 327 (M^+ $[Mn(L^3)]^+$). Elemental analysis: found (calc. for $C_{12}H_{27}ClMnN_5O_6·MeOH$): C, 34.22 (34.03); H, 6.63 (6.59); N, 15.58% (15.26%). IR spectrum (KBr disc): ν 2921m, 2850m, 1617m, 1472m, 1396s, 1121s, 1094m, 634w cm^{-1}.

[Zn(L^3)](ClO_4).. $Zn(ClO_4)_2·6H_2O$ (34.6 mg, 0.093 mmol) in MeOH (10 cm^3) was added to a solution of Li(L^3) (26.0 mg, 0.093 mmol) in MeOH (10 cm^3). The resulting solution was stirred for 3h at room temperature. The solvent was removed under reduced pressure and the residue dissolved in MeCN. Single crystals suitable for X-ray structural analysis were obtained by diffusion of Et_2O vapour (35.0 mg, 0.074 mmol, 79.3% yield). Mass spectrum (Electrospray) *m/z* = 336 (M^+ $[Zn(L^3)]^+$). Elemental analysis: found (calc. for $C_{12}H_{27}ClZnN_5O_6·2H_2O$): C, 30.22 (30.39); H, 6.63 (6.59); N, 14.58% (14.77%). IR spectrum (KBr disc): ν 3293s, 3161m, 2966w, 2919w, 2858w, 1609s, 1474w, 1400w, 1325w, 1121s, 1051m, 1006m, 799w, 634m cm^{-1}.

6.4.7 Complexes with 1-(2-hydroxyethyl)-4,7-*bis*(2-aminoethyl)-1,4,7-triazacyclononane (HL^4)

$[Mn(HL^4)](ClO_4)_2$ $Mn(ClO_4)_2{\cdot}6H_2O$ (29.6 mg, 0.082 mmol) was dissolved MeOH (10 ml) and a solution of HL^4 (21.3 mg, 0.082 mmol) in MeOH (10 cm^3) was added dropwise. The solution was stirred for 3h at room temperature. Addition of Et_2O to a concentrated solution of the complex yielded a light brown solid (24.0 mg, 0.047 mmol, 57% yield). FAB mass spectrum (3-NOBA matrix) *m/z* = 413 (M^+ $[Mn(HL^4)(ClO_4)]^+$) and 313 (M^{2+} $[Mn(HL^4)]^{2+}$). Elemental analysis: found (calc. for $C_{12}H_{29}Cl_2MnN_5O_9$): C, 28.29 (28.08); H, 5.82 (5.70); N, 13.51% (13.65%). IR spectrum (KBr disc): ν 3300m, 3262m, 2922m, 2855m, 1473m, 1109s, 1089s, 627m cm^{-1}.

$[Zn(HL^4)](ClO_4)_2$ A solution of $Zn(ClO_4)_2{\cdot}6H_2O$ (35.8 mg, 0.096 mmol) in MeOH (10 cm^3) was added MeOH to a solution of HL^4 (25.0 mg, 0.096 mmol) in MeOH (10 cm^3) and the resulting solution was stirred overnight at room temperature. Small colourless crystals were obtained by diffusion of Et_2O vapour into a solution of the complex in MeOH (30.0 mg, 0.057 mmol, 59.7% yield). FAB mass spectrum (3-NOBA matrix) *m/z* = 423 (M^+ $[Zn(HL^4)(ClO_4)]^+$) and 323 (M^{2+} $[Zn(HL^4)]^{2+}$). Elemental analysis: found (calc. for $C_{12}H_{29}Cl_2ZnN_5O_9$): C, 27.68 (27.52); H, 5.82 (5.58); N, 13.59% (13.37%). IR spectrum (KBr disc): ν 3270m, 2931m, 2863m, 1652m, 1463w, 1384m, 1299w,1122s, 1089s, 628m cm^{-1}.

6.4.8 Crystal Structure Determinations

A summary of the crystal data and refinement details for the compounds discussed in this chapter is given in Tables 6.11-6.15. Diffraction data for L^1, $[Cu(\mathbf{15})](BF_4)_2$, $[Cu(\mathbf{12})](BF_4)_2$ were collected on a Stoe Stadi-4 four-circle diffractometer equipped with an Oxford Cryosystems open-flow cryostat using graphite-monochromated Mo-K_α radiation (λ=0.71073Å). Numerical absorption corrections based on face-indexing were applied to the data for all compounds.

Data for **18** and $[Mn(L^6)](NO_3)_2{\cdot}½H_2O$ were collected on a Enraf Nonius kappaCCD area detector diffractometer and same cryostat and radiation using ω scans and corrected for Lorentz and polarisation effects; semi-empirical absorption corrections based on equivalent reflections were also applied. Data for $\{[Cu(\mathbf{16})](BF_4)_2\}_4{\cdot}4H_2O$, $[Cu(L^5)Cl_2]$, $[Cu(L^7)]Br_2$, $[Cu(L^2)](ClO_4)_2$, $[Ni(L^2)(CH_3CN)](BF_4)_2$, $[Zn(L^6)](BF_4)_2{\cdot}CH_3CN$, $[Mn(L^3)](ClO_4){\cdot}MeOH$ and $\{[Zn(L^3)]_2Li(H_2O)_3Cl(ClO_4)_2\}$ were collected on a Bruker SMART10001000 CCD area detector diffractometer equipped with an Oxford Cryosystems open-flow cryostat using graphite-monochromated Mo-K_α radiation (λ=0.71073Å). Semi-empirical absorption corrections based on equivalent reflections were also applied.

The structures of $[Cu(\mathbf{15})](BF_4)_2$, $[Ni(L^2)(CH_3CN)](BF_4)_2$ and $[Zn(L^6)](BF_4)_2{\cdot}CH_3CN$ were solved by heavy atom methods and subsequent difference-Fourier syntheses.[323] All the other structures were solved by Direct methods[322] and completed by iterative cycles of full-matrix least squares refinement and ΔF syntheses. All non-H atoms, except for those in disordered groups, were refined anisotropically. All the H atoms were placed in calculated positions and refined using a riding model[323], except those on methyl groups [except MeO groups in $[Cu(\mathbf{15})](BF_4)_2$] and on solvent molecules (MeOH or MeCN) which were located from difference maps and refined as a rigid body.

In $[Cu(\mathbf{15})](BF_4)_2$ the carbon atoms on the macrocyclic backbone and the F atoms of one BF_4^- anion were found to be disordered and were modelled using partial occupancy models over two sites (occupancy factors 0.616/0.384 for the carbon atoms and 0.602/0.398 for the BF_4^-).

In $[Cu(\mathbf{16})](BF_4)_2{\cdot}4H_2O$ the asymmetric unit contains four cations, eight anions and four H_2O molecules. Two of the cations are affected by disorder. One of the disordered cations shows disorder in the nitrile pendant arm, modelled over two sites 65:35 occupancies. The hydrogen atoms on C(17A) are also disordered. The highest residual peak in the difference Fourier lies in

this region. In the other disordered cation one of the two methoxy group is disordered and was modelled over two sites with 75:25 occupancies. Although some BF_4^- anions showed large thermal motions, Only one of them required modelling in terms of alternative atomic sites for F atoms: three of the four fluorines were each modelled over three sites 50:30:20 and restraints applied. Even so it is poorly behaved and an apparent H_2O molecule is very close to some of the F sites. There are four H_2O in the asymmetric unit, two were modelled as fully occupied, the other two were each modelled over two sites with 80:20 occupancies.

One perchlorate anion in $[Cu(L^2)](ClO_4)_2$ was found to exhibit disorder in two oxygen atoms [O(3) and O(4)], and this disorder was modelled using partial occupancy models over three sites each with occupancy factors of 0.33. In $[Ni(L^2)(CH_3CN)](BF_4)_2$ one BF_4^- anion showed disorder in F(7) and F(8). Two BF_4^- anions in $[Zn(L^6)](BF_4)_2{\cdot}CH_3CN$ were found to be disordered and were modelled using partial occupancy models over three sites with occupancy factors of 0.33 in $[Ni(L^2)(CH_3CN)](BF_4)_2$ and over two sites with occupancy factors of 0.60/0.40 for F(2), F(3) and F(4) and of 0.50 for F(5) and F(8) in $[Zn(L^6)](BF_4)_2{\cdot}CH_3CN$. In $\{[Zn(L^3)]_2Li(H_2O)_3Cl(ClO_4)_2\}$ one oxygen atom belonging to a perchlorate anion [O(8)] and one carbon atom of one pendant arm [C(2A')] were found to be disordered. The disorder was modelled by a partial occupancy model over two sites for C(2A)' and C(2A)" with occupancy factors of 0.85/0.15, respectively, and over three sites for O(8) with occupancy factors of 0.50/0.30/0.20 for O(8), O(8)' and O(8)", respectively. Appropriate restraints were applied to all bond distances and angles involving disordered atoms.

Table 6.11 Selected crystallographic data for the single crystal structure detrminations of L^1, [Cu(**15**)](BF$_4$)$_2$ and of [Cu(**16**)](BF$_4$)$_2$.

Compound	L^1	[Cu(**15**)](BF$_4$)$_2$	[Cu(**16**)](BF$_4$)$_2$
Crystal Data			
Formula	$C_{12}H_{18}N_6$	$C_{14}H_{26}N_6O_2CuB_2F_8$	$C_{17}H_{34}N_6O_3CuB_2F_8$
M / gmol^{-1}	246.32	547.57	607.66
Crystal size / mm	0.54 x 0.50 x 0.39	0.62 x 0.30 x 0.27	0.24 x 0.20 x 0.12
Crystal system	Monoclinic	Monoclinic	Triclinic
Space group	*P*2$_1$/n	*P*2$_1$/n	*P*-1
a / Å	9.892(2)	9.710(3)	10.1492(8)
b / Å	15.726(3)	16.466(5)	16.5575(14)
c / Å	9.972(2)	13.784(5)	31.057(3)
α / °	90	90	100.735(1)
β/ °	114.84(2)	95.52(3)	97.780(1)
γ / °	90	90	91.402(1)
U / Å^3	1407.7(5)	2193.6(12)	5073.8(8)
Reflections used to refine cell	35	33	5397
2θ range / °	30 to 32	25 to 31	4.88 to 55.86
Z	4	4	8
D_c / gcm^{-3}	1.162	1.658	1.591
μ / mm^{-1}	0.076	1.088	0.952
F(000)	528	1116	2504
T / K	150(2)	150(2)	150(2)
Data Collection			
Diffractometer	Stoe Stadi-4 four circle	Stoe Stadi-4 four circle	Bruker SMART1000 CCD area detector
Radiation, wavelength	MoK_α , 0.71073 Å	MoK_α , 0.71073 Å	MoK_α , 0.71073 Å
θ_{max} / °	25.03	25.04	28.92
Range of *h*	-11 → 11	-11 → 11	-13 → 13
Range of *k*	0 → 18	0 → 19	-21 → 21
Range of *l*	-9 → 11	0 → 16	-40 → 41
Measured reflections	2671	3852	47209
Unique reflections, R_{int}	2487, 0.0433	3852, --	23282, 0.034
Observed reflections	2056 [$F_o \geq 4\sigma(F_o)$]	3029 [$F_o \geq 4\sigma(F_o)$]	14322 [$F_o \geq 4\sigma(F_o)$]
Absorption correction	none	ψ-scans	Numerical
$TF_{max, min}$	--, --	0.562, 0.505	0.962, 0.753
Solution			
Method	Direct methods	Heavy atom methods	Direct methods
Using	SHELXS-97	SHELXS-97	SHELXS-97
Refinement			
Full-matrix least squares on	F^2	F^2	F^2
Using	SHELXL-97	SHELXL-97	SHELXL-97
Weighting scheme *x*, *y*[a]	0.031, 0.645	0.048, 15.835	0.066, --
Parameters refined	163	291	1345
R_1, wR_2[b]	0.0422, 0.0875	0.0639, 0.1430	0.0498, 0.1167
Goodness-of-fit (*S*)	1.148	1.060	0.925
$(\Delta/\sigma)_{max}$	0.000	0.000	0.005
$\Delta\rho_{max, min}$ / eÅ^{-3}	+0.16, -0.18	+0.80, -0.82	+1.07, -0.70

[a] $w^{-1} = [\sigma^2(F_o^2) + (xP)^2 + yP]$, $P = [MAX(F_o^2, 0) + 2F_c^2]/3$
[b] $[F_o \geq 4\sigma(F_o)]$

Table 6.12. Selected crystallographic data for the single crystal structure determinations of [Cu(L^5)Cl$_2$], **18** and [Cu(L^7)]Br$_2$.

Compound	[Cu(L^5)Cl$_2$]	**18**	[Cu(L^7)]Br$_2$
Crystal Data			
Formula	$C_{15}H_{24}N_6CuCl_2$	$C_{29}H_{38}N_4O_6S_3$·	$C_8H_{20}Br_2CuN_4$
M / gmol^{-1}	422.84	634.81	395.64
Crystal size / mm	0.29 x 0.19 x 0.15	not recorded	0.16 x 0.14 x 0.016
Crystal system	Monoclinic	Monoclinic	Orthorhombic
Space group	$P2_1/n$	$P2_1/c$	*Pnma*
a / Å	10.9750(11)	11.4876(7)	21.138(2)
b / Å	11.1671(11)	10.6016(7)	7.2918(6)
c / Å	14.9887(15)	27.6081(14)	8.2147(7)
β/ °	96.183(2)	113.567(2)	90
U / Å^3	1826.3(3)	3081.9(3)	1267.2(2)
Reflections used to refine cell	2688	4004	2614
2θ range / °	4.6 to 57.1	2 to 55	5.3 to 52.7
Z	4	4	4
D_c / gcm^{-3}	1.538	1.368	2.075
μ / mm^{-1}	1.498	0.289	8.013
F(000)	876	1344	780
T / K	150(2)	150(2)	150(2)
Data Collection			
Diffractometer	BrukerSMART1000 CCD area detector	Enraf-Nonius kappaCCD area detector	BrukerSMART1000 CCD area detector
Radiation, wavelength	MoK_α , 0.71073 Å	MoK_α , 0.71073 Å	MoK_α , 0.71073 Å
θ_{max} / °	28.65	25.00	28.72
Range of *h*	-7 → 14	-14 → 14	-27 → 27
Range of *k*	-14 → 14	-13 → 13	-10 → 9
Range of *l*	-18 → 19	-35 → 35	-9 → 9
Measured reflections	11460	24020	11448
Unique reflections, R_{int}	4452, 0.023	4154, 0.071	1808, 0.057
Observed reflections	3420 [$F_o \geq 4\sigma(F_o)$]	2744 [$F_o \geq 4\sigma(F_o)$]	1056 [$F_o \geq 4\sigma(F_o)$]
Absorption correction	Semi-empirical	Semi-empirical	Integration
$TF_{max, min}$	0.796, 0.696	0.944, 0.836	0.879, 0.355
Secondary Extinction param.	none	0.0027(7)	none
Solution			
Method	Direct methods	Direct methods	Direct methods
Using	SHELXS-97	SHELXS-97	SHELXS-97
Refinement			
Full-matrix least squares on	F^2	F^2	F^2
Using	SHELXL-97	SHELXL-97	SHELXL-97
Weighting scheme *x*, *y*[a]	0.052, --	0.077, 4.100	0.080, 5.753
Parameters refined	217	383	62
R_1, wR_2[b]	0.0310, 0.0819	0.0596, 0.1440	0.0552, 0.1450
Goodness-of-fit (*S*)	1.022	0.969	1.049
$(\Delta/\sigma)_{max}$	0.003	0.03	0.001
$\Delta\rho_{max, min}$ / eÅ^{-3}	+0.69, -0.33	+0.40, -0.49	+1.62, -1.73

[a] $w^{-1} = [\sigma^2(F_o^2) + (xP)^2 + yP]$, $P = [MAX(F_o^2, 0) + 2F_c^2]/3$
[b] $[F_o \geq 4\sigma(F_o)]$

Table 6.13. Selected crystallographic data for the single crystal structure determinations of $[Mn(L^2)](NO_3)_2$, $[Ni(L^2)CH_3CN](BF_4)_2$ and $[Cu(L^2)](ClO_4)_2$.

Compound	$[Mn(L^2)](NO_3)_2$	$[Ni(L^2)CH_3CN](BF_4)_2$	$[Cu(L^2)](ClO_4)_2$
Crystal Data			
Formula	$C_{10}H_{25}MnN_7O_6$	$C_{12}H_{28}B_2F_8N_6Ni\cdot$	$C_{10}H_{25}Cl_2CuN_5O_8$
M / gmol^{-1}	394.31	488.74	477.79
Crystal size / mm	0.45 x 0.08 x 0.08	0.48 x 0.46 x 0.35	0.30 x 0.20 x 0.07
Crystal system	Orthorhombic	Monoclinic	Monoclinic
Space group	$P2_12_12_1$	$P2_1/n$	$P2_1/c$
a / Å	7.8382(7)	8.8366(6)	9.0770(9)
b / Å	14.392(1)	12.1977(8)	12.5290(10)
c / Å	14.613(1)	18.602(1)	15.865(2)
β/ °	90	91.490(1)	91.533(2)
U / Å^3	1648.5(2)	2004.4(2)	1803.6(3)
Reflections used to refine cell	5495	6700	7298
2θ range / °	5.58 to 57.40	5.05 to 56.93	4.49 to 56.74
Z	4	4	4
D_c / gcm^{-3}	1.589	1.620	1.760
μ / mm^{-1}	0.845	1.051	1.558
F(000)	828	1008	988
T / K	150(2)	150(2)	150(2)
Data Collection			
Diffractometer	Bruker SMART1000 CCD area detector	Bruker SMART1000 CCD area detector	Bruker SMART1000 CCD area detector
Radiation, wavelength	MoK_α , 0.71073 Å	MoK_α , 0.71073 Å	MoK_α , 0.71073 Å
θ_{max} / °	28.84	28.79	28.86
Range of *h*	-10 → 10	-6 → 11	-11 → 11
Range of *k*	-19 → 19	-16 → 16	-17 → 15
Range of *l*	-19 → 12	-23 → 24	-20 → 20
Measured reflections	10415	12793	12898
Unique reflections, R_{int}	3918, 0.045	4723, 0.038	4232, 0.047
Observed reflections	3533 [$F_O \geq 4\sigma(F_O)$]	3940 [$F_O \geq 4\sigma(F_O)$]	3628 [$F_O \geq 4\sigma(F_O)$]
Absorption correction	Semi-empirical	Semi-empirical	Semi-empirical
$TF_{max, min}$	0.928, 0.436	0.746, 0.527	0.802, 0.534
Secondary Extinction param.	0.008(15)	none	none
Solution			
Method	Direct methods	Heavy atom methods	Direct methods
Using	SHELXS-97	SHELXS-97	SHELXS-97
Refinement			
Full-matrix least squares on	F^2	F^2	F^2
Using	SHELXL-97	SHELXL-97	SHELXL-97
Weighting scheme *x*, *y*[a]	0.053, --	0.078, 0.504	0.060, 0.625
Parameters refined	218	269	241
R_1, wR_2[b]	0.0329, 0.0780	0.0422, 0.1182	0.0342, 0.0920
Goodness-of-fit (*S*)	0.994	1.088	1.059
$(\Delta/\sigma)_{max}$	0.001	0.003	0.000
$\Delta\rho_{max, min}$ / eÅ^{-3}	+0.27, -0.26	+0.63, -0.70	+0.59, -0.52

[a] $w^{-1} = [\sigma^2(F_O^2) + (xP)^2 + yP]$, $P = [MAX(F_O^2, 0) + 2F_C^2\}/3$
[b] $[F_O \geq 4\sigma(F_O)]$

Table 6.14 Selected crystallographic data for the single crystal structure determinations of $[Mn(L^6)](NO_3)_2$, $[Cu(\mathbf{12})](BF_4)_2$ and $[Zn(L^6)](BF_4)_2 \cdot CH_3CN$.

Compound	$[Mn(L^6)](NO_3)_2$	$[Cu(\mathbf{12})](BF_4)_2$	$[Zn(L^6)](BF_4)_2 \cdot CH_3CN$
Crystal Data			
Formula	$C_{15}H_{37}MnN_8O_{6.5}$	$C_{12}H_{29}B_2CuF_8N_5$	$C_{17}H_{39}B_2F_8N_7Zn$
M / gmol^{-1}	488.47	480.56	580.54
Crystal size / mm	0.05 x 0.02 x 0.02	0.40 x 0.23 x 0.03	0.20 x 0.17 x 0.13
Crystal system	Orthorhombic	Orthorhombic	Monoclinic
Space group	*Fdd2*	*Pbca*	$P2_1/c$
a / Å	19.7527(8)	14.558(7)	9.866(2)
b / Å	26.0701(8)	14.192(7)	13.052(3)
c / Å	18.0195(8)	18.672(9)	20.065(4)
β/ °	90	90	99.865(5)
U / Å^3	9279.2(6)	3858(3)	2545.5(10)
Reflections used to refine cell	52463	40	3452
2θ range / °	10 to 60	20 to 26	5.17 to 55.56
Z	16	8	4
D_c / gcm^{-3}	1.399	1.655	1.515
μ / mm^{-1}	0.618	1.215	1.044
F(000)	4160	1976	1208
T / K	150(2)	150(2)	150(2)
Data Collection			
Diffractometer	Enraf Nonius kappaCCD area detector	Stoe Stadi-4 four circle	Bruker SMART1000 CCD area detector
Radiation, wavelength	MoK_α , 0.71073 Å	MoK_α , 0.71073 Å	MoK_α , 0.71073 Å
θ_{max} / °	25.10	22.48	28.65
Range of *h*	-23 → 23	0 → 15	-13 → 12
Range of *k*	-31 → 31	-3 → 15	-7 → 17
Range of *l*	-20 → 21	-20 → 0	-26 → 22
Measured reflections	52463	3327	12211
Unique reflections, R_{int}	4053, 0.232	2506, 0.0734	5860, 0.065
Observed reflections	2724 [$F_O \geq 4\sigma(F_O)$]	1362 [$F_O \geq 4\sigma(F_O)$]	3759 [$F_O \geq 4\sigma(F_O)$]
Absorption correction	Semi-empirical	Numerical	Semi-empirical
$TF_{max, min}$	0.624, 0.559	0.962, 0.753	0.881, 0.567
Solution			
Method	Direct methods	Direct methods	Direct methods
Using	SHELXS-97	SHELXS-97	SHELXS-97
Refinement			
Full-matrix least squares on	F^2	F^2	F^2
Using	SHELXL-97	SHELXL-97	SHELXL-97
Weighting scheme *x*, *y*[a]	0.080, --	0.021, 113.16	0.100, --
Parameters refined	275	253	312
R_1, wR_2[b]	0.0587, 0.1278	0.1119, 0.2034	0.0576, 0.1475
Goodness-of-fit (*S*)	0.995	1.153	0.975
$(\Delta/\sigma)_{max}$	0.001	0.008	0.002
$\Delta\rho_{max, min}$ / eÅ^{-3}	+0.78, -0.31	+0.81, -0.68	+0.65, -0.73

[a] $w^{-1} = [\sigma^2(F_O^2) + (xP)^2 + yP]$, $P = [MAX(F_O^2, 0) + 2F_C^2]/3$
[b] $[F_O \geq 4\sigma(F_O)]$

Table 6.15 Selected crystallographic data for the single crystal structure determinations of $[Mn(L^3)]ClO_4 \cdot MeOH$ and $[Zn(L^3)](ClO_4)(LiCl)_{½}(H_2O)_{1.5}$.

Compound	$[Mn(L^3)]ClO_4 \cdot MeOH$	$[Zn(L^3)](ClO_4)(LiCl)_{½}(H_2O)_{1.5}$
Crystal Data		
Formula	$C_{13}H_{30}ClMnN_5O_7$	$C_{12}H_{26}Cl_{1.5}Li_{0.5}N_5O_{7.5}Zn$
M / gmol^{-1}	458.81	482.39
Crystal size / mm	0.16 x 0.13 x 0.12	0.26 x 0.08 x 0.08
Crystal system	Monoclinic	Monoclinic
Space group	$P2_1/n$	$P2_1/c$
a / Å	8.7577(9)	15.6382(12)
b / Å	14.199(2)	8.8403(7)
c / Å	15.771(2)	29.595(2)
β/ °	92.543(2)	103.672(2)
U / Å^3	1959.2(4)	3975.5(5)
Reflections used to refine cell	5810	4413
2θ range / °	5.16 to 55.34	4.8 to 50.8
Z	4	8
D_c / gcm^{-3}	1.555	1.612
μ / mm^{-1}	0.856	1.484
F(000)	964	2000
T / K	150(2)	150(2)
Data Collection		
Diffractometer	Bruker SMART1000 CCD area detector	Bruker SMART1000 CCD area detector
Radiation, wavelength	MoK_α , 0.71073 Å	MoK_α , 0.71073 Å
θ_{max} / °	29.00	29.03
Range of *h*	-11 → 11	-21 → 13
Range of *k*	-19 → 18	-12 → 11
Range of *l*	-21 → 18	-37 → 40
Measured reflections	18071	24884
Unique reflections, R_{int}	4742, 0.039	9917, 0.063
Observed reflections	3565 [$F_O \geq 4\sigma(F_O)$]	5504 [$F_O \geq 4\sigma(F_O)$]
Absorption correction	Semi-empirical	Semi-empirical
$TF_{max, min}$	0.928, 0.737	0.638, 0.519
Solution		
Method	Direct methods	Direct methods
Using	SHELXS-97	SHELXS-97
Refinement		
Full matrix least squares on	F^2	F^2
Using	SHELXL-97	SHELXL-97
Weighting scheme *x*, *y*[a]	0.053, --	0.061, --
Parameters refined	246	498
R_1, wR_2[b]	0.0367, 0.0916	0.0575, 0.1170
Goodness-of-fit (*S*)	1.020	1.003
$(\Delta/\sigma)_{max}$	0.012	0.008
$\Delta\rho_{max, min}$ / eÅ^{-3}	+0.66, -0.51	+0.88, -1.01

[a] $w^{-1} = [\sigma^2(F_O^2) + (xP)^2 + yP]$, $P = [MAX(F_O^2, 0) + 2F_C^2\}/3$
[b] $[F_O \geq 4\sigma(F_O)]$

Chapter 7

Synthesis, solution studies and structural characterisation of complexes with [15]aneN_3O_2 derivatives

7.1 Introduction

7.1.1 Introduction to mixed oxa-aza macrocycles

Mixed donor macrocycles are a category of ligands that has been studied since the early work on macrocycles. For example, in 1969 Lehn and co-workers[7] reported the synthesis of the N_2O_4 macrocyclic system (Figure 7.1a), the 2.2.2 cryptand shown in Figure 7.1(b) the following year[436,437] and many other ligands have been synthesised since then. Mixed oxa-aza crowns may be considered to

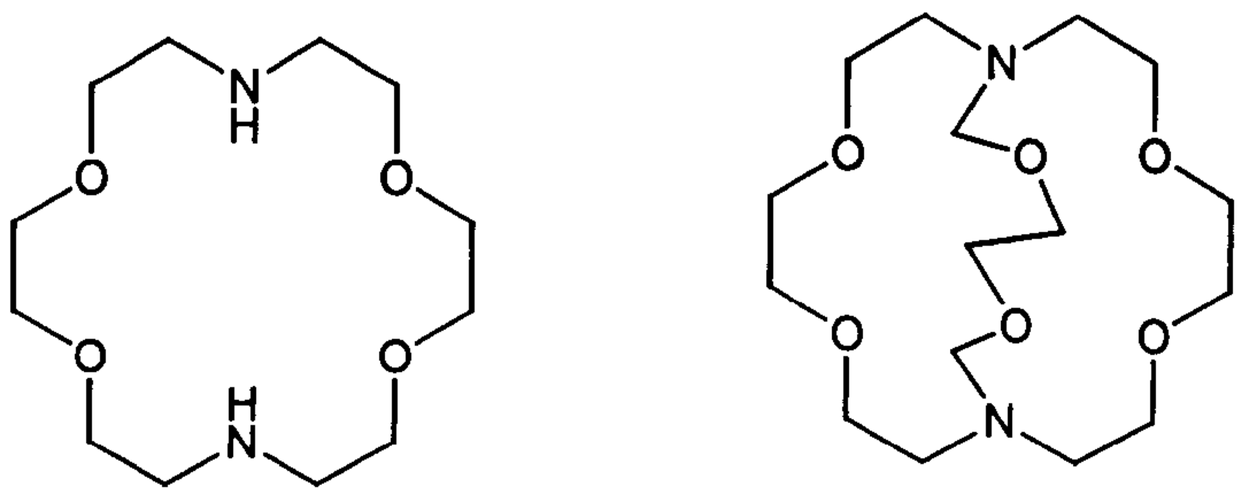

(a) (b)

Figure 7.1. (a) [18]aneN_2O_4 and (b) 2.2.2 cryptand

be intermediate between the two macrocyclic categories of crown ethers and polyamino macrocycles and, in general, their properties also tend to span those of each category.[31] Thus, they form complexes with both transition and alkali metal ions, although these are less stable than transition metal complexes with macrocycles containing only N-donors or alkali metal complexes with ligands containing only O-donors. For example, the logarithm of the binding constant for the diaza derivative shown in Figure 7.1(a) with K^+ in methanol is 2.0, whereas the analogous value for 18-crown-6 is 6.1.[31] Oxygen donors have less affinity towards transition metal ions because they form essentially electrostatic bonds with the metal ion. For example, in the crystal structure of the Cu^{II} complex of the [18]aneN_2O_4 macrocycle the Cu^{II} is located in the cavity of the macrocycle and is

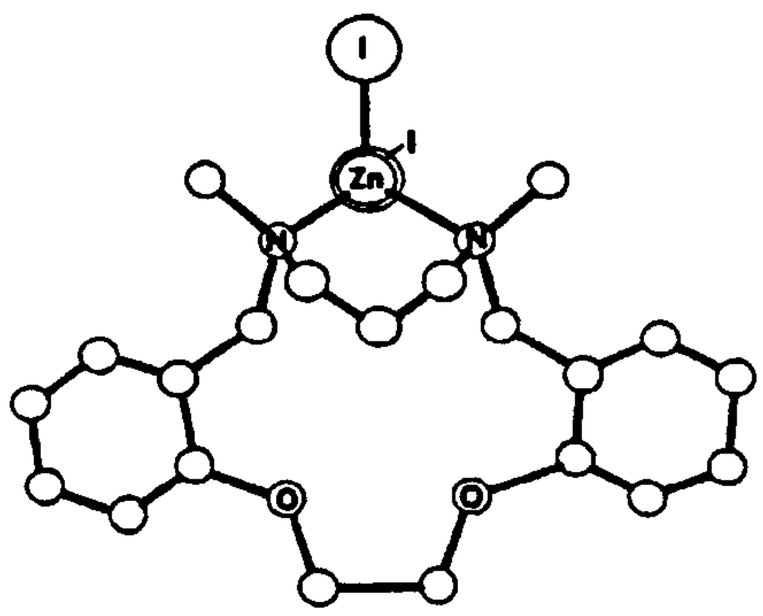

Figure 7.2. Zn^{II} crystal structure with a macrocycle containing a N_2O_2 donor set. The Zn^{II} is bound outside the macrocyclic cavity.[439]

bound by the two N-donors and by only two of the four available oxygens in the ring.[438] The oxygen donors of the ring often do not co-ordinate the transition metal ion, which sometimes also lies outside the macrocyclic cavity as in the Zn^{II} structure of a N_2O_2 macrocycle shown in Figure 7.2.[439]

Several studies have been reported on the metal-ion selectivity of these mixed macrocycles and Hancock and co-workers proposed a rule for neutral oxygen donor groups: "the addition of neutral-oxygen-donor-containing groups to a ligand will increase the selectivity of the ligand for large metal ions relative to small metal ions".[41,68] Figure 7.3 shows plots of the variation in complex stability (Δ log K) as a function of metal ion radius on addition of neutral oxygen donor groups to two mixed oxa-aza crowns.[68,440] The larger increment was observed for large metal ions such as Ba^{II}, Sr^{II} and Pb^{II} and it was suggested that this selectivity was due to the ability of larger metal ions to tolerate the steric crowding produced by addition of neutral oxygen donors. In addition, the ligands with added oxygen donors might, as a result, have a denticity that exceeds the co-ordination numbers of smaller metal ions.[41,,68] The selectivity of [18]aneN$_4$O$_2$ (Figure 7.3) for large Pb^{II} and Cd^{II} ions over the small Zn^{II} ion is not adequate for use in treating lead and cadmium poisoning. However, addition of four 2-hydroxyethyl groups to

[18]aneN$_4$O$_2$, giving THE-[18]aneN$_4$O$_2$, raises the Pb^{II}/Zn^{II} selectivity to adequate levels (Table 7.1).[440]

Table 7.1. Stability constants (log K) for the M^{II} (M = Cu, Zn, Cd and Pb) complexes with [18]aneN$_4$O$_2$ and THE-[18]aneN$_4$O$_2$.[440]

	Cu^{II}	Zn^{II}	Cd^{II}	Pb^{II}
[18]aneN$_4$O$_2$	16.27(1)	10.51(1)	10.90(1)	9.01(1)
THE-[18]aneN$_4$O$_2$	11.7(1)	5.90(1)	8.84(3)	10.73(3)

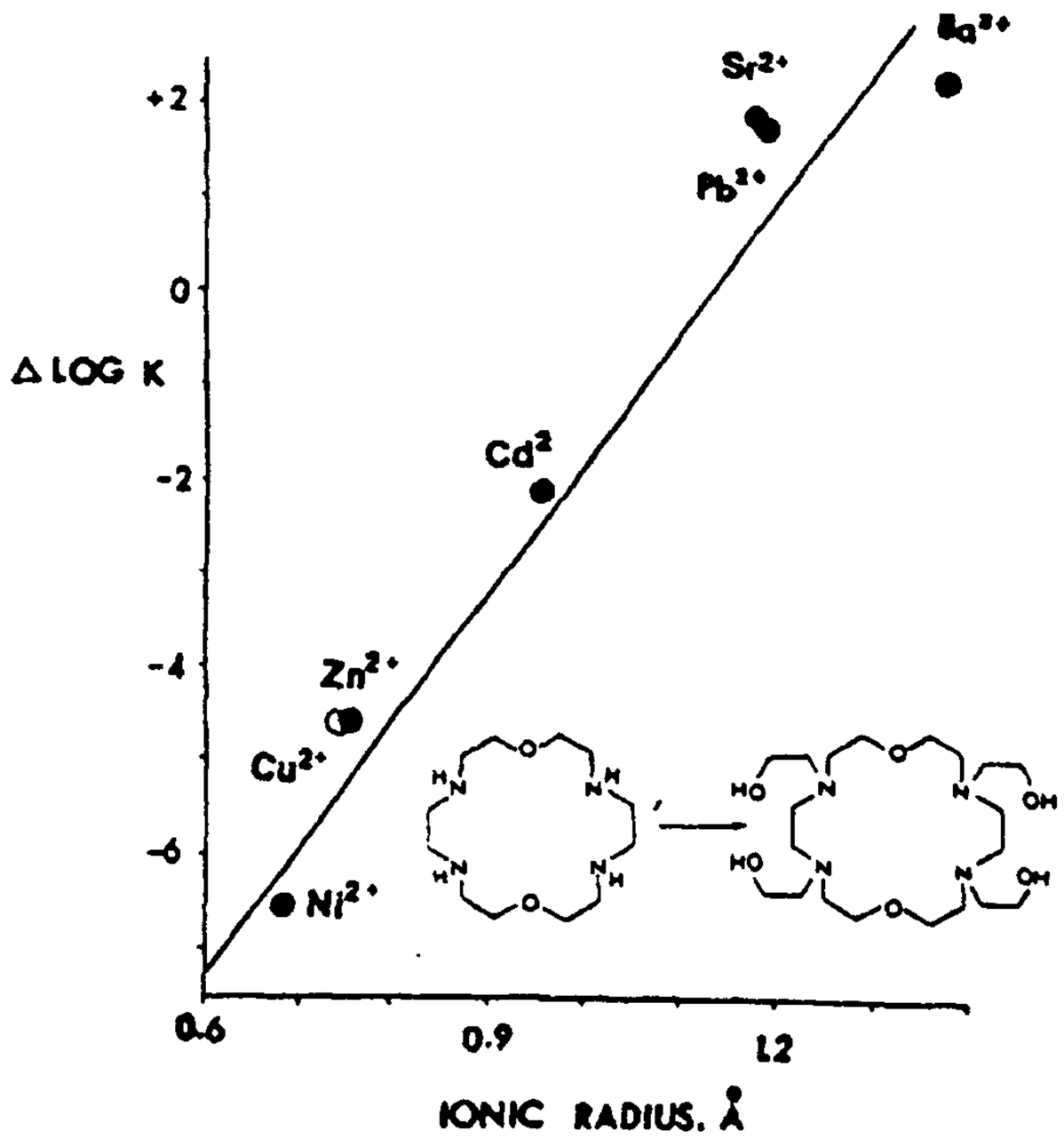

Figure 7.3. Change in complex stability (Δ log K) as a function of metal ion radius for the two macrocyclic ligands shown.[440]

7.1.2 Pendant arm derivatives of mixed oxa-aza macrocycles

The addition of pendant arms to oxa-aza macrocycles has attracted the attention of many researchers in the last twenty years and some examples have already been presented in Section 1.3. The attachment of pendant arms can change completely the binding characteristics of the ligand, which can exhibit remarkable metal ion selectivity and show specific complexation behaviour,

forming metal complexes with unusual structures.[33,41,81] Carboxylate or phosphonate pendant arm derivatives have been widely studied for the application of their lanthanide complexes as contrast agents in magnetic resonance imaging,[21,22] ligands with hydroxyalkyl or ethereal pendant groups exhibit good selectivity between large and small metal ions as discussed in the previous section,[41,68] and many other groups have been attached to the macrocyclic ring for a large variety of purposes such as the extraction of metal ions and the design of chromogenic ligands or photoresponsive systems.

Less work has been reported on mixed oxa-aza macrocycles bearing primary amino alkyl pendant arms. Lehn and Hosseini[441] have reported the synthesis of the macrocycle [24]aneN$_6$O$_2$ with six aminoethyl pendant arms (Figure 7.4a), McAuley *et al.*[442] the preparation of [9]aneN$_2$O with two aminopropyl groups (Figure 7.4b), while Zinic *et al.*[443] have described the synthesis of various oxa-aza macrocycles such as [15]aneNO$_4$, [18]aneNO$_5$ and [18]aneN$_2$O$_4$ with aminoethyl pendant arms (Figure 7.4c). However, in none of these studies has the

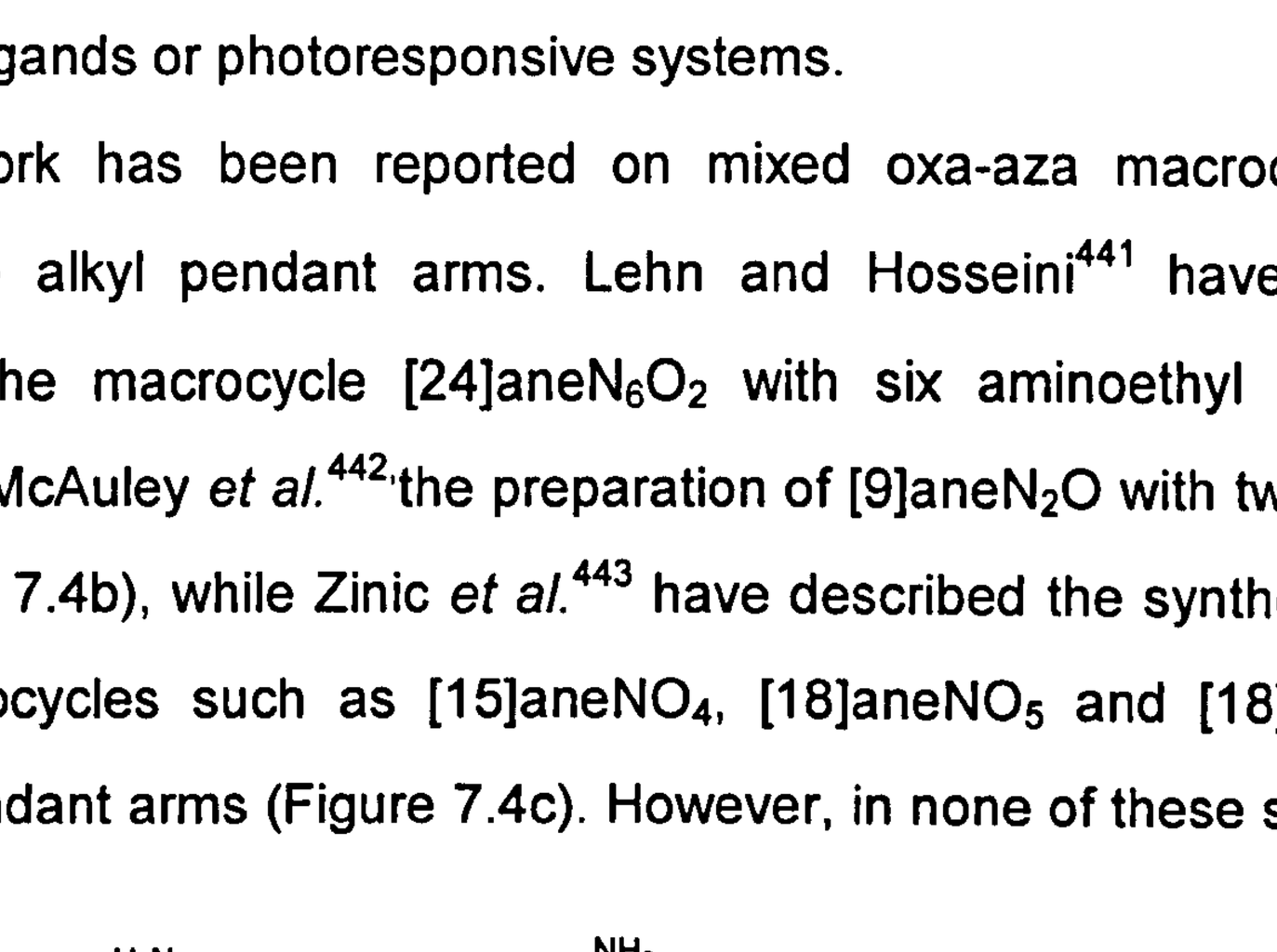

Figure 7.4. (a) [24]aneN$_6$O$_2$ bearing six aminoethyl pendant arms; (b) [9]aneN$_2$O bearing two aminopropyl groups; (c) [18]aneNO$_5$, [18]aneN$_2$O$_4$ and [15]aneNO$_4$ bearing aminoethyl pendant arms.

co-ordination chemistry of these ligands been reported. Nitrile functionalised pendant arms have been attached to aza or mixed sulphur-nitrogen macrocyles in order to prevent the polydentate ligands from encapsulating a tetrahedral metal centre such as Ag^{I}, thereby promoting the formation of polymeric compounds.[444,445] In Chapter 6, the co-ordination chemistry of the *tris*(cyanoalkyl) derivatives of [9]aneN_3 (L^1 and L^5) towards Cu^{II} was described and in Chapter 8 the Ag^{I} complexes of various polydentate ligands bearing nitrile pendant arms will be discussed in more detail.

In this chapter, the co-ordination behaviour of the ligand 1,4,7-*tris*(cyanomethyl)-1,4,7-triaza-10,13-dioxacyclopentadecane (L^8 in Figure 7.5) towards transition and post-transition metal ions will be described, with the aim of discovering whether the nitrile pendant arms dangle away from the metal centre or co-ordinate to it in some way. The co-ordination properties of the ligand 1,4,7-*tris*(2-aminoethyl)-1,4,7-triaza-10,13-dioxacyclopentadecane (L^9 in Figure 7.5),[446] which has an asymmetric disposition of the donor atoms as well as the potential for simultaneous coordination by oxygen and nitrogen donors, will also be discussed.

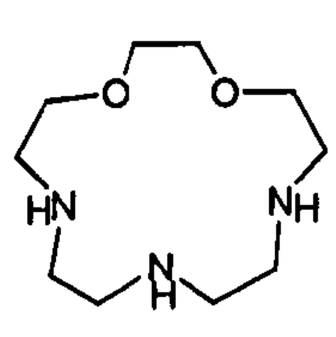

[15]aneN_3O_2

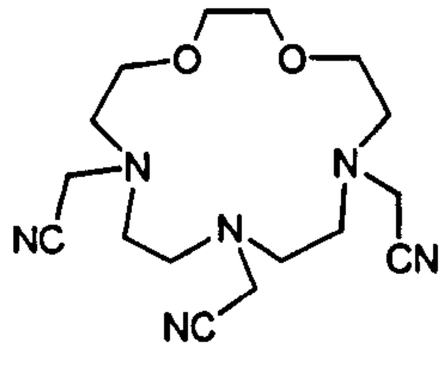

L^8

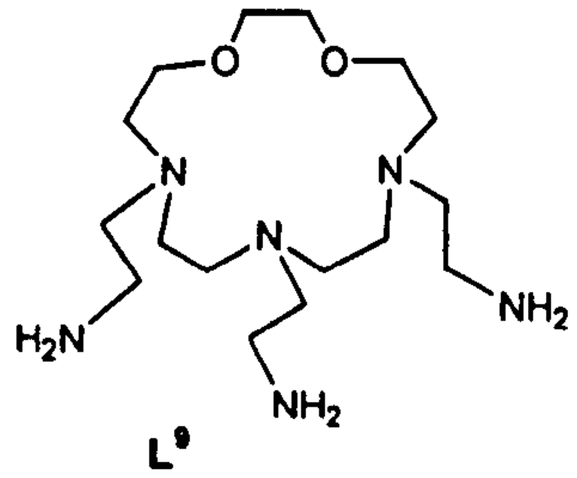

L^9

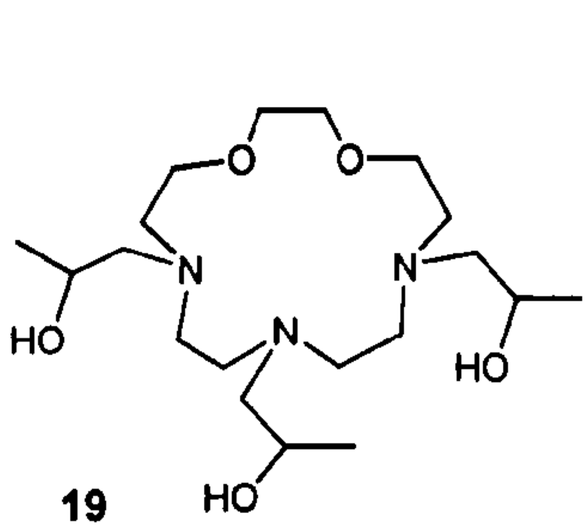

19

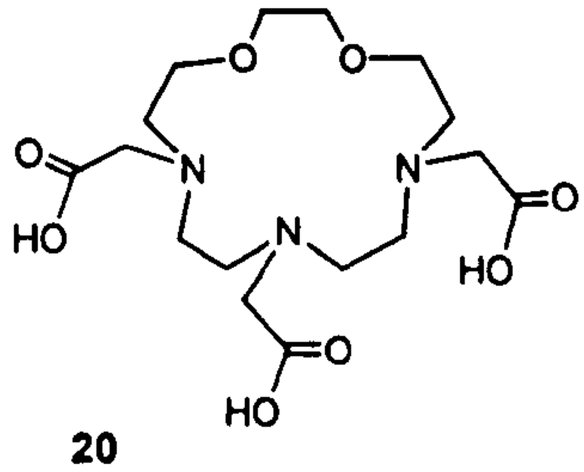

20

Figure 7.5. Ligands discussed in this chapter

Solution and structural studies have been reported on the macrocyclic precursor [15]aneN$_3$O$_2$[440,447,448] and on its derivatives with hydroxyl (**19**)[440] and carboxylate (**20**)[449] pendant groups (Figure 7.5). The co-ordination properties of these ligands will be compared to the ligands L^8 and L^9 described in this chapter.

7.2 Synthesis and structural characterisation of complexes with L^8 and L^9

7.2.1 Synthesis of ligands and complexes

The synthesis of the two ligands 1,4,7-*tris* (2-cyanomethyl)-1,4,7-triaza-10,13-dioxacyclopentadecane (L^8) and 1,4,7-*tris* (2-aminoethyl)-1,4,7-triaza-10,13-dioxacyclopentadecane (L^9) is summarised in Figure 7.6. The synthetic procedure starting from 1,4,7-triaza-10,13-dioxacyclopentadecane ([15]aneN$_3$O$_2$) is similar to that discussed previously (Section 3.3.1) for the introduction of three aminoethyl pendant arms to 1,4,7-triazacyclononane. The ligand L^8 has been prepared in 56% yield by treatment of [15]aneN$_3$O$_2$ with three equivalents of chloroacetonitrile in the presence of an excess of Et$_3$N in EtOH. Conversion into L^9 was achieved in 75% yield by reduction of L^8 with 1M BH$_3$ solution in THF followed by hydrolysis with concentrated HCl solution. The free amine was obtained by passing an aqueous solution of the hydrochloride salt of L^9 through a Dowex column. (Dowex

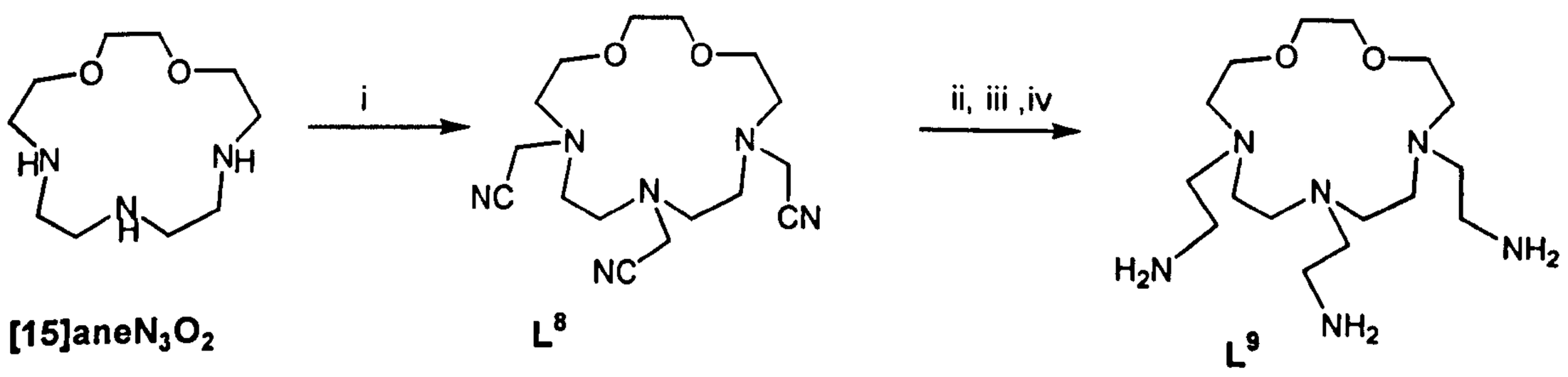

Figure 7.6. Scheme for the synthesis of L^8 and L^9: i: ClCH$_2$CN, NEt$_3$, EtOH, 18h; ii: BH$_3$·THF 1M, 48h; iii: HCl 6M, 24h; iv: Dowex 1x8-50.

1x8-50). Both products were characterised satisfactorily by ^{1}H and ^{13}C NMR spectroscopy, EI mass spectrometry and by elemental analysis.

The complexes $[M(L^8)(CH_3CN)](ClO_4)_2$ [M = Cu^{II}, Ni^{II}], $[M(L^8)](ClO_4)_2$ [M = Zn^{II} and Pb^{II}] and $[Cd(L)(NO_3)_2]$ were prepared in good yields by reacting L^8 with one equivalent of $M(ClO_4)_2 \cdot xH_2O$ or $Cd(NO_3)_2 \cdot 6H_2O$ in CH_3CN at room temperature. Elemental analytical data and mass spectra for all the complexes are consistent with these formulations.

The complexes $[M(L^9)](ClO_4)_2$ (M = Zn^{II}, Cu^{II}, Ba^{II} and Pb^{II}) and $[Cd(L^9)]Cl_2$ were obtained in good yields by reacting L^9 with one equivalent of $M(ClO_4)_2 \cdot xH_2O$ ($CdCl_2 \cdot 5/2H_2O$ for the Cd^{II} complex) in MeOH at room temperature. Elemental analytical data and mass spectra for all the complexes are consistent with the formulation $[M(L^9)](ClO_4)_2$ or $[Cd(L^9)]Cl_2$ in the case of the Cd^{II} complex.

7.2.2 Structural characterisation of complexes with L^8

Single crystals suitable for X-ray diffraction studies could be grown for all the complexes except for $[Zn(L^8)](ClO_4)_2$. $[Ni(L^8)(CH_3CN)](ClO_4)_2$ and $[Cu(L^8)(CH_3CN)](ClO_4)_2$ are isostructural (Table 7.2), with the six co-ordinate metal

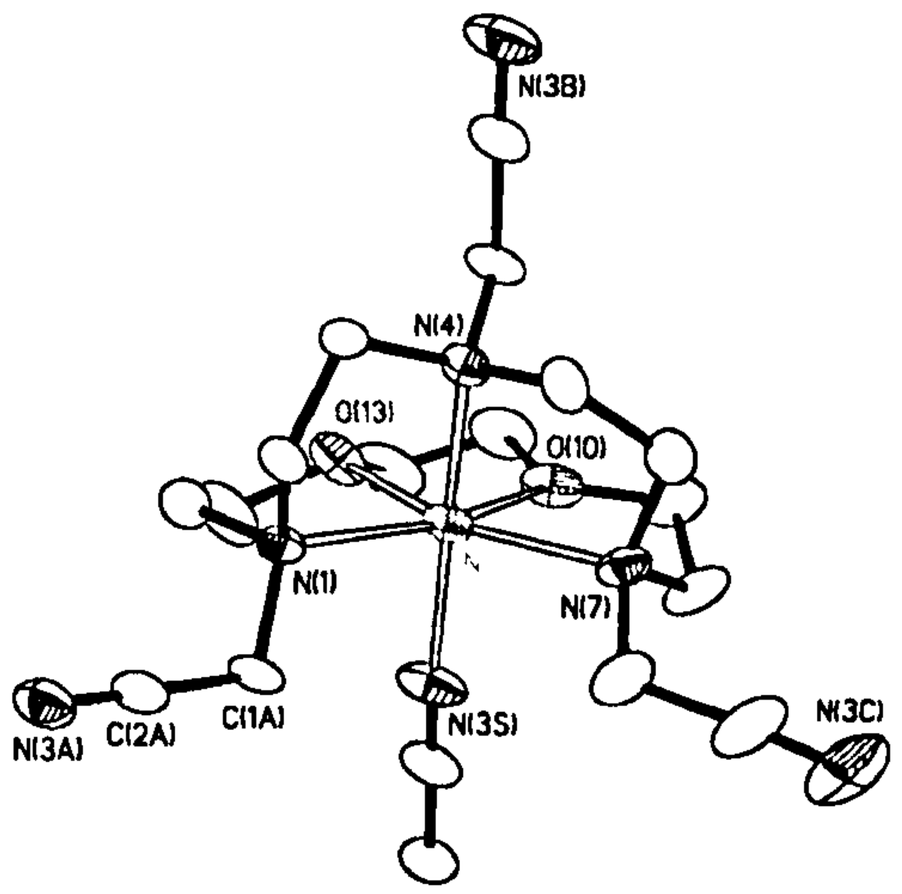

Figure 7.7. Crystal structure of the $[Ni(L^8)(CH_3CN)]^{2+}$ cation with numbering scheme adopted. Hydrogen atoms have been omitted for clarity. Displacement ellipsoids are drawn at 40% probability.

ion adopting a distorted octahedral geometry (Figures 7.7 and 7.8), being co-ordinated to the five macrocyclic ring donors (three tertiary nitrogens and two ethereal oxygens) and one acetonitrile molecule. The donor atoms in the equatorial plane are in both structures N(1), N(7), O(10) and O(13), while the axial positions are taken up by N(4) and N(3S) from the acetonitrile molecule. The r.m.s. deviation of the N and O atoms from the N_2O_2 equatorial plane is 0.036 Å for the Ni^{II} structure and 0.077 Å for the Cu^{II} complex. The difference between the two structures lies in the nature of the distortion from the octahedral geometry. The Ni^{II} structure presents a trigonal elongation with the triangular face of the octahedron formed by N(1), N(4) and N(7) elongated in respect to the O(10), O(13) and N(3S) face (bond lengths 2.110(7)-2.157(8) Å and 2.025-2.055 Å, respectively). The Cu^{II} structure presents a compression of the octahedron with the two axial bonds shorter than the four equatorial ones (see Table 7.2 for bond lengths and angles). This Jahn-Teller shortening of the axial bonds is quite rare, axial elongation being more common.[450] In the equatorial plane the two N-donors of the tertiary amine centres [N(1) and N(7)] are closer to the metal centre than the two O-donors [O(10) and O(13)] (Table 7.2).

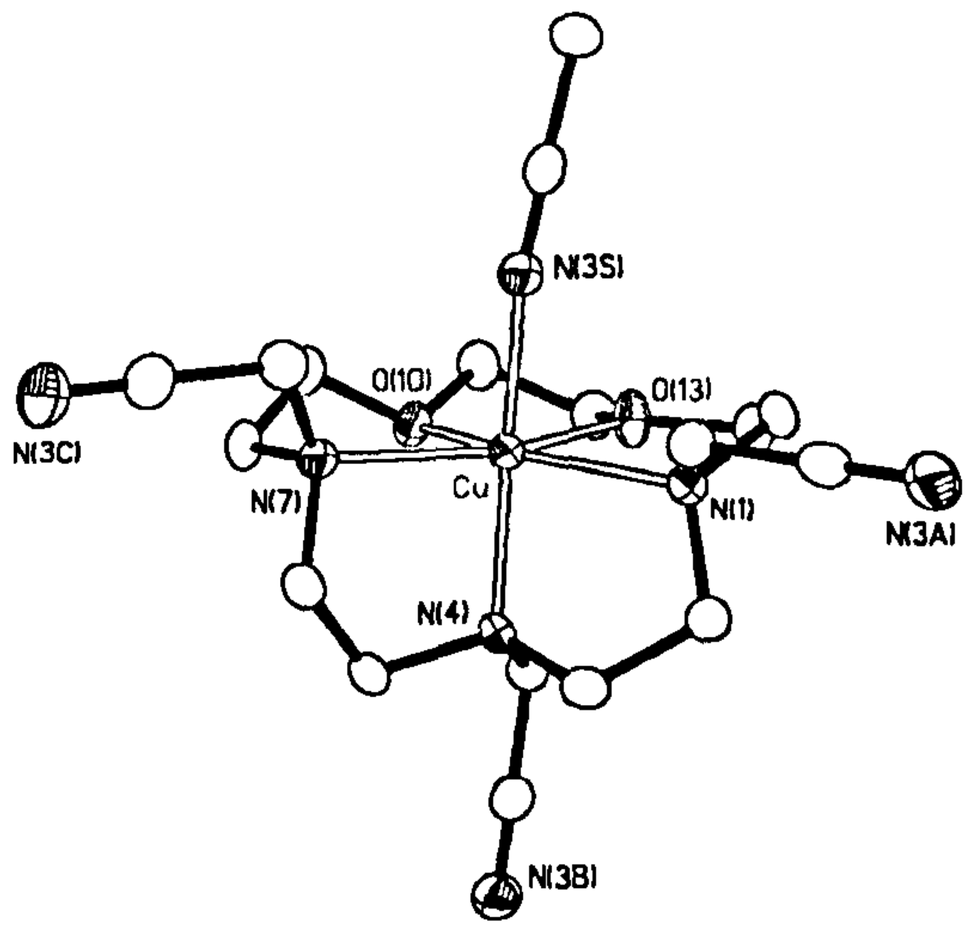

Figure 7.8. Crystal structure of the $[Cu(L^8)(CH_3CN)]^{2+}$ cation with numbering scheme adopted. Hydrogen atoms have been omitted for clarity and displacement ellipsoids are drawn at 50% probability.

Table 7.2. Selected bond lengths (Å) and angles (°) for $[Ni(L^8)(CH_3CN)](ClO_4)_2$ and $[Cu(L^8)(CH_3CN)](ClO_4)_2$.

	$[Cu(L^8)(CH_3CN)](ClO_4)_2$	$[Ni(L^8)(CH_3CN)](ClO_4)_2$
M-N(1)	2.161 (3)	2.146 (8)
M-N(4)	2.029 (3)	2.110 (7)
M-N(7)	2.136 (3)	2.157 (8)
M-O(10)	2.332 (3)	2.025 (7)
M-O(13)	2.235 (3)	2.055 (7)
M-N(3S)	1.972 (4)	2.047 (9)
N(1)-M-N(4)	84.8 (1)	83.4 (3)
N(1)-M-N(7)	138.8 (1)	123.3 (3)
N(4)-M-N(7)	86.0 (1)	83.6 (3)
N(1)-M-O(10)	143.6 (1)	158.7 (3)
N(1)-M-O(13)	75.6 (1)	81.2 (3)
N(1)-M-N(3S)	91.8 (1)	91.9 (3)
N(4)-M-O(10)	94.0 (1)	100.2 (3)
N(4)-M-O(13)	99.8 (1)	97.0 (3)
N(4)-M-N(3S)	174.7 (1)	170.0 (3)
N(7)-M-O(10)	77.0 (1)	78.0 (3)
N(7)-M-O(13)	145.5 (1)	155.2 (3)
N(7)-M-N(3S)	94.0 (1)	91.8 (4)
O(10)-M-O(13)	68.7 (1)	77.5 (3)
O(10)-M-N(3S)	91.1 (1)	87.5 (3)
O(13)-M-N(3S)	83.2 (1)	90.9 (4)

The distortion from the equatorial co-ordination geometry in both structures is clearly due to the presence of different chelate rings. While the five-membered chelate rings are very similar for $[Ni(L^8)(CH_3CN)]^{2+}$ and for $[Cu(L^8)(CH_3CN)]^{2+}$, both in the angles at the metal centre [78.0(3)-81.2(3)° and 68.7(1)-77.0(1)°, respectively] and in the distance between the donor atoms [2.555(10)-2.735(9) Å and 2.577(4)-2.786(5) Å, respectively], the angles N(1)-M-N(7) within an eight membered chelate ring are larger than the expected 90° [123.3(3)° in the Ni^{II} structure and 138.8(1)° in the Cu^{II} one]. The macrocyclic framework adopts a very similar conformation in both complexes, with eight out of fifteen torsion angles less

than 90°. In both structures the macrocycle is folded along the direction N(1)···N(7) and the dihedral angles between the two mean planes defined by the seven membered N(1)···N(7) and the ten membered N(7)···N(1) chains of the macrocycle are 90.3° in the Ni^{II} complex and 85.3° for the Cu^{II} one.

The structure of the complex $[Cd(L^8)(NO_3)_2]$ is shown in Figure 7.9 and selected bond lengths and angles are reported in Table 7.3. The Cd^{II} centre is eight co-ordinate: all the donor atoms of the macrocyclic ring co-ordinate as do two nitrate anions, one of them in a bidentate fashion. While the Cd-N bond lengths are in the range 2.436(1)-2.535(2)Å, the Cd-O distances span in the ranges 2.307(1)-2.673(1)Å, both falling in the range reported for similar bonds in other Cd^{II} complexes.[451-453] The bond length Cd-O(6) from the monodentate nitrate group [2.361(1) Å] falls within the range (2.31-2.44 Å) previously observed in this type of Cd^{II} complexes.[454-458] Cd-O lengths in bidentate nitrato complexes (which are usually asymmetrical) span a wider range (2.29-2.83 Å);[456-458] therefore, the bond lengths Cd-O(1) and Cd-O(3) of 2.307(1) and 2.673(1) Å, respectively, lie within this range. The macrocyclic framework is folded differently to that in

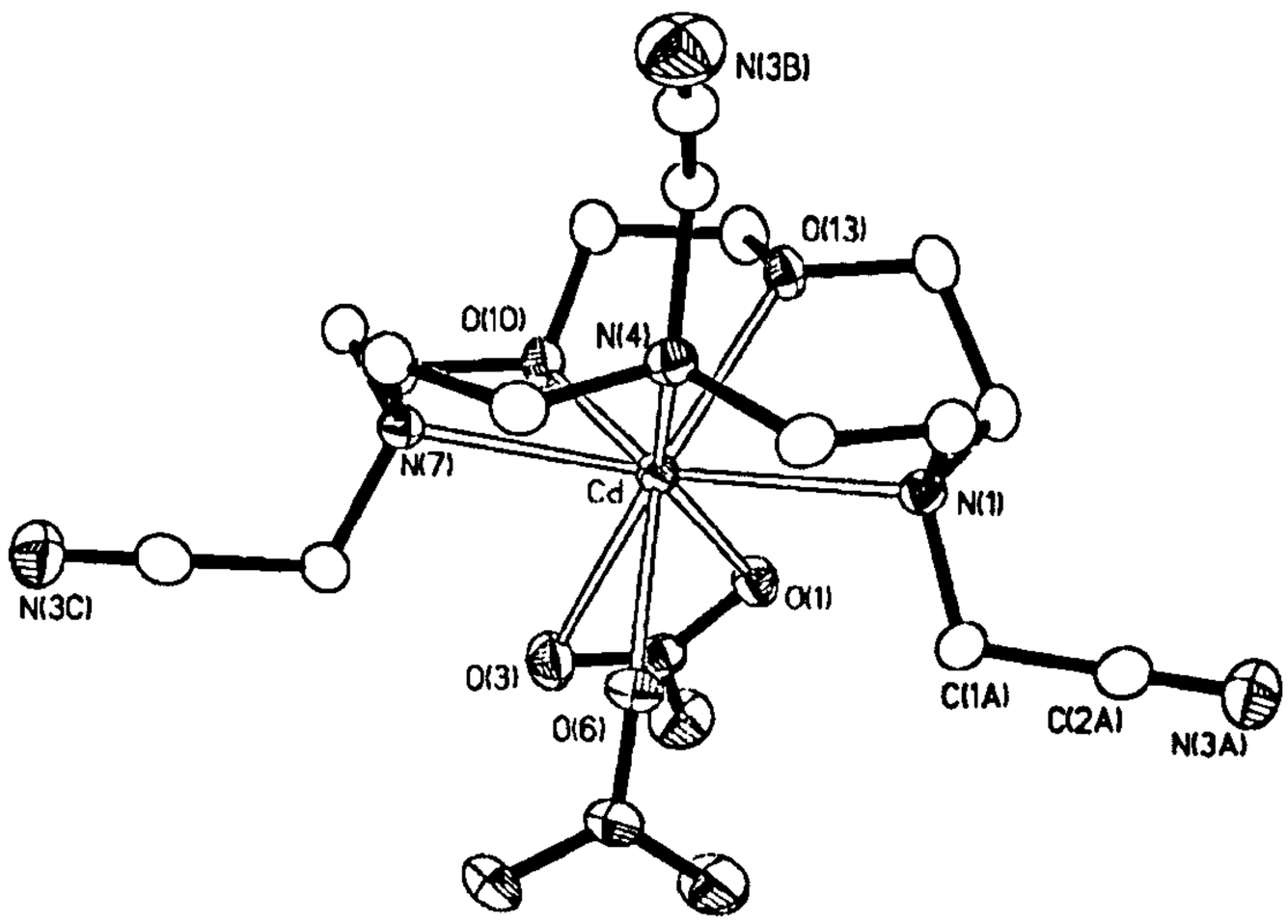

Figure 7.9. View of the $[Cd(L^8)(NO_3)_2]$ complex with numbering scheme adopted. Hydrogen atoms have been omitted for clarity and displacement ellipsoids are drawn at 50% probability.

[M(L^8)(CH$_3$CN)](ClO$_4$)$_2$ (M = Ni^{II} and Cu^{II}): here the folding is along the direction N(1)···C(9) with a dihedral angle between the two mean planes defined by the nine membered N(1)···C(9) and the eight membered C(9)···N(1) chains of the macrocycle at 59.0°.

Table 7.3. Selected bond lengths (Å) and angles (°) for [Cd(L^8)(NO$_3$)$_2$].

Cd-N(1)	2.535(2)	N(4)-Cd-O(10)	123.73(5)
Cd-N(4)	2.436(1)	O(3)-Cd-N(4)	147.72(5)
Cd-N(7)	2.474(2)	O(6)-Cd-N(4)	80.08(5)
Cd-O(10)	2.486(1)	N(7)-Cd-O(10)	71.78(5)
Cd-O(13)	2.390(1)	O(13)-Cd-N(7)	115.39(5)
Cd-O(1)	2.307(1)	O(1)-Cd-N(7)	133.17(5)
Cd-O(3)	2.672(1)	O(3)-Cd-N(7)	84.75(5)
Cd-O(6)	2.361(1)	O(6)-Cd-N(7)	85.69(5)
		O(13)-Cd-O(10)	68.03(4)
N(4)-Cd-N(1)	72.76(5)	O(1)-Cd-O(10)	78.53(5)
N(7)-Cd-N(1)	146.80(5)	O(3)-Cd-O(10)	70.50(4)
O(10)-Cd-N(1)	134.12(5)	O(6)-Cd-O(10)	138.86(5)
O(13)-Cd-N(1)	70.54(5)	O(1)-Cd-O(13)	84.28(5)
O(1)-Cd-N(1)	78.62(5)	O(3)-Cd-O(13)	123.60(5)
O(3)-Cd-N(1)	120.48(5)	O(6)-Cd-O(13)	152.28(4)
O(6)-Cd-N(1)	81.99(5)	O(3)-Cd-O(1)	51.02(5)
N(4)-Cd-N(7)	74.80(5)	O(1)-Cd-O(6)	94.17(5)
O(13)-Cd-N(4)	88.07(5)	O(3)-Cd-O(6)	73.62(5)
O(1)-Cd-N(4)	151.31(5)		

In the dinuclear complex of [Pb(L^8)]$_2$(ClO$_4$)$_4$, disorder was identified in part of the macrocyclic backbone and in one nitrile arm, and only the major component is described herein. Bond lengths and angles are reported in Table 7.4. In this crystal structure, one nitrile arm and a perchlorate anion bridge two metal ions forming a dimer as shown in Figure 7.10a. Figure 7.10b shows more clearly the co-ordination around Pb^{II} which is coordinated to nine donor atoms, although some of these bonds are longer than others (Table 7.4). Four of the five macrocyclic donors are more strongly co-ordinated to the metal centre with bond lengths in the range 2.548(8)Å–2.643(15)Å while N(1) and O(5) are at distances of

2.797(8) and 2.803(8) Å, respectively. Pb^{II} is further co-ordinated by two perchlorate oxygens, [O(8) and its symmetry equivalent O(8)'], and a nitrile group of a symmetry related molecule [N(3A)'], all at about 3 Å from the metal centre. Pb-N and Pb-O bond lengths are similar to those found in other N,O-macrocyclic complexes of Pb^{II}.[459-462,]

Table 7.4. Selected bond lengths (Å) and angles (°) for $[Pb(L^8)]_2(ClO_4)_4$. Primed atoms are related to their unprimed equivalents to the symmetry operation (-x+1, -y+2, -z+1).

Pb(1)-N(1)	2.797(8)	N(4)-Pb(1)-O(8)'	143.4(3)
Pb(1)-N(4)	2.575(10)	N(4)-Pb(1)-N(3A)'	142.7(4)
Pb(1)-N(7)	2.643(15)	O(10)-Pb(1)-N(7)	67.0(4)
Pb(1)-O(10)	2.576(14)	O(13)-Pb(1)-N(7)	120.3(3)
Pb(1)-O(13)	2.548(8)	N(7)-Pb(1)-O(5)	88.8(3)
Pb(1)-O(5)	2.803(8)	N(7)-Pb(1)-O(8)	95.8(4)
Pb(1)-O(8)	3.068(10)	N(7)-Pb(1)-O(8)'	146.7(3)
Pb(1)-N(3A)'	2.977(12)	N(7)-Pb(1)-N(3A)'	73.2(4)
Pb(1)-O(8)'	2.993(13)	O(13)-Pb(1)-O(10)	59.7(3)
		O(10)-Pb(1)-O(5)	155.7(4)
N(4)-Pb(1)-N(1)	69.0(3)	O(10)-Pb(1)-O(8)	135.1(3)
N(7)-Pb(1)-N(1)	138.2(3)	O(10)-Pb(1)-O(8)'	105.6(4)
O(10)-Pb(1)-N(1)	120.3(3)	O(10)-Pb(1)-N(3A)'	79.3(4)
O(13)-Pb(1)-N(1)	63.0(3)	O(13)-Pb(1)-O(5)	139.0(3)
N(1)-Pb(1)-O(5)	76.1(3)	O(13)-Pb(1)-O(8)	141.3(3)
N(1)-Pb(1)-O(8)	100.5(3)	O(13)-Pb(1)-O(8)'	75.7(3)
N(1)-Pb(1)-O(8)'	74.5(3)	O(13)-Pb(1)-N(3A)'	118.3(3)
N(1)-Pb(1)-N(3A)'	146.1(3)	O(5)-Pb(1)-O(8)	45.8(2)
N(4)-Pb(1)-N(7)	69.8(3)	O(5)-Pb(1)-O(8)'	95.9(2)
N(4)-Pb(1)-O(10)	91.0(4)	O(5)-Pb(1)-N(3A)'	96.4(3)
O(13)-Pb(1)-N(4)	85.5(3)	N(3A)'-Pb(1)-O(8)'	73.5(4)
N(4)-Pb(1)-O(5)	78.0(3)	N(3A)'-Pb(1)-O(8)	55.9(3)
N(4)-Pb(1)-O(8)	122.9(3)	O(8)'-Pb(1)-O(8)	65.9(4)

The macrocyclic framework assumes a folded conformation along the N(1)···N(7) direction, with a dihedral angle of 64.2° between the two mean planes defined by the seven membered N(1)···N(7) and the ten membered N(7)···N(1) chains of the macrocycle. In a recent study reported by Glusker and co-workers,[463] Pb^{II}

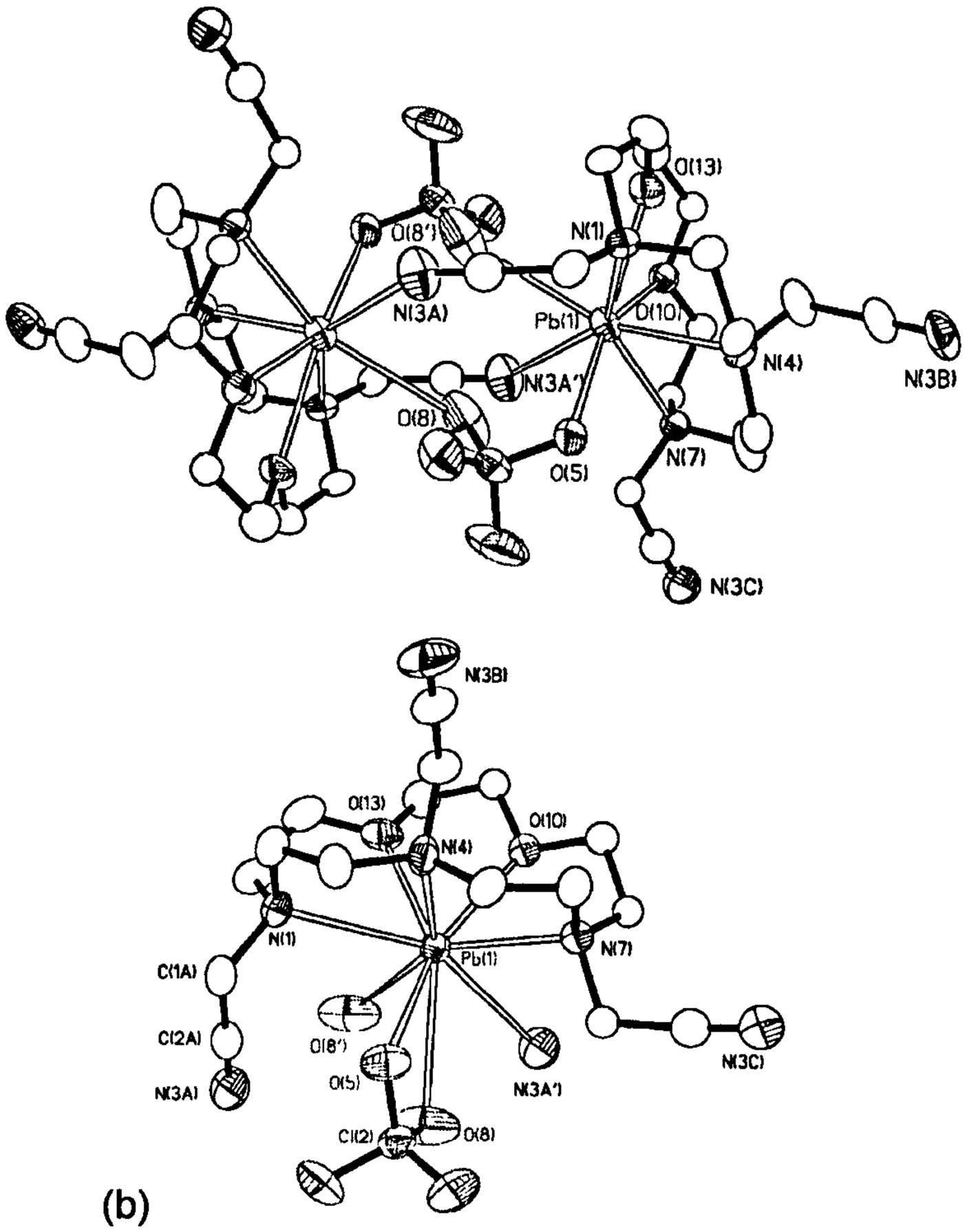

Figure 7.10. (a) Crystal structure of the $[Pb(L^8)(ClO_4)]_2^{2+}$ dinuclear cation with numbering scheme adopted. Hydrogen atoms have been omitted for clarity. Displacement ellipsoids are drawn at 40% probability; (b) clearer view of the co-ordination sphere around Pb(1). Primed atoms are related to their unprimed equivalents to the symmetry operation (-x+1, -y+2, -z+1).

structures with no stereochemically active lone pair on the metal centre have been named *holo-directed* and that ones with a gap in co-ordination geometry (stereochemically active lone pair) *hemi-directed*. In $[Pb(L^8)](ClO_4)_2$, the overall N_4O_5 donation at the Pb^{II} centre gives *holo-directed*[463] co-ordination geometry around the metal ion with the bonds to the donor atoms evenly distributed about the co-ordination sphere and the $6s^2$ lone-pair of Pb^{II} apparently stereochemically inactive. Presumably, the separation of the two metal ions within the dinuclear

species [Pb···Pb 5.087(10)Å] allows the ClO_4^- anions to act as bidentate ligands, bridging the metal centres by permitting favourable Cl–O–Pb angles. In this way, the inert lone-pair of electrons is prevented from expanding the co-ordination sphere of the Pb^{II} ions. The co-ordination sphere around the Pb^{II} centre can be described as a distorted tricapped trigonal prism (Figure 7.11). The two triangular faces formed by N(1), N(4) and O(5) and by O(10), O(8)' and N(3A)' are inclined to each other by 22.0º. The first triangular face of the prism is essentially equilateral (angle range 59.9-64.6º), but the second is more distorted, having one side and one angle larger that the other two. N(7), O(8) and O(13) cap the three rectangular faces of the prism. The two triangular faces are twisted with respect to each other: the twist between the two triangular faces can be quantified looking at the torsion angles formed by the four atoms of every rectangular face of the prism. The average of the three torsion angles in this Pb^{II} structure (one for every triangular side) is 26.0°.

It is interesting to note that the crystal structures of the Ni^{II}, Cd^{II} and Pb^{II} complexes show M-N bond lengths comparable (or sometimes longer, as in the Ni^{II} complex) with the bond distances between the metals and the O-donors of the macrocycle. This is a distinct difference with the Cu^{II} complex where the M-O bond lengths are remarkably longer than the M-N ones [2.332(3) and 2.235(3) Å against an average of 2.075 Å for M-N bonds].

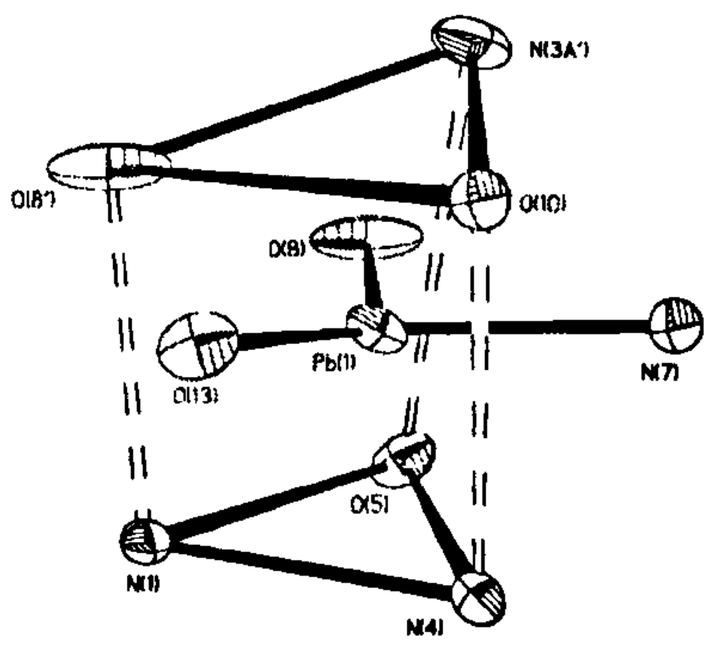

Figure 7.11. Coordination geometry about the Pb^{II} centre in $[Pb(L^8)]_2(ClO_4)_4$. Displacement ellipsoids are drawn at 30% probability.

7.2.3 Structural characterisation of complexes with L^9

Single crystals suitable for X-ray diffraction studies could be grown for all the complexes synthesised except for $[Cd(L^9)]Cl_2$. $[Zn(L^9)](ClO_4)_2$ and $[Cu(L^9)](ClO_4)_2$ are isostructural (Table 7.5) with the five-coordinate metal ion adopting a distorted square-based pyramidal geometry (Figures 7.12a and 7.12b), *via* binding to the three N-donors of the primary amines of the pendant arms and to two N-donors of the tertiary amine centres of the macrocycle. The metal centre is bound in an exocyclic manner and is situated outside the macrocyclic cavity. The two oxygens [O(10) and O(13)] and the remaining tertiary nitrogen [N(7)] from the macrocycle do not coordinate and are remote from the metal centre lying at 4.854(7), 5.114(7) and 3.492(8)Å, respectively, in $[Zn(L^9)](ClO_4)_2$ and at 4.912(3), 5.052(3) and 3.627(3)Å, respectively, in $[Cu(L^9)](ClO_4)_2$. The macrocyclic framework assumes a very similar conformation in both structures as indicated by

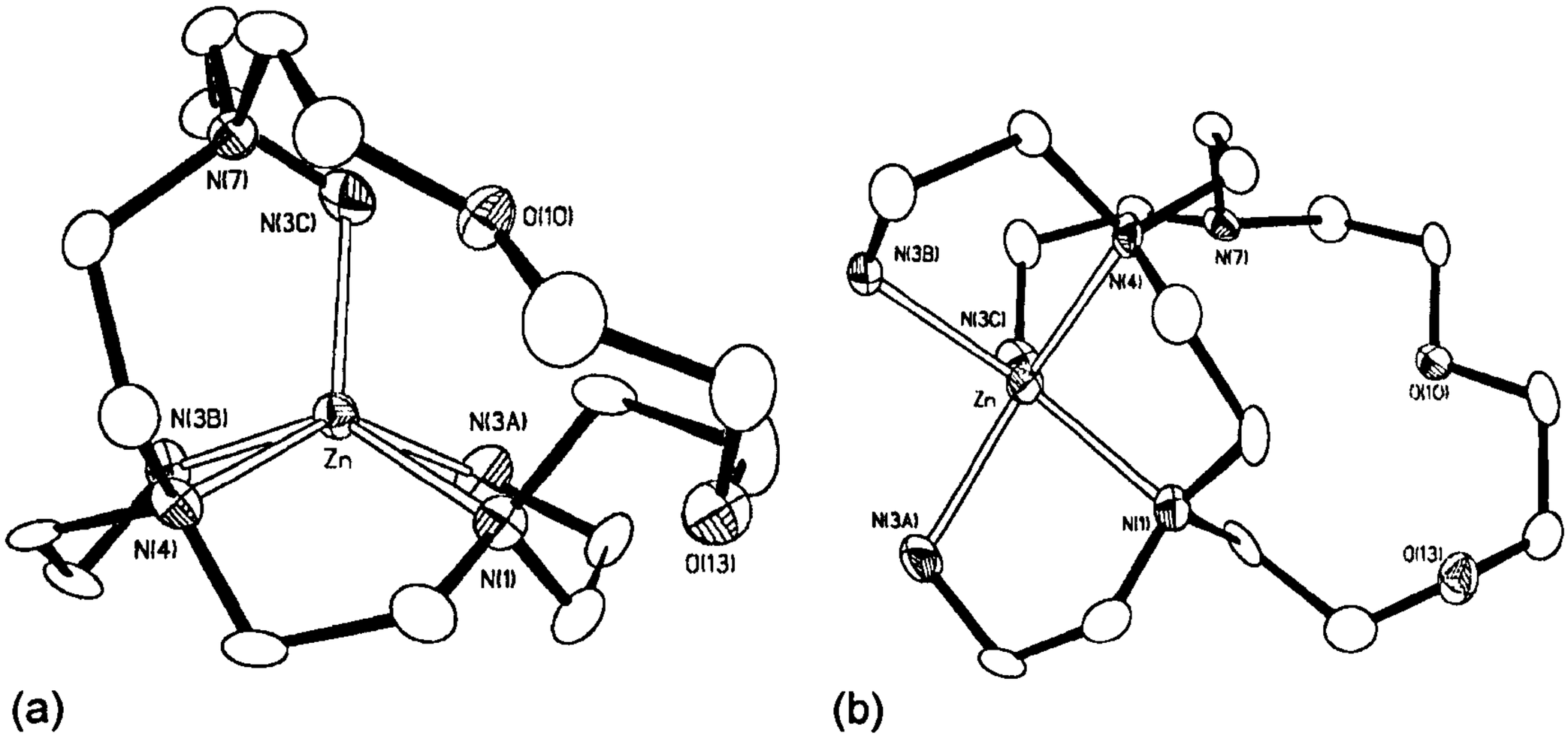

Figure 7.12. (a) Crystal structure of the cation $[Zn(L^9)]^{2+}$ with numbering scheme adopted showing the square pyramidal co-ordination geometry. Hydrogen atoms have been omitted for clarity. Displacement ellipsoids are drawn at 50% probability. (b) Alternative view of the cation $[Zn(L^9)]^{2+}$ showing the unco-ordinated part of the macrocycle.

the similar torsion angles within the macrocyclic backbones. The donor atoms forming the base of the pyramid are from two primary amines [N(3A) and N(3B)] from the pendant arms and two tertiary amines [N(1) and N(4)] from the macrocyclic framework. The r.m.s. deviation of the N atoms from the N_4 basal plane is 0.028Å for the Zn^{II} structure and 0.010Å for the Cu^{II} complex. The Zn^{II} ion lies 0.70Å and the Cu^{II} 0.51Å from their respective planes in the direction of the apical position occupied by the remaining primary amine [N(3C)]. The Zn-N(3C) apical bond forms an angle of 13.7° with the normal to the basal plane, while the Cu-N(3C) bond forms an angle of 12.7°, being in both cases very near to be perpendicular. In $[Cu(L^9)](ClO_4)_2$ the Cu-N (basal) bond lengths lie in the range 2.050(3)-2.093(3)Å and Cu-N (apical) is 2.188(4)Å. In $[Zn(L^9)](ClO_4)_2$ the corresponding bond lengths are 2.128(8)-2.221(8)Å and 2.039(9)Å (selected bond lengths and angles are in Table 7.5).

Table 7.5.. Selected bond lengths (Å) and angles (°) for $[Zn(L^9)](ClO_4)_2$ and $[Cu(L^9)](ClO_4)_2$.

Bonds	$[Zn(L^9)](ClO_4)_2$	$[Cu(L^9)](ClO_4)_2$	angles	$[Zn(L^9)](ClO_4)_2$	$[Cu(L^9)](ClO_4)_2$
M-N(1)	2.170 (8)	2.068 (3)	N(1)-M-N(4)	81.9 (3)	85.14 (12)
M-N(4)	2.211 (8)	2.093 (3)	N(1)-M-N(3A)	81.0 (3)	84.12 (13)
M-N(3A)	2.181 (9)	2.065 (3)	N(4)-M-N(3B)	81.6 (3)	84.52 (13)
M-N(3B)	2.128 (8)	2.050 (3)	N(3A)-M-N(3B)	91.9 (3)	92.43 (14)
M-N(3C)	2.039 (9)	2.188 (4)	N(1)-M-N(3B)	140.3 (4)	150.70 (14)
			N(4)-M-N(3A)	144.1 (3)	152.04 (14)
			N(3C)-M-N(1)	118.7 (4)	112.71 (13)
			N(3C)-M-N(4)	117.4 (3)	113.18 (13)
			N(3C)-M-N(3A)	98.4 (4)	94.78 (14)
			N(3C)-M-N(3B)	100.9 (4)	96.56 (14)

The difference between the Cu^{II} and Zn^{II} structures is that the apical donor is the closest to the metal centre for the Zn^{II} structure while for the Cu^{II} one the shortest bond lengths are with the basal donors as expected in a d^9 Jahn-Teller distorted complex. The square base of the pyramid is quite regular with three five-membered chelate rings formed at the metal centre; these are very similar both in the angles at the metal centre [81.0(3)°-81.9(3)° for Zn^{II} structure and 84.1(1)°-85.1(1)° for Cu^{II}] and in the distance between the nitrogens [2.83(1)-2.87(1)Å for Zn^{II} and 2.769(4)-2.814(4)Å for Cu^{II}].

It is interesting to compare the two Cu^{II} structures with L^8 and L^9 discussed in this chapter (the complex cations $[Cu(L^8)(CH_3CN)]^{2+}$ and $[Cu(L^9)]^{2+}$) with other Cu^{II} crystal structures reported with the macrocyclic precursor [15]aneN$_3$O$_2$ and its derivatives. In the Cu^{II} complex with L^8, all the atoms from the macrocycle participate in the co-ordination of the metal ion, while in all the others at least one O donor does not co-ordinate.[446,448,449] In $[Cu(L^9)]^{2+}$, the metal ion is five co-ordinate and sits outside the macrocyclic cavity with only two out of five donors of the ring interacting with the copper(II) centre.[446] The Cu^{II} complexes with [15]aneN$_3$O$_2$ and with its carboxylate pendant arm derivative are again five co-

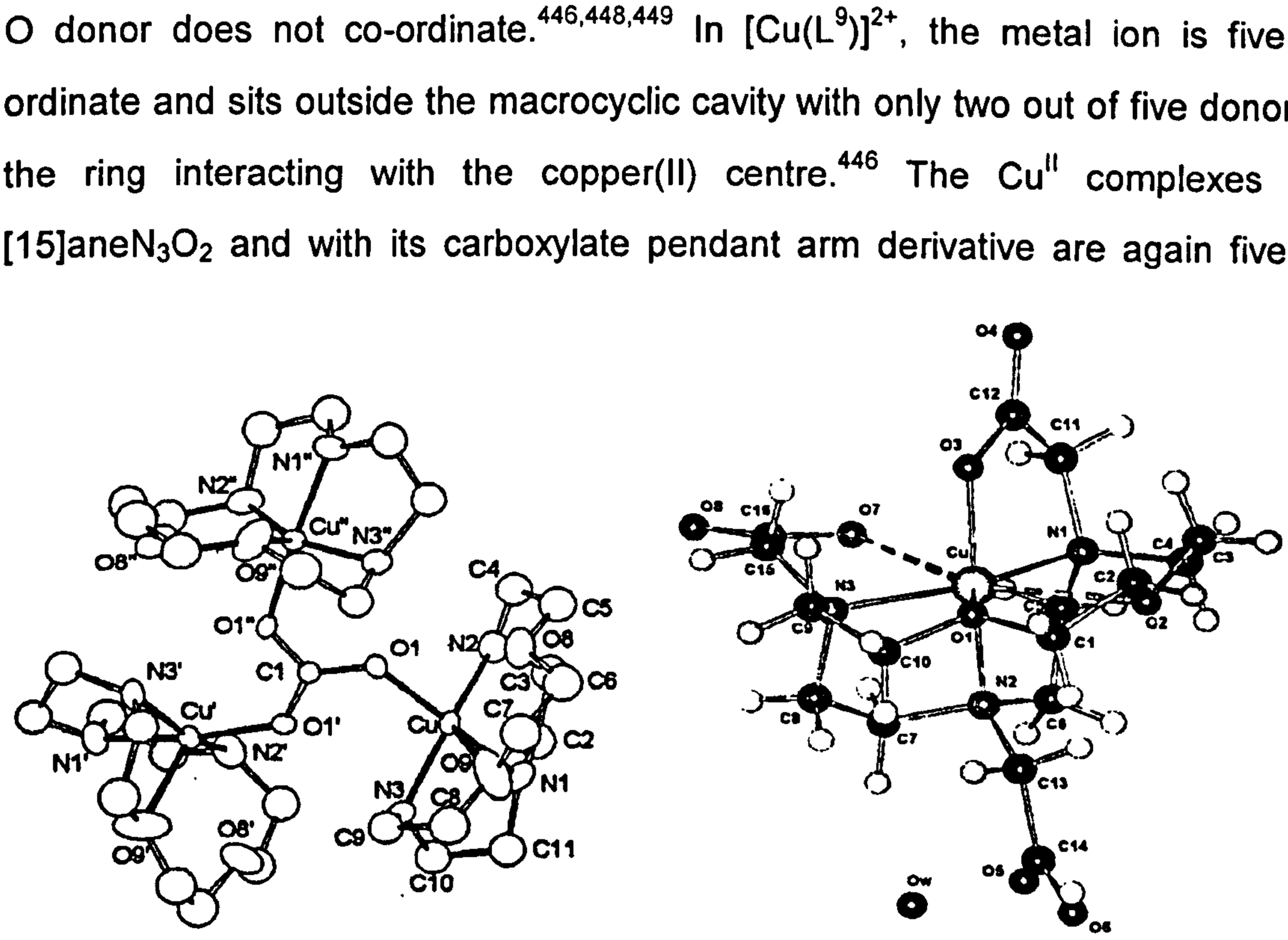

Figure 7.13. Crystal structures of the Cu^{II} complexes with (a) the macrocyclic precursor [15]aneN$_3$O$_2$ and (b) the carboxylate pendant arm derivative **20**.

ordinate. With the macrocyclic precursor [15]aneN$_3$O$_2$ a peculiar trinuclear complex with a μ_3-CO_3^{2-} bridging the three copper(II) centres has been reported (Figure 7.13a) and each Cu^{II} adopts a distorted square-pyramidal geometry with one O-donor of the macrocycle not co-ordinated.[448] In the Cu^{II} complex with the ligand containing three carboxylate donor groups, the co-ordination geometry around Cu^{II} is a distorted compressed trigonal bipyramid with one oxygen of the macrocycle interacting only very weakly with the metal centre at a distance of 2.727(4)Å (Figure 7.13b).[449] The preference for N- over O-donors, typical of Cu^{II}, requires a folded arrangement of the macrocycle, but even in this kind of arrangement the macrocyclic cavity is not too large to prevent both the O-donors of the macrocyclic ring from co-ordinating the metal ion, as demonstrated by the structure of $[Cu(L^8)(CH_3CN)]^{2+}$.

The major component of disorder on the macrocyclic backbone and one component of the disordered pendant arms for the crystal structure of $[Pb(L^9)](ClO_4)_2$ (Figure 7.14) are described in the experimental section. Selected bond lengths and angles are reported in Table 7.6. The Pb^{II} is coordinated to all eight donor atoms of the ligand, but some of these bonds are longer than others

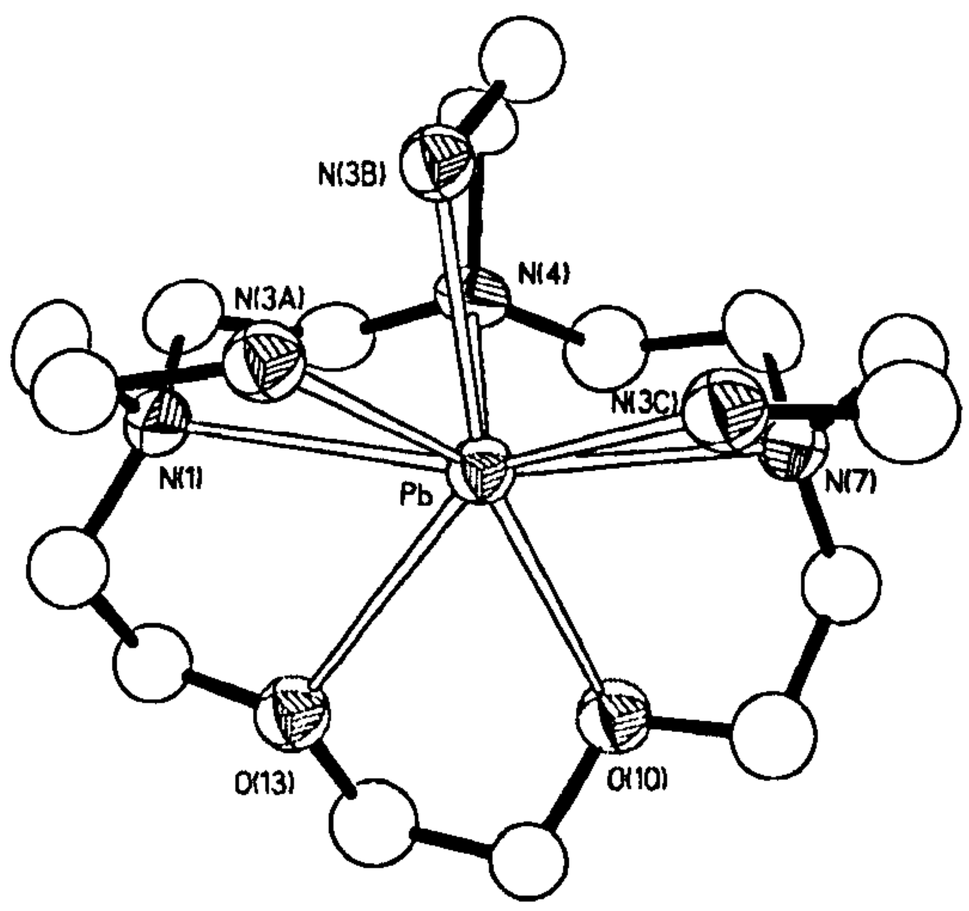

Figure 7.14. Crystal structure of the cation $[Pb(L^9)]^{2+}$ with numbering scheme adopted. Hydrogen atoms have been omitted for clarity. Displacement ellipsoids are drawn at 30% probability.

(Table 7.6). Two types of Pb-N interactions can be discerned in this structure: the three primary amines and N(4) are quite close to the lead [2.51(2)–2.65(2)Å] with bond lengths similar to those found in other N-macrocyclic complexes of lead(II).[459-462,464-466] The Pb^{II} centre is coordinated further to two other tertiary nitrogens , N(1) and N(7), with bond lengths of 2.85(1)Å and 2.80(1)Å, respectively, and to two oxygens, O(10) and O(13), at 3.05(1)Å and 3.08(1)Å, respectively. We regard these Pb···O interactions as clearly long-range, since the sum of the ionic radius of Pb^{2+} with coordination number 8 and that of O^{2-} with coordination number 3 is 2.65Å.[288]

Table 7.6. Selected bond lengths (Å) and angles (°) for $[Pb(L^9)](ClO_4)_2$.

Pb-N(1)	2.853 (10)	N(1)-Pb-N(4)	68.8 (3)	N(3C)-Pb-N(7)	67.5 (6)
Pb-N(4)	2.587 (11)	N(1)-Pb-N(7)	137.7 (4)	O(13)-Pb-N(7)	109.9(4)
Pb-N(7)	2.802 (10)	N(3A)-Pb-N(1)	67.2 (5)	O(10)-Pb-N(7)	58.8 (3)
Pb-N(3A)	2.65 (2)	N(3B)-Pb-N(1)	78.9 (5)	N(3A)-Pb-N(3B)	56.0 (7)
Pb-N(3B)	2.51 (2)	N(3C)-Pb-N(1)	146.8 (6)	N(3A)-Pb-N(3C)	81.0 (7)
Pb-N(3C)	2.60 (3)	N(4)-Pb-N(7)	62.06(9)	N(3B)-Pb-N(3C)	75.5 (8)
Pb-O(10)	3.048 (15)	N(3A)-Pb-N(4)	88.39(10)	O(10)-Pb-N(3A)	153.0 (6)
Pb-O(13)	3.083 (14)	N(3B)-Pb-N(4)	62.81(8)	O(10)-Pb-N(3B)	150.4 (5)
Pb-N(3A)'[(a)]	2.69 (3)	N(3C)-Pb-N(4)	118.7 (7)	O(10)-Pb-N(3C)	107.7 (7)
Pb-N(3B)'[(a)]	2.60 (2)	O(10)-Pb-N(4)	85.9 (4)	O(10)-Pb-O(13)	53.3 (4)
Pb-N(3C)'[(a)]	2.69 (2)	O(13)-Pb-N(4)	88.2 (4)	O(13)-Pb-N(3A)	105.9 (6)
		N(3A)-Pb-N(7)	144.0 (5)	O(13)-Pb-N(3B)	134.9 (6)
		N(3B)-Pb-N(7)	98.1 (5)	O(13)-Pb-N(3C)	147.7 (7)

[(a)] Equally populated component of the disorder not described in the text.

The effect of the lone pair of electrons on Pb^{II} on the stability and geometry of its complexes has been explained previously.[459,463,464] This lone pair can be either active or inactive, depending mostly on the nature of the donor atoms. In the structure described here two effects of a stereochemically active lone pair can be

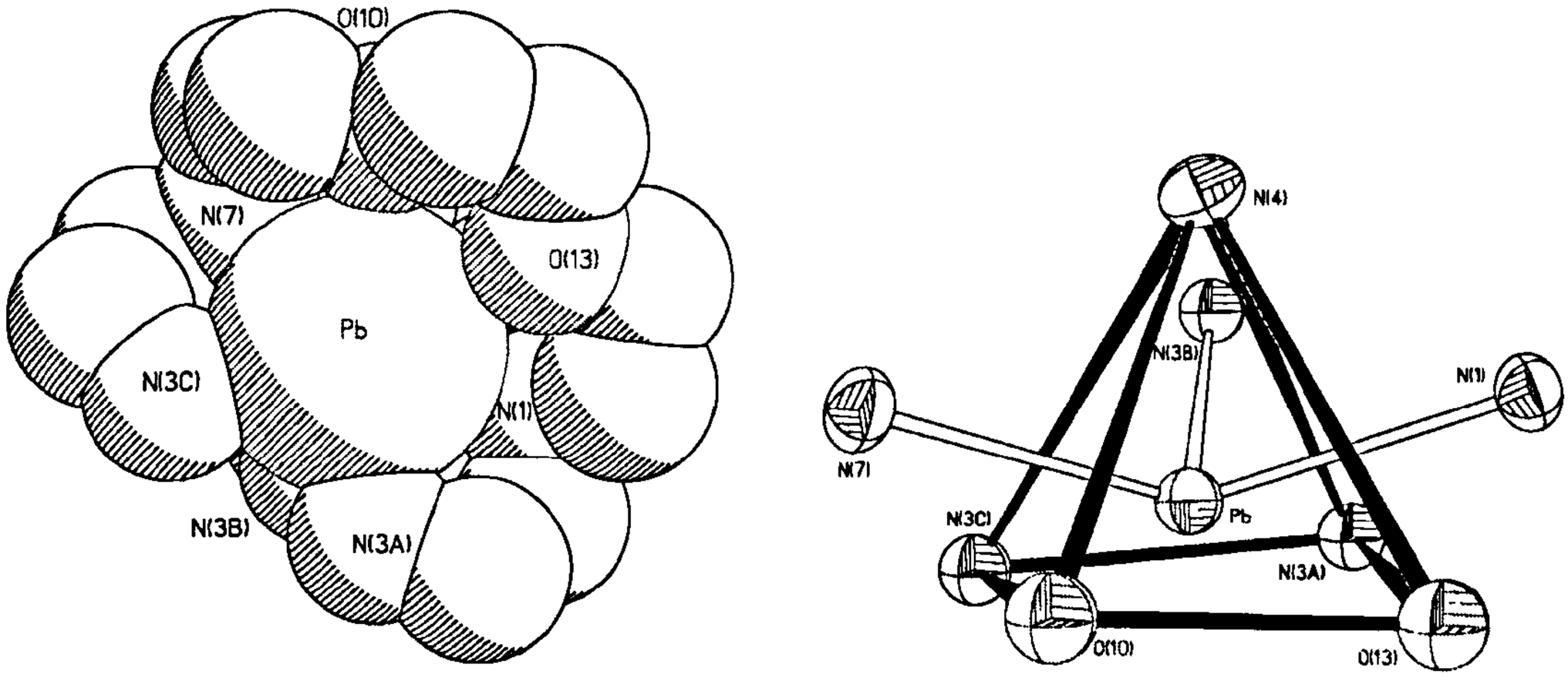

Figure 7.15. (a) Space-filling model of the complex cation $[Pb(L^9)]^{2+}$ showing the co-ordination gap at the metal centre; (b) tricapped pyramidal co-ordination geometry about the lead(II) centre in $[Pb(L^9)]^{2+}$. Displacement ellipsoids are drawn at 30% probability.

envisaged: the shortening of some of the Pb-N bonds and the presence of a gap in the coordination sphere around the metal. When Pb^{II} has an active lone pair, the apparent ionic radius decreases by about 0.3Å, which may explain the strong coordination of the four nitrogens (the Pb-N distances are around 2.5 Å). Furthermore the apparent occupation of a coordination site on Pb^{II} by the lone pair can be seen in Figure 7.15a, which shows the space-filling model for the $[Pb(L^9)]^{2+}$ complex cation. Given the very wide O(10)-Pb-N(3A) and O(13)-Pb-N(3C) angles of *ca.* 150°, it is not unreasonable to conclude that the lone pair resides between O(10), O(13), N(3A) and N(3C). This coordination mode with a gap in the coordination sphere around the metal has been named *hemi-directed* as already described in Section 7.2.2. *Hemi-directed* structures with eight coordinate Pb^{II} have been found to be quite rare in comparison to structures with no stereochemically active lone pair on Pb^{II} (*holo-directed*).[463]

The coordination sphere at the Pb^{II} centre can be described as tricapped pyramidal (Figure 7.15b). The base of the pyramid is a rectangle formed by N(3A),

N(3C), O(10) and O(13), which have an r.m.s. deviation from the basal plane of 0.085Å. The long sides are N(3C)-O(10) and N(3A)-O(13) with distances of 4.57(3) and 4.58(3)Å, respectively, while the short sides are N(3A)-N(3C) and O(10)-O(13) of 3.41(3) and 2.75(2)Å, respectively. The angles at the rectangular base are in the range 84.9(6)°-94.7(5)°. N(1), N(7) and N(3B) cap three of the four triangular faces of the pyramid, while N(4) occupies the apical position.

The structure of the complex cation $[Ba(L^9)(ClO_4)]^+$ is shown in Figure 7.16 and selected bond lengths and angles are reported in Table 7.7. The Ba^{II} centre is coordinated by all the donor atoms of the ligand plus two oxygens from one perchlorate anion, giving a coordination number of ten, as frequently found for the large Ba^{II} (the effective ionic radius of Ba^{2+} with coordination number 10 is 1.52 Å).[288] The metal ion is encapsulated by the three pendant arms and, in the side left open by the absence of pendant arms, the macrocycle is slightly bent to permit the two perchlorate O-donors to bind symmetrically, thereby completing the coordination sphere. The Ba-N bond lengths are in the range 2.889(3)-2.996(3)Å, with the three tertiary amines somewhat further from the metal centre than the three primary ones. The bond lengths between Ba^{II} and the oxygens are in the

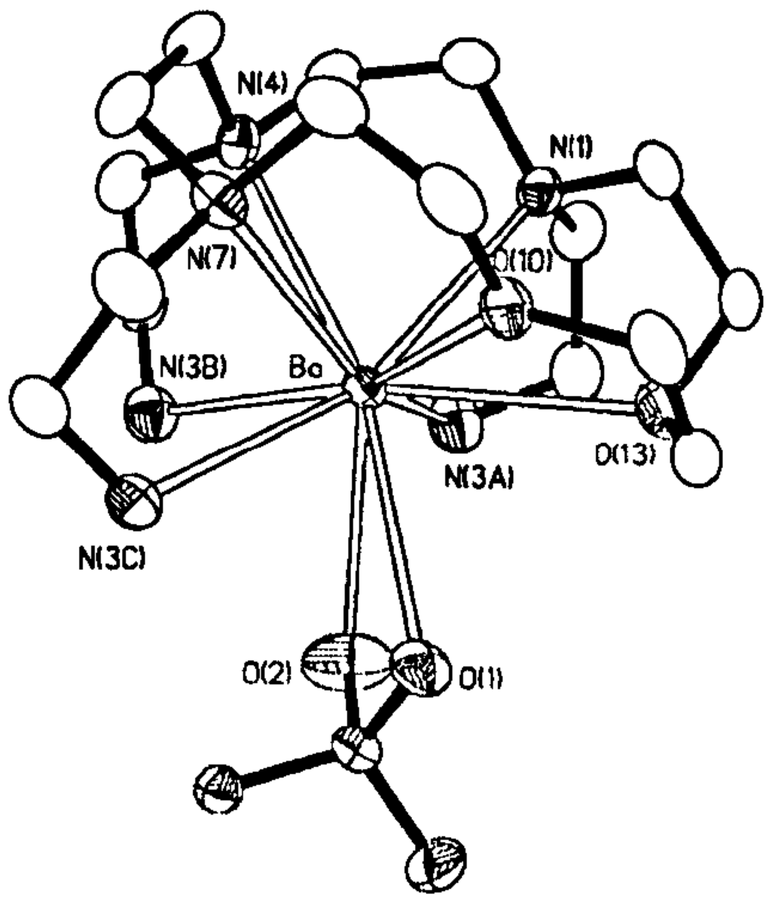

Figure 7.16. Crystal structure of the cation $[Ba(L^9)(ClO_4)]^+$ with numbering scheme adopted. Hydrogen atoms have been omitted for clarity. Displacement ellipsoids are drawn at 50% probability.

range 2.846(3)-3.015(3)Å with the perchlorate oxygens less strongly coordinated than the macrocyclic ones [O(10) and O(13)]. All the distances are in the range found in the literature.[467-471]

Table 7.7. Selected bond lenghts (Å) and angles (°) for [Ba(L^9)](ClO$_4$)$_2$.

Ba-N(1)	2.939 (3)	N(4)-Ba-N(7)	62.06(9)	O(10)-Ba-N(3C)	87.57(9)
Ba-N(4)	2.949 (3)	N(3A)-Ba-N(4)	88.39(10)	O(10)-Ba-O(13)	57.58(8)
Ba-N(7)	2.996 (3)	N(3B)-Ba-N(4)	62.81(8)	O(10)-Ba-O(1)	79.19(8)
Ba-N(3A)	2.889 (3)	N(3C)-Ba-N(4)	99.02(9)	O(10)-Ba-O(2)	123.90(8)
Ba-N(3B)	2.889 (3)	O(10)-Ba-N(4)	104.28(8)	O(13)-Ba-N(3A)	76.97(9)
Ba-N(3C)	2.902 (3)	O(13)-Ba-N(4)	122.24(8)	O(13)-Ba-N(3B)	147.26(9)
Ba-O(10)	2.846 (3)	N(4)-Ba-O(1)	163.76(8)	O(13)-Ba-N(3C)	129.89(9)
Ba-O(13)	2.911 (3)	N(4)-Ba-O(2)	131.31(8)	O(13)-Ba-O(1)	73.22(8)
Ba-O(1)	2.978 (3)	N(3A)-Ba-N(7)	150.01(10)	O(13)-Ba-O(2)	92.10(9)
Ba-O(2)	3.015 (3)	N(3B)-Ba-N(7)	97.64(9)	N(3A)-Ba-O(1)	100.94(9)
		N(3C)-Ba-N(7)	60.04(9)	N(3A)-Ba-O(2)	65.16(9)
N(1)-Ba-N(4)	64.29(9)	O(13)-Ba-N(7)	113.30(8)	N(3B)-Ba-O(1)	107.56(8)
N(1)-Ba-N(7)	98.88(9)	O(10)-Ba-N(7)	57.83(8)	N(3B)-Ba-O(2)	69.87(9)
N(3A)-Ba-N(1)	60.71(9)	O(1)-Ba-N(7)	108.97(8)	N(3C)-Ba-O(1)	65.05(9)
N(3B)-Ba-N(1)	106.57(9)	O(2)-Ba-N(7)	138.15(9)	N(3C)-Ba-O(2)	78.12(9)
N(3C)-Ba-N(1)	158.46(9)	N(3A)-Ba-N3B	70.71(10)	O(1)-Ba-O(2)	45.50(7)
O(10)-Ba-N(1)	83.92(8)	N(3A)-Ba-N(3C)	135.92(10)		
O(13)-Ba-N(1)	59.79(9)	N(3B)-Ba-N(3C)	74.45(10)		
O(1)-Ba-N(1)	131.90(8)	O(10)-Ba-N(3A)	132.74(9)		
O(2)-Ba-N(1)	122.88(9)	O(10)-Ba-N(3B)	155.00(9)		

7.3 Potentiometry measurements

7.3.1 Protonation of the ligands L^8 and L^9

The protonation equilibria of the two ligands have been studied in 0.1 mol dm^{-3} Me$_4$NCl aqueous solution at 298.1 ± 0.1 K by means of potentiometric pH measurements and the results are reported in Table 7.8, while a distribution

diagram for the species present in solution as a function of pH for the system L^9/H^+ is reported in Fig. 7.17.

The values of the protonation constants of L^8 are much lower than those found for [15]aneN$_3$O$_2$[440] (Table 7.8), possibly due to the lower basicity usually observed for tertiary amine groups.[472]

Ligand L^9 can bind up to six protons in the pH range investigated. The most interesting finding in the protonation constants is the sharp decrease in basicity observed between the third and the fourth protonation step. In fact, the values of the first three protonation constants range between 10.22 and 8.71 logarithmic units with a difference between the first and the third of only 1.5 units while the difference between the third and the fourth is *ca.* 3.4 logarithmic units. This behaviour can be rationalized by taking into account the different nature of the N-atoms of L^9, which contains three primary and three tertiary amine groups.[472] It is suggested that the first three protonation steps involve the NH_2 groups of the pendant arms. These afford the species $[H_3L^9]^{3+}$ in which the three acidic protons are located far apart from one another, thus minimizing the electrostatic repulsion between the resulting positive charges on the ligand. The species $[H_3L^9]^{3+}$ is prevalent in aqueous solution over a wide pH range (5.5-9.0, Figure 7.15). The

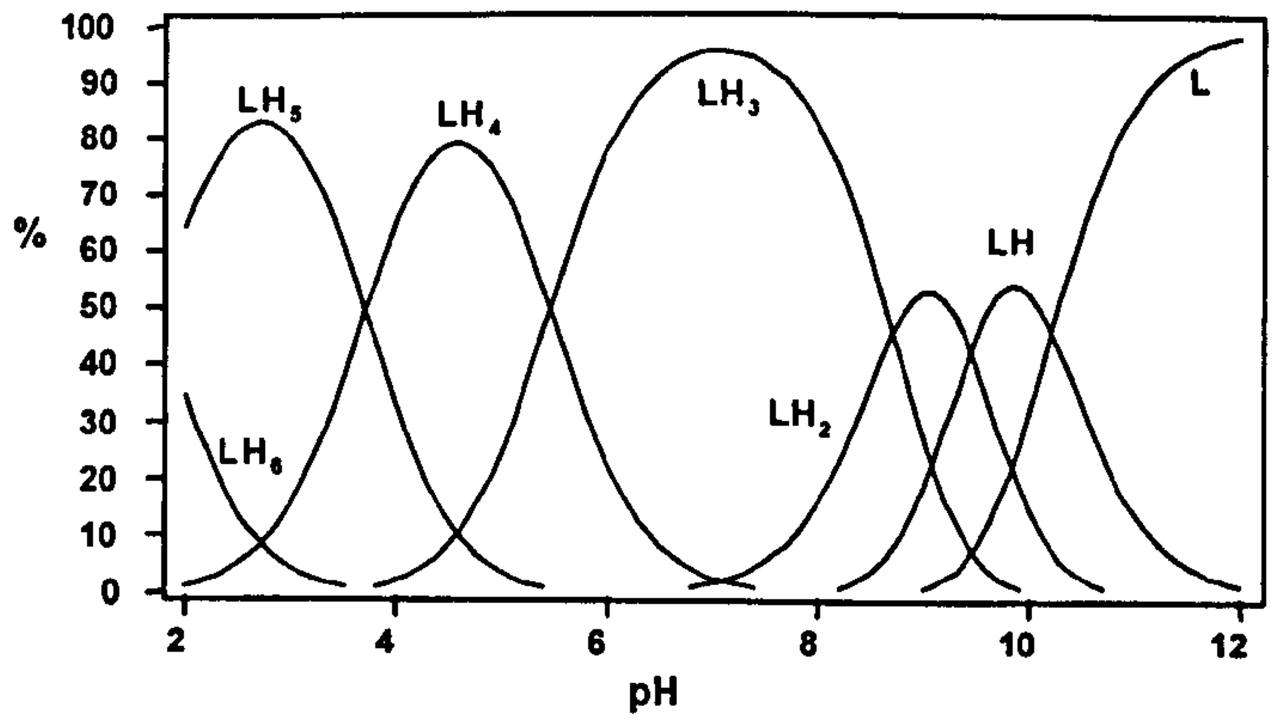

Figure 7.16. Distribution diagram of the protonated species of L^9 as function of pH (0.1 M Me$_4$NCl, 298.1 K)

subsequent protonation steps necessarily involve the sterically more protected tertiary N-centres of the macrocyclic ring, close to the already protonated primary amines. For these reasons, the last three protonation steps show much lower protonation constants (logK < 5.5) than the first three.

Table 7.8. Protonation constants (log K) of [15]aneN$_3$O$_2$[440], L[8] and L[9] determined by means of potentiometric measurements in 0.1 M Me$_4$NCl at 298.1 K

Equilibrium	[15]aneN$_3$O$_2$ [a]	L[8]	L[9]
$L + H^+ = [HL]^+$	9.29(1) [b]	9.10(3)[b]	10.22(1)[b]
$[HL]^+ + H^+ = [H_2L]^{2+}$	8.50(1)	2.94(2)	9.45(1)
$[H_2L]^{2+} + H^+ = [H_3L]^{3+}$	2.12(2)		8.71(1)
$[H_3L]^{3+} + H^+ = [H_4L]^{4+}$			5.36(1)
$[H_4L]^{4+} + H^+ = [H_5L]^{5+}$			3.70(1)
$[H_5L]^{5+} + H^+ = [H_6L]^{6+}$			2.97(1)

[a] I = 0.1 M NaNO$_3$.

[b] Values in parentheses are standard deviations on the last significant figure

7.3.2 Metal binding properties of L[8] in aqueous solution

The formation of the Cu[II], Zn[II], Cd[II] and Pb[II] complexes with L[8] has been studied by means of potentiometric measurements (298.1 K, 0.1 M Me$_4$NCl). The stability constants of the complexes are reported in Table 7.9, while the distribution diagram for the Cu[II] complexes is shown in Figure 7.18. In the case of Ni[II] the low solubility of the complex does not allow the study of its complexation equilibria in aqueous solution.

The stability of complexes with the present ligand in comparison with other cyclic or acyclic triamine compounds is considerably lower. For instance, the stability constants of the same metal complexes with the macrocyclic precursor [15]aneN$_3$O$_2$ are much higher, as can be seen in Table 7.11 (Section 7.3.4). The large decrease in stability observed for L[8] can in part be attributed to the presence of three tertiary amine groups, which usually show a lower binding ability than

primary and secondary amines. In fact, tertiary N-centres can be poorer σ-donors than primary or secondary amines, since N-functionalization prevents the formation of hydrogen bonds between water and amine groups, which contribute *via* the H_2O---H-N interaction, to the σ-donating ability of amine groups in aqueous solution.[472,473]

Table 7.5. Stability constants (log K) of the metal complexes with L^8 at 298.1 K, I = 0.1 M

reaction	log K
$L^8 + Cu^{II} \rightleftarrows [Cu(L^8)]^{2+}$	8.8(1)[a]
$[Cu(L^8)]^{2+} + H^+ \rightleftarrows [Cu(HL^8)]^{3+}$	4.7(1)
$[Cu(L^8)]^{2+} + OH^- \rightleftarrows [Cu(L^8)(OH)]^+$	6.6(1)
$[Cu(L^8)(OH)]^+ + OH^- \rightleftarrows [Cu(L^8)(OH)_2]$	3.0(1)
$L^8 + Zn^{II} \rightleftarrows [Zn(L^8)]^{2+}$	4.6(1)
$L^8 + Cd^{II} \rightleftarrows [Cd(L^8)]^{2+}$	5.6(1)
$L^8 + Pb^{II} \rightleftarrows [Pb(L^8)]^{2+}$	6.4(1)

[a] Values in parenthesis are standard deviations on the last significant figure

On the other hand, the stability constants of the present complexes are much lower even than those found for the complexes with 2,5,8-trimethyl-2,5,8-triazanonane (*e.g.* log K = 12.16 for the Cu^{II} complex),[474] which contains three

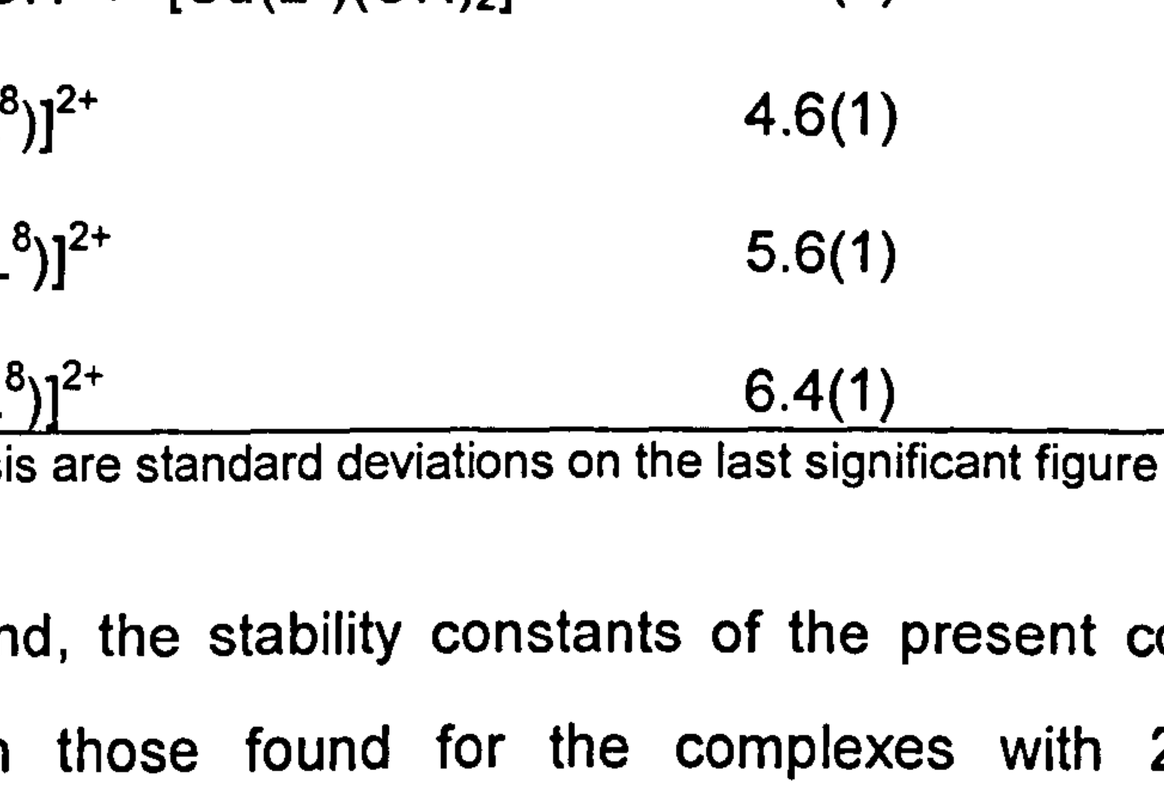

Figure 7.18. Distribution diagram for the system Cu^{II}/L^8 ($[Cu^{II}] = [L^8] = 1x10^{-3}$ M, 298.1 K, I = 0.1 M)

tertiary amine groups separated by ethylenic chains. This observation indicates that the low complex stability is not only due to the tertiary nature of nitrogen donors. Most likely, the insertion of three CH_2CN side arms on the macrocyclic backbone leads to greater rigidity in the molecule, which does not allow the donor atoms to achieve an optimal arrangement around the metal ion. In fact, the $[Cu(L^8)]^{2+}$ complex forms a protonated species $[Cu(HL^8)]^+$ at slightly acidic pH, indicating that a coordinated amine group may easily protonate and detach from the metal.

The $[Cu(L^8)]^{2+}$ complex also shows a marked tendency to form hydroxylated species at high pH. Such behaviour is usually attributed to an unsaturated coordination sphere for the metal and may suggest that in the $[Cu(L^8)]^{2+}$ complex some donors are weakly bound to the metal ion. Actually, in the solid state it has been observed (Section 7.2.2) that all the donor atoms of the macrocyclic ring co-ordinate to Cu^{II}. Two amine groups, however, are coordinated at longer distances [Cu-N(1) 2.161(3) Å, Cu-N(7) 2.136(3) Å] than those usually found in Cu^{II} complexes with oxa-aza macrocycles such as [15]aneN_3O_2, where the Cu-N bond lengths range from 1.99 to 2.05 Å.)[448] Furthermore, as previously noted, in the present complex the O-donors are also bound at longer distance than the nitrogen one. These structural data may account for the reduced thermodynamic stability of the Cu^{II} complex in aqueous solutions. It is also of interest that in the solid state the co-ordination sphere of the metal ion is effectively saturated by a solvent molecule, therefore assuming an octahedral geometry. Although conclusions regarding the co-ordination properties of ligands in solution derived from solid state data may sometimes be misleading, these observations can reasonably explain the tendency to form hydroxylated species at alkaline pH, considering that in aqueous solution one co-ordination site of the Cu^{II} would be taken by a water molecule.

Unfortunately, the low stability of the Zn^{II}, Cd^{II} and Pb^{II} complexes prevents any investigation of their complexation in the alkaline pH region, due to metal hydroxide precipitation even at slightly alkaline pH. However, the Cd^{II} and Pb^{II} complexes are somewhat more stable than the Zn^{II} complex, suggesting the involvement of the oxygen donors in co-ordination to Cd^{II} and Pb^{II}. These structural features may indicate a better fit between the large macrocyclic cavity and the larger Cd^{II} and Pb^{II} ions, leading to the observed higher stability of the Cd^{II} and Pb^{II} complexes with respect to the smaller Zn^{II} ion. Although from these potentiometric studies it cannot be concluded whether or not the nitrile arms interact with the metal ions, it can nevertheless be said that their effect is to quite drastically decrease the stability of all the metal complexes studied.

7.3.3 Metal binding properties of L^9 in aqueous solution.

The stability constants for the Cu^{II}, Zn^{II}, Cd^{II} and Pb^{II} complexes with L^9 have been measured by potentiometry under the same conditions used for the complexes of L^8 and are reported in Table 7.10, while distribution diagrams are shown in Figure 7.19. No interaction between Ba^{II} and L^9 was monitored by potentiometry under these conditions. With these metal ions L^9 forms only mononuclear complexes, all of which show a marked tendency to protonate. As shown in Figure 7.19, all complexes easily form mono and diprotonated species under alkaline to slightly acidic conditions, and in the case of Cu^{II} a triprotonated species is also formed below pH 4. The stability constants of the L^9 complexes are unusually low compared to those found for macrocyclic hexaamine ligands.[475,476] The stability constants of the L^9 complexes are much lower than those found for the corresponding complexes with 1,4,7,10,13,16-hexaazacyclooctadecane ([18]aneN$_6$) and even lower than those with 1,4,7,13-tetramethyl-1,4,7,10,13,16-hexaazacyclooctadecane (Me$_4$[18]aneN$_6$),[475,476] which contains two secondary and

four tertiary nitrogen donors. For example, the stability constants of the Cu^{II} and Zn^{II} complexes with [18]aneN$_6$ are 24.40 and 18.70 logarithmic units, respectively, and those with Me$_4$[18]aneN$_6$ 20.49 and 13.29, respectively, significantly higher than those found for the Cu^{II} and Zn^{II} complexes with L^9 (17.38 and 12.15 logarithmic units, respectively, see Table 7.10). Furthermore, the Zn^{II}, Cd^{II} and Pb^{II} complexes with these hexaazamacrocycles, in which the metals are hexacoordinated, do not show any tendency to protonate. Only the Cu^{II} complexes with Me$_4$[18]aneN$_6$ and [18]aneN$_6$ bind two protons under acidic pH, with very low protonation constants (log K < 3.5 log units for the equilibria

$$[Cu(L^9)]^{2+} + H^+ \rightleftarrows [Cu(HL^9)]^{3+}$$

or

$$[Cu(HL^9)]^{3+} + H^+ \rightleftarrows [Cu(H_2L^9)]^{4+}$$

respectively).[475,476]

Table 7.10. Stability constants (log K) of the Cu^{II}, Zn^{II}, Cd^{II} and Pb^{II} complexes with L^9 (0.1 M Me$_4$NCl, 298.1 K)

Equilibrium	Log K	Equilibrium	Log K
$Cu^{II} + L^9 \rightleftarrows [Cu(L^9)]^{2+}$	17.38(2)[a]	$Cd^{II} + L^9 \rightleftarrows [Cd(L^9)]^{2+}$	13.02(2)
$[Cu(L^9)]^{2+} + H^+ \rightleftarrows [Cu(HL^9)]^{3+}$	9.26(2)	$[Cd(L^9)]^{2+} + H^+ \rightleftarrows [Cd(HL^9)]^{3+}$	8.42(2)
$[Cu(HL^9)]^{3+} + H^+ \rightleftarrows [Cu(H_2L^9)]^{4+}$	6.01(1)	$[Cd(HL^9)]^{3+} + H^+ \rightleftarrows [Cd(H_2L^9)]^{4+}$	6.35(1)
$[Cu(H_2L^9)]^{4+} + H^+ \rightleftarrows [Cu(H_3L^9)]^{5+}$	2.98(2)		
		$Pb^{II} + L^9 \rightleftarrows [Pb(L^9)]^{2+}$	10.45(4)
$Zn^{II} + L^9 = [Zn(L^9)]^{2+}$	12.15(1)	$[Pb(L^9)]^{2+} + H^+ \rightleftarrows [Pb(HL^9)]^{3+}$	9.21(2)
$[Zn(L^9)]^{2+} + H^+ \rightleftarrows [Zn(HL^9)]^{3+}$	8.33(2)	$[Pb(HL^9)]^{3+} + H^+ \rightleftarrows [Pb(H_2L^9)]^{4+}$	5.98(1)
$[Zn(HL^9)]^{3+} + H^+ \rightleftarrows [Zn(H_2L^9)]^{4+}$	5.81(1)		
$[Zn(L^9)]^{2+} + OH^- \rightleftarrows [Zn(L^9)(OH)]^+$	2.44(6)		

Among macrocyclic ligands bearing aminoalkyl pendant arms, the octamine *N*,*N*',*N*'',*N*'''-*tetrakis*(2-aminoethyl)-1,4,8,11-tetraazacyclotetradecane (TAEC) has been investigated by Wainwright *et al.*,[477-481] with particular emphasis on the

stability of its metal complexes in aqueous solution.[477] This ligand contains four primary and four tertiary amine groups and shows a marked tendency to give binuclear complexes due to the large number of N-donors available for metal coordination. Only Cu^{II} and Cd^{II} give mononuclear $[M(TAEC)]^{2+}$ complexes in aqueous solutions, with similar or somewhat higher stability (19.9 and 13.4 logarithmic units, respectively) than that of the L^9 complexes.

It should also be noted that only extensive protonation of L^9 inhibits the formation of metal complexes. In fact, as can be seen from Table 7.10 and Figure 7.19, all the metal ions under investigation form complexes with protonated species of L^9. In particular, the equilibrium constants for the addition of the first proton to the $[M(L^9)]^{2+}$ complexes is quite high, only 1-2 log units lower than the first protonation constant of the free ligand, suggesting that protonation occurs on a nitrogen atom involved weakly, if at all, in metal coordination. This observation can partially explain the lower stability of the present metal complexes with respect to those formed with other macrocyclic hexamines.[475,476] Furthermore, L^9 contains three tertiary amine groups, which usually show lower binding ability than primary or secondary ones, as already explained in the previous section.

These observations are supported by the crystal structure analyses. In the four crystal structures reported, not all the nitrogen atoms are strongly involved in metal coordination; in particular, the crystal structures of the Cu^{II} and Zn^{II} complexes show that a tertiary amine is not bound to the metal ion. The latter is situated outside the macrocyclic cavity and therefore a large part of the macrocyclic framework, containing an amine donor, is not involved in metal coordination. Although conclusions on coordination properties of ligands in solution derived from solid state data may sometimes be misleading, these observations can reasonably explain the low values of the stability constants for these Cu^{II} and Zn^{II} complexes compared to the complexes formed with other

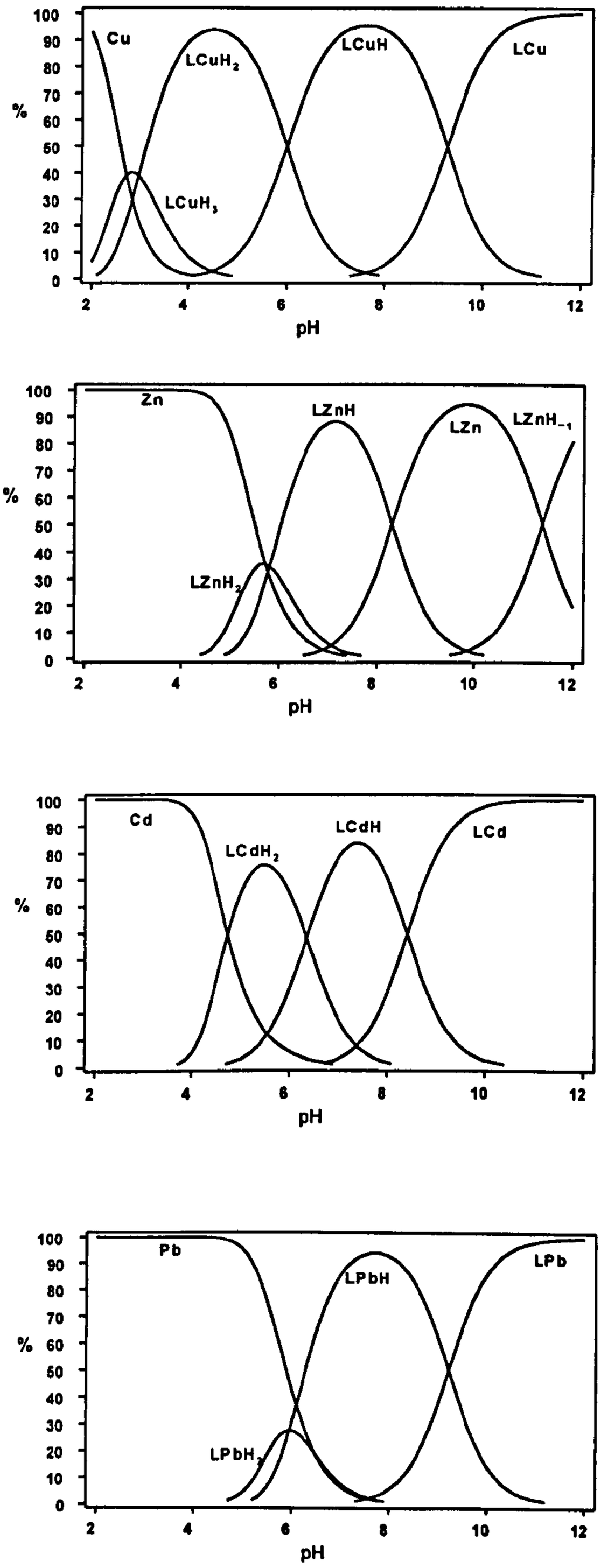

Figure 7.19 Distribution diagrams for the L^9/M^{II} systems ($[L^9] = [M^{II}] = 1 \times 10^{-3}$ M, 0.1 M NMe_4Cl, 298.1 K).

hexaamine ligands,[475,476] as well as the high values of equilibrium constants for the addition of the first proton to the complexes $[M(L^9)]^{2+}$.

Comparing the stability of the different metal complexes, it should be noted that the $[Cd(L^9)]^{2+}$ complex shows a higher thermodynamic stability than $[Zn(L^9)]^{2+}$, suggesting the involvement of the oxygen donors in the cadmium coordination sphere. Finally, looking at the stability of the Pb^{II} complex of L^9, it is been observed that adding pendant arms to a macrocycle does not increase significantly the stability constants of the Pb^{II} complexes if the metal possesses a stereochemically active lone pair.[459] For example, the stability constants of Pb^{II} complexes decrease upon adding hydroxyalkyl groups to [12]aneN_4 and [12]aneN_3O (0.83 and 0.63 logarithmic units, respectively).[459] In the case described here, there is only a small increase in stability (0.38 logarithmic units) between the Pb^{II} complex with [15]aneN_3O_2 and $[Pb(L^9)]^{2+}$ (Table 7.11).

7.3.4 Comparison between [15]aneN_3O_2 derivatives

In Table 7.11, the stability constants of the Cu^{II}, Zn^{II}, Cd^{II} and Pb^{II} complexes with the ligands discussed in this chapter ([15]aneN_3O_2, L^8, L^9, **19** and **20**) are reported.

Table 7.11. Stability constants of the metal complexes with [15]aneN_3O_2, L^8, L^9, **19** and **20** (log K).

reaction	[15]aneN_3O_2 [(a)]	L^8	L^9 [(b)]	**19** [(a)]	**20** [(c)]
$L + Cu^{II} \rightleftarrows [Cu(L)]^{2+}$	15.27(1)	8.8(1)	17.38(2)	12.68(2)	17.25(4)
$L + Zn^{II} \rightleftarrows [Zn(L)]^{2+}$	8.85(1)	4.6(1)	12.15(1)	7.21(1)	16.82(2)
$L + Cd^{II} \rightleftarrows [Cd(L)]^{2+}$	10.05(1)	5.6(1)	13.02(2)	9.15(2)	17.83(3)
$L + Pb^{II} \rightleftarrows [Pb(L)]^{2+}$	10.07(1)	6.4(1)	10.45(4)	9.09(2)	16.92(2)

a) In 0.1 M $NaNO_3$ at 298 K (ref. 440)
b) In 0.1 M Me_4NCl, 298.1 K (ref. 446)
c) In 0.1 M $(Me_4N)NO_3$, 298 K (ref. 449)

Plots of these stability constants (log K) against ionic radius (Å) are shown in Figure 7.20. The complexes with L^8 are less stable because the nitrile pendant

arms do not act as co-ordinating groups but point away from the metal centre, destabilising the entire system. The attachment of weak donor groups such as hydroxyalkyl groups (which probably do not co-ordinate) to [15]aneN$_3$O$_2$ (to form THP-[15]aneN$_3$O$_2$, **19**) caused a decrease in stability in all the complexes studied. The N-donor atoms are now all tertiary amines rather than the secondary present in the precursor [15]aneN$_3$O$_2$. Upon attachment of pendant arms containing strong donors such as primary amines (L^9) and carboxylate (**20**) almost all the M^{II} complexes show an increase in stability relative to the complexes with the macrocyclic precursor [15]aneN$_3$O$_2$. The only value that is not part of this trend is the stability constant of $[Pb(L^9)]^{2+}$, which has quite a low stability in respect to the other M^{II} complexes due to the presence of the active lone pair on the Pb^{II}, as already explained in the previous section.

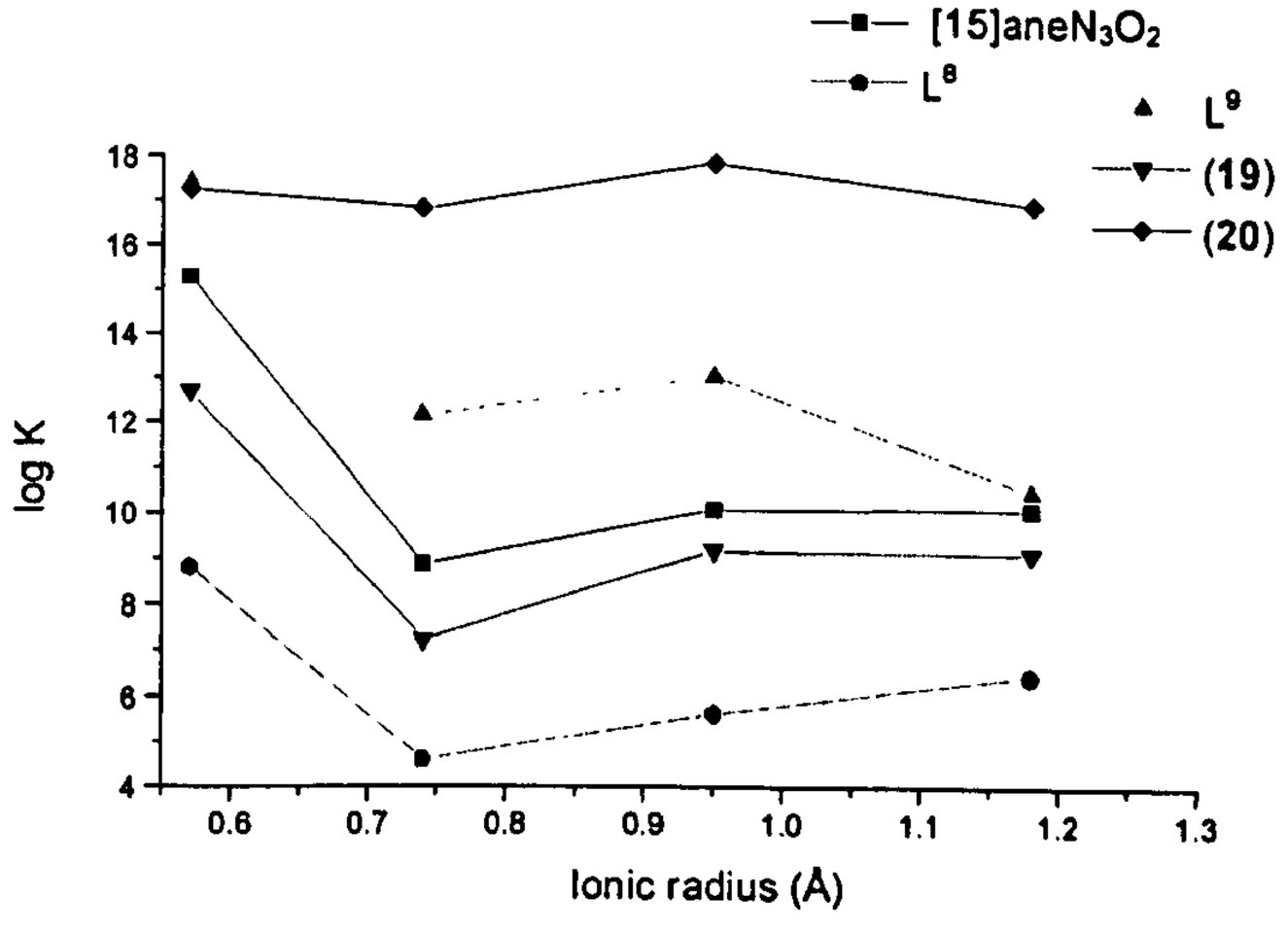

Figure 7.20. Plot of the stability constants (log K) of complexes of Cu^{II}, Zn^{II}, Cd^{II} and Pb^{II} with the the ligands discussed in this chapter ([15]aneN$_3$O$_2$, L^8, L^9, **19** and **20**) against the ionic radius (Å).

Generally, it can be noted that the Cd^{II} and Pb^{II} complexes are somewhat more stable than the Zn^{II} complex, suggesting the involvement of the oxygen

donors in co-ordination to Cd^{II} and Pb^{II}. These structural features may indicate a better fit between the large macrocyclic cavity and the larger Cd^{II} and Pb^{II} ions, leading to the observed higher stability of the Cd^{II} and Pb^{II} complexes with respect to the smaller Zn^{II} ion; this behaviour is the same for almost all the [15]aneN$_3$O$_2$ derivatives described in this chapter (Table 7.6), and can be better ascribed to the dimension of the cavity than to the different pendant arms attached to the nitrogens.

7.4 NMR spectroscopic studies

7.4.1 ^{1}H NMR spectra of complexes with L^8 and L^9

In order to further investigate the structural features of the complexes in solution, ^{1}H NMR spectra in CD_3CN were recorded at various temperatures. The proton NMR spectra of all the diamagnetic complexes with both L^8 and L^9 recorded at 300 MHz at room temperature show a complicated splitting pattern.

In the ^{1}H NMR spectra of $[Zn(L^8)]^{2+}$ and $[Cd(L^8)]^{2+}$ it is not possible to clearly assign any of the signals because of overlap. We can observe two sets of multiplets, one due to the macrocyclic protons adjacent to the amines (in the region between 2.7-3.1 ppm for $[Zn(L^8)]^{2+}$ and 2.8-3.2 ppm for $[Cd(L^8)]^{2+}$), and the other due to the protons of the CH_2CN arms and to the CH_2 adjacent to the oxygens on the ring (in the region between 3.5-4 ppm for $[Zn(L^8)]^{2+}$ and 3.6-4 ppm for $[Cd(L^8)]^{2+}$). However, for the $[Pb(L^8)]^{2+}$ complex a clearer splitting pattern can be observed in the ^{1}H NMR spectrum. A 2D-COSY experiment combined with a ^{1}H-^{13}C 2D coupling experiment allowed a partial assignment of the resonances. Two triplets of doublets have been assigned to two axial protons of the ethylenic moiety [OCH_2CH_2N] of the macrocycle. This splitting pattern is the result of the coupling between axial and equatorial protons of the two CH_2 groups of this moiety (Section 3.4.1). These two triplets of doublets at 4.23 ppm and 3.30 ppm are due

to the axial proton adjacent to the oxygen and to the nitrogen, respectively. The coupling constants are 11.4 Hz for J_{gem} for both axial protons, while J_{trans}, due to the coupling between equatorial and axial protons of different CH_2, are 3.7 and 5.5 Hz, respectively. All other peaks overlap each other, and it has not been possible to assign them; between 3.8 and 4.1 ppm a complicate multiplet, which includes the resonances of the protons of the arms, the protons of the other methylene group adjacent to the oxygen and the equatorial proton of OC*H*$_2$CH$_2$N, can be observed. Another multiplet due to the protons adjacent to the amines appears in the region between 3.0 and 3.2 ppm. The assignment of the ^{13}C spectrum of $[Pb(L^8)]^{2+}$, which does not show remarkable differences with the ^{13}C NMR spectrum of the free ligand, is reported in the experimental section.

A complex series of multiplets due to all the protons adjacent to the amines is observed between 2.2 ppm and 3.1 ppm in the case of $[Zn(L^9)]^{2+}$ and $[Cd(L^9)]^{2+}$, at 2.1-2.9 ppm for $[Ba(L^9)]^{2+}$ and at 2.5-3.4 ppm for $[Pb(L^9)]^{2+}$. The resonances due to protons adjacent to oxygen are seen in the region between 3.5 and 3.9 ppm. In all the spectra, a triplet of doublets and a doublet of doublets due to the axial and equatorial protons of the methylene group next to oxygen (OC*H*$_2$CH$_2$N) can be observed quite clearly, although in $[Zn(L^9)]^{2+}$ and $[Cd(L^9)]^{2+}$ these peaks overlap slightly. This splitting pattern is the result of the coupling with the axial and equatorial protons of the methylene group next to the nitrogen. In this region of the spectra, another multiplet can be assigned as the other methylene group adjacent to the oxygen (OC*H*$_2$). The resonances of these two methylene groups are shifted slightly downfield with respect to the resonances observed for the free ligand recorded under the same conditions. The shift is more evident for the Ba^{II} ($\Delta\delta$ = 0.18 ppm), Cd^{II} ($\Delta\delta$ = 0.11 ppm) and Pb^{II} ($\Delta\delta$ = 0.10ppm) complexes than for the Zn^{II} one ($\Delta\delta$ = 0.04ppm). This difference, although very small, can be explained by considering that in $[Zn(L^9)]^{2+}$ there is no interaction between the metal ion and the

macrocyclic oxygen centre, while in the other complexes the O-donors are coordinated to the metal ions.

7.4.2 Variable-temperature experiments

The presence of a splitting pattern where axial and equatorial protons can be detected and the peaks assigned (at least for $[Pb(L^8)]^{2+}$ in the case of the complexes with L^8) means that the complexes are quite rigid at room temperature. Variable-temperature experiments have been carried out to determine fluxionality and differences between the complexes. Upon increasing the temperature, all the peaks broaden and those due to axial and equatorial protons tend to collapse into a single broad peak. This can be explained by a loss of rigidity of the complexes and by enhanced fluxionality of the macrocycle. The Zn^{II}, Cd^{II} and Pb^{II} complexes with L^8 lose their rigidity by 40°C, perhaps due to their low stability.

In contrast, analogous experiments performed with the complexes of the ligand L^9 showed that the $[Zn(L^9)]^{2+}$ complex looses its rigidity by 40°C, while the peaks of the $[Ba(L^9)]^{2+}$ and $[Pb(L^9)]^{2+}$ spectra broaden only at 55°C and 70°C respectively. This behaviour has been rationalised in terms of the Ba^{II} and Pb^{II} complexes interacting with all the donor atoms of the ligand and thereby enhancing their stereochemical and co-ordinative rigidity. Interestingly, the complex $[Cd(L^9)]^{2+}$ shows the onset of fluxionality at 40°C, thus behaving more like the Zn^{II} complex rather than the analogous Ba^{II} or Pb^{II} complexes.

7.5 Experimental

Spectra were recorded on a Bruker DPX 300 spectrometer (^{1}H and ^{13}C NMR), on a Perkin Elmer System 2000 FT-IR Spectrometer fitted with a i-Series FT-IR microscope (FTIR on single crystal) and on a Perkin-Elmer 1600 spectrometer (FTIR, KBr discs). Elemental analytical data were obtained by the Microanalytical Service (Perkin-Elmer 240B analyser) at the University of Nottingham and EI (electron impact) mass spectra were measured using a V6 Autospec V67070E spectrometer. FAB (Fast Atom Bombardment) mass spectra were obtained by the EPSRC National Mass Spectrometry Service at the University of Swansea.

1,4,7-triaza-10,13-dioxacyclopentadecane ([15]aneN_3O_2) was prepared as described in the literature.[440] All starting materials were obtained from Aldrich Chemical Co. and were used without further purification.

7.5.1 Synthesis of 1,4,7-*tris* (cyanomethyl)-1,4,7-triaza-10,13-dioxacyclopentadecane (L^8)

[15]aneN_3O_2 (0.22 g, 1.01 mmol), chloroacetonitrile (0.25 g, 3.33 mmol), and Et_3N (10g, 0.099 mol) in EtOH (50 cm^3) were refluxed under N_2 for 18 h. After cooling, the solvent was removed by rotary evaporation to yield a red oil which was dissolved in $CHCl_3$ (50 cm^3) and washed with water (3 x 30 cm^3). The organic phase was collected and dried ($MgSO_4$). The yellow oil obtained after evaporation of the solvent was dried *in vacuo*. (0.19 g, 0.568 mmol) Yield: 56%. ^{1}H NMR ($CDCl_3$, 300.1 MHz): δ_H 3.63 (OC*H*$_2$, 4H, s), 3.63 (OC*H*$_2$CH$_2$N, 4H, t, *J* = 4.78 Hz), 2.81 (OCH$_2$C*H*$_2$N, 4H, t, *J* = 4.78 Hz), 2.78 (NC*H*$_2$, 8H, m), 3.66 (4H, s, NC*H*$_2$CN), 3.71 (2H, s, NC*H*$_2$CN) ppm. ^{13}C NMR ($CDCl_3$, 75.47 MHz): δ_C 70.4 (OCH$_2$), 69.0 (OCH$_2$CH$_2$N), 54.4 (OCH$_2$CH$_2$N), 51.9 (NCH$_2$CH$_2$N), 51.4 (NCH$_2$CH$_2$N). 43.7 (NCH$_2$CN), 43.5 (NCH$_2$CN), 115.4 (*C*N). EI mass spectrum: *m/z* found 334.2,

308.2, 267.1 for 334.4 [M^+], 308.4 [M^+-CN] and 268.4 [M^+-CH_2CN-CN] respectively. IR spectrum (KBr disk): ν 2931m, 2843m, 2235m, 1455m, 811m cm^{-1}. Elemental analysis: found (calc. for $C_{16}H_{26}N_6O_2$): C, 57.25 (57.46); H, 7.61 (7.84); N, 24.79 (25.13)%.

The hydrochloride salt of L^8 was obtained in quantitative yield by adding a 1:1 solution of HCl in EtOH to an ethanolic solution containing the free amine until precipitation of a white solid, which was filtered off and washed with EtOH. Elemental analysis: found (calc. for $C_{16}ClH_{27}N_6O_2$) C, 51.67 (51.82); H, 7.31 (7.34); N: 22.53 (22.66)%.

7.5.2 Synthesis of 1,4,7-*tris* (2-aminoethyl)-1,4,7 triaza-10,13-dioxacyclopentadecane (L^9)

1,4,7-*tris* (cyanomethyl)-1,4,7-triaza-10,13-dioxacyclopentadecane (L^8) (0.440g, 1.31 mmol) and BH_3·THF (40 cm^3, 1M solution in THF) were refluxed under N_2 for 48 h. After cooling, excess borane was destroyed by adding water (5 cm^3), then the solvent was removed *in vacuo*. The white solid obtained was dissolved in 6M HCl (50 ml) and heated under reflux for 24 h. After cooling, the solution was dried *in vacuo* to yield a white solid. The solid was dissolved in the minimum amount of water and the solution obtained was passed through a Dowex 1x8-50 column (10 g) activated with 1M sodium hydroxide. The solvent was removed under reduced pressure to yield a colourless oil (0.340g, 0.98 mmol) Yield: 75%. ^{1}H NMR: δ ($CDCl_3$) 3.59 (OCH_2, 4H, s), 3.58 (OC$H_2$$CH_2$N, 4H, t), 2.61 ($OCH_2CH_2$N, 4H, t), 2.51 (NC$H_2$, 8H, t), 2.70 (6 H, t, CH_2C$H_2$$NH_2$), 2.67 (6 H, t, C$H_2$$CH_2NH_2$), 1.5 (6 H, broad, N$H_2$) ppm. ^{13}C NMR: δ ($CDCl_3$) 70.9 ($OCH_2$), 70.6 (O$CH_2CH_2$N), 54.3 ($OCH_2CH_2$N), 53.5 ($NCH_2CH_2$N), 53.3 ($NCH_2CH_2$N) 58.7 ($NCH_2CH_2NH_2$), 39.8 ($NCH_2CH_2NH_2$) ppm. EI mass spectrum: *m/z* found 330.2, 303.2, 286.2 and 259.2 for 330.5 [M^+-NH_2], 302.4 [M^+-$CH_2CH_2NH_2$], 286.4 [M^+-

$CH_2CH_2NH_2$ -NH_2], 258.4 [M^+-2$CH_2CH_2NH_2$] respectively. Elemental analysis: found (calc. for $C_{16}H_{38}N_6O_2 \cdot H_2O$) C, 53.02 (52.72); H, 11.21 (11.06); N, 23.38 (23.05)%.

The hydrochloride salt of L^9 was obtained in quantitative yield by adding a 1:1 solution of HCl in EtOH to an ethanolic solution containing the free amine until precipitation of a white solid, which was filtered off and washed with EtOH. Elemental analysis: found (calc. for $C_{16}Cl_3H_{43}N_6O_3$) C, 40.34 (40.55); H, 9.23 (9.15); N: 17.52 (17.73)%.

7.5.3 Synthesis of the $[M(L^8)]X_2$ complexes

The appropriate metal salt MX_2 [M = Ni^{II}, Cu^{II}, Zn^{II}, Cd^{II} and Pb^{II} and X = ClO_4^- or NO_3^-] (0.06 mmol) was dissolved in CH_3CN (10 cm^3) and added to a solution of L (0.06 mmol) in CH_3CN (20 cm^3). The mixture was stirred 3h at room temperature. The solution was partially concentrated under vacuum and then addition of diethyl ether yielded a solid. The products were filtered off and dried. Single crystals suitable for X-ray analysis were obtained by diffusion of Et_2O vapour into a CH_3CN solution of the complex at room temperature for all the complexes except for $[Zn(L^8)](ClO_4)_2$.

$[Ni(L^8)(CH_3CN)](ClO_4)_2$. Yield 69.2%. FAB mass spectrum (3-NOBA matrix) m/z : 493 for $[C_{16}H_{26}N_6O_2Ni \cdot ClO_4]^+$. IR (KBr disc): 2969w, 2252m [ν (C≡N)], 1471m, 1326w, 1091s [ν (ClO_4^-)], 628m. Elemental analysis: found (calc. for $C_{16}H_{26}Cl_2N_6O_{10}Ni \cdot 2CH_3CN$): C, 35.46 (35.63); H, 6.15 (6.29); N, 13.71 (13.80)%.

$[Cu(L^8)(CH_3CN)](ClO_4)_2$. Yield 76.8%. FAB mass spectrum (3-NOBA matrix) m/z: 498 for $[C_{16}H_{26}N_6O_2Cu \cdot ClO_4]^+$. IR (KBr disc): 2910w, 2260w [ν(C≡N)], 1469m, 1338m, 1091s [ν (ClO_4^-)], 628m. Elemental analysis: found (calc. for $C_{16}H_{26}Cl_2N_6O_{10}Cu \cdot CH_3CN$): C, 33.92 (33.89); H, 4.81 (4.58); N, 15.53 (15.37)%.

[Zn(L^8)](ClO$_4$)$_2$. Yield 78.1%. FAB mass spectrum (3-NOBA matrix) m/z: 500 for $[C_{16}H_{26}N_6O_2Zn{\cdot}ClO_4]^+$. IR (KBr disc): 2907w, 2249w [ν(C≡N)], 1484m, 1382m, 1091s [ν (ClO_4^-)], 940m, 628m. Elemental analysis: found (calc. for $C_{16}H_{26}Cl_2N_6O_{10}Zn{\cdot}CH_3CN$): C, 33.57 (33.79); H, 4.46 (4.57); N, 15.29 (15.33)%.

[Cd(L^8)(NO$_3$)$_2$]. Yield 80.5%. FAB mass spectrum (3-NOBA matrix) m/z : 528 for $[C_{16}H_{26}N_6O_2Cd{\cdot}NO_3{\cdot}H_2O]^+$. IR (KBr disc): 2918w, 2263 [ν(C≡N)], 1471w, 1384s [ν (NO_3^-)], 1294s, 1100w. Elemental analysis: found (calc. for $C_{16}H_{26}N_8O_8Cd{\cdot}2H_2O$): C, 31.51 (31.67); H, 4.94 (4.98); N, 18.55 (18.46)%.

[Pb(L^8)](ClO$_4$)$_2$. Yield 83.9%. FAB mass spectrum (3-NOBA matrix) m/z: 641 for $[C_{16}H_{26}N_6O_2Pb{\cdot}ClO_4]^+$. IR (KBr disc): 2901w, 2264w [ν (C≡N)], 1464m, 1362m, 1093s [ν (ClO_4^-)], 929m, 628m. Elemental analysis: found (calc. for $C_{16}H_{26}Cl_2N_6O_{10}Pb$): C, 26.20 (25.95); H, 3.35 (3.54); N, 11.19 (11.35)%. ^{13}C NMR: δ ($CDCl_3$) 70.3 (OCH_2), 69.9 (OCH_2CH_2N), 54.1 (OCH_2CH_2N), 55.7 (NCH_2CH_2N), 46.5 (NCH_2CH_2N) 44.8 (NCH_2CN), 39.6 (NCH_2CN), 115.8 (C≡N) ppm.

7.5.4 Synthesis of the [M(L^9)]X$_2$ complexes

The appropriate metal salt M(ClO$_4$)$_2$ (M = Cu^{II}, Zn^{II}, Pb^{II} and Ba^{II}) ($CdCl_2{\cdot}5/2H_2O$ in the case of Cd^{II}) (0.06-0.07 mmol) was dissolved in MeOH (20 cm^3) and a solution of 1,4,7-*tris*(2-aminoethyl)-1,4,7-triaza-10,13-dioxacyclopentadecane (L^9) (0.06-0.07 mmol) in MeOH (20 cm^3) was added dropwise. The solution was stirred for 3h at room temperature. Partial concentration and addition of Et_2O to the solution yielded a solid which was filtered and dried *in vacuo*.

[Zn(L^9)](ClO$_4$)$_2$. Yield 77.8%. FAB mass spectrum (Glycerol/MeOH/H_2O matrix) m/z: 511 for $[C_{16}H_{38}N_6O_2Zn.ClO_4]^+$. IR (single crystal): 3337.5, 3290.5 (s, NH_2 stretch), 2937.0, 2899.0 (s, CH_2 stretch), 1592.6, 1561.7 (s, NH_2 bend), 1090.8 (s, ClO_4^-). Elemental analysis: found (calc. for $C_{16}H_{38}Cl_2N_6O_{10}Zn$): C, 31.83 (31.46);

H, 5.91 (6.27); N, 13.65 (13.76)%. Single crystals suitable for X-ray structural analysis were obtained by diffusion of Et_2O in to a MeOH solution of the complex at room temperature.

[Cu(L^9)](ClO_4)$_2$ Yield 84.5%. FAB mass spectrum (3-NOBA matrix) m/z : 510 for $[C_{16}H_{38}N_6O_2Cu{\cdot}ClO_4]^+$. IR (single crystal): 3334.7, 3286.4 (s, NH_2 stretch), 2934.2, 2895.8 (s, CH_2 stretch), 1590.6, 1560.2 (s, NH_2 bend), 1091.3 (s, ClO_4^-). Elemental analysis: found (calc. for $C_{16}H_{38}Cl_2N_6O_{10}Cu$): C, 32.04 (31.56); H, 5.93 (6.29); N, 13.69 (13.80)%. Single crystals suitable for X-ray structural analysis were obtained by diffusion of Et_2O in to a CH_3CN solution of the complex at room temperature.

[Pb(L^9)](ClO_4)$_2$ Yield 83.3%. FAB mass spectrum (3-NOBA matrix) m/z: 653 for $[C_{16}H_{38}N_6O_2Pb.ClO_4]^+$. IR (KBr disc): 2876w, 1513w, 1384w, 1121s, 1090s, 626m. Elemental analysis: found (calc. for $C_{16}H_{38}Cl_2N_6O_{10}Pb{\cdot}H_2O$): C, 25.17 (24.94); H, 4.92 (5.23); N, 10.76 (10.91)%. Single crystals suitable for X-ray structural analysis were obtained by diffusion of Et_2O in to a CH_3CN solution of the complex at room temperature.

[Ba(L^9)](ClO_4)$_2$ Yield 77.6%. FAB mass spectrum (3-NOBA matrix) m/z: 583 for$[C_{16}H_{38}N_6O_2Ba.ClO_4]^+$. IR (KBr disc): 2865w, 1498w, 1383w, 1091s, 628m. Elemental analysis: found (calc. for $C_{16}H_{38}Cl_2N_6O_{10}Ba$): C, 28.01 (28.15); H, 5.80 (5.61); N, 12.44 (12.31)%. Single crystals suitable for X-ray structural analysis were obtained by diffusion of Et_2O in to a CH_3CN solution of the complex at room temperature.

[Cd(L^9)]Cl_2 Yield 81.0%. FAB mass spectrum (NBA matrix) m/z: 494 for$[C_{16}H_{38}N_6O_2Cd.Cl]^+$. IR (KBr disc): 2878w, 1493w, 1378w, 1091s, 628m. Elemental analysis: found (calc. for $C_{16}H_{38}Cl_2N_6O_2Cd$): C, 36.76 (36.27); H, 7.40 (7.23); N, 15.93 (15.86) %.

7.5.5 Crystal Structure Determinations

Crystal data and data collection and refinement parameters for compounds $[M(L^8)(CH_3CN)](ClO_4)_2$ [M = Cu^{II}, Ni^{II}], $[Cd(L^8)(NO_3)_2]$ and $[Pb(L^8)](ClO_4)_2$ are given in Tables 7.12-7.13. The same data for compounds $[M(L^9)](ClO_4)_2$ [M = Zn^{II}, Cu^{II}, Pb^{II} and Ba^{II}] are given in Tables 7.13-7.14. Data for the Ni^{II}, Cu^{II} and Pb^{II} structures with L^8 and for the Zn^{II}, Cu^{II} and Pb^{II} structures were collected on a Stoe Stadi-4 four-circle diffractometer equipped with an Oxford Cryosystems open-flow cryostat using graphite-monochromated Mo-K_α radiation (λ=0.71073Å). Numerical absorption corrections based on face-indexing were applied to the data for all compounds. Data for the $[Cd(L^8)(NO_3)_2]$ and $[Ba(L^9)(ClO_4)]^+$ structures were collected on a Bruker SMART1000 CCD area detector diffractometer with a similar cryostat, using graphite-monochromated Mo-K_α radiation (λ=0.71073Å). Semi-empirical absorption corrections based on equivalent reflections were applied.

All the structures were solved by direct methods[322] and completed by iterative cycles of full-matrix least squares refinement and ΔF syntheses. All non-H atoms, except for those in disordered groups, were refined anisotropically. All H atoms were placed in calculated positions and refined using a riding model[323], except those on the acetonitrile molecules which were located from difference maps and refined as a rigid body. In the Zn^{II} and Cu^{II} structures with L^9 the hydrogens on the primary amines were located from difference maps and the N-H distances restrained to 0.9Å during refinement.

The perchlorate anions were found to exhibit disorder in all compounds, and this disorder was modelled using partial occupancy models over either two or three sites. In $[Ni(L^8)(CH_3CN)](ClO_4)_2$ the occupancy factor is 0.50 for O(1) and 0.33 for O(4) from a perchlorate anion found disordered over three sites [0.25 for O(1)' and O(1)", 0.33 for O(4)' and O(4)"]. Then the occupancy factor is 0.70 for all oxygens of the other perchlorate found disordered over two sites (0.30 for the

other component). In $[Cu(L^8)(CH_3CN)](ClO_4)_2$ the occupancy factor is 0.50 for two oxygens from a perchlorate anion [O(1) and O(4)] found disordered over three sites [0.25 for O(1)', O(4)' and O(1)", O(4)"]. In the $[Pb(L^8)](ClO_4)_2$ structure, disorder was identified in part of the macrocyclic backbone, in parts of the nitrile arms and in one perchlorate. It was modelled using partial occupancy models over two sites for each disordered atom. The occupancy factor is 0.60 for all the disordered atoms [from N(7) to C(12), from C(1C) to N(3C) and from O(1) to O(4)] and 0.40 for the other component. In $[Zn(L^9)](ClO_4)_2$ the occupancy factor is 0.70 for the three oxygens of one perchlorate (O1, O3 and O4) found disordered over two sites (and 0.30 for O1', O3' and O4'). In $[Cu(L^9)](ClO_4)_2$ and $[Ba(L^9)](ClO_4)_2$ the oxygens were found to be equally disordered over three sites. In the $[Pb(L^9)](ClO_4)_2$ structure, disorder was identified in part of the macrocyclic backbone and in parts of the amine arms and it was modeled using partial occupancy models over two sites for all the disordered atoms. The occupancy factor is 0.70 for the atoms from C8 to C15 and 0.30 for C8' to C15', while all the disordered atoms within the arms have occupancies of 0.5. Moreover, all the perchlorate oxygen atoms have found to be disordered, each equally over two sites, and modelling used the same method as described above. Appropriate restraints were applied to all bond distances involving disordered atoms.

7.5.6 Potentiometric measurements.

Equilibrium constants for protonation and complexation reactions with L^8 and L^9 were determined by pH measurements in 0.1 mol dm^{-3} Me_4NCl at 298.1 ± 0.1 K, by using potentiometric equipment that has been already described.[482] The combined glass electrode was calibrated as a hydrogen concentration probe by titrating known amounts of HCl with CO_2-free NaOH solutions and determining the equivalent point by Gran's method[483,484] which allows to determine the standard

potential E^0, and the ionic product of water (pK_W = 13.83(1) at 298.1 K in 0.1 mol dm^{-3} Me_4NCl). Concentrations of 0.5 x 10^{-3} – 1 x 10^{-3} mol dm^{-3} of ligand and metal ions were employed in the potentiometric measurements and three titration experiments were performed in the pH range 2 -11, each giving about 100 data points. The computer program HYPERQUAD[485] was used to calculate equilibrium constants from e.m.f. data. For each system, all titrations were treated either as single sets or as separated entities without significant variation in the values of the constants determined.

Table 7.12. Selected crystallographic data for the single crystal structures of $[Cu(L^8)(CH_3CN)](ClO_4)_2$ and $[Ni(L^8)(CH_3CN)](ClO_4)_2$.

Compound	$[Cu(L^8)(CH_3CN)](ClO_4)_2$	$[Ni(L^8)(CH_3CN)](ClO_4)_2$
Crystal Data		
Formula	$C_{16}H_{26}N_6O_2Cu\cdot CH_3CN\cdot 2ClO_4$	$C_{16}H_{26}N_6O_2Ni\cdot CH_3CN\cdot 2ClO_4$
M / gmol^{-1}	637.92	671.12
Crystal size / mm	0.35 x 0.34 x 0.10	0.29 x 0.16 x 0.15
Crystal system	Monoclinic	Monoclinic
Space group	$P2_1/n$	$P2_1/n$
a / Å	9.359(4)	9.571(4)
b / Å	17.351(3)	19.475(9)
c / Å	15.817(4)	15.663(4)
β/ °	90.59(4)	90.71(4)
U / Å^3	2568.4(14)	2919(2)
Reflections used to refine cell	40	40
θ range / °	11 to 15.5	10 to 14
Z	4	4
D_c / gcm^{-3}	1.650	1.527
μ / mm^{-1}	1.125	0.912
F(000)	1316	1388
T / K	150(2)	150(2)
Data Collection		
Diffractometer	Stoe Stadi-4 four circle	Stoe Stadi-4 four circle
Radiation, wavelength	MoK_α , 0.71073 Å	MoK_α , 0.71073 Å
θ_{max} / °	25.00	22.48
Range of *h*	-11 → 11	-10 → 10
Range of *k*	0 → 20	0 → 20
Range of *l*	-13 → 18	0 → 16
Measured reflections	4918	3797
Unique reflections, R_{int}	4513, 0.0668	3797
Observed reflections	3597 [$F_O \geq 4\sigma(F_O)$]	2644 [$F_O \geq 4\sigma(F_O)$]
Absorption correction	Numerical	Numerical
$TF_{max, min}$	0.894, 0.680	0.935, 0.823
Solution		
Method	Direct methods	Direct methods
Using	SHELXS-97	SHELXS-97
Refinement		
Full matrix least squares on	F^2	F^2
Using	SHELXL-97	SHELXL-97
Weighting scheme *x*, *y*[a]	0.052, 10.022	0.052, 10.022
Parameters refined	350	371
R_1, wR_2[b]	0.0502, 0.1152	0.0846, 0.1868
Goodness-of-fit (*S*)	1.019	1.054
$(\Delta/\sigma)_{max}$	0.004	0.077
$\Delta\rho_{max, min}$ / eÅ^{-3}	+0.66, -0.55	+0.63, -0.58

[a] $w^{-1} = [\sigma^2(F_O^2) + (xP)^2 + yP]$, $P = [MAX(F_O^2, 0) + 2F_c^2]/3$
[b] $[F_O \geq 4\sigma(F_O)]$

Table 7.13. Selected crystallographic data for the single crystal structures of $[Pb(L^8)](ClO_4)_2$, $[Cd(L^8)](NO_3)_2$ and of $[Zn(L^9)](ClO_4)_2$.

Compound	$[Pb(L^8)](ClO_4)_2$	$[Cd(L^8)(NO_3)_2]$	$[Zn(L^9)](ClO_4)_2$
Crystal Data			
Formula	$C_{16}H_{26}N_6O_2Pb{\cdot}2ClO_4$	$C_{16}H_{26}N_6O_2Cd{\cdot}CH_3CN{\cdot}2NO_3$	$C_{16}H_{38}N_6O_2Zn{\cdot}2ClO_4$
M / gmol^{-1}	740.52	611.90	610.79
Crystal size / mm	0.30 x 0.26 x 0.08	0.28 x 0.17 x 0.12	0.38 x 0.19 x 0.03
Crystal system	Triclinic	Monoclinic	Monoclinic
Space group	*P*-1	$P2_1/n$	$P2_1/n$
a / Å	8.908(6)	9.5360(8)	9.273(4)
b / Å	10.118(5)	19.221(2)	13.154(3)
c / Å	14.049(8)	13.596(4)	20.692(4)
α / °	105.86(4)	90	90
β/ °	100.72(6)	90.545(1)	101.24(5)
γ / °	92.15(5)	90	90
U / Å^3	1191.6(12)	2487.3(4)	2476(3)
Reflections used to refine cell	40	4925	42
2θ range / °	12.5 to 14	2.6 to 28.9	10 to 14
Z	2	4	4
D_c / gcm^{-3}	2.064	1.634	1.639
μ / mm^{-1}	7.368	0.939	1.271
F(000)	720	1248	1280
T / K	150(2)	150(2)	150(2)
Data Collection			
Diffractometer	Stoe Stadi-4 four circle	Bruker SMART1000 CCD area detector	Stoe Stadi-4 four circle
Radiation, wavelength	MoK_α , 0.71073 Å	MoK_α , 0.71073 Å	MoK_α , 0.71073 Å
θ_{max} / °	25.04	28.87	22.49
Range of *h*	-10 → 10	-10 → 12	-9 → 9
Range of *k*	-12 → 11	-25 → 21	0 → 14
Range of *l*	-16 → 16	-17 → 18	-22 → 22
Measured reflections	6112	17876	4228
Unique reflections, R_{int}	4203, 0.0386	6036, 0.045	3233, 0.1161
Observed reflections	3737 [$F_O \geq 4\sigma(F_O)$]	4889 [$F_O \geq 4\sigma(F_O)$]	2103 [$F_O \geq 4\sigma(F_O)$]
Absorption correction	ψ-scans	Empirical	Numerical
$TF_{max, min}$	0.354, 0.164	0.824, 0.716	0.969, 0.801
Solution			
Method	Direct methods	Direct methods	Direct methods
Using	SHELXS-97	SHELXS-97	SHELXS-97
Refinement			
Full matrix least squares on	F^2	F^2	F^2
Using	SHELXL-97	SHELXL-97	SHELXL-97
Weighting scheme *x*, *y*[a]	0.087, 13.777	0.039, 0.062	–, 20.130
Parameters refined	304	326	331
R_1, wR_2[b]	0.0573, 0.1483	0.0247, 0.0594	0.0755, 0.1236
Goodness-of-fit (*S*)	1.056	1.033	1.213
$(\Delta/\sigma)_{max}$	0.002	0.001	0.007
$\Delta\rho_{max, min}$ / eÅ^{-3}	+2.29, -3.35	+0.81, -0.43	+0.72, -0.64

[a] $w^{-1} = [\sigma^2(F_O^2) + (xP)^2 + yP]$, $P = [MAX(F_O^2, 0) + 2F_c^2]/3$
[b] $[F_O \geq 4\sigma(F_O)]$

Table 7.14. Selected crystallographic data for the single crystal structures of $[Cu(L^9)](ClO_4)_2$, $[Pb(L^9)](ClO_4)_2$ and of $[Ba(L^9)](ClO_4)_2$.

Compound	$[Cu(L^9)](ClO_4)_2$	$[Pb(L^9)](ClO_4)_2$	$[Ba(L^9)(ClO_4)]ClO_4$
Crystal Data			
Formula	$C_{16}H_{38}N_6O_2Cu{\cdot}2ClO_4$	$C_{16}H_{38}N_6O_2Pb{\cdot}2ClO_4$	$C_{16}H_{38}N_6O_2Ba{\cdot}2ClO_4$
M / gmol^{-1}	608.96	752.61	682.76
Crystal size / mm	0.38 x 0.36 x 0.11	0.54 x 0.12 x 0.08	0.12 x 0.10 x 0.04
Crystal system	Monoclinic	Monoclinic	Monoclinic
Space group	$P2_1/n$	$P2_1/c$	$P2_1/n$
a / Å	9.2446(13)	10.816(8)	9.4020(10)
b / Å	13.126(2)	15.486(9)	14.365(2)
c / Å	20.653(3)	15.844(10)	19.363(2)
β/ °	101.116(11)	98.59(6)	96.504(2)
U / Å^3	2459.7(6)	2624(3)	2598.3(5)
Reflections used to refine cell	39	16	3233
2θ range / °	10 to 16.5	11 to 13	2.53 to 23.25
Z	4	4	4
D_c / gcm^{-3}	1.644	1.905	1.745
μ / mm^{-1}	1.169	6.693	1.794
F(000)	1276	1488	1384
T / K	150(2)	220(2)	150(2)
Data Collection			
Diffractometer	Stoe Stadi-4 four circle	Stoe Stadi-4 four circle	Bruker SMART1000 CCD area detector
Radiation, wavelength	MoK_α , 0.71073 Å	MoK_α , 0.71073 Å	MoK_α , 0.71073 Å
$2\theta_{max}$ / °	24.98	26.00	28.95
Range of *h*	-10 → 10	-13 → 13	-11 → 12
Range of *k*	0 → 15	-17 → 19	-19 → 19
Range of *l*	-24 → 24	-19 → 19	-24 → 24
Measured reflections	6015	6538	26513
Unique reflections, R_{int}	4313, 0.0472	5145, 0.0762	6259, 0.104
Observed reflections	3568 [$F_O \geq 4\sigma(F_O)$]	3729 [$F_O \geq 4\sigma(F_O)$]	3553 [$F_O \geq 4\sigma(F_O)$]
Absorption correction	Numerical	Numerical	Semi-empirical
$TF_{max, min}$	0.904, 0.712	0.606, 0.468	0.894, 0.765
Solution			
Method	Direct methods	Direct methods	Direct methods
Using	SHELXS-97	SHELXS-97	SHELXS-97
Refinement			
Full matrix least squares on	F^2	F^2	F^2
Using	SHELXL-97	SHELXL-97	SHELXL-97
Weighting scheme *x*, *y*[a]	0.045, 5.495	0.092, 20.040	0.015, --
Parameters refined	349	296	322
R_1, wR_2,	0.0449, 0.1035	0.0659, 0.1635	0.0387, 0.0541
Goodness-of-fit (*S*)	1.032	1.037	0.816
$(\Delta/\sigma)_{max}$	0.077	0.003	0.036
$\Delta\rho_{max, min}$ / eÅ^{-3}	+0.75, -0.58	+2.11, -1.31	+0.63, -0.67

[a] $w^{-1} = [\sigma^2(F_O^2) + (xP)^2 + yP]$, $P = [MAX(F_O^2, 0) + 2F_c^2]/3$
[b] $[F_O \geq 4\sigma(F_O)]$

Chapter 8

Macrocyclic ligands for the synthesis of polymeric Ag^{I} complexes

8.1 Design of solid state architectures

Crystal engineering is that area of supramolecular chemistry aimed at the controlled design of metal complexes, leading to novel materials with interesting properties such as catalytic or optical activity.[110,486-490]

The assembly of organic molecules and metal ion building blocks may yield a new generation of multidimensional networks containing channels or cavities of various sizes and shapes, and many examples of inorganic superstructures have been recently reported.[490-496] The common rationale behind the formation of these molecular architectures is the interplay of preferred metal co-ordination geometry and topologically most suitable ligands leading to the controlled design of new inorganic materials.[110,486]

8.1.1 Macrocyclic complexes as building blocks

The building blocks used for the construction of multidimensional structures are normally simple multi-dentate ligands such as 4,4'-bipy, pyrazine and similar ligands with different length, spacer between the donor atoms or position of the functionalities.[490]

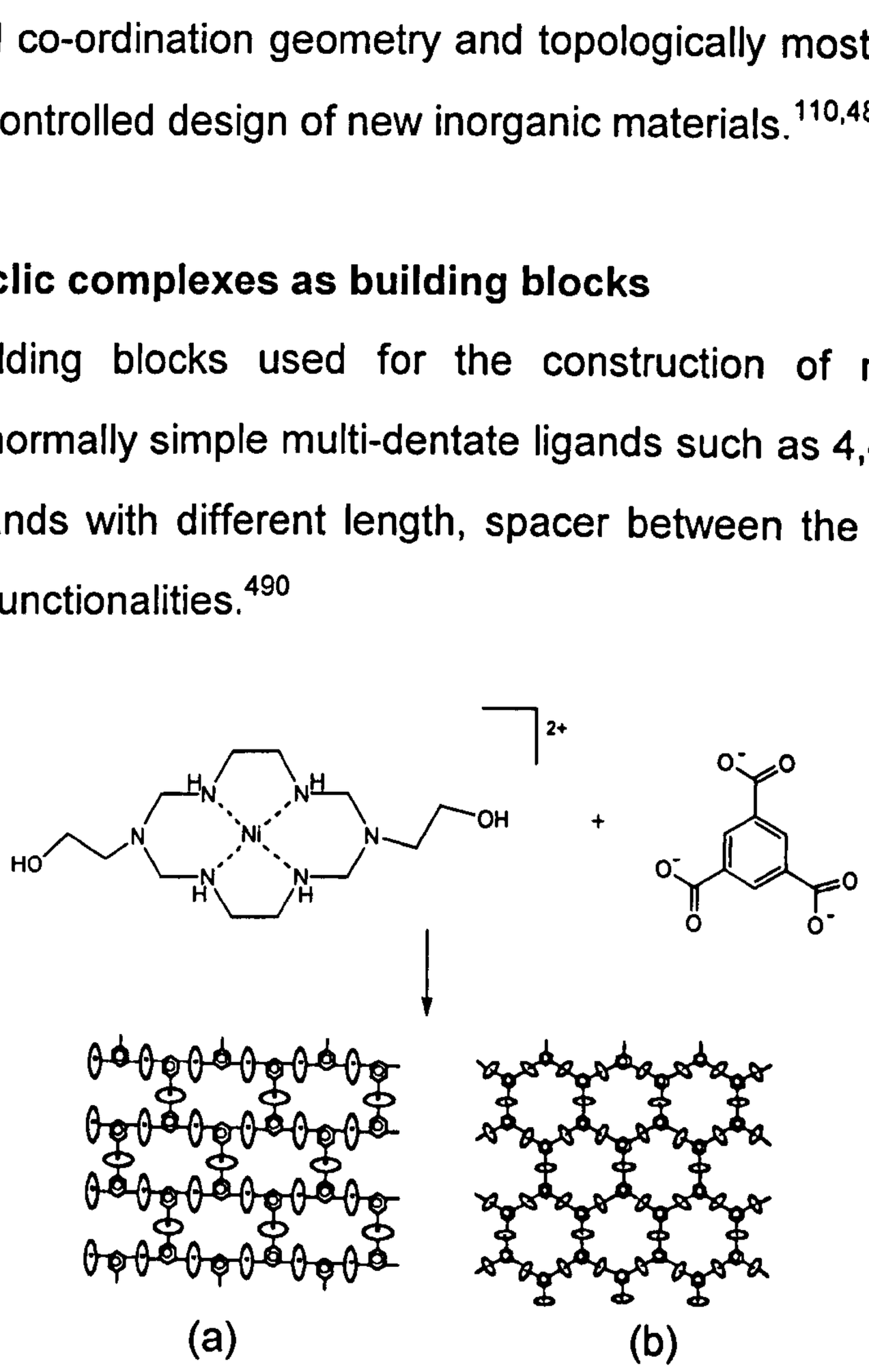

Figure 8.1. 3-D networks (a: molecular brick wall; b: molecular honeycomb) assembled by a square-planar Ni^{II} complex of an aza macrocycle bearing two hydroxyl pendant arms and 1,3,5-benzenetricarboxylate as connecting unit.

Macrocyclic complexes have seldom been employed as building blocks in crystal engineering. Suh and co-workers reported three dimensional networks assembled using a square-planar Ni^{II} complex of an aza macrocycle bearing two hydroxyl pendant arms and an organic ligand (1,3,5-benzenetricarboxylate) which connects three metal ions (Figure 8.1).[497-500] The macrocylic complex acts as a bifunctional building block involving co-ordination as well as interlayer hydrogen-bonding interactions to provide a three-dimensional structure. Depending upon which of the two carboxylate oxygens bind to the Ni^{II} complex, the two components can form molecular brick walls or molecular honeycombs (Figure 8.1).[497] Figure 8.2(a) shows the trinuclear unit of the honeycomb-like structure with the organic tricarboxylate connecting three metal complexes together. Using the terephthalate dianion as connecting unit monodimensional chains are formed (Figure 8.2b).[498] These chains are linked together by the hydrogen bonding between the pendant hydroxyl groups from one polymeric chain and the secondary amines of the macrocycles from another polymeric chain.[497,498]

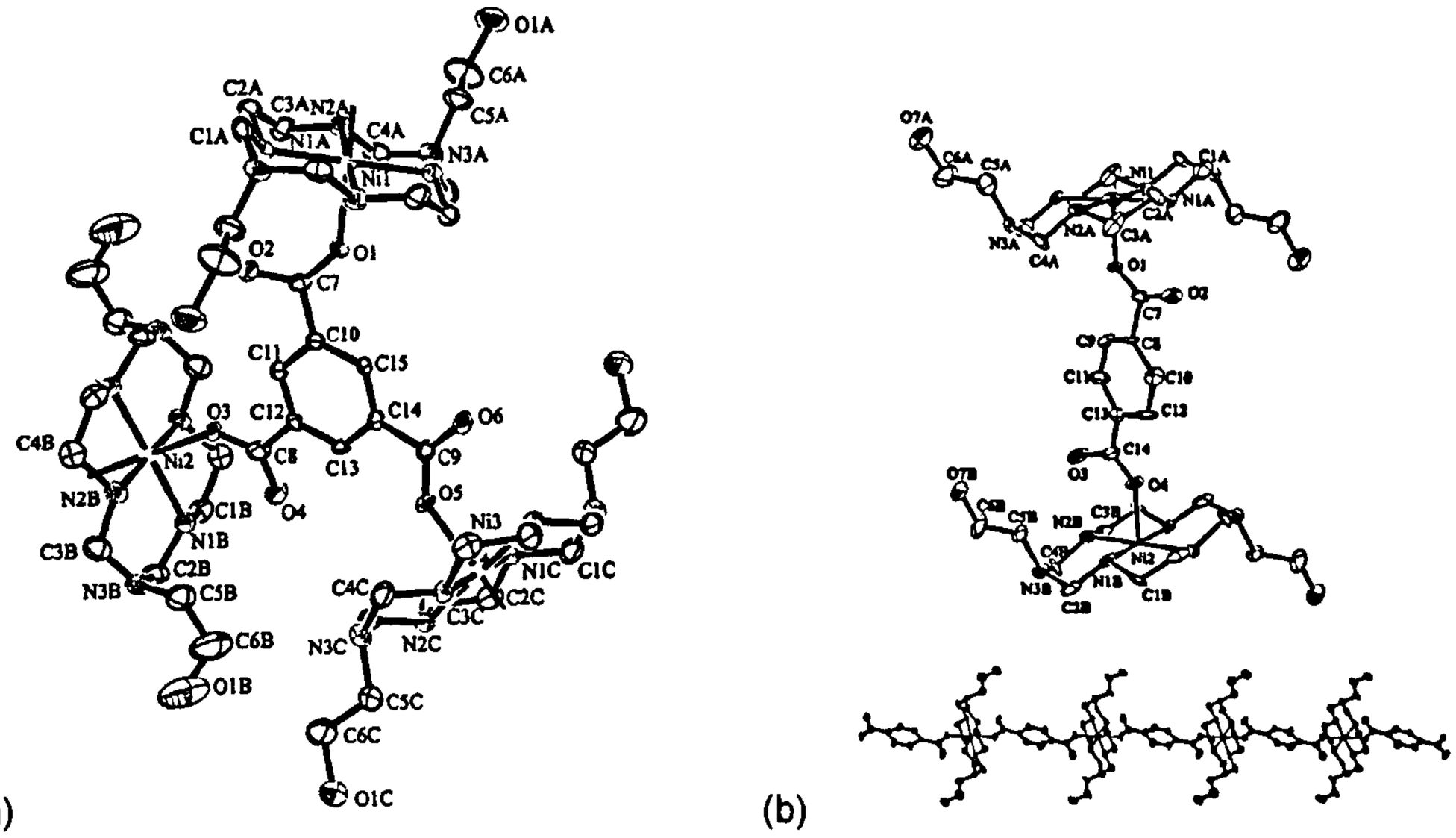

Figure 8.2. (a) Trinuclear unit of the honeycomb-like structure with the organic tricarboxylate connecting three metal complexes together and (b) with the terephthalate dianion as connecting unit monodimensional chains are formed

Another multidimensional architecture based on a polyiodide network has been obtained by reacting a macrocyclic complex ($[Ag[18]aneS_6]BF_4$) with three molar equivalents of I_2 was reported by Schröder and co-workers.[501,502] The crystal structure of $[Ag[18]aneS_6]I_7$ shows the $[Ag[18]aneS_6]^+$ cations embedded in a three dimensional polymeric polyiodide matrix of I_7^- anions (Figure 8.4). The $[Ag[18]aneS_6]^+$ cations fit very well into the cubic framework formed by I_7^- anions and therefore the formation of the cube-like $[I_7^-]_\infty$ matrix is templated by the thioether macrocyclic complex.[501,502]

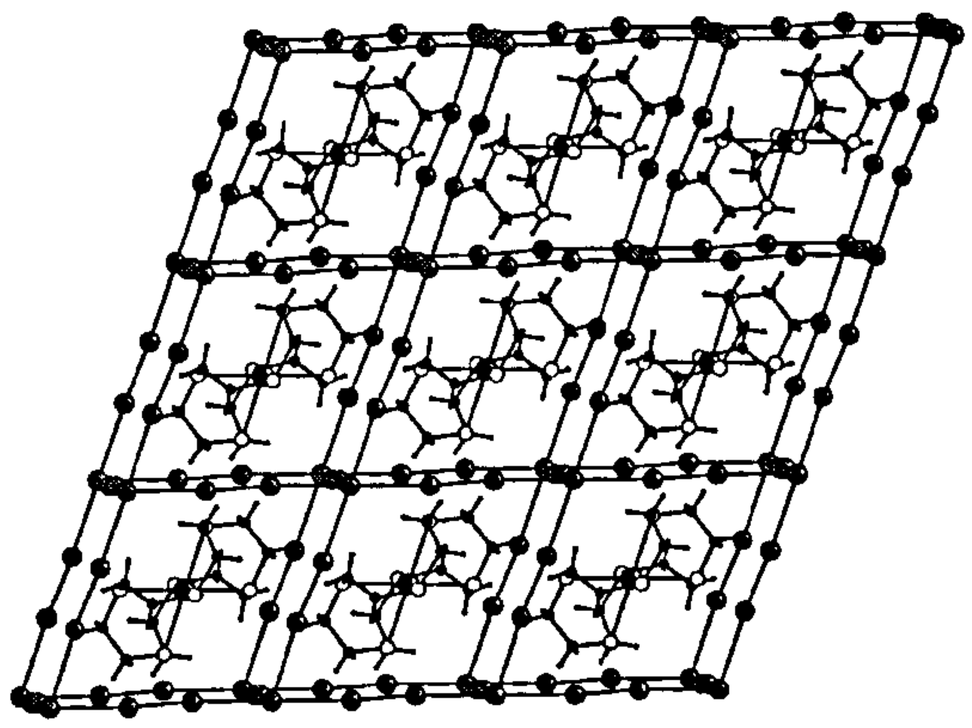

Figure 8.4. Three dimensional view of the polymeric complex $[Ag[18]aneS_6]I_7$.

8.1.2 Nitrile pendant arm macrocyclic ligands for the synthesis of polymeric Ag^{I} complexes.

In the previous section, the formation of solid state architectures in which one of the two components is a macrocyclic complex was discussed. The polymeric complexes formed directly by mixing a carefully designed ligand with a silver(I) salt will now be introduced.

Functionalised pendant arms have not been previously intentionally attached onto macrocycles for the purpose of assembling a multidentate ligand to be used in the construction of three-dimensional exocyclic solid-state architectures. It was argued that nitrile functionalised pendant arms onto a macrocycle such as $[9]aneN_3$ would prevent the resulting polydentate ligand from encapsulating tetrahedral metal centres (Ag^{I}, Cu^{I}) or forming sandwich

complexes with them, but would promote the formation of polymeric complexes.[444] The results discussed in this chapter come directly from this idea and other examples of polymeric complexes with Ag^{I} have been synthesised in the Schröder's group since then.[444,445,503]

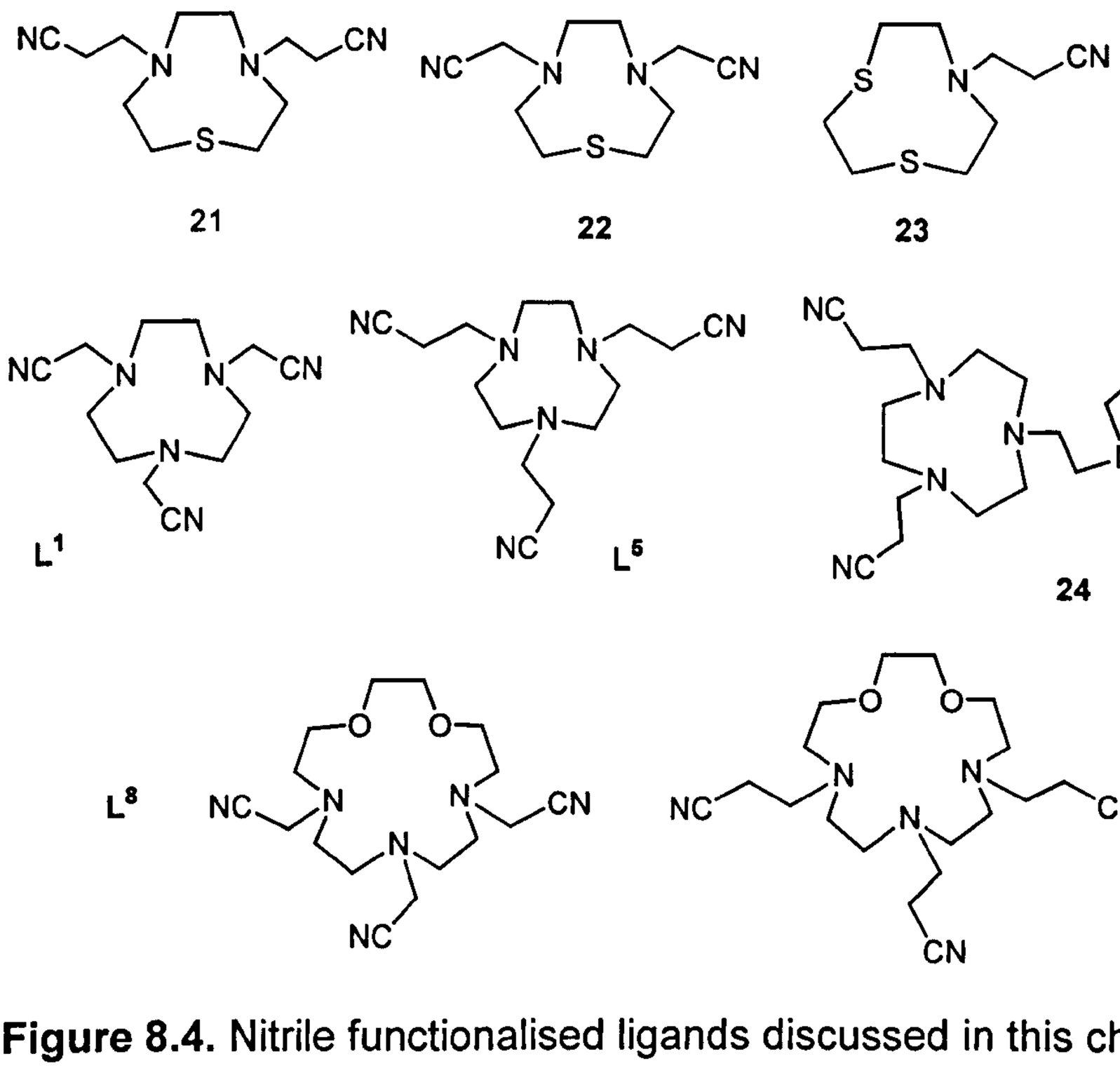

Figure 8.4. Nitrile functionalised ligands discussed in this chapter.

In his PhD work, carried out at the University of Nottingham, Vito Lippolis reported the reaction of nitrile pendant arm derivatives of [9]aneN$_2$S and [9]aneNS$_2$ (**21**, **22** and **23**, Figure 8.4) with Ag^{I} and the formation of polymeric compounds.[402,445,503] In the $[Ag(\mathbf{21})]^{+}$ complex cation, two symmetry related $[Ag(\mathbf{21})]^{+}$ units are held together in the dinuclear complex by Ag-N bonds involving one nitrile functionalised pendant arm from each ligand leaving uncoordinated the remaining two pendant arms (Figure 8.5a).[402] In this complex, further interactions between dinuclear $[Ag_2(\mathbf{21})_2]^{2+}$ fragments via nitrile groups to give a polymeric architecture were not observed. Remarkably, also the Ag^{I} complex with **22** was found to be a dimer, but this time the nitrile arms do not co-ordinate the metal centres, which instead are connected by a peculiar and unprecedented μ_2-κC:κC bridging CN^{-} possibly coming from *in situ*

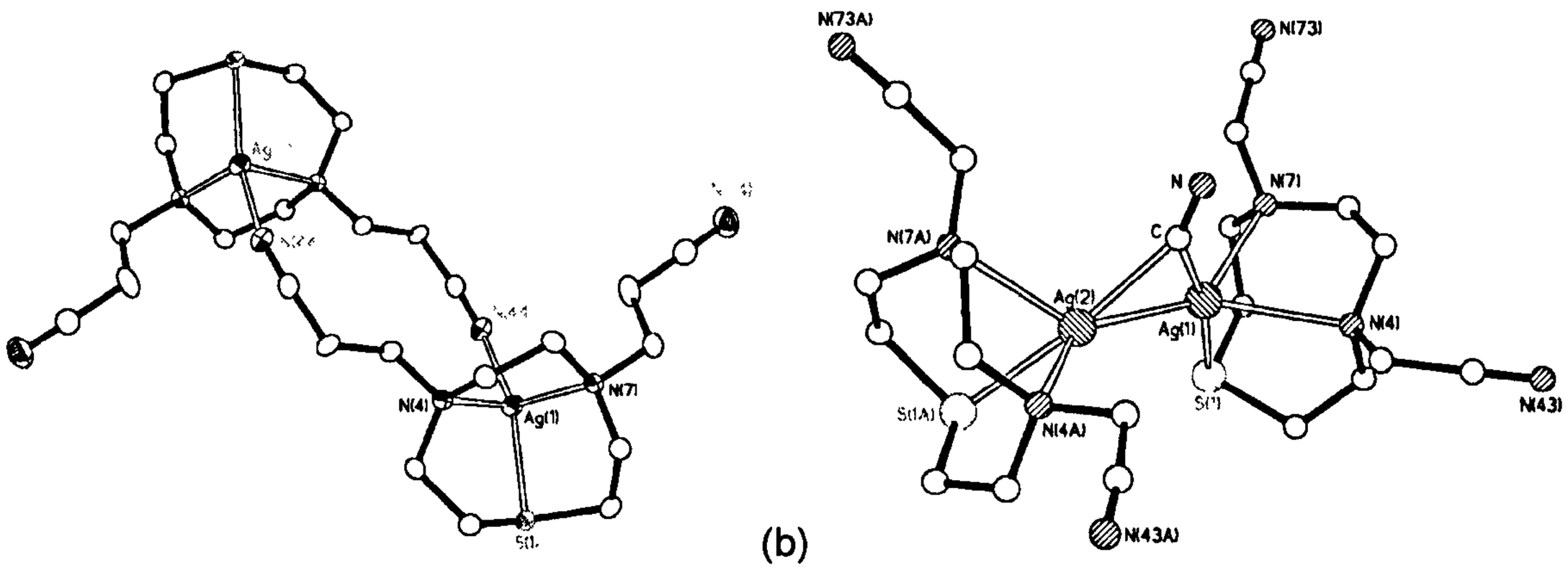

Figure 8.5. Views of the dinuclear cations (a) $[Ag_2(\mathbf{21})_2]^{2+}$ and (b) $[Ag_2(\mathbf{21})_2CN]^{+}$ with a peculiar μ_2-κC:κC CN^- bridging the two silver(I) ions.

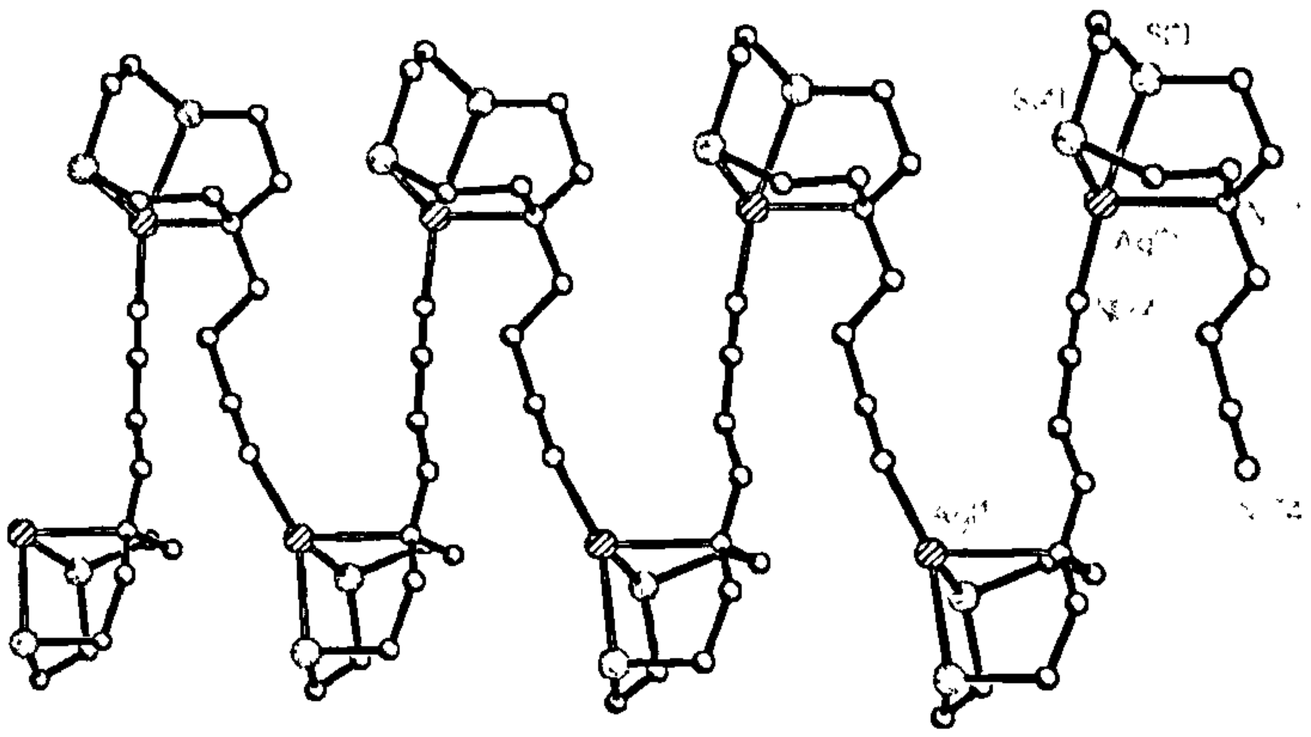

Figure 8.6. Packing diagram for the $\{[Ag(\mathbf{23})]^{+}\}_{\infty}$ polymeric chain.

decomposition of CH_3CN or of the ligand (Figure 8.5b).[445] The only Ag^{I} polymeric complex formed with ligands **21**, **22** and **23** was $[Ag(\mathbf{23})]BF_4$ as shown in Figure 8.6. In the one-dimensional sinusoidal polymer, $\{[Ag(\mathbf{23})]BF_4\}_{\infty}$, the repeating unit is the monuclear complex cation $[Ag(\mathbf{23})]^{+}$ and Ag^{I} ions are tetrahedrally co-ordinated to the three donor atoms of the macrocyclic ring and a nitrile group belonging to a symmetry-related unit.[402]

8.2 Ag^{I} complexes of nitrile functionalised macrocyclic ligands

8.2.1 Ag^{I} complexes of nitrile pendant arm derivatives of [9]aneN$_3$

The reaction of one molar equivalent of $AgPF_6$ with L^1 gave as expected a polymeric complex $\{[Ag(L^1)]PF_6\}_{\infty}$.[444] In this compound each Ag^{I} ion is co-ordinated to six N donors in a distorted octahedral co-ordination geometry, with

one face taken up by the three N donors of the triaza ring [Ag–N 2.523(4)-2.547(4) Å (Figure 8.7, Table 8.1)]. The three remaining positions are occupied by the N donors of nitrile groups belonging to three different $[Ag(L^1)]^+$ ions [Ag–N 2.311(4)-2.486(4) Å].

A three-dimensional inorganic network is therefore formed in which each molecule of L^1 is a node linked to four different Ag^{I} centres and each Ag^{I} ion represents a six-connected junction *via* NCH_2CN linkers to six other Ag^{I} ions in the overall three dimensional single network. Figures 8.8 and 8.9 show partial views of the $\{[Ag(L^1)]^+\}_\infty$ three-dimensional polymer: in the first, the chains running through the structure are distinguished by the colours of their bonds and in Figure 8.9 the methylene units belonging to the $[9]aneN_3$ frameworks are omitted to better show the six-connected single network at Ag^{I} centres. Interestingly, the structure of this polymeric cationic network does not depend on whether BF_4^- or PF_6^- is the counter anion as the channels within the polymer can accommodate both BF_4^- and PF_6^-. Six-connected single networks at Ag^{I} consisting of a cationic frame linked by molecular rods are very rare in the literature, the only reported example being the complex $[Ag(pyz)_3]SbF_6$ which is topologically related to the structure of ReO_3 or Prussian blue.[504]

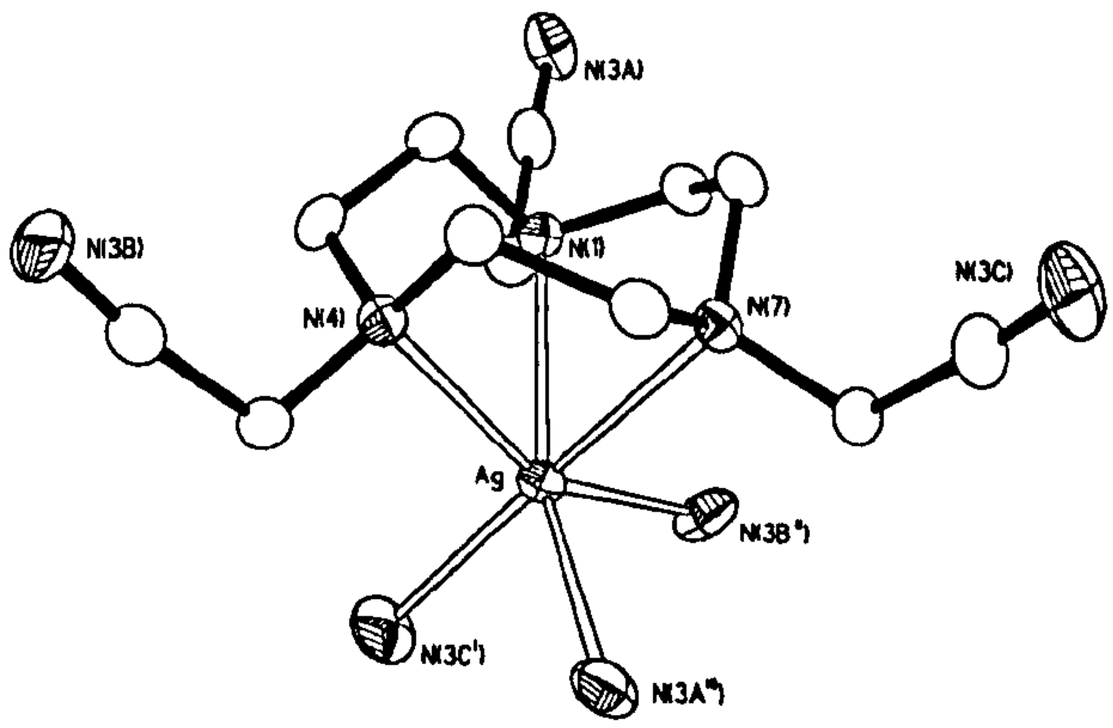

Figure 8.7. View of the co-ordination sphere in the cation $[Ag(L^1)]^+$ with the numbering scheme adopted. The nitrogen atoms N(3A^{iii}), N(3B^{ii}) and N(3C^{i}) belong to three different symmetry-related molecules of L^1 [i = x+1/2, –y+3/2, z–1/2; ii = x–1/2, –y+3/2, z–1/2; iii = –x+1/2, y+1/2, –z+1/2]. Hydrogen atoms are omitted for clarity and displacement ellipsoids are drawn at 50% probability.

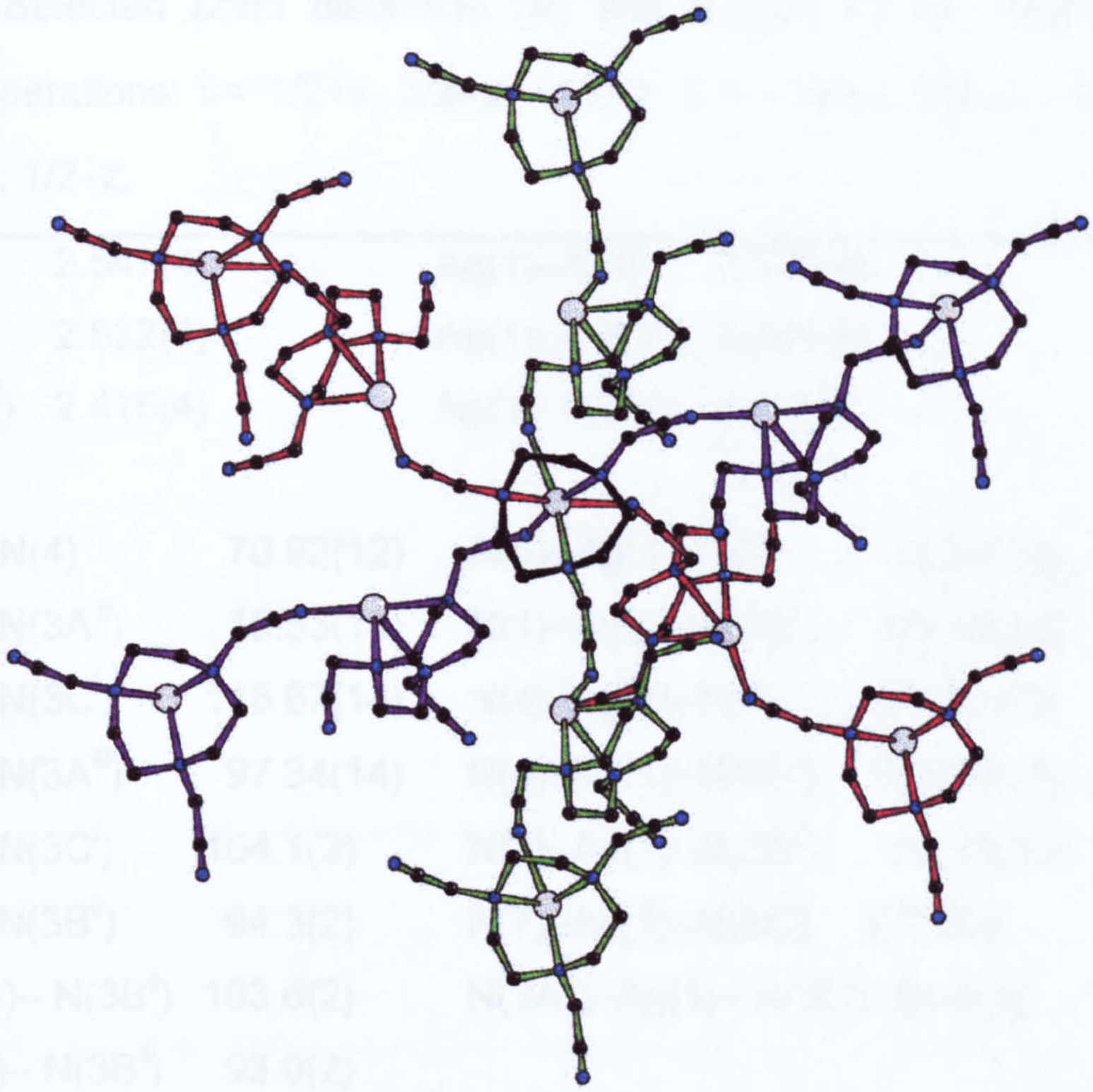

Figure 8.8. View of part of the $\{[Ag(L^1)]^+\}_\infty$ three dimensional polymer. Counter-anions are omitted for clarity and chains running through the structure are distinguished by the colours of their bonds.

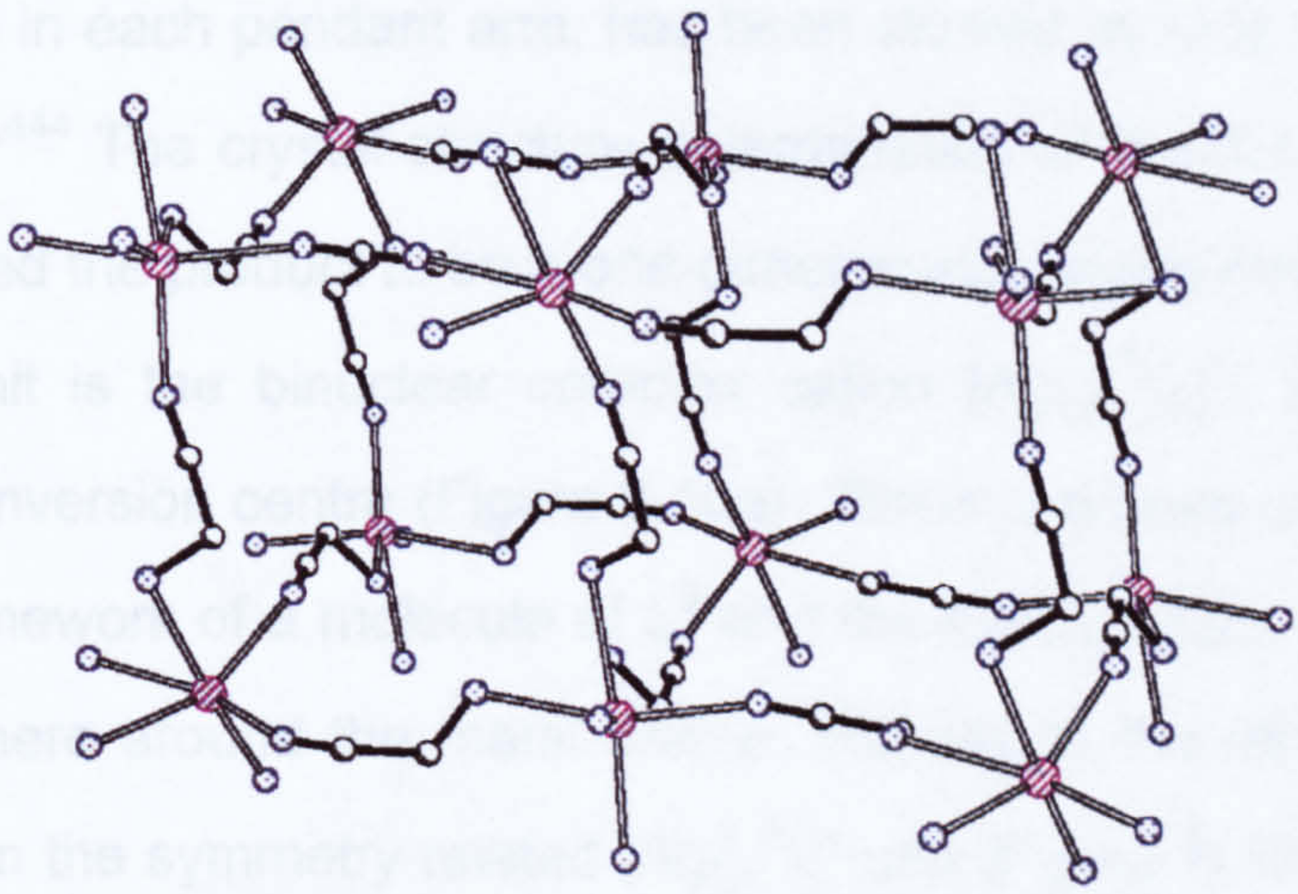

Figure 8.9. Partial view of the $\{[Ag(L^1)]^+\}_\infty$ three-dimensional polymer: the methylene units belonging to the [9]aneN_3 frameworks and counter anions are omitted for clarity to better show the six-connected single network at Ag^{I} centres.

Table 8.1. Selected bond distances (Å) and angles (°) for $\{[Ag(L^1)]PF_6\}_\infty$. Symmetry operations: i = 1/2+x, 3/2–y, –1/2+z; ii = –1/2+x, 3/2–y, –1/2+z; iii = 1/2–x, 1/2+y, 1/2–z.

Ag(1)–N(1)	2.547(4)	Ag(1)–N(4)	2.523(4)
Ag(1)–N(7)	2.532(4)	Ag(1)–N(3A^{iii})	2.486(4)
Ag(1)–N(3B^{ii})	2.415(4)	Ag(1)–N(3C^{i})	2.311(4)
N(1)–Ag(1)–N(4)	70.92(12)	N(1)–Ag(1)–N(7)	71.34(11)
N(1)–Ag(1)–N(3A^{iii})	15.53(13)	N(1)–Ag(1)–N(3B^{ii})	83.16(13)
N(1)–Ag(1)–N(3C^{i})	115.67(14)	N(4)–Ag(1)–N(7)	71.38(12)
N(4)–Ag(1)–N(3A^{iii})	97.34(14)	N(4)–Ag(1)–N(3B^{ii})	153.20(13)
N(4)–Ag(1)–N(3C^{i})	104.1(2)	N(7)–Ag(1)–N(3A^{iii})	83.58(13)
N(7)–Ag(1)–N(3B^{ii})	94.3(2)	N(7)–Ag(1)–N(3C^{i})	170.5(2)
N(3A^{iii})–Ag(1)– N(3B^{ii})	103.6(2)	N(3A^{iii})–Ag(1)– N(3C^{i})	88.8(2)
N(3C^{i})–Ag(1)– N(3B^{ii})	93.0(2)		

In the light of this result, the co-ordination chemistry towards Ag^{I} of the *tris*-cyanoethyl derivative of [9]aneN$_3$ (L^5), which differs from L^1 in having one more methylene group in each pendant arm, has been studied by Vito Lippolis during his PhD work.[402,444] The crystal structure determination of the 1:1 (metal:ligand) complex confirmed the product to be a one-dimensional zigzag polymer, in which the repeating unit is the binuclear complex cation $[Ag_2(L^5)_2]^{2+}$ lying across a crystallographic inversion centre (Figure 8.10a). Three N-donors are provided by the [9]aneN$_3$ framework of a molecule of L^5 and the fourth, which completes the co-ordination sphere around the metal centre, belongs to the nitrile group of a pendant arm from the symmetry-related $[Ag(L^5)]^+$ unit (Figure 8.10a). One of the remaining two pendant arms of L^5 interacts with an Ag^{I} centre of an inversion-related $[Ag(L^5)]^+$ binuclear fragment [Ag(1)–N(14^{ii}) 2.779(7) Å] to give an infinite zigzag polymer along the *a* axis (Figure 8.10b). Thus, simply altering the length of the pendant arm, from CH_2CN in L^1 to CH_2CH_2CN in L^5, affords a different network motif for the resulting co-ordination polymer with Ag^{I}.

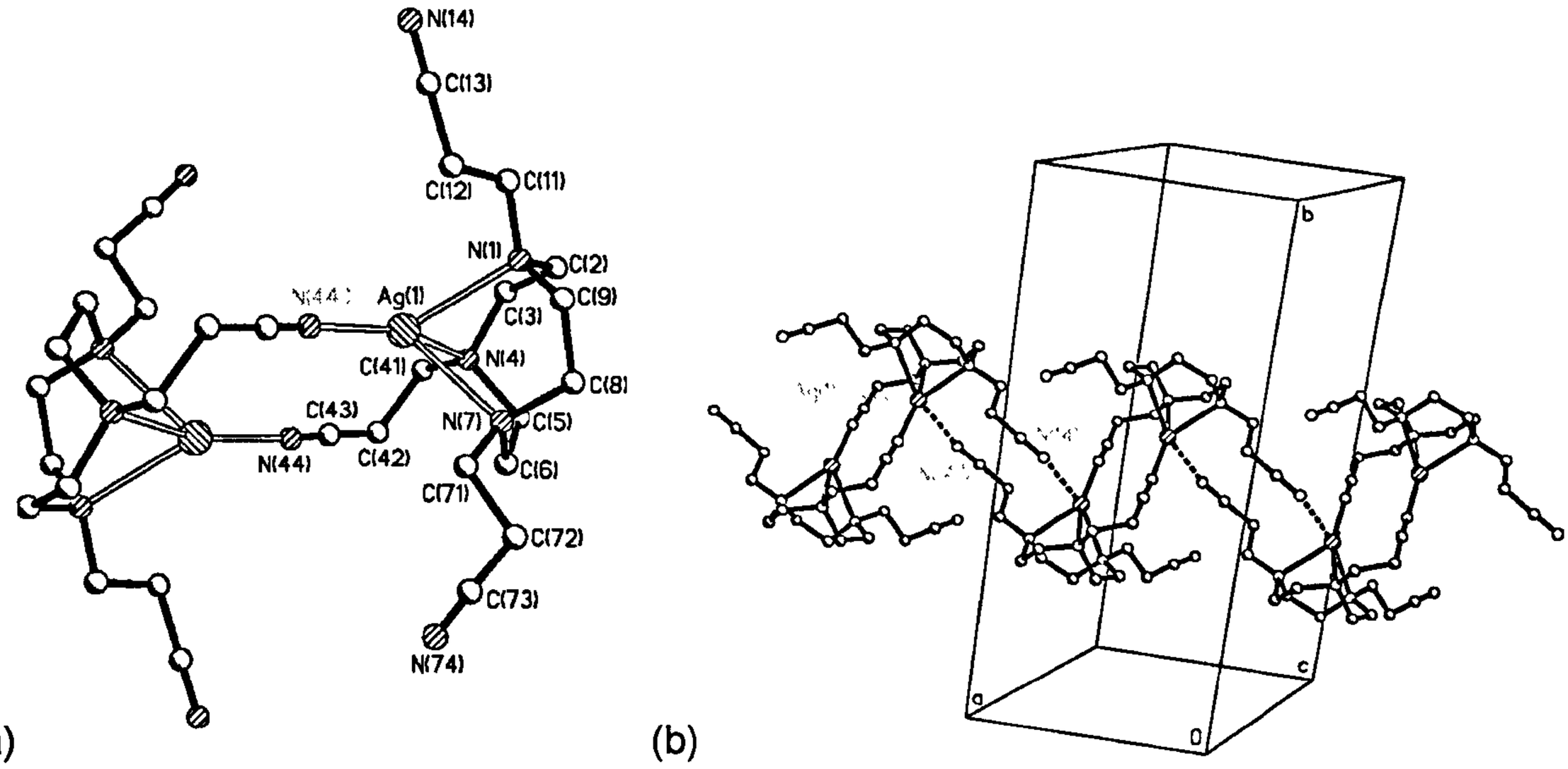

Figure 8.10. (a)View of the dinuclear cation $[Ag_2(L^5)_2]^{2+}$ and (b) packing diagram for $\{[Ag_2(L^5)_2]^{2+}\}_\infty$ polymeric chains.

Considering that nitrile pendant-arm derivatives of *bis*([9]aneN_3) ligands could represent a further step in the design of new flexible ligands suitable for the synthesis of inorganic polymers, the silver(I) complex of this ligand has been synthesised by Francesca Morale during her PhD work at the University of Nottingham. The X-ray crystal structure determination showed each [9]aneN_3 moiety in the ligand (**24**) hosting one Ag^{I} centre (Figure 8.11). Each Ag^{I} ion in the $[Ag_2(\mathbf{24})]^{2+}$ complex cation is co-ordinated to five N donors in a highly distorted

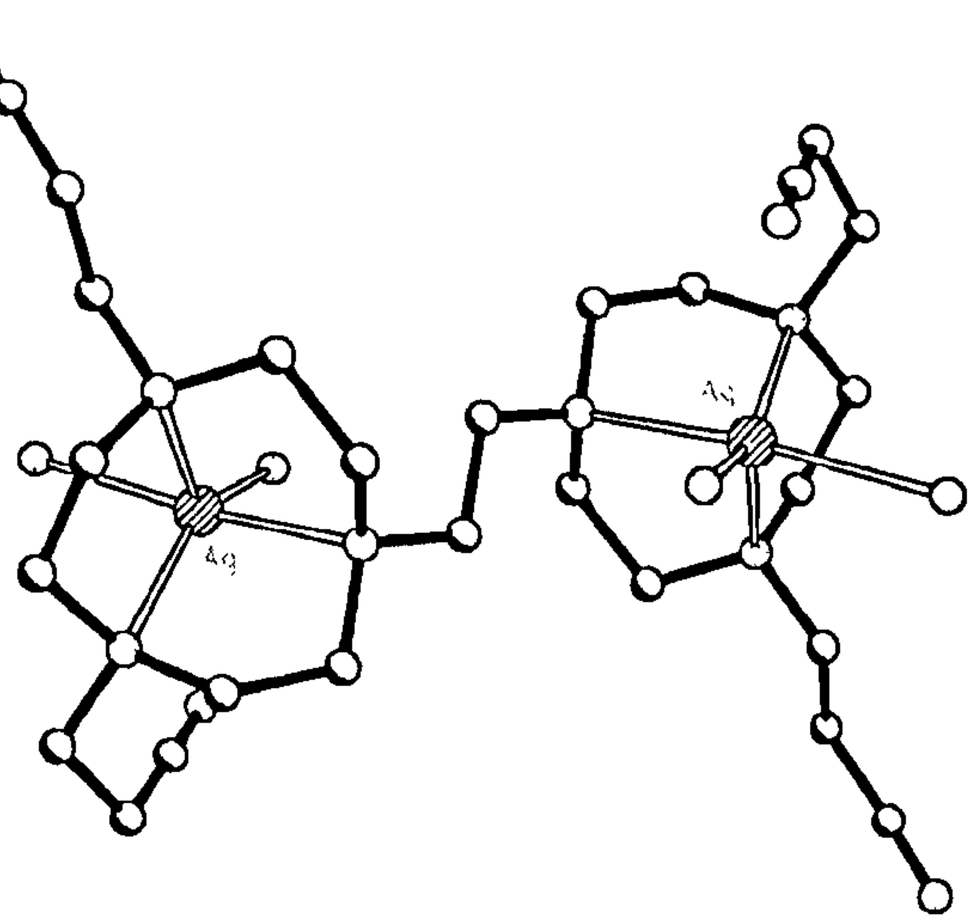

Figure 8.11. View of the co-ordination sphere around the Ag^{I} ions in the cation of $[Ag_2(\mathbf{24})][PF_6]_2$.

trigonal bipyramidal co-ordination geometry with one axial position and two equatorial positions taken up by the three N donors of the triaza ring moiety [Ag–N 2.464(4)-2.483(3) Å]. The remaining axial [Ag–N(74^{iii}) 2.501(4) Å] and equatorial [Ag–N(44^{ii}) 2.262(4) Å] sites are occupied by the N donors of nitrile groups belonging to two different $[Ag_2(\mathbf{24})]^{2+}$ complexes. The two pentadentate compartments of **24** are arranged in an *anti*-configuration similar to that found for most of the binuclear complexes of *bis*([9]aneN_3) ligands with other functionalised pendant arms.[429,430,435]

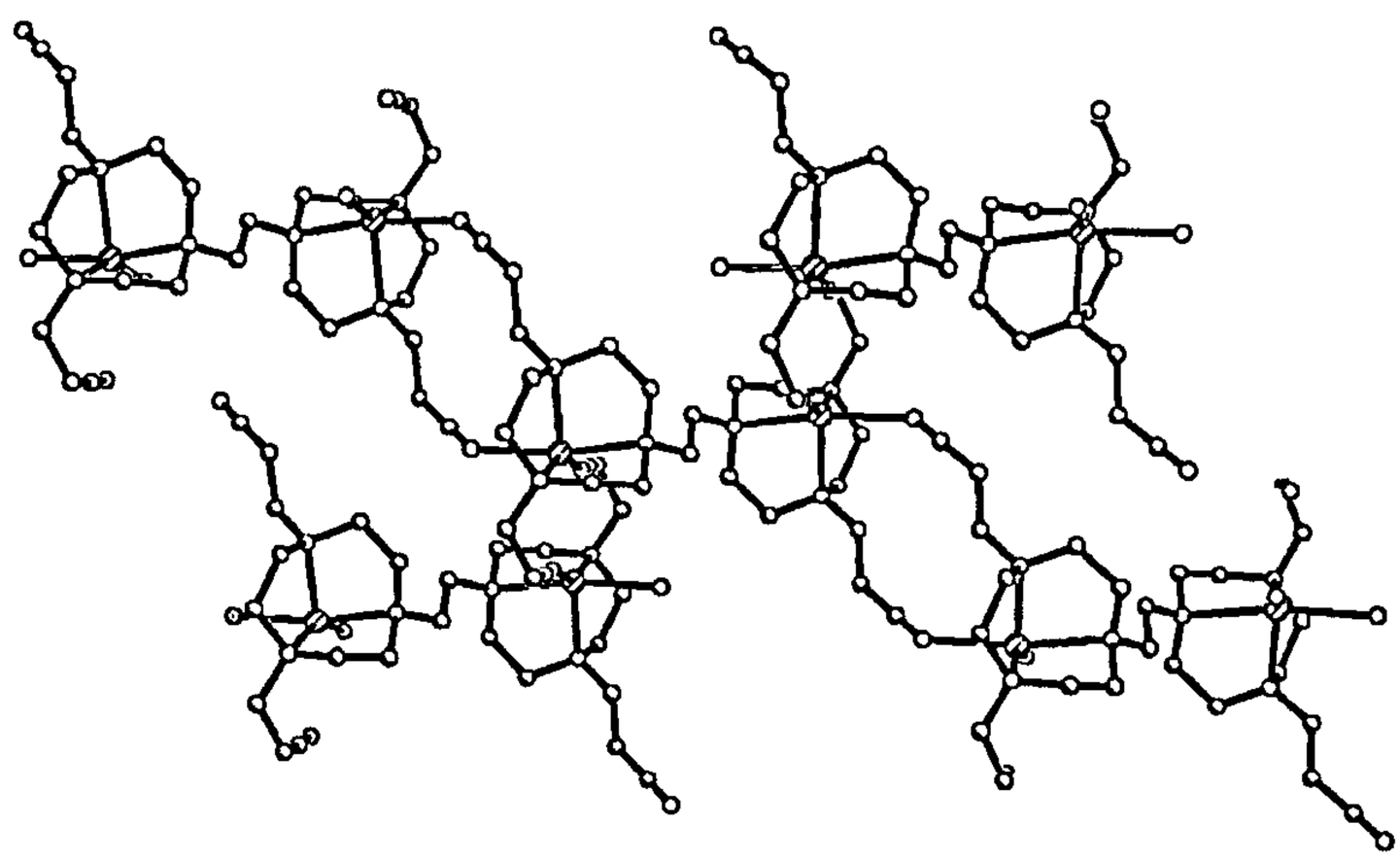

Figure 8.12. Packing diagram showing part of the $\{[Ag_2(\mathbf{24})]^{2+}\}_{\infty}$ two-dimensional polymer.

A two-dimensional inorganic network is formed where each $[Ag_2(\mathbf{24})]^{2+}$ unit is linked through its two metal centres to four symmetry-related units. Pairs of linked $[Ag_2(\mathbf{24})]^{2+}$ units share two nitrile functionalised pendant arms from the ligands and two silver(I) centres. Each five co-ordinate Ag^{I} ion is connected to other two Ag^{I} centres through two NCH_2CH_2CN linkers and to a third metal centre *via* one NCH_2CH_2N linker (Figure 8.12). A better insight into the nature of the resulting two-dimensional network can be obtained by omitting the carbon atoms of the [9]aneN_3 moieties. Ribbons of fused 12-membered rings connected at Ag^{I} spiro-centres can be envisaged in the two-dimensional architecture (Figure 8.13). Each ring comprises two metal centres and the two NCH_2CH_2CN linkers connecting

them. The mean planes containing consecutive 12-membered rings are almost perpendicular to each other. The resulting ribbons run along the [010] direction, are stacked along [100], and are connected at the metal centres *via* NCH_2CH_2N linkers.

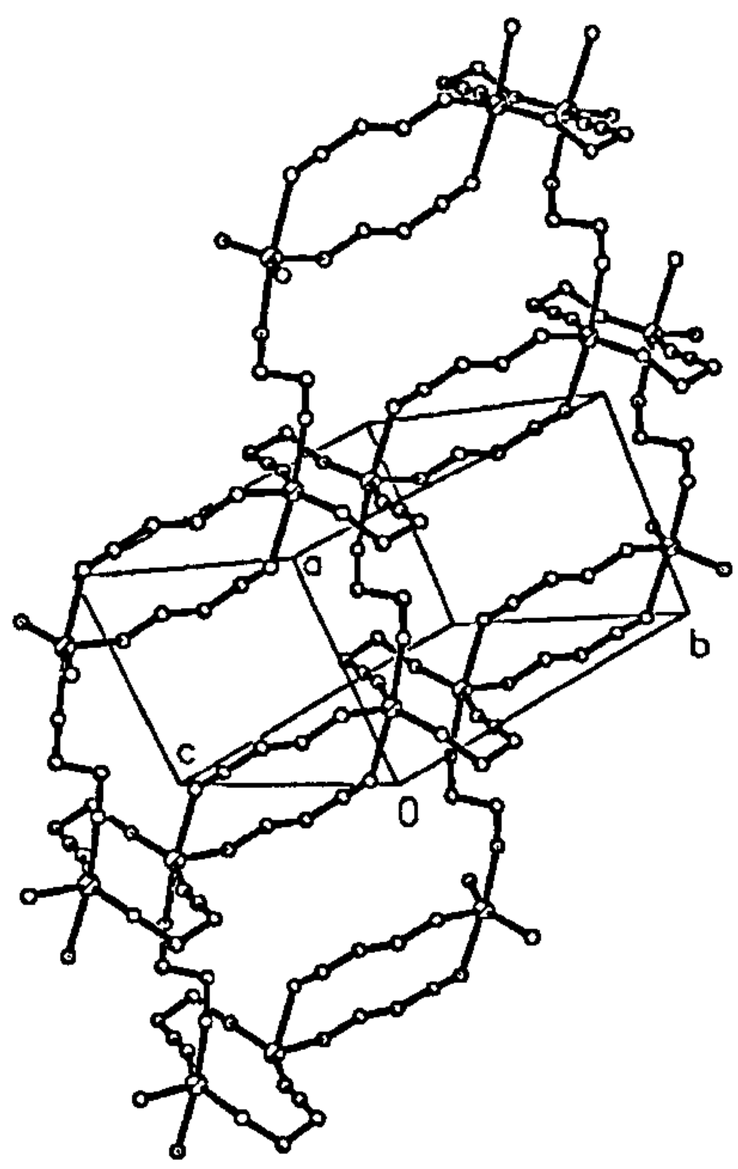

Figure 8.13. Packing diagram showing part of the $\{[Ag_2(\mathbf{24})]^{2+}\}_\infty$ two-dimensional polymer with the carbon atoms of the [9]aneN_3 moieties being omitted for clarity.

8.2.3 Ag^{I} complexes with nitrile derivatives of [15]aneN_3O_2

The ligands L^8 and L^{10} have been considered as representative examples of nitrile functionalised pendant arm derivatives of mixed oxa-aza macrocycles. They are characterised by pendant arms of different lengths and, analogously to L^1 and L^5, by an inherent stereochemical mismatch between the co-ordination preferences of the Ag^{I} ion (octahedral or tetrahedral) and the macrocyclic frameworks (potentially three co-ordinate for [9]aneN_3 and five-co-ordinate for [15]aneN_3O_2). Reaction of L^8 with one molar equivalent of $AgBF_4$ in MeCN at room temperature for 3h gave a white microcrystalline solid after addition of diethyl ether to the reaction mixture. Analytical and mass spectroscopic data were consistent with the stoichiometry $[Ag(L^8)]BF_4$. Single

crystals grown by diffusion of Et_2O vapour into a MeCN solution of the white product were subjected to X-ray diffraction studies. The structure shows the formation of a one-dimensional sinusoidal polymer, $\{[Ag(L^8)]BF_4\}_\infty$, in which the repeating unit is the mononuclear complex cation $[Ag(L^8)]^+$ (Figure 8.14, Table 8.2). Each Ag^I ion in the polymer shows a highly distorted octahedral co-ordination geometry with the equatorial positions occupied by two oxygen and two nitrogen atoms from the macrocyclic ring [Ag–O 2.514(4), 2.618(5) Å; Ag–N 2.398(4), 2.413(4) Å]. The axial positions are occupied by two nitrogen atoms, one belonging to the [15]aneN_3O_2 framework [Ag–N(4) 2.559(4) Å] and the other to the nitrile group of one of the three pendant arms of a symmetry-related $[Ag(L^8)]^+$ unit [Ag–N(3B^i) 2.377(5) Å, N(4)–Ag–N(3B^i) 158.8(2)°, i = –1/2+x, 3/2–y, –1/2+z]. The other two pendant arms of each $[Ag(L^8)]^+$ unit are unco-ordinated and are directed away from the polymeric chain which runs along the [101] direction.

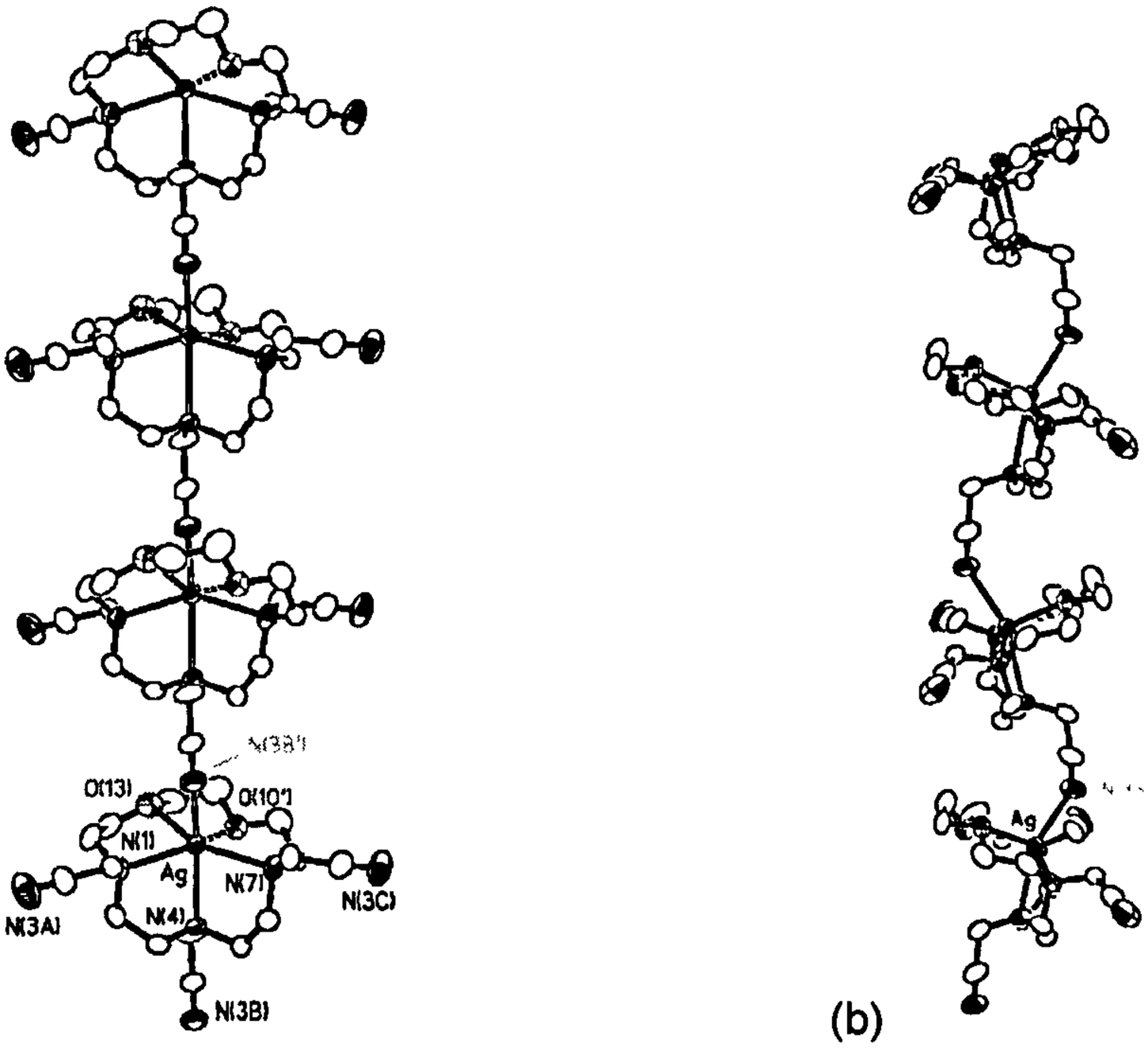

Figure 8.14. (a) Packing diagram for the $\{[Ag(L^8)]^+\}_\infty$ polymeric chain running along the [101] direction with the numbering scheme adopted. Hydrogen atoms and counter anions are omitted for clarity [i = –1/2+x, 3/2–y, –1/2+z]. Only one component of the disordered macrocyclic ligand is shown; (b) alternative view of the $\{[Ag(L^8)]^+\}_\infty$ polymeric chain showing the sinusoidal pattern.

Table 8.2. Selected bond distances (Å) and angles (°) for $\{[Ag(L^8)]BF_4\}_\infty$. Symmetry operation: i = –1/2+x, 3/2–y, –1/2+z.

Ag–N(1)	2.413(4)	Ag–N(4)	2.559(4)
Ag–N(7)	2.398(4)	Ag–O(10')	2.618(5)
Ag–O(13)	2.514(4)	Ag–N(3B^{i})	2.377(5)
N(1)–Ag–N(4)	75.37(13)	N(1)–Ag–N(7)	143.4(2)
N(1)–Ag–N(3B^{i})	96.4(2)	N(1)–Ag–O(13)	70.84(5)
N(1)–Ag–O(10')	128.4(2)	N(4)–Ag–N(7)	75.17(14)
N(4)–Ag–N(3B^{i})	158.8(2)	N(4)–Ag–O(10')	85.7(2)
N(4)–Ag–O(13)	104.16(13)	N(7)–Ag–N(3B^{i})	103.3(2)
N(7)–Ag–O(10')	70.0(2)	N(7)–Ag–O(13)	135.46(14)
O(10')–Ag–N(3B^{i})	114.0(2)	O(13)–Ag–N(3B^{i})	91.8(2)
O(10')–Ag–O(13)	65.58(14)		

The polymeric structure of $\{[Ag(L^8)]^+\}_\infty$ resembles that of the Ag^{I} complex with the cyanoethyl pendant arm derivative of [9]aneNS_2, where each Ag^{I} ion in the polymer is co-ordinated by a [2S+N] donor set from the [9]aneNS_2 macrocyclic framework and by the nitrile group of a symmetry-related unit (Figure 8.6). The major difference between the two complexes is the co-ordination environment around the metal centre (octahedral in the former and tetrahedral in the latter).

In order to ascertain whether changing the length of the pendant arms could have dramatic effects on the co-ordination chemistry of nitrile functionalised pendant arm derivatives of [15]aneN_3O_2, L^{10} has been reacted with $AgBF_4$ under the same experimental conditions used for L^8. Unfortunately, only oils were recovered from this reaction; this difficulty in crystallising the product could be a direct consequence of changing the length of the pendant arms. It has been therefore argued that changing the counter anion could alter the packing forces and thereby allowing the formation of a crystalline product. Thus, reaction of L^{10}

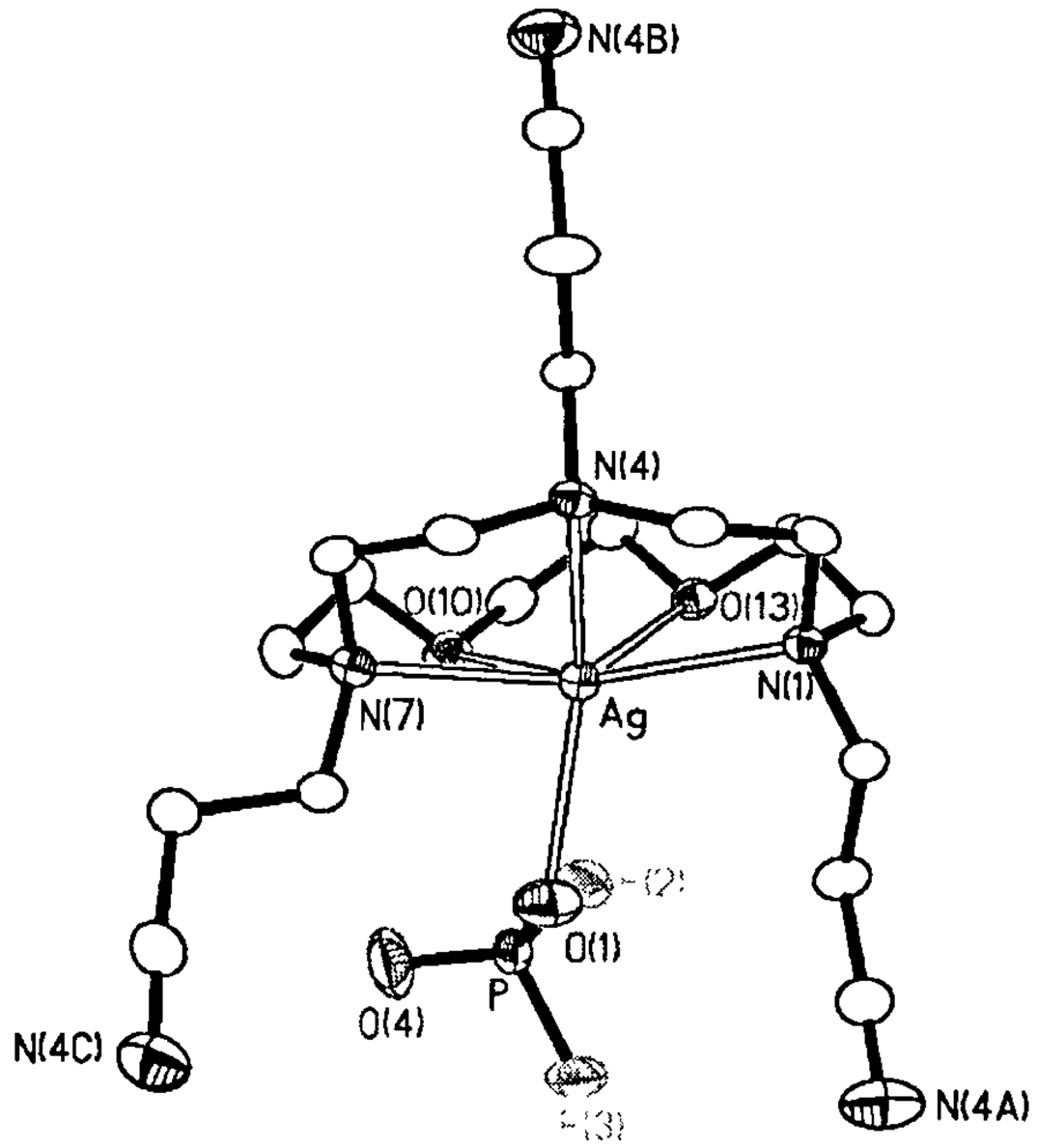

Figure 8.15. View of $[Ag(L^{10})]PF_2O_2$ with the numbering scheme adopted. Hydrogen atoms are omitted for clarity and displacement ellipsoids are drawn at 50% probability.

with one molar equivalent of $AgPF_6$ in MeCN at room temperature afforded colourless columnar crystals upon diffusion of Et_2O vapour into the reaction mixture. An X-ray diffraction analysis shows a discrete neutral mononuclear product with the formulation $[Ag(L^{10})]PO_2F_2$. By analogy with the results for $\{[Ag(L^{8})]BF_4\}_\infty$, the Ag^{I} ion in $[Ag(L^{10})]PO_2F_2$ shows a very distorted octahedral co-ordination sphere (Figure 8.15, Table 7) with one of the axial positions being occupied by an oxygen atom of a $PO_2F_2^-$ ion. Presumably, the steric requirements of the longer pendant arms in L^{10} do not allow the formation of polymeric chains of $[Ag(L^{10})]^+$ units as in $\{[Ag(L^{8})]^+\}_\infty$ (Figure 10). Rather PF_6^- is hydrolysed *in situ* to give $PO_2F_2^-$ which can complete the octahedral co-ordination sphere around the metal centre. This may explain the failure to obtain a crystalline product from the reaction of L^8 with $AgBF_4$.

Table 8.3. Selected bond distances (Å) and angles (°) for $[Ag(L^{10})]PF_2O_2$.

Ag–N(1)	2.445(2)	Ag-N(4)	2.574(2)
Ag–O(1)	2.458(2)	Ag–N(7)	2.464(2)
Ag–O(10)	2.656(2)	Ag–O(13)	2.612(2)
N(1)–Ag–N(4)	74.94(6)	N(1)–Ag–N(7)	147.04(6)
N(1)–Ag–O(1)	109.43(6)	N(1)–Ag–O(10)	135.73(6)
N(1)–Ag–O(13)	70.84(5)	N(4)–Ag–N(7)	74.87(6)
N(4)–Ag–O(1)	146.79(6)	N(4)–Ag–O(10)	116.82(5)
N(4)–Ag–O(13)	106.99(5)	N(7)–Ag–O(1)	89.25(6)
N(7)–Ag–O(10)	71.26(6)	N(7)–Ag–O(13)	131.41(6)
O(1)–Ag–O(10)	83.78(6)	O(1)–Ag–O(13)	105.38(6)
O(10)–Ag–O(13)	64.90(5)		

8.3 Macrocyclic ligands bearing quinoline pendant arms

8.3.1 Introduction to pendant arm quinoline macrocycles

Polyaza and mixed oxa-aza macrocyclic ligands bearing pendant arms with nitrogen-containing heterocycles are of interest because of their ability to form strong and selective interactions with various charged and neutral guest molecules. These ligands are particularly versatile because they combine the

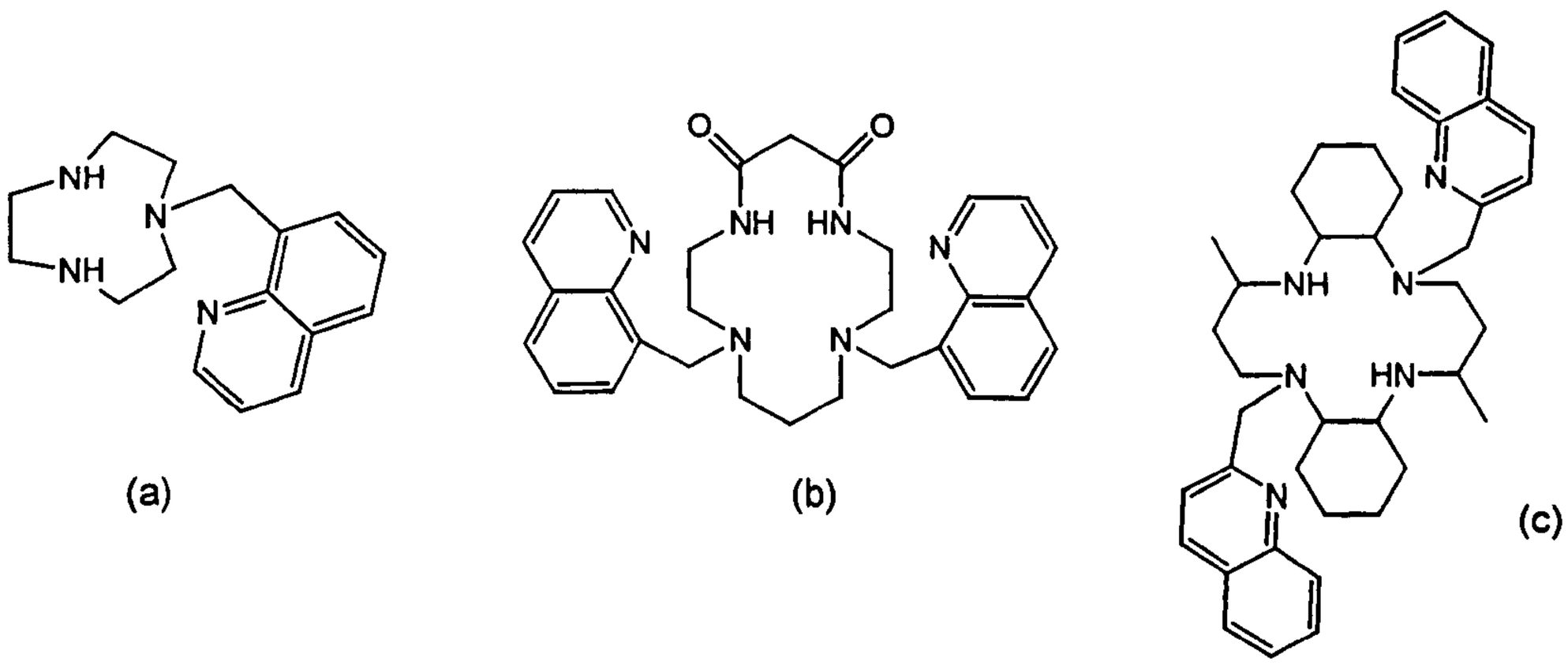

Figure 8.16. (a) mono-quinolyl derivative of [9]aneN_3; *bis*-substituted quinoline derivatives of (b) dioxocyclam and of (c) a tetraaza macrocycle with a fused cyclohexyl ring.

hard donating properties of the macrocyclic rings with the softer properties of the heterocyclic donors and have proved effective at binding both alkaline earth and transition metal ions.[505,506]

Only a few reports on quinoline derivatives have appeared in the literature and some examples of these quinoline functionalised ligands are shown in Figure 8.16.[238,505-513] In these ligands the N-donor of the heterocycle is always able to bind the metal ion co-ordinated by the macrocycle in an endocyclic manner, because of the C_2 or a C_3 linker between them and the N-donor of the ring. Figure 8.17 illustrates the structures of the Ni^{II} and Cu^{II} complexes of the ligands shown in Figure 8.16 (a) and (b), respectively, where

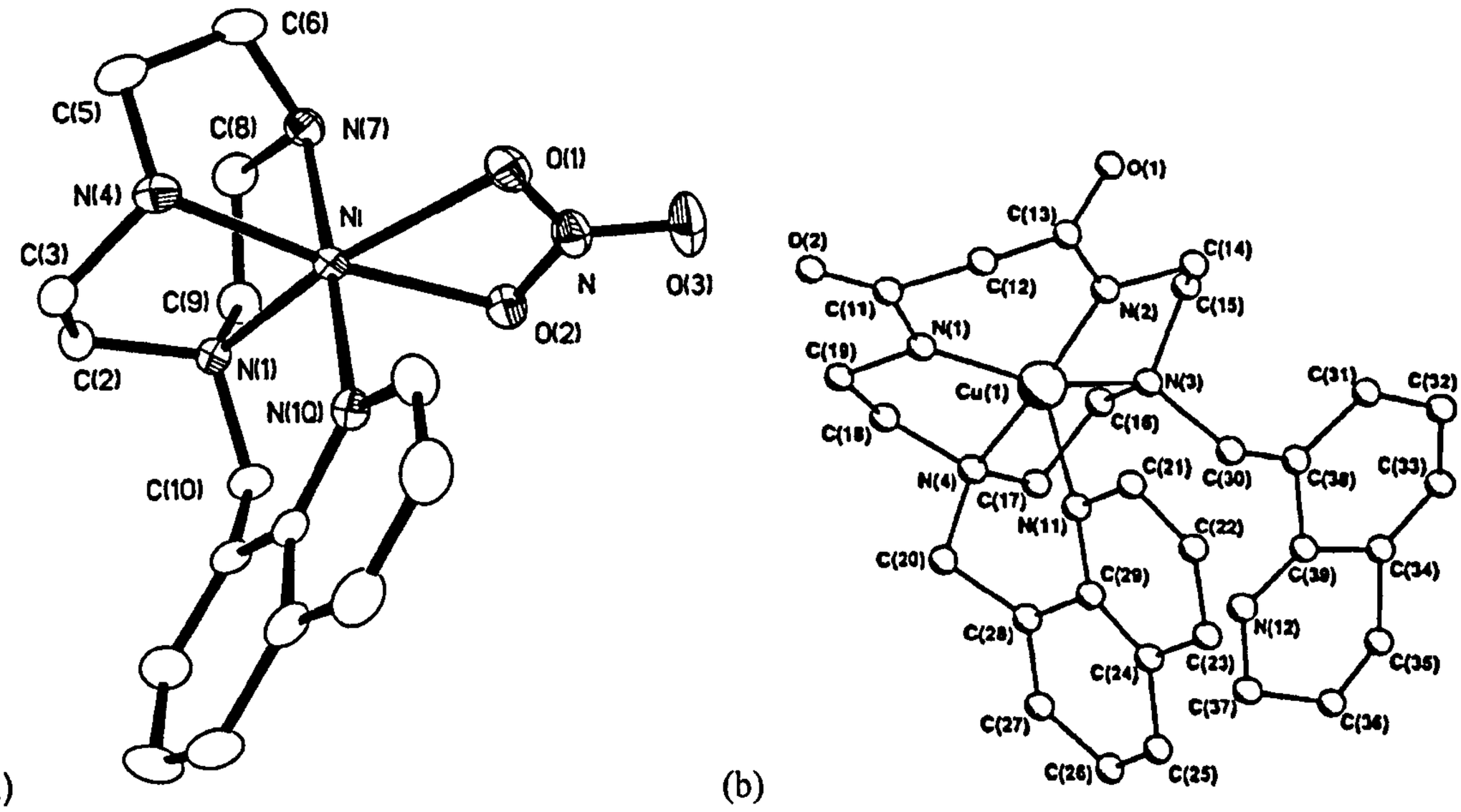

Figure 8.17. (a) crystal structure of the Ni^{II} complex with a monoquinolyl derivative of [9]aneN_3[238] and (b) crystal structure of a Cu^{II} complex with the ligand shown in Figure 8.16b showing one heterocyclic N-donor involved in the co-ordination of the metal ion.[507]

the quinoline N-donor co-ordinates the metal centre forming an endocyclic complex. Two different Cu^{II} complexes of the *bis*-substituted quinoline derivative of dioxocyclam (Figure 8.16b) have been synthesised from the same reaction mixture and their crystal structures reported.[507,508] The first of these (Figure 8.17b) shows only one of the quinoline pendant arms co-ordinated to

the metal centre forming a distorted square-based pyramidal Cu^{II} complex and the second (Figure 8.18a) exhibits only weak interactions of 2.800 and 2.686 Å between the N-donors of the quinoline subunits and the copper(II) centre which has an axially elongated octahedral geometry.[507,508] A similar co-ordination geometry has been observed in the Cu^{II} complex of the tetraaza macrocycle with fused cyclohexyl rings and bearing two quinoline pendant arms (Figure 8.16c).[509] As shown in Figure 8.18(b), only very weak interactions are observed between the N-donors of the heterocycles and the metal centre [2.948(4) Å].[509]

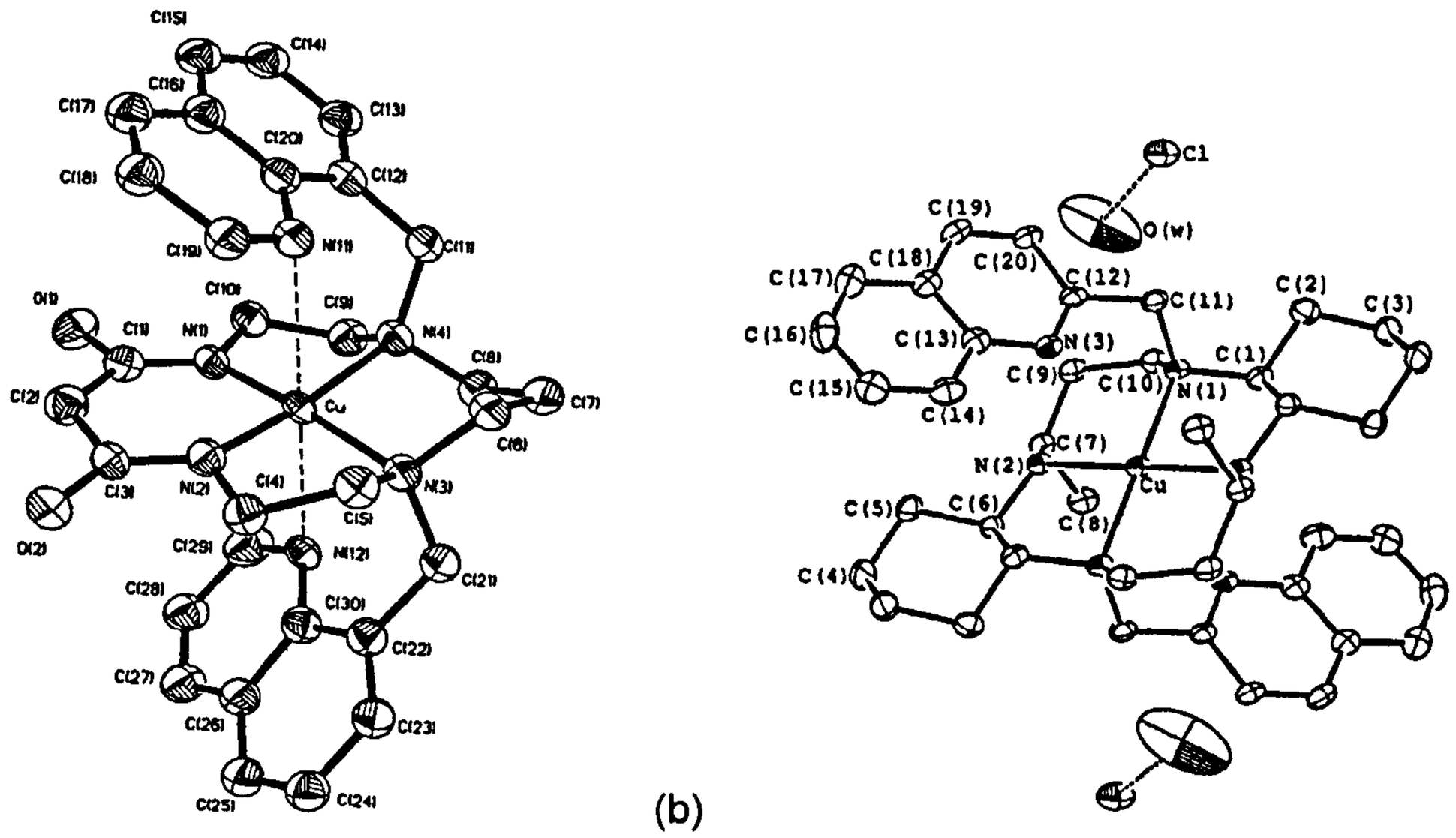

Figure 8.18. Two Cu^{II} crystal structures showing only weak interactions between the N-donors of the quinoline pendant arms and the metal ion.

Only rarely has the quinoline subunit been intentionally attached to a macrocyclic ring such that the N-donor of the heterocycle could not co-ordinate the metal ion situated inside the macrocyclic cavity.[505,510-513] The two examples shown in Figure 8.19 have been synthesised for different purposes: the one bearing 5-chloro-8-hydroxyquinoline substituents has been studied as a selective complexing agent and sensor for Mg^{2+} ions,[512] while the Zn^{2+}-cyclen derivative bearing two 4-quinolylmethyl pendant arms has been found to selectively bind and therefore recognise thymine bases in double-stranded DNA.[513] Therefore, in both cases the quinoline N-donors do not co-ordinate the

metal ion: in one case the metal centre is bound to the hydroxy group of the heterocycle and in the other the quinoline subunit is used in order to form strong π-π stacking interactions with the aromatic rings of thymine.

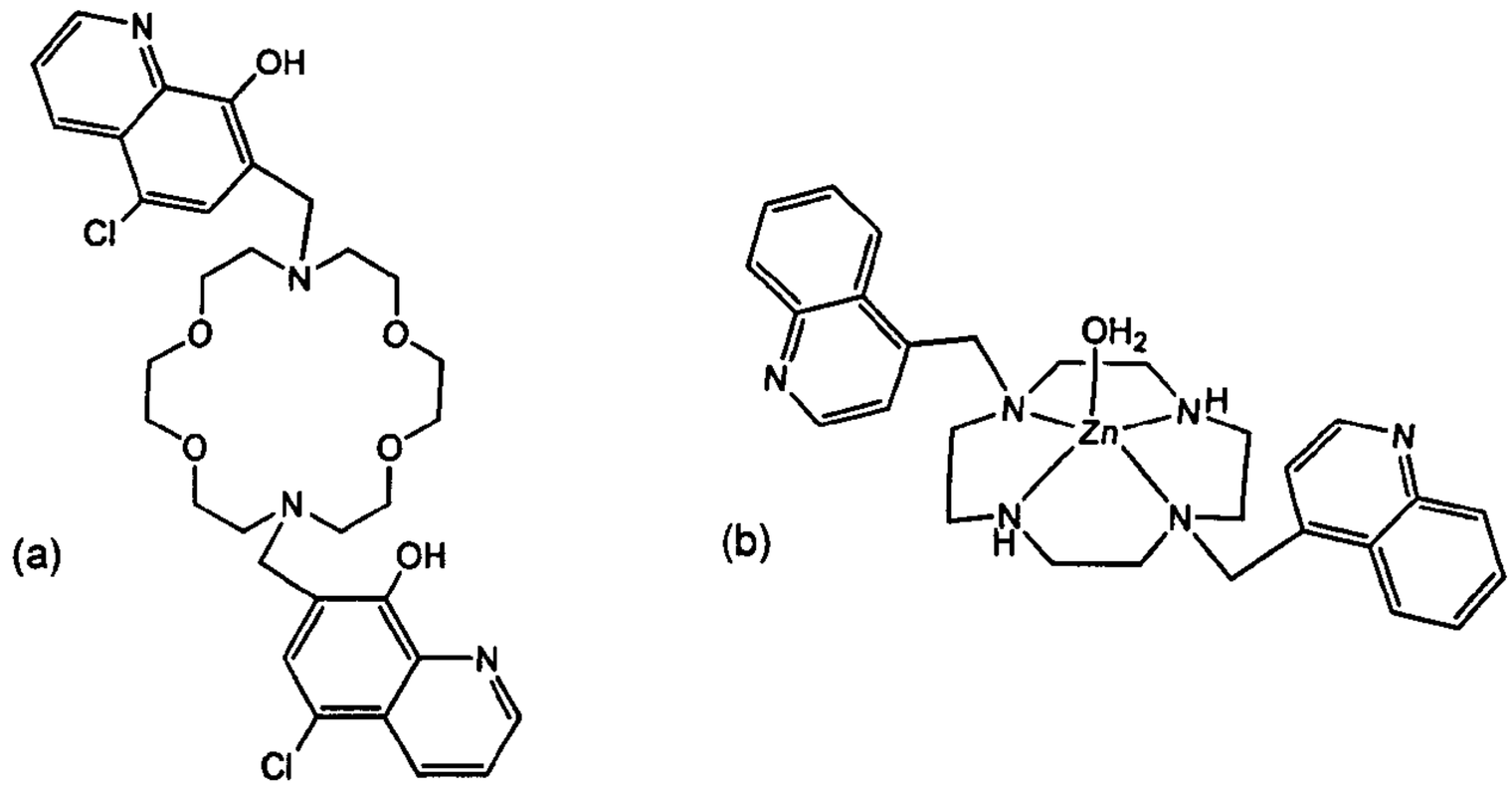

Figure 8.19. (a) An oxa-aza macrocycle with two 5-chloro-8-hydroxyquinoline units attached and (b) Zn^{2+}-cyclen derivative bearing two 4-quinolylmethyl pendant arms.

8.3.2 Ag^{I} complexes of [9]aneN_3 and [15]aneN_3O_2 derivatives bearing three 7-methylquinoline pendant arms

As in the nitrile pendant arm derivatives of [9]aneN_3 and [15]aneN_3O_2, where the nitrile group could not form endocyclic complexes with Ag^{I} but only polymeric networks, 7-methylquinoline pendant arms have been attached onto the two macrocycles [9]aneN_3 and [15]aneN_3O_2 in order to form exocyclic complexes with Ag^{I}; this is because the N-donor of the heterocyclic unit is pointing away from the metal centre and is sterically unable to co-ordinate the metal bound inside the macrocyclic cavity.

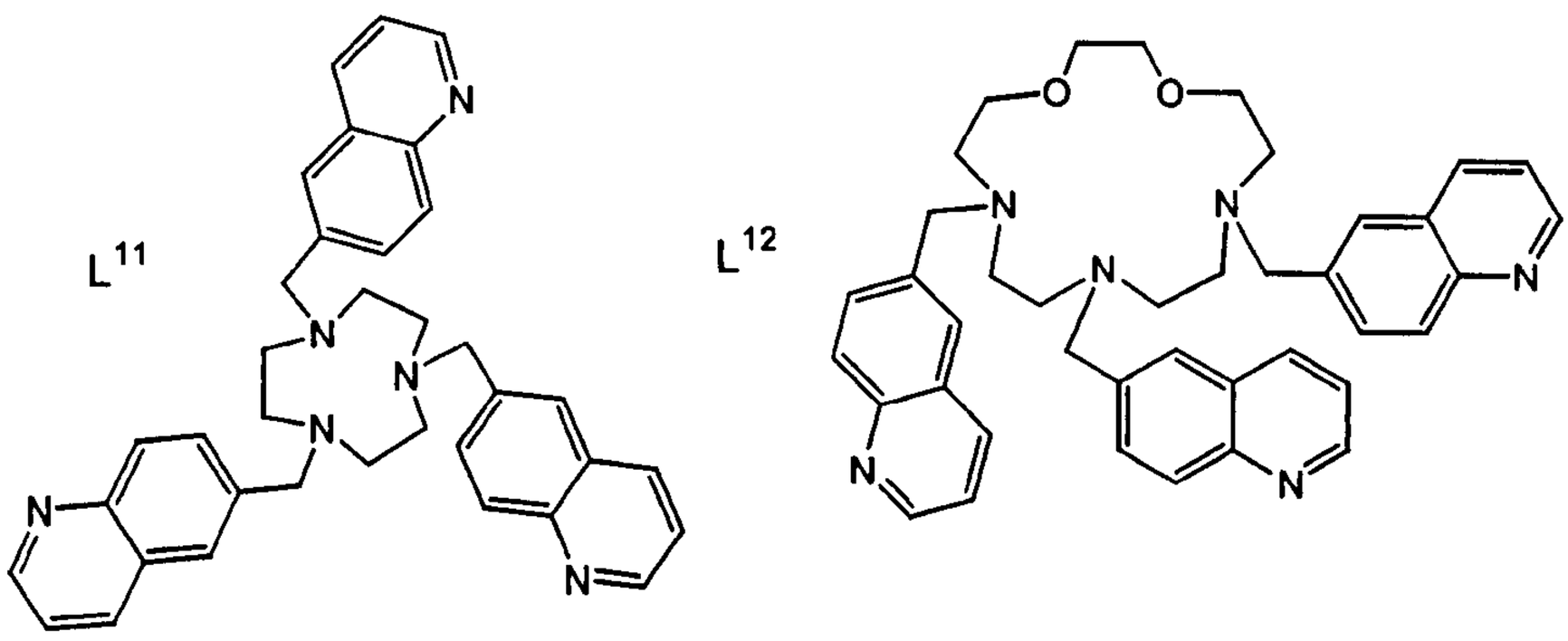

Figure 8.20. Quinoline pendant arm derivatives of [9]aneN_3 and [15]aneN_3O_2.

The synthesis of 7-bromomethylquinoline was achieved following the procedure used by Rieger *et al.*[514] for the preparation of 2-bromomethylquinoline. Reacting 7-bromomethylquinoline with [9]aneN_3 or [15]aneN_3O_2 in EtOH under anhydrous conditions gave the two ligands (Figure 8.20) in good yields. While L^{12} could be obtained sufficiently pure, the ligand L^{11} could be purified only by forming the PF_6^- salt. The reaction of two molar equivalents of $AgPF_6$ with L^{11} and L^{12} gave complexes of formula $[Ag_2(L^{11})](PF_6)_2$ and $[Ag_2(L^{12})(PF_2O_2)_2]$, respectively, on the basis of elemental analyses, IR and mass spectra.

Single crystals of $[Ag_{2.5}(L^{12})(PF_2O_2)_{2.5}\cdot CH_3CN]$, grown by diffusion of Et_2O vapour into a MeCN solution of the complex, were subjected to X-ray diffraction studies. The data revealed the presence of two and a half silver(I) ions; the counter anions have been modelled as $PF_2O_2^-$ as confirmed also by negative ES^- mass spectrum (see experimental Section 8.4.6), but the choice of the half occupied site is entirely arbitrary. The structure can be described as a dimer $\{[Ag_{2.5}(L^{12})(PF_2O_2)_{2.5}\cdot CH_3CN]_2\}$, as shown in Figure 8.21, with one Ag^{I} co-ordinated linearly by two heterocyclic N-donors [N(8B) and N(8B^{i})] and bridging

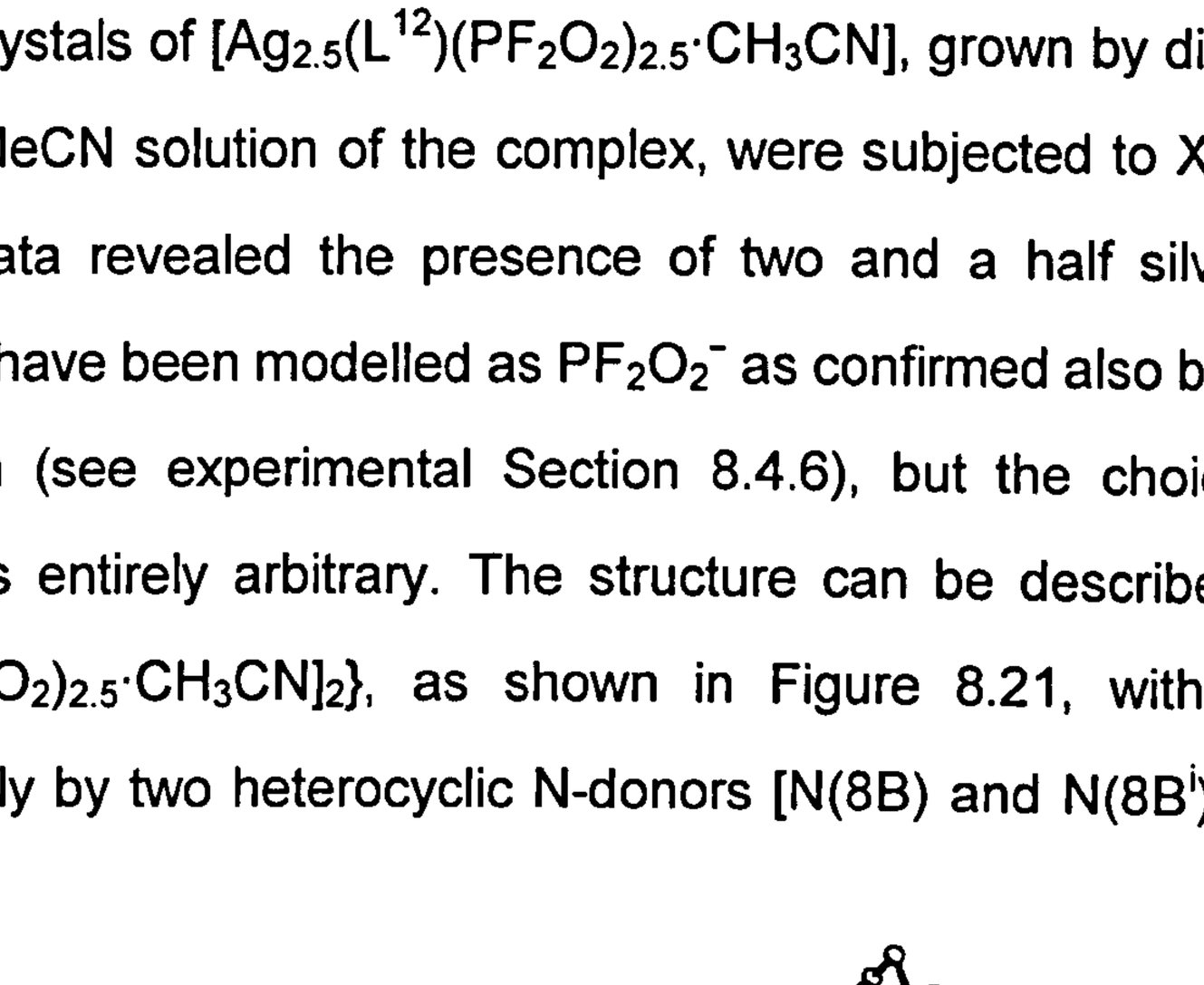

Figure 8.21. View of the dimeric cation $\{[Ag_{2.5}(L^{12})(PF_2O_2)_{1.5}\cdot CH_3CN]_2\}^+$ with the numbering scheme adopted. Hydrogen atoms have been omitted for clarity. Symmetry operation: i = -x, -y, -z+2.

the two units. One of the Ag^{I} ions [Ag(1)] is co-ordinated by one O-donor from a $PF_2O_2^-$ anion [O(1)] and by only two macrocyclic donors [N(4) and O(10)]. Ag(1) lies some distance from the other macrocyclic donors, being at 2.820(7) from N(1), 2.694(7) from N(7) and 2.720(6) from O(13). Ag(2) is bound to two quinoline N-donors from two pendant arms [N(8A) and N(8C)], to a disordered MeCN molecule (both components, N(1S) and N(1S'), are shown in Figure 8.21) and to one oxygen donor from a $PF_2O_2^-$ anion [O(9)]. The half occupied Ag(3) ion is linearly co-ordinated to two quinoline N-donors [N(8B) and the symmetry related N(8B^{i})] and coincides with the centre of the dimeric complex. The geometries around the silver(I) ions are not regular except for the exactly linear co-ordination around Ag(3). A clearer view of the asymmetric unit, where anions and solvent molecules are omitted, is shown in Figure 8.22.

Table 8.4. Selected bond distances (Å) and angles (°) for $[Ag_{2.5}(L^{12})(PF_2O_2)_{2.5}\cdot CH_3CN]$.

Ag(1)- N(4)	2.374(6)	O(1)- Ag(1)- N(4)	151.6(2)
Ag(1)- O(10)	2.571(7)	O(1)- Ag(1)- O(10)	80.3(3)
Ag(1)- O(1)	2.325(7)	N(4)- Ag(1)- O(10)	126.5(3)
Ag(2)- N(8A)	2.306(8)	N(8A)- Ag(2)- N(8C)	122.2(2)
Ag(2)- N(8C)	2.287(7)	N(8A)- Ag(2)- N(1S)	97.9(6)
Ag(2)- N(1S)	2.56(2)	N(8C)- Ag(2)- N(1S)	117.8(6)
Ag(2)- O(9)	2.578(14)	N(8A)- Ag(2)- O(9)	89.7(4)
Ag(3)- N(8B)	2.166(8)	N(8C)- Ag(2)- O(9)	98.4(4)
		N(1S)- Ag(2)- O(9)	129.7(6)
		N(8B)- Ag(3)- N(8B^{i})	180.0

Symmetry operation: i = -x, -y, -z+2

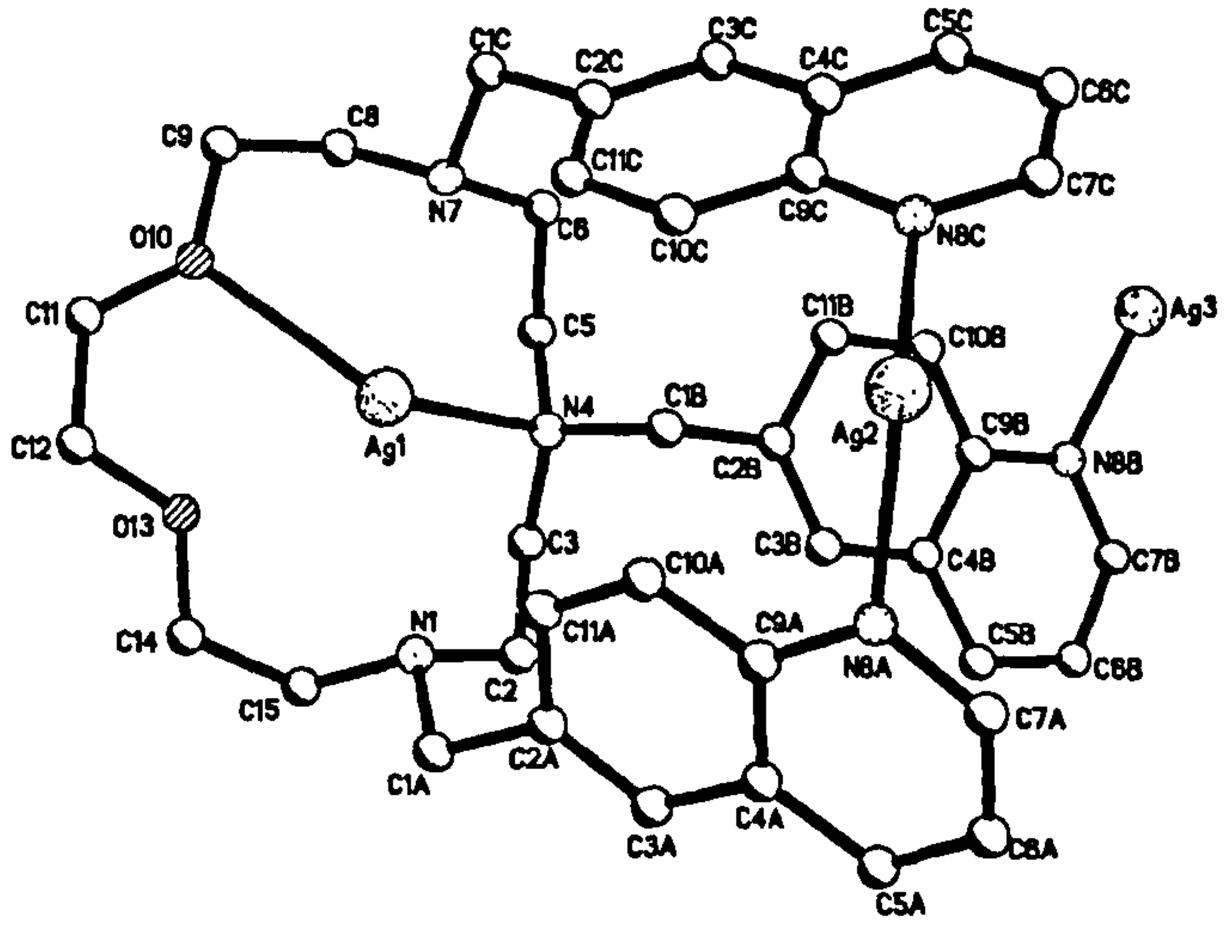

Figure 8.22. View of the asymmetric unit of $[Ag_{2.5}(L^{12})]^{2.5+}$. $PF_2O_2^-$ anions and MeCN solvent molecule are omitted for clarity.

Unfortunately, crystals of $[Ag_2(L^{11})](PF_6)_2$ were not suitable for X-ray analysis and it was not possible to determine the structural features of the complex. Although predictions of the structure of the complex without an X-ray determination can be unreliable, in view of the crystal structure of $[Ag_{2.5}(L^{12})(PF_2O_2)_{2.5}]$, it could be proposed that the Ag^{I} complex with L^{11} has one silver(I) ion bound by two heterocyclic nitrogen atoms and perhaps one or two acetonitrile molecules, and the second Ag^{I} co-ordinated by the macrocyclic N-donors and possibly one N-donor from the third quinoline group of another ligand, thereby forming a polymeric system (Figure 8.23).

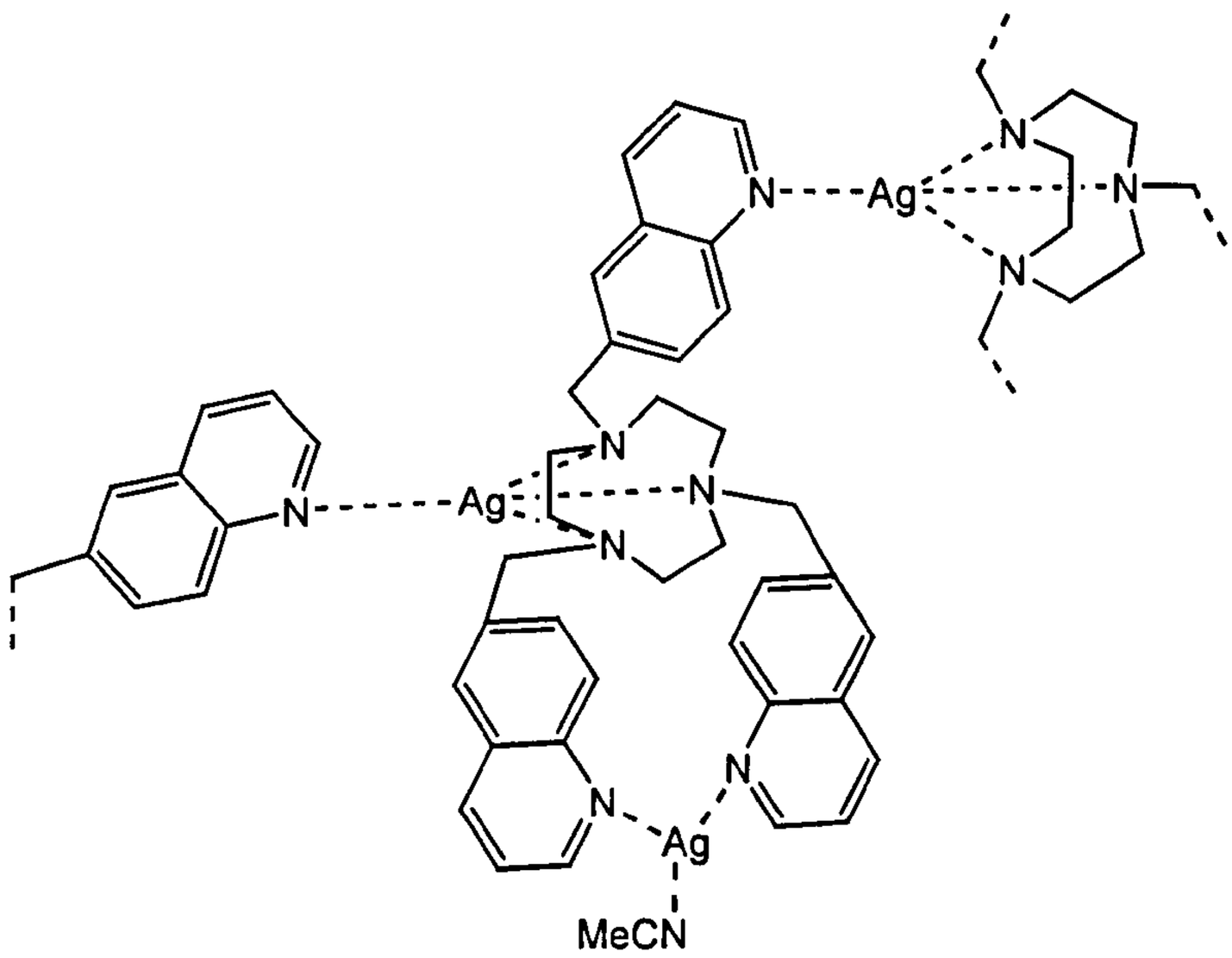

Figure 8.23. Proposed polymeric structure of $[Ag_2(L^{11})](PF_6)_2$.

8.4 Experimental

The synthesis of the ligands L^1 and L^8 has already been reported in Chapters 3 and 7, respectively. All starting materials were obtained from Aldrich Chemical Co. and were used without further purification. Microanalyses were performed by the University of Nottingham School of Chemistry Microanalytical Service. IR spectra were recorded as KBr discs using a Perkin-Elmer 598 spectrometer over the range 200-4000 cm^{-1}. Fast atom bombardment (FAB), electron impact (EI) and electrospray (ES) mass spectra were recorded at the EPSRC Centre for Mass Spectroscopy at the University of Swansea.

8.4.1 Synthesis of 1,4,7-*tris*(cyanoethyl)-1,4,7-triaza-10,13-dioxacyclopentadecane (L^{10})

[15]aneN_3O_2 (0.22 g, 1.01 mmol) was refluxed in acrylonitrile (20 cm^3) under N_2 for 16 h. After cooling, the solvent was removed by rotary evaporation to yield a colourless oil which was dried *in vacuo* (0.29 g, 77% yield). ^{1}H NMR ($CDCl_3$, 300.1 MHz): δ_H 3.59 (OC*H*$_2$, 4H, s), 3.58 (OC*H*$_2$CH$_2$N, 4H, t, *J* = 4.70 Hz), 2.80 (OCH$_2$C*H*$_2$N, 4H, t, *J* = 4.70 Hz), 2.75 (NC*H*$_2$, 8H, t, *J* = 5.16 Hz), 2.88 (C*H*$_2$CH$_2$CN, 6H, t, *J* = 6.77 Hz), 2.45 (CH$_2$C*H*$_2$CN, 6H, t, *J* = 6.77 Hz). ^{13}C NMR ($CDCl_3$, 75.47 MHz): δ_C 119.1 (*C*N), 70.8 (O*C*H$_2$), 70.6 (OCH$_2$*C*H$_2$N), 54.0 (OCH$_2$*C*H$_2$N), 53.1 (NCH$_2$*C*H$_2$N), 52.9 (NCH$_2$*C*H$_2$N), 51.5 (NCH$_2$*C*H$_2$CN), 51.4 (NCH$_2$*C*H$_2$CN), 17.1 (*C*H$_2$CN), 16.9 (NCH$_2$*C*N). EI$^+$ mass spectrum: *m/z*: 376 (*M*$^+$), 350 (*M*$^+$-CN), 321 (*M*$^+$-CH$_2$CH$_2$CN). Found (calc. for $C_{19}H_{32}N_6O_2$): C, 60.40 (60.61); H, 8.40 (8.57); N, 22.20% (22.32%). IR spectrum (KBr disk): ν 2924m, 2853m, 2246m, 1459m, 1384m, 1113s, 801m cm^{-1}.

8.4.2 Synthesis of silver(I) complexes with L^1, L^8 and L^{10}

{[Ag(L^1)][PF_6]}$_\infty$. A mixture of silver hexafluorophosphate (19.5 mg, 0.077 mmol) and 1,4,7-*tris*(cyanomethyl)-1,4,7-triazacyclononane (L^1) (19.0 mg, 0.077 mmol) in acetonitrile (15 cm^3) was stirred for 3h at room temperature. The

solvent was partially removed under reduced pressure and Et_2O vapour was allowed to diffuse into the remaining solution. Colourless crystals suitable for X-ray structural analysis were obtained (28.9 mg, 75.3% yield). M.p.: 212-214 °C. ^{1}H NMR (CD_3CN, 300.1 MHz, 298K): δ_H 2.14 (12H, s, NCH_2CH_2N), 2.75 (6H, s, NCH_2CN). Found (calc. for $C_{12}H_{18}PF_6N_6Ag$): C, 29.10 (28.88); H, 3.83 (3.63); N, 19.15% (18.84%). FAB mass spectrum (3-NOBA matrix) *m/z*: 353 for $[^{107}Ag(L^1)]^+$. IR spectrum (KBr disc) ν: 2930 m, 2843 s, 2247 (s, CN stretch), 1457 s, 1337 s, 1113 s, 995 s, 881 s.

$\{[Ag(L^1)][BF_4]\}_\infty$. Silver tetrafluoroborate (15.0 mg, 0.077 mmol) was dissolved in acetonitrile (15 cm^3) and a solution of 1,4,7-*tris*(cyanomethyl)-1,4,7-triazacyclononane (L^1) (19.0 mg, 0.077 mmol) in acetonitrile (15 cm^3) was added dropwise. The solution was stirred for 3 h at room temperature. Single crystals suitable for X-ray structural analysis were obtained by diffusion of diethyl ether vapour into an acetonitrile solution of the complex at room temperature (24.2 mg, 71.4% yield). FAB mass spectrum (3-NOBA matrix) *m/z:* 353 for $[^{107}Ag(L^1)]^+$. Found (calc. for $C_{12}H_{18}BF_4N_6Ag$): C, 32.81 (32.68); H, 4.04 (4.11); N, 19.15% (19.06%). IR spectrum (KBr disc) ν: 2925 m, 2873 m, 2245 (m, CN stretch), 1384 s, 1084 s.

$[Ag(L^8)]BF_4$. $AgBF_4$ (16.0 mg, 0.082 mmol) was dissolved in acetonitrile (15 cm^3) and a solution of L^8 (27.4 mg, 0.082 mmol) in acetonitrile (15 cm^3) was added dropwise. The solution was stirred for 3 h at room temperature. Addition of diethyl ether yielded a white solid (34.3 mg, 79.3% yield). Single crystals suitable for X-ray structural analysis were obtained by diffusion of diethyl ether vapour into an acetonitrile solution of the complex at room temperature. ^{1}H NMR (CD_3CN, 300.1 MHz, 298 K): δ_H 3.64 (4H, s, OCH_2), 3.59 (4H, t, J = 4.63 Hz, OCH_2CH_2N), 2.88 (4H, t, J = 4.63 Hz, OCH_2CH_2N), 2.79 (8H, s, NCH_2), 3.81 (4H, s, NCH_2CN), 3.82 (2H, s, NCH_2CN). FAB mass spectrum (3-NOBA matrix) *m/z*: 441; calc. for $[^{107}Ag(L^8)BF_4]^+$. Found (calc. for $C_{16}H_{26}BF_4N_6O_2Ag$):

C, 36.40 (36.32); H, 5.02 (4.95); N, 14.51% (14.36%). IR spectrum (KBr disc): ν 2920m, 2858m, 2238m, 1384s, 1084s cm^{-1}.

$[Ag(L^{10})]PF_2O_2$. $AgPF_6$ (18.2 mg, 0.072 mmol) was dissolved in acetonitrile (15 cm^3) and a solution of 1,4,7-*tris*(cyanoethyl)-1,4,7-triaza-10,13-dioxacyclopentadecane (L^{10}) (27.1 mg, 0.072 mmol) in acetonitrile (15 cm^3) was added dropwise. The solution was stirred for 3 h at room temperature. Single crystals suitable for X-ray structural analysis were obtained by diffusion of diethyl ether vapour into an acetonitrile solution of the complex at room temperature (19.9 mg, 47.8% yield). ^1H NMR (CD_3CN, 300.1 MHz, 298 K): δ_H 3.62 (4H, s, OCH_2), 3.56 (4H, t, J = 4.37 Hz, OCH_2CH_2N), 2.76 (4H, t, J = 4.37 Hz, OCH_2CH_2N), 2.68 (8H, s NCH_2), 3.11 (2H, t, J = 7.33 Hz, CH_2CH_2CN), 3.04 (4H, t, J = 7.22 Hz, CH_2CH_2CN), 2.63 (4H, t, J = 7.22 Hz, CH_2CH_2CN), 2.54 (2H, t, J = 7.33, CH_2CH_2CN). ES mass spectrum *m/z*: 483; calc. for $[^{107}Ag(L^9)]^+$ 484 (the $PF_2O_2^-$ anion was also detected: *m/z*: 101). Found (calc. for $C_{19}H_{32}AgF_2N_6O_4P$): C, 38.75 (38.99); H, 5.63 (5.51); N, 14.25% (14.36%). IR spectrum (KBr disc): ν 2854s, 2246m, 1312s, 1160s, 850s, 498s cm^{-1}.

8.4.3 Synthesis of 7-bromomethylquinoline

7-Methylquinoline (1.865 g, 0.0130 mol) was dissolved in CCl_4 (60 cm^3) and N-bromosuccinimide (2.564 g, 0.0144 mol) was added under N_2. A catalytic amount of 2,2'-azobis(2-methylpropionitrile) (AIBN) (62 mg, 0.38 mmol) was added slowly to the suspension and the resulting mixture was refluxed for 5 h under N_2. After cooling, the reaction mixture was filtered and the solvent was removed by rotary evaporation to yield a yellow oil. Re-crystallisation from petroleum ether (60-80°C) at –10°C yielded colourless crystals which were filtered, dried *in vacuo* and stored under N_2. (1.55 g, 6.98 mmol, 53.7% yield). ^1H NMR ($CDCl_3$): δ_H 4.66 (CH_2Br, 2H, s), 7.39-7.43 (C*H* arom., 1H, m), 7.72-7.76 (C*H* arom., 1H, m), 7.81 (C*H* arom., 1H, d), 8.08-8.14 (C*H* arom., 2H, m),

8.91-8.93 (C*H* arom., 1H, m). EI^{+} mass spectrum: *m/z*: 221(M^{+}). Found (calc. for $C_{10}H_8NBr$): C, 53.85 (54.10); H, 3.51(3.65); N, 6.18% (6.30%).

8.4.4 Synthesis of 1,4,7-*tris*(7-methylquinolyl)-1,4,7-triazacyclononane (L^{11})

A solution of 7-bromoquinoline (0.806 g, 3.63 mmol) in freshly distilled EtOH (100 cm^3, cooled in an ice bath) was added over 1 h to a suspension of [9]aneN_3 (0.155 g, 1.20 mmol) and K_2CO_3 (0.75 g, 5.40 mmol) in dry EtOH (150 cm^3). The reaction mixture was refluxed under N_2 for 15 minutes and then stirred at room temperature for 2 days. The solvent was removed under reduced pressure to yield a yellow oil which was dissolved in $CHCl_3$ (100 cm^3) and washed with water (2 × 50 cm^3). The organic phase was collected and dried over $MgSO_4$. After filtration, the solvent was removed under reduced pressure to give a pale yellow oil. Purification was achieved *via* the formation of the HPF_6 salt, by adding a few drops of concentrated HPF_6 into an EtOH solution of the ligand and filtering the pale green solid obtained (0.85 g, 9.26 mmol, 77.2% yield). ^1H NMR (CD_3CN): δ_H 2.90-3.03 (CH_2 ring, 12H, m), 4.07 (CH_2 arms, 6H, s), 7.43 (C*H* arom., 1H, d, J = 8.86 Hz), 7.84 (C*H* arom., 1H, q, J_1= 8.38 Hz, J_2= 4.96 Hz), 8.02 (C*H* arom., 1H, s), 8.09 (C*H* arom., 1H, d, J = 8.73 Hz), 8.74 (C*H* arom., 1H, d, J = 8.15 Hz) and 9.01 (C*H* arom., 1H, d, J = 4.87 Hz) ppm. ^{13}C NMR (CD_3CN): δ_C 50.21 (CH_2 ring), 60.00 (CH_2 arms), 123.45, 125.69, 131.09, 135.20, 144.46, 148.62 (*C*H arom), 129.69, 136.76 and 142.25 (*C* arom) ppm. FAB mass spectrum (3-NOBA matrix): *m/z* 553 (M^{+}). Found (calc. for $C_{36}H_{38.5}N_6P_{2.5}F_{15}$): C, 46.66 (47.12); H, 4.45 (4.23); N, 8.83% (9.16%). IR spectrum (KBr disk): ν 2924m, 2849m, 1506m, 1384s, 1325m, 1172m, 1114s, 839m, 557m cm^{-1}.

8.4.5 Synthesis of 1,4,7-*tris*(7-methylquinolyl)-1,4,7-triaza-10,13-dioxacyclopentadecane (L^{12})

A solution of 7-bromoquinoline (0.358 g, 1.61 mmol) in freshly distilled EtOH (60 cm^3, cooled in an ice bath) was added over 1 h to a suspension of

[15]aneN_3O_2 (0.117 g, 0.54 mmol) and K_2CO_3 (0.40 g, 2.90 mmol) in dry EtOH (100 cm^3). The reaction mixture was stirred at room temperature for 2 days. The solvent was removed under reduced pressure to yield a yellow oil which was dissolved in $CHCl_3$ (80 cm^3) and washed with water (2 × 40 cm^3). The organic phase was collected, dried over $MgSO_4$, filtered and dried under reduced pressure to give a pale yellow oil which had to be stored under N_2 (0.29 g, 0.045 mmol, 83.6% yield). ^1H NMR ($CDCl_3$): δ_H 2.75-2.93 (NCH_2 ring, 12H, m), 3.60-3.66 (OCH_2 ring, 8H, m), 3.74 (CH_2 arms, 6H, s), 7.31-7.34 (C*H* arom., 1H, m), 7.56-7.96 (C*H* arom., 4H, m), 8.82-8.86 (C*H* arom., 1H, m) ppm. FAB mass spectrum (3-NOBA matrix): *m/z* 641 (M^+). Found (calc. for $C_{50}H_{64}N_6O_2$): C, 76.49 (76.88); H, 8.45 (8.26); N, 10.93% (10.76%). IR spectrum (KBr disk): ν 2924m, 2854m, 1504m, 1384s, 1303m, 1175s, 1125m, 841m cm^{-1}.

8.4.6 Synthesis of silver(I) complexes with L^{11} and L^{12}

[$Ag_2(L^{11})(PF_6)2$. A mixture of silver hexafluorophosphate (27.8 mg, 0.110 mmol) and 1,4,7-*tris*(7-methylquinolyl)-1,4,7-triazacyclononane (L^{11}) (30.5 mg, 0.055 mmol) in CH_3CN (15 cm^3) was stirred for 3h at room temperature. The solvent was partially removed under reduced pressure and Et_2O vapour was allowed to diffuse into the remaining solution, thereby affording colourless crystals (38.6 mg, 0.036 mmol, 65.9% yield). Mass spectrum (electrospray) *m/z*: 661 for [$^{107}Ag(L^{11})]^+$. Found (calc. for $C_{36}H_{36}P_2F_{12}N_6Ag_2$): C, 39.92 (40.86); H, 3.01 (3.43); N, 7.48% (7.94%). IR spectrum (KBr disc) ν 2926m, 2849w, 1635m, 1506m, 1384s, 1304m, 1140s, 843m cm^{-1}.

[$Ag_2(L^{12})(PF_2O_2)_2$. $AgPF_6$ (21.2 mg, 0.084 mmol) was dissolved acetonitrile (15 ml) and a solution of 1,4,7-*tris*(7-methylquinolyl)-1,4,7-triaza-10,13-dioxacyclopentadecane (L^{12}) (27.1 mg, 0.042 mmol) in CH_3CN (15 cm^3) was added dropwise. The solution was stirred for 3 h at room temperature. Single crystals suitable for X-ray structural analysis were obtained by diffusion of Et_2O

vapour into a CH_3CN solution of the complex at room temperature (20.2 mg, 45.5% yield). Mass spectrum (electrospray) *m/z*: 957 for $[^{107}Ag_2(L^{12})(PF_2O_2)]^+$ and 749 for $[^{107}Ag(L^{12})]^+$ (the PF_2O_2 anion was also detected: *m/z*: 101). Found (calc. for $C_{52}H_{67}Ag_2F_4N_7O_6P_2$): C, 50.03 (50.38); H, 5.83 (5.45); N, 7.65% (7.91%). IR spectrum (KBr disc) ν 2925m, 2854s, 1496m, 1385s, 1160s, 850s, 498s cm^{-1}.

8.4.7 Crystal structures determination

Crystal data and refinement details for all the structures are reported in Tables 8.5 and 8.6. The crystals were cooled using an Oxford Cryosystem open-flow nitrogen cryostat. Data were collected on a Stoe Stadi-4 four circle diffractometer using ω–θ scans for $\{[Ag(L^1)]PF_6\}_\infty$; for $\{[Ag(L^1)]BF_4\}_\infty$, $\{[Ag(L^8)]BF_4\}_\infty$, $[Ag(L^{10})]PF_2O_2$ and $[Ag_{2.5}(L^{12})(PF_2O_2)_{2.5}\cdot CH_3CN]$ data were collected on a Bruker SMART1000 CCD area detector diffractometer using ω scans. Data were corrected for Lorentz and polarisation effects and absorption corrections were applied using ψ-scan methods for the data collected on the four circle diffractometer and semi-empirical methods for the data collected on the area detector diffractometer. All the structures were solved by direct methods using the *SHELXS* program[322] followed by least squares refinement and difference Fourier synthesis.[323] All non-H atoms were refined anisotropically and H atoms were introduced at calculated positions and thereafter incorporated into a riding model with $U_{iso}(H) = 1.2U_{eq}(C)$.

In $\{[Ag(L^8)]BF_4\}_\infty$ the BF_4^- ion and part of the [15]aneN_3O_2 framework were both found to be disordered. The disorder in the BF_4^- ion was modelled by two equally occupied sites for each F atom to give two tetrahedra coincident at the boron. The components were refined isotropically with restraints to impose tetrahedral geometry on each. The disorder in the macrocyclic ligand was modelled with C(5), C(6), C(8) and O(10) each disordered over two sites with the occupancy factor 0.65 for the major components of C(5), C(6) and C(8)

and 0.7 for that of O(10). Appropriate restraints were applied to the bond lengths of the disordered portion of the macrocyclic ligand with both components being refined isotropically.

In $[Ag_{2.5}(L^{12})(PF_2O_2)_{2.5}\cdot CH_3CN]$ two $PF_2O_2^-$ anions and the MeCN molecule were found to be disordered and this disorder was modelled using partial occupancy models over two sites. F(5), F(6) and the MeCN molecule [N(1S), C(1S) and C(2S)] are the major components with occupancy factors of 0.6. O(10), F(11) and F(12) are part of the $PF_2O_2^-$ anion which was arbitrarily chosen to be the half occupied one and they have occupancy factor 0.3 (O(10'), F(11') and F(12') have occupancy of 0.2). Appropriate restraints were applied to bond lengths and angles involving the disordered atoms.

Table 8.5 Selected crystallographic data for the single crystal structures of $\{[Ag(L^1)]PF_6\}_\infty$, $\{[Ag(L^1)]BF_4\}_\infty$and of $\{[Ag(L^8)]BF_4\}_\infty$.

Compound	$\{[Ag(L^1)]PF_6\}_\infty$	$\{[Ag(L^1)]BF_4\}_\infty$	$\{[Ag(L^8)]BF_4\}_\infty$
Crystal Data			
Formula	$C_{12}H_{18}F_6N_6PAg$	$C_{12}H_{18}F_4N_6BAg$	$C_{16}H_{26}F_4N_6O_2BAg$
M / $gmol^{-1}$	499.16	441.00	529.11
Crystal size / mm	0.50 x 0.43 x 0.26	0.45 x 0.24 x 0.22	0.30 x 0.12 x 0.06
Crystal system	Monoclinic	Monoclinic	Monoclinic
Space group	$P2_1/n$	$P2_1/n$	$P2_1/n$
a / Å	10.652(9)	10.3140(10)	9.876(4)
b / Å	15.400(9)	14.846(2)	15.316(3)
c / Å	10.924(6)	10.6040(10)	14.823(4)
β/ °	92.14(6)	93.543(2)	108.022(2)
U / $Å^3$	1791(2)	1620.6(3)	2132.1(5)
Reflections used to refine cell	26	5089	4803
θ range / °	12.5 to 17	2.41 to 27.59	2.55 to 27.65
Z	4	4	4
D_c / gcm^{-3}	1.851	1.807	1.648
μ / mm^{-1}	1.283	1.293	1.005
F(000)	992	880	1072
T / K	150(2)	150(2)	150(2)
Data Collection			
Diffractometer	Stoe Stadi-4 four circle	Bruker SMART1000 CCD area detector	Bruker SMART1000 CCD area detector
Radiation, wavelength	MoK_α , 0.71073 Å	MoK_α , 0.71073 Å	MoK_α , 0.71073 Å
θ_{max} / °	25.02	28.67	28.93
Range of *h*	-12 → 12	-13 → 13	-11 → 13
Range of *k*	0 → 18	-19 → 18	-19 → 20
Range of *l*	-12 → 12	-14 → 13	-20 → 14
Measured reflections	5626	14047	13541
Unique reflections, R_{int}	3151, 0.0440	3848, 0.020	5006, 0.052
Observed reflections	2895 [[$F_O \geq 4\sigma(F_O)$]	3553 [$F_O \geq 4\sigma(F_O)$]	3617 [$F_O \geq 4\sigma(F_O)$]
Absorption correction	ψ-scans	Semi-empirical	Semi-empirical
$TF_{max, min}$	0.7314, 0.5662	0.825, 0.677	0.888, 0.600
Solution			
Method	Direct methods	Direct methods	Direct methods
Using	SHELXS-97	SHELXS-97	SHELXS-97
Refinement			
Full matrix least squares on	F^2	F^2	F^2
Using	SHELXL-97	SHELXL-97	SHELXL-97
Weighting scheme *x*, *y*[a]	0.041, 4.892	0.031, 0.972	--, 20.130
Parameters refined	247	217	263
R_1, wR_2[b]	0.0364, 0.0940	0.0206, 0.0556	0.0476, 0.1242
Goodness-of-fit (*S*)	1.078	1.077	0.991
$(\Delta/\sigma)_{max}$	0.045	0.005	0.035
$\Delta\rho_{max, min}$ / $eÅ^{-3}$	+0.97, -1.02	+0.71, -0.40	+1.02, -0.89

[a] $w^{-1} = [\sigma^2(F_O^2) + (xP)^2 + yP]$, $P = [MAX(F_O^2, 0) + 2F_C^2\}/3$
[b] $[F_O \geq 4\sigma(F_O)]$

Table 8.5 Selected crystallographic data for the single crystal structures of $[Ag(L^{10})(PF_2O_2)]$ and of $[Ag_{2.5}(L^{12})(PF_2O_2)_{2.5}]$.

Compound	$[Ag(L^{10})(PF_2O_2)]$	$[Ag_{2.5}(L^{12})(PF_2O_2)_{2.5}]$
Crystal Data		
Formula	$C_{19}H_{32}F_2N_6O_4PAg$	$C_{42}H_{46}F_5N_7O_7P_{2.5}Ag_{2.5}$
M / $gmol^{-1}$	585.35	1202.96
Crystal size / mm	0.32 x 0.15 x 0.08	0.20 x 0.12 x 0.08
Crystal system	Monoclinic	Triclinic
Space group	$P2_1/c$	P-1
a / Å	9.8248(4)	12.3033(11)
b / Å	14.6417(7)	14.6638(13)
c / Å	17.5430(8)	16.2768(14)
α / °	90	63.492(1)
β/ °	105.747(1)	70.964(1)
γ / °	90	76.334(2)
U / $Å^3$	2428.9(2)	2469.8(4)
Reflections used to refine cell	6833	4777
2θ range / °	2.42 to 28.95	2.5 to 23.05
Z	4	2
D_c / gcm^{-3}	1.601	1.618
μ / mm^{-1}	0.948	1.138
F(000)	1200	1206
T / K	150(2)	150(2)
Data Collection		
Diffractometer	Bruker SMART1000 CCD area detector	Bruker SMART1000 CCD area detector
Radiation, wavelength	MoK_α , 0.71073 Å	MoK_α , 0.71073 Å
θ_{max} / °	28.95	28.67
Range of h	-13 → 5	-16 → 16
Range of k	-19 → 19	-19 → 18
Range of l	-23 → 23	-20 → 21
Measured reflections	15628	19676
Unique reflections, R_{int}	5930, 0.051	10954, 0.046
Observed reflections	4670 [$F_O \geq 4\sigma(F_O)$]	6044 [$F_O \geq 4\sigma(F_O)$]
Used reflections	5712	5712
Absorption correction	Semi-empirical	Semi-empirical
$TF_{max, min}$	0.875, 0.752	0.894, 0.757
Solution		
Method	Direct methods	Direct methods
Using	SHELXS-97	SHELXS-97
Refinement		
Full matrix least squares on	F^2	F^2
Using	SHELXL-97	SHELXL-97
Weighting scheme x, y[a]	0.039, --	0.167, --
Parameters refined	298	591
R_1, wR_2[b]	0.0299, 0.0679	0.0822, 0.2472
Goodness-of-fit (S)	0.982	1.055
$(\Delta/\sigma)_{max}$	0.001	0.005
$\Delta\rho_{max, min}$ / $eÅ^{-3}$	+0.81, -0.40	+1.49, -1.55

[a] $w^{-1} = [\sigma^2(F_O^2) + (xP)^2 + yP]$, $P = [MAX(F_O^2, 0) + 2F_C^2\}/3$
[b] $[F_O \geq 4\sigma(F_O)]$

References

1 N. F. Curtis, *J. Chem. Soc.*, 1960, 4409.

2 N. F. Curtis and D. A. House, *Chemistry & Industry*, 1961, 1708.

3 C. J. Pedersen, *J. Am. Chem. Soc.*, 1967, **89**, 7017.

4 M. C. Thompson and D. H. Busch, *J. Am. Chem. Soc.*, 1964, **86**, 3651.

5 J. E. Richman and T. J. Atkins, *J. Am. Chem. Soc.*, 1974, **96**, 2268.

6 S. Ogawa, T. Tamaguchi and N. Gotoh, *J. Chem. Soc., Perkin Trans. I*, 1974, 976.

7 B. Dietrich, J. M. Lehn and J. P. Sauvage, *Tetrahedron Lett.*, 1969, **34**, 2885.

8 C. J. Pedersen, *J. Org. Chem.*, 1971, **36**, 254.

9 J. M. Lehn, *Accounts Chem. Res.*, 1978, **11**, 49.

10 I. Bertini and *et al.*, *Bioinorganic Chemistry*; University Science Books: Mill Valley, California, 1994.

11 R. E. Dickerson and I. Geis: *Hemoglobin*; Benjamin/Cummings: Menlo Park, California, 1983.

12 K. S. Suslick and T. J. Reinert, *J. Chem. Educ.*, 1985, **62**, 974.

13 J. J. Katz, *J. Am. Chem. Soc.*, 1969, **91**, 2661.

14 R. Cammark, *Adv. Inorg. Chem.*, 1988, **32**, 297.

15 F. P. Guengerich and T. L. Macdonald, *Accounts Chem. Res.*, 1984, **17**, 9.

16 S. Lindskog, *Adv. Inorg. Biochem.*, 1982, **4**, 115.

17 T. G. Spiro, *Iron-Sulfur Proteins*; Wiley: New York, 1982.

18 A. G. Sykes, *Adv. Inorg. Chem.*, 1990, **36**, 377.

19 W. A. Volkert and T. J. Hoffman, *Chem. Rev.*, 1999, **99**, 2269.

20 Z. J. Guo and P. J. Sadler, *Angew. Chem., Int. Ed.*, 1999, **38**, 1513.

21 R. B. Lauffer, *Chem. Rev.*, 1987, **87**, 901.

22 P. Caravan, J. J. Ellison, T. J. McMurry and R. B. Lauffer, *Chem. Rev.*, 1999, **99**, 2293.

23 R. Bergonzi, L. Fabbrizzi, M. Licchelli and C. Mangano, *Coord. Chem. Rev.*, 1998, **170**, 31.

24 P. D. Beer, *Acc. Chem. Res.*, 1998, **31**, 71.

25 B. Fabre and J. Simonet, *Coord. Chem. Rev.*, 1998, **180**, 1211.

26 E. Kimura and T. Koike, *Chem. Soc. Rev.*, 1998, **27**, 179.

27 B. L. Valeur and I. Leray, *Coord. Chem. Rev.*, 2000, **205**, 3.

28 A. F. de Silva, D.B. Fox, A.J.M. Huxley and T.S. Moody, *Coord. Chem. Rev.*, 2000, **205**, 41.

29 J. M. Lehn, *Angew. Chem., Int. Ed. Engl.*, 1988, **27**, 89.

30 A. F. Williams, C. Floriani and A. E. Merbach *Perspective in Coordination Chemistry*; VCH publishers, Inc.: Weinheim, 1992.

31 L. F. Lindoy, *The Chemistry of Macrocyclic Ligand Complexes*; Cambridge University Press: Cambridge, 1989.

32 C. J. Pedersen, *Angew. Chem., Int. Ed. Engl.,* 1988, **27**, 1021.

33 G. W. Gokel, *Crown ethers and cryptands*; Royal Society of Chemistry: Cambridge, 1991.

34 N. F. Curtis, *Coord. Chem. Rev.,* 1968, **3**, 3.

35 K. E. Krakowiak, J. S. Bradshaw and D. J. Zameckakrakowiak, *Chem. Rev.,* 1989, **89**, 929.

36 A. J. Blake and M. Schröder, *Adv. Inorg. Chem.,* 1990, **35**, 1.

37 A. M. Caminade and J. P. Majoral, *Chem. Rev.,* 1994, **94**, 1183.

38 H. W. Roesky, H. Djarrah, J. Lucas, M. Noltemeyer and G. M. Sheldrick, *Angew. Chem., Int. Ed. Engl.,* 1983, **22**, 1006.

39 E. G. Hope and W. Levason, *Coord. Chem. Rev.,* 1993, **122**, 109.

40 S. G. Murray and F. R. Hartley, *Chem. Rev.,* 1981, **81**, 365.

41 R. D. Hancock, H. Maumela and A. S. deSousa, *Coord. Chem. Rev.,* 1996, **148**, 315.

42 J. P. Danks, N. R. Champness and M. Schröder, *Coord. Chem. Rev.,* 1998, **174**, 417.

43 E. Weber and F. Vogtle, *Justus Liebigs Annales Chemistry,* 1976, 891.

44 P. H. Smith, J. R. Brainard, D. E. Morris, G. D. Jarvinen and R. R. Ryan, *J. Am. Chem. Soc.,* 1989, **111**, 7437.

45 C. R. Lucas, L. Shuang, M. J. Newlands and E. J. Gabe, *Can. J. Chem.,* 1990, **68**, 1357.

46 H. Okawa, H. Furutachi and D. E. Fenton, *Coord. Chem. Rev.,* 1998, **174**, 51.

47 J. E. Kickham and S. J. Loeb, *Inorg. Chem.,* 1995, **34**, 5656.

48 C. Bazzicalupi, A. Bencini, A. Bianchi, C. Giorgi, V. Fusi, A. Masotti, B. Valtancoli, A. Roque and F. Pina, *Chem. Commun.,* 2000, 561.

49 A. Bencini, M. A. Bernardo, A. Bianchi, V. Fusi, C. Giorgi, F. Pina and B. Valtancoli, *Eur. J. Inorg. Chem.,* 1999, 1911.

50 A. J. Blake, J. Casabo, F. A. Devillanova, L. Escriche, A. Garau, F. Isaia, V. Lippolis, R. Kivekas, V. Muns, M. Schröder, R. Sillanpaa and G. Verani, *J. Chem. Soc., Dalton Trans.,* 1999, 1085.

51 C. D. Gutsche and J. A. Levine, *J. Am. Chem. Soc.*, 1982, **104**, 2652.

52 P. Schmitt, P. D. Beer, M. G. B. Drew and P. D. Sheen, *Angew. Chem., Int. Ed. Engl.*, 1997, **36**, 1840.

53 C. O. Dietrich-Buchecker, J. P. Sauvage and J. M. Kern, *J. Am. Chem. Soc.*, 1984, **106**, 3043.

54 J. P. Sauvage, *Acc. Chem. Res.*, 1998, **31**, 611.

55 D. J. Cram, *Angew. Chem., Int. Ed.*, 1986, **25**, 1039.

56 F. A. Cotton and G. Wilkinson, *Advanced Inorganic Chemistry*; 5th Ed.; Wiley: New York, 1988.

57 A. E. Martell, R. D. Hancock and R. J. Motekaitis, *Coord. Chem. Rev.*, 1994, **133**, 39.

58 D. K. Cabbiness and D. W. Margerum, *J. Am. Chem. Soc.*, 1969, **91**, 6540.

59 L. L. Diaddario, L. L. Zimmer, T. E. Jones, L. S. W. L. Sokol, R. B. Cruz, E. L. Yee, L. A. Ochrymowycz and D. B. Rohrabacher, *J. Am. Chem. Soc.*, 1979, **101**, 3511.

60 D. H. Busch and N. A. Stephenson, *Coord. Chem. Rev.*, 1990, **100**, 119.

61 R. M. Clay, M. Micheloni, P. Paoletti and W. V. Steele, *J. Am. Chem. Soc.*, 1979, **101**, 4119.

62 R. M. Clay, H. McCormac, M. Micheloni and P. Paoletti, *Inorg. Chem.*, 1982, **21**, 2494.

63 R. M. Clay, S. Corr, M. Micheloni and P. Paoletti, *Inorg. Chem.*, 1985, **24**, 3330.

64 J. M. Desper, S. H. Gellman, R. E. Wolf and S. R. Cooper, *J. Am. Chem. Soc.*, 1991, **113**, 8663.

65 R. M. Izatt, J. S. Bradshaw, S. A. Nielsen, J. D. Lamb and J. J. Christensen, *Chem. Rev.*, 1985, **85**, 271.

66 C. J. Pedersen and H. K. Frensdorff, *Angew. Chem., Int. Ed.*, 1972, **11**, 16.

67 R. G. Pearson, *J. Am. Chem. Soc.*, 1963, **85**, 3533.

68 R. D. Hancock and A. E. Martell, *Chem. Rev.*, 1989, **89**, 1875.

69 A. E. Martell and R. M. Smith, *Critical Stability Constants*; Suppl. 2, 1989.

70 R. D. Hancock, *Pure Appl. Chem.*, 1986, **58**, 1445.

71 V. J. Thom and R. D. Hancock, *J. Chem. Soc., Dalton Trans.*, 1985, 1877.

72 L. Y. Martin, L. J. De Hayes, L. F. Zompa and D. H. Busch, *J. Am. Chem. Soc.*, 1974, **96**, 4047.

73 V. J. Thom, C. C. Fox, J. C. A. Boeyens and R. D. Hancock, *J. Am. Chem. Soc.*, 1984, **106**, 5947.

74 M. J. Vandermerwe, J. C. A. Boeyens and R. D. Hancock, *Inorg. Chem.*, 1985, **24**, 1208.

75 W. N. Setzer, C. A. Ogle, G. S. Wilson and R. S. Glass, *Inorg. Chem.*, 1983, **22**, 266.

76 S. M. Hart, J. C. A. Boeyens, J. P. Michael and R. D. Hancock, *J. Chem. Soc., Dalton Trans.*, 1983, 1602.

77 P. Chaudhuri and K. Wieghardt, *Prog. Inorg. Chem.*, 1987, **35**, 329.

78 D. J. Cram, *Angew. Chem., Int. Ed. Engl.*, 1988, **27**, 1009.

79 T. A. Kaden, *Top. Curr. Chem.*, 1984, **121**, 157.

80 P. V. Bernhardt and G. A. Lawrance, *Coord. Chem. Rev.*, 1990, **104**, 297.

81 G. W. Gokel, *Chem. Soc. Rev.*, 1992, **21**, 39.

82 K. P. Wainwright, *Coord. Chem. Rev.*, 1997, **166**, 35.

83 J. S. Bradshaw, K. E. Krakowiak, R. L. Bruening, B. J. Tarbet, P. B. Savage and R. M. Izatt, *J. Org. Chem.*, 1988, **53**, 3190.

84 J. S. Bradshaw, K. E. Krakowiak, R. M. Izatt, R. L. Bruening and B. J. Tarbet, *J. Heterocycl. Chem.*, 1990, **27**, 347.

85 H. Stetter and W. Frank, *Angew. Chem., Int. Ed.*, 1976, **15**, 686.

86 R. Delgado and J. Dasilva, *Talanta,* 1982, **29**, 815.

87 A. E. Martell, R. J. Motekaitis, E. T. Clarke, R. Delgado, Y. Z. Sun and R. Ma, *Supramol. Chem.*, 1996, **6**, 353.

88 S. Chaves, R. Delgado and J. Dasilva, *Talanta,* 1992, **39**, 249.

89 V. J. Thom, M. S. Shaikjee and R. D. Hancock, *Inorg. Chem.*, 1986, **25**, 2992.

90 T. Arishima, K. Hamada and S. Takamoto, *Nippon Nagaku Kaishi,* 1973, 1119.

91 H. Hama and S. Takamoto, *Nippon Nagaku Kaishi,* 1975, 1182.

92 M. Matsu-ura, F. Tani, S. Nakayama, N. Nakamura and Y. Naruta, *Angew. Chem., Int. Ed.*, 2000, **39**, 1989.

93 L. Ma, T. T. Tibbits and E. R. Kantrovitz, *Protein Science,* 1995, **4**, 1498.

94 E. Kimura and T. Koike, *J. Chem. Soc., Chem. Commun.*, 1998, 1495.

95 C. Bazzicalupi, A. Bencini, E. Berni, A. Bianchi, V. Fedi, V. Fusi, C. Giorgi, P. Paoletti and B. Valtancoli, *Inorg. Chem.*, 1999, **38**, 4115.

96 J. W. Whittaker, *Metalloenzymes involving Amino Acid Residue and related Radicals*; Marcel Dekker: New York, 1994; Vol. 30.

97 N. Ito, S. E. V. Phillips, C. Stevens, Z. B. Ogel, M. J. McPherson, J. N. Keen, K. D. S. Yadav and P. F. Knowles, *Nature,* 1991, **350**, 87.

98 M. M. Whittaker, P. J. Kersten, N. Nakamura, J. SandersLoehr, E. S. Schweizer and J. W. Whittaker, *J. Biol. Chem.,* 1996, **271**, 681.

99 J. A. Halfen, V. G. Young and W. B. Tolman, *Angew. Chem., Int. Ed. Engl.,* 1996, **35**, 1687.

100 J. A. Halfen, B. A. Jazdzewski, S. Mahapatra, L. M. Berreau, E. C. Wilkinson, L. Que and W. B. Tolman, *J. Am. Chem. Soc.,* 1997, **119**, 8217.

101 J. Muller, T. Weyhermuller, E. Bill, P. Hildebrandt, L. Ould, Moussa, T. Glaser and K. Wieghardt, *Angew. Chem., Int. Ed.,* 1998, **37**, 616.

102 P. Chaudhuri, M. Hess, J. Muller, K. Hildenbrand, E. Bill, T. Weyhermuller and K. Wieghardt, *J. Am. Chem. Soc.,* 1999, **121**, 9599.

103 D. E. De Vos, S. de Wildeman, B. F. Sels, P. J. Grobet and P. A. Jacobs, *Angew. Chem., Int. Ed.,* 1999, **38**, 980.

104 R. M. Izatt, R. L. Bruening, J. S. Bradshaw, J. D. Lamb and J. J. Christensen, *Pure Appl. Chem.,* 1988, **60**, 453.

105 Y. Habata and S. Akabori, *Coord. Chem. Rev.,* 1996, **148**, 97.

106 G. W. Gokel, J. E. Trafton, A. E. Kaifer, L. Echegoyen and S. Shinkai, *Cation Binding by Macrocycles*; Y. Inoue and G.W. Gokel Eds., Dekker: New York, 1990.

107 I. M. Atkinson, J. D. Chartres, G. W. Everett, X. K. Ji, L. F. Lindoy, O. A. Matthews, G. V. Meehan, B. W. Skelton, G. Wei and A. H. White, *J. Chem. Soc., Dalton Trans.,* 2000, **7**, 1191.

108 T. Hirano, K. Kikuchi, Y. Urano, T. Higuchi and T. Nagano, *Angew. Chem., Int. Ed.,* 2000, **39**, 1052.

109 A. P. deSilva, H. Q. N. Gunaratne, T. Gunnlaugsson, A. J. M. Huxley, C. P. McCoy, J. T. Rademacher and T. E. Rice, *Chem. Rev.,* 1997, **97**, 1515.

110 J. M. Lehn, *Supramolecular Chemistry: Concepts and Perspectives*; VCH Publishers, Inc., 1995.

111 G. R. Choppin, M. F. Tweedle, J. C. G. Bunzli, C. F. G. C. Geraldes and A. D. Sherry, *Lanthanide Probes in Life, Chemical and Earth Sciences*; J. C. G. Bunzli and G.R. Choppin Eds., Elsevier: Amsterdam, 1989.

112 R. M. Izatt, K. Pawlak, J. S. Bradshaw and R. L. Bruening, *Chem. Rev.,* 1991, **91**, 1721.

113 L. Thunus and R. Lejeune, *Coord. Chem. Rev.,* 1999, **184**, 125.

114 V. Wing-Wah Yam and K. Kam-Wing Lo, *Coord. Chem. Rev.,* 1999, **184**, 157.

115 N. Sabbatini, M. Guardigli and J. M. Lehn, *Coord. Chem. Rev.,* 1993, **123**, 201.

116 G. Mathis, *Clin. Chem.,* 1995, **41**, 1391.

117 E. F. G. Dickson, A. Pollak and E. P. Diamandis, *J. Photochem. Photobiol. B-Biol.,* 1995, **27**, 3.

118 D. Parker and J. A. G. Williams, *J. Chem. Soc., Dalton Trans.,* 1996, 3613.

119 D. Parker, P. K. Senanayake and J. A. G. Williams, *J. Chem. Soc., Perkin Trans. 2,* 1998, 2129.

120 D. Parker, *Coord. Chem. Rev.,* 2000, **205**, 109.

121 J. L. Sessler, N. A. Tvermoes, J. Davis, P. Anzenbacher, K. Jursikova, W. Sato, D. Seidel, V. Lynch, C. B. Black, A. Try, B. Andrioletti, G. Hemmi, T. D. Mody, D. J. Magda and V. Kral, *Pure Appl. Chem.,* 1999, **71**, 2009.

122 J. L. Sessler and R. A. Miller, *Biochem. Pharmacol.,* 2000, **59**, 733.

123 P. R. Selvin, T. M. Rana and J. E. Hearst, *J. Am. Chem. Soc.,* 1994, **116**, 6029.

124 J. Coates, P. G. Sammes and R. M. West, *J. Chem. Soc., Chem. Commun.,* 1995, 1107.

125 C. J. Anderson and M. J. Welch, *Chem. Rev.,* 1999, **99**, 2219.

126 S. Aime, M. Botta, S. G. Crich, G. Giovenzana, G. Palmisano and M. Sisti, *Bioconjugate Chem.,* 1999, **10**, 192.

127 S. Aime, M. Botta, M. Fasano and E. Terreno, *Chem. Soc. Rev., 1*998, **27**, 19.

128 U. Casellato, S. Tamburini, P. Tomasin, P. A. Vigato, S. Aime, A. Barge and M. Botta, *Chem. Commun.,* 2000, 145.

129 P. Mansfield and P.G. Morris, *NMR Imaging in Biomedicine*; Academic Press: New York, 1982.

130 S. W. Young, *Magnetic Resonance Imaging: Basic Principles*; Raven Press, New Raven Press: New York, 1988.

131 P. A. Rinck, *Magnetic Resonance in Medicine*; Blackwell: Oxford, U.K., 1993.

132 A. D. Nunn, K. Linder and M. F. Tweedle, *Q. J. Nucl. Med.,* 1997, **41**, 155.

133 K. Kumar, *J. Alloy. Compd.,* 1997, **249**, 163.

134 S. M. Rocklage, D. Worah and S. H. Kim, *Magn. Reson. Med.,* 1991, **22**, 216.

135 W. P. Cacheris, S. C. Quay and S. M. Rocklage, *Magn. Reson. Imaging,* 1990, **8**, 467.

136 P. Wedeking, K. Kumar and M. F. Tweedle, *Magn. Reson. Imaging,* 1992, **10**, 641.

137 K. Kumar, M. F. Tweedle, M. F. Malley and J. Z. Gougoutas, *Inorg. Chem.,* 1995, **34**, 6472.

138 N. R. Puttagunta, W. A. Gibby and G. T. Smith, *Invest. Radiol.,* 1996, **31**, 739.

139 R. Ramasamy, D. M. Defreitas, W. Jones, F. Wezeman, R. Labotka and C. Geraldes, *Inorg. Chem.,* 1990, **29**, 3979.

140 L. Banci, I. Bertini and C. Luchinat, *Coord. Chem. Rev., 1*996, **150**, 1, 296.

141 L. Banci, I. Bertini and C. Luchinat, *Nuclear and Electron Relaxation*; VCH Publishers, Inc.: Weinheim, 1991.

142 M. Botta, *Eur. J. Inorg. Chem.,* 2000, 399.

143 S. H. Koenig and R. D. Brown, *Prog. Nucl. Magn. Reson. Spectrosc.,* 1990, **22**, 487.

144 S. Aime, M. Botta, E. Garino, S. G. Crich, G. Giovenzana, R. Pagliarin, G. Palmisano and M. Sisti, *Chem., Eur. J.,* 2000, **6**, 2609.

145 S. Aime, M. Botta, M. Fasano, S. G. Crich and E. Terreno, *Coord. Chem. Rev.,* 1999, **186**, 321.

146 S. Aime, M. Botta, M. Fasano and E. Terreno, *Acc. Chem. Res.,* 1999, **32**, 941.

147 J. A. Peters, J. Huskens and D. J. Raber, *Prog. Nucl. Magn. Reson. Spectrosc.,* 1996, **28**, 283.

148 B. G. Jenkins, E. Armstrong and R. B. Lauffer, *Magn. Reson. Med.,* 1991, **17**, 164.

149 R. C. Brasch, *Magn. Reson. Med.,* 1991, **22**, 282.

150 A. S. Batsanov, A. Beeby, J. I. Bruce, J. A. K. Howard, A. M. Kenwright and D. Parker, *Chem. Commun.,* 1999, 1011.

151 K. I. Hardcastle, M. Botta, M. Fasano and G. Digilio, *Eur. J. Inorg. Chem.,* 2000, 971.

152 M. Botta, *First COST D1 European Workshop*, Coimbra, 1995, pp 24, Abstract book.

153 S. Aime, M. Botta, S. G. Crich, G. B. Giovenzana, R. Pagliarin, M. Piccinini, M. Sisti and E. Terreno, *J. Biol. Inorg. Chem.,* 1997, **2**, 470.

154 S. Aime, M. Botta, S. G. Crich, G. Giovenzana, R. Pagliarin, M. Sisti and E. Terreno, *Magn. Reson. Chem.,* 1998, **36**, S200.

155 C. Geraldes, A. D. Sherry, P. Vallet, F. Maton, R. N. Muller, T. D. Mody, G. Hemmi and J. L. Sessler, *J. Magn. Reson. Imaging,* 1995, **5**, 725.

156 J. Hall, R. Haner, S. Aime, M. Botta, S. Faulkner, D. Parker and A. S. de Sousa, *New J. Chem.,* 1998, **22**, 627.

157 J. Lisowski, J. L. Sessler, V. Lynch and T. D. Mody, *J. Am. Chem. Soc.,* 1995, **117**, 2273.

158 J. L. Sessler, T. D. Mody, G. W. Hemmi, V. Lynch, S. W. Young and R. A. Miller, *J. Am. Chem. Soc.,* 1993, **115**, 10368.

159 S. W. Young, F. Qing, A. Harriman, J. L. Sessler, W. C. Dow, T. D. Mody, G. W. Hemmi, Y. P. Hao and R. A. Miller, *Proc. Natl. Acad. Sci. U. S. A.,* 1996, **93**, 6610.

160 K. E. Kellar, P. M. Henrichs, R. Hollister, S. H. Koenig, T. Eck and D. Wei, *Magn. Reson. Med.,* 1997, **38**, 712.

161 E. Toth, L. Helm, K. E. Kellar and A. E. Merbach, *Chem., Eur. J.,* 1999, **5**, 1202.

162 E. Toth, D. Pubanz, S. Vauthey, L. Helm and A. E. Merbach, *Chem., Eur. J.,* 1996, **2**, 1607.

163 L. D. Margerum, B. K. Campion, M. Koo, N. Shargill, J. J. Lai, A. Marumoto and P. C. Sontum, *J. Alloy. Compd.,* 1997, **249**, 185.

164 L. H. Bryant, M. W. Brechbiel, C. C. Wu, J. W. M. Bulte, V. Herynek and J. A. Frank, *Proc. 6th Intl. Soc. Magn. Reson. Med. Conference*, Sidney, Australia, 1998.

165 L. H. Bryant, M. W. Brechbiel, C. C. Wu, J. W. M. Bulte, V. Herynek and J. A. Frank, *J. Magn. Reson. Imaging,* 1999, **9**, 348.

166 C. Corot, M. Schaefer, S. Beaute, P. Bourrinet, S. Zehaf, V. Benize, M. Sabatou and D. Meyer, *Acta Radiol.,* 1997, **38**, 91.

167 P. F. Sieving, A. D. Watson and S. M. Rocklage, *Bioconjugate Chem.,* 1990, **1**, 65.

168 C. Curtet, F. Maton, T. Havet, M. Slinkin, A. Mishra, J. F. Chatal and R. N. Muller, *Invest. Radiol.,* 1998, **33**, 752.

169 S. Aime, M. Botta, S.G. Crich, G. Giovenzana, G. Palmisano, M. Sisti, *Chem. Commun.,* 1999, 1577.

170 J. A. Meyer, *American Surgery,* 1974, **179**, 88.

171 R. J. Gillies, Z. Liu and Z. Bhujwalla, *Am. J. Physiology.,* 1994, C195.

172 Y. Aoki, K. Akagi, Y. Tanaka, J. Kawai and M. Takahashi, *Invest. Radiol.,* 1996, **31**, 680

173 D. J. Parmelee, R. C. Walovitch, H. S. Ouellet and R. B. Lauffer, *Invest. Radiol.,* 1997, **32**, 741.

174 R. B. Lauffer, D. J. Parmelee, S. U. Dunham, H. S. Ouellet, R. P. Dolan, S. Witte, T. J. McMurry and R. C. Walovitch, *Radiology,* 1998, **207**, 529.

175 R. A. Wallace, J. P. Haar, D. B. Miller, S. R. Woulfe, J. A. Polta, K. P. Galen, M. R. Hynes and K. Adzamli, *Magn. Reson. Med.,* 1998, **40**, 733.

176 S. Aime, M. Botta, M. Fasano, S. G. Crich and E. Terreno, *J. Biol. Inorg. Chem.*, 1996, **1**, 312.

177 S. Aime, M. Botta, L. Frullano, S.G. Crich, G.B. Giovenzana, R. Pagliarin, G. Palmisano and M. Sisti, *Chem., Eur. J.*, 1999, **5**, 1253.

178 R. B. Lauffer, T. J. McMurry, S. O. Dunham, D. M. Scott, D. J. Parmelee and S. Dumas, 1997, PCT Int. Appl. WO9736619.

179 W. H. Li, S. E. Fraser and T. J. Meade, *J. Am. Chem. Soc.*, 1999, **121**, 1413.

180 S. R. Zhang, K. C. Wu and A. D. Sherry, *Angew. Chem., Int. Ed.*, 1999, **38**, 3192.

181 R. A. Moats, S. E. Fraser and T. J. Meade, *Angew. Chem., Int. Ed. Engl.*, 1997, **36**, 726.

182 P. L. Anelli, I. Bertini, M. Fragai, L. Lattuada, C. Luchinat and G. Parigi, *Eur. J. Inorg. Chem.*, 2000, 625.

183 M. G. B. Drew, *Coord. Chem. Rev.*, 1977, **24**, 179.

184 L. J. Guggenberger and E. L. Muetterties, *J. Am. Chem. Soc.*, 1976, **98**, 7221.

185 F. Uggeri, S. Aime, P. L. Anelli, M. Botta, M. Brocchetta, C. Dehaen, G. Ermondi, M. Grandi and P. Paoli, *Inorg. Chem.*, 1995, **34**, 633.

186 M. R. Spirlet, J. Rebizant, J. F. Desreux and M. F. Loncin, *Inorg. Chem.*, 1984, **23**, 359.

187 S. S. Jurisson and J. D. Lydon, *Chem. Rev.*, 1999, **99**, 2205.

188 S. Liu and D. S. Edwards, *Chem. Rev.*, 1999, **99**, 2235.

189 K. Kukulski, J. Liniecki, D. Brykalski, O. Zadrozna and J. Kapuscinski, *Nucl. Med. Comm.*, 1995, **16**, 747.

190 H. B. Wester, J. Brokmann, F. Rosch, W. Wutz, H Herzog, P. SmithJones, B. Stolz, C. Bruns, G. Stocklin, *Nucl. Med. Biol.*, 1997, **24**, 275.

191 H. R. Herzog, F. Rosch, J. Brockmann, H. Muhlensiepen, M. Kohle, B. Stolz, P. Marbach and H.W. MullerGartner, *J. Nucl. Med.*, 1997, **38**, 215.

192 S. Jurisson, D. Berning, W. Jia and D. S. Ma, *Chem. Rev.*, 1993, **93**, 1137.

193 D. E. Reichert, C.J. Anderson and M.J. Welch, *Chemistry & Industry*, 1998, 731.

194 J. L. Sessler, W. C. Dow, D. Oconnor, A. Harriman, G. Hemmi, T. D. Mody, R. A. Miller, F. Qing, S. Springs, K. Woodburn and S. W. Young, *J. Alloy. Compd.*, 1997, **249**, 146.

195 W. F. Goeckeler, D. E. Troutner, W. A. Volkert, B. Edwards, J. Simon and D. Wilson, *Nucl. Med. Biol.*, 1986, **13**, 479.

196 J. Simon, D. A. Wilson, S. A. Baughman, D. Leggett, W. F. Goeckeler, L. Stringham, W. A. Volkert and K. McMillian, *Proc. VII Intl. Symp. Radiopharm.Chem.,* 1988; Vol. 7, pp 359.

197 J. C. Lattimer, L. A. Corwin, J. Stapleton, W. A. Volkert, G. J. Ehrhardt, A. R. Ketring, J. E. Hewett, J. Simon and W. F. Goeckeler, *J. Nucl. Med.,* 1990, **31**, 586.

198 A. R. Fritzberg, L. M. Gustavson, M. D. Hylarides and J. M. Reno, *Chemical and Structural Approaches to Rational Drug Design*; D.B. Weiner, M.V. Williams, Eds.; CRC Press: Boca Raton, 1995.

199 O. W. Press, F. R. Appelbaum, J. F. Early and I. D. Bernstein, *Biological Therapy Cancer Update,* 1994, **4**, 1.

200 M. K. Moi, C. F. Meares, W. C. Cole and S. J. Denardo, *Abstr. Pap. Am. Chem. Soc.,* 1985, **189**, 30.

201 D. J. Buchsbaum, *Cancer Therapy with Radiolabelled Antibodies*; D.M. Goldenberg, Ed.; CRC Press: Boca Raton, 1995.

202 W. C. Eckelman and R. E. Gibson, *Nuclear Imaging in Drug Discovery, Development and Approval*; H.D. Burns, R.E. Gibson, R. Dannals and P. Siegl Eds; Birkhauser: Boston, 1993.

203 D. A. Goodwin, C. F. Meares and M. Osen, *J. Nucl. Med., 1*998, **39**, 1813.

204 J. C. Reubi, *Q. J. Nucl. Med.,* 1997, **41**, 63.

205 A. Heppeler, S. Froidevaux, H. R. Macke, E. Jermann, M. Behe, P. Powell and M. Hennig, *Chem., Eur. J.,* 1999, **5**, 1974.

206 A. Otte, E. Jermann, M. Behe, M. Goetze, H. C. Bucher, H. W. Roser, A. Heppeler, J. MuellerBrand and H. R. Maecke, *Eur. J. Nucl. Med.,* 1997, **24**, 792.

207 M. deJong, W. H. Bakker, E. P. Krenning, W. A. P. Breeman, M. E. Van der Pluijm, B. F. Bernard, T. J. Visser, E. Jermann, M. Behe, P. Powell and H. R. Macke, *Eur. J. Nucl. Med.,* 1997, **24**, 368.

208 J. R. Duncan, M. T. Stephenson, H. P. Wu and C. J. Anderson, *Cancer Res.,* 1997, **57**, 659.

209 B. F. Bernard, E. P. Krenning, W. A. P. Breeman, E. J. Rolleman, W. H. Bakker, T. J. Visser, H. Macke and M. de Jong, *J. Nucl. Med.,* 1997, **38**, 1929.

210 H. Akizawa, Y. Arano, T. Uezono, M. Ono, Y. Fujioka, T. Uehara, A. Yokoyama, K. Akaji, Y. Kiso, M. Koizumi and H. Saji, *Bioconjugate Chem.,* 1998, **9**, 662.

211 J. J. Peterson and C. F. Meares, *Bioconjugate Chem.,* 1999, **10**, 553, 557.

212 D. S. Wilbur, D. K. Hamlin, K. R. Buhler, P. M. Pathare, R. L. Vessella, P. S. Stayton and R. To, *Bioconjugate Chem.,* 1998, **9**, 322.

213 Y. Arano, *Q. J. Nucl. Med.,* 1998, **42**, 262.

214 R. S. Dickins, J. A. K. Howard, C. L. Maupin, J. M. Moloney, D. Parker, J. P. Riehl, G. Siligardi and J. A. G. Williams, *Chem., Eur. J.,* 1999, **5**, 1095.

215 A. Casnati, C. Fisher, M. Guardigli, A. Isernia, I. Manet, N. Sabbatini and R. Ungaro, *J. Chem. Soc., Perkin Trans. 2,* 1996, 395.

216 M. H. V. Werts, M. A. Duin, J. W. Hofstraat and J. W. Verhoeven, *Chem. Commun.,* 1999, 799.

217 S. Petoud, J. C. G. Bunzli, F. Renaud, C. Piguet, K. J. Schenk and G. Hopfgartner, *Inorg. Chem.,* 1997, **36**, 5750.

218 M. Elhabiri, R. Scopelliti, J. C. G. Bunzli and C. Piguet, *Chem. Commun.,* 1998, 2347.

219 S. Aime, M. Botta, D. Parker and J. A. G. Williams, *J. Chem. Soc., Dalton Trans.,* 1995, 2259.

220 A. Beeby, I. M. Clarkson, R. S. Dickins, S. Faulkner, D. Parker, L. Royle, A. S. de Sousa, J. A. G. Williams and M. Woods, *J. Chem. Soc., Perkin Trans. 2,* 1999, 493.

221 M. P. Lowe and D. Parker, *Chem. Commun.,* 2000, 707.

222 K. Wieghardt, *Pure Appl. Chem.,* 1988, **60**, 509.

223 R. I. Haines and A. McAuley, *Coord. Chem. Rev.,* 1981, **39**, 77.

224 H. Koyama and T. Yoshino, *Bull. Chem. Soc. Jpn.,* 1972, **96**, 481.

225 T. J. Atkins, J. E. Richman and W. F. Oetle, *Org. Synth.,* 1978, **58**, 86.

226 B. A. Sayer, J. P. Michael and R. D. Hancock, *Inorg. Chim. Acta, Letters,* 1983, **77**, L63.

227 S. L. Whitbread, J. M. Weeks, P. Valente, M. A. Buntine, S. F. Lincoln and K. P. Wainwright, *Aust. J. Chem.,* 1997, **50**, 853.

228 J. Huskens and A. D. Sherry, *J. Chem. Soc., Dalton Trans.,* 1998, 177.

229 J. Robb and R. D. Peacock, *Inorg. Chim. Acta,* 1986, **121**, L15.

230 I. A. Fallis, L. J. Farrugia, N. M. Macdonald and R. D. Peacock, *J. Chem. Soc., Dalton Trans.,* 1993, 2759.

231 D. A. Moore, P. E. Fanwick and M. J. Welch, *Inorg. Chem.,* 1990, **29**, 672.

232 U. Bossek, D. Hanke, K. Wieghardt and B. Nuber, *Polyhedron,* 1993, **12**, 1.

233 J. L. Sessler, J. W. Sibert and V. Lynch, *Inorg. Chim. Acta,* 1994, **216**, 89.

234 C. S. John, C. E. Costello and E. O. Schlemper, *Polyhedron,* 1992, **11**, 2651.

235 D. J. Evans, G. Garcia, G. J. Leigh, M. S. Newton and M. D. Santana, *J. Chem. Soc., Dalton Trans.,* 1992, 3229.

236 A. J. Blake, I. A. Fallis, S. Parsons, S. A. Ross and M. Schröder, *J. Chem. Soc., Dalton Trans* , 1996, 525.

237 A. J. Blake, I. A. Fallis, A. Heppeler, S. Parsons, S. A. Ross and M. Schröder, *J. Chem. Soc., Dalton Trans.,* 1996, 31.

238 R. S. Grimditch, PhD Thesis: *Synthesis and complexation of pendant arm aza macrocycles*; University of Nottingham, 1996.

239 G. W. Bushnell, D. G. Fortier and A. McAuley, *Inorg. Chem.,* 1988, **27**, 2626.

240 A. D. Kirk, P. Hoggard and H. U. Gudel, *Inorg. Chim. Acta,* 1995, **238**, 45.

241 O. D. Gupta, J. G. Chen, R. L. Kirchmeier and J. M. Shreeve, *Inorg. Chem.,* 1998, **37**, 5342.

242 A. Hammershoi and A. M. Sargeson, *Inorg. Chem., 1*983, **22**, 3554.

243 S. G. Taylor, M. R. Snow and T. W. Hambley, *Aust. J. Chem.,* 1983, **36**, 2359.

244 L. Tei, G. Baum, A. J. Blake, D. Fenske and M. Schröder, *J. Chem. Soc., Dalton Trans.,* 2000, 2793.

245 T. Beissel, K. S. Burger, G. Voigt, K. Wieghardt, C. Butzlaff and A. X. Trautwein, *Inorg. Chem.,* 1993, **32**, 124.

246 E. Kimura, Y. Kodama, T. Koike and M. Shiro, *J. Am. Chem. Soc.,* 1995, **117**, 8304.

247 A. E. Martell, K. N. Raymond, V. L. Pecoraro and F. L. Weitl, *Development of Iron Chelators for Clinical Use*; A.E. Martell, W.F. Anderson and D.G. Badman Eds.; Elsevier, North Holland, New York, 1981.

248 W. R. Harris, C. J. Carrano, S. R. Copper, S. R. Sofen, A. Avdeef, J. V. McArdel and K. N. Raymond, *J. Am. Chem. Soc., 1*979, **101**, 6097.

249 A. E. Martell, R. J. Motekaitis and M. J. Welch, *J. Chem. Soc., Chem. Commun.,* 1990, 1748.

250 E. T. Clarke and A. E. Martell, *Inorg. Chim. Acta,* 1991, **186**, 103.

251 S. M. Moerlein, M. J. Welch, K. N. Raymond and F. L. Weitl, *J. Nucl. Med.,* 1981, **22**, 710.

252 C. J. Mathias, M. J. Welch, M. A. Green, J. A. Thomas, A. E. Martell and Y. Sun, *J. of Labelled Compounds & Radiopharm.,* 1986, **23**, 1221.

253 C. J. Mathias, Y. Z. Sun, M. J. Welch, M. A. Green, J. A. Thomas, K. R. Wade and A. E. Martell, *Nucl. Med. Biol.,* 1988, **15**, 69.

254 C. J. Broan, J. P. L. Cox, A. S. Craig, R. Kataky, D. Parker, A. Harrison, A. M. Randall and G. Ferguson, *J. Chem. Soc., Perkin Trans. 2,* 1991, 87.

255 A. S. Craig, I. M. Helps, K. J. Jankowski, D. Parker, N. R. A. Beeley, B. A. Boyce, M. A. W. Eaton, A. T. Millican, K. Millar, A. Phipps, S. K. Rhind, A. Harrison and C. Walker, *J. Chem. Soc., Chem. Commun.,* 1989, 794.

256 J. P. L. Cox, A. S. Craig, I. M. Helps, K. J. Jankowski, D. Parker, M. A. W. Eaton, A. T. Millican, K. Millar, N. R. A. Beeley and B. A. Boyce, *J. Chem. Soc., Perkin Trans. 1,* 1990, 2567.

257 I. M. Helps, D. Parker, K. J. Jankowski, J. Chapman and P. E. Nicholson, *J. Chem. Soc., Perkin Trans. 1,* 1989, 2079.

258 J. R. Morphy, D. Parker, R. Kataky, M. A. W. Eaton, A. T. Millican, R. Alexander, A. Harrison and C. Walker, *J. Chem. Soc., Perkin Trans. 2,* 1990, 573.

259 P. H. Walton and K. N. Raymond, *Inorg. Chim. Acta,* 1995, **240**, 593.

260 A. D. Moore, M. J. Welch, K. R. Wade, A. E. Martell and R. J. Motekaitis, *7th Int. Symp. Radiopharmaceutical Chem.*, Groningen, The Nederlands, 1988.

261 D. A. Moore, P. E. Fanwick and M. J. Welch, *Inorg. Chem.,* 1989, **28**, 1504.

262 G. Winkelmann, D. van der Helm and J. B. E. Neilands, *Iron Transport in Microbes, Plants and Animals*; VCH Publishers, Inc.: Weinheim, 1987.

263 D. Bradley, *New Scientist,* 1991, **129**, 35.

264 U. Auerbach, U. Eckert, K. Wieghardt, B. Nuber and J. Weiss, *Inorg. Chem.,* 1990, **29**, 938.

265 U. Auerbach, T. Weyhermuller, K. Wieghardt, B. Nuber, E. Bill, C. Butzlaff and A. X. Trautwein, *Inorg. Chem.,* 1993, **32**, 508.

266 O. Schlager, K. Wieghardt, H. Grondey, A. Rufinska and B. Nuber, *Inorg. Chem.,* 1995, **34**, 6440.

267 O. Schlager, K. Wieghardt and B. Nuber, *Inorg. Chem.,* 1995, **34**, 6449.

268 O. Schlager, K. Wieghardt and B. Nuber, *Inorg. Chem.,* 1995, **34**, 6456.

269 T. Beissel, T. Glaser, F. Kesting, K. Wieghardt and B. Nuber, *Inorg. Chem.,* 1996, **35**, 3936.

270 V. Alexander, *Chem. Rev.,* 1995, **95**, 273.

271 D. E. Fenton and P. A. Vigato, *Chem. Soc. Rev.,* 1988, **17**, 69.

272 P. Guerriero, P. A. Vigato, D. E. Fenton and P. C. Hellier, *Acta Chem. Scand.,* 1992, **46**, 1025.

273 L. M. Vallarino, *Handbook of the Physics and Chemistry of Rare Hearths*; K.A. Gschneidner Jr. and L. Eyring Eds.; Elsevier Science Publishers B. V.; Amsterdam, 1991; Vol. 15, Chapter 104.

274 C. Piguet, C. Edder, H. Nozary, F. Renaud, S. Rigault and J. C. G. Bunzli, *J. Alloy. Compd.*, 2000, **303**, 94.

275 J. P. Costes, A. Dupuis, G. Commenges, S. Lagrave and J. P. Laurent, *Inorg. Chim. Acta,* 1999, **285**, 49.

276 A. Smith, S. J. Rettig and C. Orvig, *Inorg. Chem.,* 1988, **27**, 3929.

277 D. J. Berg, S. J. Rettig and C. Orvig, *J. Am. Chem. Soc.,* 1991, **113**, 2528.

278 E. C. Alyea, A. Malek and A. E. Vougioukas, *Can. J. Chem., Revue Canadienne De Chimie,* 1982, **60**, 667.

279 O. Kocian, K. W. Chiu, R. Demeure, B. Gallez, C. J. Jones and J. R. Thornback, *J. Chem. Soc., Perkin Trans. 1,* 1994, 527.

280 J. P. Costes, F. Dahan, A. Dupuis, S. Lagrave and J. P. Laurent, *Inorg. Chem.,* 1998, **37**, 153.

281 P. V. Bernhardt, B. M. Flanagan and M. J. Riley, *Aust. J. Chem.,* 2000, **53**, 229.

282 A. J. Blake, D. M. J. Doble, W. S. Li and M. Schröder, *J. Chem. Soc., Dalton Trans.,* 1997, 3655.

283 D. M. J. Doble, PhD thesis: *Complexes and aggregates of imino carboxylates*; University of Nottingham, 1998.

284 L. W. Yang, S. Liu, S. J. Rettig and C. Orvig, *Inorg. Chem.,* 1995, **34**, 4921.

285 S. J. Archibald, A. J. Blake, M. Schröder and R. E. P. Winpenny, *J. Chem. Soc., Chem. Commun.,* 1994, 1669.

286 S. J. Archibald, A. J. Blake, S. Parsons, M. Schröder and R. E. P. Winpenny, *J. Chem. Soc., Dalton Trans.,* 1997, 173.

287 U. Casellato, S. Tamburini, P. Tomasin, P. A. Vigato and M. Botta, *Inorg. Chim. Acta,* 1996, **247**, 143.

288 R. D. Shannon, *Acta Crystallogr., Sect. A, 1*976, **32**, 751.

289 F. A. Dunand, S. Aime and A. E. Merbach, *J. Am. Chem. Soc.,* 2000, **122**, 1506.

290 M. R. Spirlet, J. Rebizant, M. F. Loncin and J. F. Desreux, *Inorg. Chem.,* 1984, **23**, 4278.

291 J. F. Desreux, *Inorg. Chem., 1*980, **19**, 1319.

292 S. Aime, M. Botta and G. Ermondi, *Inorg. Chem.,* 1992, **31**, 4291.

293 S. Aime, A. S. Batsanov, M. Botta, R. S. Dickins, S. Faulkner, C. E. Foster, A. Harrison, J. A. K. Howard, J. M. Moloney, T. J. Norman, D. Parker, L. Royle and J. A. G. Williams, *J. Chem. Soc., Dalton Trans.*, 1997, 3623.

294 L. Di Bari, G. Pintacuda and P. Salvadori, *Eur. J. Inorg. Chem.*, 2000, 75.

295 J. P. Jesson, *NMR of Paramagnetic Molecules*; G.N. La Mar and W.DeW. Horrocks, Eds.; Academic Press Inc.; New York, 1973.

296 I. Bertini and C. Luchinat, *NMR of Paramagnetic Molecules in Biological Systems*; Benjamin-Cummings; Boston, MA, 1986.

297 B. Bleaney, *J. Mag. Reson., 1*972, **8**, 91.

298 I. Bertini and R. S. Drago, *ESR and NMR of Paramagnetic Species in Biological and Related Systems*; D. Reidel Publishing Company; Dordrech, Holland, 1980.

299 S. Aime and M. Botta, *Inorg. Chim. Acta,* 1990, **177**, 101.

300 B. G. Jenkins and R. B. Lauffer, *Inorg. Chem.,* 1988, **27**, 4730.

301 S. Aime, M. Botta, M. Fasano, M. P. M. Marques, C. Geraldes, D. Pubanz and A. E. Merbach, *Inorg. Chem.,* 1997, **36**, 2059.

302 C. Geraldes, A. M. Urbano, M. C. Alpoim, M. A. Hoefnagel and J. A. Peters, *J. Chem. Soc., Chem. Commun.,* 1991, 656.

303 C. Geraldes, A. M. Urbano, M. A. Hoefnagel and J. A. Peters, *Inorg. Chem.,* 1993, **32**, 2426.

304 K. Roth, G. Bartholomae, H. Bauer, T. Frenzel, S. Kossler, J. Platzek, B. Raduchel and H. J. Weinmann, *Angew. Chem., Int. Ed. Engl.,* 1996, **35**, 655.

305 T. Frenzel, K. Roth, S. Kossler, B. Raduchel, H. Bauer, J. Platzek and H. J. Weinmann, *Magn. Reson. Med.,* 1996, **35**, 364.

306 S. Aime, M. Botta, M. Fasano, E. Terreno, P. Kinchesh, L. Calabi and L. Paleari, *Magn. Reson. Med.,* 1996, **35**, 648.

307 C. S. Zuo, J. L. Bowers, K. R. Metz, T. Nosaka, A. D. Sherry and M. E. Clouse, *Magn. Reson. Med.,* 1996, **36**, 955.

308 J. Rohovec, I. Lukes and P. Hermann, *New J. Chem.,* 1999, **23**, 1129.

309 D. M. J. Doble and M. Schröder, *International Patent*, WO 98/39288, 1998.

310 J. Huskens, J. A. Peters, H. Vanbekkum and G. R. Choppin, *Inorg. Chem.,* 1995, **34**, 1756.

311 J. Huskens, A. D. Kennedy, H. Vanbekkum and J. A. Peters, *J. Am. Chem. Soc.*, 1995, **117**, 375.

312 M. C. Alpoim, A. M. Urbano, C. Geraldes and J. A. Peters, *J. Chem. Soc., Dalton Trans.,* 1992, 463.

313 P. Caravan, T. Hedlund, S. Liu, S. Sjoberg and C. Orvig, *J. Am. Chem. Soc.,* 1995, **117**, 11230.

314 C. A. M. Vijverberg, J. A. Peters, A. P. G. Kieboom and H. Vanbekkum, *Recueil Des Travaux Chimiques Des Pays Bas, J. Royal Netherlands Chem. Soc.,* 1980, **99**, 403.

315 J. A. Peters and M. S. Nieuwenhuizen, *J. Magn. Reson.,* 1985, **65**, 417.

316 M. S. Nieuwenhuizen, J. A. Peters, A. Sinnema, A. P. G. Kieboom and H. Vanbekkum, *J. Am. Chem. Soc.,* 1985, **107**, 12.

317 C. Cossy and A. E. Merbach, *Pure Appl. Chem.,* 1988, **60**, 1785.

318 C. Cossy, A. C. Barnes, J. E. Enderby and A. E. Merbach, *J. Chem. Phys.,* 1989, **90**, 3254.

319 L. Helm, F. Foglia, T. Kowall and A. E. Merbach, *Journal of Physics, Condensed Matter,* 1994, **6**, A137.

320 E. Brucher, J. Glaser, I. Grenthe and I. Puigdomenech, *Inorg. Chim. Acta, F, Block Elements Articles and Letters,* 1985, **109**, 111.

321 W. Herrendorf, *Habitus, program for absorption corrections*, University of Giessen, Germany, 1995.

322 G. M. Sheldrick, *Acta Crystallogr., Sect A, 1*990, **46**, 461.

323 G. M. Sheldrick, *SHELXS-97*, University of Göttingen, Germany, 1997.

324 I. Lazar, R. Ramasamy, E. Brucher, C. Geraldes and A. D. Sherry, *Inorg. Chim. Acta,* 1992, **195**, 89.

325 M. I. Kabachnik, T. Y. Medved, Y. M. Polikarpov, B. K. Shcherbakov, F. I. Bel'skii, E. I. Matrosov and M. P. Pasechnik, *Izv. Akad. Nauk SSSR, Ser. Khim., 1*984, 769.

326 C. Geraldes, A. D. Sherry and W. P. Cacheris, *Inorg. Chem.,* 1989, **28**, 3336.

327 C. Geraldes, R. D. Brown, W. P. Cacheris, S. H. Koenig, A. D. Sherry and M. Spiller, *Magn. Reson. Med.,* 1989, **9**, 94.

328 J. Huskens and A. D. Sherry, *J. Am. Chem. Soc., 1*996, **118**, 4396.

329 W. Clegg, P. B. Iveson and J. C. Lockhart, *J. Chem. Soc., Dalton Trans.,* 1992, 3291.

330 A. D. Sherry, *J. Alloy. Compd.,* 1997, **249**, 153.

331 A. D. Sherry, C. Geraldes and W. P. Cacheris, *Inorg. Chim. Acta,* 1987, **139**, 137.

332 A. D. Sherry, C. R. Malloy, F. M. H. Jeffrey, W. P. Cacheris and C. Geraldes, *J. Magn. Reson.*, 1988, **76**, 528.

333 C. Geraldes, A. D. Sherry, I. Lazar, A. Miseta, P. Bogner, E. Berenyi, B. Sumegi, G. E. Kiefer, K. McMillan, F. Maton and R. N. Muller, *Magn. Reson. Med.,* 1993, **30**, 696.

334 S. Aime, A. S. Batsanov, M. Botta, J. A. K. Howard, D. Parker, K. Senanayake and J.A.G. Williams, *Inorg. Chem.,* 1994, **33**, 4696.

335 I. Lazar, A. D. Sherry, R. Ramasamy, E. Brucher and R. Kiraly, *Inorg. Chem.*, 1991, **30**, 5016.

336 K. P. Pulukkody, T. J. Norman, D. Parker, L. Royle and C. J. Broan, *J. Chem. Soc., Perkin Trans. 2,* 1993, 605.

337 J. Vanwestrenen and A. D. Sherry, *Bioconjugate Chem.,* 1992, **3**, 524.

338 A. D. Sherry, J. Ren, J. Huskens, E. Brucher, E. Toth, C. Geraldes, M. Castro and W. P. Cacheris, *Inorg. Chem.,* 1996, **35**, 4604.

339 C. Geraldes, A. D. Sherry and G. E. Kiefer, *J. Magn. Reson.*, 1992, **97**, 290.

340 A. Harrison, C. A. Walker, K. A. Pereira, D. Parker, L. Royle, K. Pulukkody and T. J. Norman, *Magn. Reson. Imaging,* 1993, **11**, 761.

341 J. Rohovec, P. Vojtisek, P. Hermann, J. Mosinger, Z. Zak and I. Lukes, *J. Chem. Soc., Dalton Trans.,* 1999, 3585.

342 J. Rohovec, P. Vojtisek, P. Hermann, J. Ludvik and I. Lukes, *J. Chem. Soc., Dalton Trans.,* 2000, 141.

343 D. Parker, K. Pulukkody, T. J. Norman, A. Harrison, L. Royle and C. Walker, *J. Chem. Soc., Chem. Commun.,* 1992, 1441.

344 S. Aime, M. Botta, D. Parker and J. A. G. Williams, *J. Chem. Soc., Dalton Trans.,* 1996, 17.

345 W. D. Kim, G. E. Kiefer, J. Huskens and A. D. Sherry, *Inorg. Chem.,* 1997, **36**, 4128.

346 J. M. Ren and A. D. Sherry, *Inorg. Chim. Acta,* 1996, **246**, 331.

347 J. G. VanEmous, M. G. J. Nederhoff, T. J. C. Ruigrok and C. J. A. VanEchteld, *Journal of Molecular and Cellular Cardiology,* 1997, **29**, 85.

348 N. Bansal, M. J. Germann, V. Seshan, G. T. Shires, C. R. Malloy and A. D. Sherry, *Biochemistry,* 1993, **32**, 5638.

349 V. Seshan, M. J. Germann, P. Preisig, C. R. Malloy, A. D. Sherry and N. Bansal, *Magn. Reson. Med.,* 1995, **34**, 25.

350 R. Ramasamy, M. Castro, D. M. Defreitas and C. Geraldes, *Biochimie,* 1992, **74**, 777.

351 J. vanHaveren, L. DeLeon, R. Ramasamy, J. vanWestrenen and A. D. Sherry, *NMR in Biomedicine,* 1995, **8**, 197.

352 R. Ramasamy, I. Lazar, E. Brucher, A. D. Sherry and C. R. Malloy, *Febs Letters,* 1991, **280**, 121.

353 *CRC Handbook of Chemistry and Physics, 53rd Edn.*; R.C. Weast Ed., The Chemical Rubber Company:, 1972.

354 S. Aime, M. Botta, L. Milone and E. Terreno, *Chem. Commun.,* 1996, 1265.

355 A. Beeby, R. S. Dickins, S. Faulkner, D. Parker and J. A. G. Williams, *Chem. Commun.,* 1997, 1401.

356 M. P. Lowe, P. Caravan, S. J. Rettig and C. Orvig, *Inorg. Chem.,* 1998, **37**, 1637.

357 M. P. Lowe, S. J. Rettig and C. Orvig, *J. Am. Chem. Soc.,* 1996, **118**, 10446.

358 R. Karaman, A. Goldblum, E. Breuer and H. Leader, *J. Chem. Soc., Perkin Trans. 1,* 1989, 765.

359 S. Hoeft and K. Roth, *Chem. Ber., Recueil,* 1993, **126**, 869.

360 V. Jacques and J. F. Desreux, *Inorg. Chem.,* 1994, **33**, 4048.

361 S. Parkin, B. Moezzi and H. Hope, *J. Appl. Cryst.*, 1995, **28**, 53

362 M. Studer and T. A. Kaden, *Helv. Chim. Acta, 1*986, **69**, 2081.

363 M. Studer, A. Riesen and T. A. Kaden, *Helv. Chim. Acta, 1*989, **72**, 307.

364 H. Z. Cai and T. A. Kaden, *Helv. Chim. Acta, 1*993, **76**, 557.

365 N. W. Alcock, F. McLaren, P. Moore, G. A. Pike and S. M. Roe, *J. Chem. Soc. Chem. Commun., 1*989, 629.

366 G. R. Weisman, D. J. Vachon, V. B. Johnson and D. A. Gronbeck, *J. Chem. Soc., Chem. Commun., 1*987, 886.

367 J. L. Sessler, J. W. Sibert and V. Lynch, *Inorg. Chem., 1*990, **29**, 4143.

368 Z. Kovacs and A. D. Sherry, *Tetrahedron Lett., 1*995, **36**, 9269.

369 C. J. Broan, K. J. Jankowski, R. Kataky and D. Parker, *J. Chem. Soc., Chem. Commun., 1*990, 1738.

370 C. J. Broan, E. Cole, K. J. Jankowski, D. Parker, K. Pulukkody, B. A. Boyce, N. R. A. Beeley, K. Millar and A. T. Millican, *Synthesis,* 1992, 63.

371 D. Schulz, T. Weyhermuller, K. Wieghardt and B. Nuber, *Inorg. Chim. Acta,* 1995, **240**, 217.

372 D. Schulz, T. Weyhermuller, K. Wieghardt, C. Butzlaff and A. X. Trautwein, *Inorg. Chim. Acta,* 1996, **246**, 387.

373 D. Odom, C. J. Gramer, V. G. Young, S. A. Hilderbrand and S. E. Sherman, *Inorg. Chim. Acta,* 2000, **297**, 404.

374 A. J. Blake, I. A. Fallis, R. O. Gould, S. Parsons, S. A. Ross and M. Schröder, *J. Chem. Soc., Dalton Trans.,* 1996, 4379.

375 G. A. McLachlan, G. D. Fallon, R. L. Martin, B. Moubaraki, K. S. Murray and L. Spiccia, *Inorg. Chem.,* 1994, **33**, 4663.

376 G. A. McLachlan, G. D. Fallon, R. L. Martin and L. Spiccia, *Inorg. Chem.,* 1995, **34**, 254.

377 A. J. Blake, J. P. Danks, W.-S. Li, V. Lippolis and M. Schröder, *J. Chem. Soc., Dalton Trans.,* 2000, 3034.

378 L. J. Farrugia, P. A. Lovatt and R. D. Peacock, *Inorg. Chim. Acta,* 1996, **246**, 343

379 M. W. Brechbiel, T. J. McMurry and O. A. Gansow, *Tetrahedron Lett.,* 1993, **34**, 3691.

380 D. G. Fortier and A. McAuley, *J. Am. Chem. Soc.,* 1990, **112**, 2640.

381 L. R. Gahan, G. A. Lawrence and A. M. Sargeson, *Aust. J. Chem.,* 1982, **35**, 1119.

382 F. McLaren, P. Moore and A. M. Wynn, *J. Chem. Soc., Chem. Commun.,* 1989, 798.

383 I. A. Fallis, P. C. Griffiths, P. M. Griffiths, D. E. Hibbs, M. B. Hursthouse and A. L. Winnington, *Chem. Commun.,* 1998, 665.

384 A. J. Blake, I. A. Fallis, R. O. Gould, S. Parsons, S. A. Ross and M. Schröder, *J. Chem. Soc., Chem. Commun.,* 1994, 2467.

385 P. D. Beer and D. Gao, *Chem. Commun.,* 2000, 443.

386 C. Stockheim, L. Hoster, T. Weyhermuller, K. Wieghardt and B. Nuber, *J. Chem. Soc., Dalton Trans.,* 1996, 4409.

387 M. Di Vaira, F. Mani and P. Stoppioni, *Inorg. Chim. Acta,* 1998, **273**, 151.

388 J. P. Andre, H. R. Maecke, M. Zehnder, L. Macko and K. G. Akyel, *Chem. Commun.,* 1998, 1301.

389 K. Kumar, C. A. Chang, L. C. Francesconi, D. D. Dischino, M. F. Malley, J. Z. Gougoutas and M. F. Tweedle, *Inorg. Chem.,* 1994, **33**, 3567.

390 R. B. Shukla, *J. Magn. Reson. Ser. A,* 1995, **113**, 196

391 G. Sosnovsky and J. Lukszo, *Z.Naturforsch.(B),* 1994, **49**, 1580.

392 W. DeW. Horrocks and D. R. Sudnick, *J. Am. Chem. Soc.,* 1979, **101**, 334.

393 W. DeW. Horrocks and D. R. Sudnick, *Acc. Chem. Res.*, 1981, **14**, 384.

394 A. Bencini, L. Fabbrizzi and A. Poggi, *Inorg. Chem.,* 1981, **20**, 2544.

395 L. F. Lindoy, G. V. Meehan and N. Svenstrup, *Synthesis,* 1998, 1029.

396 R. A. Michelin, M. Mozzon and R. Bertani, *Coord. Chem. Rev.,* 1996, **147**, 299.

397 H. Endres, *Comprehensive Coordination Chemistry*; G. Wilkinson, R. D. Gillard and J. A. McCleverty Eds.; Pergamon, Oxford, 1987; vol 2, pp 261.

398 S. J. Bryan, P. G. Huggett, K. Wade, J. A. Daniels and J. R. Jennings, *Coord. Chem. Rev.,* 1982, **44**, 149.

399 D. H. Busch Ed., *Reactions of Coordinated Ligands and Homogeneous Catalysis*; Advances in Chemistry; Am. Chem. Soc.: Washington, DC, 1963.

400 K. R. Dunbar, *Comments Inorg. Chem.*, 1992, **13**, 313.

401 H. Aneetha, Y. H. Lai, S. C. Lin, K. Panneerselvam, T. H. Lu and C. S. Chung, *J. Chem. Soc., Dalton Trans.,* 1999, 2885.

402 V. Lippolis, PhD thesis: *Studies on the Coordination Chemistry of Macrocyclic Ligands*, The University of Nottingham, 2000.

403 C. S. Chin, D. Chong, B. Lee, H. Jeong, G. Won, Y. Do and Y. J. Park, *Organometallics,* 2000, **19**, 638.

404 N. V. Kaminskaia, I. A. Guzei and N. M. Kostic, *J. Chem. Soc., Dalton Trans.,* 1998, 3879.

405 P. Paul and K. Nag, *Inorg. Chem.,* 1987, **26**, 1586.

406 G. Lazarevski, M. Vinkovic, G. Kobrehel and S. Dokic, *Tetrahedron,* 1994, **50**, 12201.

407 F. Barbot, *Tetrahedron Lett.,* 1989, **30**, 185.

408 M. Pfau, A. Felk and G. Revial, *Tetrahedron Lett.,* 1994, **35**, 1549.

409 H. Winter, Y. Maeda, H. Mitsuya and J. Zemlicka, *J. Med. Chem.,* 1996, **39**, 3300.

410 J. March, *Advanced Organic Chemistry*, 4th ed.; Wiley Interscience, 1992; pp 887-888, 892, 903-904.

411 M. Wada and T. Shimohigashi, *Inorg. Chem.*, 1976, **15**, 954.

412 P. Paul and K. Nag, *J. Chem. Soc., Dalton Trans.,* 1988, 2373.

413 A. W. Zanella and P. C. Ford, *Inorg Chem.*, 1975, **14**, 42-47 and 700-701

414 T. Uchiyama, Y. Toshiyasu, Y. Nakamura, T. Miwa and S. Kawaguchi, *Bull. Chem. Soc. Jpn.,* 1981, **54**, 181.

415 F. P. Fanizzi, F. P. Intini, L. Maresca and G. Natile, *J. Chem. Soc., Dalton Trans.,* 1990, 199.

416 D. Fraccarollo, R. Bertani, M. Mozzon, U. Belluco and R. A. Michelin, *Inorg. Chim. Acta,* 1992, **201**, 15.

417 F. P. Fanizzi, F. P. Intini and G. Natile, *J. Chem. Soc., Dalton Trans.,* 1989, 947.

418 J. M. Casas, M. H. Chisholm, M. V. Sicilia and W. E. Streib, *Polyhedron,* 1991, **10**, 1573.

419 R. Breslow, R. Fairweather and J. Keana, *J. Am. Chem. Soc.,* 1967, **89**, 2135.

420 R. Breslow and M. Schmir, *J. Am. Chem. Soc.,* 1971, **93**, 4960.

421 D. A. Buckingham, P. Morris, A. M. Sargeson and A. Zanella, *Inorg. Chem.,* 1977, **16**, 1910.

422 C. R. Clark and R. W. Hay, *J. Chem. Soc., Dalton Trans.,* 1974, 2148.

423 R. Cini, P. A. Caputo, F. P. Intini and G. Natile, *Inorg. Chem.,* 1995, **34**, 1130.

424 G. Villain, A. Gaset and P. Kalck, *J. Molecular Catalysis,* 1981, **12**, 103.

425 C. M. Jensen and W. C. Trogler, *J. Am. Chem. Soc.,* 1986, **108**, 723.

426 A. J. Blake, P. Hubberstey, U. Suksangpanya and C. L. Wilson, *J. Chem. Soc., Dalton Trans.,* 2000, 3873.

427 D. G. Fortier and A. McAuley, *J. Chem. Soc., Dalton Trans.,* 1991, 101.

428 I. A. Fallis, R. D. Farley, K. M. A. Malik, D. M. Murphy and H. J. Smith, *J. Chem. Soc., Dalton Trans.,* 2000, 3632.

429 S. J. Brudenell, L. Spiccia and E. R. T. Tiekink, *Inorg. Chem.,* 1996, **35**, 1974.

430 S. J. Brudenell, L. Spiccia, A. M. Bond, P. Comba and D. C. R. Hockless, *Inorg. Chem., 1*998, **37**, 3705.

431 P. Chaudhuri, K. Oder, K. Wieghardt, B. Nuber and J. Weiss, *Inorg. Chem.,* 1986, **25**, 2818.

432 R. R. Holmes, *Progr. Inorg. Chem.,* 1984, **32**, 119.

433 R. R. Holmes, *J. Am. Chem. Soc.,* 1984, **106**, 3745.

434 S. C. Rawle, A. J. Clarke, P. Moore and N. W. Alcock, *J. Chem. Soc., Dalton Trans.,* 1992, 2755.

435 S. J. Brudenell, L. Spiccia, A. M. Bond, G. D. Fallon, D. C. R. Hockless, G. Lazarev, P. J. Mahon and E. R. T. Tiekink, *Inorg. Chem.,* 2000, **39**, 881.

436 B. Dietrich, J., M. Lehn and J. P. Sauvage, *J. Chem. Soc., Chem. Comm.,* 1970, 1055.

437 B. Dietrich, J., M. Lehn, J. P. Sauvage and J. Blanzat, *Tetrahedron,* 1973, **29**, 1629.

438 M. Herceg and R. Weiss, *Inorg. Nucl. Chem. Lett.,* 1970, **6**, 435.

439 G. Anderegg, A. Ekstrom, L. F. Lindoy and R. J. Smith, *J. Am. Chem. Soc.*, 1980, **102**, 2670.

440 R. D. Hancock, R. Bhavan, P. W. Wade, J. C. A. Boeyens and S. M. Dobson, *Inorg. Chem.*, 1989, **28**, 187.

441 M. W. Hosseini and J. M. Lehn, *J. Am. Chem. Soc.*, 1987, **109**, 7047.

442 K. A. Beveridge, A. McAuley and C. Xu, *Inorg. Chem.*, 1991, **30**, 2074.

443 M. Zinic, S. Alihodzic and V. Skaric, *J. Chem. Soc., Perkin Trans. 1*, 1993, 21.

444 L. Tei, V. Lippolis, A. J. Blake, P. A. Cooke and M. Schröder, *Chem. Commun.*, 1998, 2633.

445 V. Lippolis, A. J. Blake, P. A. Cooke, F. Isaia, W. S. Li and M. Schröder, *Chem., Eur. J.*, 1999, **5**, 1987.

446 L. Tei, A. Bencini, A.J. Blake, B. Valtancoli, C. Wilson and M. Schröder, *J. Chem. Soc., Dalton Trans.*, 2000, 4122.

447 M. F. Cabral and R. Delgado, *Helv. Chim. Acta*, 1994, **77**, 515.

448 C. Bazzicalupi, A. Bencini, A. Bianchi, F. Corana, V. Fusi, C. Giorgi, P. Paoli, P. Paoletti, B. Valtancoli and C. Zanchini, *Inorg. Chem.*, 1996, **35**, 5540.

449 M. F. Cabral, R. Delgado, M. T. Duarte and M. Teixeira, *Helv. Chim. Acta*, 2000, **83**, 702.

450 M. Gerloch, *Inorg. Chem.*, 1981, **20**, 638.

451 K. R. Adam, K. P. Dancey, A. J. Leong, L. F. Lindoy, B. J. McCool, M. McPartlin and P. A. Tasker, *J. Am. Chem. Soc.*, 1988, **110**, 8471.

452 K. R. Adam, S. P. H. Arshad, D. S. Baldwin, P. A. Duckworth, A. J. Leong, L. F. Lindoy, B. J. McCool, M. McPartlin, B. A. Tailor and P. A. Tasker, *Inorg. Chem.*, 1994, **33**, 1194.

453 R. Iwamoto and H. Wakano, *J. Am. Chem. Soc.*, 1976, **98**, 3764.

454 R. W. Turner, P. F. Rodesiler and E. L. Amma, *Inorg. Chim. Acta, Bioinorg. Chem.*, 1982, **66**, L13.

455 B. Viossat, P. Khodadad and N. Rodier, *Acta Crystallogr. Sect. B, Struct. Commun.*, 1982, **38**, 3075.

456 B. Viossat, P. Khodadad and N. Rodier, *Acta Crystallogr. Sect. C, Cryst. Struct. Commun.*, 1984, **40**, 24.

457 N. W. Alcock, E. H. Curzon and P. Moore, *J. Chem. Soc., Dalton Trans.*, 1984, 2813.

458 A. F. Cameron, D. W. Taylor and R. H. Nuttall, *J. Chem. Soc., Dalton Trans.*, 1972, 1608.

459 R. D. Hancock, M. S. Shaikjee, S. M. Dobson and J. C. A. Boeyens, *Inorg. Chim. Acta*, 1988, **154**, 229.

460 I. W. Nowell, *Acta Crystallogr. Sect. B, Struct. Commun.*, 1979, **35**, 1891.

461 B. Metz and R. Weiss, *Acta Crystallogr. Sect. B, Struct. Commun.*, 1973, **29**, 1088.

462 B. Metz and R. Weiss, *Inorg. Chem.*, 1974, **13**, 2094.

463 L. Shimoni, Livny, J. P. Glusker and C. W. Bock, *Inorg. Chem.*, 1998, **37**, 1853.

464 K. Wieghardt, M. Kleineboymann, B. Nuber, J. Weiss, L. Zsolnai and G. Huttner, *Inorg. Chem.*, 1986, **25**, 1647.

465 M. G. B. Drew and S. M. Nelson, *Acta Crystallogr. Sect. B, Struct. Commun.*, 1979, **35**, 1594.

466 N. W. Alcock, E. H. Curzon and P. Moore, *J. Chem. Soc., Dalton Trans.*, 1979, 1486.

467 T. Tsubomura, T. Sato, K. Yasaku, K. Sakai, K. Kobayashi and M. Morita, *Chem. Lett.*, 1992, 731.

468 H. Adams, N. A. Bailey, S. R. Collinson, D. E. Fenton, C. J. Harding and S. J. Kitchen, *Inorg. Chim. Acta*, 1996, **246**, 81, 88.

469 R. Bhavan, R. D. Hancock, P. W. Wade, J. C. A. Boeyens and S. M. Dobson, *Inorg. Chim. Acta*, 1990, **171**, 235.

470 D. Esteban, D. Banobre, R. Bastida, A. de Blas, A. Macias, A. Rodriguez, T. Rodriguez, Blas, D. E. Fenton, H. Adams and J. Mahia, *Inorg. Chem.*, 1999, **38**, 1937.

471 D. Esteban, D. Banobre, A. de Blas, T. Rodriguez, Blas, R. Bastida, A. Macias, A. Rodriguez, D. E. Fenton, H. Adams and J. Mahia, *Eur. J. Inorg. Chem.*, 2000, 1445.

472 A. Bencini, A. Bianchi, E. Garcia, Espana, M. Micheloni and J. A. Ramirez, *Coord. Chem. Rev.*, 1999, **188**, 97.

473 G. Golub, H. Cohen, P. Paoletti, A. Bencini and D. Meyerstein, *J. Chem. Soc., Dalton Trans.*, 1996, 2055.

474 E. Kimura, T. Koike, M. Kodama and D. Meyerstein, *Inorg. Chem.*, 1989, **28**, 2998.

475 A. Bencini, A. Bianchi, P. Dapporto, V. Fusi, E. Garciaespana, M. Micheloni, P. Paoletti, P. Paoli, A. Rodriguez and B. Valtancoli, *Inorg. Chem.*, 1993, **32**, 2753.

476 A. Bencini, A. Bianchi, C. Giorgi, P. Paoletti, B. Valtancoli, V. Fusi, E. GarciaEspana, J. M. Llinares and J. A. Ramirez, *Inorg. Chem.*, 1996, **35**, 1114.

477 L. H. Tan, M. R. Taylor, K. P. Wainwright and P. A. Duckworth, *J. Chem. Soc., Dalton Trans.*, 1993, 2921.

478 K. P. Wainwright, *J. Chem. Soc., Dalton Trans.*, 1983, 1149.

479 I. Murase, M. Mikuriya, H. Sonoda and S. Kida, *J. Chem. Soc.-Chem. Commun.*, 1984, 692.

480 I. Murase, M. Mikuriya, H. Sonoda, Y. Fukuda and S. Kida, *J. Chem. Soc., Dalton Trans.*, 1986, 953.

481 I. Murase, I. Ueda, N. Marubayashi, S. Kida, N. Matsumoto, M. Kudo, M. Toyohara, K. Hiate and M. Mikuriya, *J. Chem. Soc.,Dalton Trans.*, 1990, 2763.

482 A. Bianchi, L. Bologni, P. Dapporto, M. Micheloni and P. Paoletti, *Inorg. Chem.*, 1984, **23**, 1201.

483 G. Gran, *Analyst* (London), 1952, **77**, 661.

484 F. J. Rossotti and H. Rossotti, *J. Chem. Educ.*, 1965, **42**, 375.

485 P. Gans, A. Sabatini and A. Vacca, *Talanta*, 1996, **43**, 1739.

486 "*The crystal as a supramolecular entity*", G. R. Desiraju Ed., Wiley, Chichester (UK), 1995.

487 H. Gudbjartson, K. Biradha, K. M. Poirier and M. J. Zaworotko, *J. Am. Chem. Soc.*, 1999, **121**, 2599.

488 M. Fujita, M. Aoyagi, F. Ibukuro, K. Ogura and K. Yamaguchi, *J. Am. Chem. Soc.*, 1998, **120**, 611.

489 B. Olenyuk, J. A. Whiteford, A. Fechtenkotter and P. J. Stang, *Nature*, 1999, **398**, 796.

490 A. J. Blake, N. R. Champness, P. Hubberstey, W. S. Li, M. A. Withersby and M. Schröder, *Coord. Chem. Rev.*, 1999, **183**, 117.

491 T. L. Hennigar, D. C. MacQuarrie, P. Losier, R. D. Rogers and M. J. Zaworotko, *Angew. Chem., Int. Ed. Engl.*, 1997, **36**, 972.

492 W. T. A. Harrison and L. Hannooman, *Angew. Chem., Int. Ed. Engl.*, 1997, **36**, 640.

493 L. Carlucci, G. Ciani, D. M. Proserpio and A. Sironi, *J. Am. Chem. Soc.*, 1995, **117**, 4562.

494 B. F. Hoskins, R. Robson and D. A. Slizys, *J. Am. Chem. Soc.*, 1997, **119**, 2952.

495 A. J. Blake, N. R. Champness, S. S. M. Chung, W. S. Li and M. Schröder, *Chem. Commun.*, 1997, 1675.

496 A. J. Blake, N. R. Champness, S. S. M. Chung, W. S. Li and M. Schröder, *Chem. Commun.,* 1997, 1005.

497 H. J. Choi and M. P. Suh, *J. Am. Chem. Soc.,* 1998, **120**, 10622.

498 H. J. Choi and M. P. Suh, *Inorg. Chem.,* 1999, **38**, 6309.

499 H. J. Choi, T. S. Lee and M. P. Suh, *Angew. Chem., Int. Ed.,* 1999, **38**, 1405.

500 S. Ferlay, T. Mallah, J. Vaissermann, F. Bartolome, P. Veillet and M. Verdaguer, *Chem. Commun.,* 1996, 2481.

501 A. J. Blake, R. O. Gould, S. Parsons, C. Radek and M. Schröder, *Angew. Chem., Int. Ed. Engl.,* 1995, **34**, 2374.

502 A. J. Blake, F. A. Devillanova, R. O. Gould, W. S. Li, V. Lippolis, S. Parsons, C. Radek and M. Schröder, *Chem. Soc. Rev.,* 1998, **27**, 195.

503 A. J. Blake, J. P. Danks, V. Lippolis, S. Parsons and M. Schröder, *New J. Chem.,* 1998, **22**, 1301.

504 L. Carlucci, G. Ciani, D. M. Proserpio and A. Sironi, *Angew. Chem., Int. Ed. Engl.,* 1995, **34**, 1895.

505 A. V. Bordunov, P. C. Hellier, J. S. Bradshaw, N. K. Dalley, X. L. Kou, X. X. Zhang and R. M. Izatt, *J. Org. Chem.,* 1995, **60**, 6097.

506 H. Tsukube, K.Yamashita, T.Iwachido and M. Zenki, *Tetrahedron Lett.*, 1989, **30**, 3983.

507 X. H. Bu, D. L. An, Y. T. Chen, M. Shionoya and E. Kimura, *J. Chem. Soc., Dalton Trans.,* 1995, 2289.

508 X. H. Bu, Z. H. Zhang, D. L. An, Y. T. Chen, M. Shionoya and E. Kimura, *Inorg. Chim. Acta,* 1996, **249**, 125.

509 K. Y. Choi and I. H. Suh, *Inorg. Chim. Acta,* 2000, **299**, 128.

510 Z. X. Yang, J. S. Bradshaw, X. X. Zhang, P. B. Savage, K. E. Krakowiak, N. K. Dalley, N. Su, R. T. Bronson and R. M. Izatt, *J. Org. Chem.*, 1999, **64**, 3162.

511 N. Su, J. S. Bradshaw, X. X. Zhang, H. Song, P. B. Savage, G. P. Xue, K. E. Krakowiak and R. M. Izatt, *J. Org. Chem.,* 1999, **64**, 8855.

512 L. Prodi, F. Boletta, M. Montalti, N.Zaccheroni, P. B. Savage, J. S. Bradshaw and R. M. Izatt, *Tetrahedron Lett.*, 1998, **39**, 5451.

513 E. Kikuta, M. Murata, N. Katsube, T. Koike and E. Kimura, *J. Am. Chem. Soc.,* 1999, **121**, 5426.

514 B. Rieger, A. S. Abusurrah, R. Fawzi and M. Steiman, *J. Organomet. Chem.*, 1995, **497**, 73.